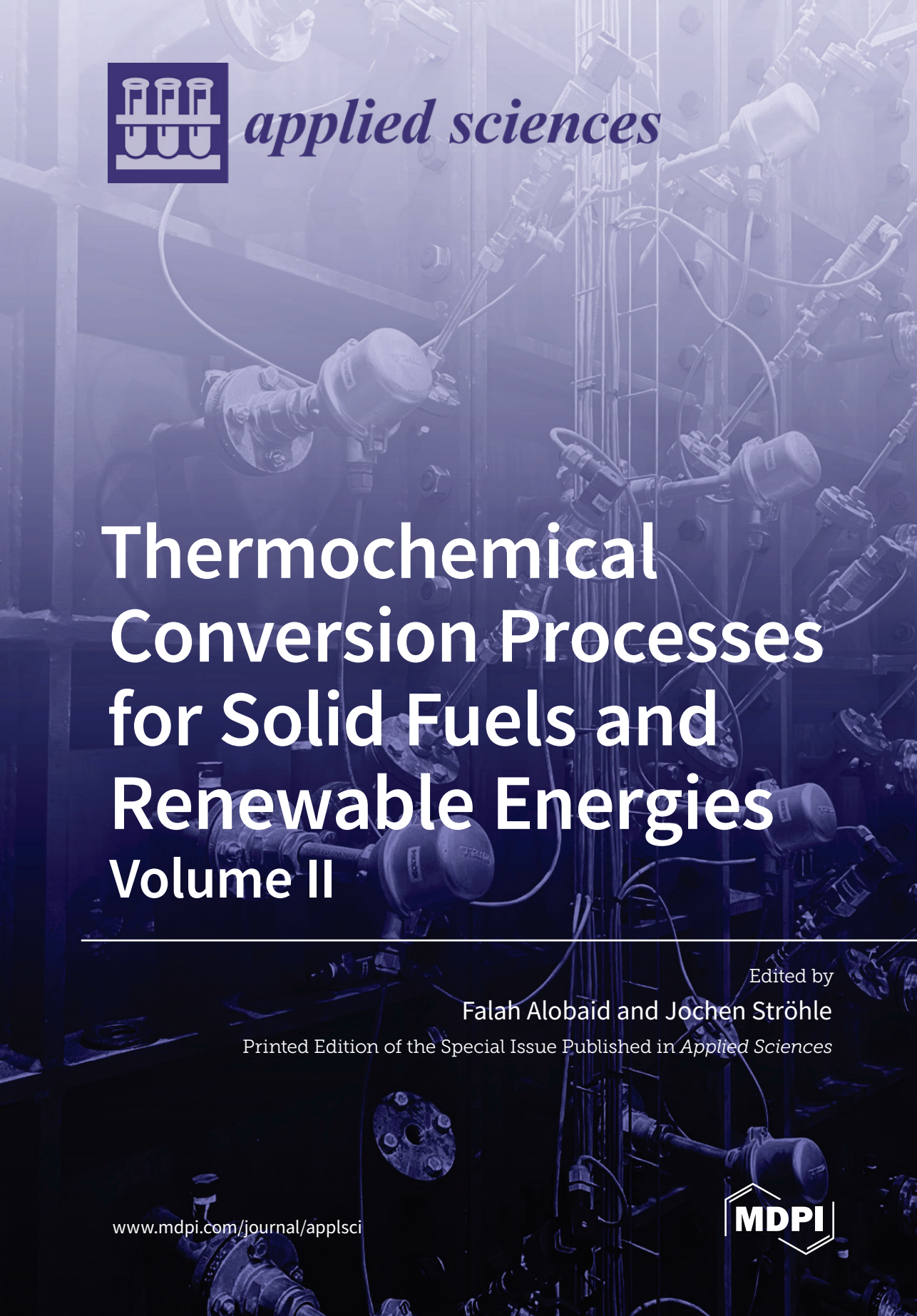

applied sciences

Thermochemical Conversion Processes for Solid Fuels and Renewable Energies

Volume II

Edited by

Falah Alobaid and Jochen Ströhle

Printed Edition of the Special Issue Published in *Applied Sciences*

www.mdpi.com/journal/applsci

MDPI

Thermochemical Conversion Processes for Solid Fuels and Renewable Energies: Volume II

Thermochemical Conversion Processes for Solid Fuels and Renewable Energies: Volume II

Editors

Falah Alobaid
Jochen Ströhle

MDPI • Basel • Beijing • Wuhan • Barcelona • Belgrade • Manchester • Tokyo • Cluj • Tianjin

Editors

Falah Alobaid
Institute for Energy Systems and Technology, Technische Universität Darmstadt, 64287 Darmstadt, Germany

Jochen Ströhle
Institute for Energy Systems and Technology, Technische Universität Darmstadt, 64287 Darmstadt, Germany

Editorial Office
MDPI
St. Alban-Anlage 66
4052 Basel, Switzerland

This is a reprint of articles from the Special Issue published online in the open access journal *Applied Sciences* (ISSN 2076-3417) (available at: https://www.mdpi.com/journal/applsci/special_issues/thermochemical_conversion_volume_II).

For citation purposes, cite each article independently as indicated on the article page online and as indicated below:

LastName, A.A.; LastName, B.B.; LastName, C.C. Article Title. *Journal Name* **Year**, *Volume Number*, Page Range.

ISBN 978-3-0365-5145-6 (Hbk)
ISBN 978-3-0365-5146-3 (PDF)

Cover image courtesy of Falah Alobaid.

Contents

About the Editors

Falah Alobaid

Priv.-Doz. Dr.-Ing. habil. Falah Alobaid received his Ph.D. degree with the highest distinction from the Technical University of Darmstadt, Germany, in 2013 for his work on the CFD-DEM model. His dissertation was awarded the energy special prize of the Technical University of Darmstadt in 2014. He has since served as the research group leader at the Institute for Energy Systems and Technology at the Technical University of Darmstadt. In 2018, he received his habilitation degree in energy systems (habilitation lecture: Energy Storage Technologies), which was then followed by receiving the academic title "Privatdozent" in 2019. He has vast experience and a notable track record for research in the field of numerical simulation of energy systems and the associated engineering processes using one-dimensional dynamic process simulation and three-dimensional computational fluid dynamics. He published more than 100 papers as first author and second author in renowned peer-reviewed journals as well as numerous conference contributions and many patents.

Jochen Ströhle

Dr.-Ing. Jochen Ströhe is the deputy director of the Institute for Institute of Energy Systems and Technology at Darmstadt University of Technology. He has extensive experience in the field of power plant engineering, especially in combustion/gasification processes for solid fuels and related CO_2 capture technologies, with key competencies in modelling and simulation of multiphase flows and power plant processes as well as in experimental investigations in pilot test plants.

applied sciences

MDPI

Editorial

Special Issue "Thermochemical Conversion Processes for Solid Fuels and Renewable Energies: Volume II"

Falah Alobaid *, Jochen Ströhle and Bernd Epple

Institute for Energy Systems and Technology, Technical University of Darmstadt, Otto-Berndt- Straße 2, 64287 Darmstadt, Germany; jochen.stroehle@est.tu-darmstadt.de (J.S.); bernd.epple@est.tu-darmstadt.de (B.E.)
* Correspondence: falah.alobaid@tu-darmstadt.de; Tel.: +49-(0)-6151-16-23004

1. Introduction

The increasing share of renewable energy sources draws attention to a critical challenge. The availability of wind turbines and photovoltaic solar cells is limited and difficult to predict. They usually provide a fluctuating feed-in to the grid, so energy reserves, e.g., conventional thermal power plants or energy storage systems, are necessary to establish a balance between electricity supply and demand. To maintain the security of supply and improve the flexibility of future power systems, various solutions can be adopted, such as improving the efficiency of technical processes in areas such as thermal power plants, as well as cement and metallurgy industries, the use of advanced thermochemical conversion technologies such as gasification, the expansion of high-voltage transmission infrastructure, the promotion of renewable energy sources, the use of large-scale energy storage systems, and the use of highly flexible power generation units with carbon capture and utilisation, such as combined-cycle power plants.

Given this background, and to support the development of thermochemical conversion processes for solid fuels and renewable energy, this Special Issue addresses the following topics, among others:

- Gasification and combustion of biomass, refuse-derived fuel, tire-derived fuel, solid recovered fuel, sewage sludge, and low-rank coal;
- Technological combinations of thermochemical conversion processes based on renewable sources (power-to-fuel);
- Carbon capture, storage, and utilisation (CCS/U) technologies (carbon-capture-to-fuel);
- Renewable energy for heating and cooling to reduce peak demand, with energy storage systems to mitigate grid imbalances;
- CFD and process simulations of thermochemical conversion processes for solid fuels and renewables.

The editors are pleased to present to the scientific community the best and latest advances in thermochemical conversion processes for solid fuels and renewable energy in this second volume of a compact, peer-reviewed Special Issue. This new Special Issue is a continuation of the previous Special Issue "Thermochemical Conversion Processes for Solid Fuels and Renewable Energies", which was closed in October 2020 including 10 valuable, peer-reviewed papers [1]. The second volume of the Special Issue contains fundamental scientific studies on the latest research progress in the development and optimisation of gasification processes, renewable energy source "solar energy", the synthesis of new hybrid nanocomposites and nanofluids, carbon capture, and energy storage systems. The submitted manuscripts were reviewed by recognised and expert reviewers. Manuscripts were accepted only if they made a clear contribution to technical and scientific knowledge and highlighted the most important recent developments and new findings in this field of research. Accordingly, 22 manuscripts were submitted, and 15 of them were accepted and published in this Special Issue (acceptance rate of 68%).

Citation: Alobaid, F.; Ströhle, J.; Epple, B. Special Issue "Thermochemical Conversion Processes for Solid Fuels and Renewable Energies: Volume II". *Appl. Sci.* **2022**, *12*, 7478. https://doi.org/10.3390/app12157478

Received: 20 July 2022
Accepted: 22 July 2022
Published: 26 July 2022

2. Special Issue Findings

A summary of the accepted manuscripts with their main contributions is presented below.

1. The first contribution included in this Special Issue was submitted by Schmid, M.; Hafner, S.; and Scheffknecht, G., from the University of Stuttgart, Institute of Combustion and Power Plant Technology, Germany [2]. In this work, sewage sludge gasification was investigated using a 20 kW bubbling fluidised bed test facility (see Figure 1). Steam and oxygen were used as gasification agents, and in situ generated sewage sludge ash was applied as bed material. The influence of the main operating parameters such as gasification temperature, oxygen ratio, steam to carbon ratio, and fluidisation velocity on the composition of the produced raw gas (CO, H_2, CO_2, H_2S, CH_4, C_xH_y, COS, NH_3, and tar) was determined. The authors found that the raw gas had high H_2 and CO concentrations of up to 0.37 m^3/m^3 and 0.18 m^3/m^3, respectively, making it suitable for the synthesis of fuels and chemicals. By adjusting the steam-to-carbon ratio (by the water gas shift reaction), the H_2/CO ratio of the syngas could be targeted for different synthesis products such as synthetic natural gas (H_2/CO = 3) or Fischer–Tropsch products (H_2/CO = 2). The analysis of the bed ash showed that the cadmium and mercury content was drastically reduced by the gasification process. Ash is appropriate as a secondary raw material to produce phosphorus or phosphate fertilisers.

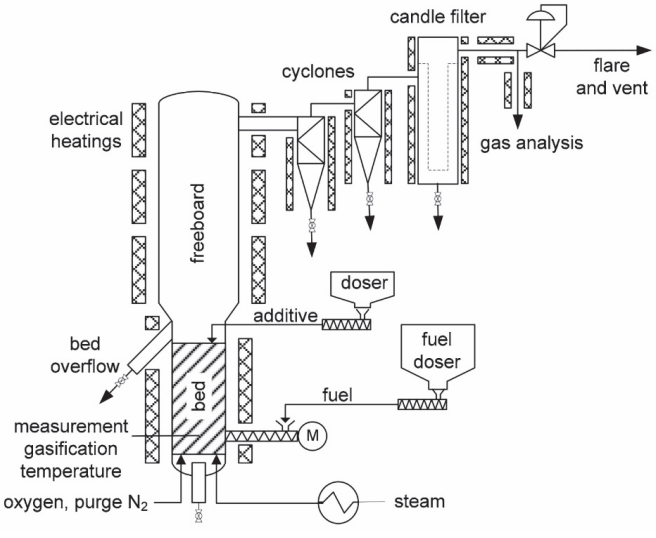

Figure 1. Schematic flow diagram of 20 kW fluidised bed gasification facility at the University of Stuttgart [2].

2. The second article, which was written by Kubonova, L.; Janakova L.; Malikova P.; Drabinova S.; Dej M.; Smelik R.; Skalny P.; and Heviankova S., from the VSB-Technical University of Ostrava, Czech Republic, dealt with the thermochemical utilisation of sewage sludge based on thermogravimetric analysis (TGA) [3]. Since sewage sludge is difficult to use as a feedstock due to its high moisture and ash content, its energy utilisation is increased by adding suitable waste materials (various types of plastics, used tires, and paper waste). Fifty-five waste mixtures were prepared in different volume ratios, a visual comparison was made, and high and low calorific values were measured. It was found that thermoplastics with sewage sludge and low-density polyethylene with sewage sludge had the lowest residual masses and the highest weight loss rates. Higher pyrolysis temperatures have always resulted in higher gas

volume yields, as observed in many previous studies, e.g., [4]. The authors claimed that the highest average mass yield was reached in the pyrolysis of plastics. The most suitable material and temperature combinations to produce pyrolysis oils and gases were the blends of thermoplastics with sewage sludge and low-density polyethylene with sewage sludge.

3. Solar absorption cooling systems are more advantageous than other cooling systems such as vapour compression because the peak cooling load nearly coincides with the available solar energy. The most common working fluid pairs are water/lithium bromide (H_2O-LiBr) (water as refrigerant and lithium bromide as a solvent, especially for air conditioning and process cooling) and ammonia/water (NH_3-H_2O) (ammonia as refrigerant and water as a solvent, especially for frozen food applications). The authors of the third article (Al-Falahi, A.; Alobaid, F.; and Epple, B., from the Technical University of Darmstadt, Germany) carried out a thermo-economic analysis to compare different configurations of solar absorption cooling systems used for thermal cooling processes [5]. While the first solar absorption cooling system used H_2O-LiBr as the working fluid pair, the second absorption cooling system adopted NH_3-H_2O. Parabolic trough collectors and evacuated tube collectors were applied under the same operating conditions as a source of thermal energy for both systems. The results showed that parabolic trough collectors combined with H_2O-LiBr provided lower design aspects and minimum rates of hourly costs (5.2 USD/h), followed by evacuated tube collectors with H_2O-LiBr (5.6 USD/h). Furthermore, it was found that H_2O-LiBr provided a lower thermo-economic product cost (0.14 USD/GJ) compared with NH_3-H_2O (0.16 USD/GJ). The thermal ratio (absorption refrigeration cycle coefficient of performance) was between 0.5 and 0.9.
4. The authors of the fourth article (Nguyen, N.M.; Alobaid F.; and Epple, B., from the Technical University of Darmstadt, Germany, and Can Tho University, Vietnam) developed an Aspen plus model for steam gasification of biomass to investigate the influence of operating parameters on the gasification process under steady-state conditions [6]. To consider the hydrodynamic, reaction kinetic decomposition of biomass and pyrolysis yield distribution, external FORTRAN codes were written and implemented in the developed model. The numerical results were compared with the measurement obtained from a 5 kW_{th} bubbling fluidised bed test rig, showing good agreement. A slight discrepancy between the simulation model and the measured data was observed, which is due to the limitations of the model, i.e., simplified calculations of the hydrodynamics and kinetics of the bed and the absence of tar decomposition reactions. The authors claimed that the gasification process is favoured at higher temperatures. Under such conditions, hydrogen production and carbon conversion efficiency increased, while the percentage of carbon monoxide and methane in the product gas decreased. Increasing the amount of steam in the reactor promoted biomass gasification performance. The ratio of steam to biomass increased the content and yield of hydrogen in the product gas and significantly improved the gas yield and carbon conversion efficiency.
5. The fifth contribution included in this Special Issue is by Lucantonio, S.; Di Giuliano, A.; and Gallucci, K., from the University of L'Aquila, Italy [7]. This study investigated the chemical looping gasification of wheat straw pellets as part of the European research project entitled Chemical Looping Gasification for Sustainable Production of Biofuels (CLARA; G.A. 817841 [8]). The focus was on wheat straw pellet pre-treatment, i.e., torrefaction and torrefaction-washing. After pre-treatment, the devolatilisation of individual pellets was carried out in a laboratory-scale fluidised bed of sand at 700, 800, and 900 °C to both quantify and analyse the product gas released from differently pre-treated types of biomass. The experimental data were evaluated using integral average parameters such as gas yield (H_2/CO mole ratio) and carbon conversion. For all biomasses, increasing the devolatilisation temperature between 700 and 900 °C improved the thermochemical conversion in terms of gas yield, carbon

conversion, and H_2/CO mole ratio in the product gas. As for the pre-treatments, the main evidence was observed in the overall improvement in product gas quality (i.e., composition) and quantity compared with the untreated pellets. Negligible differences were observed between the different pre-treatments, mainly owing to the peak quantities that showed an improvement in the H_2/CO mole ratio in correlation with the increase in torrefaction temperature from 250 to 270 °C.

6. The authors of the sixth article published by Al-Maliki, A. K. W.; Mahmoud S. N.; Al-Khafaji, M. H. H.; Alobaid, F.; and Epple, B., from the Technical University of Darmstadt, Germany, and the University of Technology, Iraq, developed a dynamic process simulation model to improve the efficiency of parabolic trough power plants and their associated control structures [9]. The model was created using advanced process simulation software (APROS) [10] and validated against an existing Andasol II solar power plant in Spain. The study focused on control circuits used in the thermal storage system of a parabolic trough power plant during the charging/discharging cycle. In the charging phase, the heat transfer fluid (Therminol VP-1) from the solar field at a temperature of 393 °C heated the molten salt (sodium and potassium nitrates), which was pumped from a cold tank into a hot tank and stored in a temperature of about 386 °C. The charging phase continued until the maximum capacity of stored thermal energy of about 1025 MW_{th} h was reached. During the discharge phase, the hot molten salt heated the heat transfer fluid (Therminol VP-1), to be used in the power block via the heat exchangers. The molten salt left the heat exchangers and entered the cold tank at a temperature of approximately 292 °C. Accordingly, the thermal storage system provides the thermal power at the nominal load (125.75 MW_{th}) for about 7.5 h in the evening time. The authors stated that the main results of this study should help researchers and designers understand the advanced control structures used in parabolic trough power plants. For more studies on the dynamic simulation of solar power plants, see this review paper [11].
7. The seventh article in this Special Issue addressed an important topic currently under research as an effective technology for the gasification of solid fuels such as biomass and refuse-derived fuels to produce valuable products, e.g., methanal or Fischer–Tropsch synthesis (see Figure 2). Here, recent developments related to the biomass-based chemical looping gasification process were reported by the authors (Nguyen, N. M.; Alobaid F.; Dieringer, P.; and Epple, B., from the Technical University of Darmstadt, Germany, and Can Tho University, Vietnam) [12]. The influence of process parameters such as gasification temperature, steam-to-biomass ratio, oxygen-carrier-to-biomass ratio, and biomass characteristics on the performance of the chemical looping gasification process was discussed. Furthermore, improvements in syngas purification technologies were shown to reduce problems associated with breakdowns and plugging, as well as efficiency losses. The latest experimental and simulation/modelling studies and their basic assumptions were described in detail. The authors pointed out that the proof of concept has been carried out for a pilot scale system from a few kW up to one MW. This is the basis for the scaling up of the process, which is required for commercial power plant and syngas production together with CO_2 capture. Finally, the review paper emphasised current research topics, highlighted research gaps, and identified opportunities for future applications of the biomass-based chemical looping gasification process.
8. The authors of the eighth article (Al-Maliki, A.K.W.; Al-Hasnawi, G.T.A.; Abdul Wahhab, A.H.; Alobaid, F.; and Epple, B., from the Technical University of Darmstadt, Germany, and the University of Technology, Iraq) presented a detailed dynamic model of an existing parabolic trough solar power plant using the advanced process simulation software (APROS) [13]. The authors claimed that the developed model is the first in the literature that analyses the dynamic interaction of all parts of a parabolic trough solar power plant, including the solar field, thermal storage system, and power block (see Figure 3), and described the heat transfer fluid and steam-water

paths in detail. Furthermore, all control circuits such as drum level and steam bypass controllers were included in the developed model. The model was first validated using measured data from an existing Andasol II solar power plant in Spain. In the next step, the validated model was applied to determine the best operating strategy based on direct normal irradiance variations during the day. The operating strategy used in this model was effective compared with the decisions made by operators during cloudy conditions, as it improved the performance of the power plant and increased the operating hours.

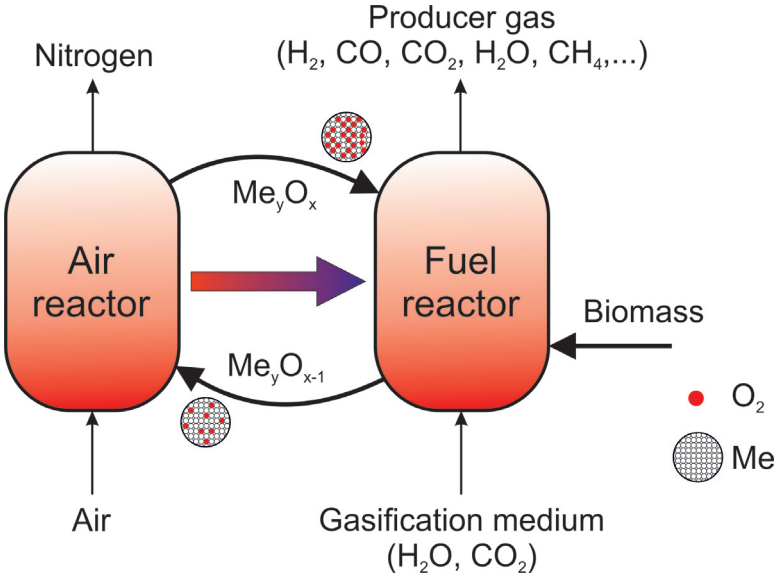

Figure 2. Schematic flow diagram of the chemical looping gasification process.

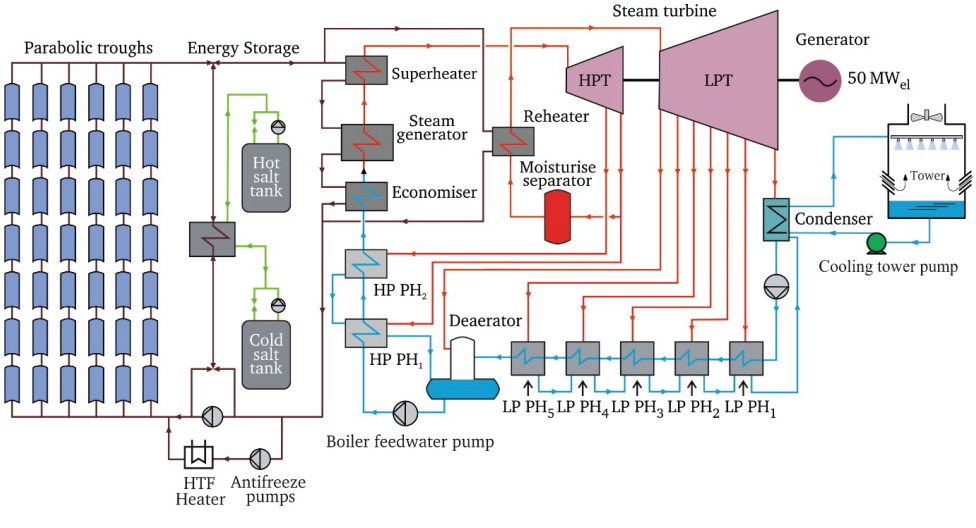

Figure 3. Schematic flow diagram of parabolic trough solar power plant [13].

9. The authors of the ninth article, Almoslh, A.; Alobaid, F.; Heinze, C.; and Epple, B., from the Technical University of Darmstadt, Germany, built and operated an absorber test rig for CO_2 capture [14]. The study aimed to assess the effect of gas flow rate on the hydrodynamic characteristics of the sieve tray including wet tray pressure drop, total tray pressure drops, dry tray pressure drops, liquid holdup, clear liquid height, and froth height. It was found that the inlet gas flow rate has a considerable influence on the hydrodynamic characteristics of the sieve tray. While increasing the inlet gas flow rate up to a certain value improved the liquid retention capacity, raising the inlet gas flow rate above this value did not increase the liquid holdup. There was a relationship between absorber performance and the liquid holdup on the sieve tray. The performance of the CO_2 absorber increased due to the rise in liquid holdup caused by the increase in inlet flow rate. The interface between the gaseous and liquid phases varied with a change in gas flow rate. The increase in froth height is a parameter that provides information about how large the interface is between the gaseous and liquid phases. Finally, the authors found that the hydrodynamic properties of the shell are crucial for the choice of optimal absorber operating conditions.
10. The main contribution of the tenth article is related to molten salt energy storage systems. The authors (Al-Maliki, A.K.W.; Alobaid, F.; Keil, A.; and Epple, B., from the Technical University of Darmstadt, Germany, and the University of Technology, Iraq) created a numerical model of a molten salt energy storage system used in existing Andasol II solar power plant in Spain [15]. The storage model was validated by comparing the results with measured data from the real power plant. A system analysis and system optimisation were then performed, and the stand-alone concept of the thermal storage system was introduced. Stand-alone means an isolated deployment of the storage system without a solar power plant. At lower peak power demands, the storage medium was heated with surplus electrical energy and later fed back into the electrical grid via a steam cycle at higher peak power demands (see Figure 4). The system was then further optimised by modelling four different types of storage medium (Andasol 2 (base), SSalt max, Hitec, and carbonate salt) with different temperature differences in the cold and hot tanks. From the comparison, the most preferred storage medium was found to be carbonate salt, as it increased both the efficiency and the capacity. The largest increase in efficiency in terms of electricity generation could also be achieved with carbonate salt (18.2%), while the increase for SSalt max and Hitec was 9.5% and 7.4%, respectively.

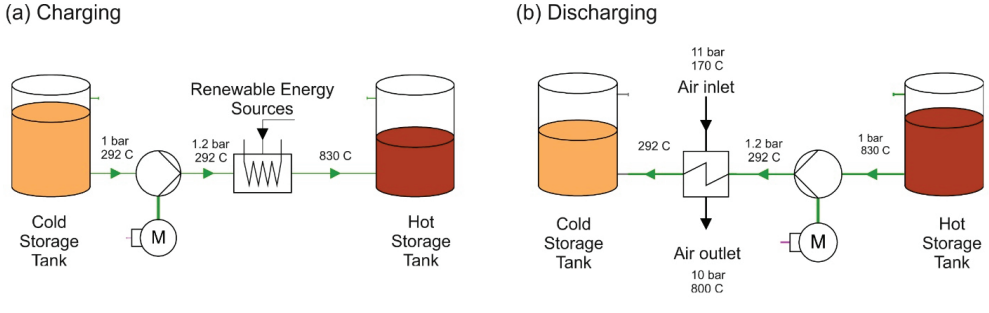

Figure 4. Schematic flow diagram of stand-alone molten salt energy storage system: (**a**) during charge mode and (**b**) discharge mode [15].

11. In the eleventh article of this Special Issue, the authors Judran, K. H.; Al-Hasnawi, G. T. A.; Al Zubaid, N. F.; Al-Maliki, A. K. W.; Alobaid, F.; and Epple, B., from the Technical University of Darmstadt, Germany, and the University of Technology, Iraq, prepared a new nanofluid that has the potential to be used in various applications such as working fluids in cooling systems [16]. A novel, two-step technique (co-precipitation

method) was used to prepare an efficient magnesium oxide–deionised water (MgO-DW) nanofluid without using surfactants and/or organic base fluids. Then, the influence of the volume concentration of the nanopowder and the duration of the ultrasonic treatment on the stability and thermophysical properties of the MgO-DW nanofluid at room temperature was investigated. Based on the experimental assessment, the co-precipitation method was successfully applied to prepare crystalline and pure MgO nanopowder, with an average particle size of 33 nm. Scanning electron microscopy (SEM) images demonstrated unique feathery or fluffy-like nanostructures of the MgO nanopowder that was prepared with volume concentrations ranging from 0.05% to 0.25% and ultrasonic treatment times ranging from 45 to 180 min at ambient temperature. The introduction of MgO nanoparticles to conventional liquid such as deionised water improved the thermal conductivity, with the highest value of thermal conductivity improvement of 25.08% observed at a volume concentration of 0.25% and ultrasonic treatment time of 180 min. The impact of ultrasonic treatment duration on the improvement of thermal conductivity was relatively like the impact of nanoparticle volume concentration. However, this conductivity improvement was limited after an ultrasonication duration of 135 min. The measurements of dynamic viscosity showed that it was directly proportional to the volume concentration of MgO-DW nanofluid until the highest value of 0.0052 [Pa s] was reached at a higher volume solid content of 0.25% of MgO-DW nanofluid. By contrast, increasing the ultrasonic treatment time resulted in a sharp decrease in the dynamic viscosity of the nanofluid samples. It was found that a MgO-DW nanofluid with good dispersion stability, high thermal conductivity, and low viscosity could be generated by controlling the ultrasonic time and/or volume concentration.

12. The authors of the twelfth article in this Special Issue (Aghel, B.; Janati, S.; Alobaid, F.; Almoslh, A.; and Epple, B., from the Technical University of Darmstadt, Germany, and Kermanshah University of Technology, Iran) provided a review article on the possible application of nanofluids in CO_2 absorption [17]. Fossil fuel conversion (e.g., combustion or gasification) and industrial processes are now the main sources of CO_2 emissions, along with forestry and land use, including livestock. Reducing greenhouse gas emissions is, therefore, essential to mitigate climate change and its devastating environmental consequences. Carbon capture and storage (CCS) or carbon dioxide utilisation (CCU) technologies are one of the most environmentally friendly options for reducing anthropogenic greenhouse gas emissions. However, these technologies are currently associated with significant efficiency losses, resulting in higher CO_2 avoidance costs. Owing to the advent of nanotechnology and its unique advantages in various fields, a new approach was introduced using suspended particles in a base fluid (suspension) to achieve maximum absorption efficiency and minimum energy consumption through CO_2 capture. In this review article, the performance of nanofluids, preparation methods, and their stability, which is one of the most important factors to prevent sedimentation of nanofluids, were discussed. The objective of this article was to present the factors contributing to CO_2 absorption by nanofluids in an easy-to-understand manner, focusing on the role of base fluids and the reasons for their selection. Based on research in the literature, the authors claimed that nanofluids are an effective way to increase CO_2 absorption compared with the base fluid, which can reduce host plant energy consumption.
13. The thirteenth article in this Special Issue focused on evaluating the thermal performance of a tubular heat exchanger equipped with combined basket-twisted tape inserts. Here, the authors, Khafaji, Q.A.H.; Wahhab, A.A.H.; Alsaedi, S.S; Maliki, A.K.W.; Alobaid, F.; and Epple, B., from the Technical University of Darmstadt, Germany, and the University of Technology, Iraq, experimentally investigated the properties of tubular heat exchangers [18]. For this purpose, a test rig was built, equipped with novel inserts, and finally operated under different conditions. Air was used as the working medium, and a constant wall heat flux was provided for turbu-

lent discharge conditions ($6000 \leq Re \leq 19{,}500$). Two inserts were used to improve heat transfer: First, bascule turbulators were inserted into the heat exchanger with a constant pitch ratio (PR = 150 mm), and second, basket turbulators together with a twisted tape were installed in the core of the basket turbulators. The results showed that the Nusselt numbers were 131.8%, 169.5%, 187.7%, and 206.5% higher than those of a plain heat exchanger for basket turbulators and the combined basket-twisted tape inserts with y/w = 6, 3, and 2, respectively. On average, the maximum thermal efficiency of the elevated tubular heat exchanger was 1.63 times higher than that of the simple heat exchanger, which is due to a binary basket-shaped band for a twist ratio y/w equal to 2 at constant pump power. Finally, practical correlations for the Nusselt number and friction characteristics were developed and presented.

14. The fourteenth article in this Special Issue dealt with the microstructural analysis and mechanical characteristics of hybrid nanocomposites of aluminium (Al), ferric oxide (Fe_2O_3), and silver (Ag). The aluminium alloys can be used in many fields such as electronics, aerospace, and automotive due to their properties such as lightness, strength, wear, and corrosion resistance. The authors (Salman, D.K.; Maliki, A.K.W.; Alobaid, F.; and Epple, B., from the Technical University of Darmstadt, Germany, and the University of Technology, Iraq) aimed to specify the microstructure and investigate the mechanical properties of Al alloys, into which different amounts of Fe_2O_3 (3, 6, 9, 12, and 15 wt.%) were introduced with a constant Ag content of 1 wt.% [19]. The Al/Fe_2O_3 + Ag hybrid nanocomposite samples were synthesised via powder metallurgy, and the microstructure was visualised via field-emission scanning electron microscopy (FESEM) and X-ray diffraction (XRD) investigations. Furthermore, mechanical experiments, such as microhardness tests, compression tests, and wear tests, were performed to estimate the mechanical properties of the hybrid nanocomposites. The FESEM and XRD results showed that the Fe_2O_3 and Ag nanoparticles were uniformly distributed and dispersed in the Al matrix. Compared with pure Al, the mechanical test values increased with increasing weight percentages of the reinforcing nanoparticles up to 12 wt.% Fe_2O_3. Here, the microhardness was 34.19 HV, the compressive strength was 89.9 MPa, and the wear rate was about 1.8×10^{-8} g/cm for Al + 12 wt.% Fe_2O_3 + 1 wt.% Ag. The authors claimed that the results of this work demonstrated an improvement in the mechanical properties of aluminium alloys.
15. The last article of this Special Issue was published by Salman, D.K.; Maliki, A.K.W.; Alobaid, F.; and Epple, B., from the Technical University of Darmstadt, Germany, and the University of Technology, Iraq [20]. Here, the authors synthesised a nickel–titanium—silver (Ni-Ti-Ag) shape memory alloy by casting to investigate its microstructure and mechanical properties. Ag (grain size 1 mm) was integrated into Ni-Ti alloys with different weight percentages (0, 1.5, 3, and 4.5 wt.% Ag) to prepare shape memory alloys using a vacuum arc remelting (VAR) furnace. The microstructural analysis was performed using field-emission scanning electron microscopy (FESEM) and X-ray diffraction (XRD), whereas the transformation temperatures of the Ni-Ti-Ag shape memory alloy were obtained via a differential scanning calorimetry (DSC) investigation. The results showed that Ag was homogeneously distributed in the Ni-Ti alloy. In addition, two primary phases (martensite phase and austenite phase) were formed with few impurities. The XRD investigation indicated that the number of Ag peaks showed an increase with the enhancement in Ag weight fraction. The DSC investigation revealed that the austenite transformation temperature began at -1.6 °C, and the transformation temperatures increased with increasing Ag content to 19.7 °C, 12.7 °C, and 12.3 °C, respectively. Increasing Ag content significantly affected the mechanical properties of the Ni-Ti base alloy in terms of its compressive strength and microhardness. The highest value of compressive strength was reached for the alloy with 3 wt.% Ag, whereas the microhardness tests showed a minor decrease with the increase in Ag weight fraction.

3. Conclusions

In this second volume of a compact, peer-reviewed Special Issue, the editors are proud to present the recent advances in thermochemical conversion processes for solid fuels and renewable energy to the scientific community. A total of 22 manuscripts were submitted, of which 15 manuscripts (2 reviews and 13 regular articles) were accepted and published in this Special Issue, representing an acceptance rate of 68%. One-third of the studies published (five articles) addressed the gasification of low-value solid fuels (e.g., biomass) treated with a single fluidised bed gasifier at the early stages of their development and, of late, with double fluidised bed gasification systems such as chemical loop gasification. The most common renewable energy source "solar energy" had a considerable share in this Special Issue, with three articles. Two publications dealt with parabolic trough solar power plants and the associated control structure for power generation, while one article addressed solar absorption cooling systems using water/lithium bromide and ammonia/water as the working fluid pair. Three other articles focused on the synthesis of new hybrid nanocomposites and nanofluids that have the potential to be used in various applications such as working fluids in heating and cooling systems, as well as in electronics, aerospace, and automotive applications. Carbon capture was covered in two articles in this Special Issue, but unfortunately, CO_2 utilisation technologies (carbon-capture-to-fuel) were not mentioned. One published article reported the evaluation of the thermal performance of a tubular heat exchanger equipped with combined basket-twisted tape inserts, which is crucial for increasing the heat exchanger efficiency. Another article was published dealing with energy storage systems for mitigating grid imbalances. Here, a new stand-alone molten-salt energy storage system was presented and dynamically simulated.

We believe that the new findings on thermochemical conversion technologies amassed in this Special Issue will be of great benefit to the readers of *Applied Sciences*. All contributions have been published online, free of charge, and without restrictions on access.

Author Contributions: F.A. was responsible for writing, reviewing, and editing this Editorial. J.S. and B.E. have read and agreed to the published version of the manuscript. All authors have read and agreed to the published version of the manuscript.

Funding: This research received no external funding.

Acknowledgments: The editors would like to thank the Associate Editors and their teams, for the provision of excellent technical support and organisational guidance for this Special Issue. In addition, a great thank you goes to all the reviewers for reviewing the above-mentioned manuscripts. Their professional evaluations greatly contributed to improving the quality of the submissions for this Special Issue. The editors also gratefully acknowledge the support of the German Research Foundation (DFG) and the Open Access Publishing Fund of the Technical University of Darmstadt.

Conflicts of Interest: The author declares no conflict of interest.

References

1. Alobaid, F.; Ströhle, J. Special issue "thermochemical conversion processes for solid fuels and renewable energies". *Appl. Sci.* **2021**, *11*, 1907. [CrossRef]
2. Schmid, M.; Hafner, S.; Scheffknecht, G. Experimental parameter study on synthesis gas production by steam-oxygen fluidized bed gasification of sewage sludge. *Appl. Sci.* **2021**, *11*, 579. [CrossRef]
3. Kubonova, L.; Janakova, I.; Malikova, P.; Drabinova, S.; Dej, M.; Smelik, R.; Skalny, P.; Heviankova, S. Evaluation of waste blends with sewage sludge as a potential material input for pyrolysis. *Appl. Sci.* **2021**, *11*, 1610. [CrossRef]
4. Zhou, H.; Wu, C.; Onwudili, J.A.; Meng, A.; Zhang, Y.; Williams, P.T. Influence of process conditions on the formation of 2–4 ring polycyclic aromatic hydrocarbons from the pyrolysis of polyvinyl chloride. *Fuel Process. Technol.* **2016**, *144*, 299–304. [CrossRef]
5. Al-Falahi, A.; Alobaid, F.; Epple, B. Thermo-Economic Comparisons of Environmentally Friendly Solar Assisted Absorption Air Conditioning Systems. *Appl. Sci.* **2021**, *11*, 2442. [CrossRef]
6. Nguyen, N.M.; Alobaid, F.; Epple, B. Process simulation of steam gasification of torrefied woodchips in a bubbling fluidized bed reactor using aspen plus. *Appl. Sci.* **2021**, *11*, 2877. [CrossRef]
7. Lucantonio, S.; Di Giuliano, A.; Gallucci, K. Influences of the Pretreatments of Residual Biomass on Gasification Processes: Experimental Devolatilizations Study in a Fluidized Bed. *Appl. Sci.* **2021**, *11*, 5722. [CrossRef]

8. Dieringer, P.; Marx, F.; Alobaid, F.; Ströhle, J.; Epple, B. Process Control Strategies in Chemical Looping Gasification—A Novel Process for the Production of Biofuels Allowing for Net Negative CO_2 Emissions. *Appl. Sci.* **2020**, *10*, 4271. [CrossRef]
9. Al-Maliki, W.A.K.; Mahmoud, N.S.; Al-Khafaji, H.M.; Alobaid, F.; Epple, B. Design and Implementation of the Solar Field and Thermal Storage System Controllers for a Parabolic Trough Solar Power Plant. *Appl. Sci.* **2021**, *11*, 6155. [CrossRef]
10. Al-Maliki, W.A.K.; Hadi, A.S.; Al-Khafaji, H.M.; Alobaid, F.; Epple, B. Dynamic Modelling and Advanced Process Control of Power Block for a Parabolic Trough Solar Power Plant. *Energies* **2021**, *15*, 129. [CrossRef]
11. Alobaid, F.; Mertens, N.; Starkloff, R.; Lanz, T.; Heinze, C.; Epple, B. Progress in dynamic simulation of thermal power plants. *Prog. Energy Combust. Sci.* **2017**, *59*, 79–162. [CrossRef]
12. Nguyen, N.M.; Alobaid, F.; Dieringer, P.; Epple, B. Biomass-based chemical looping gasification: Overview and recent developments. *Appl. Sci.* **2021**, *11*, 7069. [CrossRef]
13. Al-Maliki, W.A.K.; Al-Hasnawi, A.G.T.; Abdul Wahhab, H.A.; Alobaid, F.; Epple, B. A Comparison Study on the Improved Operation Strategy for a Parabolic trough Solar Power Plant in Spain. *Appl. Sci.* **2021**, *11*, 9576. [CrossRef]
14. Almoslh, A.; Alobaid, F.; Heinze, C.; Epple, B. Experimental Study of the Influence of Gas Flow Rate on Hydrodynamic Characteristics of Sieve Trays and Their Effect on CO_2 Absorption. *Appl. Sci.* **2021**, *11*, 10708. [CrossRef]
15. Al-Maliki, W.A.K.; Alobaid, F.; Keil, A.; Epple, B. Dynamic Process Simulation of a Molten-Salt Energy Storage System. *Appl. Sci.* **2021**, *11*, 11308. [CrossRef]
16. Judran, H.K.; Al-Hasnawi, A.G.T.; Al Zubaidi, F.N.; Al-Maliki, W.A.K.; Alobaid, F.; Epple, B. A High Thermal Conductivity of MgO-H2O Nanofluid Prepared by Two-Step Technique. *Appl. Sci.* **2022**, *12*, 2655. [CrossRef]
17. Aghel, B.; Janati, S.; Alobaid, F.; Almoslh, A.; Epple, B. Application of Nanofluids in CO_2 Absorption: A Review. *Appl. Sci.* **2022**, *12*, 3200. [CrossRef]
18. Khafaji, H.Q.; Abdul Wahhab, H.A.; Alsaedi, S.S.; Al-Maliki, W.A.K.; Alobaid, F.; Epple, B. Thermal Performance Evaluation of a Tubular Heat Exchanger Fitted with Combined Basket–Twisted Tape Inserts. *Appl. Sci.* **2022**, *12*, 4807. [CrossRef]
19. Salman, K.D.; Al-Maliki, W.A.K.; Alobaid, F.; Epple, B. Microstructural Analysis and Mechanical Properties of a Hybrid Al/Fe_2O_3/Ag Nano-Composite. *Appl. Sci.* **2022**, *12*, 4730. [CrossRef]
20. Salman, K.D.; Al-Maliki, W.A.K.; Alobaid, F.; Epple, B. Microstructural Analysis and Mechanical Characterization of Shape Memory Alloy Ni-Ti-Ag Synthesized by Casting Route. *Appl. Sci.* **2022**, *12*, 4639. [CrossRef]

applied sciences

MDPI

Article

Experimental Parameter Study on Synthesis Gas Production by Steam-Oxygen Fluidized Bed Gasification of Sewage Sludge

Max Schmid *, Selina Hafner and Günter Scheffknecht

Institute of Combustion and Power Plant Technology, University of Stuttgart, Pfaffenwaldring 23, D-70569 Stuttgart, Germany; Selina.Hafner@ifk.uni-stuttgart.de (S.H.); Guenter.Scheffknecht@ifk.uni-stuttgart.de (G.S.)
* Correspondence: deu@ifk.uni-stuttgart.de

Featured Application: The experimental data can be applied for designing or modeling of fluidized bed sewage sludge gasifiers for synthesis gas production.

Abstract: The conversion of biogenic residues to fuels and chemicals via gasification and synthesis processes is a promising pathway to replace fossil carbon. In this study, the focus is set on sewage sludge gasification for syngas production. Experiments were carried out in a 20 kW fuel input bubbling fluidized bed facility with steam and oxygen as gasification agent. In-situ produced sewage sludge ash was used as bed material. The sensitivity of the key operation parameters gasifier temperature, oxygen ratio, steam to carbon ratio, and the space velocity on the syngas composition (H_2, CO, CO_2, CH_4, C_xH_y, H_2S, COS, NH_3, and tars) was determined. The results show that the produced syngas has high H_2 and CO concentrations of up to 0.37 $m^3\ m^{-3}$ and 0.18 $m^3\ m^{-3}$, respectively, and is thus suitable for synthesis of fuels and chemicals. By adjusting the steam to carbon ratio, the syngas' H_2 to CO ratio can be purposely tailored by the water gas shift reaction for various synthesis products, e.g., synthetic natural gas (H_2/CO = 3) or Fischer–Tropsch products (H_2/CO = 2). Also, the composition and yields of fly ash and bed ash are presented. Through the gasification process, the cadmium and mercury contents of the bed ash were drastically reduced. The ash is suitable as secondary raw material for phosphorous or phosphate fertilizer production. Overall, a broad database was generated that can be used for process simulation and process design.

Keywords: gasification; sewage sludge; syngas; sulfur; tar; ammonia; biofuel; synthesis stoichiometry; operation parameters; nutrient recovery; circular economy

Citation: Schmid, M.; Hafner, S.; Scheffknecht, G. Experimental Parameter Study on Synthesis Gas Production by Steam-Oxygen Fluidized Bed Gasification of Sewage Sludge. *Appl. Sci.* **2021**, *11*, 579. https://doi.org/10.3390/app11020579

Received: 1 December 2020
Accepted: 28 December 2020
Published: 8 January 2021

1. Introduction

The mitigation of climate change requires the substitution of fossil carbon in carbonaceous fuels and goods by renewable carbon sources. Renewable carbon sources are, for instance, biomasses, such as wood or energy crops. However, the current available biomass feedstock cannot satisfy the massive amount of fossil carbon that is currently utilized worldwide. Therefore, also the utilization of carbon from available biogenic residues and waste streams has to be considered in order to replace as much fossil carbon as possible. Sewage sludge is a not avoidable residue with a quantity of over 10×10^9 kg a^{-1} on dry basis in Europe [1], over 12×10^9 kg a^{-1} in the USA [2] (1999 only 7×10^9 kg a^{-1} [3]), and over 6×10^9 kg a^{-1} in China with a steep increase [4]. Besides the utilization of the energy and carbon contents of sewage sludge, the recovery of phosphorous (e.g., from sewage sludge ash) to close the nutrient cycle and the safe recycling or disposal of hazardous components such as heavy metals are also of great importance [5]. Therefore, a change from the currently mostly practiced sewage sludge disposal methods, e.g., land-"use", landfill, and co-incineration in coal-fired power plants or cement plants, to mono-treatment recycling methods is required in order to fulfill the goals of a circular economy and climate change mitigation. For instance in Germany, the need of phosphorous recovery has already

been put into regulation [6]. The utilization of sewage sludge as fuel is also economically favorable as high disposal fees are attainable.

A conversion process is needed to practically replace fossil carbon with renewable carbon in established products such as transport fuels, chemicals or plastics. A promising and very flexible conversion process considering feedstock quality and product choice is the thermochemical gasification that generates a high calorific syngas which can be further converted to the desired product in a downstream catalytic synthesis [7]. Such a gasification process is the steam-oxygen fluidized bed gasification, that produces a nitrogen-lean and thus high calorific syngas, that is rich in hydrogen and carbon monoxide, and thus can be used for synthesis of fuels (e.g., synthetic natural gas, dimethyl ether, kerosene) and chemicals (methanol, plastic monomers) [8]. Also, the recovery of phosphorous can be achieved well from gasification-derived sewage sludge ash [9–11].

As gasification agent, a mixture of steam and oxygen is used to provide the necessary heat for the endothermic gasification process through partial fuel oxidation. Therefore only a single fluidized bed reactor is needed, which simplifies the process layout in contrast to the allothermal indirect dual fluidized bed (DFB) steam gasification [12,13]. The needed oxygen can be generated by an on-site power-to-gas facility that produces oxygen as by-product from water electrolysis, by a state of the art cryogenic air separation unit (ASU) with acceptable energy consumption of 720 kJ per kg O_2 [14,15] or tentatively in future by air separation with membranes. The sewage sludge has to be dried in order to be utilized in fluidized bed gasification. To minimize the energy consumption for drying, a combination of mechanical dewatering (e.g., centrifuge) to a dry matter fraction of around 0.25 kg kg^{-1}, solar drying, and thermal drying using low temperature heat will finally obtain a dry matter fraction of around 0.9 kg kg^{-1} that can be used for fluidized bed gasification [16].

In the steam-oxygen gasification, the gasifier is operated at temperatures of about 850 °C which enables the thermochemical decomposition of fuel into permanent gases, tars, char and ash. The so produced char and tars are then gasified or reformed by reaction with oxygen and steam. The raw syngas is comprised of H_2O, H_2, CO, CO_2, CH_4, light hydrocarbons (mostly C_2H_4), and tars (larger hydrocarbons, e.g., aromatics and polyaromatics).

Steam-oxygen gasification of wood and biogenic residues has been studied by other researches [15,17–24], however there is not as much data available as on other gasification processes. Results from these literature references are summarized in previous work of this author [14], but also in the results section of this paper these references are used for a comparison of results where applicable. Also, semi-commercial demonstration plants for the steam-oxygen fluidized bed gasification of biomass have already been in operation with a thermal input of 18 MW [25] and 100 MW [26,27]. The technical results of these endeavors were encouraging, underlining the potential of the technology. However, for sewage sludge, little fuel data were available. This is why this paper is needed, and constitutes one core goal of this paper.

The product gas contains beside the desired syngas species, tars and other impurities. Especially for sewage sludge, a high H_2S and NH_3 concentration is observed in the syngas which is not tolerated by downstream synthesis catalysts [28]. Therefore, gas cleaning is required before synthesis. Reducing the costs of gas cleaning is important for the economic feasibility of the process [29]. To design and develop the entire process chain consisting of gasification, gas cleaning, and synthesis, detailed information on the product gas quality and composition, including impurities such as tars, sulfur-species, and ammonia, is needed.

The reduction of tars and impurities by primary measures such as active bed materials is considered economically and technically favorable compared to secondary measures [30,31]. A CaO-containing bed material, e.g., achieved by addition of limestone ($CaCO_3$) or dolomite is catalytically active for cracking and steam reforming of tars [28,32,33] and acts as sorbent to capture H_2S ($CaO + H_2S \leftrightarrow CaS + H_2O$) and COS ($CaO + COS \leftrightarrow CaS + CO_2$) [31,34,35]. This work delivers experimental data on the application of this sulfur capture for sewage sludge gasification and its temperature dependency.

This study continues the author's previous research on steam-oxygen gasification wherein sewage sludge gasification was compared to straw and wood gasification [14] and the influence of limestone as bed additive for sewage sludge gasification was investigated [36]. In this paper, a deeper look is cast on the effect of operation conditions on the gasification performance. These insights are important to validate process models and to support process design.

2. Materials and Methods

2.1. Fuel and Bed Material

The sewage sludge used in this work originated mainly from the municipal waste water treatment plant Häldenmühle in Marbach am Neckar in south-west Germany. A minor fraction of the sludge (less than 0.2 kg kg^{-1}) came from the municipal wastewater treatment plants "Beilstein" and "Oberes Bottwartal" that are also located in south-west Germany. Those treatment plants delivered the sludge to the drying facility of Bioenergie Bottwartal GmbH&Co.KG, where the sludge was dried thermally with hot flue gases from a biogas CHP. After drying, the fuel had particle sizes of 5–10 mm, which might already be suitable for application in commercial fluidized beds. To suit the used experimental facility, the dried sewage sludge was crushed with a beater mill using a 2 mm sieve. The sewage sludge, gasified in the experiments, had high N, S, Cl, and ash contents. The ash summed up to almost half of the fuels dry mass. Therefore, the ash itself was used as bed material.

The proximate and elemental analysis is given in Table 1. The composition of this sewage sludge lies within the ranges reported by [37], wherein information on organic and non-organic components of typical sewage sludge is also given.

Table 1. Sewage sludge proximate and elemental analysis; au: as used (raw), daf: dry ash free, wf: water free, fc: fixed carbon, vm: volatile matter.

Proximate Analysis in kg kg^{-1}					Elemental Analysis in kg kg^{-1}				
γ_{H2O}	γ_{ash}	γ_{fc}	γ_{vm}	γ_{C}	γ_{H}	γ_{O}	γ_{N}	γ_{S}	γ_{Cl}
au	wf				daf				
0.065	0.476	0.082	0.918	0.510	0.069	0.320	0.075	0.024	0.002

For some experiments, limestone was used as bed additive without pre-calcination. The calcination took then place in-situ in the gasifier releasing CO_2. The limestone type "Messinghausener Sand 0.3–0.7" was obtained from LHOIST Germany/Rheinkalk GmbH with origin Messinghausen in Germany and consisted of the sieve fraction 0.3 mm–0.7 mm.

Table 2 shows the mineral composition of sewage sludge ash and limestone. The major elements are Si, Ca, P, Al, and Fe. Heavy metal concentrations in the dry sewage sludge are presented in Table 9.

Table 2. Main elements of sewage sludge ash and limestone.

	Elemental Analysis in kg kg^{-1}									
	γ_{Al2O3}	γ_{CaO}	γ_{Fe2O3}	γ_{K2O}	γ_{MgO}	γ_{Na2O}	γ_{P2O5}	γ_{SO3}	γ_{SiO2}	γ_{CO2}
Sewage Sludge Ash	0.129	0.223	0.103	0.017	0.028	0.004	0.162	0.045	0.292	-
Limestone	0.001	0.526	0.001	-	0.009	0.001	-	-	0.057	0.405

The particle sizes of the used solids are shown in Table 3. The dried sewage sludge had a wide range in particle sizes. During the gasification process, the sewage sludge particles seemed to release their volatile components with only a slight decrease in particle size, as the comparison of the particle sizes of sewage sludge and its ash showed. The limestone reduced its particle size during its residence time in the gasifier due to calcination and abrasion and was finer than the sewage sludge ash. Comprehensive particle size distributions on these materials are given in [14].

Table 3. Particle sizes of fuel and bed materials.

	$d_{p,10}$	$d_{p,50}$	$d_{p,90}$
		in μm	
Sewage Sludge	200	1010	2100
Sewage Sludge Bed Ash	170	520	1700
Limestone	300	650	1200
Calcined Limestone	165	370	640

2.2. Experimental Facility

A 20 kW fuel input fluidized bed facility was used in this work. It is shown schematically in Figure 1. The bubbling fluidized bed reactor is 3.5 m high and has an internal diameter of 0.15 m in the fluidized bed region and 0.20 m in the freeboard above. The facility is equipped with several thermocouples and pressure transducers. Electrical heating allowed to control and adjust the temperature inside the gasifier and to compensate unwanted heat losses that are inherent to a research scale facility. Preheated steam was injected through six bubble cap nozzles to fluidize the bed. Oxygen could due to technical reasons not be mixed with the steam like in an industrial plant but was introduced through two additional bubble cap nozzles. For safety reasons N_2 was added to the oxygen stream to reduce the O_2 concentration to 0.75 m^3 m^{-3}. The mass flow of N_2 and O_2 in these gas feeds was controlled by automatic mass flow controllers.

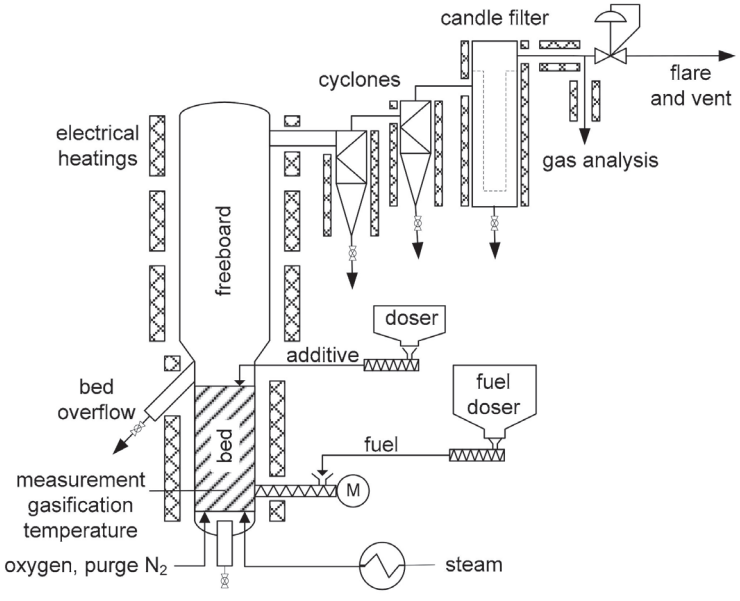

Figure 1. 20 kW fluidized bed gasification facility.

Dried sewage sludge was dosed gravimetrically with a screw feeder into the lower part of the fluidized bed, for which a small amount of nitrogen purge gas was also required. As a result of the high ash content in sewage sludge, the bed material was continuously removed during the gasification process by an overflow port to maintain a constant bed height.

For some experiments limestone was used as additive, which was dosed gravimetrically by a second doser through a port above the fluidized bed. A double ball-valve lock was used for pressure sealing.

After the gasifier, the product gas is cleaned from particles by two cyclones and a candle filter, which are heated to 400 °C to prevent tar condensation. The gas passed a pressure control valve before it was combusted in a flare.

2.3. Analysis Methods

Three slipstreams of the product gas were extracted for gas measurements after the candle filter of the facility. H_2, CO, CO_2, and CH_4 were measured continuously in a combined NDIR and thermal conductivity gas analyzer (ABB AO2020), whereas hydrocarbons from C_2 to C_4 (C_xH_y), H_2S and COS were semi-continuously (every 3 min) analyzed with a Varian CP-4900 Micro-GC. The slipstream for these devices was lead from the facility through a heated filter and a heated hose (both 180 °C) directly into 4 chilled impinger bottles, wherein the gas passed through an equal mixture of isopropanol and a 0.30 kg kg^{-1} sulfuric acid aquatic solution for tar removal. Afterwards the gas was lead through an impinger bottle with a 0.15 kg kg^{-1} sulfuric acid aquatic solution at ambient temperature to capture evaporated isopropanol. By these means, tars were removed to prevent damage to the analytical equipment, but due to the low *p*H value of the solution, H_2S and COS remained in the gas.

The continuous online gas measurement was also used to measure the dry volume flow of the syngas by a dilution method. After the candle filter, the syngas was diluted by a known N_2-stream controlled by a mass flow controller. The permanent gas concentrations were measured before and after the dilution. The syngas volume flow was calculated from the concentration changes.

The second sample line was used for wet chemical NH_3 measurement according to a modified VDI 3838 [38] guideline: An impinger bottle was used to absorb the gaseous ammonia in a 1 mol L^{-1} H_2SO_4-solution. For tar and humidity removal an isopropanol impinger bottle was arranged before the absorption solution. To avoid NH_3 loss in the isopropanol bottle, the pH value was increased by adding NaOH. The samples were analyzed with UV-Vis spectroscopy.

The third sample line was used for tar measurement, where a heated filter and heated hose at 350 °C were used. Tars were measured by extractive sampling and analysis according to the tar protocol CEN/TS 15439 [39]. For this, a quantified volume of the product gas was directed through cooled isopropanol washing bottles, wherein the tars were solved and condensed. The collected isopropanol-tar samples were analyzed by two methods as follows.

(i) In the gravimetric analysis the isopropanol is vaporized out of the sample to gain a solvent free tar residue from whose mass the gravimetric tar concentration is derived. According to [40] this sample covers all "heavy" tar species with a molar mass over approximately 180 g mol^{-1} (phenanthrene). Also tars with lower molar mass can be detected with this method, but with decreasing molar mass the detectability of tar species by gravimetric analysis decreases. Very "light" species, such as benzene, toluene, and xylene (BTX), are not detected or only to a small extend by gravimetric analysis. The gravimetric tar concentration is particularly important to assess the amount of very heavy tars with high boiling temperatures, that may condense easily on cold facility parts (e.g., gas coolers, valves) and can cause blockage and operation failure. The gravimetric analysis is performed three times for each tar sample and a mean value was calculated. As a novel method, elemental analysis of C, H, N, S, and Cl, as well as the heating value of the gravimetric tar was conducted for some samples to assess its composition.

(ii) With gas chromatography (GC) analysis of the isopropanol-tar sample, actual tar components can be individually intentified and quantified. Especially "light" species can be detected very well. These species are partially still present after gas cooling, condensation and possibly after gas washing and thus have to be considered for downstream equipment. On the contrary, heavy tar species can only be detected up to a certain molar mass with a GC, in this work this was pyrene with 202 g mol^{-1}. Quantification of all evaluated tar species was conducted with GC-FID by the institute of energy and process engineering of

FAU University of Erlangen-Nuremberg with the following equipment and specifications: Agilent GC 7890A, column CP Sil 8 CB (L = 25 m, d = 0.25 mm), temperature programme: 3 min at 40 °C, heating rate 4.7 K min^{-1} to 300 °C [41]. For simplification, benzene is also considered a tar component despite the fact that it is not named as tar in most of the literature.

Elemental and heating value analysis of fuel and gravimetric tar residues were conducted by a CHN-analyzer and combustion in a bomb calorimeter with wet sampling and ion-chromatography of S and Cl. Inorganic elemental analysis of sewage sludge ash and limestone was done by using acid digestion with subsequent ICP analysis.

Particle size distributions were measured by sieve analysis and with a laser diffraction particle size analyser.

2.4. Experimental Parameters

The main operation parameters for the steam-oxygen gasification process are gasification temperature, steam to carbon ratio, oxygen ratio, weight hourly space velocity and the bed material type.

For the choice of the gasification temperature, the following trade-off needs to be considered: Higher temperatures lead to faster gasification reactions and thus improved char and tar conversion but, on the other hand, can result in bed agglomeration when fuels with low temperature ash melting behaviour like straw are used. Also, higher gasification temperatures require more oxygen and thus reduce the overall conversion efficiency. The used bed material, sewage sludge ash, has a rather high ash melting temperature of 1200 °C but it already begins sintering at about 900 °C [42]. Therefore, the maximum bed temperature should be kept below that. In this work gasification temperatures from 650 °C to 900 °C were investigated to generate insight in the temperature influence on the process. Because of the advantages of higher gasification rates and lower tar yields, it is expected that an industrial sewage sludge gasifier will be operated at a temperature above 800 °C but below 900 °C, so as to prevent sintering and agglomeration of the bed.

The steam to carbon ratio, n_{SC}, describes the ratio of the total mole flow of water, including the fuel's moisture, to the mole flow of biomass carbon introduced into the gasifier:

$$n_{SC} = \frac{\dot{N}_{\mathrm{H2O,steam}} + \dot{N}_{\mathrm{H2O,\ moist}}}{\dot{N}_{\mathrm{C,fuel}}} \quad (1)$$

Generally, higher n_{SC} results in a reduced energetic efficiency as additional steam needs to be introduced to the gasifier. On the other hand, low S/C ratios can reduce char conversion and cause higher tar yields. The water-gas-shift reaction ($CO + H_2O \leftrightarrow H_2 + CO_2$) is severely influenced by the steam to carbon ratio, since H_2O pushes the equilibrium to the right side. Therefore, the H_2 yield as well as the H_2/CO-ratio, that is important for downstream synthesis processes, can be increased with increasing S/C ratio.

The oxygen ratio n_{O2} (analogue to air ratio λ in combustion processes), often also referred to as equivalence ratio ER, expresses the ratio of the amount of oxygen actually used in the process to the amount of oxygen which would be required for the stoichiometric oxidation of the fuel:

$$\mathrm{n_{O_2}} = \frac{\dot{N}_{\mathrm{O_2}}}{\dot{N}_{\mathrm{O_2,stoic}}} \quad (2)$$

In a technical process, n_{O2} cannot be chosen independently of the gasifier's temperature, but is a function thereof. However, due to the electrical heating of the experimental facility used in this work, n_{O2} is not coupled with the gasifier temperature and hence needs to be set by the operator. Nevertheless, in order to simulate industrially relevant conditions within the experiments, n_{O2} was chosen according to adiabatic conditions. These calculations resulted in ranges of n from 0.2 to 0.3. To generate comparable conditions, the base case of n_{O2} = 0.25 was chosen.

T weight hourly space velocity, n_{WHSV}, is the ratio of the fuel feeding rate to bed inventory mass:

$$n_{\mathrm{WHSV}} = \frac{\dot{M}_{fuel,daf}}{M_{bed}} \quad (3)$$

Therefore n_{WHSV} is a design value that brings the fuel load and the size of the fluidized bed reactor vessel in correlation. The n_{WHSV} is correlated reciprocally to the fuel residence or space time in the bed. That means, for higher n_{WHSV} the fuel has a shorter residence time in the bed.

The limestone additive ratio n_{CaCO3} expresses the mass ration of limestone additive to sewage sludge feed.

$$n_{CaCO_3} = \frac{\dot{M}_{CaCO_3}}{\dot{M}_{fuel,ar}} \quad (4)$$

The superficial velocity u_0 in the fluidized bed was calculated by dividing the volume flow of steam and oxygen at operation conditions by the cross sectional area A_{gasifier} of the gasifier (d_{gasifier} = 0.15 m):

$$n_{CaCO_3} = \frac{\dot{M}_{\mathrm{CaCO_3}}}{\dot{M}_{\mathrm{fuel,ar}}} \quad (5)$$

The minimum fluidizing velocity u_{mf} was derived from the particle Reynolds number at minimum fluidizing conditions $Re_{\mathrm{p,mf}}$ which was calculated according to Kunii and Levenspiel and Wen and Yu.

$$u_0 = \frac{\dot{V}_{\mathrm{H_2O,steam}} + \dot{V}_{\mathrm{O_2}}}{A_{\mathrm{gasifier}}} \quad (6)$$

The experimental parameters are summarized in Table 4.

2.5. Experimental Procedure

Prior to the experiments, the gasifier was heated to the desired bed temperature with around 7 kg of bed material, consisting of sewage sludge ash. The flows of sewage sludge, steam and oxygen were adjusted according to the desired experimental parameters. When the temperature and gas concentrations were steady, the experimental point commenced. Each experimental point was held in steady state conditions for at least 30 min and mean values for the continuously recorded data were calculated over this period. The tar and NH_3 measurements, with a duration of 20 min each, were conducted during steady state operation conditions.

For the experiments with limestone as bed additive, a respective batch of limestone was added prior to the experiment to set up the desired fraction of CaO in the bed. After that, a continuous dosing of limestone with the additive ratio of 0.25 kg kg^{-1} (mass limestone per sewage sludge as used) was started.

Table 4. List of all experimental of this work with respective operation conditions.

Variation	Run	ϑ	n_{SC}	n_{O2}	n_{WHSV}	$\dot{m}_{fuel}$	m_{bed}	n_{CaCO3}	u_0	$u_0 u_{mf}^{-1}$
		°C	mol mol^{-1}	mol mol^{-1}	h^{-1}	kg h^{-1}	kg	kg kg^{-1}	m s^{-1}	-
n_{O2}	O1	848	1.03	0.20	0.49	7.2	6.1	0	0.34	4.5
	O2/ref	842	1.05	0.25	0.44	7.1	7.8	0	0.36	4.7
	O3	842	1.01	0.27	0.41	7.2	7.6	0	0.36	4.8
	O4	852	1.04	0.28	0.49	7.2	7.2	0	0.37	5.0
n_{SC}	S1	852	0.59	0.24	0.52	11.3	7.4	0	0.37	5.0
	S2/ref	842	1.05	0.25	0.44	7.1	7.8	0	0.36	4.7
	S3	839	1.48	0.25	0.43	7.2	7.3	0	0.47	6.3
	S4	849	1.98	0.26	0.54	7.0	6.8	0	0.60	8.0
ϑ	ϑ1	659	1.03	0.26	0.54	7.0	6.8	0	0.29	3.9
	ϑ2	778	0.97	0.26	0.53	7.1	7.1	0	0.32	4.2
	ϑ3/ref	842	1.05	0.25	0.47	7.1	7.8	0	0.36	4.7
	ϑ4	894	1.03	0.25	0.50	7.0	7.3	0	0.37	4.9
ϑ with $CaCO_3$ additive	ϑCa1	655	1.01	0.25	0.48	6.9	5.8	0.25	0.28	3.8
	ϑCa2	708	1.04	0.26	0.26	6.9	7.6	0.25	0.31	4.1
	ϑCa3	770	1.06	0.26	0.29	6.8	7.4	0.25	0.33	4.3
	ϑCa4	798	1.12	0.28	0.40	6.4	7.9	0.25	0.33	4.5
	ϑCa5	844	1.08	0.27	0.38	6.6	8.4	0.25	0.35	4.6
	ϑCa6	897	1.26	0.26	0.48	7.0	7.1	0.25	0.43	5.7
n_{WHSV}	W1	848	1.21	0.25	0.27	7.2	12.9	0	0.41	5.4
	W2/ref	842	1.05	0.25	0.44	7.1	7.8	0	0.36	4.7
	W3	829	1.02	0.26	0.71	13.6	9.4	0	0.67	9.0
	W4	849	0.99	0.26	1.19	7.0	2.9	0	0.34	4.5
	W5	846	0.95	0.26	1.29	13.9	5.3	0	0.65	8.7

2.6. Thermochemical Equilibrium Calculations for Sulfur Capture with Calcium

The thermochemical equilibrium can be used to calculate the theoretical optimum of the H_2S and COS capture by reaction with CaO during gasification [34,43]. CaO is present in sewage sludge ash but can also be added in form of limestone ($CaCO_3$) bed additive. The H_2S and COS capture follows the equilibrium reaction equations [31,34,44,45]:

$$CaCO_3 \leftrightarrow CaO + CO_2 \quad (7)$$

$$H_2S + CaO \leftrightarrow CaS + H_2O \quad (8)$$

$$COS + CaO \leftrightarrow CaS + CO_2 \quad (9)$$

Since, in the gasifier, a reducing atmosphere is present, no $CaSO_4$ can be formed, but instead, CaS.

With the data from Tables 1 and 2, the molar ratio of calcium and sulfur fed into the gasifier by the sewage sludge can be calculated:

$$n_{Ca,S} = \frac{\dot{N}_{Ca,\,fuel}}{\dot{N}_{S,\,fuel}} \quad (10)$$

It can be seen that the sewage sludge has enough CaO present in its ash to capture all of the sludge's sulfur ($n_{Ca,S}$ = 3.5 mol mol^{-1}). However, sulfur capture can only occur until the equilibrium concentration of H_2S and COS is reached in the syngas. Since also H_2O and CO_2 are part of the relevant chemical equations (Equations (4)–(6)), the total syngas atmosphere influences the equilibrium concentrations of H_2S and COS. Hence, equilibrium calculations of the whole gasification process needed to be performed.

For this, the software FactSage 7.3, described in [46], with the database FactPS (pure substances) including all species relevant for this gasification process was used. FactSage's numerical solver then calculated the product composition where the Gibbs energy is at its minimum–the thermodynamic equilibrium:

$$\Delta G_R \overset{!}{=} 0 \tag{11}$$

The input masses necessary for the gasification of 1 kg sewage sludge as used together with the gasification agents according to Tables 5 and 6 were entered into the FactSage solver. The gasification temperature was set. All calculations were done for ambient pressure of 1 bar. The database FactPS was used. Then, the equilibrium product composition, including the permanent gases like H_2, CO, CO_2, as well as H_2S and COS, was calculated. From this result, the equilibrium concentrations of H_2S and COS were calculated as volume fraction based on the dry syngas.

Table 5. Fuel input masses for FactSage equilibrium calculation for gasification of 1 kg as used sewage sludge, ash components other than CaO were neglected.

$m_{H2O,moist}$	m_C	m_H	m_O	m_N	m_S	m_{Cl}	m_{CaO}
in kg							
0.065	0.250	0.034	0.157	0.037	0.012	0.001	0.098

Table 6. Gasification agent input masses and operation parameters for FactSage® equilibrium calculation for gasification of 1 kg as used sewage sludge.

Variation	Operation Parameters				Input Gasification Agent	
	p	ϑ	n_{O2}	n_{SC}	m_{O2}	m_{H2O}
	in bar	in °C	in mol mol^{-1}	in mol mol^{-1}	in kg	in kg
ref/n_{WHSV}	1	850	0.25	1	0.212	0.309
ϑ	1	550 . . . 1000	0.25	1	0.212	0.309
n_{O2}	1	850	0 . . . 1	1	0...1	0.309
n_{SC}	1	850	0.25	0 . . . 4	0.212	0 . . . 1.5

3. Results and Discussion

In this paper experimental runs investigating the influence of key operation parameters on sewage sludge gasification are presented. The actual operation values for these runs are summarized Table 4.

3.1. Permanent Gases

In this chapter the influence of the operation parameters on the permanent gas composition and yields are shown. The concentration of the permanent gases H_2, CO, CO_2, CH_4 and C_xH_y (C_2 to C_4 hydrocarbons) are given as volume fractions on a dry N_2-free basis and the permanent gas yield as dry N_2-free volume in STP conditions (273.17 K, 101,300 Pa) per mass of dry ash free sewage sludge. In addition, the water concentration is shown as volume fraction on wet N_2-free basis.

3.1.1. Variation of Oxygen Ratio n_{O2}

Figure 2 shows the influence of the oxygen ratio n_{O2} on the permanent gases at constant temperature ϑ. With increasing oxygen ratio, the H_2 concentration decreased and the CO_2 and H_2O concentration increased. Also, a slight decrease of CO was observed. This reflects the increased combustion of H_2 and CO to H_2O and CO_2 due to the higher oxygen supply. The CH_4 and C_yH_y concentrations were not influenced by the oxygen ratio in the investigated range. A rather constant value was observed for the gas yield.

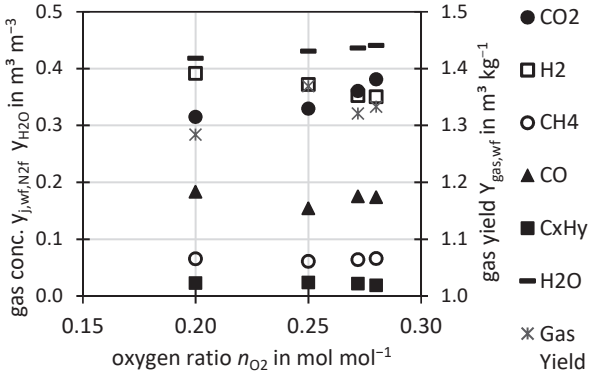

Figure 2. Permanent gas concentrations in dry N_2-free basis, for H_2O wet N_2-free basis and dry N_2-free gas yield per dry ash free fuel at different oxygen ratios n_{O2} and constant ϑ.

In most experiments found in the literature, other parameters such as temperature also varied when different n_{O2} were investigated. Therefore, it is difficult to compare the trends [22,47–49]. For coal gasification in a steam-oxygen blown slightly pressurized spouting bed at 940 °C [50], n_{O2} variation also showed increasing CO_2 concentration whereas H_2 and CO were increasing until $n_{O2} = 0.35$ but then decreased with increasing n_{O2}. The reference connects this to increased gas yield and carbon conversion up to $n_{O2} = 0.35$ followed by constant values for higher n_{O2}. The trend of higher y_{CO2} for higher n_{O2} in that reference is fitting well to this work. The variation of gas yield and carbon conversion with n_{O2} is significantly dependent on the fuel reactivity and temperature, which could be the explanation for the differences between both studies.

3.1.2. Variation of Temperature ϑ

Figure 3 shows the influence of the gasification temperature ϑ on the permanent gases for a constant n_{O2}. With increasing temperature, the gas yield increased due to higher carbon conversion to permanent gases. Also the H_2 and CO concentration increased and the H_2O concentration decreased with increasing temperature, which is also related to an increased fuel conversion by steam gasification. No influence was seen on CH_4 and C_xH_y concentrations. Similar trends were found for steam-air gasification of corn straw [51] and sewage sludge [32] also, with regard to the N_2-free basis, and similar gas concentrations of all permanent gases were reported. Also, the temperature influence in steam-oxygen gasification of wood is reported in literature [22] and shows similar trends compared to this study concerning H_2, CO_2, and gas yield. However, differences were reported in the trend of the CO, CH_4, and C_xH_y concentrations, which decreased slightly with temperature in the reference whereas in this study they slightly increased (CO) or stayed constant (CH_4, C_xH_y). Similar trends to this study were also obtained by steam gasification of sewage sludge in the same gasifier operated in DFB mode [52].

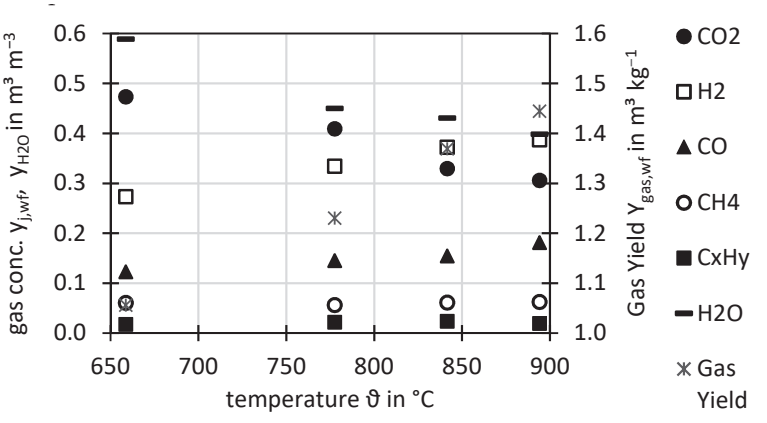

Figure 3. Permanent gas concentrations in dry N_2-free basis, for H_2O wet N_2-free basis and dry N_2-free gas yield per dry ash free fuel for different temperatures ϑ at constant n_{O2}.

3.1.3. Variation of Steam to Carbon Ratio n_{sc}

Figure 4 shows the influence of the steam to carbon ratio n_{SC} on the permanent gases. The n_{SC} had a strong influence on the permanent gas composition, since H_2 and CO_2 strongly increased and CO decreased with n_{SC}. This was due to the water gas shift reaction ($CO + H_2O \leftrightarrow H_2 + CO_2$) that was driven to the right side by adding steam. Therefore also the dry gas yield rose, since water was converted to H_2. The CH_4 and C_xH_y concentrations were mostly unaffected. Naturally, as more steam was introduced, the H_2O concentration increased with n_{SC}. Parameter variation in steam-oxygen gasification of wood in a comparable facility was conducted by [22] and in air-steam gasification of corn straw by [51], where similar trends for H_2, CO, CO_2 and H_2O were found, but other than in this work, a slight decrease of CH_4 and C_xH_y was reported with increasing n_{SC} in the reference. High CO and lower H_2 and CO_2 concentrations at low n_{SC} as in this work were also reported by [21]. For steam-air gasification of refuse-derived fuel in a rotary kiln also a rise in gas yield with n_{SC} was reported [53].

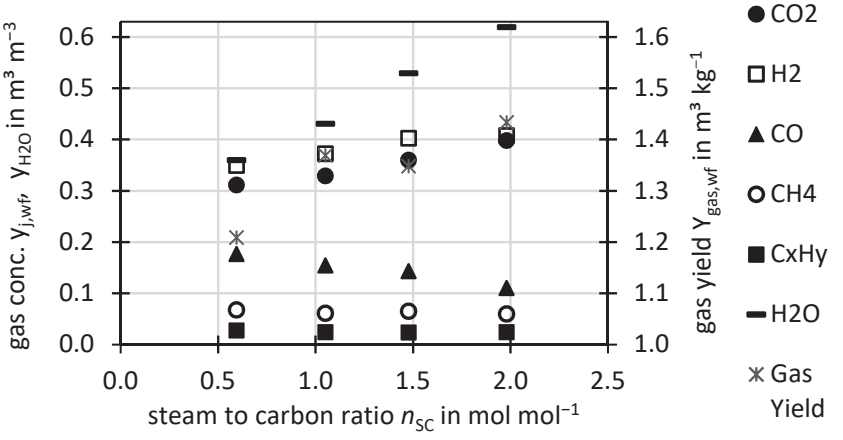

Figure 4. Permanent gas concentrations for different n_{SC} in dry N_2-free basis, for H_2O wet N_2-free basis and dry N_2-free gas yield per dry ash free fuel.

These results indicate, that through a higher n_{SC} a conversion of CO to H_2 and CO_2 can be achieved to improve the H_2-yield or to adjust the H_2/CO-ratio. However, higher n_{SC} requires more energy-intensive steam production, so that in practice it always needs to be considered if a higher n_{SC} or a downstream catalytic WGS unit, which are currently developed for uncleaned syngas [54], is preferred.

3.1.4. Variation of Weight Hourly Space Velocity n_{WHSV}

Figure 5 shows the influence of the weight hourly space velocity n_{WHSV}, given in mass flow of dry ash-free sewage sludge per bed inventory mass, on the permanent gases. It has to be mentioned, that n_{WHSV} was changed, both, by variation of fuel throughput and bed inventory as can be seen in Table 4. For the gases CO, CO_2, CH_4, and C_xH_y, no clear trend was observed for different n_{WHSV}. A slight decrease for the H_2 concentration with increased n_{WHSV} was present, which could be related to slightly decreased water-gas-shift reaction due to the decreasing residence time of the gas. Similar behavior was reported for sewage sludge steam-air gasification by [15], where for a higher turnover rate, respectively higher n_{WHSV}, lower H_2 concentrations, and no or only little change in the other permanent gas concentrations were found.

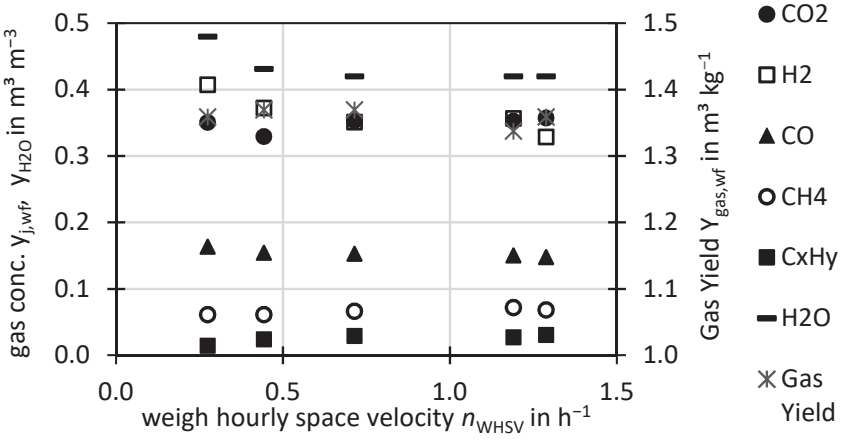

Figure 5. Permanent gas concentrations for different n_{WHSV} in dry N_2-free basis, for H_2O wet N_2-free basis and dry N_2-free gas yield per dry ash free fuel.

3.2. Tar Concentration

As described previously, tar sampling was conducted wet chemically and two sample analysis methods were used: GC analysis and gravimetric analysis. By GC analysis 18 tar species (named in [14]) were quantified. In the following, the GC tars are shown as ECN tar classes [40]. The majority of the GC-detectable tars were found to be benzene, toluene, xylene (BTX) included in the here used classes "benzene" and "ECN3". In previous work [36] it was found, that also unneglectable amounts of heterocyclic species, mainly pyridine, are present in tar from sewage sludge gasification. However, pyridine was not quantified in the GC analysis presented in this work since the used GC was not calibrated for that.

The gravimetric analysis detects mostly heavy tars, but also inorganic components e.g., salts from ammonia, sulfur and chlorine can be present (see previous work [14,36]). The carbon mass fraction in the gravimetric tars was found to be around 0.5 kg kg^{-1}, which has to be considered when using the presented tar concentrations for calculating a carbon mass balance.

All concentrations are shown as tar mass per volume of dry and N_2-free syngas in STP conditions. The tar yields can be calculated by multiplying the tar concentration with the gas yields from Section 3.1.

In the following, the influence of different operation conditions on the tar concentrations are shown. In this study the influence of the operation parameters n_{O2}, ϑ, n_{SC}, n_{WHSV} is shown. The tar concentration is also significantly dependent on the catalytic activity of the bed material e.g. in case of limestone or dolomite addition which was not subject of this work but was investigated in literature [51].

3.2.1. Variation of Oxygen Ratio n_{O2}

Figure 6 shows the influence of the oxygen ratio n_{O2} on the tar concentration. The gravimetric tar concentration is dropping slightly with increasing oxygen ratio. This could be related to enhanced tar oxidation. Since due to technical reasons only one GC analysis was performed for this parameter variation, no trend can be observed.

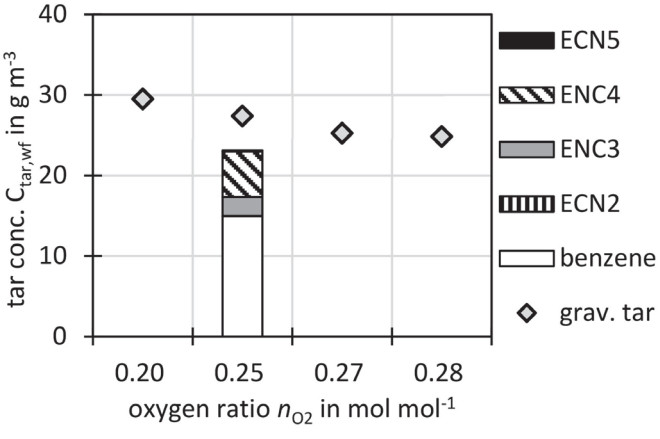

Figure 6. Gravimetric and GC tar concentrations dry, N_2-free and STP basis at different oxygen ratios n_{O2} and constant ϑ.

Again, although n_{O2} was varied by several researchers [22,47–49], in all found references, other significant parameters such as temperature were altered as well. Therefore, no exclusive variation of n_{O2} was found in the literature. This study can thus at least shed some light on the behaviour of gravimetric tar concentration at different n_{O2}.

3.2.2. Variation of Temperature ϑ

Figure 7 shows the tar concentration at different gasification temperatures ϑ. At the 659 °C a very high gravimetric tar concentration of 98 g m^{-3} was measured. When the temperature was increased to 778 °C the concentration drastically dropped to 31 g m^{-3}. With further temperature increase, the gravimetric tar concentration steadily dropped to 27 g m^{-3} and 21 g m^{-3} for 842 °C and 894 °C, respectively. As known [55], at low gasification temperatures, considerable fractions of the fuel are not converted into small molecules, but form large tar molecules which are detected well by gravimetric analysis. At higher temperatures those gravimetric tars are cracked or reformed into smaller tar species or into permanent gases.

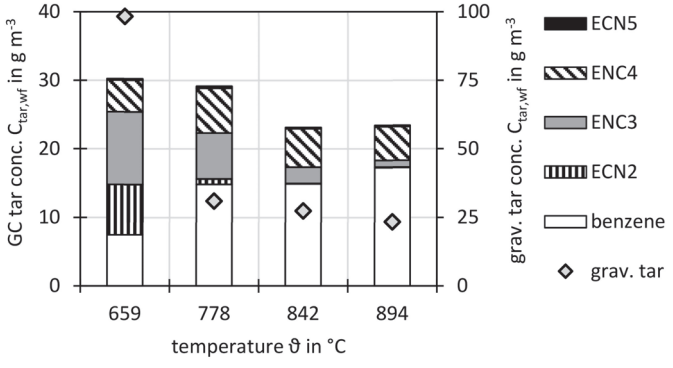

Figure 7. Gravimetric and GC tar concentrations on dry, N_2-free and STP basis at different gasifier temperatures.

The total GC tar concentration was 31 g m^{-3} at 659 °C. When the temperature was increased, the GC tars were found to be decreasing slightly but steadily to 23 g m^{-3} at 894 °C. It has to be noted that the concentration of tar species from ECN2 and ECN3 classes decreased severely with temperature, while benzene is increasing.

In the literature, overall similar behaviour is reported [22,47,52,56–59].

3.2.3. Variation of Steam to Carbon Ratio n_{SC}

Figure 8 shows the tar concentrations against steam to carbon ratio n_{SC}, where a decrease of the gravimetric tar concentration with increasing n_{SC} was observed. This could be due to the known [55,60] effect of higher steam concentrations on reforming of gravimetric tars. The GC tars stayed rather constant over n_{SC}. This corresponds well to other gasification experiments where higher steam concentrations also reduced tar concentrations [22,60,61].

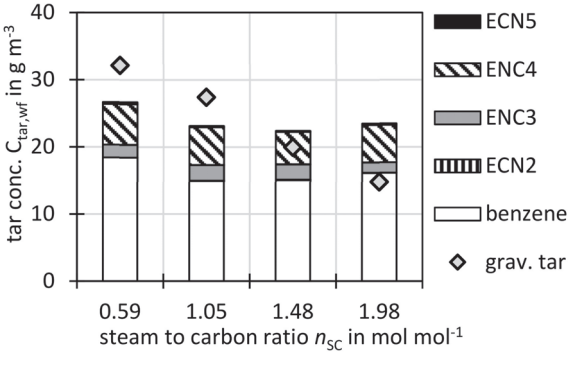

Figure 8. Gravimetric and GC tar concentrations on dry, N_2-free and STP basis at different steam to carbon ratios n_{SC}.

3.2.4. Variation of Weight Hourly Space Velocity n_{WHSV}

Figure 9 shows the tar concentration against the weight hourly space velocity n_{WHSV}. For the gravimetric tars no clear trend was observed. It also has to be noted that the point at n_{WHSV} = 1.3 h^{-1} was conducted with a higher fuel mass flow of around 14 kg h^{-1} compared to around 7 kg h^{-1} (see Table 4) for the other points. Despite that, the tar concentration for the points at n_{WHSV} = 1.2 h^{-1} and 1.3 h^{-1} were found to be similar.

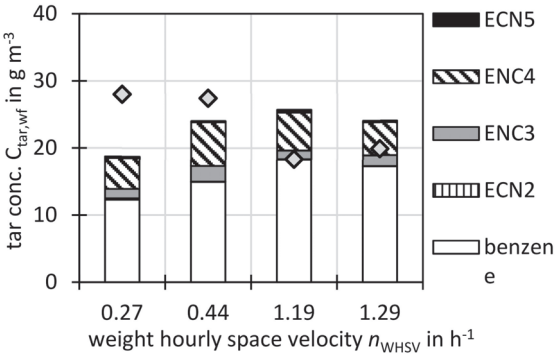

Figure 9. Gravimetric and GC-MS tar concentrations on dry, N_2-free and STP basis at different weight hourly space velocities.

When comparing the two gravimetric tar concentrations lower n_{WHSV} with the two ones at higher n_{WHSV}, a decrease can be seen. For the GC tars no trend is visible. However, a more comprehensive study is needed to fully assess the influence of n_{WHSV} on tar concentration.

In literature [15] for steam-air gasification it was reported that tar concentration is slightly increased with higher "turnover rate" respective higher n_{WHSV}. For steam gasification, [56] found slightly increased gravimetric tar yields but constant GC tar yields for increasing n_{WHSV} which is consistent with this work.

3.2.5. Gravimetric Tar Composition and Heating Value

For some runs, the gravimetric tar sample was retrieved after the completed gravimetric analysis and analysed. Figure 10 shows the elemental composition of gravimetric tars. It can be seen that the carbon mass fraction is only around 0.5 kg kg^{-1} compared to up to 0.87 kg kg^{-1} for tar from wood [14]. Also, significant amounts of S, N, and Cl were found in sewage sludge gravimetric tar in this study. It is therefore assumed that, when applied for sewage sludge derived syngas, the gravimetric analysis does not only sample typical tar species (e.g., PAH), but also salts like NH_4Cl, $(NH_4)_2CO_3$, and $(NH_4)_2SO_4$ that are formed from NH_3, HCl, and H_2S which are present in high concentrations in the syngas. This hypothesis is supported by the measured higher heating value of the gravimetric tars, which were found to be around 25 MJ/kg and are thus around 40% below the heating value of a typical gravimetric tar species (e.g., naphthalene 40 MJ kg^{-1}).

Figure 10. Elemental analysis and heating values of gravimetric tars.

3.3. H_2S and COS Concentration

In this chapter the concentrations of the gaseous sulfur species H_2S and COS are discussed.

3.3.1. Variation of Oxygen Ratio n_{O2}

Figure 11 shows the measured H_2S and COS concentrations as well as the equilibrium concentrations, calculated with FactSage® (see Section 2.6), over the oxygen ratio n_{O2}. All concentrations are presented in water free (wf) and N_2-free basis. For oxygen ratios from 0.20 to 0.28, H_2S concentrations between 2000 × 10^{-6} m^3 m^{-3} and 3000 × 10^{-6} m^3 m^{-3} were measured at the respective conditions of 847 ± 5 °C. From the measurements of this work, it is hard to deduct a specific trend for H_2S, but it can be noted that the two points at higher n_{O2} show slightly higher concentrations. For COS only one measurement was performed of 60 × 10^{-6} m^3 m^{-3} at n_{O2} = 0.2 mol mol^{-1}.

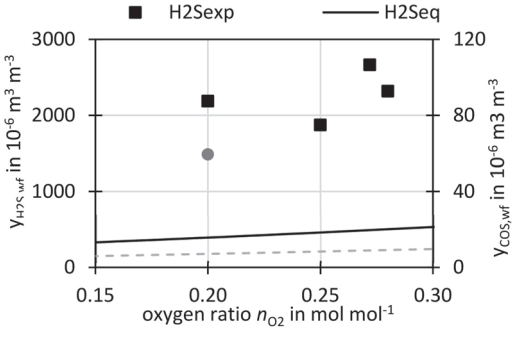

Figure 11. Measured and equilibrium H_2S and COS concentrations on dry and N_2-free basis at different oxygen ratios n_{O2} and constant ϑ.

The equilibrium predicts a slight increase of H_2S and COS concentration with n_{O2}. This is related to higher feed of oxygen to the gasifier at higher n_{O2}, leading to the formation of H_2O and CO_2. This drives Equations (5) and (6) away from sulfur capture following Le Chatelier's principle.

3.3.2. Variation of Temperature ϑ

Figure 12 shows the H_2S concentration and Figure 13 the COS concentration at different temperatures for cases with the reference bed material, sewage sludge ash, but also for runs with limestone additive. Additionally, the H_2S and COS concentrations in the thermochemical equilibrium, calculated by the software FactSage® as described Section 2.6 are shown.

A strong dependence of the concentration of the two sulfur species on the temperature could be observed in the experiment as well as in the equilibrium calculations. At low temperatures high concentrations of up to 7653 × 10^{-6} m^3 m^{-3} for H_2S and up to 215 × 10^{-6} m^3 m^{-3} for COS were measured with sewage sludge ash as bed material. With increasing temperatures the H_2S and COS concentrations were decreasing until a minimum was reached before the concentration increased again at higher temperatures. This is related to the facts, that sewage sludge ash contains CaO which is can capture sulfur through reactions Equations (5) and (6) which are exothermic and therefore favored at lower temperatures. However the calcination reaction (Equation (4)) is favored at higher temperatures. The overlay of calcination and sulfur capture leads to the here seen temperature dependency.

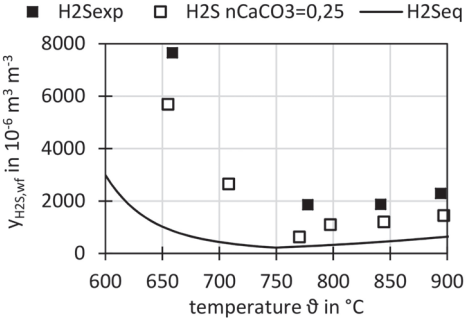

Figure 12. Measured and equilibrium H_2S concentration on dry and N_2-free basis at different temperatures ϑ.

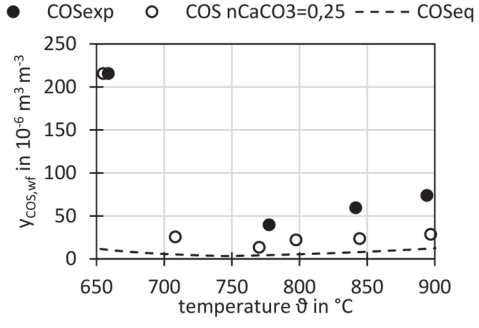

Figure 13. Measured and equilibrium COS concentration on dry and N_2-free basis at different temperatures ϑ.

For the case with limestone additive, a similar trend was observed but consequently lower concentrations were measured. The equilibrium has a similar trend as the experiments, but shows for all cases lower concentrations, which is in agreement with the fact that the equilibrium predicts optimal sulfur capture and thus the lowest possible concentration. The lowest measured concentration without limestone additive was 1855×10^{-6} m^3 m^{-3} at 778 °C and with limestone additive the lowest concentration was 624×10^{-6} m^3 m^{-3} at 770 °C. With the limestone additive the H_2S concentration could thus be reduced by around factor 3 at these temperatures. The absolute equilibrium minimum is was calculated for 740 °C with 243×10^{-6} m^3 m^{-3}.

For COS similar behavior was observed, at 770 °C–778 °C the concentration for sewage sludge ash bed is 40×10^{-6} m^3 m^{-3}, with limestone additive it is reduced to 13×10^{-6} m^3 m^{-3}, also by factor 3. The COS minimum equilibrium concentration was calculated for 740 °C with 6×10^{-6} m^3 m^{-3}.

As said, with further increasing temperatures the measured and equilibrium H_2S and COS concentrations are rising again. At the reference temperature of 840 °C, which is also a very common temperature to operate sewage sludge incinerators and gasifiers [62], slightly higher concentrations of H_2S with 1873×10^{-6} m^3 m^{-3} and COS of 59×10^{-6} m^3 m^{-3} were observed without additive. Again, the limestone additive brings a reduction. It was noticed that, with limestone additive, the COS concentrations can be brought very close to the equilibrium for all investigated temperatures above 750 °C, while for H_2S, the concentrations with additive still have some distance to the equilibrium.

In literature [34,43], similar trends of H_2S concentrations over temperature in the presence of CaO were also reported in experiments and equilibrium calculations.

3.3.3. Variation of Steam to Carbon Ratio n_{SC}

Figure 14 shows the H_2S and COS concentrations for different steam to carbon ratios n_{SC}. The measured H_2S concentrations increased with n_{SC}. The lowest S/C ratio tested was 0.6 mol mol^{-1} which lowered the H_2S concentration to 1340 $\times$ 10^{-6} m^3 m^{-3}. A similar trend was found by [34]. This follows well the trend of the equilibrium where the H_2S concentrations are increasing with n_{SC} following Le Chatelier's principle: With higher n_{SC}, more steam is introduced into the gasifier, driving Equation (5) to the left towards less H_2S capture.

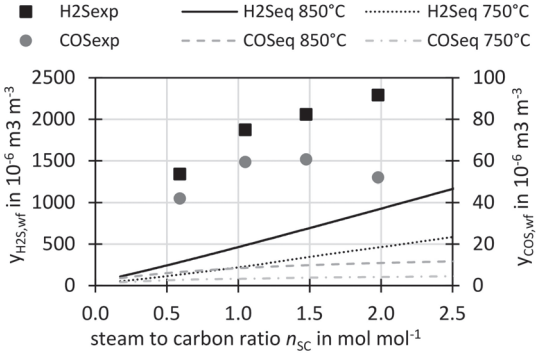

Figure 14. Measured and equilibrium H_2S and COS concentration on dry and N_2-free basis at different steam to carbon ratios, additionally equilibrium calculations for ϑ = 750 °C are showing the best possible sulfur capture.

The measured COS concentration stayed on the same level throughout the n_{SC} variation, whereas the equilibrium predicts a very small increase. Since steam is not present in Equation (6), n_{SC} has no direct effect on COS capture. However through the water gas shift reaction, steam addition also produces more CO_2 influencing the COS capture.

Additionally, the equilibrium for 750 °C is shown since sulfur capture is maximized at this temperature. It can be seen that, at operation conditions of 750 °C and low n_{SC}, very low concentrations are achievable according to the equilibrium.

In literature [34,43], similar trends of H_2S concentrations over n_{SC} in the presence of CaO were also reported in experiments and equilibrium calculations.

3.3.4. Variation of Weight Hourly Space Velocity n_{WHSV}

Figure 15 shows the H_2S and COS concentration at different fuel space velocities n_{WHSV}. For the measured values, no specific trend could be observed. Since the equilibrium already assumes infinite residence time of the fuel, it cannot produce trends of the space velocity and thus a constant equilibrium concentration is shown.

3.4. NH_3 Concentration

Figure 16 shows the measured NH_3 concentrations in the syngas with respect to different operation conditions. As indicated above, NH_3 was measured wet chemically. Therefor these measurements were not performed for every experimental point. Due to the limited points, it is not always possible to deduct a clear trend, therefore further studies with more comprehensive NH_3 analysis are needed.

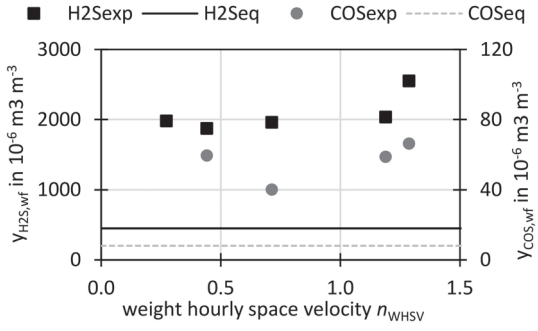

Figure 15. Measured and equilibrium H_2S and COS concentration at different fuel space velocities.

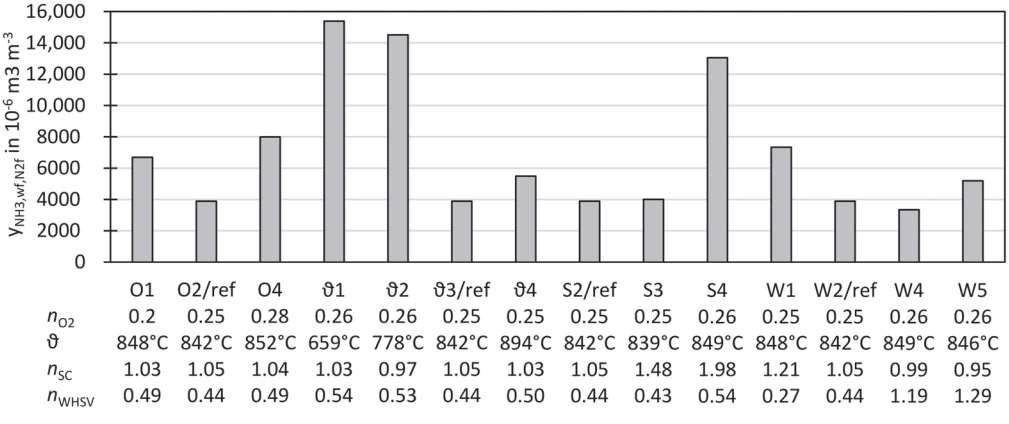

	O1	O2/ref	O4	ϑ1	ϑ2	ϑ3/ref	ϑ4	S2/ref	S3	S4	W1	W2/ref	W4	W5
n_{O2}	0.2	0.25	0.28	0.26	0.26	0.25	0.25	0.25	0.25	0.26	0.25	0.25	0.26	0.26
ϑ	848°C	842°C	852°C	659°C	778°C	842°C	894°C	842°C	839°C	849°C	848°C	842°C	849°C	846°C
n_{SC}	1.03	1.05	1.04	1.03	0.97	1.05	1.03	1.05	1.48	1.98	1.21	1.05	0.99	0.95
n_{WHSV}	0.49	0.44	0.49	0.54	0.53	0.44	0.50	0.44	0.43	0.54	0.27	0.44	1.19	1.29

Figure 16. Compilation of all conducted NH_3 measurements.

For most runs, NH_3 concentrations of between 4000 × 10^{-6} m^3 m^{-3} and 8000 × 10^{-6} m^3 m^{-3} were measured. However, for runs with lower ϑ or with higher n_{SC} higher NH_3 concentrations of up to 15,000 × 10^{-6} m^3 m^{-3} were measured.

It can be concluded that NH_3 is present in considerable concentrations in sewage sludge derived syngas, which is clearly related to the high nitrogen content in the fuel. Other research also shows high NH_3 concentration for high N-containing fuels such as sewage sludge [14,52], manure [52], peat [26], or coal [63]. It has to be noted that steam-oxygen gasification seams to show considerably lower NH_3 concentration than steam gasification [52] in the same facility at IFK University of Stuttgart. Literature also reports decreasing NH_3 concentrations with increasing temperature, which is in line with this study [64].

3.5. Ash Yields and Carbon Contents

Depending on the process design, different kinds of ash streams are produced and are usually divided in bed ash and fly ash. Carbon contained in ashes leaves the reactor ungasified and therefore reduces the conversion efficiency of the process.

3.5.1. Bed Ash

In the used research facility as well as in some commercial sewage sludge gasifiers [65], the bed ash is the main ash stream since granular dried sludge is used as fuel. The bed ash is therefore also serving as bed material. Since constantly new bed ash is produced, it is

discharged continuously over an overflow. In this work, the bed ash had a particle size of $d_{p,50}$ = 520 µm and was only slightly smaller than the used fuel (see [14] for detailed particle distribution).

The bed ash yield per dry fuel is around 0.41 kg/kg as calculated from the difference of the fuels ash content (proximate analysis Table 1) and the measured fly ash yields (Table 6). The carbon content of the bed material after discharge from the reactor was around 0.017 kg/kg at a reference gasification temperature of 850 °C however for lower temperature the carbon content was found to be higher up to 0.04 kg/kg at 668 °C (Table 7).

Table 7. Fly ash and bed ash yields and carbon content.

run	ϑ	n_{SC}	n_{O2}	n_{WHSV}	$Y_{ash,fly}$	$Y_{ash,bed,bal}$	$¥_{C,ash,fly}$	$¥_{C,ash,bed}$
ϑ1	659	1.03	0.259	0.54	0.072	0.404	0.110	0.045
ϑ2	778	0.97	0.256	0.53	0.063	0.413	0.092	0.031
ref	842	1.05	0.250	0.47	0.062	0.414	0.085	0.017
ϑ4	894	1.03	0.254	0.51	0.059	0.417	0.047	0.006
W1	848	1.21	0.252	0.27	0.065	0.411	0.066	0.016
SC4	849	1.98	0.256	0.54	0.070	0.406	0.055	0.014

3.5.2. Fly Ash

Smaller sized fuel particles, dust produced by attrition in the bed or soot formed by fuel conversion are entrained from the fluidized bed and are considered fly ash. As described in Section 2.2, this fly ash is in the used research facility captured by a primary cyclone, a secondary cyclone and a ceramic candle filter. The yields of the respective fly ash fractions for the reference run (n_{O2} = 0.25, ϑ = 842, n_{SC} = 1.05 mol mol^{-1}) are $Y_{ash,prim.cyclone}$ = 0.051 kg kg^{-1}, $Y_{ash,sec.cyclone}$ = 0.008 kg kg^{-1} and $Y_{ash,filter}$ = 0.003 kg kg^{-1}. It can be seen that the majority of the fly ash is separated by the primary cyclone.

In Table 7, the fly ash yield and the carbon mass fraction are shown for different runs, wherein all respective fly ash fractions (prim. cyclone, sec. cyclone, filter) have been cumulated. It can be seen that the fly ash yield per fuel mass is for all presented runs between 0.059 kg kg^{-1} and 0.072 kg kg^{-1}. The carbon mass fraction of the fly ash varied between 0.047 kg kg^{-1} and 0.110 kg kg^{-1} and was found to be dependent on gasification temperature.

3.6. Ash Main Elements and Heavy Metal Content

Table 8 shows the main elemental analysis of the ash fractions of the reference run. It can be seen that the elemental composition for all ash fractions was similar. The major components of the ash were calcium, silica, phosphorous, aluminium and iron. These elements originated from the mineral content of waste water and additives for phosphorous precipitation. Due to the high phosphorous content, the ash can be used as fertilizer if it fulfils the respective regulations or as raw material for industrial fertilizer production.

Table 9 shows the heavy metal concentration in dry sewage sludge and the ash fractions from the gasification experiments. Also the German legal limits for fertilizers [66] in general and specifically for the deployment of sewage sludge as fertilizer [67] are given. It can be seen that the used dry sewage sludge already fulfils the legal limits for all components except Thallium. Depending on the species, the concentration of the heavy metals in the ashes are different to those of the sewage sludge. For more volatile elements such as Cd, Pb and Tl, the concentration in the bed ash is reduced compared to the sewage sludge, but these elements are found again in the fly ashes with increased concentrations. It is gratifying, that the bed ash is therefore, compared to sewage sludge, depleted of Cd, Hg, Tl and has reduced Pb concentrations. The bed ash fulfils all legal limits except of Nickel, however the high Ni concentrations of the bed ash are assumed to come from the high temperature steel pipe of the reactor and are not attributed to the Ni present in the sewage sludge. Since in industrial plants are refractory lined, the industrial ash is expected to meet the Ni limits. The bed ash is only slightly below the Cu limit, though.

Table 8. Ash main elemental analysis.

	Bed Ash	Fly Ash		
	Overflow	**Prim. Cyclone**	**Sec. Cyclone**	**Filter**
	mass fraction in kg kg^{-1}			
Al_2O_3	0.105	0.105	0.107	0.108
BaO	0.001	0.001	0.001	0.001
CaO	0.235	0.252	0.302	0.335
Fe_2O_3	0.098	0.095	0.115	0.108
K_2O	0.015	0.017	0.014	0.011
MgO	0.025	0.029	0.031	0.031
MnO_2	0.003	0.002	0.003	0.002
Na_2O	0.004	0.004	0.004	0.003
P_2O_5	0.141	0.128	0.137	0.135
SO_3	0.040	0.033	0.033	0.028
SiO_2	0.307	0.267	0.228	0.228
SrO	0.001	0.001	0.001	0.001
TiO_2	0.005	0.006	0.006	0.006

Table 9. Heavy metal concentration in sewage sludge and ash fractions, for comparison: German legal limit. [a] German fertilizer law (DüMV), [b] German sewage sludge treatment law (AbklärV2017), [c] for dry sewage sludge with 8% P_2O_5, [d] for ash with 12% P_2O_5, [e] stricter limits for Cr^{VI}: 2 mg kg^{-1}.

	Sewage Sludge	**Bed Ash**	**Prim. Cyclone**	**Sec. Cyclone**	**Filter**	**German Legal Limit**
	mass fraction of trace elements in mg/kg					
As	10	38	40	86	38	40 [a]
Be	1	1	1	1	1	-
Cd	1.7	0.2	3.3	29	0	4 [a,c]/6 [a,d]
Co	3	29	29	41	29	-
Cr	377	828	1018	1939	828	900 [a]/2 [e]
Cu	515	865	946	1552	865	900 [b]
Hg	0.4	0.0	0.1	0.5	0.0	1 [a]
Mo	7	25	36	81	25	-
Ni	25	592	4639	6338	592	80 [a]
Pb	60	134	219	710	134	150 [a]
Sb	2	15	12	23	15	-
Se	13	43	103	217	43	-
Sn	134	75	122	195	75	-
Tl	3	<0.3	<0.3	<0.3	<0.3	1 [a]
V	31	52	53	64	52	-
Zn	1010	1607	1589	2291	1607	4000 [b]

It has to be noted, that in this study only the total value of chrome was measured, but not Cr^{VI} for which strict limits are imposed [66]. However, from a commercial air-blown sewage sludge fluidized bed gasifier the heavy metal concentrations of the bed ash were reported, and the Cr^{VI} concentration was below 0.5 mg kg^{-1} and with that below the legal limit [62]. From this commercial facility also very low concentrations of Cd, Hg and Tl were reported, each below 0.2 mg kg^{-1}, 0.05 mg kg^{-1} and 0.5 mg kg^{-1}, respectively, and Pb was reported with 20 mg kg^{-1}. These values correspond well to the findings of this study. The Ni concentration was reported to be much lower in the commercial gasifier, underlining the hypothesis that, in this study, the Ni loading of the ash came from the high temperature steel of the reactor pipe. Arsenic, at 3 mg kg^{-1}, was reported to be much lower in the commercial gasifier compared to this study, however there could also be differences in the sewage sludge composition, which is not considered in [62].

3.7. Hydrodynamic Behavior of the Sewage Sludge Ash Bed Material

Overall, the fluidization behaviour of the bed material was good during the experiments. The facility was in operation with sewage for around 25 trial days with each a gasification operation of 4 h to 8 h. In most cases the experimental conditions were varied several times per day to investigate different experimental points. During the majority of the experiments, stable hydrodynamical conditions were reached quickly, visible by a constant pressure drop over the fluidized bed.

However, bed melting and agglomeration have been observed on few occasions for operation points with low superficial fluidization velocity of $u_0 < 0.2$ m s^{-1} corresponding to $u_0\ u_{mf}{}^{-1} < 3$ and temperatures over 850 °C. In these cases at the beginning stable condition could be reached, but then a rapid temperature rise accompanied with partial bed material melting and agglomeration was triggered by a short interruption of the fuel supply. After that, fluidization was not possible anymore and the agglomerated bed material needed to be removed from the reactor. Such short fuel supply interruptions also occurred at other operation points with higher fluidization velocity, but no negative effect was present there. Leading to the explanation, that after the fuel supply interruption the endothermic effect of the fuel conversion ceased and the further supplied oxygen could exothermally oxidize char and reduced metals (e.g., FeO) in the bed. Due to the low fluidization velocity, the bed was poorly mixed and therefore the temperature could rise above the ash melting temperature locally at the gasifier bottom. The authors therefore advise to always ensure a good bed material mixing by maintaining sufficient fluidization velocity of $u_0\ u_{mf}{}^{-1} >> 3$. However, it is likely that this problem was more prominent in the small electrically heated research reactor than in a bigger industrial facility.

3.8. Carbon Balance

Figure 17 shows the carbon yields for different gasifier temperatures. On the left y-axis, the carbon yield in tars, in bed ash and in fly ash is shown. On the right y-axis, the carbon yield in the syngas main components (CO, CO_2, CH_4, C_xH_y) as well as the total sum of all measured carbon yields is depicted.

The carbon yield in tars was calculated as sum of carbon in gravimetric tars as measured from gravimetric tar concentration (Figure 7) and its elemental analysis (Figure 10) as well as the carbon in benzene, toluene and xylene (ECN3 in Figure 7) taken from the GC analysis. This approach adds the light tars to the gravimetric tars to represent a total tar amount. The carbon yield in tars decreased with temperature, since the tars are thermally cracked at higher temperatures.

The carbon yield in bed ash and fly ash decreased with increasing temperature since more char was gasified, e.g., by the water-gas reaction at higher temperatures due to faster reaction rates.

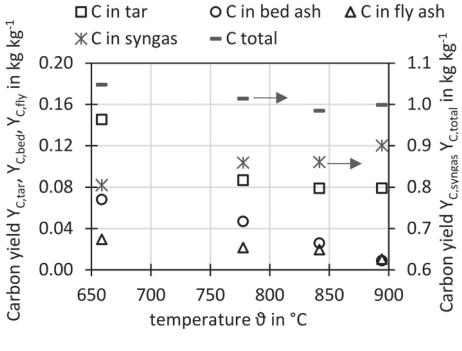

Figure 17. Carbon balance: Yield of carbon in syngas, tar, bed ash, fly ash and total sum for different gasifier temperatures.

The carbon yield in the syngas main components increased with temperature, since at higher temperature more char and tar is converted to gases such as CO, CO_2, and CH_4.

The total carbon yield sum for all shown carbon points are close to 1 kg kg^{-1}, which means that almost the same amount of carbon was found in the products than introduced with the sewage sludge.

4. Conclusions and Outlook

This work offers a comprehensive experimental study of the steam-oxygen gasification of sewage sludge for synthesis gas production in a 20 kW fluidized bed plant. The experimental results can be utilized for process design and to set-up and validate a gasifier model, since product gas, char, tar and impurity yields as well as their dependencies on the operation conditions are presented.

Since the gas yield was enhanced and the tar yield decreased with increasing gasification temperature it can be concluded, that the gasification temperature should be chosen as high as practically feasible (i.e., 850 °C to 900 °C) taking into account the ash melting behavior.

The H_2/CO-ratio can be controlled by altering the steam to carbon ratio n_{SC} as steam promotes the water gas shift reaction. It could be shown that the H_2/CO-ratio could be tailored to 2 (e.g., for methanol or DME-production) or 3 (for methanation) with a reasonable range of n_{SC}.

In the investigated process, the majority of the ash is received as bed ash. Hazardous cadmium, mercury and thallium, contained in the sewage sludge, is evaporated in the gasification process, therefore the bed ash was found to be free of or very lean in those elements, which is beneficial for the ash application for fertilizer production. Since the sewage sludge ash contains calcium, the majority of the sludge's sulfur is bound in the bed ash. By adding limestone to the gasifier this sulfur capture is enhanced and the H_2S and COS concentrations in the syngas are lowered.

Overall, the steam-oxygen gasification proved to be an efficient and technically feasible process for sewage sludge treatment. The process can play a role in closing the loop for carbon by converting the organic fraction of sewage sludge to carbon-containing bio-fuels or chemicals as well as in closing the loop for phosphorous that can be recovered from the heavy metal lean ash. Therefore, in future, this process can be considered as an alternative to fluidized bed incineration.

Author Contributions: Conceptualization, experimental work, data evaluation, writing—original draft: M.S.; measurement and analysis methodology: M.S. and S.H.; review and editing: M.S., S.H., G.S. All authors have read and agreed to the published version of the manuscript.

Funding: The work was funded by the federal state of Baden-Württemberg in the framework of the BW-PLUS program (BWB 15004).

Institutional Review Board Statement: Not applicable.

Informed Consent Statement: Not applicable.

Data Availability Statement: The data presented in this study are available on request from the corresponding author.

Acknowledgments: The experiments in this work were carried out within the Res2CNG project at IFK University of Stuttgart. The authors gratefully acknowledge the cooperation with the project partners and the financial support from the federal state of Baden-Württemberg. Furthermore the practical support of lab engineer Tim Seitz and the whole IFK-DEU department is acknowledged.

Conflicts of Interest: The authors declare no conflict of interest.

Abbreviations

au	as used
daf	dry ash free
CHP	combined heat and power plant
DME	dimethyl ether
ER	Equivalence ratio, synonymous to oxygen ratio n_{O2}
fc	fixed carbon
FID	flame ionizing detector
GC	gas chromatography
SNG	Substitute Natural Gas
vm	volatile matter
wf	water free

Symbols

A	m^2	cross sectional area
Ar_p	-	Archimedes number of particle
C_{tar}	g m^{-3}	tar mass per volume of dry and N_2-free gas in STP conditions
d_p	µm	particle size
γ_j	kg kg^{-1}	mass fraction of element j in solid sample
m	kg	mass
$\dot{m}$	kg h^{-1}	mass flow
N	mol	substance amount
$\dot{N}$	mol h^{-1}	mole flow
$n_{Ca,S}$	mol mol^{-1}	molar ratio of calcium feed to sulfur feed
n_{CaCO3}	kg kg^{-1}	limestone additive ratio
n_{O2}	mol mol^{-1}	oxygen ratio
n_{SC}	mol mol^{-1}	steam to carbon ratio
n_{WHSV}	h^{-1}	weight hourly space velocity of dry ash free fuel in bed
$Re_{p,mf}$	-	Reynolds number for particle at minimum fluidizing condition
u_0	m s^{-1}	superficial velocity
u_{mf}	m s^{-1}	minimal fluidization velocity
Y_{gas}	m^3 kg^{-1}	gas yield (volume of dry and N_2-free gas in STP conditions per mass of dry ash free fuel)
$y_{j,}$	m^3 m^{-3}	gas concentration (volume fraction)
ΔG_R	kJ mol^{-1}	Gibbs reaction enthalpy

References

1. Milieu Ltd; WRc; RPA. Environmental, Economic and Social Impacts of the Use of Sewage Sludge on Land: Final Report Part I. Available online: https://ec.europa.eu/environment/archives/waste/sludge/pdf/part_i_report.pdf (accessed on 5 January 2021).
2. Seiple, T.E.; Coleman, A.M.; Skaggs, R.L. Municipal wastewater sludge as a sustainable bioresource in the United States. *J. Environ. Manag.* **2017**, *197*, 673–680. [CrossRef] [PubMed]
3. United States Environmental Protection Agency, Municipal and Industrial Solid Waste Division. Biosolids Generation, Use, and Disposal in The United States. 1998. Available online: https://www.epa.gov/sites/production/files/2018-12/documents/biosolids-generation-use-disposal-us.pdf (accessed on 24 February 2020).
4. Yang, G.; Zhang, G.; Wang, H. Current state of sludge production, management, treatment and disposal in China. *Water Res.* **2015**, *78*, 60–73. [CrossRef] [PubMed]
5. Gorazda, K.; Tarko, B.; Werle, S.; Wzorek, Z. Sewage sludge as a fuel and raw material for phosphorus recovery: Combined process of gasification and P extraction. *Waste Manag.* **2018**, *73*, 404–415. [CrossRef] [PubMed]
6. BGB German law, Verordnung über die Verwertung von Klärschlamm, Klärschlammgemisch und Klärschlammkompost (Klärschlammverordnung - AbfKlärV): Regulation on the recovery of sewage sludge, Sewage sludge mixture and sewage sludge compost. 2017. Available online: https://www.gesetze-im-internet.de/abfkl_rv_2017/AbfKl%C3%A4rV.pdf (accessed on 5 January 2021).
7. Dos Santos, R.G.; Alencar, A.C. Biomass-derived syngas production via gasification process and its catalytic conversion into fuels by Fischer Tropsch synthesis: A review. *Int. J. Hydrogen Energy* **2020**, *45*, 18114–18132. [CrossRef]
8. Sikarwar, V.S.; Zhao, M.; Clough, P.; Yao, J.; Zhong, X.; Memon, M.Z.; Shah, N.; Anthony, E.J.; Fennell, P.S. An overview of advances in biomass gasification. *Energy Environ. Sci.* **2016**, *9*, 2939–2977. [CrossRef]

9. Zanelli, A. Producing Fertilizers with Recycled Phosphate. Available online: http://icl-group-sustainability.com/reports/producing-fertilizers-with-recycled-phosphate (accessed on 5 January 2021).
10. Arnout, S.; Nagels, E. Modelling thermal phosphorus recovery from sewage sludge ash. *Calphad* **2016**, *55*, 26–31. [CrossRef]
11. Herzel, H.; Krüger, O.; Hermann, L.; Adam, C. Sewage sludge ash—A promising secondary phosphorus source for fertilizer production. *Sci. Total. Environ.* **2016**, *542*, 1136–1143. [CrossRef]
12. Thunman, H.; Seemann, M.; Vilches, T.B.; Maric, J.; Pallares, D.; Ström, H.; Berndes, G.; Knutsson, P.; Larsson, A.; Breitholtz, C.; et al. Advanced biofuel production via gasification—lessons learned from 200 man-years of research activity with Chalmers' research gasifier and the GoBiGas demonstration plant. *Energy Sci. Eng.* **2018**, *6*, 6–34. [CrossRef]
13. Koppatz, S.; Pfeifer, C.; Rauch, R.; Hofbauer, H.; Marquard-Moellenstedt, T.; Specht, M. H2 rich product gas by steam gasification of biomass with in situ CO2 absorption in a dual fluidized bed system of 8 MW fuel input. *Fuel Process. Technol.* **2009**, *90*, 914–921. [CrossRef]
14. Schmid, M.; Beirow, M.; Schweitzer, D.; Waizmann, G.; Spörl, R.; Scheffknecht, G. Product gas composition for steam-oxygen fluidized bed gasification of dried sewage sludge, straw pellets and wood pellets and the influence of limestone as bed material. *Biomass—Bioenergy* **2018**, *117*, 71–77. [CrossRef]
15. Roche, E.; De Andrés, J.M.; Narros, A.; Rodríguez, M.E. Air and air-steam gasification of sewage sludge. The influence of dolomite and throughput in tar production and composition. *Fuel* **2014**, *115*, 54–61. [CrossRef]
16. Kelessidis, A.; Stasinakis, A.S. Comparative study of the methods used for treatment and final disposal of sewage sludge in European countries. *Waste Manag.* **2012**, *32*, 1186–1195. [CrossRef] [PubMed]
17. De Andrés, J.M.; Roche, E.; Narros, A.; Rodríguez, M.E. Characterisation of tar from sewage sludge gasification. Influence of gasifying conditions: Temperature, throughput, steam and use of primary catalysts. *Fuel* **2016**, *180*, 116–126. [CrossRef]
18. Morgano, M.T.; Leibold, H.; Richter, F.; Stapf, D.; Seifert, H. Screw pyrolysis technology for sewage sludge treatment. *Waste Manag.* **2018**, *73*, 487–495. [CrossRef]
19. Lee, U.; Dong, J.; Chung, J. Experimental investigation of sewage sludge solid waste conversion to syngas using high temperature steam gasification. *Energy Convers. Manag.* **2018**, *158*, 430–436. [CrossRef]
20. Chen, S.; Sun, Z.; Zhang, Q.; Hu, J.; Xiang, W. Steam gasification of sewage sludge with CaO as CO 2 sorbent for hydrogen-rich syngas production. *Biomass Bioenergy* **2017**, *107*, 52–62. [CrossRef]
21. Barisano, D.; Canneto, G.; Nanna, F.; Alvino, E.; Pinto, G.; Villone, A.; Carnevale, M.; Valerio, V.; Battafarano, A.; Braccio, G. Steam/oxygen biomass gasification at pilot scale in an internally circulating bubbling fluidized bed reactor. *Fuel Process. Technol.* **2016**, *141*, 74–81. [CrossRef]
22. Gil, J.; Aznar, M.P.; Caballero, M.A.; Francés, E.; Corella, J. Biomass Gasification in Fluidized Bed at Pilot Scale with Steam−Oxygen Mixtures. Product Distribution for Very Different Operating Conditions. *Energy Fuels* **1997**, *11*, 1109–1118. [CrossRef]
23. Berrueco, C.; Recari, J.; Güell, B.M.; Del Alamo, G. Pressurized gasification of torrefied woody biomass in a lab scale fluidized bed. *Energy* **2014**, *70*, 68–78. [CrossRef]
24. Berrueco, C.; Montane, D.; Güell, B.M.; Del Alamo, G. Effect of temperature and dolomite on tar formation during gasification of torrefied biomass in a pressurized fluidized bed. *Energy* **2014**, *66*, 849–859. [CrossRef]
25. Bengtsson, S. VVBGC demonstration plant activities at Värnamo. *Biomass Bioenergy* **2011**, *35*, S16–S20. [CrossRef]
26. Koljonen, J.; Kurkela, E.; Wilén, C. Peat-based HTW-plant at Oulu. *Bioresour. Technol.* **1993**, *46*, 95–101. [CrossRef]
27. Meng, X.; De Jong, W.; Fu, N.; Verkooijen, A.H. Biomass gasification in a 100 kWth steam-oxygen blown circulating fluidized bed gasifier: Effects of operational conditions on product gas distribution and tar formation. *Biomass Bioenergy* **2011**, *35*, 2910–2924. [CrossRef]
28. Abdoulmoumine, N.; Adhikari, S.; Kulkarni, A.; Chattanathan, S.A. A review on biomass gasification syngas cleanup. *Appl. Energy* **2015**, *155*, 294–307. [CrossRef]
29. Göransson, K.; Söderlind, U.; He, J.; Zhang, W. Review of syngas production via biomass DFBGs. *Renew. Sustain. Energy Rev.* **2011**, *15*, 482–492. [CrossRef]
30. Stevens, D.J. *Hot Gas. Conditioning: Recent Progress with Larger-Scale Biomass Gasification Systems; Update and Summary of Recent Progress*; NREL: Golden, CO, USA, 2001.
31. Dou, B.; Wang, C.; Chen, H.; Song, Y.; Xie, B.; Xu, Y.; Tan, C. Research progress of hot gas filtration, desulphurization and HCl removal in coal-derived fuel gas: A review. *Chem. Eng. Res. Des.* **2012**, *90*, 1901–1917. [CrossRef]
32. De Andrés, J.M.; Narros, A.; Rodríguez, M.E. Behaviour of dolomite, olivine and alumina as primary catalysts in air–steam gasification of sewage sludge. *Fuel* **2011**, *90*, 521–527. [CrossRef]
33. Abu El-Rub, Z.; Bramer, E.A.; Brem, G. Review of Catalysts for Tar Elimination in Biomass Gasification Processes. *Ind. Eng. Chem. Res.* **2004**, *43*, 6911–6919. [CrossRef]
34. Husmann, M.; Zuber, C.; Maitz, V.; Kienberger, T.; Hochenauer, C. Comparison of dolomite and lime as sorbents for in-situ H2S removal with respect to gasification parameters in biomass gasification. *Fuel* **2016**, *181*, 131–138. [CrossRef]
35. Meng, X.; De Jong, W.; Pal, R.; Verkooijen, A.H. In bed and downstream hot gas desulphurization during solid fuel gasification: A review. *Fuel Process. Technol.* **2010**, *91*, 964–981. [CrossRef]
36. Schmid, M.; Hafner, S.; Biollaz; Schneebeli, J.; Waizmann, G.; Scheffknecht, G. Steam-oxygen gasification of sewage sludge: Reduction of tar, H2S and COS with limestone as bed additive. *Biomass Bioenergy* **2021**. in review.

37. Syed-Hassan, S.S.A.; Wang, Y.; Hu, S.; Su, S.; Xiang, J. Thermochemical processing of sewage sludge to energy and fuel: Fundamentals, challenges and considerations. *Renew. Sustain. Energy Rev.* **2017**, *80*, 888–913. [CrossRef]
38. Fachbereich Umweltmesstechnik. *Stationary Source Emissions—Measurement of Ammonia (and Gaseous Ammonium Compounds)—Manual Method*; Technical Report for Verein Deutscher Ingenieure; Verein Deutscher Ingenieure: Düsseldorf, Germany, September 2017.
39. *Biomass Gasification—Tar and Particles in Product Gases—Sampling and Analysis*; Technical Report for BSI; BSI: London, UK, March 2007.
40. Kiel, J.H.A.; Paasen, S.V.B. *Tar Formation in a Fluidised-Bed Gasifier*; Energy Research Centre of the Netherlands: Petten, The Netherlands, 2001; Volume 1, pp. 1–58.
41. Neubert, M.; Reil, S.; Wolff, M.; Pöcher, D.; Stork, H.; Ultsch, C.; Meiler, M.; Messer, J.; Kinzler, L.; Dillig, M.; et al. Experimental comparison of solid phase adsorption (SPA), activated carbon test tubes and tar protocol (DIN CEN/TS 15439) for tar analysis of biomass derived syngas. *Biomass Bioenergy* **2017**, *105*, 443–452. [CrossRef]
42. Wang, L.; Skjevrak, G.; Hustad, J.E.; Grønli, M.G. Sintering characteristics of sewage sludge ashes at elevated temperatures. *Fuel Process. Technol.* **2012**, *96*, 88–97. [CrossRef]
43. Husmann, M.; Müller, M.; Zuber, C.; Kienberger, T.; Maitz, V.; Hochenauer, C. Application of BaO-Based Sulfur Sorbent for in Situ Desulfurization of Biomass-Derived Syngas. *Energy Fuels* **2016**, *30*, 6458–6466. [CrossRef]
44. Delgado, J.; Aznar, M.P.; Corella, J. Calcined Dolomite, Magnesite, and Calcite for Cleaning Hot Gas from a Fluidized Bed Biomass Gasifier with Steam: Life and Usefulness. *Ind. Eng. Chem. Res.* **1996**, *35*, 3637–3643. [CrossRef]
45. Al-Otoom, A.Y.; Ninomiya, Y.; Moghtaderi, B.; Wall, T.F. Coal Ash Buildup on Ceramic Filters in a Hot Gas Filtration System. *Energy Fuels* **2003**, *17*, 316–320. [CrossRef]
46. Bale, C.; Bélisle, E.; Chartrand, P.; Decterov, S.; Eriksson, G.; Hack, K.; Jung, I.-H.; Kang, Y.-B.; Melançon, J.; Pelton, A.; et al. FactSage thermochemical software and databases—recent developments. *Calphad* **2009**, *33*, 295–311. [CrossRef]
47. Ruoppolo, G.; Miccio, F.; Brachi, P.; Picarelli, A.; Chirone, R. Fluidized Bed Gasification of Biomass and Biomass/Coal Pellets in Oxygen and Steam Atmosphere. *Chem. Eng. Trans.* **2013**, *32*, 595–600. [CrossRef]
48. Choi, Y.-K.; Cho, M.-H.; Kim, J.-S. Steam/oxygen gasification of dried sewage sludge in a two-stage gasifier: Effects of the steam to fuel ratio and ash of the activated carbon on the production of hydrogen and tar removal. *Energy* **2015**, *91*, 160–167. [CrossRef]
49. Sandeep, K.; Dasappa, S. Oxy-steam gasification of biomass for hydrogen rich syngas production using downdraft reactor configuration. *Int. J. Energy Res.* **2013**, *38*, 174–188. [CrossRef]
50. Xiao, R.; Zhang, M.; Jin, B.; Huang, Y.; Zhou, H. High-Temperature Air/Steam-Blown Gasification of Coal in a Pressurized Spout-Fluid Bed. *Energy Fuels* **2006**, *20*, 715–720. [CrossRef]
51. Guo, S.; Wei, X.; Li, J.; Che, D.; Liu, H.; Sun, B.; Wang, Q. Experimental Study on Product Gas and Tar Removal in Air–Steam Gasification of Corn Straw in a Bench-Scale Internally Circulating Fluidized Bed. *Energy Fuels* **2020**, *34*, 1908–1917. [CrossRef]
52. Schweitzer, D.; Gredinger, A.; Schmid, M.; Waizmann, G.; Beirow, M.; Spörl, R.; Scheffknecht, G. Steam gasification of wood pellets, sewage sludge and manure: Gasification performance and concentration of impurities. *Biomass Bioenergy* **2018**, *111*, 308–319. [CrossRef]
53. Molino, A.; Iovane, P.; Donatelli, A.; Braccio, G.; Chianese, S.; Musmarra, D. Steam Gasification of Refuse-Derived Fuel in a Rotary Kiln Pilot Plant: Experimental Tests. *Chem. Eng. Trans.* **2013**, *32*, 337–342. [CrossRef]
54. Chianese, S.; Fail, S.; Binder, M.; Rauch, R.; Hofbauer, H.; Molino, A.; Blasi, A.; Musmarra, D. Experimental investigations of hydrogen production from CO catalytic conversion of tar rich syngas by biomass gasification. *Catal. Today* **2016**, *277*, 182–191. [CrossRef]
55. Milne, T.A.; Evans, R.J.; Abatzaglou, N. Biomass Gasifier "Tars": Their Nature, Formation, and Conversion. *INIS* **1998**, *1*, 33052766.
56. Poboss, N. Experimental investigation of the absorption enhanced reforming of biomass in a 20 kWth dual fluidized bed system. *Int. J. Thermodyn.* **2012**, *15*. [CrossRef]
57. Wolfesberger, U.; Aigner, I.; Hofbauer, H. Tar content and composition in producer gas of fluidized bed gasification of wood-Influence of temperature and pressure. *Environ. Prog. Sustain. Energy* **2009**, *28*, 372–379. [CrossRef]
58. Pfeifer, C.; Koppatz, S.; Hofbauer, H. Steam gasification of various feedstocks at a dual fluidised bed gasifier: Impacts of operation conditions and bed materials. *Biomass Convers. Biorefinery* **2011**, *1*, 39–53. [CrossRef]
59. Fuchs, J.; Schmid, J.C.; Müller, S.; Mauerhofer, A.M.; Benedikt, F.; Hofbauer, H. The impact of gasification temperature on the process characteristics of sorption enhanced reforming of biomass. *Biomass Convers. Biorefinery* **2020**, *10*, 925–936. [CrossRef]
60. Poboss, N. Experimentelle Untersuchung der sorptionsunterstützten Reformierung. Ph.D. Thesis, University of Stuttgart, Stuttgart, Germany, 2016. Available online: http://elib.uni-stuttgart.de/bitstream/11682/8873/1/Dissertation_Norman_Poboss.pdf (accessed on 2 April 2020).
61. Hafner, S.; Schmid, M.; Spörl, R.; Scheffknecht, G. Experimental Investigation of the Sorption Enhanced Gasification of Biomass in a Dual Fluidized Bed Pilot Plant. In Proceedings of the 27th European Biomass Conference (EUBCE), Lisbon, Portugal, 27–30 May 2019.
62. Kopf SynGas GmbH & Co. KG. Klärschlammverwertung: Nachhaltige Phosphornutzung aus Vergasungsaschen. Available online: https://suelzle-kopf.de/wp-content/uploads/sites/3/2018/07/aschenutzung-phosphor-suelzle-kopf-syngas.pdf (accessed on 5 January 2021).

63. De Jong, W.; Andries, J.; Hein, K.R. Coal/biomass co-gasification in a pressurised fluidised bed reactor. *Renew. Energy* **1999**, *16*, 1110–1113. [CrossRef]
64. Hongrapipat, J.; Saw, W.-L.; Pang, S. Removal of ammonia from producer gas in biomass gasification: Integration of gasification optimisation and hot catalytic gas cleaning. *Biomass Convers. Biorefinery* **2012**, *2*, 327–348. [CrossRef]
65. Kopf SynGas GmbH & Co. KG. Klärschlammverwertung. Umweltfreundlich. Wirtschaftlich. Zukunfstsweisend. Available online: https://suelzle-kopf.de/wp-content/uploads/sites/3/2017/07/15-11_Imagebrosch%c3%bcre_S%c3%bclzle_Kopf_SynGas.pdf (accessed on 2 April 2020).
66. DüMV. Verordnung über das Inverkehrbringen von Düngemitteln, Bodenhilfsstoffen, Kultursubstraten und Pflanzenhilfsmitteln (Düngemittelverordnung—DüMV). Available online: https://www.gesetze-im-internet.de/d_mv_2012/D%C3%BCMV.pdf. (accessed on 5 January 2021).
67. AbklärV. Verordnung über die Verwertung von Klärschlamm,Klärschlammgemisch und Klärschlammkompost(Klärschlammverordnung—AbfKlärV). Available online: https://www.gesetze-im-internet.de/abfkl_rv_2017/AbfKl%C3%A4rV.pdf. (accessed on 5 January 2021).

applied sciences

MDPI

Article

Evaluation of Waste Blends with Sewage Sludge as a Potential Material Input for Pyrolysis

Lenka Kubonova [1], Iva Janakova [2,*], Petra Malikova [2], Silvie Drabinova [2], Milan Dej [1], Roman Smelik [2], Pavel Skalny [3] and Silvie Heviankova [2]

[1] Energy Research Center, VSB-Technical University of Ostrava, 17. listopadu 2172/15, 70800 Ostrava, Czech Republic; lenka.kubonova@vsb.cz (L.K.); milan.dej@vsb.cz (M.D.)
[2] Faculty of Mining and Geology, VSB-Technical University of Ostrava, 17. listopadu 2172/15, 70800 Ostrava, Czech Republic; petra.malikova@vsb.cz (P.M.); silvie.drabinova@vsb.cz (S.D.); roman.smelik.st@vsb.cz (R.S.); silvie.heviankova@vsb.cz (S.H.)
[3] Faculty of Mechanical Engineering, VSB-Technical University of Ostrava, 17. listopadu 2172/15, 70800 Ostrava, Czech Republic; pavel.skalny@vsb.cz
* Correspondence: iva.janakova@vsb.cz; Tel.: +420-596-993-575

Abstract: In line with the requirements of the circular economy, the European Union's waste management legislative changes also concern the treatment of sewage sludge. Although sewage sludge production cannot be prevented, its quantities may be reduced by the synergetic effect of energy recovery via choosing a proper technology. Sewage sludge is difficult to apply as fuel alone, because of its high moisture and ash content. However, its energy use will be increased by adding suitable waste materials (different types of plastics, waste tires and paper rejects). Most recently, the thermal utilization of sewage sludge via incineration or pyrolysis has grown in importance. This article describes the fuel parameters of particular waste materials and of their blends with sewage sludge in connection with laboratory-scale thermal decomposition in an inert atmosphere, for their potential use in a semi-pilot plant pyrolysis unit. For pyrolytic application, the results of thermogravimetric analysis are needed in order to know the maximal temperature of thermal decomposition in an inert atmosphere, maximal mass losses, and weight loss rates. The samples of different thermoplastics mixed with sewage sludge, and low-density polyethylene blends with sewage sludge, had the lowest residual masses (70–74%) and the highest weight loss rates (11–19%/min). On the other hand, the blend of polyester rejects from tire processing, paper rejects and sewage sludge had the second highest residual mass (60%) and the lowest weight loss rate (3%/min).

Keywords: sewage sludge; plastics; waste blends; thermogravimetric analysis; pyrolysis

Citation: Kubonova, L.; Janakova, I.; Malikova, P.; Drabinova, S.; Dej, M.; Smelik, R.; Skalny, P.; Heviankova, S. Evaluation of Waste Blends with Sewage Sludge as a Potential Material Input for Pyrolysis. *Appl. Sci.* **2021**, *11*, 1610. https://doi.org/10.3390/app11041610

Academic Editor: Falah Alobaid

Received: 13 January 2021
Accepted: 5 February 2021
Published: 10 February 2021

1. Introduction

The large quantities of waste and waste packaging produced by consumer society are a risk factor for both human health and ecosystems. During waste production and its disposal, secondary substances may escape into the environment, the constituents of which may be contaminated. The substances contained in waste and packaging can enter the human body through the food chain, and thus negatively affect human health [1,2].

In the Czech Republic (an EU country with 10 million inhabitants), the annual production of corporate waste has been around 22 million tons. In terms of the origin of this waste, a constant trend can be observed in the increasing production of waste particularly by companies engaged in the treatment, collection, and processing of industrial or municipal waste. This includes waste from municipal waste treatment facilities and wastewater treatment plants (so-called secondary waste). However, these materials are not perceived as waste only, but represent secondary raw materials due to their energy potential. At present, the key waste management trend is to move towards a circular economy [3], product reuse, recycling, and the conversion of waste to energy [4], instead of mining

and the additional landfills that lead to the issue of land scarcity [4,5]. Beside the EU waste policies that restrict landfilling (99/31/EC on the landfill of waste) while promoting waste prevention, minimization, and recycling, legislation also focuses on the treatment of sewage sludge—91/271/EEC on urban waste water treatment, and 86/278/EEC on the use of sewage sludge in agriculture [6–8].

Sewage sludge (SS) is an unavoidable waste arising in connection with wastewater treatment. In the EU, the production of SS dry matter per capita is estimated to be 90 g per day [9], meaning that the current annual production of sewage sludge dry matter exceeds 12 million tons. It can be expected that with a growth in the population, and pressures on the construction of new wastewater treatment plants (WWTPs), the production of SS will soar. The development of SS production in tons of dry matter in the Czech Republic, and a comparison of the development in SS disposal in a percentage ratio, in the years 2009–2018 are shown in Figure 1 below.

While a similar trend has been observed in several other EU countries due to stricter registrations or new regulations, Figure 1 implies that the total production of SS in the Czech Republic is growing. As a counter-measure, most SS has been applied directly, particularly in land reclamation projects. On the other hand, the quantities of composted SS are likely to continue to fall due to the stricter requirement for compost sanitization. Most recently, the "thermal utilization" of SS from WWTPs via incineration or pyrolysis has grown in importance, and this area is expanding due to the currently tightening legislation. Pyrolysis is considered advantageous for the decomposition of organic pollutants, the neutralization of pathogens, the reduction of waste, the application for a wide range of products, and significant energy recovery [10].

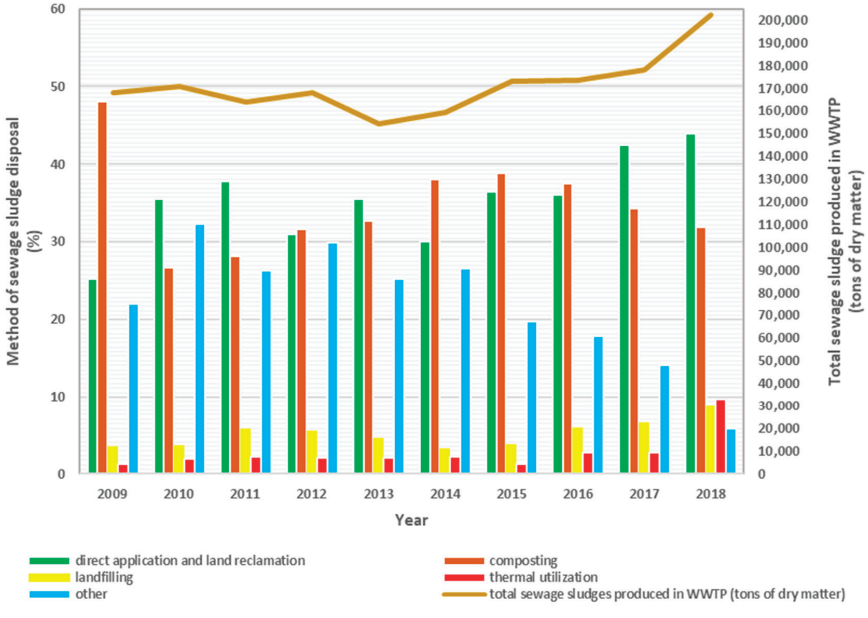

Figure 1. Proportional comparison of sewage sludge disposal in the Czech Republic in the years 2009–2018, modified according to [11].

Referring back to the circular economy principle, and trends for reducing waste, it must be emphasized that the formation of SS cannot be prevented. Besides excess biomass from biological treatment, SS contains heavy metals and drug residues. Research is heading towards solutions regarding the choice of SS disposal technologies to reduce its quantity, while maximizing its energy potential [12]. However, this shows that SS is difficult to use

on its own as fuel, due to its high moisture content [13–15]. After dewatering (depending on the equipment used—filter presses, centrifuges, etc.), the SS dry matter can range from 15 to 32 wt. %. The calorific value of such SS is very low. The calorific value of dried SS is comparable to brown coal or wood biomass in terms of energy content [16–18]. The low heating value of SS dry matter is 17–18 MJ/kg for raw SS, 14–16 MJ/kg for activated SS, and 8–12 MJ/kg for stabilized SS [19].

Therefore, we assume that with mixing SS with other waste materials (various types of plastics, waste tires, and paper rejects), the energy use of SS will increase. When preparing alternative fuels via the synergetic disposal of waste, it is advisable to concentrate on the disposal of waste occurring in large quantities, as well as to select waste materials originating close to the source, so as to eliminate transportation, storage, and handling costs. Further, indicative calorific values of the original waste products are summarized.

Plastic waste can be converted into valuable fuels [20,21]. Plastics meet the requirement of widely used packaging materials. These materials are also suitable for handling and transport, and their material properties allow for easy molding. Plastics are polymeric substances that can be divided into two main types. First, those that soften when heated are called thermoplastics, which account for 80% of plastics currently in production, e.g., high-density polyethylene (HDPE), low-density polyethylene (LDPE), polyethylene terephthalate (PET), polypropylene (PP). The second type of plastics that harden when heated are called thermosets [22]. In terms of energy potential, the high heating value of plastics is 46.5 and 44 MJ/kg for PE and PP respectively, and 22.8 MJ/kg for polyester (PES) fibers [23,24].

The remaining waste materials used for the experiments were used tires and paper rejects. Used tires account for a significant share of all rubber waste. The high heating value of tires is similar to that of black coal (30 MJ/kg) [25]. The paper and pulp industries create large amounts of solid waste and wastewater that have to be treated. The methods for converting paper mill waste into energy are discussed [26]. As for the energy potential of paper, its low heating value is 14.11 MJ/kg [27].

It is necessary to find technical solutions that will enable the efficient management of the described waste in order to reduce environmental pollution and meet the requirements of the circular economy [28]. One of the technologies available to deal with these types of waste is pyrolysis. A number of articles have focused on the co-pyrolysis of sewage sludge with other types of feedstocks, such as agricultural waste [29,30], wood waste [31] or lignite [32]. The aim of this article is to describe the energy parameters and simulate the thermal decomposition at the laboratory scale of individual waste materials and novel blends (i.e., different types of waste plastics, paper rejects and polyester waste from tire processing) with SS in an inert atmosphere. This research is important for learning about the discrete processes taking place during pyrolysis, and how the composition of different waste blends changes. Appropriately selected waste blends will be further tested in a semi-pilot plant pyrolysis unit for their energy recovery.

2. Materials and Methods

2.1. Description and Physical Appearance of Input Waste

The photographs of all samples, i.e., raw sewage sludge and input waste, are shown in Figure 2. The description and physical appearance of the input waste are as follows:

- 1, 2—SS—sewage sludge from the municipal wastewater treatment plant, which is anaerobically stabilized, blackish-brown in color, lumpy, with an earthy odor, and very wet. The projected WWTP capacity is 207,000 PT (population total), and HRT (hydraulic retention time) is in the range of 26–32 days depending on temperature;
- 3—LDPE—recycled LDPE from separated collection and sorting lines. This material was wet during processing. It is a flexible (even soft) material, but it is also tough and hard to grind;
- 4—TP—a mixture of crushed sorted hard thermoplastics. Colored materials (mixture of PP and PE) have a low weight, are tenacious and strong, and are easy to grind;

- 5—RDF—polyethylene foils, bags and sorted municipal solid waste (MSW) without PET and hardened plastics. This material was rather wet, contained impurities (clay etc.) and was hard to grind due to its consistency;
- 6—PES—polyester waste (PES) from tire processing contains crushed pieces of tire (styrene–butadiene rubber) and PES textile fiber in the form of small fluffy clumps up to 20 mm in size. It is a loose, non-sticky material that is easy to handle and has a grey color;
- 7—PR—paper rejects with a composition of paper and plastic in the ratio of 50:50. It consists of small plastic particles and paper pulp (cellulose). These fibers are simply bonded under pressure to form solid shapes, and have medium humidity and a light brown color.

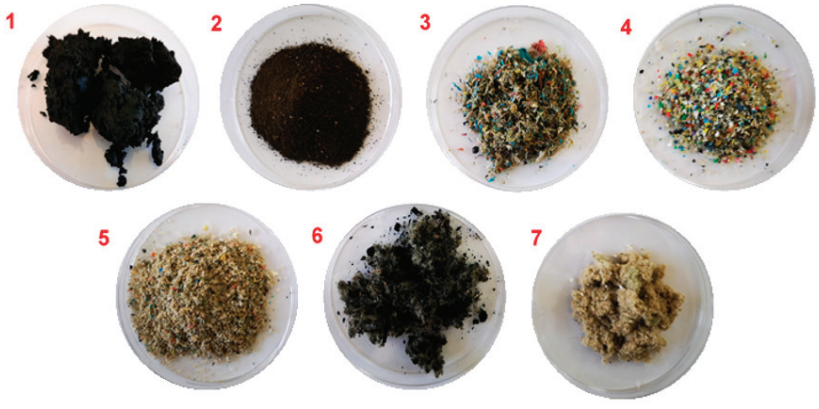

Figure 2. Consistency of 1—raw SS (moisture 72 wt. %) and visualization of waste inputs: 2—dry SS (sewage sludge), 3—LDPE (low-density polyethylene), 4—TP (thermoplastics (non-specified)), 5—RDF (residual derived fuel), 6—PES (polyester), 7—PR (paper rejects).

2.2. Waste Blends Preparation

Six waste materials were selected for experimental tests. The high and low heating values were measured for each waste blend (55 in total). These values were key parameters for the selection of suitable waste blends for the further study of thermochemical conversion processes. Information on the average dry matter or moisture and bulk density of selected waste materials is summarized in Table S1. Specifically, these were sewage sludge from a public wastewater treatment plant (SS), low-density polyethylene rejects (LDPE), non-specified thermoplastics (TP), solid residual fuel (RDF), polyester rejects from tire processing (PES), and paper rejects (PR). All the above parameters were measured according to the standards [33–35]. Except for SS, all materials were ground to a fraction <2 mm on a laboratory mill IKA MF 10 basic (IKA®-Werke GmbH & Co. KG, Staufen, Germany). From each of the individual materials, two and three mixtures were formed together with SS. In total, 55 waste blends in various volume ratios were prepared.

Because SS has an average moisture content of about 72 wt. %, this moisture level was an advantage for mixing with other types of waste. SS served as a binder for individual components. The first "binder tests" were aimed at forming granular mixtures being prepared in volume and weight ratios, respectively. After weighing the individual components of the mixtures, the waste blends were then mixed on a laboratory mixer HOBART—HSM 10 (HOBART GmbH, Offenburg, Germany). The blends were then spread on the surface and freely dried in the laboratory at room temperature for 1 week.

The dry matter or moisture of the blends were always measured after their preparation and after a week of drying. Then, gross and net calorific values and other parameters were determined. From 55 experimental blends, 8 blends were selected on the basis of the highest measured values of gross and net calorific values. In addition, 4 were double

blends and 4 were triple blends. The individual ratios, the combinations of waste materials, the moisture and dry matter, and the gross and net calorific values of selected mixtures are shown in Table S2.

The description and physical appearance of waste blends are shown in Figure 3.

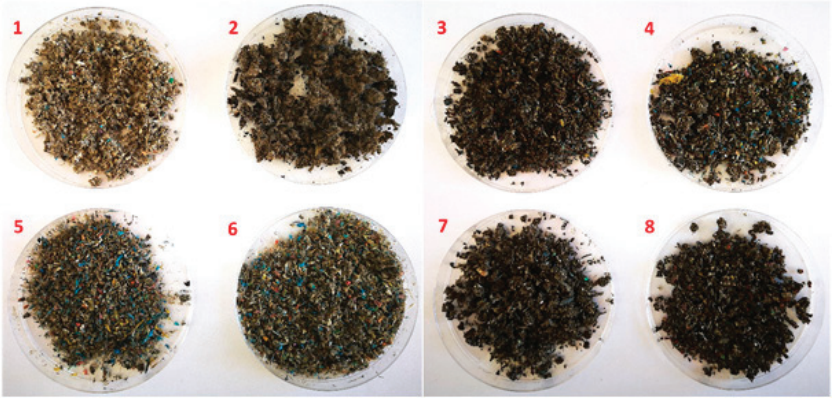

Figure 3. Visualization of 8 selected experimental waste blends (1—3RDF:SS:PR, 2—3PES:SS:PR, 3—4LDPE:SS, 4—4LDPE:2SS:PR, 5—6LDPE:SS, 6—3LDPE:SS:PR, 7—RDF:SS, 8—3TP:SS).

1. The 3RDF:SS:PR blend was light brown in color with a slight odor. The material was light.
2. The 3PES:SS:PR blend was grey with a slight odor. The material was not compact. It consisted of separate pieces of rubber and fluffy PES fibers mixed with sludge.
3. The 4LDPE:SS blend had a good structure. It was slightly damp. LDPE formed a compact mass with sewage sludge.
4. The 4LDPE:2SS:PR blend was well workable and was light black in color. It was slightly damp. Small pieces of LDPE can be seen in the mixture. LDPE formed a compact mass with sewage sludge.
5. The 6LDPE:SS blend was rather dry and did not form a compact mass. Due to the large proportion of LDPE, small colored pieces were visible in the mixture. The mixture was blackish brown in color with a musty smell.
6. The 3LDPE:SS:PR blend was rather dry and did not form a compact mass. The mixture was dark brown in color with a slight odor.
7. The RDF:SS blend was very moist with a strong odor. The mixture was hard to mix together. The individual grains stuck together and formed a lumpy structure.
8. The 3TP:SS blend was very moist with a slight specific odor. The discrete grains stuck together and formed a lumpy structure.

2.3. Analyses of Physical Properties

2.3.1. Proximate Analysis

The moisture, ash, fixed carbon and volatile matter were analyzed.

Total moisture: Raw samples (approximately 50 g) were dried at 105 °C in a laboratory dryer and weighed, and the moisture content was calculated [36].

Moisture of analytical samples: Analytical samples (2 × 1 g) were dried in glass weighing bottles in a laboratory dryer at 105 °C, then weighed, and moisture content was calculated [37].

Determination of ash content: Analytical samples (2 × 1 g) were annealed in ceramic dishes in a laboratory oven at 550 °C and weighed, and ash content was calculated. The content of combustible matter in the sample was calculated [38].

Determination of volatile combustible matter content: Analytical samples (2 × 1 g) were annealed in a crucible with a lid in a laboratory oven at 900 °C, then weighed, and volatile combustible matter content was calculated [39].

2.3.2. Ultimate Analysis

The carbon, hydrogen, nitrogen and sulfur in the samples were determined using an analyzer LECO CHN628 (LECO Corporation, St. Joseph, MI, USA) with the additional module 628 S (LECO Corporation, St. Joseph, MI, USA). The principle of C, H, and N determination is based on the combustion of the sample in an oxygen atmosphere at 950 °C, and then measuring the concentration of CO_2 and H_2O in the burned gases using the IR detector, and of N_2 using the thermal conductivity (TC) detector [40]. The sulfur is determined by burning the sample in an oxygen atmosphere at 1350 °C and measuring the SO_2 concentration in the burned gases using an IR detector [41]. The oxygen content in fuel was calculated, O^d = 100-ash^d-C^d-H^d-N^d-S^d (in percentage, ^{d} means in dry matter) [42].

2.3.3. High and Low Heating Values (HHV, LHV)

The gross calorific value (high heating value; HHV) of the fuels was determined by setting the calorimetry with the calorimeter LECO AC600 (LECO Corporation, St. Joseph, MI, USA) [43]. The principle of the method is based on the combustion of the sample in the form of a bomb of calorimeter, and measuring the increase in the temperature of the water bath with a calorimeter. The net calorific value (low heating value LHV) of the fuels was calculated.

2.4. Thermogravimetric Analysis

Thermogravimetric (TG) analysis was performed with the analyzer STA 449 F1 Jupiter (Netzsch-Gerätebau GmbH, Selb, Germany). The TG conditions were 30–1000 °C, 10 °C/min, 100 mL/min N_2 (50 mL/min purge + 50 mL/min protective), and isotherm at 1000 °C for 15 min (20 ml/min O_2 + 50 mL/min N_2 protective). An Al_2O_3 crucible was used for a sample mass of 20–21 mg. TG analysis was used to determine the maximum temperature before constant weight loss, and to determine the maximum weight loss as information for the further pyrolysis treatment of waste blends.

2.5. Statistical Analysis

Statistical analysis was carried out using the *MATLAB*® software. Kruskal–Wallis tests, Dunn's test, Shapiro–Wilk test and Levene's test were performed.

3. Results and Discussion

3.1. Analysis of Input Waste

The analytical results of input waste are summarized in Table S1. Bulk density was an important parameter in waste blend preparation. The plastics, paper rejects and tire waste ash yields were much lower than that of the sewage sludge (49 wt. %). Typical raw sewage sludge has a high moisture content, in our case 72 wt. %, but the samples were analyzed after drying. The SS had a low carbon content (approximately 28 wt. % in dry matter), and a high oxygen content. There were relatively high values for nitrogen and sulfur in SS. The nitrogen in SS has its origin in the microorganisms used for water purification. The sewage sludge is characterized by a much lower HHV than other waste inputs, because of the higher inorganic content and because of the high oxygen content. The composition of SS differs within the literature; however, the authors of Refs. [44,45], for instance, showed comparable values for the chemical composition of sewage sludge.

A higher ash content and lower HHV means less efficient fuel [46]. In Figure 4, the highest ash content and the lowest HHV were determined for SS; on the other hand, RDF has the lowest ash content and the second highest HHV. Mixing the plastics with SS may improve the characteristics of oil and char derived from pyrolytic treatment [10].

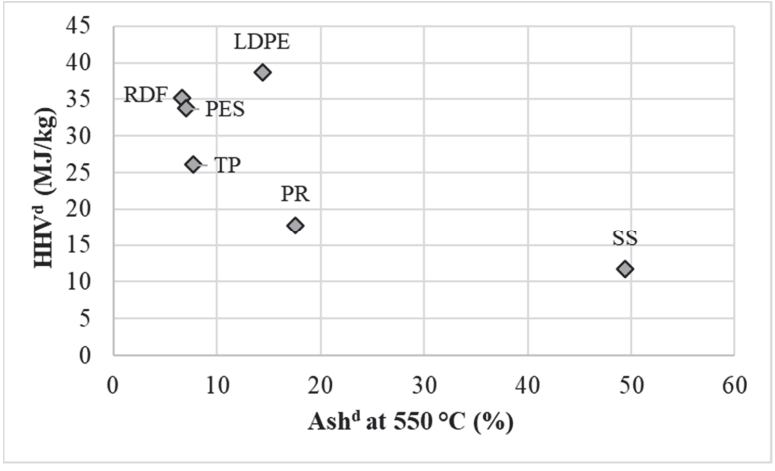

Figure 4. The HHV^d (MJ/kg) and ash^d at 550 °C (%), ^{d} means in dry matter.

Certain studied plastics, such as RDF, TP and LDPE, have higher volatile matter and weight loss than PR, PES and SS, so there is more chance of the decomposition of volatile matter, and in turn high oil and gas yields (Figure 5) [10].

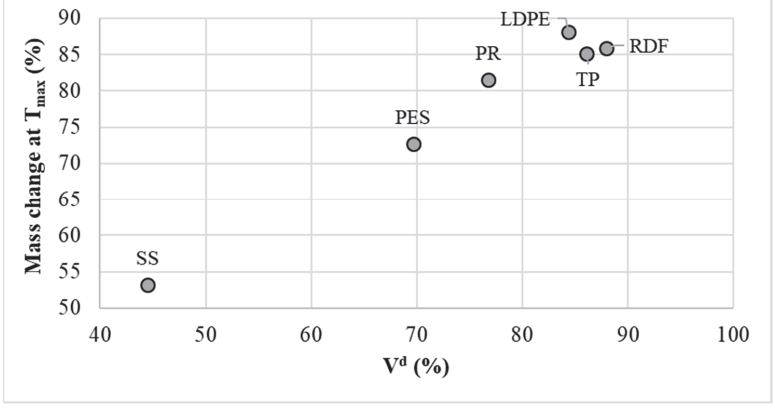

Figure 5. Mass change at T_{max} (%) from TGA and volatile matter V^d (%).

It is apparent from Figure 6 that the combustible matter of SS is the lowest in quantity, while the highest amount of combustible matter with the highest C/H ratio is in TP and PES. The C/H ratio in biomass affects the yields of char, tar, and gas [47]. A higher C/H content means a higher production of char and a lower production of tar, and the opposite holds for lower C/H content. A comparison with pyrolytic products is the aim of future investigations.

3.2. Composition of Waste Blends and Results of Physical Properties of Waste Blends

The compositions of the selected and further-tested waste blends are summarized in Table S2. The results of the proximate and ultimate analyses, and high and low heating values, are shown herein. The International Solid Waste Association set a guideline that specifies that the average LHV of waste should be at least 7 MJ/kg, so that it can be used as an energy source in the pyrolysis process [48]. For all waste blends, the LHV was above this level, and was higher than the LHV of SS (Figure 7).

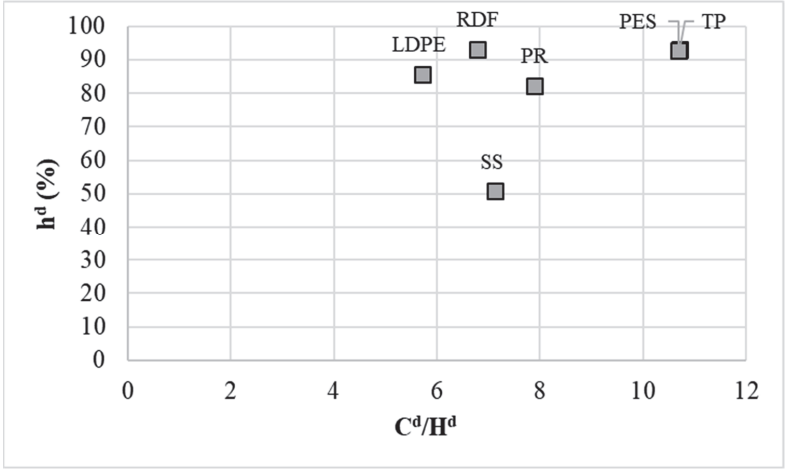

Figure 6. Combustible matter h^d (%) and the ratio C^d/H^d, ^{d} means in dry matter.

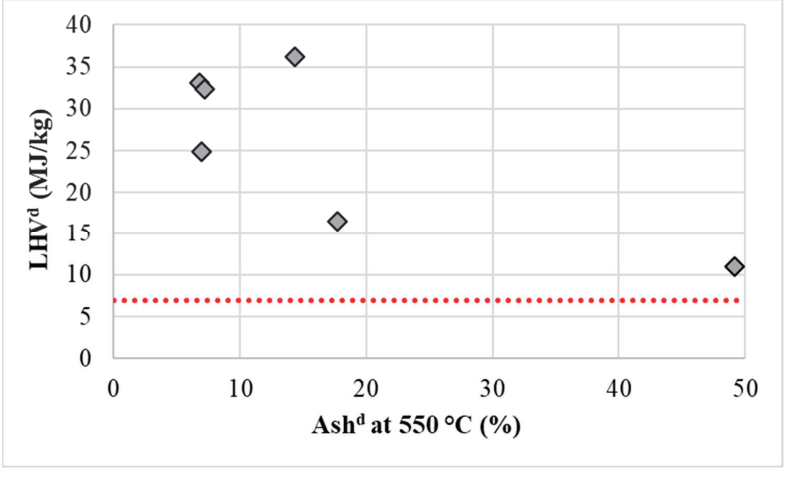

Figure 7. The LHV^d (MJ/kg) and ash^d at 550 °C (%).

3.3. Thermogravimetric Analysis of Wastes and Their Blends

TG analysis was performed for the determination of the minimal temperature for the maximal yield of pyrolysis products, and the maximal mass losses of wastes and their blends.

3.3.1. Input Materials

For all samples, a typical weight loss up to approx. 100 °C is associated with the removal of water from the sample during its pyrolysis decomposition. The highest decrease is seen for the sample of sewage sludge and paper rejects, which is related to the high moisture content (Table S1). The results for the TGA/DTG of the input waste materials are shown in Table 1, and the TG curves of the input waste materials are shown in Figure 8. The temperatures of maximum weight loss in the TGA experiments for the input waste materials are shown in Figure S1.

Table 1. Results of TGA/DTG for the input waste materials.

Inlet Material	Tmax	Mass Change at Tmax	T1	Weight Loss Rate at T1
	°C	%	°C	%/min
LDPE	998.9	88.09	479.9	26.98
RDF	999.0	85.85	469.1	11.73
TP	998.8	85.13	429.3	13.77
PR	998.9	81.55	348.1	11.85
PES	998.8	72.66	378.6	6.16
SS	998.9	53.19	325.2	1.62

Note: T1 is the temperature of highest mass loss determined from the DTG curves.

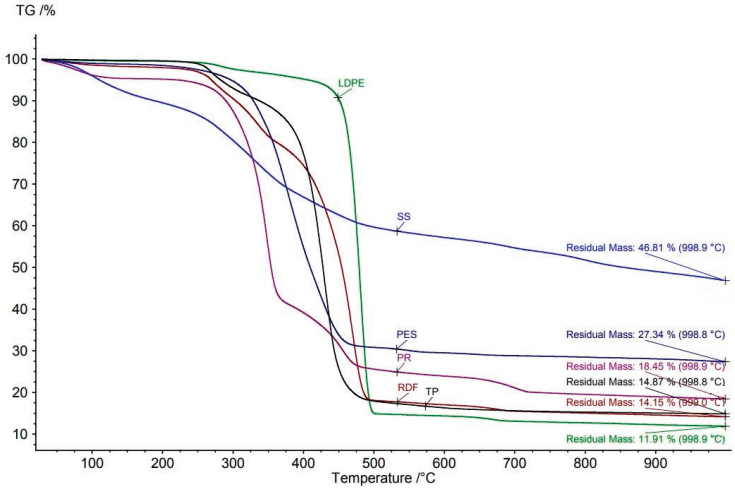

Figure 8. TG curves of input waste materials.

Sewage Sludge

For the sample of SS, (1) the first interval of decomposition was between 100 and 200 °C, which is related to the decomposition of sewage sludge components (biodegradable organic material and bacterial matter); (2) the second interval was between 200 and 520 °C, which related to the decomposition of organic matter (hydrocarbons between 200 and 390 °C, proteins, sugars, aliphatic compounds of SS between 390 and 520 °C); (3) at temperatures above 520 °C, the volatile matter evaporates from the carbon residue (secondary pyrolysis), and weight loss associated with organic matter may continue up to 600 °C; (4) at temperatures above 600 °C, inorganic material (e.g., CaCO3, ash in SS) decomposes [10,49]. As described in a recent review [10], there is a difference in the pyrolysis product (tar and char) yields under fast and slow pyrolysis. Slow pyrolysis generally leads to higher char yield and lower tar yield than fast pyrolysis.

Plastics

For all samples containing plastics, a weight loss of up to 500 °C is typical, which is associated with the pyrolysis decomposition of a particular plastic. The thermal degradation of plastics takes place via a chain mechanism—fission reactions involving serial and parallel reactions (individual reactions overlap) [50]. The thermal decomposition of plastics takes place in several steps: chain radical mechanism → initiation → H-abstraction → beta-scission → radical recombination [51].

Thermal decomposition is related to the chemical structure and complexity of the substance. PP decomposes at lower temperatures than HDPE due to tertiary carbons in the polymer structure, as described by [52]. In our experiments, the plastics decomposed in the

order PES > TP > LDPE, from lower to higher temperatures. LDPE and TP decomposed in a narrow temperature range. For pure plastics, there should be no carbon residue [53], which is not the case for our plastic materials.

The PES sample is characterized by the TG decomposition curve of tires [54], which decomposes at two temperatures (361 and 410 °C). The first step is attributed to the presence of natural rubber, while the second step to a blend of butadiene rubber with styrene-butadiene rubber [55].

Paper Rejects

For all samples containing paper waste, a typical weight loss appeared at a temperature of approx. 250–350 °C, which is not typical for pure plastics. This proportion is greater than the proportion of the thermal decomposition of plastics (approx. 350–470 °C) [56].

The residual mass was recorded in the order, from highest to lowest: SS > PES > PR > TP > RDF > LDPE. The weight loss rate (%/min) was recorded in the following order, from highest to lowest: LDPE > TP > PR > RDF > PES > SS. The mixing of sewage sludge with other waste is desirable, as the mass loss should increase, as well as the weight loss rate of the prepared waste blends.

The temperature and weight reproducibility of LDPE are shown in Figure S2.

3.3.2. Waste Blends

The results of the thermogravimetric analysis of waste blends are not comparable with those in the literature because they are unique and have not been reported. According to the authors' knowledge, the study of Zaker et al. [57] published the results of the co-pyrolysis of sewage sludge with LDPE. Therein, the samples containing 25%, 50% and 75% mass percentage of LDPE were tested. As is apparent, greater amounts of LDPE in the blend mean that the TG curve is similar to the pyrolysis behavior of LDPE, which was seen in our case. In the study of Hu et al. [58], the isothermal pyrolysis of polyethylene, paper towel and textiles, and their mixture in a ratio of 4:1:1, was carried out in a fixed bed reactor between 475 °C and 550 °C.

The TGA/DTG results of waste blends are summarized in Table 2. The temperatures of maximum weight losses in the thermal TGA experiments for waste blends are shown in Figure S3.

For all samples, a typical weight loss up to approx. 100 °C was associated with the removal of water from the samples during their pyrolysis decomposition.

Sewage Sludge

For all samples containing sewage sludge, a gradual weight loss is typical, with the greatest weight distribution up to 500 °C, and further thermal decomposition is visible at a temperature of 660–670 °C [54].

Plastics

For all samples containing plastics, a weight loss of up to 500 °C is typical and is associated with the pyrolysis decomposition of a particular plastic.

For the LDPE:SS samples (4:1 and 6:1), a TG curve of LDPE decomposition is typical [50,53] due to the higher content of LDPE in the samples; see Figure 9.

The shape of the TG curve is similar for RDF:SS and 3TP:SS samples (Figure 10). The pyrolysis decomposition of the plastic waste mixture prevails. For hardened plastics, pyrolysis decomposition occurs at lower temperatures (419 °C) than PE without hardened plastics (462 °C). The sample containing hard plastics (TP) shows a sharp drop in weight in a narrower temperature range than for the sample containing PE + RDF.

Paper Rejects

For all samples containing paper rejects, there is a typical weight loss in the temperature range of approx. 250–350 °C [56].

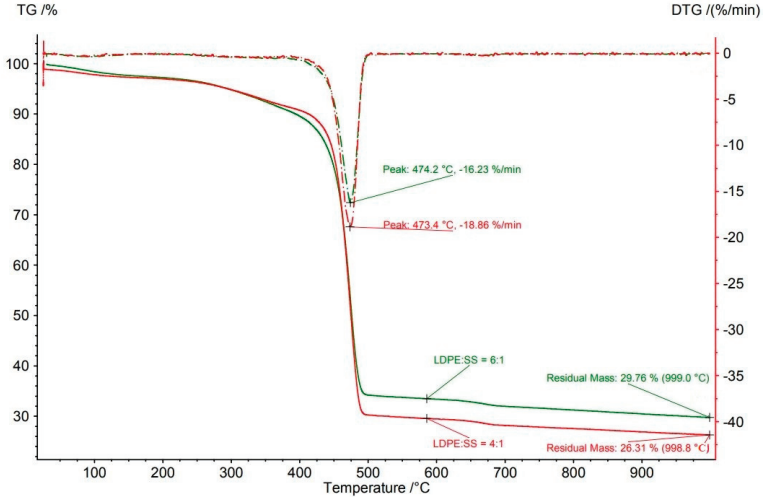

Figure 9. TG/DTG curves of LDPE:SS in 2 different volume ratios.

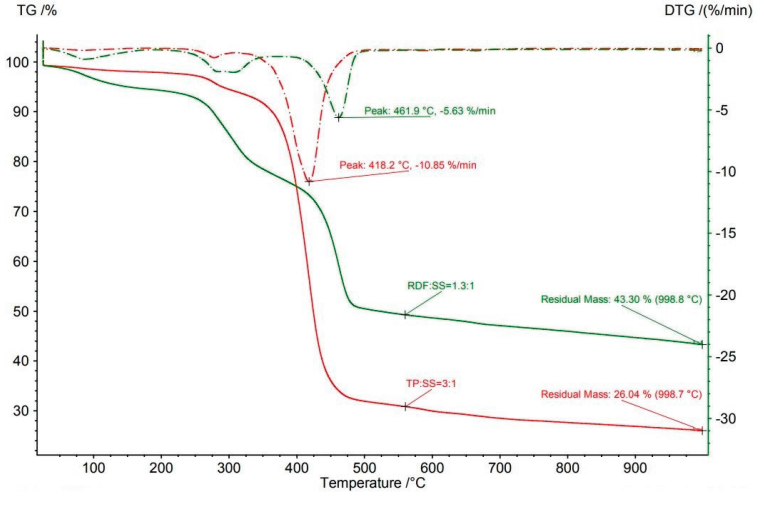

Figure 10. TG/DTG curves of RDF:SS and TP:SS in 2 different volume ratios.

The TG curves of the LDPE:SS:PR samples (3:1:1 and 4:2:1) are shown in Figure 11. The TG degradation of LDPE is dominant for these samples [50,53]. The course of the TG curves is similar, and the residual mass is very similar. Higher humidity was observed in the sample LDPE:SS:PR = 3:1:1 (greater mass loss up to 100 °C).

The TG curves for the PES:SS:PR and RDF:SS:PR samples are similar up to a temperature of approx. 300 °C (Figure 12). The sample containing PES decomposes at two temperatures for a temperature range of approx. 300–500 °C, while the RDF sample decomposes in a narrow temperature range of 400–500 °C.

The shape of the TG curve of 3RDF:SS:PR is similar to the 3LDPE:SS:PR sample (Figure 13). They also have similar weight losses at similar decomposition temperatures.

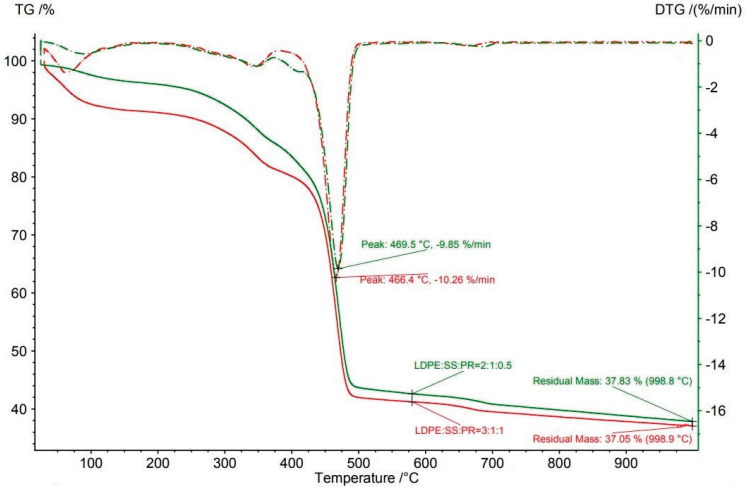

Figure 11. TG/DTG curves of LDPE:SS:PR in 2 different volume ratios.

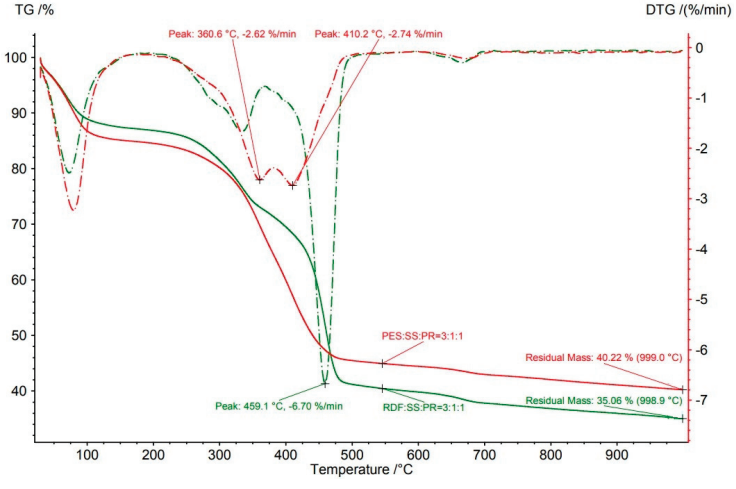

Figure 12. TG/DTG curves of PES:SS:PR and RDF:SS:PR in the same volume ratio.

Table 2. TGA/DTG results of waste blends.

Waste Blend	Volume Ratio	Tmax	Mass Change at Tmax	T1	Mass Change at T1	Weight Loss Rate at T1
		°C	%	°C	%	%/min
TP:SS	3:1	998.7	74.0	418.2	67.0	10.9
LDPE:SS	4:1	998.8	73.7	473.4	72.7	18.9
LDPE:SS	6:1	998.9	70.2	474.2	67.8	16.2
RDF:SS:PR	3:1:1	998.9	64.9	459.1	32.6	6.7
LDPE:SS:PR	3:1:1	998.9	63.0	466.4	39.4	10.3
LDPE:SS:PR	4:2:1	998.8	62.2	469.5	48.1	9.9
PES:SS:PR	3:1:1	999.0	59.8	360.6 *		2.6
PES:SS:PR	3:1:1	999.0	59.8	410.2 *	39.7	2.7
RDF:SS	1.3:1	998.8	56.7	461.9	31.7	5.6

Note: * Thermal decomposition within the range 250–500 °C occurred at two temperatures (Figure 13

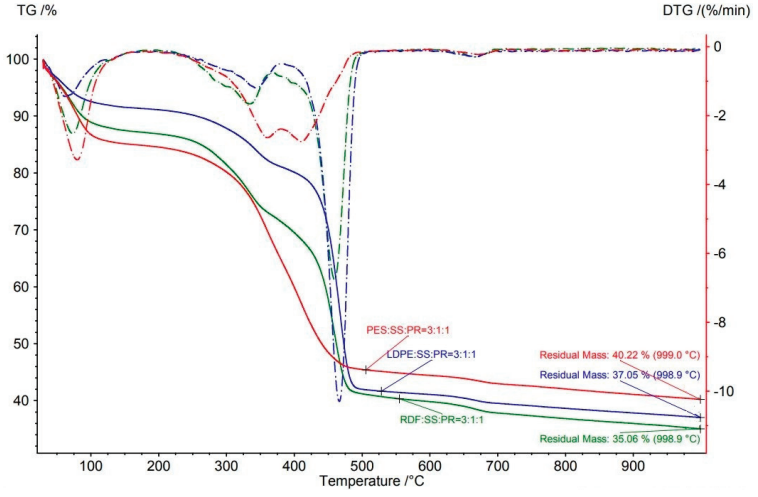

Figure 13. TG/DTG curves of RDF:SS:PR, LDPE:SS:PR and PES:SS:PR in the same volume ratios (3:1:1).

The weight loss rate (%/min) is highest in the order LDPE:SS > 3TP:SS > LDPE:SS:PR. The lowest weight loss rate is for 3PES:SS:PR. These values are important for comparison with future semi-pilot plant pyrolysis experiments.

3.3.3. Comparison of TG with Weight Loss at 900 °C (Gravimetric Analysis)

TGA showed that volatile matter was generally the most abundant component in the sludge blends. Volatile matter on a dry basis ranged from 54.1 wt. % to 73.8 wt. % for different sludge blends (Table S2). The volatile matter of input sewage sludge was 44.5 wt. %, which is a similar value for sewage sludge samples as was presented by Ref. [59].

The residual weight for the input waste materials at 900 °C from TGA was (from highest to lowest order): SS > PES > PR > TP > RDF > LDPE. The chemically simpler the substance, the lower the residual weight.

The residual weight for waste blends at 900 °C from TGA was (from highest to lowest order): RDF:SS > 3PES:SS:PR > 4LDPE:2SS:PR > 3DLPE:SS:PR > 3RDF:SS:PR > 6LDPE:SS > 4LDPE:SS > 3TP:SS.

The weight loss in the RT–900 °C range measured by TGA fits within the accuracy of the measurement (Section 3.3.1), with the weight drop measured in a muffle furnace for input waste materials (Figure S4). There is a bigger discrepancy for waste blends (especially for RDF:SS and 3LDPE:SS:PR). The reason is due to the inhomogeneity of waste blends (Figure S5).

The co-pyrolysis of SS with tested waste at laboratory scale showed a higher weight loss in the temperature range of 200–600 °C, so there is more chance of the decomposition of volatile matter into high oil and gas yields [10].

3.3.4. Statistical Evaluation

Multivariate testing was used to evaluate whether TG is statistically comparable for various ranges of temperatures. Every input material (LDPE, PES, PR, etc.) was split into ten groups for temperatures, in the following intervals: [0 °C, 100 °C], [100 °C, 200 °C] . . . [900 °C, 1000 °C]. Every measurement was tested separately to decide if there are significant differences in TG for various temperature intervals. Furthermore, the same temperature intervals were compared for different input materials. According to the Shapiro–Wilk test, they are not normally distributed, and the even variances are not equal for all groups (Levene's test), meaning that the ANOVA test with post hoc Tukey HSD test could not

be realized. Instead, a Kruskal–Wallis with pos hoc Dunn's test was used. Applying a Kruskal–Wallis test we determined whether the TG for different temperature intervals is the same. The p-value was always close to zero, so we rejected the hypothesis that the medians of all groups are equal. According to Dunn's test we found that every neighboring group shows no difference in terms of median values.

Moreover, the Kruskal–Wallis test was used to compare the medians for the same temperature interval, which had the same median value between different input materials. Even in this case we always reject the null hypothesis that all medians are equal. Table S3 displays the cases wherein the medians show no statistically significant difference (according to Dunn´s post hoc test).

4. Conclusions

Comprehensive characterization provided concrete data for the optimization and modeling of the pyrolysis treatment of sewage sludge and its blends with various waste samples. Sewage sludge could be classified as a suitable feedstock for thermochemical conversion processes, with 61.2% organic contents (mass loss between 100 and 600 °C) and HHV of 11.8 MJ/kg on a dry basis. However, the HHV of sewage sludge is low, and therefore it is suitable to mix sewage sludge with selected waste for further pyrolytic applications, and thus achieve the synergetic effect of disposing of certain types of waste. Waste materials (different types of plastics, waste tires, and waste paper) were selected based on their availability to eliminate transportation, storage, and handling costs. For pyrolytic applications, the results from thermogravimetric analyses are required in order to know the maximal temperature of thermal decomposition in an inert atmosphere, maximal mass losses, and weight loss rates. The residual mass was in this order, from highest to lowest: SS > PES > PR > TP > RDF > LDPE. Furthermore, 55 waste blends were prepared in various volume ratios. The visual comparison carried out and HHV was measured for each waste blend, and these were key parameters for the selection of suitable waste blends. It is apparent from the thermogravimetric analysis that all waste blends thermally decomposed up to the temperature 500 °C, with the maximal weight loss rate. The residual mass for waste blends at 900 °C from TGA was in the following order, from highest to lowest: RDF:SS > 3PES:SS:PR > 4LDPE:2SS:PR > 3LDPE:SS:PR > 3RDF:SS:PR > 6LDPE:SS > 4LDPE:SS > 3TP:SS. Thermoplastics with sewage sludge (3TP:SS) and LDPE with sewage sludge (LDPE:SS) had the lowest residual masses and the highest weight loss rates. On the other hand, the waste blend of polyester waste with sewage sludge and paper rejects (3PES:SS:PR) had the second highest residual mass and the lowest weight loss rate.

The conversion of input materials into oils and gases is strongly dependent on the pyrolysis temperature, which was also confirmed by TGA/DTG analysis. Higher pyrolysis temperatures have always led to higher gas volume yields, as observed in many previous studies [60–62]. We confirmed that the highest average mass yield was observed during the pyrolysis of plastics. In conclusion, the most suitable combinations of materials and temperature from TGA for the production of pyrolysis oils and gases are the 3TP:SS and 4LDPE:SS waste blends. Further research will focus on applied pyrolysis in a semi-pilot plant unit with analyses of outputs.

Supplementary Materials: The following are available online at https://www.mdpi.com/2076-3417/11/4/1610/s1, Figure S1: Temperatures of maximum weight losses in TGA experiments for inlet waste materials, Figure S2: TGA reproducibility of LDPE waste material, Figure S3: Temperatures of maximum weight losses in thermal TGA experiments for waste blends, Figure S4: Comparison of mass change measured by TGA and by the standard method in a muffle oven, Figure S5: Comparison of mass change measured by TGA and by the standard method in a muffle oven, Table S1: Analytical results of input waste materials, Table S2: Analytical results of waste blends, Table S3: Comparable groups.

Author Contributions: Conceptualization, L.K. and I.J.; methodology, L.K. and P.M.; software, P.S.; validation, I.J. and R.S., formal analysis, I.J. and S.D.; investigation, L.K., M.D.; resources, R.S.; data curation, L.K. and P.S.; writing—original draft preparation, L.K., I.J. and P.M.; writing—

review and editing, L.K., S.D., S.H. and M.D.; visualization, P.M.; supervision, S.H., I.J. and L.K.; project administration, S.D.; funding acquisition, S.H., M.D. All authors have read and agreed to the published version of the manuscript.

Funding: This research received no external funding.

Institutional Review Board Statement: Not applicable.

Informed Consent Statement: Not applicable.

Acknowledgments: This study was supported by the Institute of clean technologies for mining and utilization of raw materials for energy use, reg. No. LO1406. Further, it was supported by the ERDF/ESF project "Research on the identification of combustion of unsuitable fuels and systems of self-diagnostics of boilers combustion solid fuels for domestic heating" (No. CZ.02.1.01/0.0/0.0/18_069/0010049).

Conflicts of Interest: The authors declare no conflict of interest. The funders had no role in the design of the study; in the collection, analyses, or interpretation of data; in the writing of the manuscript, or in the decision to publish the results.

Abbreviations

EU	European Union
HHV	high heating value
HRT	hydraulic retention time
LDPE	low density polyethylene
LHV	low heating value
MSW	municipal solid waste
OLR	organic loading rate
PES	polyester
PR	paper rejects
PT	population total
RDF	residual derived fuel (polyethylene foils, bags and sorted municipal solid waste)
SS	sewage sludge
TG	thermogravimetric
TP	thermoplastics (non-specified)

References

1. Baggio, P.; Baratieri, M.; Gasparella, A.; Longo, G.A. Energy and environmental analysis of an innovative system based on municipal solid waste (MSW) pyrolysis and combined cycle. *Appl. Therm. Eng.* **2008**, *28*, 136–144. [CrossRef]
2. Letcher, T.M.; Vallero, D.A. *Waste: A Handbook for Management*; Elsevier: New York, NY, USA, 2011.
3. EP. *Directive 2019/904/EC of the European Parliament and of the Council of 5 June 2019 on the Reduction of the Impact of Certain Plastic Products on the Environment*; European Parliament: Brussels, Belgium, 2019; p. 19.
4. EP. *Directive 2018/2001/EC of the European Parliament and of the Council of 11 December 2018 on the Promotion of the Use of Energy from Renewable Sources*; European Parliament: Brussels, Belgium, 2018; pp. 82–209.
5. Smol, M.; Duda, J.; Czaplicka-Kotas, A.; Szołdrowska, D. Transformation towards circular economy (CE) in municipal waste management system: Model solutions for poland. *Sustainability* **2020**, *12*, 4561. [CrossRef]
6. EP. *Directive 91/271/EEC of 21 May 1991 Concerning Urban Waste-Water Treatment*; European Parliament: Brussels, Belgium, 1991.
7. EP. *Directive 99/31/EC of 26 April 1999 on the Landfill of Waste*; European Parliament: Brussels, Belgium, 1999.
8. EP. *Directive 2000/60/EC of the European Parliament and of the Council of 23 October 2000 on Water Protection (Water Framework Directive)*; European Parliament: Brussels, Belgium, 2000.
9. Bianchini, A.; Bonfiglioli, L.; Pellegrini, M.; Saccani, C. Sewage sludge management in Europe: A critical analysis of data quality. *Int. J. Environ. Waste Manag.* **2016**, *18*, 226–238. [CrossRef]
10. Gao, N.; Kamran, K.; Quan, C.; Williams, P.T. Thermochemical conversion of sewage sludge: A critical review. *Progress Energy Combust. Sci.* **2020**, *79*, 100843. [CrossRef]
11. Wanner, F. *Treatment of Sewage Sludge in the Czech Republic*; Sovak: Prague, Czech Republic, 2019; p. 23.
12. Raheem, A.; Sikarwar, V.S.; He, J.; Dastyar, W.; Dionysiou, D.D.; Wang, W.; Zhao, M. Opportunities and challenges in sustainable treatment and resource reuse of sewage sludge: A review. *Chem. Eng. J.* **2018**, *337*, 616–641. [CrossRef]
13. Mills, N.; Pearce, P.; Farrow, J.; Thorpe, R.B.; Kirkby, N.F. Environmental & economic life cycle assessment of current & future sewage sludge to energy technologies. *Waste Manag.* **2014**, *34*, 185–195. [CrossRef] [PubMed]

14. Tic, W.J.; Guziałowska-Tic, J.; Pawlak-Kruczek, H.; Woźnikowski, E.; Zadorożny, A.; Niedźwiecki, Ł.; Wnukowski, M.; Krochmalny, K.; Czerep, M. Novel concept of an installation for sustainable thermal utilization of sewage sludge. *Energies* **2018**, *11*, 748. [CrossRef]
15. Winkler, M.K.H.; Bennenbroek, M.H.; Horstink, F.H.; van Loosdrecht, M.C.M.; van de Pol, G.J. The biodrying concept: An innovative technology creating energy from sewage sludge. *Bioresour. Technol.* **2013**, *147*, 124–129. [CrossRef] [PubMed]
16. Fuwape, J.A. Charcoal and fuel value of agroforestry tree crops. *Agroforest. Syst.* **1993**, *22*, 175–179. [CrossRef]
17. Openshaw, K. Energy values of unprocessed biomass, charcoal and other biomass fuels and their role in greenhouse gas mitigation and energy use. In Proceedings of the Advances in Environmental Science and Energy Planning, Canary Islands, Spain, 10–12 January 2015; pp. 30–40.
18. Praspaliauskas, M.; Pedišius, N. A review of sludge characteristics in Lithuania's wastewater treatment plants and perspectives of its usage in thermal processes. *Renew. Sustain. Energy Rev.* **2017**, *67*, 899–907. [CrossRef]
19. Cao, Y.; Pawłowski, A. Sewage sludge-to-energy approaches based on anaerobic digestion and pyrolysis: Brief overview and energy efficiency assessment. *Renew. Sustain. Energy Rev.* **2012**, *16*, 1657–1665. [CrossRef]
20. Kasar, P.; Sharma, D.K.; Ahmaruzzaman, M. Thermal and catalytic decomposition of waste plastics and its co-processing with petroleum residue through pyrolysis process. *J. Clean. Prod.* **2020**, *265*, 121639. [CrossRef]
21. EP. *Directive 2008/98/EC of the European Parliament and of the Council of 19 November 2008 on Waste*; European Parliament: Brussels, Belgium, 2008; pp. 3–30.
22. Singhabhandhu, A.; Tezuka, T. The waste-to-energy framework for integrated multi-waste utilization: Waste cooking oil, waste lubricating oil, and waste plastics. *Energy* **2010**, *35*, 2544–2551. [CrossRef]
23. Diaz-Silvarrey, L.S.; McMahon, A.; Phan, A.N. Benzoic acid recovery via waste poly(ethylene terephthalate) (PET) catalytic pyrolysis using sulphated zirconia catalyst. *J. Anal. Appl. Pyrol.* **2018**, *134*, 621–631. [CrossRef]
24. Osborn, P. *Handbook of Energy Data and Calculations*; Butterworth–Heinemann: London, UK, 1985.
25. Choi, G.-G.; Oh, S.-J.; Kim, J.-S. Scrap tire pyrolysis using a new type two-stage pyrolyzer: Effects of dolomite and olivine on producing a low-sulfur pyrolysis oil. *Energy* **2016**, *114*, 457–464. [CrossRef]
26. Gopal, P.M.; Sivaram, N.M.; Barik, D. Chapter 7—Paper industry wastes and energy generation from wastes. In *Energy from Toxic Organic Waste for Heat and Power Generation*; Barik, D., Ed.; Woodhead Publishing: Cambridge, UK, 2019; pp. 83–97.
27. Pokhrel, D.; Viraraghavan, T. Treatment of pulp and paper mill wastewater—A review. *Sci. Total Environ.* **2004**, *333*, 37–58. [CrossRef] [PubMed]
28. Dobrotă, D.; Dobrotă, G. An innovative method in the regeneration of waste rubber and the sustainable development. *J. Clean. Prod.* **2018**, *172*, 3591–3599. [CrossRef]
29. Naqvi, S.R.; Hameed, Z.; Tariq, R.; Taqvi, S.A.; Ali, I.; Niazi, M.B.K.; Noor, T.; Hussain, A.; Iqbal, N.; Shahbaz, M. Synergistic effect on co-pyrolysis of rice husk and sewage sludge by thermal behavior, kinetics, thermodynamic parameters and artificial neural network. *Waste Manag.* **2019**, *85*, 131–140. [CrossRef]
30. Wang, Z.; Liu, K.; Xie, L.; Zhu, H.; Ji, S.; Shu, X. Effects of residence time on characteristics of biochars prepared via co-pyrolysis of sewage sludge and cotton stalks. *J. Anal. Appl. Pyrol.* **2019**, *142*, 104659. [CrossRef]
31. Chen, Q.; Liu, H.; Ko, J.; Wu, H.; Xu, Q. Structure characteristics of bio-char generated from co-pyrolysis of wooden waste and wet municipal sewage sludge. *Fuel Process. Technol.* **2019**, *183*, 48–54. [CrossRef]
32. Yang, X.; Yuan, C.; Xu, J.; Zhang, W. Potential method for gas production: High temperature co-pyrolysis of lignite and sewage sludge with vacuum reactor and long contact time. *Bioresource Technol.* **2015**, *179*, 602–605. [CrossRef] [PubMed]
33. CEN/TS. *Solid Recovered Fuels—Determination of Bulk Density*; CEN: Brussels, Belgium, 2010; Volume CEN/TS 15401:2010.
34. EN. *Characterization of Sludges—Determination of Dry Residue and Water Content*; EN: Brussels, Belgium, 2000; Volume EN 12880:2000.
35. EN. *Characterization of—Sampling of Waste Materials—Framework for the Preparation and Application of a Sampling Plan*; EN: Brussels, Belgium, 2005; Volume EN 14899:2005.
36. CEN/TS. *Solid Recovered Fuels—Determination of Moisture Content Using the Oven Dry Method—Part 2: Determination of Total Moisture Content by a Simplified Method*; CEN: Brussels, Belgium, 2010; Volume CEN/TS 15414-2:2010.
37. EN. *Solid Recovered Fuels—Determination of Moisture Content Using the Oven Dry Method—Part 3: Moisture in General Analysis Sample*; EN: Brussels, Belgium, 2011; Volume EN 15414-3:2011.
38. EN. *Solid Recovered Fuels—Determination of Ash Content*; EN: Brussels, Belgium, 2011; Volume EN 15403:2011.
39. EN. *Solid Recovered Fuels—Determination of the Content of Volatile Matter*; EN: Brussels, Belgium, 2011; Volume EN 15402:2011.
40. EN. *Solid Recovered Fuels—Methods for the Determination of Carbon (C), Hydrogen (H) and Nitrogen (N) Content*; EN: Brussels, Belgium, 2011; Volume EN 15407:2011.
41. ISO. *Solid Mineral Fuels—Determination of Sulfur by IR Spectrometry*; International Organization for Standardization: Geneva, Switzerland, 2006; Volume ISO 19579.
42. ISO. *Solid Biofuels—Conversion of Analytical Results from One Basis to Another*; ISO: Geneva, Switzerland, 2016; Volume ISO 16993:2016.
43. EN. *Solid Recovered Fuels—Determination of Calorific Value*; EN: Brussels, Belgium, 2011; Volume EN 15400:2011.
44. Fonts, I.; Gea, G.; Azuara, M.; Ábrego, J.; Arauzo, J. Sewage sludge pyrolysis for liquid production: A review. *Renew. Sustain. Energy Rev.* **2012**, *16*, 2781–2805. [CrossRef]

45. Magdziarz, A.; Werle, S. Analysis of the combustion and pyrolysis of dried sewage sludge by TGA and MS. *Waste Manag.* **2014**, *34*, 174–179. [CrossRef]
46. Calvo, L.F.; Otero, M.; Jenkins, B.M.; García, A.I.; Morán, A. Heating process characteristics and kinetics of sewage sludge in different atmospheres. *Thermochim. Acta* **2004**, *409*, 127–135. [CrossRef]
47. Hu, X.; Guo, H.; Gholizadeh, M.; Sattari, B.; Liu, Q. Pyrolysis of different wood species: Impacts of C/H ratio in feedstock on distribution of pyrolysis products. *Biomass Bioenergy* **2019**, *120*, 28–39. [CrossRef]
48. Fetene, Y.; Addis, T.; Beyene, A.; Kloos, H. Valorisation of solid waste as key opportunity for green city development in the growing urban areas of the developing world. *J. Environ. Chem. Eng.* **2018**, *6*, 7144–7151. [CrossRef]
49. Folgueras, M.B.; Alonso, M.; Díaz, R.M. Influence of sewage sludge treatment on pyrolysis and combustion of dry sludge. *Energy* **2013**, *55*, 426–435. [CrossRef]
50. Das, P.; Tiwari, P. Thermal degradation kinetics of plastics and model selection. *Thermochim. Acta* **2017**, *654*, 191–202. [CrossRef]
51. Chowlu, A.C.K.; Reddy, P.K.; Ghoshal, A.K. Pyrolytic decomposition and model-free kinetics analysis of mixture of polypropylene (PP) and low-density polyethylene (LDPE). *Thermochim. Acta* **2009**, *485*, 20–25. [CrossRef]
52. Marcilla, A.; García-Quesada, J.C.; Sánchez, S.; Ruiz, R. Study of the catalytic pyrolysis behaviour of polyethylene–polypropylene mixtures. *J. Anal. Appl. Pyrol.* **2005**, *74*, 387–392. [CrossRef]
53. Anene, A.F.; Fredriksen, S.B.; Sætre, K.A.; Tokheim, L.-A. Experimental study of thermal and catalytic pyrolysis of plastic waste components. *Sustainability* **2018**, *10*, 3979. [CrossRef]
54. Grigiante, M.; Ischia, M.; Baratieri, M.; Dal Maschio, R.; Ragazzi, M. Pyrolysis analysis and solid residue stabilization of polymers, waste tyres, spruce sawdust and sewage sludge. *Waste Biomass Valorizat.* **2010**, *1*, 381–393. [CrossRef]
55. Acevedo, B.; Fernández, A.M.; Barriocanal, C. Identification of polymers in waste tyre reinforcing fibre by thermal analysis and pyrolysis. *J. Anal. Appl. Pyrol.* **2015**, *111*, 224–232. [CrossRef]
56. Arenales Rivera, J.; Pérez López, V.; Ramos Casado, R.; Sánchez Hervás, J.-M. Thermal degradation of paper industry wastes from a recovered paper mill using TGA. Characterization and gasification test. *Waste Manag.* **2016**, *47*, 225–235. [CrossRef] [PubMed]
57. Zaker, A.; Chen, Z.; Zaheer-Uddin, M.; Guo, J. Co-pyrolysis of sewage sludge and low-density polyethylene—A thermogravimetric study of thermo-kinetics and thermodynamic parameters. *J. Environ. Chem. Eng.* **2020**, 104554. [CrossRef]
58. Hu, D.H.; Chen, M.Q.; Huang, Y.W.; Wei, S.H.; Zhong, X.B. Evaluation on isothermal pyrolysis characteristics of typical technical solid wastes. *Thermochim. Acta* **2020**, *688*, 178604. [CrossRef]
59. Chan, W.P.; Wang, J.-Y. Comprehensive characterisation of sewage sludge for thermochemical conversion processes—Based on Singapore survey. *Waste Manag.* **2016**, *54*, 131–142. [CrossRef] [PubMed]
60. Honus, S.; Kumagai, S.; Fedorko, G.; Molnár, V.; Yoshioka, T. Pyrolysis gases produced from individual and mixed PE, PP, PS, PVC, and PET—Part I: Production and physical properties. *Fuel* **2018**, *221*, 346–360. [CrossRef]
61. Quan, C.; Gao, N.; Song, Q. Pyrolysis of biomass components in a TGA and a fixed-bed reactor: Thermochemical behaviors, kinetics, and product characterization. *J. Anal. Appl. Pyrol.* **2016**, *121*, 84–92. [CrossRef]
62. Zhou, H.; Wu, C.; Onwudili, J.A.; Meng, A.; Zhang, Y.; Williams, P.T. Influence of process conditions on the formation of 2–4 ring polycyclic aromatic hydrocarbons from the pyrolysis of polyvinyl chloride. *Fuel Process. Technol.* **2016**, *144*, 299–304. [CrossRef]

applied sciences

MDPI

Article

Thermo-Economic Comparisons of Environmentally Friendly Solar Assisted Absorption Air Conditioning Systems

Adil Al-Falahi *, Falah Alobaid and Bernd Epple

Institute for Energy Systems and Technology, Technical University Darmstadt, Otto-Berndt-Straße 2, 64287 Darmstadt, Germany; falah.alobaid@est.tu-darmstadt.de (F.A.); bernd.epple@est.tu-darmstadt.de (B.E.)
* Correspondence: adil.al-falahi@est.tu-darmstadt.de; Tel.: +49-6151-16-20724; Fax: +49-0-6151-16-22690

Abstract: Absorption refrigeration cycle is considered a vital option for thermal cooling processes. Designing new systems is needed to meet the increasing communities' demands of space cooling. This should be given more attention especially with the increasing conventional fossil fuel energy costs and CO_2 emission. This work presents the thermo-economic analysis to compare between different solar absorption cooling system configurations. The proposed system combines a solar field, flashing tank and absorption chiller: two types of absorption cycle H_2O-LiBr and NH_3-H_2O have been compared to each other by parabolic trough collectors and evacuated tube collectors under the same operating conditions. A case study of 200 TR total cooling load is also presented. Results reveal that parabolic trough collector combined with H_2O-LiBr (PTC/H_2O-LiBr) gives lower design aspects and minimum rates of hourly costs (5.2 $/h) followed by ETC/$H_2O$-LiBr configuration (5.6 $/h). H_2O-LiBr gives lower thermo-economic product cost (0.14 $/GJ) compared to the NH_3-H_2O (0.16 $/GJ). The absorption refrigeration cycle coefficient of performance ranged between 0.5 and 0.9.

Keywords: thermo-economic; aqua-ammonia; lithium bromide-water; absorption systems; design; solar collectors

Citation: Al-Falahi, A.; Alobaid, F.; Epple, B. Thermo-Economic Comparisons of Environmentally Friendly Solar Assisted Absorption Air Conditioning Systems. *Appl. Sci.* **2021**, *11*, 2442. https://doi.org/10.3390/app11052442

Academic Editor: Paride Gullo

Received: 26 January 2021
Accepted: 5 March 2021
Published: 9 March 2021

1. Introduction

Today, the substitution of traditional energy sources by renewable ones has becomes urgently needed for the clean and sustainable development of the energy sector worldwide. Climate change, the world's noticeable growth in population number, and the improvement in standard conditions of living make cooling demands to increase significantly. According to the International Institute of Refrigeration reports, approximately 15% of total electricity production in the world is used for refrigeration and air conditioning [1]. About 80% of the global electricity is produced from fossil fuels, which increases the emissions of greenhouse gases significantly [2]. Solar thermally activated cooling systems are more attractive than the other type because of the near concurrence of peak cooling loads with the available solar power. Taking into account the deficiency in electrical power in most developing countries, all these previous factors make solar cooling technology a suitable and clean alternative for a big problem. Current studies of solar thermal cooling technology should strive to realize modern, low-cost, energy-efficient, high-temperature collectors, and to develop a high-performance, low-temperature enabled air conditioning technology [3]. In particular, there has to be a determination to find the optimal operational capabilities that make the optimum total performance of the device to be reached despite the apparent specific use of high-efficiency technology. Today, absorption chillers are the most mature technology. Therefore, solar thermal absorption cooling units might be a great option to reduce the usage of electricity in cooling and obtain economic gains [4–6].

There are different technologies to produce cold (cooling of industrial processes, conservation of products, air conditioning, etc.) with solar energy (and with solar thermal energy in particular). Syed et al. [7] performed a simple economic analysis comparing

eight different configurations of solar cooling systems. These configurations contemplated reasonable combinations of refrigeration (ejector, compression, and absorption) and solar electric drive (with photovoltaic collectors) or thermal drive (flat plate collectors FPC, evacuated tube collector ETC, and parabolic through collector PTC). They concluded that solar thermal systems using absorption refrigeration are the most economical; in particular those with low temperature (flat collectors coupled with single-effect absorption), solar collectors account for the highest life cycle costs in all the configurations analyzed.

In the solar thermal sector, the main technologies integrated with absorption cooling systems are FPC, ETC, and PTC [8]. Parabolic through collectors have been analyzed in many types of research through single impact absorption cycles. Li et al. [9] inspected experimentally the performance of this configuration for Kunming, China, and they concluded that 56 m^2 of PTCs can drive H_2O-LiBr absorption cycle with 6 TR cooling capacity to serve the cooling requirements of a meeting room of 102 m^2. Besides this, they analyzed appropriate methods for improving cooling performance. In Iran, Mazloumi et al. [10] proved that 57.6 m^2 of PTC, storage tank of 1.26 m^3 equipped with absorption system can satisfyingly meet building cooling load. The system operated from 6:00 to 19:00.

Shirazi et al. [11] compared three configurations of H_2O-LiBr solar absorption cooling system with TRNSYS 17. The first one was a single effect absorption integrated with ETC. The second and third configurations were double and triple effect systems, respectively, with PTC. The results revealed that the use of multi-effect absorption solar cycles was not advantageous over single-effect solar systems when the fraction of direct normal irradiation is less than 60% of the total global solar irradiation. Furthermore, the analysis of cost results indicated that a fraction of minimum direct normal irradiation of about 70% was required for solar-powered multi-effect cooling systems in order to be cost-effective in comparison to single-effect solar cooling systems.

The use of ETC to provide refrigeration in Saudi Arabia has been examined by Khan et al. [12], and they demonstrated that the use of 116 m^2 of ETC can lead to satisfying results with 10 kW cooling capacity of NH_3–H_2O absorption refrigeration system.

Rajasekar et al. [13] examined a single effect NH_3-H_2O chiller of one KW, which was using an evacuated tube solar collector. They deduced that the optimum coefficient of performance (COP) was accomplished at the temperature of the generator of 83.2 °C and while the evaporator temperature was 23.59 °C. A comparison was achieved among their accomplished COP values with standard absorption solar cooling systems.

Flores et al. [14] compared the operation of the absorption cooling system with different working pairs and presented a computer program to study H_2O-LiBr, NH_3-H_2O, and the other four pairs' performance. They found that due to crystallization problems, the H_2O-LiBr pair operates at a small range of vapor temperature operation specifically at generator temperature of 75–95 °C. In the case of the NH_3-H_2O system, the range of generator temperature was 78–120 °C. The condenser, evaporator, and absorber temperatures were 40 °C, 10 °C, and 35 °C, respectively, for a cooling load of 1 kW for each working pair.

Many researchers have carried out exergetic analysis studies for different thermal solar absorption cooling systems. Gebreslassie et al. [15] studied an exergy analysis for all components in the absorption cycle. They found that the largest exergy destruction occurs at the absorbers and generators. In the same regard, Kilic et al. [16] utilized the first and second laws of thermodynamics to develop a mathematical model for single stage H_2O-LiBr refrigeration cycle and they proved that the system COP increases with the increase of generator and evaporator temperature, while system COP decreases as condenser and absorber temperature increases. In the same regard, Ahmet Karkas et al. [17] carried out energy analysis for absorption cooling cycles and states that, above 0 °C, the cycles of H_2O-LiBr cooling are more effective based on thermodynamics laws. Dincer et al. [18] investigated procedures of calculating the total exergy, both chemical and physical exergy for the absorption cooling system, using the realization of a series of programming algorithms, with the help of the correlations supplied in the Engineering Equation Solver (EES).

Related to thermo-economics, Lu and Wang [19] analyzed economically three types of solar cooling systems. The first one was an adsorption system integrated with ETC solar collector the cycle employing water and silica gel as a working solution. The second system was a single-effect (H_2O-LiBr) absorption system connected by an efficient compound parabolic concentrating solar collector. Finally, the last system was a double-effect (H_2O-LiBr) absorption cycle equipped with PTC. They deduced that the third system had the highest solar coefficient of performance (COP). They also concluded that the cooling chiller can be driven at an ambient temperature of 35 °C from 14:30 to 17:00.

In recent years, the studies that have contributed to the improvement of the performance of absorption systems are related to hybrid absorption. Colorado and Rivera [20] have compared various refrigeration systems by vapor compression with a hybrid system(compression/absorption) based on the 1st and 2nd laws of thermodynamics; in the compression cycle, they utilized R134a and CO_2 as refrigerants, and for absorption cycle, they used H_2O-LiBr as an operating mixture. The hybrid system has a cascade heat exchanger, in this case, the condenser of the compression cycle is considered the evaporator of the absorption cycle. The study aims to enhance the efficiency and reduce the energy consumption in the compressor. The research results show that the hybrid system consumes 45% less electricity than the simple compression cycle. Likewise, the coefficient of performance (COP) achieved with the hybrid system was higher with R134a refrigerant.

A major benefit of the absorption cooling system is the opportunity to use different heat sources to drive the generator of absorption. Wang et al. [21] investigated the optimal heat sources for different absorption cooling system applications. The heat released from the exhaust gases of boilers, internal combustion engines, and gas turbines could be utilized as a heat source for an absorption system. Du et al. [22] constructed a prototype of a single-stage NH_3-H_2O cooling system that operated with a heat discarded from a diesel engine through an active open-pipe heating method, which was designed to provide a uniform amount of available heat. The authors designed the heat exchanger to recover energy discarded for a specific capacity, combining the processes of condensation and absorption in a refrigeration unit by circulating a solution that had been previously cooled.

Finally, two latest thermo-economic comparative studies by authors in this field need to be mentioned [23,24], which compared the use of ETC and PTC integrated with H_2O-LiBr and/or NH_3-H_2O absorption chiller energetically and financially. They found that, generally, PTC in both cases (PTC-H_2O-LiBr/NH_3-H_2O) is the best option with large capacities and the use of (ETC-H_2O-LiBr/NH_3-H_2O) as a next alternative.

The previous literature review states that there are a lot of investigations on thermal absorption cooling systems field and most of them deal with LiBr-H_2O or H_2O-NH_3 as working pairs, and that most of them used traditional absorption cycles. Numerous ideas on thermodynamic and economic studies are being examined. In general, for each comparative research, only one technique was investigated. In this direction, this work is a comparative analysis of four common solar thermal cooling systems. More specifically, it compares the use of two kinds of collectors (ETC and PTC) for the solar part and the absorption cycles H_2O-LiBr and NH_3-H_2O with each other under the same operating conditions.

The innovation of this work has arisen from the method of combination of solar field and absorption cycle by using flash tank as the investigated thermal enhancement method. To the authors' knowledge, no article available in literature has dealt with the proposed integration from that side, and in general, comparative researches are restricted. Therefore, this work is innovative because it systematically presents a comparison between four configurations. The solar cooling plant introduced in this work is suitable for medium and high loads of cooling. This may be reasonable for coastal and tourist spots along with the solar beam areas like the Middle East, North Africa (MENA), and Gulf regions.

The main objective of this work is to improve and compare between the various configuration of absorption refrigeration cycles by various solar thermal collectors. In this sense, steady-state energetic, exergetic, cost, and design techniques of modeling are performed for

an absorption cooling system powered by solar energy. The optimal operating condition of the system is reported as well. The following outlines were withdrawn in this work:

- Two different types of absorption cycles in different working conditions were studied. The selection process involved the optimum operating conditions.
- Comparison was made of two different types of solar thermal collectors when combined with an absorption chiller.
- The mathematical model has been carried out in detail.
- The comparison was performed based on the terms of energy, exergy, design, cost, and thermo-economic. Design technique of modeling has been adopted in this study.
- Based on the optimized selection, a detailed case study was performed for a cooling load of 700~800 kW.

2. System Description

As mentioned previously, the proposed system combines two systems: a solar power system and an absorption air conditioning (AAC) system. The solar power system includes a thermal solar collector and flash tank. Basically, the plant is driven by solar energy. The current proposed absorption cooling systems (H_2O-LiBr/NH_3-H_2O) integrated with (PTC/ETC) are displayed in Figure 1.

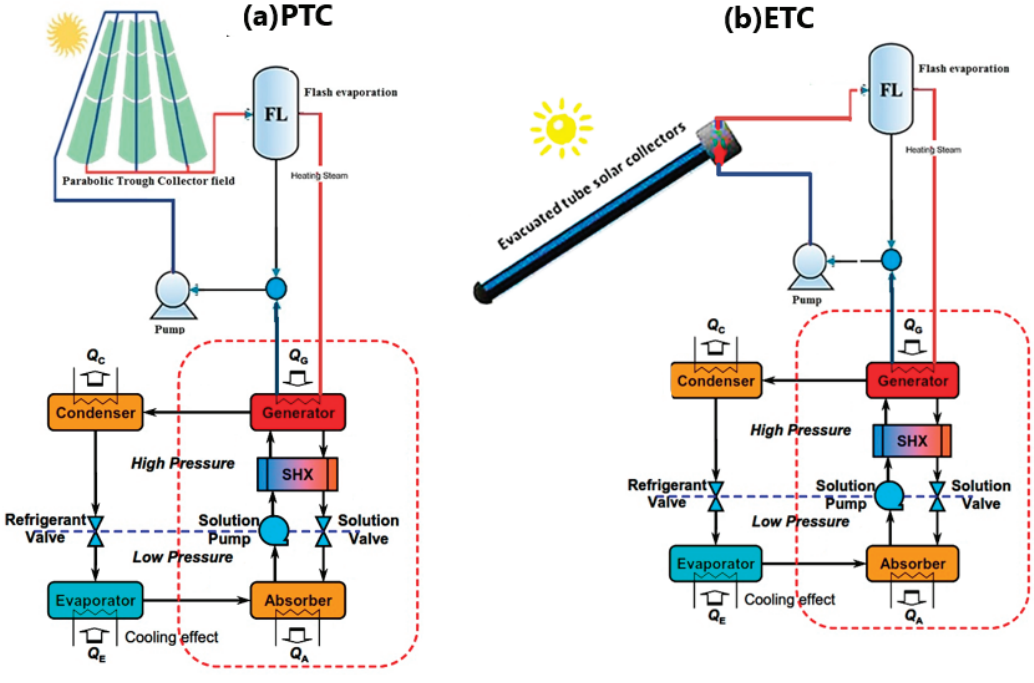

Figure 1. Absorption air-conditioning system integrated with solar thermal collector. (**a**) Parabolic trough collector PTC; (**b**) Evacuated tube collector ETC [24].

Solar field loop combines a set of PTCs or ETCs. Water is employed as a working fluid. Solar radiation is collected and concentrated on the water by solar collectors. In simulation, solar intensity is assumed to be constant to accomplish the steady-state condition. Subsequently, the water with high temperature enters the flash tank to generate steam, and the condensed water is collected in the bottom of the flash tank and then back to the solar collector's field via the heat release. The AAC unit is a single-stage H_2O-LiBr or NH_3-H_2O

type. Flash tank steam condensation in the AAC generator results in the boiling of the solution and separation of the refrigerant (water or ammonia vapor). At the generator outlet, there is a two-phase flow. The steam phase involves the vapor of the refrigerant, which moves forward into a condenser unit; the liquid phase is a mixture (absorbent-refrigerant) with a low concentration of refrigerant (strong solution). Then, this solution is returned through a throttle valve to the absorber. In the AAC condenser, heat is removed from the refrigerant to the cooling water. The refrigerant is then throttled to fulfill the required temperature at the evaporator in which the chilled water acquires its low temperature needed for the cooling application. Besides this, the heat transfer results in a change in the thermodynamic state of the refrigerant from a saturated mixture of liquid and vapor to superheated vapor. The evaporated refrigerant is cooled, condensed, and mixed with the LiBr or water in the absorber forming a dilute solution. The refrigerant-absorber mixture causes an exothermic reaction, whereby the heat released in this process is discharged from the solution to the other stream via cooling water delivered from the secondary cooling system (air or cooling tower). The absorption process results in a mass flow of diluted solution leaving the absorber. Finally, the dilute solution is pumped back to the generator and so on. To enhance the AAC performance, strong and weak solutions exchange heat through a liquid-liquid heat exchanger. The utilization of the economizer increases the coefficient of performance (COP) by reducing heat released into the absorber and heat delivered to the generator. COP of a single effect system is defined as the relationship between the heat flow eliminated in the evaporator (cooling capacity) vs. the heat flow into the generator and the energy consumption of the pump. The single effect is represented by the basic absorption cycle, half effect, double effect, triple, and multi-effect absorption cycles. The term "effect" refers to the times that the driving heat is used by the absorption system, and the number of generators refers to the number of effects.

3. Methodology, Design Development Software, and Assumptions

The design of an absorption air conditioning cycle (AAC) requires a considerable amount of calculation. This makes it an extremely complex, cumbersome, and time-consuming process. That is why we chose to use software that facilitates it. MATLAB is a powerful software package for scientific computing, focusing on numerical calculations, matrix operations, and especially the applications of science and engineering. It can be used as a simple matrix calculator, but its main interest lies in the hundreds of functions—both general purpose and specialized—that it has, as well as its possibilities for graphic visualization.

In this work, the four configurations proposed model was coded in the MATLAB program, which allows you to establish a numerical method for solving the proposed model and makes it possible to solve the mathematical model of the simulator and provide the obtained results. Since it is a platform that allows making sequences of mathematical calculations, it is possible to model physical phenomena in the form of equations. In order to build the simulator, it is necessary to enter the equations with their respective nomenclatures and establish the criteria to be followed for the resolution of the sequence of steps. The origin of the physical characteristics is taken from the NIST chemistry book on their website [25]. More information about the optimization techniques considered in this work is given in Refs. [23,24], to minimize techno-economic costs. Table 1 shows parameters considered for the simulation of the four different system proposed configurations. In simulation, solar intensity is assumed to be constant to accomplish the steady-state condition. In all the absorption cycles, the energy input was used in the form of steam. For the thermodynamic, exergetic, and cost analysis, the equations that were applied are described in the following sections.

Table 1. Design data for the solar absorption system configurations [24].

Unit Process	Assigned Data	Calculated Data
Absorption air-conditioning cycle (AAC)/(ETC/PTC)	✓ Solar radiation: 500 W/m^2 ✓ Ambient temperature: 25 °C ✓ Average relative humidity: 15% ✓ ETC top temperature: 100–200 °C ✓ PTC top temperature: 200–300 °C ✓ Absorber temperature: 30–35 °C ✓ Generator temperature: 80–90 °C ✓ Condenser temperature: 40–45 °C ✓ Hot air temperature: 35 °C ✓ Target cooled air temperature: 20 °C ✓ Evaporator temperature: 5–10 °C ✓ Cooling load: 176–700 kW (50–200 TR) ✓ Condenser effectiveness: 80% ✓ Fan system efficiency: 85% ✓ Pumping system efficiency: 75% ✓ Plant life time: 20 years ✓ Interest rate: 5% ✓ Load factor: 90% ✓ Specific electric power cost: 0.065 $/kWh ✓ Water steam is the solar field working fluid	**Solar Field:** ➢ Solar field top pressure, bar ➢ Solar field pressure loss, bar ➢ Total solar field area, m^2 ➢ Solar field thermal load, kW ➢ Number of solar collectors, # ➢ Solar field mass flow rate, kg/s ➢ Solar field inlet temperature, °C ➢ Efficiency, % ➢ Exergy destruction, kW **Flash Tank:** ➢ * Flash tank design data ➢ Total mass flow rate, kg/s ➢ Dryness fraction, % ➢ Flash tank water flow rate, kg/s ➢ Steam flow rate, kg/s ➢ Exergy destruction, kW **AAC Unit:** ➢ Weak & strong solutions, kg/s ➢ * Design data ➢ Thermal power, kW ➢ Total cycle flow rate, kg/s ➢ Generator power, kW ➢ Cooling fan power, kW ➢ Coefficient of performance (COP) ➢ COPmax ➢ Relative performance ➢ Exergy destruction, kW **Pump:** ➢ Power, kW ➢ Outlet temperature, °C ➢ Exergy destruction, kW **Cost & Performance:** ➢ Units hourly costs, $/h ➢ Total hourly costs, $/h ➢ Total power, kW ➢ LPC, $/kWh ➢ Thermo-economic cost, $/GJ ➢ Total exergy destruction rate, kW
Notes:	■ Data are run out based on steady-state operating conditions. ■ Ambient temperature is fixed as 25 °C for all process runs. ■ Solar radiation is fixed at 500 W/m^2. ■ * Design data means area, length, width, etc.	

4. Mathematical Model

The studied system components are modeled and simulated depending on both first and second laws of thermodynamics. As a first step in modeling this system, the study is implemented depending on steady state basis at a constant value of solar radiation intensity. An explanation of the mathematical model of each part is clarified in the following subsections.

4.1. ETC Modeling

An immediate efficiency of the ETC solar collector can be calculated by the solar irradiance, average collector temperature, and environmental temperature based on its characteristic curve. For ETC, the curve adopted is specified by Equation (1) [26,27].

$$\eta_{etc} = \eta_o - a_1\left(\frac{T_o - T_{amb}}{I_s}\right) - a_2\left(\frac{T_o - T_{amb}}{I_s}\right)^2 .I_s \quad (1)$$

where, η_{etc} is the ETC efficiency, $\eta_o = 0.665$, $a_1 = 2.9$ W/m^2. °C, $a_2 = 0.0019$ W/m^2. °C^2, I_s is the solar flux (W/m^2), T_o is the exit top temperature of the collector (°C), and T_{amb} (°C) is the ambient temperature. The thermal load of the collector Q_{th} (kW) is calculated according to Equation (2).

$$Q_{th} = \dot{M_{col}} \times C_p \times (T_o - T_i) \quad (2)$$

where, $\dot{M_{col}}$ is the mass flow rate in kg/s.

The total surface area of the collector A_t(m^2), is calculated from the equation of the energy balance of the collector as a dependency of the efficiency using:

$$A_t = \frac{Q_{th}}{\eta_{etc} \times I_s} \quad (3)$$

The aperture area of the ETC module A_{etc}, m^2, can be calculated as:

$$A_{etc} = D_t \times L_t \times NOT \quad (4)$$

where, D_t and L_t is the diameter and length of the tube in (m), respectively, and NOT is the tube numbers of each module. The total number of ETCs, NOC could be estimated from the following relation:

$$NOC = \frac{A_t}{A_{etc}} \quad (5)$$

The loops number NOL, area of the loop A_{loop}, and the length of each loop, L_{loop} could be computed by allocating the hydraulic mass flow rate $\dot{M_{hyd}}$, kg/s.

$$NOL = \frac{\dot{M_{col}}}{\dot{M_{hyd}}} \quad (6)$$

$$A_{loop} = \frac{A_t}{NOL} \quad (7)$$

$$L_{loop} = \frac{A_{loop}}{L_t} \quad (8)$$

4.2. PTC Modeling

For the medium-high temperature of PTCs, the relevant efficiency can be found in Equation (9) [27]:

$$\eta_{ptc} = \eta_o - a_{11}(T_o - T_{amb}) - a_{21}\left(\frac{T_o - T_{amb}}{I_s}\right) - a_{31}\left(\frac{T_o - T_{amb}}{I_s}\right)^2 \quad (9)$$

where, $a_{11} = 4.5 \times 10^{-6}$ 1/ °C, $a_{21} = 0.039$ W/m^2. °C, $a_{31} = 3 \times 10^{-4}$ W^2/m^2. °C^2, $\eta_o = 0.75$.

The thermodynamic performance of a PTC is expressed as:

$$\eta_{PTC} = \frac{Q_u}{A_{PTC} \times I_s} \quad (10)$$

where, η_{PTC} is the collector thermal efficiency; Qu is the useful thermal power (W); A_{PTC} is the aperture area of the collector (m^2); and Is is the solar radiation (W/m^2). Modifying Equation (10) results in Equation (11):

$$A_{PTC} = \frac{Q_u}{\eta_{PTC} \times I_s} \tag{11}$$

The ground area necessary for solar collector implementation, however, is larger than the collector's aperture area. This value ranges from about three to four times the collector's aperture area, due to the space between the collectors in addition to the space needed for the pipes and other system accessories. The useful thermal energy of the collectors can exist according to the following relationship:

$$Q_u = M_{col}^{\cdot} \times \Delta h_{o-i} \tag{12}$$

Here, Δh is the enthalpy difference of through collector in kJ/kg, and $M_{col}^{\cdot}$ is the mass flow rate in kg/s. The total length of PTC, L_{PTC} is then calculated depending on the width of the collector W_c (m) and the diameter of the glass envelope D_{env} (m):

$$L_{PTC} = \frac{A_{PTC}}{W_c - D_{env}} \tag{13}$$

By identifying the total mass flow rate, which is estimated based on the load of the boiler heat exchanger, and assigning a hydraulic mass flow rate to be the input, the entire number of loops N_{loop}, area of the loop A_{loop}, the width of the loop W_{loop}, and the solar PTC's number ($N_{PTC's}$) are calculated as follows:

$$N_{loop} = \frac{M_{col}^{\cdot}}{M_{hyd}^{\cdot}} \tag{14}$$

$$A_{loop} = \frac{A_{PTC}}{N_{loop}} \tag{15}$$

$$W_{loop} = \frac{A_{loop}}{L_m} \tag{16}$$

where, L_m (m) is assigned as the length of the module.

$$N_{PTC's} = \frac{A_{PTC}}{L_m(W_c - D_{env})} \tag{17}$$

Overall pressure drops P_{tloss} are determined based on the major and minor drops over the length of the field. The general loss-equation is carried out as follows [28,29]:

$$P_{tloss} = N_{loop} \times \Delta P_{loop} \tag{18}$$

where,

$$\Delta P_{loop} = \frac{32 \times f \times L_{loop} \times {M_{hyd}^{\cdot}}^2}{\rho \times \pi^2 \times D_t} \tag{19}$$

D_t is the inner tube diameter(m).

$$f = [(1.82 \times \log Re) - 1.64]^{-2} \tag{20}$$

$$Re = 4 \times \frac{M_{hyd}^{\cdot}}{\mu \times \pi \times D_t} \tag{21}$$

4.3. Flash Tank Modeling

The design parameters of the cyclone flash tank have been derived in the following manner:

Tank inlet and outlet tube steam area A_{t_i} is determined according to the velocity of steam V_{st}, m/s, and the density of vapor ρ_v, kg/m^3:

$$A_{t_i} = \frac{M_{st}}{\rho_v \times V_{st}} \tag{22}$$

Tube diameter D_t (m):

$$D_t = \left(\frac{A_{t_i} \times 4}{\pi}\right)^{0.5} \tag{23}$$

Height of flash tank H_{fst} (m) [29]:

$$H_{fst} = 7.15 \times D_t \tag{24}$$

Flash tank width W_{fst} (m):

$$W_{fst} = 3.5 \times D_t \tag{25}$$

Flash tank total volume Vol_{fst} (m^3):

$$Vol_{fst} = \left(\frac{Pi}{4}\right) \times {W_{fst}}^2 \times H_{fst} \tag{26}$$

The flashing enthalpy h_{fsh} equals the fluid enthalpy that comes from the solar collector h_{col}, kJ/kg:

$$h_{fsh} = h_{col} \tag{27}$$

The flashing dryness fraction X_{fsh} is used to quantify the amount of water within steam and it is estimated depending on the enthalpy of flashing h_{fsh}, liquid enthalpy h_f, (kJ/kg), and dry vapor enthalpy h_g (kJ/kg):

$$X_{fsh} = \frac{h_{fsh} - h_f}{h_g - h_f} \tag{28}$$

The total mass flow rate M_{total} (kg/s) and non-vaporized water M_w (kg/s) were calculated using Equations (29) and (30), respectively:

$$M_{total} = \frac{M_{st}}{X_{fsh}} \tag{29}$$

$$M_w = \left(1 - X_{fsh}\right) \times M_{total} \tag{30}$$

4.4. Pump Modeling

The work of the pump W_p, kW may be determined using the following relation [30]:

$$W_p = M_{total} \times \frac{\Delta P}{\rho} \times \eta_p \tag{31}$$

where, ΔP (kPa) represents the difference in total pressure and it is computed as:

$$\Delta P = P_{high} + P_{loss} \tag{32}$$

Outlet pump enthalpy h_{po} (kJ/kg):

$$h_{po} = \left(\frac{W_p}{M_{total}}\right) + h_{pi} \tag{33}$$

4.5. Absorption Chiller Modeling

The absorption cycle was developed for a capacity of cooling and specific temperature ranges. Table 1 shows the input parameters considered for the simulation of the absorption chiller. The mathematical model that was developed for the study of single-effect absorption cycles is based on the theory reported by the authors [23,24]. The following assumptions are considered for analyzing absorption systems:

- Analysis is carried out in steady-state conditions.
- The refrigerant leaving the condenser is in a saturated liquid state.
- The refrigerant when leaving the evaporator is in the saturated vapor state.
- Temperature at the outlet of the absorber and the generator belong to mixing equilibrium and the conditions of separation, respectively.
- The pressure drops through the pipes and heat exchangers are negligible.
- The heat exchange among the system and the environment are negligible.

The thermodynamic analysis model of the absorption cycle components is done with the help of basic balances, mass balance, energy balance, and solution phase equilibrium, and the general formulation are listed as follows:

$$\sum m_i - \sum m_o = 0 \tag{34}$$

$$\sum m_i x_i - \sum m_o x_o = 0 \tag{35}$$

$$\sum m_i h_i - \sum m_o h_o = 0 \tag{36}$$

where, m , x, and h denote mass, concentration, and enthalpy for inlet (i) and outlet (o) of the component, respectively. The total energy balance for the absorption cycle is specified as follows:

$$Q_e + Q_g = Q_c + Q_a + W_p \tag{37}$$

where, Q_e is the thermal load on the evaporator, kW; Q_g is the heat added to the Generator, kW; Q_c is the heat expelled from the condenser, kW; Q_a is the absorber thermal power, kW; and W_p represents the pump work, kW. For performance calculations, the COP is defined as follows:

$$COP = \frac{Q_e}{Q_g} \tag{38}$$

The max COP of the ideal cycle is given by:

$$COP_{max} = \frac{(T_e + 273.15) \times (T_g - T_a)}{(T_g + 273.15) \times (T_c - T_e)} \tag{39}$$

The relative performance ratio RPR can be estimated as:

$$RPR = \frac{COP}{COP_{max}} \tag{40}$$

From the analysis thermodynamic, data are obtained to obtain thermo-physical properties and to dimension the system components.

4.6. Thermo-Economic Model

In this part, the proposed system is mathematically analyzed to be evaluated it using thermo-economic approach (exergy and cost). Thermo-economic is the branch of engineering that combines exergy analysis and cost principles to provide the system

designer or operator with information not available through conventional energy analysis and economic evaluation. Thermo-economic balance for any unit is performed based on exergy and cost balances.

The availability (exergy) and cost have been estimated based on the formulas reported in Refs. [31–35]. The equation of availability for any system is a fixed point; a stable flow process with first and second thermodynamic laws can be applied. By ignorance of kinetic and potential energy alterations, the following equation can be used to describe the form of availability [31]:

$$A_2 - A_1 = A_q + A_w + A_{fi} - A_{fo} - I \tag{41}$$

where, $A_2 - A_1 = 0$ is the change of availability without flow in a steady-state condition; $A_q = \sum_J \left(1 - T_{amb}/T_J\right) Q_J$ is the transfer of availability due to heat exchange among the control volume and its surroundings; $A_w = -W_{cv} + P_o(V_2 - V_1)$ is equivalent to negative work value generated by the control volume W_{cv}. In certain instances, though, the control volume has a fixed volume; therefore, A_w can be simplified, and $I = T_{amb}.S_{gen}$ is the destruction availability of the process. Flow availability is specified as $A_{fi,o} = \sum_{i,o} m_{i.o} a_{fi,o}$. Hence, the general form in steady-state condition would become:

$$0 = A_q + A_w + A_{fi} - A_{fo} - I \tag{42}$$

In a conventional economic evaluation, a balance of costs for the total system running in a steady state is established as following [32]:

$$\sum_{out} C_{\cdot} = \sum_{in} C_{\cdot} + Z^{IC\&OM} \tag{43}$$

where, $C_{\cdot}$ is the rating of cost based on in and out streams, and $Z^{IC\&OM}$ are related to capital expenditure and operational and maintenance costs. In the calculation of exergy costs, a cost is identified for every exergy stream. Hence, for the incoming and outgoing matter streams that have attached exergy exchange rates $E_{i,o}^{\cdot}$, power $W^{\cdot}$, and the exergy exchange rate assigned to the heat release $E_{\dot{q}}^{\cdot}$, Equation (43) can be written as follows:

$$C_{i,o}^{\cdot} = c_{i,o} E_{i,o}^{\cdot} \tag{44}$$

$$C_w^{\cdot} = c_w W^{\cdot} \tag{45}$$

$$C_q^{\cdot} = c_q E_q^{\cdot} \tag{46}$$

where, $c_{i,o}, w, q$ represent the average cost for each unit of exergy in (USD/kJ) for inlet (i), outlet (o), power (w), and energy (q) respectively. The following relationships are used to estimate the costs per hour:

For cost analysis, the amortization factor A_f is computed depend on:

$$A_f = \frac{i.(1+i)^{LTp}}{(1+i)^{LTp} - 1} \tag{47}$$

The collector's estimated cost of investment IC_{col} (USD) is determined according to the area correlation given below:

$$IC_{col} = 150 \times A_{col}^{0.95} \tag{48}$$

The cost of operation and maintenance OMC_{col} is then calculated (USD):

$$OMC_{col} = 0.15 \times IC_{col} \tag{49}$$

Total annual cost TAC_{col} (USD/y) is considered to depend on the parameters of operation and maintenance costs and investment costs, as indicated below:

$$TAC_{col} = (IC_{col} + OMC_{col}) \times A_f \tag{50}$$

Hourly costs are calculated Z_{col} (USD/h):

$$Z_{col} = \frac{TAC_{col}}{OH \times 365} \tag{51}$$

where, OH is operating hours (h)

Flashing tank investment cost IC_{fsh} (USD) is calculated according to the total volume of the tank Vol_{fst} correlation:

$$IC_{fsh} = \frac{Vol_{fst} \times 6300}{3.8} \tag{52}$$

The total annual cost TAC_{fsh} USD/y is measured by:

$$TAC_{fsh} = IC_{fsh} \times A_f \tag{53}$$

Hourly costs are calculated Z_{fsh} (USD/h):

$$Z_{fsh} = \frac{TAC_{fsh}}{OH \times 365} \tag{54}$$

Absorption cycle investment cost IC_{aac} (USD), is estimated on the base of the correlation of total area as:

$$IC_{aac} = 150 \times A_{aac}^{0.8} \tag{55}$$

Total annual cost TAC_{aac} (USD/y) is then estimated:

$$TAC_{aac} = IC_{aac} \times A_f, \tag{56}$$

Hourly costs are calculated Z_{aac} (USD/h):

$$Z_{aac} = \frac{TAC_{aac}}{OH \times 365} \tag{57}$$

Pump investment cost IC_p (USD) It is estimated on pump power correlation:

$$IC_p = 3500 \times W_p^{0.47} \tag{58}$$

Total annual cost TAC_p (USD/y) It is estimated on:

$$TAC_p = IC_p \times A_f \tag{59}$$

Hourly costs are calculated Z_p (USD/h):

$$Z_p = \frac{TAC_p}{OH \times 365} \tag{60}$$

Total hourly costs Z_{tot} (USD/hr) It is estimated on all parameters:

$$Z_{tot} = Z_{col} + Z_{fsh} + Z_{aac} + Z_p \tag{61}$$

Total Plant Costs TPC (USD/y) is also identified based on the total annual costs for all units:

$$TPC = TAC_{col} + TAC_{fsh} + TAC_{aac} + TAC_p \tag{62}$$

The cumulative thermo-economic equation is determined based on the expense and exergy flow of the cycles (USD/GJ):

$$c_p = 1000 \times \left(\frac{(W_{tot} \times c_w) + \left(\frac{Z_{tot}}{3600} \right)}{Ex_{f_o}} \right) \quad (63)$$

where, c_p is the thermo-economic product cost (USD/GJ), c_w is the energy price in (USD/kWh) (~0.065), and W_{tot} is the cycle power(kW), while Ex_{f_o} is the exergy stream outlet from the system to the user (kW).

5. Results and Analysis

The purpose of the simulation study was to indicate which combination of the absorption cycle model and solar thermal collector provides the most accurate information in order to bring the cost down. The investigated unit has never been studied before. Therefore, no experimental data is available, but the complete design can be used for this study. The application of design data promises reliable results. A common problem for numerical studies of a large-scale system capacity is the lack of validation data. One approach to resolve this problem is the usage of very detailed models and special simulation tools. In this study, the detailed design data values from Table 1 were used for the simulation of the solar absorption cooling system.

5.1. Water-Lithium Bromide (H_2O-LiBr) Cycle Results

5.1.1. Effect of Top Solar Field Temperature

The simulation data delivers temperature data of solar field at various cooling loads (50–150TR), and at different solar collector working temperature values (100–200 °C for ETC and 200–300 °C for PTC). Figures 2 and 3 depict the obtained results based on the influence of the temperature of the solar collector on the other design parameters, such as mass flow rates, and design aspects. Figures 2a and 3a show the impact of the solar collector temperature on solar field mass flow rate. The mass flow rate shows a strong temperature dependency. Higher temperature of the solar collector also causes a large decline in the mass flow rate of the solar field. The primary cause for this effect was referring to the energy balance throughout the solar field as provided in this partnership $Q_{th} = M_{col}^{\cdot} \times C_p \times (T_o - T_i)$.

Even so, in contrast with the ETC, the PTC yielded a lower average mass flow rate dependent on an increase in top temperature. The solar field area also has an increasing influence depending on the temperature rise. This effect is shown in Figures 2b and 3b. The increase in the outlet temperature is quite certain to increase the area of the solar field. However, the PTC is registered less in the total area vs. the ETC. Figures 2c and 3c represent a significant impact on flash tank volume by the increase in solar collector temperature. Even so, in comparison with the ETC, PTC showed low tank volume results.

The total solar thermal energy variations due to the change in the upper temperature of the solar field have been depicted in Figures 2d and 3d. Raising the upper solar field temperature increases solar thermal power in the entire solar field in both cases. The exit temperature is an important value for designing the solar field. For ETC collectors and PTC solar collectors, a temperature level of 150~200 °C and 250~300 °C are suggested in this study. Based on the current obtained results, it is quite interesting to assign the operating temperature as follows:

- T_a = 35 °C.
- T_c = 43 °C.
- T_e = 7~10 °C.
- T_g = 85~90 °C.
- ETC T_{high} = 150~200 °C.
- PTC T_{high} = 250~300 °C.

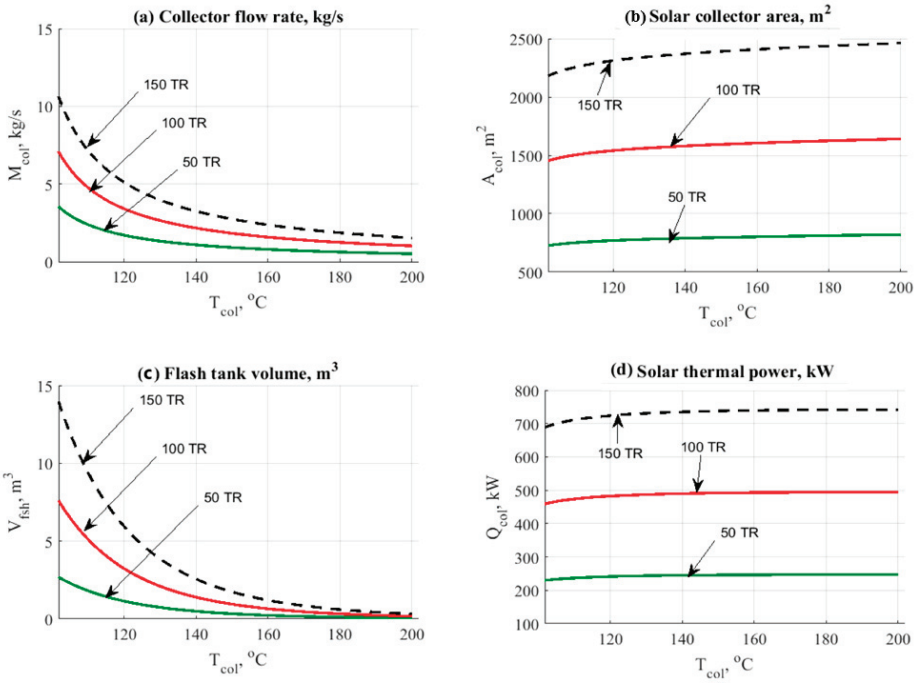

Figure 2. Data results for ETC/H_2O-LiBr cycle vs. variation in exit upper temperature of the solar field. (**a**) Collector flow rate. (**b**) Solar collector area. (**c**) Flash tank volume. (**d**) Solar thermal power.

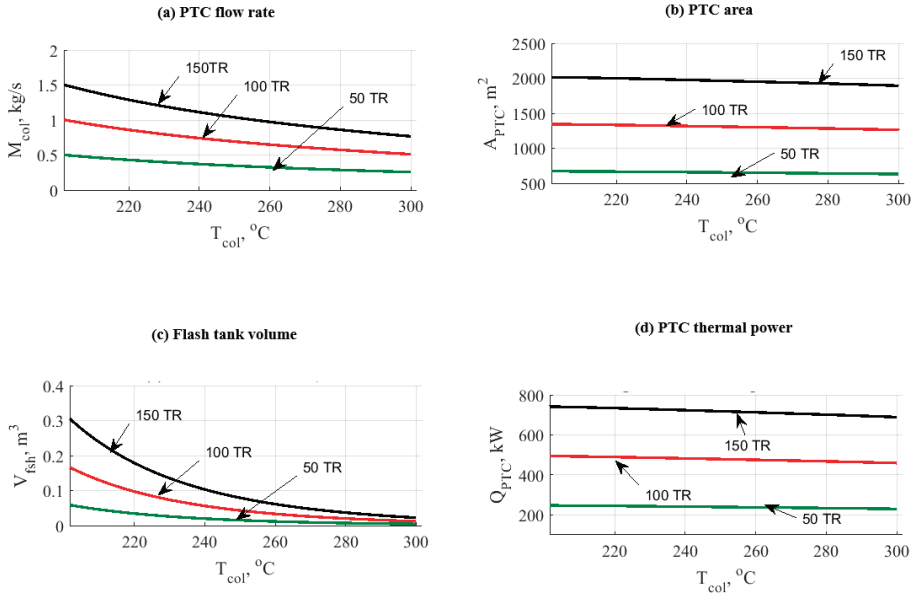

Figure 3. Data results for PTC/H_2O-LiBr cycle vs. variation in exit upper temperature of the solar field. (**a**) Collector flow rate. (**b**) Solar collector area. (**c**) Flash tank volume. (**d**) Solar thermal power.

5.1.2. Effect of Cooling Load

Figures 4 and 5 demonstrate the influence of cooling load on cycles ETC/H_2O-LiBr and PTC/H_2O-LiBr. The two figures addressed the influence on the costs per hour, the cost of the levelized power, and the cost of the thermo-economic product. The thermo-economic parameter is very important because it reflect the combination between cost and exergy. At the same time, the exergy is also reflecting the maximum available work (gain) that be extracted from any system putting in consideration the entropy generation minimization. As expected, the trend in the figure has been increasing due to the load and energy consumption of all units. The solar collectors showed the largest hourly cost values compared to the corresponding other units, as illustrated in Figures 4a and 5a.

Even so, the PTC is reported to be 12% lower than the ETC associated with the hourly cost variable. The key factor was the rise in the working temperature of the collector (250 °C vs. 150 °C). More steam is produced for the AAC cycle by raising the collector temperature. The influence of increasing cooling load on pumps and flashing tanks is illustrated in Figures 4b and 5b. The figures clearly show that the pumps register slightly higher than the flash tank by the total work required.

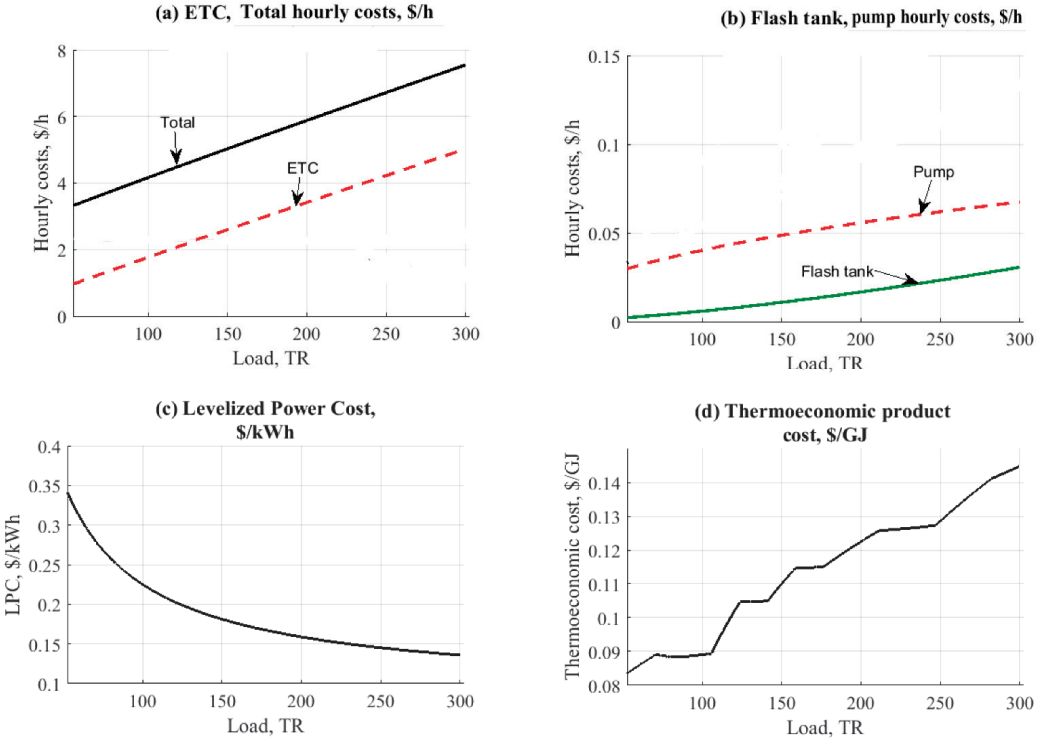

Figure 4. Data results for ETC-H_2O-LiBr cycle vs. change in cooling load. (**a**) ETC total hourly cost. (**b**) Flash tank and pump hourly cost. (**c**) Levelized power cost. (**d**) Thermo-economic product.

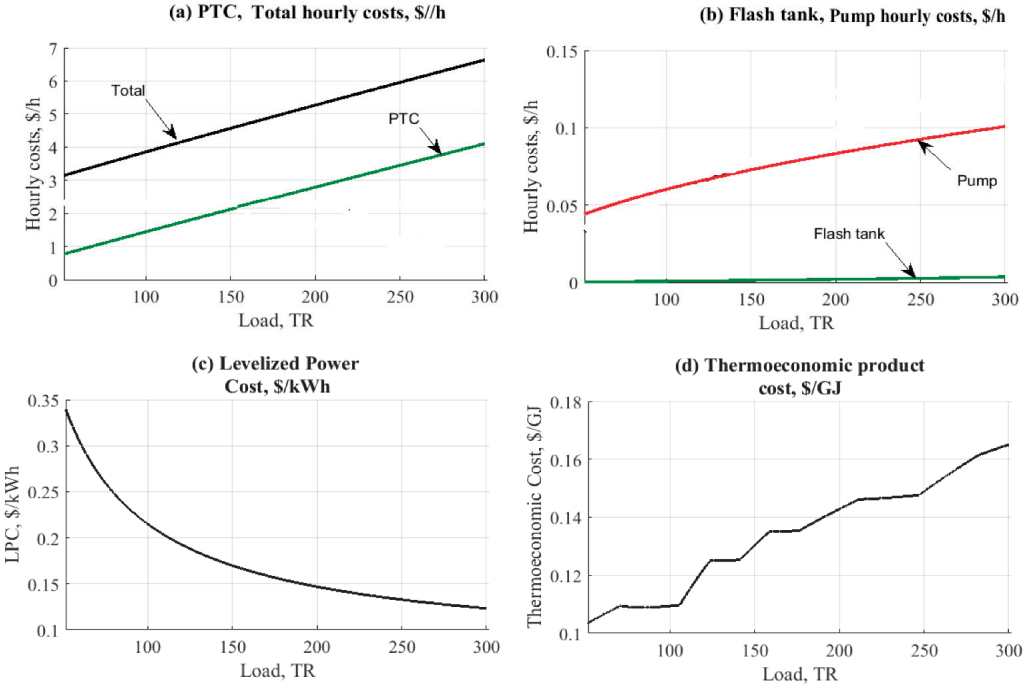

Figure 5. Data results for PTC-H_2O-LiBr cycle vs. change in cooling load. (**a**) PTC total hourly cost. (**b**) Flash tank and pump hourly cost. (**c**) Levelized power cost. (**d**) Thermo-economic product.

Figures 4c and 5c demonstrate the impact of cooling on the cost of levelized power, $/kWh. The outcomes are almost the same depending on the approximate results of the related pumping unit in both configurations. The leveled power cost varied from 0.15 $/kWh to 0.35 $/kWh. A similar close was observed when comparing the cost of the thermo-economic product. For both configurations, the outcomes have been centralized at 0.08 to 0.14~0.16 $/GJ with a minor advantage to the ETC (Figures 4d and 5d). As expected, a higher load will increase the exergy cost. Both PTC and ETC have been identified as the main reason for such an effect due to the large area that is required for covering the load.

5.2. Ammonia-Water (NH_3-H_2O) Cycle Results

5.2.1. Effect of Top Solar Field Temperature (NH_3-H_2O)

The upper temperature of the solar field is considered a very significant factor within this cycle. Figures 6 and 7 demonstrate the changes in the performance and design variables for both ETC and PTC installations. The temperature range for ETC was 110 °C up to 200 °C. For PTC, the temperature range was 150 °C up to 300 °C.

Figure 6a indicates the influence of the top ETC temperature on the mass flow rate of the solar field. The figure also shows that a rise in the upper temperature reduces the overall mass flow rate in the solar field as a common result of the energy balance. An identical trend was also observed in Figure 7a that depicts the PTC operation. Even so, the PTC granted smaller flow rates, leading to a lower cost. The difference is considerable when comparing 50 kg/s to 300 kg/s @150TR for the ETC and 15 kg/s to 65 kg/s @150TR for the PTC.

Figures 6b and 7b display the influence of solar field temperature on the design area of the solar collectors. The variations on the two figures were not massive, even though the lowest area, i.e., the lowest cost and control is reported for the PTC as anticipated. Raising the temperature of PTC will reduce both the loops and unit numbers as well. The number of loop variables is influenced by the total area of the PTC needed for the load. For instance, the ETC at 150TR would consume around 45,000 m^2 to 50,000 m^2. However, the PTC in the same operating conditions will require approximately 45,000 m^2 down to 40,000 m^2.

For both situations, the volume of the flash tank has been depicted in Figures 6c and 7c. The distinction is very obvious with the PTC advantage. Increasing the upper-temperature level of the solar field will reduce the volume of the flashing tank. However, the ETC would require bigger tanks due to a massively lower dryness fraction relative to the PTC process.

For ETC, Figure 6d represents the effect on the thermal power, kW; the rise in working temperature also enhances the solar thermal energy. Figure 7d demonstrates the influence on the thermal power of the PTC. The figure exhibits a descending behavior concerning the upper solar field temperature increase. In general, the increase in AAC unit load would require a larger solar field area, resulting in the mass flow rate increase.

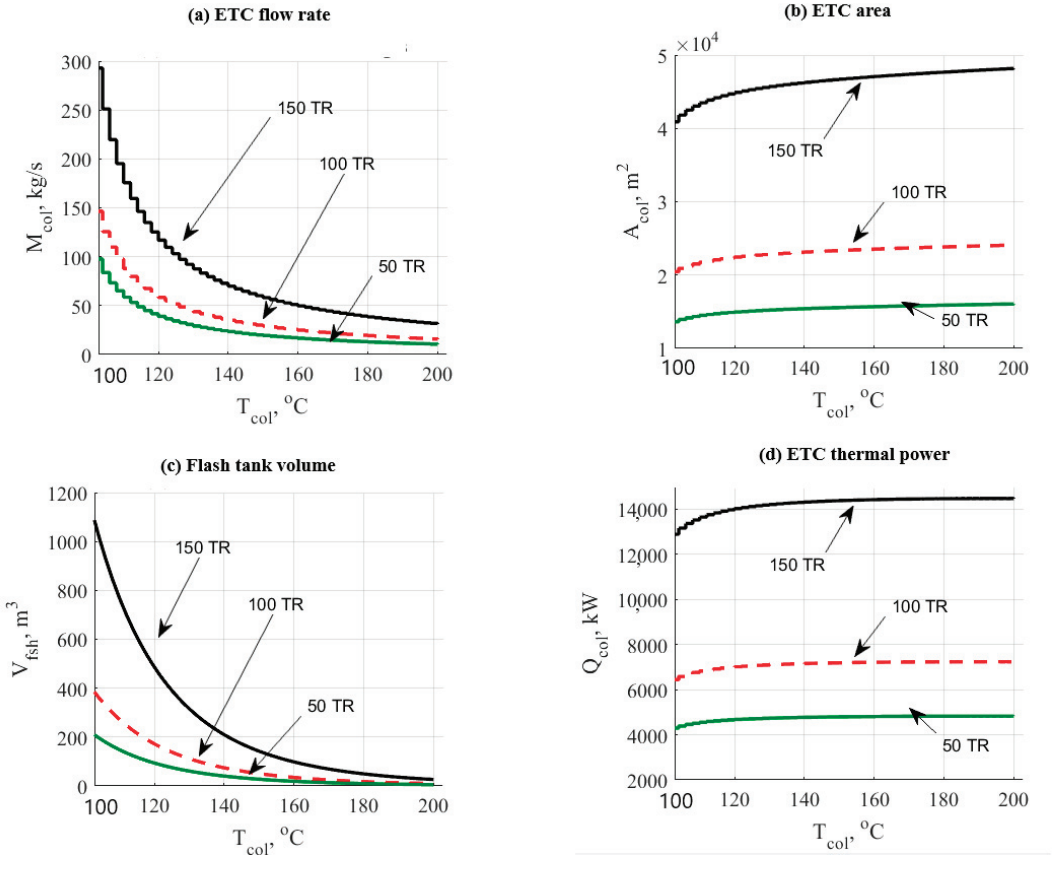

Figure 6. Data results for ETC/NH_3- H_2O cycle vs. variation in upper temperature of the solar field. (**a**) Collector flow rate. (**b**) Solar collector area. (**c**) Flash tank volume. (**d**) Solar thermal power.

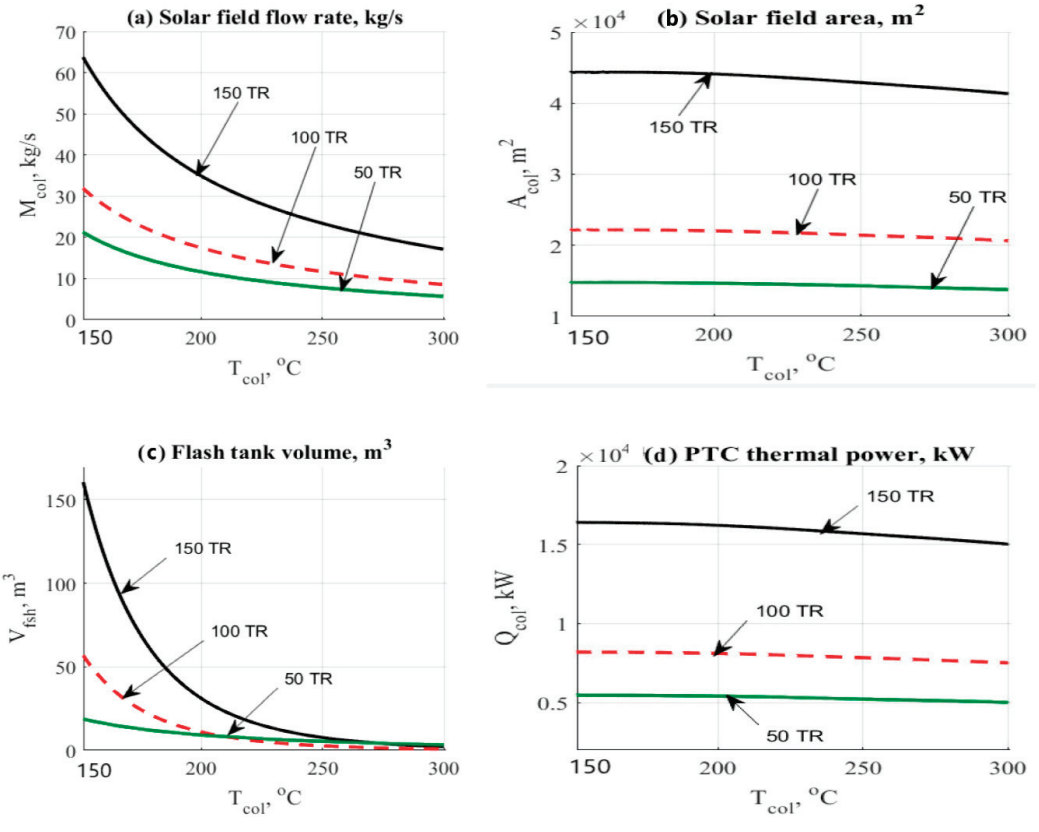

Figure 7. Data results for PTC/NH_3- H_2O cycle vs. variation in upper temperature of the solar field. (**a**) Collector flow rate. (**b**) Solar collector area. (**c**) Flash tank volume. (**d**) Solar thermal power.

Ranges of 150~200 °C and 250~300 °C are advocated for ETC and PTC solar thermal collectors in this paper. Depending on the latest data achieved, it is quite important to assign the working temperature as follows:

- T_a = 35 °C.
- T_c = 43 °C.
- T_e = 7~10 °C.
- T_g = 85~90 °C.
- ETC T_{high} = 150~200 °C.
- PTC T_{high} = 250~300 °C.

5.2.2. Effect of Cooling Load Effect (NH_3-H_2O)

The effect of cooling capacity on the ETC-NH_3-H_2O and PTC-NH_3-H_2O configurations is illustrated in Figures 8 and 9. The two figures cover the impact on the costs per hour, the cost of the leveled energy, and the cost of the thermo-economic product. The trend in the figure was, as predicted, in a variable mode owing to the energy load and required by all units. The solar collectors showed the largest hourly cost values among the other units as illustrated in Figures 8a and 9a.

However, the PTC was lower by 8% against the ETC, associated with the variable cost of hour metric. This was mainly due to the increase in the collector's working temperature (250 °C vs. 150 °C). The increase in the temperature of the collector would produce further steam for the AAC unit. Pumps and flashing tanks are seen in Figures 8b and 9b. It is clear from the figures that the flashing tank is recorded higher than the pump unit based on the total tank volume. PTC operation was recorded lower in flashing tank hourly cost because it has lower tank volume 0.2–0.3 $/h vs. 0.5–2.2 $/h. Figures 8c and 9c display the impact of cooling capacity on the cost of levelized power rate, $/kWh. The outcomes are almost the same depending on the approximate results of the related pumping unit in both configurations. The leveled power cost varied from 0.07 $/kWh to 0.08 $/kWh for PTC and ETC, respectively. Identical close behavior was observed when compared related to the cost of the thermo-economic product. The results ranged from $0.1 to $1/GJ in both configurations with a smaller advantage for the ETC (Figures 8d and 9d).

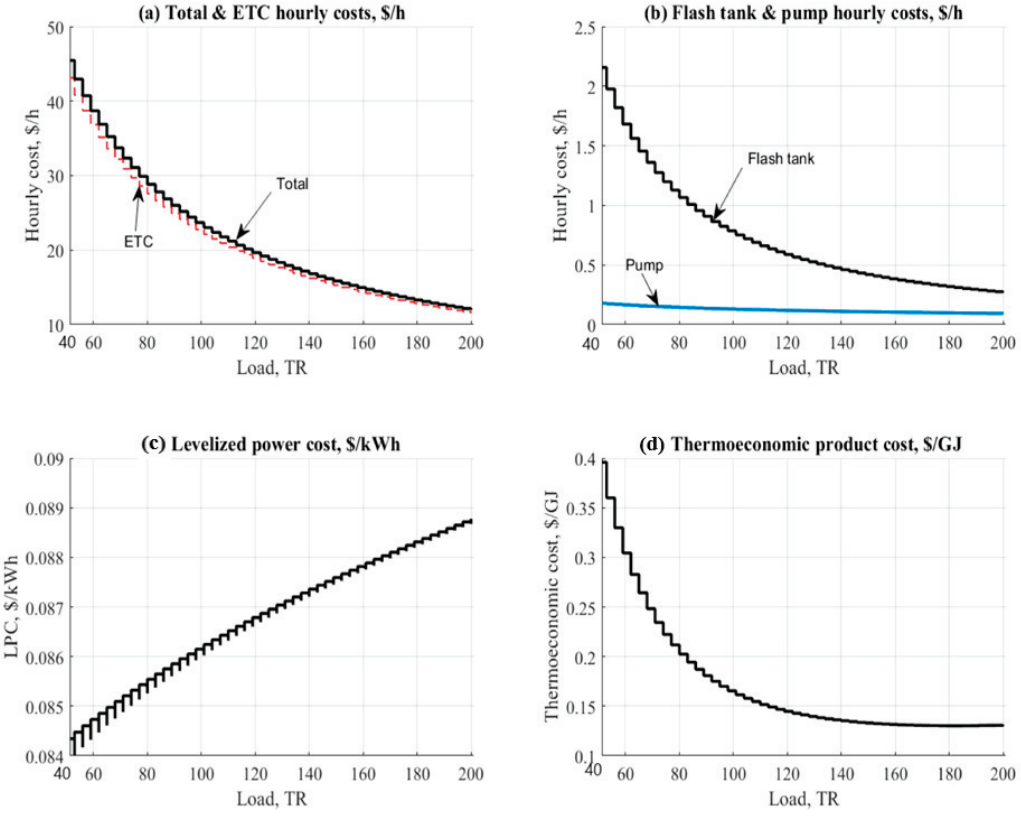

Figure 8. Data results for ETC/NH_3-H_2Ocycle vs. cooling load. (**a**) ETC total hourly cost. (**b**) Flash tank and pump hourly cost. (**c**) Levelized power cost. (**d**) Thermo-economic product.

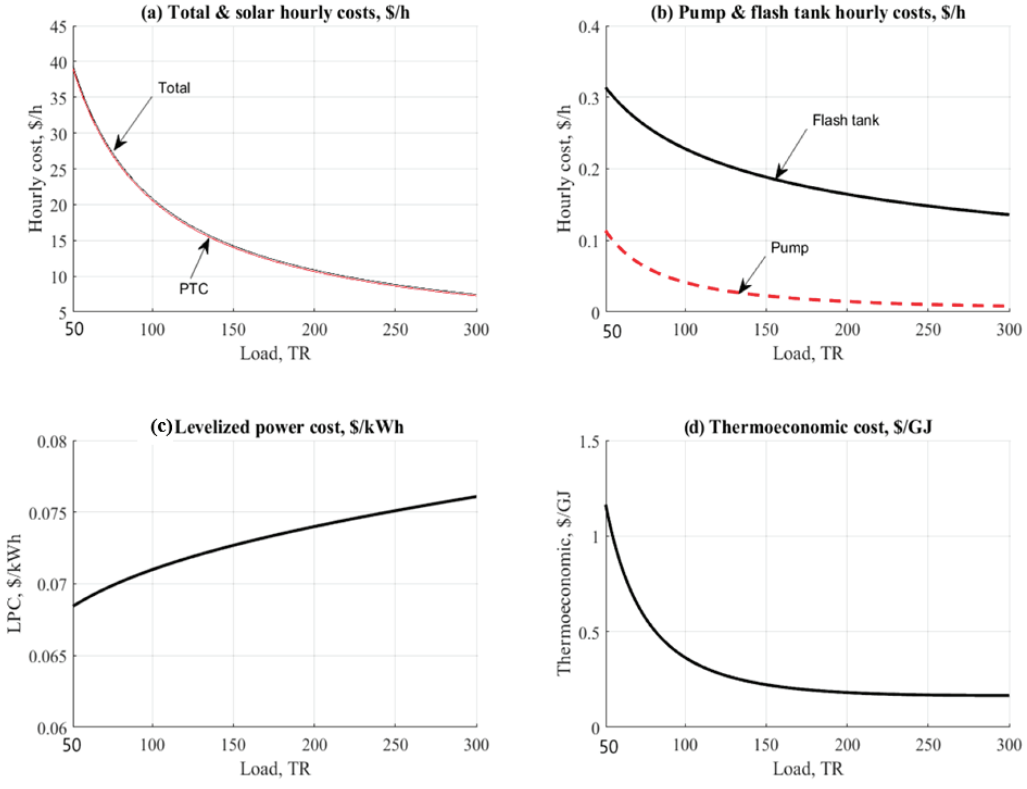

Figure 9. Data results for PTC/NH_3-H_2O cycle vs. cooling load. (**a**) PTC total hourly cost. (**b**) Flash tank and pump hourly cost. (**c**) Levelized power cost. (**d**) Thermo-economic product.

5.3. Case Study Results

The case study introduced in this section compares all the configurations at a specified load point. This case study was conducted in a sports hall situated in Baghdad, Iraq. The stadium costs $14 million, and the 3000-seat capacity indoor sports facilities are focused on basketball, volleyball, and athletics. The entire project employs central air conditioning for an air-cooled absorption chiller of 700~800 kW. Its evaporator would be designed to operate in the range of 7~12 °C. Table 2 reports the results data in the case of using the solar absorption cooling cycle for all installations. A cooling load of 200TR was chosen for comparison. The ambient working conditions are set to a specified amount for simplicity. Regarding the results of the solar field, the PTC/H_2O-LiBr configuration proved to be the lowest in the required area, which is quite significant for decreasing the required area. The ETC/H_2O-LiBr was the next one. The same behavior was observed in PTC/NH_3-H_2O vs. ETC/NH_3-H_2O configurations. With respect to design features that include the design of the flash tank, the operation of the PTC/H_2O-LiBr configuration provided the lowest results, and this was very advantageous by 0.11 m^3, while the ETC/H_2O-LiBr has 1 m^3 and the PTC/NH_3-H_2O had 3.8 m^3. We also observed the same trend concerning the exergy destruction and dryness fraction. Exergy destruction analysis showed that the most critical part in the system that causes the highest percent of the exergy destruction is the solar collectors due to the big difference between the highest exergy input, as it depends on the sun temperature, and the exergy output due to the heat transfer to the heat carrier fluid (water). Consequently, in order to decrease the solar collector's exergy loss, the heat transfer between the solar radiation and the heat carried fluid has to be enhanced

through new designs and investigations. For the entire AAC, the highest exergy loss was experienced in the absorber and generator. Therefore, special attention must be considered in the design of these components. The AAC was found to be lower in design results based on the H_2O-LiBr operation. The results expose that PTC is regarded as a cycling advantage for ETC operation. The idle driving steam has been reported by PTC/H_2O-LiBr with 0.4 kg/s, which led to a reduced volume of the flashing tank and solar field area. The COP value was substantial relative to the H_2O-LiBr cycle. For cost per hour, PTC/H_2O-LiBr was noticed to be the lowest among the others. By reaching 5.2 $/hr, PTC/$H_2O$-LiBr was identified as the best alternative for this case study. The lowest hourly costs for the solar array were regarded as the vital term to judge the cost of the system. The thermo-economic cost was almost the same for all configurations in the range of 0.14–0.16 $/GJ with an advantage for H_2O-LiBr configuration.

Table 2. Case study results @ 200 TR cooling load.

Solar Radiation, W/m^2		500		
T_{amb}, °C		25		
T_a, T_e, T_g, T_c, T_{col}, °C	=30, 10, 90, 40, 175	=30, 10, 90, 40, 175	=30, 10, 90, 40, 250	=30, 10, 90, 40, 250
Load, TR		200		
Target cooled air, °C		20		
Interest rate, %		5		
Load factor, %		95		
Plant life time, yr		20		
Electric cost, $/kWh		0.065		
Pumps efficiency, %		75		
Configuration:	**ETC-H_2O/LiBr**	**ETC-NH_3/H_2O**	**PTC-LiBr/H_2O**	**PTC-NH_3/H_2O**
		Solar field:		
Total solar field area, m^2	3022	11,880	2433	11,020
Solar thermal power, kW	918.6	3612	890	4051
Inlet temperature, °C	91.64	91.82	92.66	92.04
Mass flow rate, kg/s	2.582	10.17	1.327	8.727
Inlet exergy, kW	1436	5646	1136	4217
Exergy destruction, kW	1191	4683	930	5143
		Flash tank:		
Height/Width, m	1.742/0.852	3.381/1.655	0.837/0.41	2.743/1.343
Volume, m^3	0.9942~1	7.276	0.1106	3.883
Total flow rate, kg/s	2.582	10.17	1.327	8.727
Water content, kg/s	2.1	8.551	0.897	6.91
Dryness fraction	0.1667	0.1595	0.324	0.208
Exergy destruction, kW	134.3	391.1	180.8	515.6
		AAC unit:		
Q_a, kW	743.3	1251	743.3	1153
A_a, m^2	190.5	23.37	190.5	21.3
M_{str}, kg/s	1.391	1.428	1.391	1.428
M_{wk}, kg/s	1.092	0.778	1.092	0.778
$X_{a\text{-}hex}$	0.4893	–	0.4893	–
$X_{hex\text{-}NH_3}$	–	0.4554	–	0.4554
A_{hex}, m^2	1.313	7.837	1.313	6.73
Q_g, kW	787.8	1407	787.8	1256
A_g, m^2	4.299	5.123	4.299	4.574

Table 2. *Cont.*

Driving steam flow, kg/s	0.4034	2.07	0.4034	1.848
$X_{g\text{-}hex}$	0.6233	–	0.6233	–
Q_c, kW	747.8	694.9	747.8	694.9
A_c, m^2	37.45	9.1	37.45	9.1
M_r, kg/s	0.299	0.6505	0.299	0.6505
Q_e, kW	703.4	703.4	703.4	703.4
A_e, m^2	36.35	41.15	36.35	41.15
FHP, kW	29.33~30	70.64	29.33~30	70.64
M_{air}, kg/s	68	119.5~120	68	119.5~120
COP/COP_{max}	0.89/1.56	0.5/1.559	0.89/1.56	0.5/1.559
RPR	0.573	0.3206	0.573	0.3591
Exergy destruction, kW	729.9	1010	729.9	977.3
Pump unit:				
W_p, kW	3.204	12.63	7.338	18.97~19
Exergy destruction, kW	14.8	64.7	12.33	62.25
Cost & Thermo-economics:				
Z_{col}, $/h$	3.918	11.75	2.604	10.93
Z_{fsh}, $/h$	0.02	0.11	0.001	0.06
Z_{aac}, $/h$	0.121	0.0487	0.121	0.04716
Z_{p+f}, $/h$	0.055	0.256	0.1743	0.2652
Z_{tot}, $/h$	4.114	12.16	2.9	11.3
LPC, $/kWh$	0.165	0.089	0.1557	0.0744
cp, $/GJ$	0.1474	0.144	0.1602	0.1554

6. Conclusions

This study introduced different configurations of solar-assisted absorption air conditions (AAC) cycles. The proposed system is powered by solar energy. The system configuration combines solar field (PTC/ETC), flashing tank, and absorption chiller (H_2O-LiBr/NH_3-H_2O). A case study of 200 TR cooling is applied to the simulation program. Energetic and exegetic results are presented and have revealed that:

- Design aspects such as solar area and flashing tank volume were found have a great influence on the cycle cost.
- Among all configurations, PTC-H_2O-LiBr gives a remarkable result comparing against the ETC.
- For case study, PTC-H_2O-LiBr was recorded the best based on design and hourly costs. The required solar area was in the range of 2000~2500 m^2. Meanwhile, the total hourly cost was in the range of 4~5 $/h, which is quite attractive.
- Absorption chiller coefficient of performance was in the range of 0.5 to 0.9.
- The total rate of exergy destruction of the AAC was in the range of 55 kW.
- Solar field harvests a larger amount of exergy destruction rates for all configurations due to the large area and mass flow rate effect. PTC-H_2O-LiBr resulted in a 930~1000 kW of exergy destruction rate comparing against PTC-NH_3-H_2O, which resulted a value of 4600~5000 kW.
- PTC-H_2O-LiBr gives the lowest values related to exergy destruction rates for all units.
- PTC-H_2O-LiBr gives the lowest value of flashing tank design aspects such as width 0.4~0.5 m, height 0.8 m, and volume 0.11 m^3. ETC-H_2O-LiBr comes next with a total flashing tank equal to ~1 m^3.

- The thermo-economic cost is almost the same for all configurations in the range of 0.14–0.16 $/GJ with an advantage for H_2O-LiBr configuration.
- It is quite clear that PTC-H_2O-LiBr followed by ETC-H_2O-LiBr have remarkable results according to the terms of energy, design, and cost. Generally, PTC system is considered the best choice for H_2O-LiBr or NH_3-H_2O.

Author Contributions: Methodology, A.A.-F.; software, A.A.-F.; investigation, A.A.-F.; writing—original draft preparation, A.A.-F.; writing—review and editing, A.A.-F. and F.A.; supervision, B.E.; All authors have read and agreed to the published version of the manuscript.

Funding: This research received no external funding.

Institutional Review Board Statement: Not applicable.

Informed Consent Statement: Not applicable.

Data Availability Statement: Not applicable.

Acknowledgments: The corresponding author would like to thank the Technical University of Darmstadt, enabling the open-access publication of this paper.

Conflicts of Interest: The authors declare no conflict of interest.

Nomenclature

A	Availability: kW, Area:m^2
A_t	Tube cross sectional area, m^2
A_f	Amortization factor, 1/y
AAC	Absorption Air Conditioning
C	Thermo-economic cost stream, $/kJ
C_p	Specific heat capacity, kJ/kg °C @ constant pressure
COP	Coefficient of Performance
D	Diameter, m
D_{env}	Collector glass envelope diameter, m
E	Exergy stream, kW
ETC	Evacuated Tube Collector
FPT	Flat Plate Collector
f	Function
FHP	Fan power, kW
H, h	Height, m, Enthalpy, kJ/kg
I_s	Solar intensity, W/m^2
i	Interest rate, %
L	Length, m
L_m	Module length, m
LPC	Levelized Power Cost, $/kWh
LTp	Plant life time, y
M	Mass flow rate, kg/s
NOT	Number of Tubes
NOC	Number of Collectors
NOL	Number of Loops
OH	Operating hours
PTC	Parabolic Through Collector
P	Power (Kw), or Pressure, kPa
ΔP	Pressure, kPa
Q	Thermal power, kW
RPR	Relative Performance Ratio
Re	Raynold's Number
S, s	Entropy, kJ/kg °C

T	Temperature, °C
V, Vol	Volume, cm^3
v	Velocity, m/s
W	Power, Work, kW
W_c	Collector width, m
X	Concentration percentage, %
Z	Hourly cost, $/h
Subscripts	
a, abs	Absorber
air	Air
amb	Ambient
c	Condenser
col	Collector
e	Evaporator
etc	Evacuated tube collector
f	Liquid phase
fan	Fan
fsh	Flashing tank
fst	Flashing steam
g	Generator, vapor phase
i	Inlet
$loop$	Loop
o	Out
p	Pump
ptc	Parabolic trough collector
$p_{i,o}$	Pump inlet and outlet
q	Heat
r	Refrigerant
s	Steam
st	Steam
w	Water
Greek	
η	Efficiency, %
ρ	Density, kg/m^3
μ	Dynamic viscosity, Pa.s

References

1. Wang, R.Z.; Wu, J.Y.; Dai, Y.J.; Wang, W.; Jiangzhou, S. *Adsorption Refrigeration*; China Mechanical Industry Press: Beijing, China, 2002.
2. IEA. *Global CO_2 Emissions in 2019*; IEA: Paris, France, 2020. Available online: https://www.iea.org/articles/global-co2-emissions-in-2019 (accessed on 10 September 2020).
3. Al-Alili, A.; Hwang, Y.; Radermacher, R. Review of solar thermal air conditioning technologies. *Int. J. Refrig.* **2014**, *39*, 4–22. [CrossRef]
4. Mone, C.D.; Chau, D.S.; Phelan, P.E. Economic feasibility of combined heat and power and absorption refrigeration with commercially available gas turbines. *Energy Convers. Manag.* **2001**, *42*, 1559–1573. [CrossRef]
5. Rodríguez-Muñoz, J.L.; Belman-Flores, J.M. Review of diffusion–absorption refrigeration technologies. *Renew. Sustain. Energy Rev.* **2014**, *30*, 145–153. [CrossRef]
6. Bataineh, K.; Taamneh, Y. Review and recent improvements of solar sorption cooling systems. *Energy Build.* **2016**, *128*, 22–37. [CrossRef]
7. Syed, A.; Maidment, G.G.; Tozer, R.M.; Missenden, J.F. A Study of the Economic Perspectives of Solar Cooling Schemes. In Proceedings of the CIBSE National Conference, Part 2, London, UK, 14 October 2002.
8. Balaras, C.A.; Hans-Martin, H.; Wiemken, E.; Grossman, G. Solar cooling: An overview of European applications design guidelines. *ASHRAE J.* **2006**, *48*, 14.
9. Li, M.; Xu, C.; Hassanien, R.H.E.; Xu, Y.; Zhuang, B. Experimental investigation on the performance of a solar powered lithium bromide–water absorption cooling system. *Int. J. Refrig.* **2016**, *71*, 46–59. [CrossRef]

10. Mazloumi, M.; Naghashzadegan, M.; Javaherdeh, K.J.E.C. Simulation of solar lithium bromide–water absorption cooling system with parabolic trough collector. *Energy Convers. Manag.* **2008**, *49*, 2820–2832. [CrossRef]
11. Shirazi, A.; Taylor, R.A.; White, S.D.; Morrison, G.L. Multi-effect absorption chillers powered by the sun: Reality or reverie. *Energy Procedia* **2016**, *91*, 844–856. [CrossRef]
12. Zacarías, A.; Venegas, M.; Lecuona, A.; Ventas, R.; Carvajal, I. Experimental assessment of vapour adiabatic absorption into solution droplets using a full cone nozzle. *Exp. Therm. Fluid Sci.* **2015**, *68*, 228–238. [CrossRef]
13. Rajasekar, D.; Ponshanmugakumar, A.; Rajavel, R. Design and Performance Validation of Vapour Absorption Solar Air Conditioning System. *Int. J. Future Revolut. Comput. Sci. Commun. Eng.* **2017**, *3*, 115–119.
14. Flores, V.H.F.; Román, J.C.; Alpírez, G.M. Performance analysis of different working fluids for an absorption refrigeration cycle. *Am. J. Environ. Eng.* **2014**, *4*, 1–10.
15. Gebreslassie, B.H.; Medrano, M.; Boer, D. Exergy analysis of multi-effect water–LiBr absorption systems: From half to triple effect. *Renew. Energy* **2010**, *35*, 1773–1782. [CrossRef]
16. Kilic, M.; Kaynakli, O. Second law-based thermodynamic analysis of water-lithium bromide absorption refrigeration system. *Energy* **2007**, *32*, 1505–1512. [CrossRef]
17. Karakas, A.; Egrican, N.; Uygur, S. Second-law analysis of solar absorption-cooling cycles using lithium bromide/water and ammonia/water as working fluids. *Appl. Energy* **1990**, *37*, 169–187. [CrossRef]
18. Dincer, I.; Ratlamwala, T.A.H. Fundamentals of Absorption Refrigeration Systems. In *Integrated Absorption Refrigeration Systems*; Springer: Cham, Switzerland, 2016; pp. 1–25.
19. Lu, Z.S.; Wang, R.Z. Experimental performance investigation of small solar air-conditioning systems with different kinds of collectors and chillers. *Solar Energy* **2014**, *110*, 7–14. [CrossRef]
20. Colorado, D.; Rivera, W. Performance comparison between a conventional vapor compression and compression-absorption single-stage and double-stage systems used for refrigeration. *Appl. Therm. Eng.* **2015**, *87*, 273–285. [CrossRef]
21. Wang, Y.; Wang, C.; Feng, X. Optimal match between heat source and absorption refrigeration. *Comput. Chem. Eng.* **2017**, *102*, 268–277. [CrossRef]
22. Du, S.; Wang, R.Z.; Chen, X. Development and experimental study of an ammonia water absorption refrigeration prototype driven by diesel engine exhaust heat. *Energy* **2017**, *130*, 420–432. [CrossRef]
23. Al-Falahi, A.; Alobaid, F.; Epple, B. Design and Thermo-economic Comparisons of Large Scale Solar Absorption Air Conditioning Cycles. *Case Stud. Therm. Eng.* **2020**, *22*, 100763. [CrossRef]
24. Al-Falahi, A.; Alobaid, F.; Epple, B. Thermo-Economic Evaluation of Aqua-Ammonia Solar Absorption Air Conditioning System Integrated with Various Collector Types. *Entropy* **2020**, *22*, 1165. [CrossRef] [PubMed]
25. NIST Chemistry WebBook, SRD 69. Available online: https://webbook.nist.gov/chemistry/name-ser/ (accessed on 3 October 2020).
26. Vakiloroaya, V.; Ha, Q.; Skibniewski, M.J. Modeling and experimental validation of a solar-assisted direct expansion air conditioning system. *Energy Build.* **2013**, *66*, 524–536. [CrossRef]
27. Carles Bruno, J.; López-Villada, J.; Letelier, E.; Romera, S.; Coronas, A. Modelling and Optimisation of Solar Organic Rankine Cycle Engines for Reverse Osmosis Desalination. *Appl. Therm. Eng.* **2008**, *28*, 2212–2226. [CrossRef]
28. Nafey, A.S.; Sharaf, M.A.; García-Rodríguez, L. A New Visual Library for Design and Simulation of Solar Desalination Systems (SDS). *Desalination* **2010**, *259*, 197–207. [CrossRef]
29. Eldean, M.A.S.; Soliman, A.M. A new visual library for modeling and simulation of renewable energy desalination systems (REDS). *Desalin. Water Treat.* **2013**, *51*, 6905–6920. [CrossRef]
30. Singh, R.; Kumar, D.R. Theoritical Analysis of Nh3-H2o Refrigeration System Coupled with Diesel Engine: A Thermodynamic Study. *IOSR J. Mech. Civ. Eng.* **2014**, *11*, 29–36. [CrossRef]
31. Li, K.W. *Applied Thermodynamics: Availability Method and Energy Conversion*; CRC Press: Boca Raton, FL, USA, 1995.
32. Bejan, A.; Tsatsaronis, G.; Moran, M.J. *Thermal Design and Optimization*; Wiley: New York, NY, USA, 1996; Chapter 8.
33. Sharaf, M.A.; Nafey, A.S.; García-Rodríguez, L. Author's Personal Copy Thermo-Economic Analysis of Solar Thermal Power Cycles Assisted MED-VC (Multi Effect Distillation-Vapor Compression) Desalination Processes. *Energy* **2011**, *36*, 2753–2764. [CrossRef]
34. Sharaf, M.; Nafey, A.; Desalination, L.G.-R. Exergy and Thermo-Economic Analyses of a Combined Solar Organic Cycle with Multi Effect Distillation (MED) Desalination Process. *Desalination* **2011**, *272*, 135–147. [CrossRef]
35. Castro, M.M.; Song, T.W.; Pinto, J.M. Minimization of operational costs in cooling water systems. *Chem. Eng. Res. Des.* **2000**, *78*, 192–201. [CrossRef]

applied sciences

MDPI

Article

Process Simulation of Steam Gasification of Torrefied Woodchips in a Bubbling Fluidized Bed Reactor Using Aspen Plus

Nhut M. Nguyen [1,2,*], Falah Alobaid [1] and Bernd Epple [1]

[1] Institute for Energy Systems and Technology, Technical University of Darmstadt, Otto-Berndt-Straße 2, 64287 Darmstadt, Germany; falah.alobaid@est.tu-darmstadt.de (F.A.); bernd.epple@est.tu-darmstadt.de (B.E.)
[2] Department of Chemical Engineering, Campus II 3/2 Street, Can Tho University, Can Tho 900000, Vietnam
* Correspondence: nhut.nguyen@est.tu-darmstadt.de; Tel.: +49-6151-16-22673

Abstract: A comprehensive process model is proposed to simulate the steam gasification of biomass in a bubbling fluidized bed reactor using the Aspen Plus simulator. The reactor models are implemented using external FORTRAN codes for hydrodynamic and reaction kinetic calculations. Governing hydrodynamic equations and kinetic reaction rates for char gasification and water-gas shift reactions are obtained from experimental investigations and the literature. Experimental results at different operating conditions from steam gasification of torrefied biomass in a pilot-scale gasifier are used to validate the process model. Gasification temperature and steam-to-biomass ratio promote hydrogen production and improve process efficiencies. The steam-to-biomass ratio is directly proportional to an increase in the content of hydrogen and carbon monoxide, while gas yield and carbon conversion efficiency enhance significantly with increasing temperature. The model predictions are in good agreement with experimental data. The mean error of CO_2 shows the highest value of 0.329 for the steam-to-biomass ratio and the lowest deviation is at 0.033 of carbon conversion efficiency, respectively. The validated model is capable of simulating biomass gasification under various operating conditions.

Keywords: steam gasification; biomass; bubbling fluidized bed; Aspen Plus simulation; hydrogen production

Citation: Nguyen, N.M.; Alobaid, F.; Epple, B. Process Simulation of Steam Gasification of Torrefied Woodchips in a Bubbling Fluidized Bed Reactor Using Aspen Plus. *Appl. Sci.* **2021**, *11*, 2877. https://doi.org/10.3390/app11062877

Academic Editor: Francesco Calise

Received: 2 March 2021
Accepted: 18 March 2021
Published: 23 March 2021

1. Introduction

Biomass has been considered as one of the most important primary and renewable energy resources for the production of heat, electricity, hydrogen, chemicals, and liquid fuels due to its carbon-neutral renewable and abundant quantity. Furthermore, the energy production from biomass is advantageous to other renewable sources such as wind energy, hydropower, solar energy, etc. [1].

Gasification is a partial oxidation process at high temperatures, which can convert organic or fossil fuel-based carbonaceous materials into gaseous fuel including mainly H_2, CO, CO_2, and CH_4. In the presence of steam, the product gas has been generated with 30–60% of H_2 content and a calorific value of 10–18 MJ/Nm^3 [2,3]. Thus, steam gasification of biomass is an effective and efficient technology for sustainable hydrogen production without a carbon footprint [4].

Generally, three reactor configurations can be used for biomass gasification, i.e., the entrained flow, fixed bed, and fluidized bed reactors. The fluidized bed gasifiers show advantages for biomass conversion due to the perfect contact between gas and solid, increasing heat and mass transfer characteristics, and improving temperature control. An experimental investigation of gasification of torrefied woody biomass was conducted by Berrueco et al. [5] in a pressurized fluidized bed, evaluating the effect of pressure and torrefaction level on the yield and composition of the products. The authors found that the

pressure could result in a decline in CO and H_2 levels, whereas CO_2 and CH_4 yield increase. Chen et al. [6] observed that the cold gasification efficiency of torrefied bamboo rose by 88% compared to raw bamboo. Furthermore, char gasification reactions are one of the most important reactions in biomass gasification. Many kinetic studies have been carried out through the thermogravimetric analysis instrument (TGA) to determine the kinetic parameters of char gasification [7–12]. Some reaction kinetic models have been proposed for char gasification. They could be categorized into two groups such as theoretical and semiempirical models. Four conversion models have been investigated for char gasification reactions, i.e., volumetric model, shrinking core model, random pore model, and Johnson model [9,13]. Additionally, the Langmuir-Hinshelwood reaction model has been used extensively as a kinetic model for heterogeneous reactions, particularly char gasification with steam and carbon dioxide [14].

Along with the computational progress, the numerical simulation could help bypass a long planning and construction process of experimental studies, provide low-cost methods for the proper design and project realization. Mathematical models are developed to describe the physical and chemical phenomena occurring inside the gasifier and to understand the effect of various operating and design parameters on the process performance. The model also is used to predict the behavior of gasification at off-design conditions and the optimum operating parameters [15]. The main simulation methods can be categorized as the thermal equilibrium model, kinetic model, numerical model, and artificial neural network [15–27]. The thermodynamic equilibrium model is simple and provides the preliminary comparison and assessment of the gasification process [28]. There are three equilibrium modeling approaches, such as the restricted equilibrium model, empirical correlation-based model, and the model based on a combination of hydrodynamic and kinetic aspects [29].

The Aspen Plus process simulator, which is developed to facilitate physical, chemical, and biological calculations, has been used commonly in various studies to simulate coal and biomass gasification. Due to the complex nature of tar, most of the studies in the literature have not considered tar calculations. Tar is a product of the thermal decomposition process of biomass, including condensed oils such as olefins, phenols, aromatics, etc. Few Aspen Plus models of biomass gasification have been reported on tar and its kinetics. For example, a mathematical model of biomass gasification in a bubbling bed reactor was developed in Aspen Plus with a sub-model for tar generation and cracking [30]. This study has defined tar and its cracking kinetics to improve the model performance and its credibility. Nikoo et al. [31] proposed a process model for biomass gasification using external FORTRAN subroutines for both hydrodynamic and reaction kinetic calculations simultaneously in Aspen Plus. A process model was developed to simulate the air-stream gasification of biomass in a bubbling fluidized bed reactor [17]. This model was based on chemical reaction rates, empirical correlations of pyrolysis mass yields, and hydrodynamic parameters. A simulation was performed in the Aspen program for steam gasification of rice husk to evaluate the influence of gasification temperature and steam-to-biomass ratio on product gas composition [32]. The model was developed based on the chemical equilibrium to predict the gas composition of the process. A model is developed based on Gibbs free energy minimization applying the restricted equilibrium method to study the influence of key parameters on the performance of steam gasification of biomass [33].

The high amount of volatile matter in biomass and the complexity of biomass reaction kinetics in fluidized beds have hindered the simulation of biomass gasification. Many studies ignored the kinetics of char gasification and developed their gasification model based on Gibbs equilibrium. Additionally, in a typical fluidized bed gasifier, solid fuels and bed material are fluidized by a mixture of gases resulting in good solid-gas heat and mass transfer. Consequently, hydrodynamic behavior is a crucial factor in a fluidized bed gasifier influencing strongly the performance of the gasification process. Therefore, reliable process simulation studies on biomass gasification are still limited, resulting in a lack of understanding of the fundamentals of the biomass-based gasification process.

This study has been developed in Aspen Plus based on the previous studies with some improvements to provide a good understanding of biomass gasification in terms of the effect of operating parameters on the process performance and the phenomena occurring in a bubbling fluidized bed gasifier. The proposed model based on a combination of both hydrodynamic and reaction kinetic calculations simultaneously is capable of predicting the steady-state performance of a negative gauge pressure bubbling fluidized bed gasifier. Due to the complexity of biomass characteristics, the mass yields of pyrolytic products released from torrefied wood chips were determined by the model of Neves et al. [34] according to the biomass proximate and ultimate analyses. Char gasification kinetics obtained from experimental investigations are to determine the reaction rate of char gasification. Three chemical reactions, i.e., char gasification with steam and CO_2 and water–gas shift reactions are taken into consideration in the model to calculate variations of components in biomass gasification. Due to the lack of a library model to simulate fluidized bed units in the Aspen Plus simulator, external FORTRAN codes are implemented with input data to simulate an operation of a bubbling fluidized bed gasifier. The validity and accuracy of the model are evaluated by comparing the numerical result obtained with the experimental data of biomass steam gasification.

2. Modeling Methods

In the test rig, silica sand is used as bed material. Biomass is fed continuously and reacts with steam to produce syngas, mainly comprising hydrogen, carbon monoxide, carbon dioxide, and methane. The model is developed based on hydrodynamic and reaction rate kinetic calculations at the isothermal condition.

2.1. Process Assumption

For the modeling of the biomass gasification process, the following assumptions were considered:

- The process is modeled in steady-state and isothermal conditions.
- The reactive gases are H_2, CO, CO_2, CH_4, and H_2O.
- N_2, NH_3, H_2S, and SO_2 are considered chemically inert components in gasification reactions.
- The char is modeled with only components of carbon black and ash.
- All gases are uniformly distributed within the emulsion phase.
- Particles are spherical and of uniform size. Their average diameter remains unchanged during the gasification.
- Char gasification starts in the dense zone and completes in the freeboard.
- Ash and sand are chemically inert under process conditions.

For the hydrodynamic calculation, the following assumptions were made:

- There are two regions in the fluidized bed reaction: bed and freeboard.
- The bubbling regime is maintained in the bed region.
- The volumetric flow rate of gas increases along with the reactor height, corresponding to the gas products generated.
- The mixing of solid particles in the reactor is perfect.
- The reactor is divided into many control volumes with constant hydrodynamic parameters.
- The fluidized bed is one-dimensional.

2.2. Experimental Facility

The experimental reactor comprises a circular column with 54.5 mm inner diameter and 550 mm length, and a porous gas distributor plate at the bottom shown in Figure 1. Pressure and temperature sensors are installed at 90, 350, and 550 mm along the reactor. Two electrical heating elements are used to heat the reactor. 800 g of silica sand is filled up in the reactor as bed material due to its good mechanical properties and no active role. Sand's properties are shown in Table 1. The solid fuel is filled in a hopper and fed continuously into the reactor at 90 mm height through a screw feeder. A gas mixture is pre-heated to 300 °C before being injected into the reactor through a porous distributor. A

part of the product gas is extracted from the reactor to a gas analysis unit, ABB URAS 206 analyzers. A summary of the continuous measuring methods and the maximum relative error is shown in Table 2.

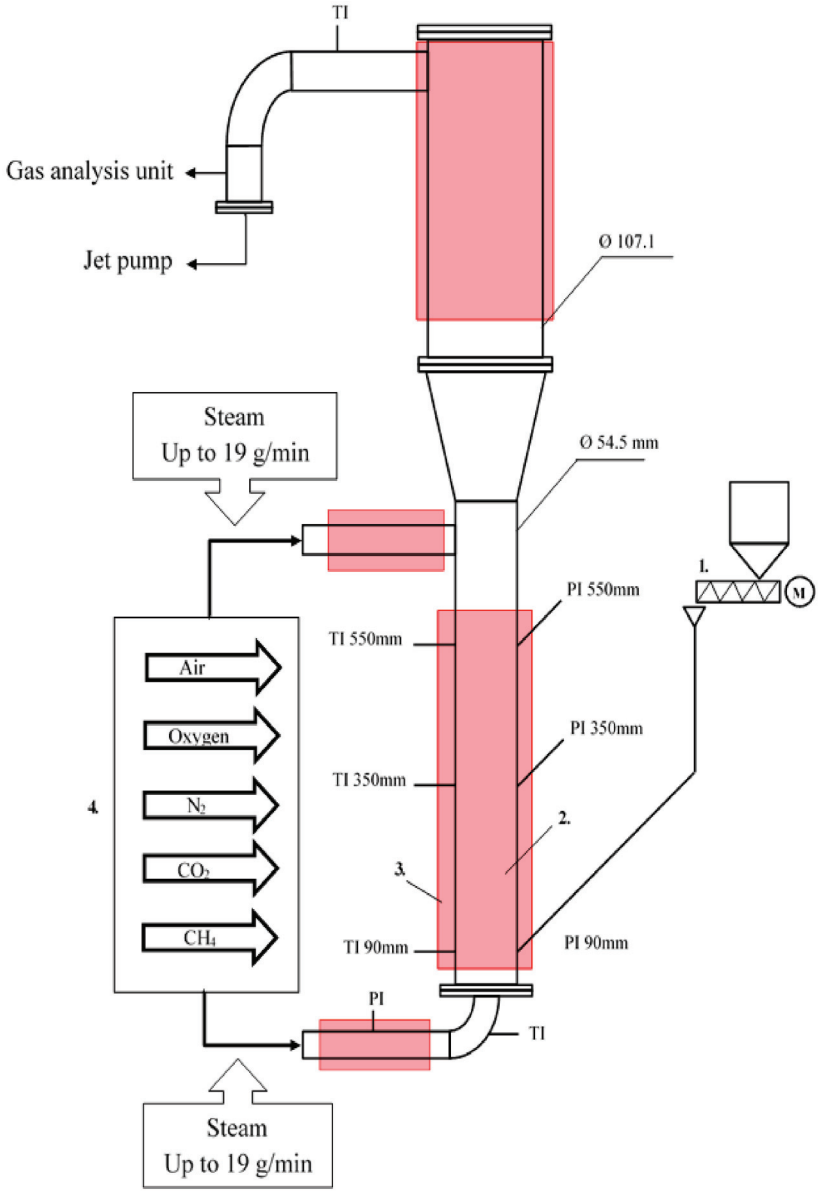

Figure 1. Schematic configuration of the bubbling fluidized bed test rig. 1—screw conveyor for feeding fuel; 2—bubbling fluidized bed reactor; 3—electrical heater; 4—gas distribution system.

Table 1. Experimental setup parameters used in the simulation.

Fluidized Bed Reactor	
Temperature (°C)	800–900
Pressure (bar)	0.92
Diameter (m)	0.0545
Height (m)	0.55
Bed Material (Silica Sand)	
Mean particle size (m)	177×10^{-6}
Density (kg/m^3)	2650
Mass weight (kg)	0.8
Steam	
Temperature (°C)	300
Flow rate (kg/h)	0–0.084
Concentration (%)	0–33.33

Table 2. The method for continuous measurement of the gas composition.

Species	Method	Range	Unit	Rel. Error in %
CO_2	Infrared	0–100	Vol.%	<0.5
CO	Infrared	0–20	Vol.%	<0.5
CH_4	Infrared	0–5	Vol.%	<0.5
H_2	Paramagnetic	0–20	Vol.%	<0.5
O_2	Paramagnetic	0–25	Vol.%	<0.5

2.3. Reaction Kinetics

The biomass gasification in the presence of steam includes a series of complex and competing reactions, including homogeneous and heterogeneous reactions. These reactions occur simultaneously in four overlapping steps, i.e., drying, thermal decomposition, oxidation, and reduction. The overall reaction of biomass steam gasification is described as follows:

$$\text{Biomass} + H_2O \rightarrow H_2 + CO + CO_2 + CH_4 + \text{l hydrocarbon} + \text{Tar} + \text{Char} \quad (1)$$

Initially, the moisture content of biomass reduces to less than 5% [35]. Then, devolatilization and cracking of weaker chemical bonds takes place at a temperature ranging from 250 to 700 °C [36], producing various fractions: gas, a liquid/condensed, and a solid [37–41]. In this step, the biomass converts into solid char which can range from 5% to 10% for fluidized bed reactors, or 20% to 25% for fixed-bed reactors [37–41]. The volatiles and solid char react with limited oxygen in the oxidation stage to produce mainly CO, CO_2, and H_2O, and the heat from this stage can supply to the endothermic reactions ((2) and (3)). The unreacted char is converted by steam and CO_2 to form the final gaseous products [36,42]. The yield of hydrogen from steam gasification is significantly higher than that of fast pyrolysis followed by a steam reforming of char.

$$C + \alpha H_2O \rightarrow (2 - \alpha)\, CO + (\alpha - 1)\, CO_2 + \alpha H_2 \text{ (Water-gas reaction)} \quad (2)$$

$$C + CO_2 \rightarrow 2CO \text{ (Boudourd reaction)} \quad (3)$$

where α has been experimentally determined in the range of 1.5–1.1 at 750–900 °C [43]. For the proposed model, the selected value of α was 1.3, showing good agreement with experimental data.

Water–gas shift reaction and steam reforming reaction occur simultaneously according to gasification conditions, playing a key factor for hydrogen production:

$$CO + H_2O \rightarrow CO_2 + H_2 \quad (4)$$

$$CH_4 + H_2O \rightarrow CO + H_2 \quad (5)$$

The carbon in the char is gasified with steam and CO_2 ((2) and (3)). The reaction rate kinetics of char gasification are calculated when fluidized with steam and carbon dioxide as follows [44]:

$$\left[\frac{dX_C}{dt}\right]_{H_2O} = \frac{k_{H_2O}P_{H_2O}}{1 + K_{H_2O}P_{H_2O} + K_{H_2}P_{H_2}}(1 - X_C) \quad (6)$$

$$\left[\frac{dX_C}{dt}\right]_{CO_2} = \frac{k_{CO_2}P_{CO_2}}{1 + K_{CO_2}P_{H_2O} + K_{CO}P_{CO}}(1 - X_C) \quad (7)$$

The kinetic parameters of char gasification can be found in Table 3.

Table 3. Kinetic parameters for char gasification obtained from experimental results.

H_2O		CO_2		Unit
k_{0,H_2O}	1.02×10^{11}	k_{0,CO_2}	9.62×10^{10}	$kPa^{-1}\ min^{-1}$
E_{a1,H_2O}	281.86	E_{a1,CO_2}	284.36	kJ/mol
K_{0,H_2O}	60.34	K_{0,CO_2}	3.63	kPa^{-1}
E_{a2,H_2O}	61.69	E_{a2,CO_2}	40.08	kJ/mol
K_{0,H_2}	1.56×10^{-10}	$K_{0,CO}$	2.24×10^{-10}	kPa^{-1}
E_{a3,H_2}	−203.46	$E_{a3,CO}$	−195.64	kJ/mol

The water–gas shift reaction (WGSR) (R4) takes place in a homogeneous phase. In this model, the WGSR is assumed to occur in all regions in the reactor. Thus, the reaction rate kinetics of the WGSR is calculated as [45]:

$$\frac{dF_{WGS,i}}{dV_j} = (1 - \varepsilon_j)k_{0,WGS}e^{-\frac{E_{WGS}}{RT}}C_{CO}^{0.5}C_{H_2O} \quad (8)$$

where ε_j is the porosity of the bed in the region j with volume V_j. The pre-exponential factor of the kinetic constant is $k_{0,WGS} = 7.97 \times 10^9\ (m^3/mol)^{0.5}.s^{-1}$ and the activation energy is $E_{WGS} = 274.5$ kJ/mol.

2.4. Hydrodynamic Calculation

The hydrodynamic properties of the bubbling fluidized bed reactor have a significant effect on the fuel conversion during biomass gasification. Here, the calculation equations and empirical correlations, reported in the literature, have been used to determine the hydrodynamic parameters, considering that the model is divided into two regions: bed and freeboard.

2.4.1. Bed Hydrodynamic

The minimum fluidization velocity for small particles have been introduced by Kunii and Levenspil [46] as follows:

$$Ar = \frac{d_p^3\rho_g(\rho_s - \rho_g)g}{\mu^2} \quad (9)$$

$$u_{mf} = \frac{33.7\mu}{d_p\rho_g}\left(\sqrt{1 + 3.59 \times 10^{-5}Ar} - 1\right) \quad (10)$$

The correlations were developed to determine the volume fraction occupied by bubbles in a fluidized bed [32].

$$B = 1 + \frac{10.978\left(u_f - u_{mf}\right)^{0.738} \rho_s^{0.376} d_p^{1.006}}{u_{mf}^{0.937} \rho_g^{0.126}} \quad (11)$$

$$\delta_b = 1 - 1/B \quad (12)$$

The following relation gives the bed void fraction:

$$\varepsilon_f = \delta_b + (1 - \delta_b)\varepsilon_{mf} \quad (13)$$

2.4.2. Freeboard Dynamics

The volume fraction of solid varies along with the height of the freeboard. The void fraction of the freeboard is determined by the following equation.

$$1 - \varepsilon_{fb} = (1 - \varepsilon_f) \exp(-az) \quad (14)$$

where a is the decay constant of solid particles in the freeboard, a is determined from the graph with the following range [47]:

$$a = \frac{1.3}{u_f} \quad (15)$$

with:

$$u_f \leq 1.25 \text{ m/s} \quad (16)$$

$$d_p \leq 800 \text{ μm} \quad (17)$$

2.5. Aspen Plus Model

The biomass gasification model involves various stages in Aspen Plus. The overall gasification process is illustrated in Figure 2. The biomass decomposition is simulated in the RYIELD block. The product distribution is determined by the model of Neves et al. [34] based on the proximate and ultimate analyses of biomass (listed in Tables 4 and 5). The volatile components obtained from pyrolysis simulated the volatile reactions in the RGIBBS reactor with the assumption that these reactions follow the Gibb equilibrium. The char gasification is modeled in two RSTOIC reactors, corresponding to bed and freeboard. The hydrodynamics and kinetics have been written in two external FORTRAN codes. The products then go through CYCLONE to separate gas products from solid impurities.

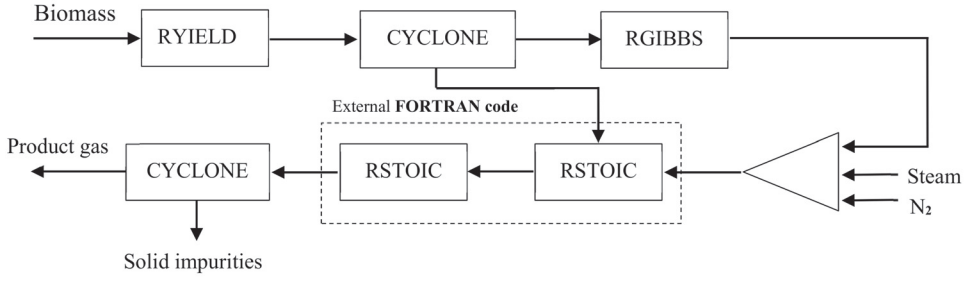

Figure 2. Biomass gasification model flow chart in Aspen Plus.

Table 4. Main properties of the torrefied woodchips.

	Property	Value	Note
Proximate analysis (wt.%)	Moisture	5.28	As received
	Volatile matter	70.75	As received
	Fixed carbon	22.82	As received
	Ash	1.15	As received
Ultimate analysis (wt.% daf)	C	54.46	Dry basis
	H	5.99	Dry basis
	O	39.31	Dry basis
	N	0.24	Dry basis
	S	0.00254	Dry basis
HHV (MJ/kg)		20.97	As received
LHV (MJ/kg)		19.26	As received
Bulk density (kg/m^3)		161.71	As received
Mean particle diameter (μm)		296.65	Mass-weighted average diameter

Table 5. Mass yield distribution (wt.%) from biomass decomposition.

Component	Wt.%	Component	wt.%
Ash	1.09	H_2O	11.05
CO	46.9	N_2	0.22
C	17.53	CO_2	6.69
CH_4	15.39	H_2S	0.0025
H_2	1.12		

2.5.1. Biomass Characteristics

The torrefied woodchips, a feedstock in this study, were ground and sieved to a particle size of 200 to 850 μm. The proximate analysis of all samples was conducted following the DIN norms 18122, 18123, and 18134 standard test methods for ash, volatile matter, fixed carbon, and moisture determination, respectively. The ultimate analysis was carried out using an elemental analyzer (Elementar vario MACRO cube) with a measurement deviation <0.1%. The feedstock characteristics are shown in Table 4.

2.5.2. Biomass Decomposition

Devolatilization (pyrolysis) is a thermal decomposition of biomass at high temperatures in an inert atmosphere. Biomass pyrolysis includes extremely complex reactions that convert biomass into a mixture of gases, char, and liquid (tars). In this work, the Aspen Plus yield reactor, RYIELD, is used to simulate the decomposition of biomass. The mass yield distribution of pyrolysis products is derived from a pyrolysis model [34] based on the biomass proximate and ultimate analyses. Tars and larger hydrocarbons are assumed to be converted directly to methane and carbon monoxide in this study. The summary of mass product yields from the biomass decomposition is presented in Table 5.

2.5.3. Char Gasification

Char gasification is performed in the Aspen Plus STOIC reactor, RSTOIC, by using an external FORTRAN code to calculate hydrodynamic parameters and reaction rate kinetics. As mentioned above, the reactor is divided into two regions, bed and freeboard, each region is simulated by one RSTOIC. In FORTRAN code, each RSTOIC is divided into a finite number of equal volumes. Hydrodynamic parameters are determined by a series of equations and correlations in Section 2.4. Biomass gasification is a complex series of competing reactions. To simplify the process, this study only takes account of the water gas reaction, Boudourd reaction, and the water–gas shift reaction in the kinetic calculation. Their reaction rate kinetics are presented in Section 2.3.

2.5.4. Calculation Procedure

The model equations, given in previous sections, are implemented in Fortran codes. A flow chart for the calculation procedure is shown in Figure 3. Input data, such as reactor configuration, gasification conditions, the characteristics of biomass, bed material and gases, kinetic parameters, etc. are described in Tables 1–5. Firstly, it is necessary to make assumptions of molar values of components and initial carbon conversion in the reactor as well as bed properties such as bed height and bed volume. For the analysis, the volume of the reactor is divided into N divisions. Then, hydrodynamic and kinetic aspects are calculated discretely for dense and lean zones through the model equations described in previous sections, employing an iterative procedure. The calculation ends once all divisions have been calculated and the error does not exceed 10^{-4}. The output data, such as the concentration profiles of components, solid conversion and fluidization properties, etc. are obtained along the entire reactor.

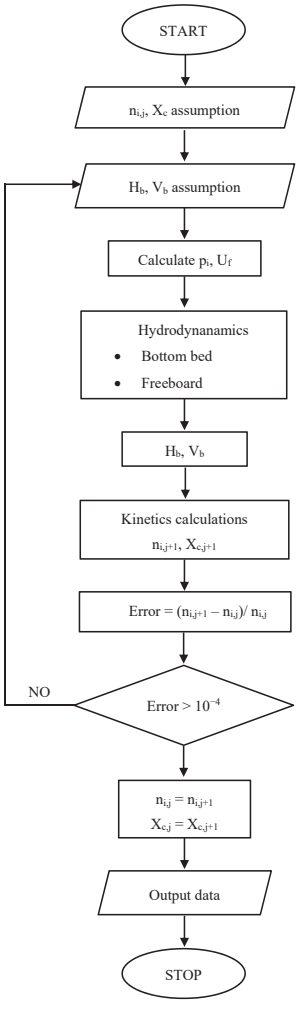

Figure 3. Simplified flow diagram of simulation calculation.

2.6. Model Validation

Simulation results were compared with experimental data and the deviation between simulation and experiment was determined. The sum of the squared deviation method is applied to determine the accuracy of the simulation.

$$RSS = \sum_{i=1}^{N} \left(\frac{y_{ie} - y_{ip}}{y_{ie}} \right)^2 \quad (18)$$

$$RSS = \frac{RSS}{N} \quad (19)$$

$$Mean\ error = \sqrt{MRSS} \quad (20)$$

3. Results and Discussion

This study investigated the effects of important parameters, namely, steam-to-biomass ratio (SBR) and gasification temperature during steam gasification of biomass through the Aspen Plus process flow model at steady-state conditions. One parameter varies, while the others are kept constant. To validate the simulation results, the experimental data from steam gasification of torrefied biomass in a bubbling fluidized bed reactor were used [47].

The isothermal experimental investigations of steam gasification of biomass were carried out in a pilot-scale bubbling fluidized bed reactor (Figure 1) using silica sand as bed material. The performance of biomass gasification was analyzed to assess the influence of operating parameters, i.e., gasification temperature, steam-to-biomass ratio, equivalence ratio. During the investigations, each operating parameter varied in the desired range, while other parameters were fixed at known values. After reaching steady conditions, the variations of gas composition were recorded and analyzed for the process performance. A detailed experimental description and its results are presented in a publication [47].

3.1. Effect of Gasification Temperature

The gasification temperature is a crucial parameter in biomass gasification. In this study, three temperatures ranging between 800 and 900 °C were investigated, while the steam-to-biomass ratio was fixed at 1.2 for the steam gasification. The effects of gasification temperature on the gas composition (on dry basic and N_2 free) are presented in Figure 4. The simulation results indicate that the content of H_2 increases with elevated temperature, while the CH_4 content decreases considerably. Furthermore, the content of CO rose from 800 to 850 °C, then dropped down to 21.98% at 900 °C. It is noteworthy that the CO_2 fraction showed an opposite trend. Moreover, operating temperature also enhanced the gas yield produced and CCE by 1.28 $Nm^3/kg_{biomass}$ and 51.97% from 800 to 900 °C, respectively (shown in Figures 5 and 6). A similar trend is observed in the experimental results.

The effect of operating temperature on the process performance of steam gasification of biomass can be attributed to endothermic and exothermic reactions in biomass gasification [42,48]. According to Le Chatelier's principle and dynamic equilibrium, the endothermic reactions ((2), (3), and (5)) are strengthened with elevated temperature, increasing the contents of hydrogen and carbon monoxide, while reducting in methane fraction. Additionally, the water–gas shift reaction can be promoted by the high contents of carbon monoxide and steam in the gasifier, resulting in a decline of carbon monoxide in the product gas. These reactions take place simultaneously in the reactor; thus, there is a considerable rise in H_2 content and fluctuations in the values of other components at high temperatures.

Elevated temperature favors the rate of char gasification reactions and the water–gas shift reaction, which can result in increased dry gas yield and the decreasing unreacted char. Therefore, increasing operating temperature improves biomass conversion and hydrogen production in steam gasification of torrefied biomass.

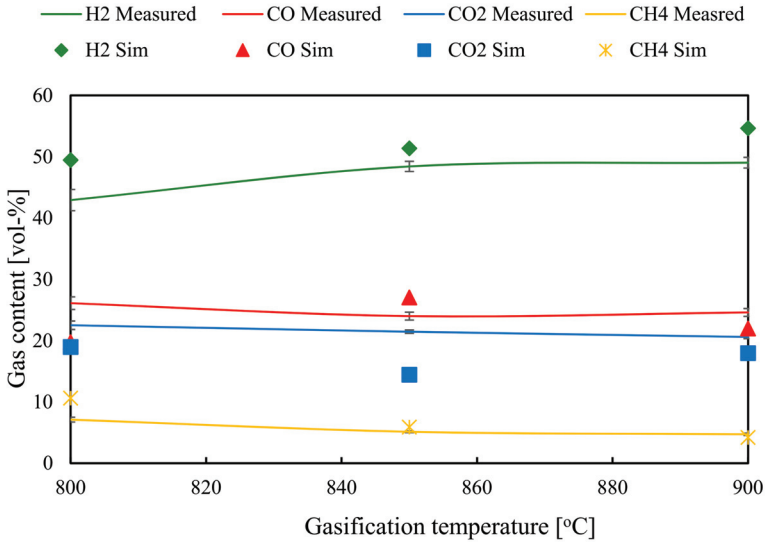

Figure 4. Effect of gasification temperature on the gas composition.

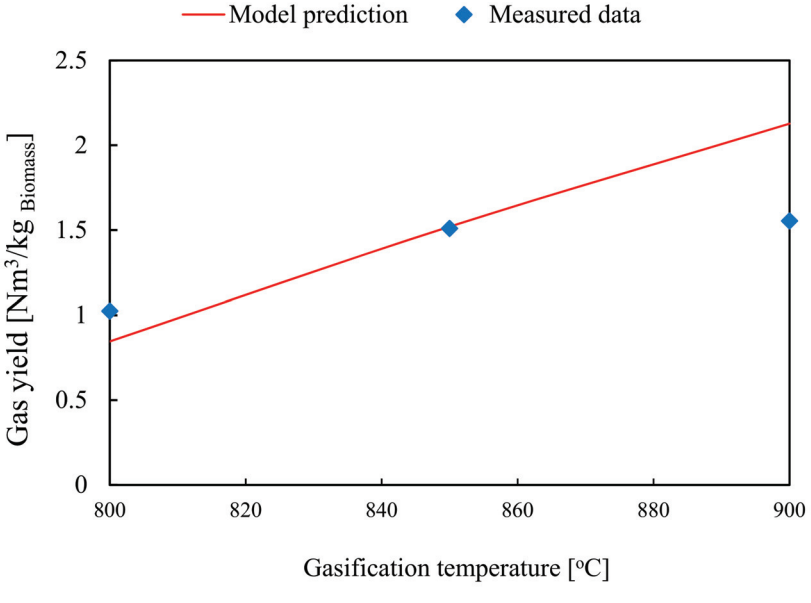

Figure 5. Effect of gasification temperature on the gas yield.

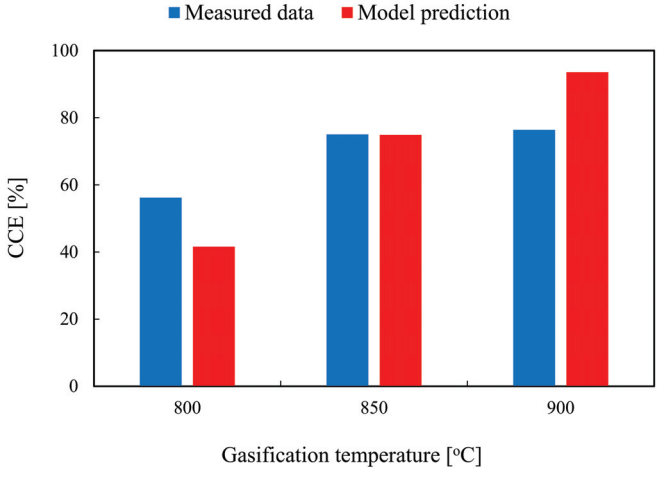

Figure 6. Effect of gasification temperature on carbon conversion efficiency.

Data analysis of the effect of gasification temperature is shown in Table 6. The mean errors of H_2 and CH_4 are the lowest and highest values, respectively. These errors are acceptable to predict the performance of the biomass gasification process. The differences between simulation and experimental results in the effect of gasification temperature are due to some simplified calculations and assumptions during the simulation. Biomass produces more tar and heavier hydrocarbons at lower temperatures, and they are decomposed at high temperatures. Tars released during biomass decomposition are assumed to be converted completely into CO and CH_4; therefore, the effect of temperature on tar production and decomposition is generally ignored in this study. Additionally, some reactions, i.e., steam reforming, char combustion, and hydrogen combustion, etc. are not considered in FORTRAN kinetic calculations, resulting in the high content of H_2 and CH_4 and the dry gas yield as well as the low fraction of CO_2 compared to experimental results. The equilibrium assumption replaces methane for all other hydrocarbons in the product gas and a negligible deviation of methane content between simulation and experimental results as observed in Figure 4.

Table 6. Analysis of data.

Parameters	Mean Error					
	H_2	CO	CO_2	CH_4	Gas Yield	CCE
T (°C)	0.115	0.17	0.222	0.303	0.235	0.2
SBR	0.193	0.174	0.329	0.134	0.076	0.033

3.2. Effect of Steam-to-Biomass Ratio

The steam-to-biomass ratio (SBR) represents a ratio of the mass flow rate of steam to biomass fed into the reactor [48]. Along with operating temperature, the steam-to-biomass ratio is a crucial operating parameter that affects significantly hydrogen production from biomass gasification [49]. The SBR was investigated in this study ranging from 0 to 1.6, and the temperature was at 850 °C.

In the following Figures 7–12, the simulation results were compared with experimental data for gas composition at various steam-to-biomass ratios. Generally, the H_2 and CO_2 fractions increase (see Figures 7 and 8), while CO and CH_4 show a downward trend (Figures 9 and 10). In the range of 0 to 0.9, the H_2 concentration rises considerably. Afterward, its increase slows down in the higher SBRs. A steady rise in the content of CO_2

is found in the SBR range from 0.7 to 1.6, reaching a peak of 16.1% at the SBR of 1.6. Those trends of the model predictions are similar to those found from the experimental data. Compared with other species, the difference between simulation results and experimental data in CH_4 content is the lowest, while in the case of CO_2, the fraction is the highest with the mean error of 0.329. The simulation results for hydrogen and carbon monoxide also display a good qualitative prediction of experimental data in the whole range of SBR. The mean errors of the effect of SBR on gas composition, presented in Table 6, are in acceptable ranges.

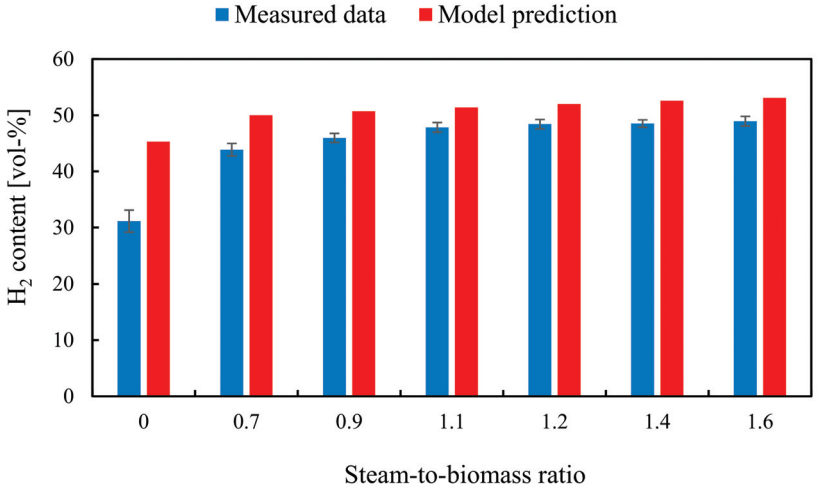

Figure 7. Effect of SBR on the hydrogen content.

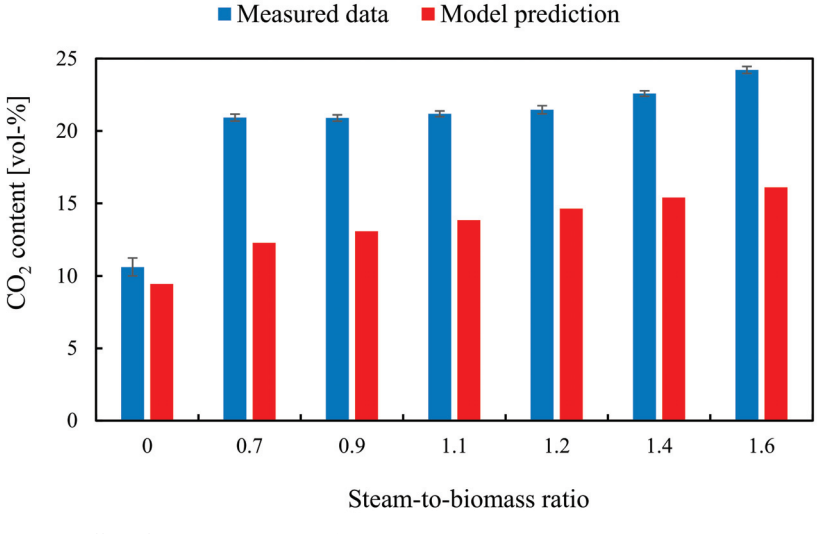

Figure 8. Effect of SBR on carbon dioxide content.

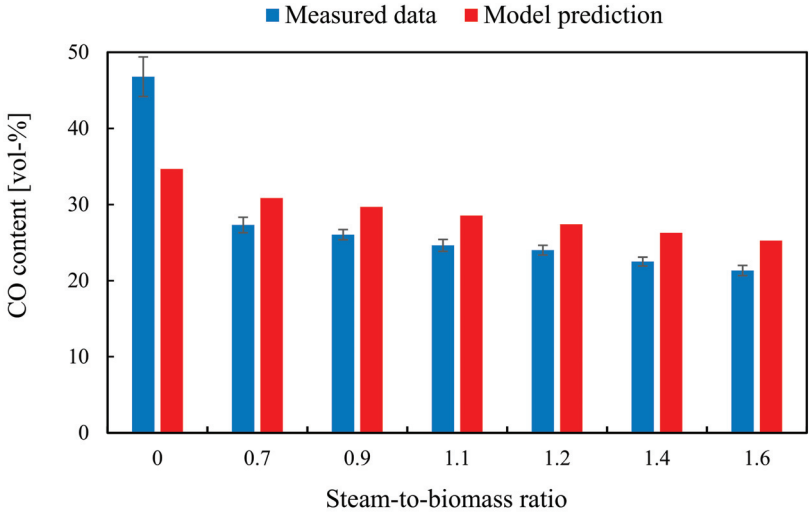

Figure 9. Effect of SBR on carbon monoxide content.

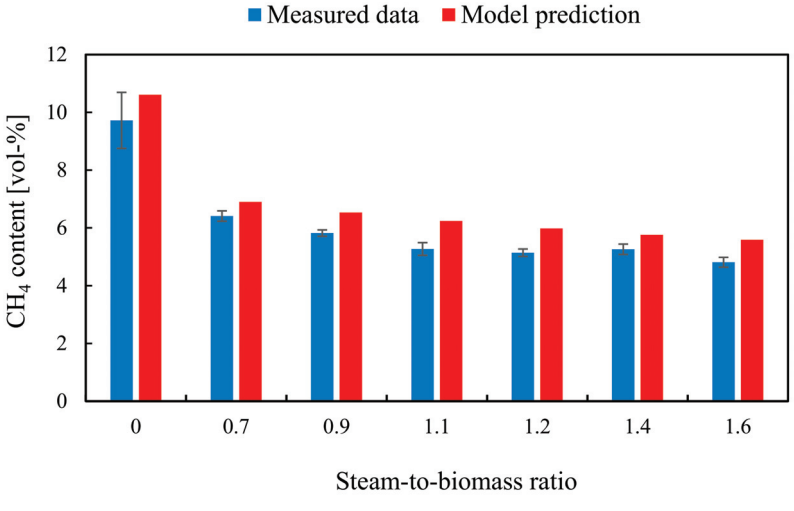

Figure 10. Effect of SBR on methane content.

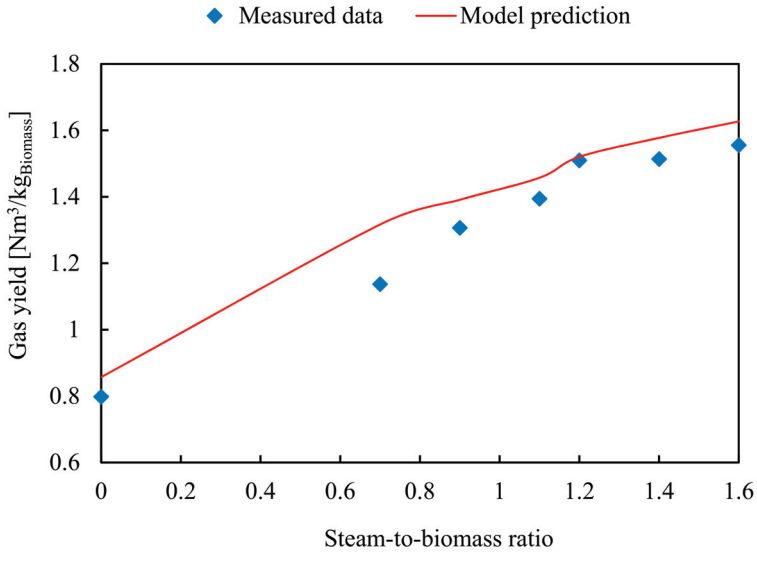

Figure 11. Effect of SBR on dry gas yield.

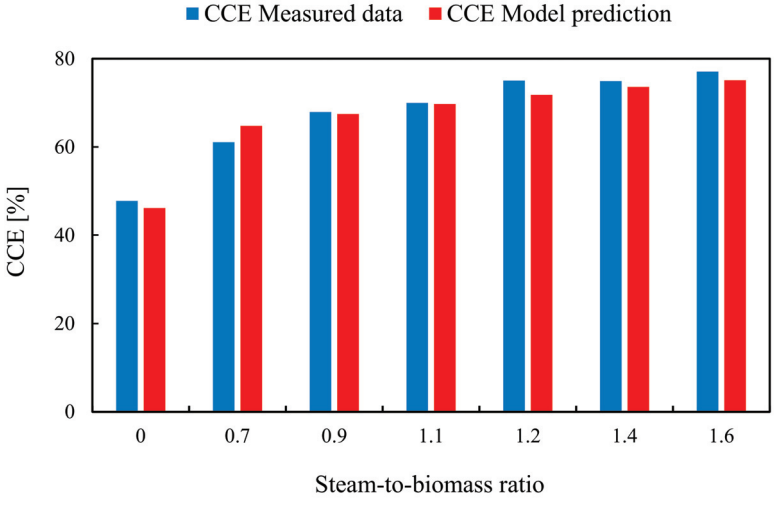

Figure 12. Effect of SBR on carbon conversion efficiency.

The dry gas yield of the product gas as a function of SBR is illustrated in Figure 11. As can be seen in the figure, the gas yield increases rapidly until an SBR of 0.9 before slowing down. It is noted that simulation results for gas yield are better in agreement with measured data from SBR of 1.2. Its mean error is about 0.17 that is acceptable for the investigation of steam-to-biomass ratios.

Figure 12 shows the comparison of the simulation results with the measured data for carbon conversion efficiency versus the SBR in the range of 0–1.6. Increasing trends of CCE are observed in both simulation and experimental results. A high SBR improves the gasification process and increases efficiency. The efficiency rises considerably at low SBRs, then its rate decelerates at high SBRs. The high accuracy of model predictions in carbon conversion efficiency compared to experimental data is determined by the mean error of 0.033.

The effect of SBR on the performance of biomass gasification is mainly due to the reactions with the presence of steam. The high amount of steam in the gasifier promotes char gasification and water–gas shift reactions, resulting in increasing hydrogen production and the amount of char consumed. The largest difference in CO_2 content is observed in this evaluation. This error is due to the combustion reactions of char and CO which are neglected. Additionally, this difference could be attributed to equilibrium assumptions. As discussed above, the main error of the simulation is likely attributed to simplified calculations and assumptions during the simulation. The ignorance of the effect of tar and some reactions causes the differences between simulation results and experimental data. In the presence of steam in the gasifier, the steam reforming reaction increases the decomposition of tar components at high temperatures. Generally, the model predictions and their error are capable of simulating the gasification performance under various steam-to-biomass ratios.

In summary, the study has developed a kinetic model which incorporates both reactor hydrodynamics and reaction rate kinetics to simulate biomass gasification in a bubbling fluidized bed reactor. The model is validated against experimental data at the same operating parameter range in terms of gasification temperature and steam-to-biomass ratio. It is noted that high agreement has been found with experimental results in most cases with the mean error ranging from approximately 0.033 to 0.329 (when fractions and yields of gas components and carbon conversion efficiency are considered). The trends observed in both simulation and experimental investigations are similar. There are slight deviations during the comparisons due to model assumptions. Additionally, the equilibrium model assumes that the reactions can reach a complete equilibrium, while the experimental conditions deviate from the ideal operating conditions, resulting in those errors. Finally, the model is capable of predicting the performance of biomass gasification in a bubbling fluidized bed and is sufficient to provide a good understanding of the phenomena occurring inside the gasifier.

4. Conclusions

In this work, an Aspen plus model for the steam gasification of biomass was developed to investigate the effect of operating parameters on the gasification process at steady-state conditions. Hydrodynamic and reaction kinetic calculations were implemented in external FORTRAN codes. Pyrolysis yield distribution obtained from the model of Neves was used to determine the mass yields of the decomposition of torrefied biomass. The simulation results for the product gas composition and carbon conversion efficiency versus gasification temperature and steam-to-biomass ratio were validated by the experimental data. The following relevant conclusions can be obtained from this study:

1. At higher temperatures, the gasification process is favored. Here, the hydrogen production and the carbon conversion efficiency are increased, while the amount of carbon monoxide and methane in the product gas is decreased.
2. Increasing the steam amount in the reactor promotes the performance of biomass gasification. The SB steam-to-biomass ratio strongly enhances the content and yield of hydrogen in the product gas as well as improves the gas yield and the carbon conversion efficiency.
3. It is noteworthy that the model predictions are in good agreement with the experimental data, and the model is capable of simulating the performance of biomass gasification under various operating conditions, i.e., operating temperature and steam-to-biomass ratio. The minor deviations between the simulation model and the measured data are related to the model limitations, i.e., simplified calculations in bed hydrodynamics and kinetics.

The model-predicted values showed good agreement with experimental data. The errors of the simulation compared to experimental investigations could be attributed to process assumptions to simplify the calculations and the lack of tar decomposition reactions as well as the chemical equilibrium. The residence time in a fluidized bed gasifier might be not sufficient to reach equilibrium conditions in the experimental conditions. In further

studies, tar decomposition and combustion reactions are taken into consideration along with sufficient hydrodynamic calculations to reduce the deviations in the simulation of biomass gasification.

Author Contributions: N.M.N. is responsible for administration, conceptualization, the original draft, and the applied methodology. The simulation was conducted by N.M.N. F.A. supported the writing process with his reviews and edits. B.E. supervised the research progress and the presented work. All authors have read and agreed to the published version of the manuscript.

Funding: This research received no external funding. The corresponding author would like to thank the Technical University of Darmstadt, enabling the open-access publication of this paper.

Institutional Review Board Statement: Not applicable.

Informed Consent Statement: Not applicable.

Data Availability Statement: The data presented in this study are available in the article.

Conflicts of Interest: The authors declare no conflict of interest.

References

1. Sikarwar, V.S.; Zhao, M.; Fennell, P.S.; Shah, N.; Anthony, E.J. Progress in biofuel production from gasification. *Prog. Energy Combust. Sci.* **2017**, *61*, 189–248. [CrossRef]
2. McKendry, P. Energy production from biomass (Part 3): Gasification technologies. *Bioresour. Technol.* **2002**, *83*, 55–63. [CrossRef]
3. Basu, P. Chapter 5—Gasification Theory and Modeling of Gasifiers. In *Biomass Gasification and Pyrolysis*; Basu, P., Ed.; Academic Press: Boston, MA, USA, 2010; pp. 117–165. [CrossRef]
4. Spath, P.L.; Dayton, D.C. *Preliminary Screening—Technical and Economic Assessment of Synthesis Gas to Fuels and Chemicals with Emphasis on the Potential for Biomass-Derived Syngas*; National Renewable Energy Lab.: Golden, CO, USA, 2003. [CrossRef]
5. Berrueco, C.; Recari, J.; Güell, B.M.; Alamo, G.D. Pressurized gasification of torrefied woody biomass in a lab scale fluidized bed. *Energy* **2014**, *70*, 68–78. [CrossRef]
6. Chen, W.-H.; Chen, C.-J.; Hung, C.-I.; Shen, C.-H.; Hsu, H.-W. A comparison of gasification phenomena among raw biomass, torrefied biomass and coal in an entrained-flow reactor. *Appl. Energy* **2013**, *112*, 421–430. [CrossRef]
7. Dupont, C.; Nocquet, T.; Da Costa, J.A.; Verne-Tournon, C. Kinetic modelling of steam gasification of various woody biomass chars: Influence of inorganic elements. *Bioresour. Technol.* **2011**, *102*, 9743–9748. [CrossRef]
8. Xiao, R.; Yang, W. Kinetics characteristics of straw semi-char gasification with carbon dioxide. *Bioresour. Technol.* **2016**, *207*, 180–187. [CrossRef]
9. Wang, G.; Zhang, J.; Hou, X.; Shao, J.; Geng, W. Study on CO_2 gasification properties and kinetics of biomass chars and anthracite char. *Bioresour. Technol.* **2015**, *177*, 66–73. [CrossRef] [PubMed]
10. Fermoso, J.; Gil, M.V.; Pevida, C.; Pis, J.J.; Rubiera, F. Kinetic models comparison for non-isothermal steam gasification of coal–biomass blend chars. *Chem. Eng. J.* **2010**, *161*, 276–284. [CrossRef]
11. Bouraoui, Z.; Jeguirim, M.; Guizani, C.; Limousy, L.; Dupont, C.; Gadiou, R. Thermogravimetric study on the influence of structural, textural and chemical properties of biomass chars on CO_2 gasification reactivity. *Energy* **2015**, *88*, 703–710. [CrossRef]
12. Dahou, T.; Defoort, F.; Thiéry, S.; Grateau, M.; Campargue, M.; Bennici, S.; Jeguirim, M.; Dupont, C. The Influence of Char Preparation and Biomass Type on Char Steam Gasification Kinetics. *Energies* **2018**, *11*, 2126. [CrossRef]
13. Molina, A.; Mondragón, F. Reactivity of coal gasification with steam and CO_2. *Fuel* **1998**, *77*, 1831–1839. [CrossRef]
14. Ergun, S.; Mines, U.S.B.O. *Kinetics of the Reactions of Carbon Dioxide and Steam with Coke*; U.S. Government Printing Office: Boston, MA, USA, 1962.
15. Suraj, P.; George, J.; Arun, P.; Muraleedharan, C. Theoretical and experimental feasibility study of groundnut shell gasification in a fluidized bed gasifier. *Biomass Convers. Biorefinery* **2020**, *10*, 735–742. [CrossRef]
16. Rupesh, S.; Muraleedharan, C.; Arun, P. ASPEN plus modelling of air–steam gasification of biomass with sorbent enabled CO_2 capture. *Resour. Technol.* **2016**, *2*, 94–103. [CrossRef]
17. Beheshti, S.; Ghassemi, H.; Shahsavan-Markadeh, R. Process simulation of biomass gasification in a bubbling fluidized bed reactor. *Energy Convers. Manag.* **2015**, *94*, 345–352. [CrossRef]
18. Yan, L.; Lim, C.J.; Yue, G.; He, B.; Grace, J.R. One-dimensional modeling of a dual fluidized bed for biomass steam gasification. *Energy Convers. Manag.* **2016**, *127*, 612–622. [CrossRef]
19. Aghaalikhani, A.; Schmid, J.C.; Borello, D.; Fuchs, J.; Benedikt, F.; Hofbauer, H.; Rispoli, F.; Henriksen, U.B.; Sárossy, Z.; Cedola, L. Detailed modelling of biomass steam gasification in a dual fluidized bed gasifier with temperature variation. *Renew. Energy* **2019**, *143*, 703–718. [CrossRef]
20. Shahbaz, M.; Taqvi, S.A.; Loy, A.C.M.; Inayat, A.; Uddin, F.; Bokhari, A.; Naqvi, S.R. Artificial neural network approach for the steam gasification of palm oil waste using bottom ash and CaO. *Renew. Energy* **2019**, *132*, 243–254. [CrossRef]

21. Zhou, L.; Yang, Z.; Tang, A.; Huang, H.; Wei, D.; Yu, E.; Lu, W. Steam-gasification of biomass with CaO as catalyst for hydrogen-rich syngas production. *J. Energy Inst.* **2019**, *92*, 1641–1646. [CrossRef]
22. Eri, Q.; Peng, J.; Zhao, X. CFD simulation of biomass steam gasification in a fluidized bed based on a multi-composition multi-step kinetic model. *Appl. Therm. Eng.* **2018**, *129*, 1358–1368. [CrossRef]
23. Ghasemzadeh, K.; Khosravi, M.; Tilebon, S.S.; Aghaeinejad-Meybodi, A.; Basile, A. Theoretical evaluation of PdAg membrane reactor performance during biomass steam gasification for hydrogen production using CFD method. *Int. J. Hydrogen Energy* **2018**, *43*, 11719–11730. [CrossRef]
24. Ostermeier, P.; Fischer, F.; Fendt, S.; DeYoung, S.; Spliethoff, H. Coarse-grained CFD-DEM simulation of biomass gasification in a fluidized bed reactor. *Fuel* **2019**, *255*, 115790. [CrossRef]
25. Kraft, S.; Kirnbauer, F.; Hofbauer, H. CPFD simulations of an industrial-sized dual fluidized bed steam gasification system of biomass with 8 MW fuel input. *Appl. Energy* **2017**, *190*, 408–420. [CrossRef]
26. Chen, T.; Ku, X.; Lin, J.J.C. CFD simulation of the steam gasification of millimeter-sized char particle using thermally thick treatment. *Combust. Flame* **2020**, *213*, 63–86. [CrossRef]
27. Yang, S.; Fan, F.; Wei, Y.; Hu, J.; Wang, H.; Wu, S. Three-dimensional MP-PIC simulation of the steam gasification of biomass in a spouted bed gasifier. *Energy Convers. Manag.* **2020**, *210*, 112689. [CrossRef]
28. George, J.; Arun, P.; Muraleedharan, C. Stoichiometric Equilibrium Model Based Assessment of Hydrogen Generation through Biomass Gasification. *Procedia Technol.* **2016**, *25*, 982–989. [CrossRef]
29. Mirmoshtaghi, G.; Li, H.; Thorin, E.; Dahlquist, E. Evaluation of different biomass gasification modeling approaches for fluidized bed gasifiers. *Biomass Bioenergy* **2016**, *91*, 69–82. [CrossRef]
30. Kaushal, P.; Tyagi, R. Advanced simulation of biomass gasification in a fluidized bed reactor using ASPEN PLUS. *Renew. Energy* **2017**, *101*, 629–636. [CrossRef]
31. Nikoo, M.B.; Mahinpey, N. Simulation of biomass gasification in fluidized bed reactor using ASPEN PLUS. *Biomass Bioenergy* **2008**, *32*, 1245–1254. [CrossRef]
32. Acar, M.; Böke, E. Simulation of Biomass Gasification Process Using Aspen Plus. In Proceedings of the 14th International Conference of Combustion, Karabük, Turkey, 25–27 April 2018.
33. Pala, L.P.R.; Wang, Q.; Kolb, G.; Hessel, V. Steam gasification of biomass with subsequent syngas adjustment using shift reaction for syngas production: An Aspen Plus model. *Renew. Energy* **2017**, *101*, 484–492. [CrossRef]
34. Neves, D.; Thunman, H.; Matos, A.; Tarelho, L.; Gómez-Barea, A. Characterization and prediction of biomass pyrolysis products. *Prog. Energy Combust. Sci.* **2011**, *37*, 611–630. [CrossRef]
35. Puig-Arnavat, M.; Bruno, J.C.; Coronas, A. Review and analysis of biomass gasification models. *Renew. Sustain. Energy Rev.* **2010**, *14*, 2841–2851. [CrossRef]
36. Molino, A.; Chianese, S.; Musmarra, D. Biomass gasification technology: The state of the art overview. *J. Energy Chem.* **2015**, *25*, 10–25. [CrossRef]
37. Li, X.T.; Grace, J.R.; Lim, C.J.; Watkinson, A.P.; Chen, H.P.; Kim, J.R. Biomass gasification in a circulating fluidized bed. *Biomass Bioenergy* **2004**, *26*, 171–193. [CrossRef]
38. Lv, P.M.; Xiong, Z.H.; Chang, J.; Wu, C.Z.; Chen, Y.; Zhu, J.X. An experimental study on biomass air–steam gasification in a fluidized bed. *Bioresour. Technol.* **2004**, *95*, 95–101. [CrossRef] [PubMed]
39. Gómez-Barea, A.; Arjona, R.; Ollero, P. Pilot-Plant Gasification of Olive Stone: A Technical Assessment. *Energy Fuels* **2005**, *19*, 598–605. [CrossRef]
40. Roos, C.J. *Clean Heat and Power Using Biomass Gasification for Industrial and Agricultural Project*; U.S. Department of Energy Clean Energy Application Center: Washington, DC, USA, 2010; p. 64.
41. Carlassara, L. Modeling and Optimization of Biomass Gasification Systems. Master's Thesis, Technical University of Denmark, Kongens Lyngby, Denmark, 2009.
42. Parthasarathy, P.; Narayanan, K.S. Hydrogen production from steam gasification of biomass: Influence of process parameters on hydrogen yield—A review. *Renew. Energy* **2014**, *66*, 570–579. [CrossRef]
43. Matsui, I.; Kunii, D.; Furusawa, T. Study of fluidized bed steam gasification of char by thermogravimetrically obtained kinetics. *J. Chem. Eng. Jpn.* **1985**, *18*, 105–113. [CrossRef]
44. Abad, A.; Gayán, P.; de Diego, L.F.; García-Labiano, F.; Adánez, J. Fuel reactor modelling in chemical-looping combustion of coal: 1. model formulation. *Chem. Eng. Sci.* **2013**, *87*, 277–293. [CrossRef]
45. Abad, A.; Adánez, J.; de Diego, L.F.; Gayán, P.; García-Labiano, F.; Lyngfelt, A. Fuel reactor model validation: Assessment of the key parameters affecting the chemical-looping combustion of coal. *Int. J. Greenh. Gas Control* **2013**, *19*, 541–551. [CrossRef]
46. Kunii, D.; Levenspiel, O. CHAPTER 3—Fluidization and Mapping of Regimes. In *Fluidization Engineering*, 2nd ed.; Kunii, D., Levenspiel, O., Eds.; Butterworth-Heinemann: Boston, MA, USA, 1991; pp. 61–94. [CrossRef]
47. Nguyen, N.M.; Alobaid, F.; May, J.; Peters, J.; Epple, B. Experimental study on steam gasification of torrefied woodchips in a bubbling fluidized bed reactor. *Energy* **2020**, *202*, 117744. [CrossRef]
48. Udomsirichakorn, J.; Salam, P.A. Review of hydrogen-enriched gas production from steam gasification of biomass: The prospect of CaO-based chemical looping gasification. *Renew. Sustain. Energy Rev.* **2014**, *30*, 565–579. [CrossRef]
49. Florin, N.H.; Harris, A.T. Hydrogen production from biomass coupled with carbon dioxide capture: The implications of thermodynamic equilibrium. *Int. J. Hydrogen Energy* **2007**, *32*, 4119–4134. [CrossRef]

applied sciences

MDPI

Article

Influences of the Pretreatments of Residual Biomass on Gasification Processes: Experimental Devolatilizations Study in a Fluidized Bed

Stefania Lucantonio, Andrea Di Giuliano and Katia Gallucci *

Department of Industrial and Information Engineering and Economics (DIIIE), University of L'Aquila, Piazzale E. Pontieri 1-loc. Monteluco di Roio, 67100 L'Aquila, Italy; stefania.lucantonio@student.univaq.it (S.L.); andrea.digiualiano@univaq.it (A.D.G.)

* Correspondence: katia.gallucci@univaq.it; Tel.: +39-0862-434213

Abstract: The European research project CLARA (chemical looping gasification for sustainable production of biofuels, G.A. 817841) investigated chemical looping gasification of wheat straw pellets. This work focuses on pretreatments for this residual biomass, i.e., torrefaction and torrefaction-washing. Devolatilizations of individual pellets were performed in a laboratory-scale fluidized bed made of sand, at 700, 800, and 900 °C, to quantify and analyze the syngas released from differently pretreated biomasses; experimental data were assessed by integral-average parameters: gas yield, H_2/CO molar ratio, and carbon conversion. A new analysis of devolatilization data was performed, based on information from instantaneous peaks of released syngas, by simple regressions with straight lines. For all biomasses, the increase of devolatilization temperature between 700 and 900 °C enhanced the thermochemical conversion in terms of gas yield, carbon conversion, and H_2/CO ratio in the syngas. Regarding pretreatments, the main evidence is the general improvement of syngas quality (i.e., composition) and quantity, compared to those of untreated pellets; only slighter differentiations were observed concerning different pretreatments, mainly thanks to peak quantities, which highlighted an improvement of the H_2/CO molar ratio in correlation with increased torrefaction temperature from 250 to 270 °C. The proposed methods emerged as suitable straightforward tools to investigate the behavior of biomasses and the effects of process parameters and biomass nature.

Keywords: devolatilization; biomass pretreatments; wheat straw pellets; syngas; gas yield; carbon conversion; fluidized bed

Citation: Lucantonio, S.; Di Giuliano, A.; Gallucci, K. Influences of the Pretreatments of Residual Biomass on Gasification Processes: Experimental Devolatilizations Study in a Fluidized Bed. *Appl. Sci.* **2021**, *11*, 5722. https://doi.org/10.3390/app11125722

Academic Editors: Falah Alobaid and Jochen Ströhle

Received: 2 June 2021
Accepted: 18 June 2021
Published: 20 June 2021

1. Introduction

The EU's Renewable Energy Directive (RED II) has set the goal of achieving a 14% renewable energy share in the transport sector by 2030 [1], and residual biomasses and agro-industrial waste can be exploited as sources to produce sustainable second generation biofuels [2], which are expected to significantly reduce greenhouse gas emissions [2,3].

The gasification of residual biomass, to produce advanced biofuels, is a promising technology to achieve the goals of RED II. Gasification is a mature thermochemical conversion process suitable for biomasses, with syngas (mixture of H_2, CO, CO_2, CH_4, possibly diluted by steam and/or N_2 [4]) as the main product; syngas is primarily used to generate heat and electricity, and is potentially exploitable to synthesize advanced biofuels (the latter option has not yet been fully implemented at the industrial scale) [5]. Gasification consists of partial oxidation of the carbon contained in the biomass (or in other carbonaceous fuels) at high temperature (750–1150 °C [6]), using a controlled amount of an oxidant agent (air, pure oxygen, steam, or mixtures of them) [6]. Pure oxygen ensures the production of a high heating value and nitrogen-free syngas, the latter feature being advantageous for the synthesis of biofuels; however, the provision of pure oxygen requires an air separation

unit (ASU), which is usually associated with high capital and operational costs [5]. The chemical looping gasification (CLG) process is a new gasification concept, which avoids nitrogen dilution without requiring an ASU and allows for decent fuel conversions [5,7,8]. The difference between CLG and conventional gasification methods is represented by the oxygen source: the gaseous oxidant agents are replaced by the lattice oxygen provided by metal oxides (Me_xO_y) [9]. These metal oxides for CLG are called oxygen carriers (OC). A suitable reactor configuration for CLG is the dual fluidized bed reactor: one fluidized bed works as a gasifier (steam and/or CO_2 as fluidizing agents, while the OC particles provide oxygen); the other bed works as a burner (air as the oxidizing and fluidizing agent, the OC recovers oxygen); the OC particles continuously circulate from one bed to the other [10].

The ongoing European research project CLARA (chemical looping gasification for sustainable production of biofuels, G.A. 817841 [11]) aims to develop an efficient technology to produce liquid fuels by the Fischer–Tropsch synthesis [12], which converts the syngas obtained by the CLG of selected biogenic residues [13]. Concretely, CLARA's final objective is to prove the feasibility of a complete residual biomass-to-fuel chain up to the 1 MW_{th} scale in an industrially relevant environment, with a target cold gas efficiency of 82%, carbon conversion of 98%, and the level of tar in outlet syngas lower than 1 mg Sm^{-3} [14,15]. Even though CLG is rather flexible concerning the nature of raw solid fuel, one of the main focuses and novelty points of CLARA deals with the study of biomass pretreatments, carried out in order to improve fuel performances during their thermochemical conversion, in terms of fuel energy density and avoidance of sintering/agglomeration phenomena of fluidized bed particles with fuel ashes [15,16].

CLARA has selected wheat straw as a residual biomass of interest for CLG, investigating the effects from several pretreatments, such as torrefaction, washing, addition of minerals; those pretreatments, described in detail elsewhere [15–17], were mainly focused on the issue of agglomeration avoidance during the reduction-oxidation cycles of CLG, involving both OC particles and biomass ashes [15]. This work focuses on torrefaction and washing influences on the pyrolytic behavior of pretreated biomass.

Torrefaction is a mild form of pyrolysis at temperatures ranging between about 200 and 300 °C, in an inert environment [18]. Tumuluru et al. [18] reported that biomass torrefaction improves its physical properties, such as: grindability; particle size and distribution; pelletability; proximate and ultimate composition (moisture, carbon, and hydrogen content); calorific value; storability, thanks to increased resistance towards biological degradation. Ru et al. [19] investigated physicochemical characteristics of fast-growing poplar, torrefied at 200, 225, 250, 275, and 300 °C; they found that: (i) torrefaction reduced biomass hemicellulose content because of dehydration, deacetylation, and cleavage of ether linkages; (ii) H/C decreases while O/C and heating value increase as the torrefaction temperature is increased. Stelte et al. [20] focused on the correlation between wheat straw torrefaction (in the range 150–300 °C) and pelletizing properties, concluding that the pelletizing process results in mechanically strong pellets (with higher heating value and reduced moisture adsorption) for torrefaction temperature lower than or equal to 250 °C. Di Giuliano et al. [15], thanks to the research carried out at CENER (Centro Nacional de Energías Renovables), found that torrefaction was effective in the removal of Cl from wheat straw, therefore suggesting this pretreatment as a de-chlorinating operation, which prevents the formation of pollutants derived from Cl and the accelerated corrosion issues in facilities for thermochemical processes, such as CLG.

The washing pretreatment may be used to remove alkali and alkaline earth metals (AAEM) [15,21]. Cen et al. [21] studied the AAEM content and the pyrolytic behavior of rice straw, washed with water, aqueous HCl solution or aqueous phase bio-oil; they found that K, Ca, Mg, and Na were removed thanks to washing by each of the three liquids, with removal efficiencies always between 90–100% as to the HCl solution and aqueous phase bio-oil, while quite lower with water (~80% for K, ~10% for Ca, ~25% for Mg, and ~75% for Na); with regard to the pyrolytic behavior of washed rice straw, they found that the pretreatment with water had little effect on developed non-condensable gases.

This work thoroughly investigates the influence of some pretreatments on the thermochemical decomposition of wheat straw and the produced syngas. In this regard, experiments were carried out involving devolatilizations in a fluidized bed made up of sand. Devolatilization is a key step of a generic gasification process, and strongly influences the amount and composition of the produced gas [22], so devolatilization results may detect possible primary effects of pretreatments on the thermochemical behavior of wheat straw. The fluidized bed made up of inert sand was chosen in so that: (i) biomasses could be studied in a reactor configuration similar to that of CLG developed in the CLARA project; (ii) possible redox effects from solids (such as OC) could be excluded and only those influences strictly due to biomass pretreatments could emerge. Devolatilization tests were performed on pellets of differently pretreated biomasses, firstly elaborating data by methods described elsewhere [10,23]. In addition, a further analysis of the same data was introduced, based on information taken from the instantaneous peaks of gas release during devolatilizations, treated by simple regressions with straight lines. This represents a point of novelty, since the introduced method is quite straightforward as far as both experimental and mathematical approaches are concerned.

2. Materials and Methods

2.1. Investigated Biomasses

The biomass investigated in this work is wheat straw, one of the biogenic residues selected within the CLARA project [10,15,16,24]. Wheat straw was in the form of pellets, useful to facilitate their transport, storage, and handling, and closer to its possible commercial utilization. Those wheat straw pellets underwent some pretreatments, i.e., torrefaction and torrefaction followed by washing, as described extensively elsewhere [10,15–17,25]. The torrefied and torrefied-washed pellets were also compared to the untreated wheat straw pellets (studied elsewhere [10]), which were considered as a reference material to infer the effects from pretreatments on syngas, if any. From here on, biomasses are named as indicated in Table 1. These biomasses were characterized by proximate and ultimate analyses, which allowed determining the moisture and ash contents, and the elemental composition; some of these data are available in [17,24] and were used in Equation (3) of this work. Chemical analysis and ash melting tests were also performed on investigated biomasses, as reported by Di Giuliano et al. [15], to quantify respectively the content of inorganics and the melting temperature of biomass ashes.

Table 1. Names of biomasses investigated in this work with specification of the related pretreatment.

Name of Biomass	Characteristic of the Pellet
WSP	Wheat Straw Pellet
WSP-T1	Wheat Straw Pellet—Torrefied at T1 = 250 °C
WSP-T2	Wheat Straw Pellet—Torrefied at T2 = 260 °C
WSP-T3	Wheat Straw Pellet—Torrefied at T3 = 270 °C
WSP-T1W	Wheat Straw Pellet—Torrefied at T1 and Washed
WSP-T2W	Wheat Straw Pellet—Torrefied at T2 and Washed
WSP-T3W	Wheat Straw Pellet—Torrefied at T3 and Washed

2.2. Bed Material and Conditions of Devolatilization Tests

Devolatilizations were carried out in a laboratory scale fluidized bed reactor. The granular bed was made up of sand, an inert material used to perform devolatilizations in the absence of particles with proven oxidizing properties (such as OC exploited in CLG). The physical properties of sand are summarized in Table 2. Nitrogen (N_2) was used as the fluidizing gas, to avoid the provision of external oxygen, at 1.5 times the minimum fluidization velocity of sand, so to ensure similar fluid-dynamic conditions for all tests. Under the selected conditions (700, 800, and 900 °C in N_2), sand particles (Table 2) belong to the Group B of generalized Geldart classification [26]. The minimum fluidization velocities

(u_{mf}), calculated according to the method adopted by Di Giuliano et al. [15,27,28], are summarized in Table 2.

Table 2. Physical and fluid-dynamic properties of sand, adapted from [10]: particles diameter (d_p) and particle density (ρ_p); minimum fluidization velocity (u_{mf}) in N_2 as a function of temperature (T), with the indication of the related generalized Geldart Group [26].

Material		**Sand**
d_p **(µm)**		212–250
ρ_p **(kg m^{-3})**		2.6×10^3
T **(°C)**	u_{mf} **(cm s^{-1})**	**Generalized Geldart Group [27]**
700	2.4	B
800	4.4	B
900	2.9	B

2.3. Experimental Apparatus and Procedure for Devolatilization Tests

Devolatilization tests, as anticipated in Section 2.2, were carried out for all biomasses listed in Table 1 at three temperature levels (700, 800, and 900 °C), with N_2 as the fluidizing agent, in a fluidized bed made up of sand. The related experimental apparatus at laboratory-scale was depicted and fully described in detail elsewhere [10,23]. For the sake of clarity, it is also briefly described in the following.

A mass flow controller allowed N_2 to be fed into the windbox of a cylindrical quartz reactor (5 cm internal diameter), in which the devolatilizations took place. Sand was loaded inside, in such a quantity to form a 7.5 cm high bed (1.5 times the internal diameter of the reactor). The reactor was heated by a cylindrical electric furnace, with temperature controlled by a thermocouple directly submerged in the bed. The syngas produced by devolatilizations left the reactor freeboard together with N_2, and both passed through an ice trap, which operated a first separation of condensable species and entrained fine solids. Downstream, a double-pipe condenser (ethylene glycol on the shell-side at −4°C, gas flow on the tube-side) allowed the forced separation of water and other condensable substances. The dry and cold syngas passed through filters for a further cleaning, then reached gas detectors: (i) a micro-gas chromatograph (µGC) (Agilent 490, Agilent Technologies Italia S.p.A., Cernusco sul Naviglio (MI), Italy), to identify the hydrocarbons in the syngas (qualitative identification from a not exhaustive list of detected species, as discussed in [10,23]); (ii) an online ABB station, with analyzers measuring the volumetric concentrations of H_2, CO, CO_2, CH_4, and hydrocarbons expressed in ppm of "equivalent C_3H_8". From here on, equivalent C_3H_8 is named "$C_3H_{8,eq.}$" and such quantity excludes CH_4, separately measured and accounted.

2.4. Processing of Devolatilization Data

For each pair "biomass kind-temperature", three repetitions of devolatilization were performed (i.e., three pellets of the same kind were devolatilized at each temperature).

Each pellet was devolatilized individually and completely before feeding the following one. Because of this procedure, as already evidenced in [10,23], the experimental process is intrinsically at unsteady-state.

Thanks to the hypothesis of N_2 as the internal standard, it was possible to determine the instantaneous molar flow rates of the gases ($F_{i,out}$, with i as the generic gaseous species produced by the devolatilization tests, quantified by the ABB system: H_2, CO, CO_2, CH_4, $C_3H_{8,eq.}$). Figure 1 (Section 3.1) shows examples of these instantaneous flow rates from individual devolatilizations as functions of time (t), characteristically shaped as asymmetric peaks [29,30].

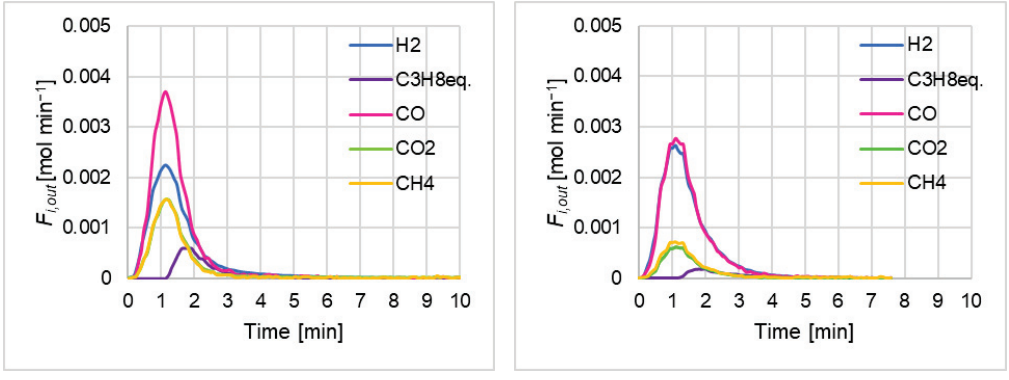

Figure 1. Example of H_2, CO, CO_2, CH_4, and $C_3H_{8,eq}$. outlet molar flow rates ($F_{i,out}$) as functions of time, produced by devolatilizations in the sand fluidized bed of (**a**) WSP at 800 °C; (**b**) WSP-T1 at 900 °C. WSP data adapted from [10].

The evaluation of devolatilization performances by integral-average values, already proposed by the same research team in [10,23], was adopted in this work to calculate: gas yield (η^{av}, Equation (1)); H_2/CO molar ratio (λ^{av}, Equation (2)); carbon conversion ($\chi_c{}^{av}$, Equation (3)); the superscript "av" means "integral-average".

$$\eta^{av} = \frac{\sum_i \int F_{i,out}\, dt}{m_p} with\ i = H_2, CO, CO_2, CH_4\ and\ C_3H_{8,eq.}\ ;\ m_p = mass\ of\ pellet\ (g) \quad (1)$$

$$\lambda^{av} = \frac{\int F_{H_2,out}\, dt}{\int F_{CO,out}\, dt} \quad (2)$$

$$\chi_C{}^{av} = \frac{12\ (g\ mol^{-1}) \times \sum_j [n_j \times \int F_{j,out}\ dt]}{m_p \times \left(1 - \frac{\%moisture_{ar}}{100}\right) \times \left(1 - \frac{\%ash_{db}}{100}\right) \times \left(\frac{\%C_{daf}}{100}\right)} \times 100$$
$$with\ j = CO, CO_2, CH_4\ and\ C_3H_{8,eq.}\ ;\ m_p = mass\ of\ pellet\ (g)$$
$$n_j = number\ of\ carbons\ atoms\ in\ j \quad (3)$$
$$\%moisture_{ar} = moisture\ content\ as\ wt\%\ in\ as\ recieived\ (ar)\ biomass \%ash_{db} =$$
$$ash\ content\ as\ wt\%\ in\ biomass\ on\ dry\ basis\ (db)$$
$$\%C_{daf} = elemental\ carbon\ as\ wt\%\ in\ biomass\ on\ dry\ ash\ free\ basis\ (daf)$$

As to these parameters (Equations (1)–(3), the arithmetic average out of the three repetitions and the related standard deviation were calculated for each set "biomass kind-temperature", and the resulting values were represented by bar-charts in Figure 2 (Section 3.1).

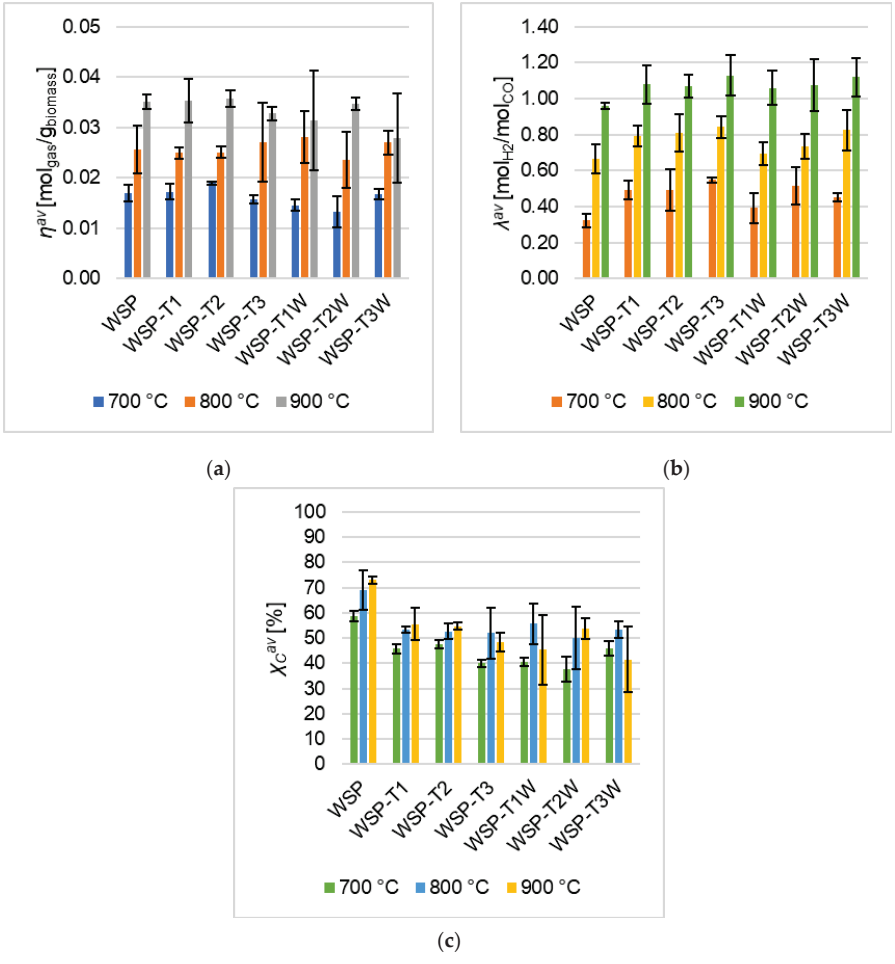

Figure 2. Experimental results of devolatilization tests for all kind of pellets, as functions of temperature (700, 800, and 900°C): (**a**) integral average gas yield (η^{av}, Equation (1)); (**b**) integral average H_2/CO molar ratio (λ^{av}, Equation (2)); (**c**) integral average carbon conversion (χ_c^{av}, Equation (3)); WSP data adapted from [10].

This work introduces a further method to analyze devolatilization performances, which focuses on the quantitatively most representative moment of unsteady-state devolatilizations of individual pellets, i.e., the top of $F_{i,out}$ devolatilization peaks as functions of time (see Figure 1), when the highest gas release occurred.

The procedure to elaborate this data follows:

1. for each set "biomass kind-temperature" and for each of the three repetitions, the highest released flow rate (i.e., peak top of $F_{i,out}$ in Figure 1) was identified for each quantified species (i = H_2, CO, CO_2, CH_4, and $C_3H_{8,eq.}$);
2. a neighborhood of 7 $F_{i,out}$ experimental points was selected, centered on the considered peak top;
3. the arithmetic average ($F'^{p}_{i,out}$, Equation (4), where "p" superscript means "peak") was calculated out of these 7 points.

In addition, the distribution among peaks of released gases—namely H_2, CO, CO_2, CH_4, and $C_3H_{8,eq.}$—was calculated, in terms of molar fractions on a nitrogen-free basis

($Y^p_{i,out}$, Equation (5)). For each temperature value and each gaseous species, three points were obtained (one per test), corresponding to the three repetitions for each kind of biomass; therefore, for the generic gaseous species i, 9 values of $Y^p_{i,out}$ were obtained, evenly distributed on the three temperature levels 700, 800, 900 °C.

$$F^p_{i,out} = \frac{\sum_{k=1}^{7} F_{i,out,k}}{7} \quad with\ i = H_2, CO, CO_2, CH_4\ and\ C_3H_{8,eq.}\ ;\ k = number\ of\ experimental\ point \tag{4}$$

$$Y^p_{i,out} = \frac{F^p_{i,out}}{\sum_i F^p_{i,out}} with\ i = H_2, CO, CO_2, CH_4\ and\ C_3H_{8,eq} \tag{5}$$

Moreover, a parameter called "specific maximum gas production" (*SMGP*) was introduced and calculated by Equation (6). This parameter is a local value expressed as a specific gas yield per unit of biomass and unit of time, which focuses on the devolatilization phenomenon around the peak top of released gas flow rate.

$$SMGP = \frac{\sum_i F^p_{i,out}}{m_p} with\ i = H_2, CO, CO_2, CH_4\ and\ C_3H_{8,eq.}\ ;\ m_p = mass\ of\ pellet\ (g) \tag{6}$$

Analogously to $Y^p_{i,out}$, 9 *SMGP* values resulted for each kind of biomass, evenly distributed on the three temperature levels 700, 800, 900 °C.

For each 9-points set of $Y^p_{i,out}$ or *SMGP* as functions of devolatilization temperature, a regression was performed by means of dedicated Microsoft Excel tool, under the assumption of straight line (Equation (7)) as the modeling equation for $Y^p_{i,out}$ or *SMGP* dependency on devolatilization temperature (T). This assumption was supported by observing the approximately linear trends of devolatilization performances experimentally determined by Zeng et al. [30], with tests at different temperature levels, progressively increased by 50 °C in the range 600–900 °C.

$$Z = m\ T[^\circ C] + q with\ Z = Y^p_{i,out}\ or\ SMGP\ ;\ m = slope\ ; q = intercept\ at\ T = 0 \tag{7}$$

3. Results

Figure 1 shows two examples of results (out of 63), obtained from devolatilizations of individual pellets, expressed in terms of $F_{i,out}$. As already reported by [10,23], $F_{i,out}$ curves as functions of time have an asymmetrical shape, due to the unsteady-state of each devolatilization.

3.1. Results from Devolatilization Tests: Integral-Average Quantities

Figure 2 shows the overall results of the devolatilization tests carried out using sand as the bed material, in anoxic conditions due to N_2 supply, at three temperature levels (700, 800, and 900 °C). The data of the three repetitions of the untreated WSP pellets were adapted from [10]. The bar-charts in Figure 2 summarize the devolatilization results in terms of integral-average parameters: (i) gas yield (η^{av}, Equation (1)), (ii) H_2/ CO molar ratio (λ^{av}, Equation (2)), and (iii) carbon conversion (χ^{av}_C, Equation (3)), calculated by the procedure described in Section 2.4. For each set "biomass kind-temperature" in Figure 2, the bar heights represent the average values of the considered quantity out of the three repetitions, the associated error bars represent the related standard deviations.

3.2. Results from Devolatilization Peaks: Regression Analyses

As described in Section 2.4, the molar fractions on N_2-free basis ($Y^p_{i,out}$, Equation (5)) of the gases and the *SMGP* (Equation (6)) were calculated, focusing on the peaks top of gas release during devolatilizations of individual pellets.

Figure 3 shows the results of this calculations from devolatilizations of WSP pellets at each temperature level, provided with regression straight lines (Equation (7)). For the sake

of clarity, the slopes (m, Equation (7)) and y-axis intercepts (q, Equation (7)) of regression straight lines were collected in Table 3 for devolatilizations of WSP pellets.

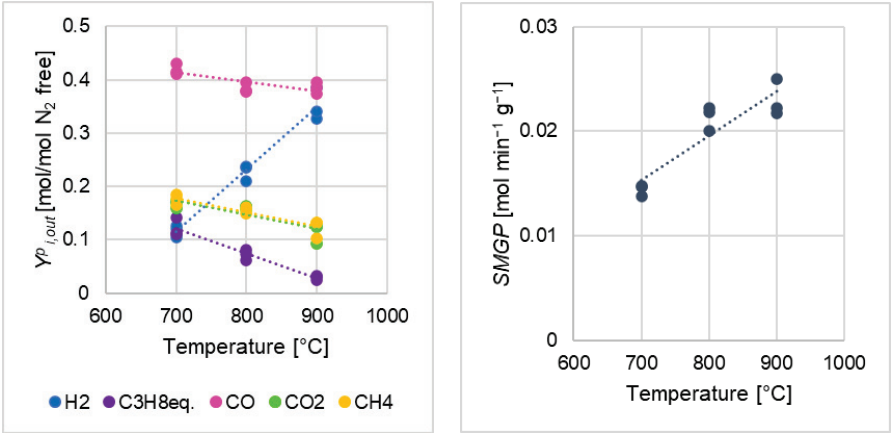

(**a**) (**b**)

Figure 3. Experimental results from devolatilization peaks for WSP pellets as functions of temperature (points), with regression straight lines (dotted): (**a**) molar fractions on N_2 free-basis of produced gases at devolatilization peaks ($Y^p_{i,out}$ Equation (5)); (**b**) SMGP (Equation (6)).

Table 3. Slopes (m, Equation (7)) and y-axis intercepts (q, Equation (7)) of the regression straight lines of $Y^p_{i,out}$ (Equation (5), i = H_2, CO, CO_2, CH_4, and $C_3H_{8,eq.}$) and *SMGP* (Equation (6)), for WSP pellets.

Species of Gas	m [Mol Mol N_2 Free^{-1} °C^{-1}]	q [Mol Mol N_2 Free^{-1}]
H_2	1.170×10^{-3}	-7.050×10^{-1}
$C_3H_{8eq.}$	-4.622×10^{-4}	4.440×10^{-1}
CO	-1.730×10^{-4}	5.340×10^{-1}
CO_2	-2.686×10^{-4}	3.622×10^{-1}
CH_4	-2.672×10^{-4}	3.648×10^{-1}
SMGP	m [mol min^{-1} g^{-1} °C^{-1}]	q [mol min^{-1} g^{-1}]
	4.293×10^{-1}	-1.475×10^{-2}

Figures 4 and 5 show the results of peak analyses on devolatilizations data for torrefied (WSP-T1, WSP-T2, WSP-T3) and torrefied-washed pellets (WSP-T1W, WSP-T2W, WSP-T3W). In order to facilitate comparisons, the graphs of the molar fractions ($Y^p_{i,out}$, Equation (5)) of the six pellets were collected in Figure 4, while Figure 5 collects the graphs of *SMGP* for the same biomasses. Tables 4 and 5 are associated with Figures 4 and 5, respectively, reporting the coefficients m and q (Equation (7)) of regression straight lines.

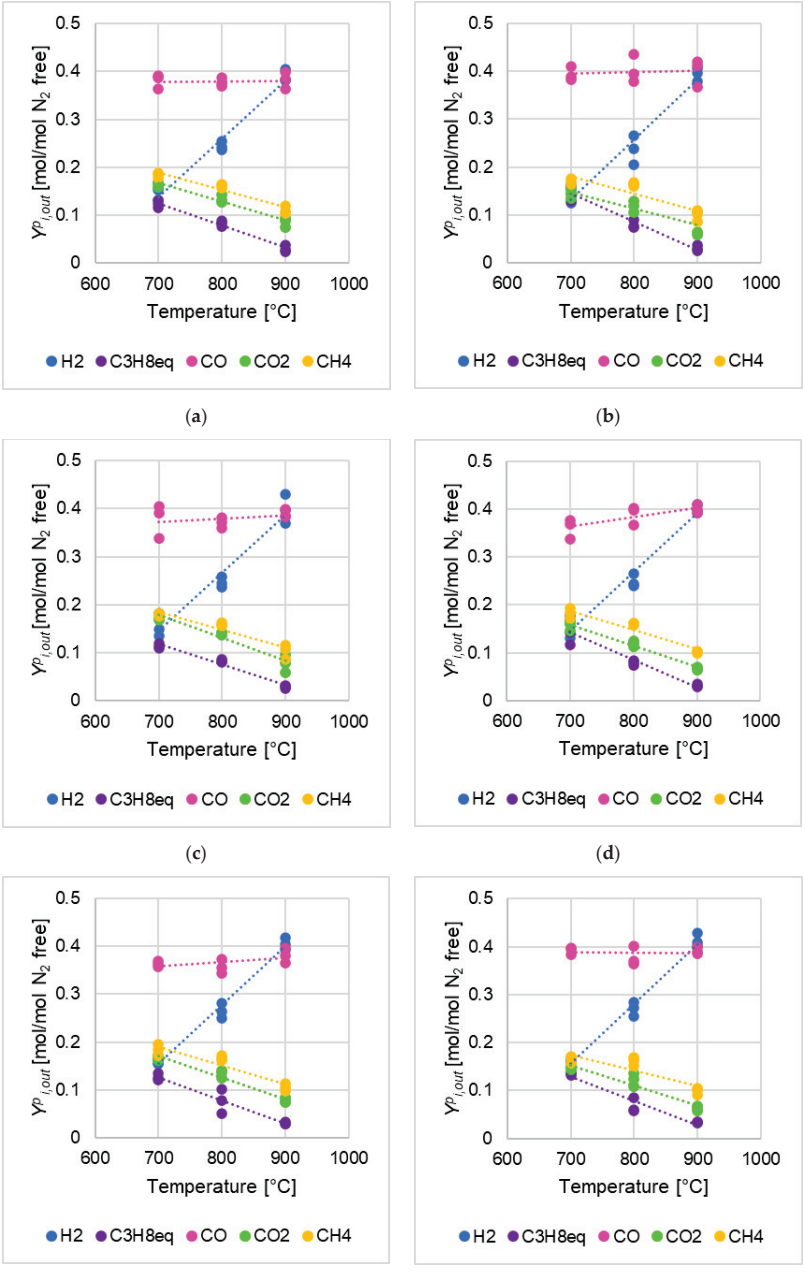

Figure 4. Experimental results from devolatilizations of torrefied and torrefied-washed pellets. Molar fractions on N_2 free-basis of produced gases at devolatilization peaks ($Y^{p}_{i,out}$, Equation (5)), as functions of temperature (points), with regression straight lines (dotted), for: (**a**) WSP-T1; (**b**) WSP-T1W; (**c**) WSP-T2; (**d**) WSP-T2W; (**e**) WSP-T3; and (**f**) WSP-T3W.

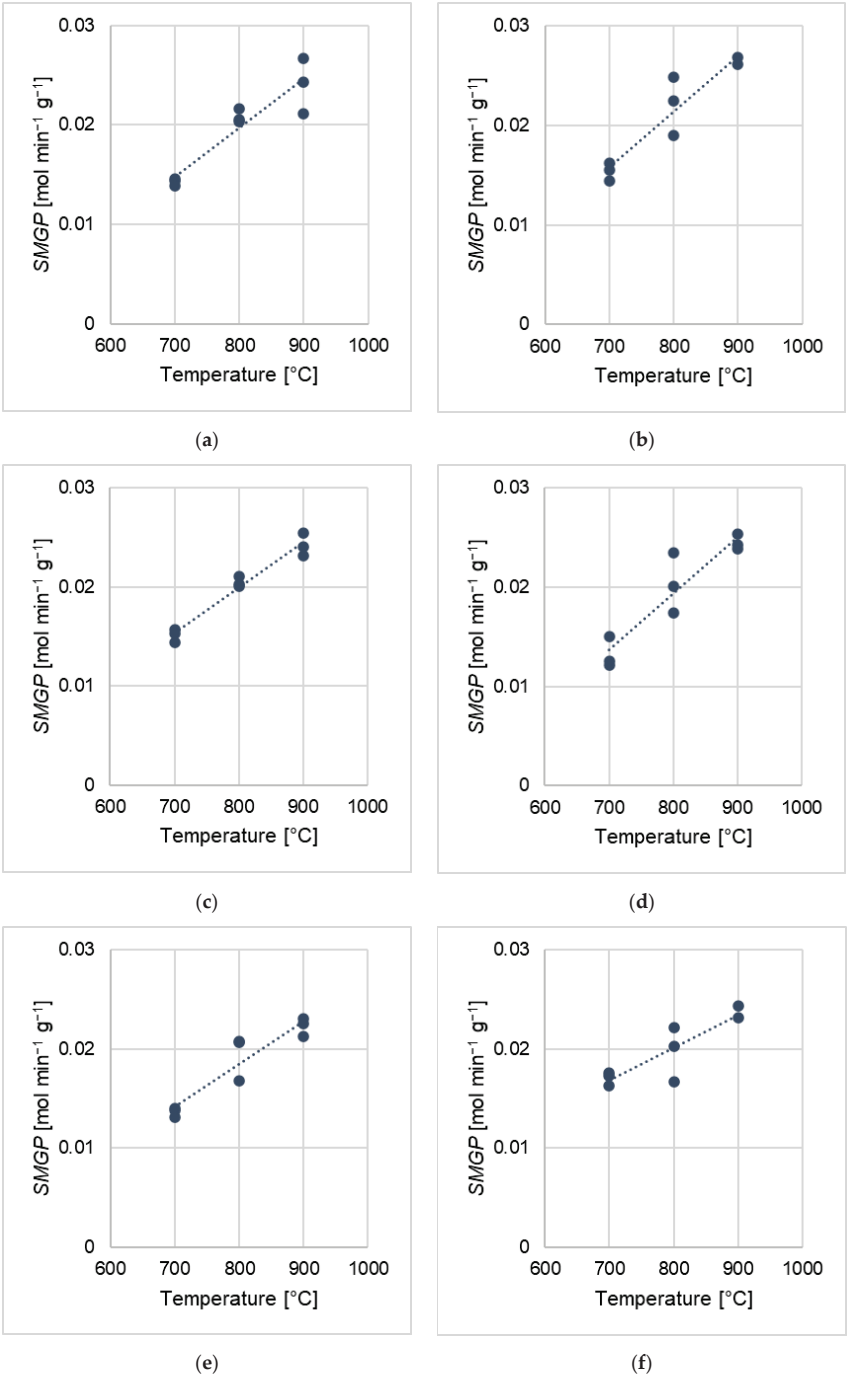

Figure 5. Experimental results from devolatilizations of torrefied and torrefied-washed pellets. *SMGP* (Equation (6)) as a function of temperature (points), with regression straight lines (dotted), for: (**a**) WSP-T1; (**b**) WSP-T1W; (**c**) WSP-T2; (**d**) WSP-T2W; (**e**) WSP-T3; (**f**) WSP-T3W.

Table 4. Slopes (m, Equation (7)) and y-axis intercepts (q, Equation (7)) of the regression straight lines of $Y^{p}_{i,out}$ (Equation (5), i = H_2, CO, CO_2, CH_4, and $C_3H_{8,eq.}$) for torrefied and torrefied-washed pellets.

Type of Biomass	Species of Gas	m (Mol Mol N_2 Free^{-1} °C^{-1})	q (Mol Mol N_2 Free^{-1})
WSP-T1	H_2	1.213×10^{-3}	-7.106×10^{-1}
	C_3H_{8eq}	-4.654×10^{-4}	4.514×10^{-1}
	CO	8.298×10^{-6}	3.733×10^{-1}
	CO_2	-3.932×10^{-4}	4.429×10^{-1}
	CH_4	-3.631×10^{-4}	4.429×10^{-1}
WSP-T2	H_2	1.217×10^{-3}	-7.064×10^{-1}
	C_3H_{8eq}	-4.272×10^{-4}	4.177×10^{-1}
	CO	6.025×10^{-5}	3.311×10^{-1}
	CO_2	-4.774×10^{-4}	5.125×10^{-1}
	CH_4	-3.721×10^{-4}	4.450×10^{-1}
WSP-T3	H_2	1.221×10^{-3}	-6.999×10^{-1}
	C_3H_{8eq}	-4.802×10^{-4}	4.624×10^{-1}
	CO	9.178×10^{-5}	2.936×10^{-1}
	CO_2	-4.400×10^{-4}	4.780×10^{-1}
	CH_4	-3.924×10^{-4}	4.659×10^{-1}
WSP-T1W	H_2	1.255×10^{-3}	-7.466×10^{-1}
	C_3H_{8eq}	-5.867×10^{-4}	5.553×10^{-1}
	CO	2.963×10^{-5}	3.747×10^{-1}
	CO_2	-3.447×10^{-4}	3.892×10^{-1}
	CH_4	-3.535×10^{-4}	4.274×10^{-1}
WSP-T2W	H_2	1.224×10^{-3}	-7.107×10^{-1}
	C_3H_{8eq}	-5.705×10^{-4}	5.420×10^{-1}
	CO	1.980×10^{-4}	2.247×10^{-1}
	CO_2	-4.458×10^{-4}	4.715×10^{-1}
	CH_4	-4.053×10^{-4}	4.725×10^{-1}
WSP-T3W	H_2	1.256×10^{-3}	-7.236×10^{-1}
	C_3H_{8eq}	-5.044×10^{-4}	4.821×10^{-1}
	CO	-3.523×10^{-6}	3.903×10^{-1}
	CO_2	-4.187×10^{-4}	4.457×10^{-1}
	CH_4	-3.295×10^{-4}	4.054×10^{-1}

Table 5. Slopes (m, Equation (7)) and y-axis intercepts (q, Equation (7)) of the regression straight lines of *SMGP* (Equation (6)) for torrefied and torrefied-washed pellets.

Biomass	m [Mol Min^{-1} g^{-1} °C^{-1}]	q [Mol Min^{-1} g^{-1}]
WSP-T1	4.882×10^{-5}	-1.933×10^{-2}
WSP-T2	4.534×10^{-5}	-1.636×10^{-2}
WSP-T3	4.312×10^{-5}	-1.605×10^{-2}
WSP-T1W	5.648×10^{-5}	-2.380×10^{-2}
WSP-T2W	5.618×10^{-5}	-2.560×10^{-2}
WSP-T3W	3.297×10^{-5}	-6.241×10^{-3}

4. Discussion

Before a detailed discussion of devolatilization results, it is worth to stress that this study aimed to strictly examine the influences from wheat straw pretreatments and devolatilization temperatures on pellets thermochemical behavior. For this reason, tests were carried out in an inert atmosphere and with a unique bed material, devoid of those oxidative properties typical of the OC investigated within CLARA project [5,10,15,31]. In such a way, results did not depend on the type of bed material or any external oxygen supply.

4.1. Integral-Average Quantities

Figure 2 highlights that the devolatilization temperature is a parameter with a significant effect on devolatilization performances, whatever the considered biomass kind; for all biomasses, the gas yield (η^{av}, Equation (1), Figure 2a) and the H_2/CO molar ratio (λ^{av}, Equation (2), Figure 2b) grew as the temperature was increased. With regard to the carbon conversion (χ_C^{av}, Equation (3), Figure 2c), the difference between values at 800 and 900 °C was not always evident (net of standard deviations), so that trends with respect to temperature were not as much clear as in the case of η^{av} and λ^{av}. Anyway, one can state that the temperature increasing from 700 to 800 °C always improved χ_C^{av}. As a matter of fact, Wang et al. [32] reported how the gas yield, the carbon conversion and the H_2 and CO content in the syngas increased as the devolatilization temperature was increased, with experiments on sawdust pellets in a fluidized bed reactor, within the range 750–950 °C. Consequently, considerations about Figure 2 may suggest that one should obtain the best performance of thermochemical conversion of wheat straw biomasses by operating at the highest tested temperature (900 °C).

In general, the increase in gas yield (η^{av}, Equation (1), Figure 2a) is not necessarily accompanied by an improvement in syngas quality (e.g., in terms of H_2/CO ratio for Fischer-Tropsch synthesis). Remarkably, in the case of study of this work, the H_2/CO molar ratio (λ^{av}, Equation (2), Figure 2b) grew together with gas yield (η^{av}, Equation (1), Figure 2a) as the temperature was increased; in other words, there is a general improvement in the quality and quantity of the syngas due to the increase of devolatilization temperature, which in turn appeared to enhance the extent of reforming and cracking reactions.

In addition to the devolatilization temperature influence, minor effects due to pretreatments were observed on devolatilization performances.

A comparison between the results of torrefied pellets (WSP-T1, WSP-T2, WSP-T3) and those of WSP, suggested that:

- the η^{av} of torrefied pellets was close to that of WSP (Figure 2a), with differences even less evident if standard deviations are taken into account;
- the λ^{av} of torrefied pellets is slightly higher than that of WSP (Figure 2b);
- with torrefied pellets, a substantial decrease of the χ_C^{av} emerged in comparison to the same quantity of WSP (Figure 2c); this is in agreement with the expected effects of the torrefaction pretreatment (defined elsewhere [17]). As highlighted by Fan et al. [33], torrefaction can lead to a reduction of carbon conversion in the thermochemical conversion of the biomass, because of devolatilization, polycondensation, and carbonization which occur during the pretreatment; as a matter of fact, Niu et al. [34] referred that torrefaction increased the elemental carbon content per unit of mass, because of the release of volatiles (such as water and CO_2), which in turn made the biomass properties shift towards those of coal [35].

With regard to torrefied samples (WSP-T1, WSP-T2, WSP-T3), a further focus was performed on effects of torrefaction temperature:

- no evident influences emerged on gas yield (η^{av}, Equation (1), Figure 2);

The highest H_2/CO molar ratio (λ^{av}, Equation (2), Figure 2b) resulted for WSP-T3; Zhang et al. [36] found that 270 °C was the best torrefaction temperature for pelletized pine and spruce sawdust, among investigated values of 240, 270, 300, and 330 °C: they carried out devolatilizations by thermogravimetric measurements and determined, by kinetic analyses, that the activation energy of H_2 release was minimum when the torrefaction temperature was equal to T3 (270 °C).

Concerning the torrefied-washed samples (WSP-T1W, WSP-T2W, WSP-T3W), a comparison with the corresponding torrefied pellets (WSP-T1, WSP-T2, WSP-T3) evidenced that η^{av} (Figure 2a), λ^{av} (Figure 2b), and χ_C^{av} (Figure 2c) did not substantially vary, net of standard deviations. The washing pretreatment after torrefaction did not produce significant improvements, at least in terms of gas yield, H_2/CO molar ratio, and carbon conversion. These results can be justified by considering that the washing pretreatment

with water was strictly applied to remove AAEM from the biomass [37]. On the other hand, it is worth to stress that the washing pretreatment improves some other properties of wheat straw from the gasification process point of view, since the release of contaminants (e.g., KCl, H_2S) is preliminary reduced, and therefore the post-processing requirements in the cleaning unit of syngas may decrease [17].

4.2. Peak Quantities

Figures 4 and 5 summarize the results of devolatilization data analysis focused on peak quantities.

In general, for all kinds of biomass, Figures 3a and 4 suggest that:

- $Y^p_{CH_4,out}$, $Y^p_{CO_2,out}$, $Y^p_{C_3H_{8,\ eq.},out}$ (Equation (5)) decreased as the devolatilization temperature was increased, for all kinds of biomasses; qualitative identification analyses with the μGC AGILENT 490 found a high number of hydrocarbons species at 700 °C (*i*-C_4H_{10}, *n*-C_4H_{10}, C_5H_{12}, i-C_5H_{12}, *n*-C_5H_{12}, C_6H_6, C_2H_4/C_2H_2, C_2H_6, C_3H_8, C_3H_4), just some of them at 800 °C (*n*-C_4H_{10}, C_6H_6, C_2H_4/C_2H_2, C_2H_6, C_3H_8), while at 900 °C none of them was detected;
- $Y^p_{H2,out}$ (Equation (5)) increased as the temperature was increased for all kinds of biomasses;
- $Y^p_{CO,out}$ (Equation (5)) of pretreated pellets (Figure 4), was quite constant or slightly increased as the temperature was increased, while $Y^p_{CO,out}$ of WSP (Figure 3a) decreased.

These observations matched well with the discussion about integral-average parameters in Section 4.1, which highlighted that the higher the devolatilization temperature the higher the H_2/CO ratio, hypothesizing an enhancement of reforming and cracking reactions of hydrocarbons due to the increasing of devolatilization temperature.

Tables 3 and 4 show the coefficients *m* and *q* of regression straight lines obtained for $Y^p_{i,out}$:

- *m* is an index of the effects due to the variations of devolatilization temperature on the $Y^p_{i,out}$ distribution in the syngas; for a generic gaseous species *i*, a positive *m* means that $Y^p_{i,out}$ increases as the temperature was increased (and vice versa), and the higher of the absolute value of *m*, the more abrupt the $Y^p_{i,out}$ variation due to temperature (somehow related to similar temperature effects represented by values of the Arrhenius activation energy);
- *q* may not have a proper physical-chemical interpretation for a given *i* species (anyway, it is likely interpretable analogously to the preexponential factor of Arrhenius function); in any case, being *m* equal, the higher the *q* the greater the tendency of a given biomass to release *i*;

Overall, for all investigated biomasses, *m* and *q* values related to $Y^p_{i,out}$ (*i* = H_2, CO, CO_2, CH_4, and $C_3H_{8,eq.}$, Equation (5)) did not severely differ one to another for each considered gaseous species (Tables 3 and 4); this was in agreement with the abovementioned observations about Figures 3a and 4, which generally showed quite similar trends and absolute values for $Y^p_{i,out}$ of the seven investigated biomasses.

Nevertheless, without prejudice to what was said in the previous sentence, the quantifications offered by *m* and *q* highlighted some minor differences between the behaviors of biomasses, associated to their devolatilization peaks; in this regard, Figure 6 compares regression lines obtained by *m* and *q* values from Tables 3 and 4 for $Y^p_{i,out}$ (*i* = H_2, CO, CO_2, CH_4, and $C_3H_{8,eq.}$, Equation (5)):

- WSP appeared as less likely to release H_2 (Figure 6b) and more likely to release CO_2 (Figure 6d) than pretreated wheat straw pellets; this could be related to the results of Qing et al. [38], who experimentally found that carbonaceous gases (CO_2 and CO) are more easily released than H_2 during the preliminary torrefaction pretreatment;

- With regard to CH_4 release (Figure 6a), a significant differentiation between WSP and pretreated wheat straw pellets emerged at 900 °C, with $Y^p_{CH_4,out}$ of WSP resulting as the highest value at that temperature;
- As to CO (Figure 6c), a poorer influence from devolatilization temperature emerged, also taking into account the distribution of the $Y^p_{CO,out}$ experimental points which originated the regression lines (Figure 4);
- As far as hydrocarbons are concerned (C_3H_{8eq}, Figure 6e), at 700 °C WSP-T1W and WSP-T2W showed the highest $Y^p_{C_3H_{8\ eq},out}$, but at higher temperatures, the behavior of all biomasses became uniform;
- When considering torrefied (WSP-T1, WSP-T2, WSP-T3) and torrefied-washed pellets (WSP-T1W, WSP-T2W, WSP-T3W) as two groups, they showed a slight behavioral difference in terms of CO_2 peak release (Figure 6d); for all other gas components, when individually considered, clear effects ascribable to the specific pre-treatment or the variation of torrefaction temperature could not be inferred;
- For each biomass, the H_2/CO molar ratio related to peak analyses ($Y^p_{H_2,out}/Y^p_{CO,out}$) was calculated as the ratio between the respective $Y^p_{H_2,out}$ and $Y^p_{CO,out}$ straight lines in Figure 6b,c at a given temperature, obtaining the results summarized in Table 6; remarkably, a direct influence from torrefaction temperature emerged: the higher this parameter, the greater the H_2/CO molar ratio related to peaks (with a negligible exception of the very close values of WSP-T2W and WSP-T3W at 700 °C), in fair agreement with evidences obtained by the analysis of integral-average quantities and the already cited literature evidence from Zhang et al. [36] (Section 4.1); in addition, relative percentage variation of H_2/CO ratio related to peaks were calculated with WSP values as references ($\Delta(H_2/CO)^p$, Table 6), and WSP-T3 always exhibited the greatest variation at each temperature, with the absolutely most pronounced at 700 °C.

Table 6. Peak analyses at 700, 800, and 900 °C: H_2/CO molar ratio related to peaks, obtained as the ratio between regression lines of $Y^p_{H_2,out}$ and $Y^p_{CO,out}$ (Equation (7), m and q from Tables 3 and 4) for each biomass; relative percentage variation of H2/CO ratio related to peaks, referred to WSP values $\Delta(H_2/CO)^p$.

Biomass	700 °C		800 °C		900 °C	
	$Y^p_{H_2,out}/Y^p_{CO,out}$ ($mol_{H2}\ mol_{CO}{}^{-1}$)	$\Delta(H_2/CO)^p$ (%)	$Y^p_{H_2,out}/Y^p_{CO,out}$ ($mol_{H2}\ mol_{CO}{}^{-1}$)	$\Delta(H_2/CO)^p$ (%)	$Y^p_{H_2,out}/Y^p_{CO,out}$ ($mol_{H2}\ mol_{CO}{}^{-1}$)	$\Delta(H_2/CO)^p$ (%)
WSP	0.28	0	0.58	0	0.92	0
WSP-T1	0.37	32	0.68	17	1.00	9
WSP-T2	0.39	41	0.70	21	1.01	10
WSP-T3	0.43	57	0.75	29	1.06	15
WSP-T1W	0.33	21	0.65	11	0.95	4
WSP-T2W	0.40	46	0.70	20	0.97	5
WSP-T3W	0.40	45	0.73	24	1.05	14

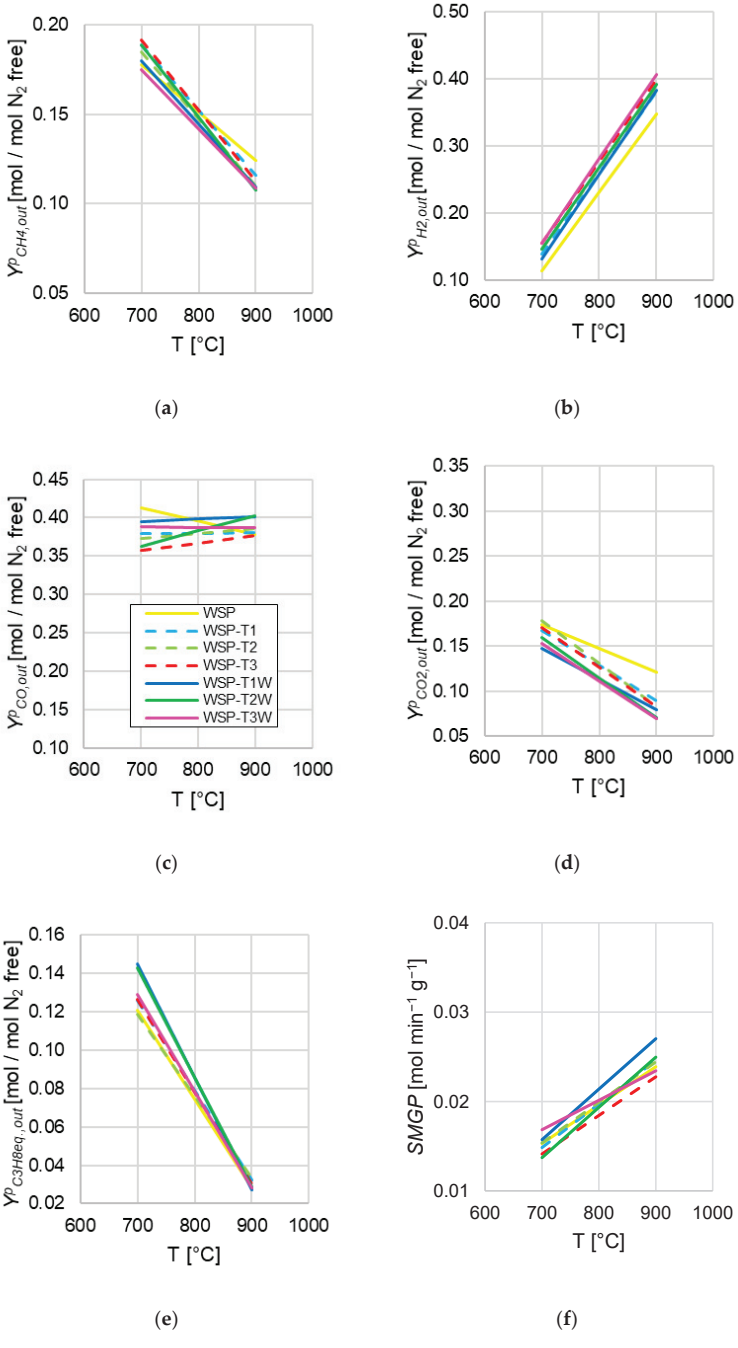

Figure 6. Regression lines obtained from data at the top of devolatilization peaks, compared for investigated biomasses: (**a**) $Y^p_{CH_4,out}$ (Equation (5)); (**b**) $Y^p_{H_2,out}$ (Equation (5)); (**c**) $Y^p_{CO,out}$ (Equation (5)); (**d**) $Y^p_{CO_2,out}$ (Equation (5)); (**e**) $Y^p_{C_3H_8eq.,out}$ (Equation (5)); (**f**) SMGP (Equation (6)); the legend in (**c**) is valid for the entire Figure.

Figure 5 and Table 5 summarize the results from the regression data analysis regarding the *SMGP* parameter (Equation (6)).

Figures 3b and 5 suggest that the predominant effect on *SMGP* derives from the increase of the devolatilization temperature: for all the biomasses, *SMGP* increased as the devolatilization temperature was increased, in agreement with the integral average gas yield (η^{av}, Equation (1), Figure 2a). This corroborates the reliability of both analysis methods.

Overall, by comparing *SMGP* lines in Figure 6f, substantial differences did not emerge in relation to pretreatments.

5. Conclusions

In this work, devolatilization tests of untreated and pretreated wheat straw pellets were carried out at three temperature levels (700, 800, and 900 °C), in a fluidized bed made up of sand.

Integral-average gas yield, H_2/CO molar ratio, and carbon conversion were determined from gas release data obtained by devolatilizations of individual pellets. Whatever the considered biomass, all these parameters increased as the temperature was increased, with a general improvement in syngas quality and productivity. Concerning the specific pretreatments:

- No evident influences on the integral-average gas yield emerged;
- All pretreated wheat straw pellets showed integral-average H_2/CO molar ratios higher than those of untreated wheat straw: the highest value was recorded for wheat straw pellet torrefied at 270 °C (the highest explored devolatilization temperature);
- Integral-average carbon conversion of untreated wheat straw pellets was significantly higher that of pretreated pellets;
- The washing pretreatment after torrefaction did not produce significant improvements in term of integral-average gas yield, H_2/CO molar ratio, and carbon conversion, when compared to only-torrefied ones.

Because of the intrinsically unsteady-state of devolatilizations (performed for individual pellets), a new analysis method of devolatilization data was proposed, focused on the peak in the experimental curves of released flow rates of syngas components (CO, CO_2, H_2, CH_4, and hydrocarbons as $C_3H_{8,eq.}$). Trends of syngas compositions as functions of devolatilization temperature were obtained by regressions with straight lines. Similarly, trends regarding the parameter "specific maximum gas production" were also obtained. As to fractions of gas species, the regressed trends offered some further information, which were not inferred from the previous integral-average analysis:

- The higher the devolatilization temperature, the greater the H_2 fraction in the syngas, at the expenses of CO_2, CH_4, and hydrocarbons;
- All pretreatments improved the H_2/CO molar ratio related to peaks, in comparison to the same ratio obtained from untreated wheat straw;
- A direct influence from torrefaction temperature emerged on H_2/CO molar ratio related to peaks, corroborating the less clear indication obtained by the integral average analyses.

Observations from the two kinds of analysis were in fair agreement with literature.

The integral average estimations and the regression peak analysis both appeared as general and straightforward methods to investigate the thermochemical behavior of biomasses, as well as the influences from operating conditions and biomass nature. Together with the experimental procedure of devolatilization of a few pellets, they constitute a faster and simpler procedure to select the more promising biomasses and operating conditions during a preliminary screening phase, in comparison to a more complex and time-demanding experimental campaign based on a continuous gasification process.

An additional outcome of this work is the provision of elaborated experimental data for further studies with modeling purposes, which also allow careful extrapolation (out of the experimentally explored temperature range) by means of linear regressed trends.

As a general remark, the torrefaction pretreatment brings in several advantages (e.g., grindability, pelletability, storability, increased heating value, higher H_2/CO molar ratio in devolatilized syngas), while the related operational costs may be limited—thanks to the low required temperatures—and easily compensated via heat recoveries in the intensified industrial configuration of a CLG plant.

Author Contributions: Conceptualization, A.D.G. and K.G.; methodology, A.D.G. and K.G.; software, S.L. and A.D.G.; validation, A.D.G. and K.G.; formal analysis, A.D.G. and K.G.; investigation, S.L., A.D.G. and K.G.; resources, K.G.; data curation, S.L., A.D.G. and K.G.; writing—original draft preparation, S.L.; writing—review and editing, S.L., A.D.G. and K.G.; visualization, S.L. and A.D.G.; supervision, A.D.G. and K.G.; project administration, K.G.; funding acquisition, K.G. All authors have read and agreed to the published version of the manuscript.

Funding: This research and the APC were funded by the Horizon 2020 Framework program of the European Union, CLARA project, G.A. 817841.

Data Availability Statement: The data presented in this study are available on request from the corresponding author.

Acknowledgments: The production and characterization of biomass pellets by the research team of National Renewable Energy Centre of Spain (CENER) is acknowledged, occurred within the CLARA project. The authors warmly thank Giampaolo Antonelli for his technical support.

Conflicts of Interest: The authors declare no conflict of interest. The funders had no role in the design of the study; in the collection, analyses, or interpretation of data; in the writing of the manuscript, or in the decision to publish the results.

References

1. EUR-Lex—32018L2001—EN—EUR-Lex. Available online: https://eur-lex.europa.eu/legal-content/en/TXT/?uri=CELEX:32018L2001 (accessed on 7 November 2020).
2. Molino, A.; Larocca, V.; Chianese, S.; Musmarra, D. Biofuels production by biomass gasification: A review. *Energies* **2018**, *11*, 811. [CrossRef]
3. Naik, S.N.; Goud, V.V.; Rout, P.K.; Dalai, A.K. Production of first and second generation biofuels: A comprehensive review. *Renew. Sustain. Energy Rev.* **2010**, *14*, 578–597. [CrossRef]
4. Amaro, J.; Rosado, D.J.M.; Mendiburu, A.Z.; dos Santos, L.R.; de Carvalho, J.A. Modeling of syngas composition obtained from fixed bed gasifiers using Kuhn–Tucker multipliers. *Fuel* **2021**, *287*, 119068. [CrossRef]
5. Dieringer, P.; Marx, F.; Alobaid, F.; Ströhle, J.; Epple, B. Process control strategies in chemical looping gasification-A novel process for the production of biofuels allowing for net negative CO_2 emissions. *Appl. Sci.* **2020**, *10*, 4271. [CrossRef]
6. Heidenreich, S.; Foscolo, P.U. New concepts in biomass gasification. *Prog. Energy Combust. Sci.* **2015**, *46*, 72–95. [CrossRef]
7. Mattison, T.; Hildor, F.; Li, Y.; Linderholm, C. Negative emissions of carbon dioxide through chemical-looping combustion (CLC) and gasification (CLG) using oxygen carriers based on manganese and iron. *Mitig. Adapt. Strateg. Glob. Chang.* **2020**, *25*, 497–517. [CrossRef]
8. Mendiara, T.; García-Labiano, F.; Abad, A.; Gayán, P.; de Diego, L.F.; Izquierdo, M.T.; Adánez, J. Negative CO2 emissions through the use of biofuels in chemical looping technology: A review. *Appl. Energy* **2018**, *232*, 657–684. [CrossRef]
9. Mohamed, U.; Zhao, Y.; Yi, Q.; Shi, L.; Wei, G.; Nimmo, W. Evaluation of life cycle energy, economy and CO2 emissions for biomass chemical looping gasification to power generation. *Renew. Energy* **2021**. [CrossRef]
10. Di Giuliano, A.; Lucantonio, S.; Gallucci, K. Devolatilization of residual biomasses for chemical looping gasification in fluidized beds made up of oxygen-carriers. *Energies* **2021**, *14*, 311. [CrossRef]
11. CLARA—Chemical Looping Gasification for Sustainable Production of Biofuels. Available online: https://clara-h2020.eu/ (accessed on 26 May 2021).
12. Faba, L.; Díaz, E.; Ordóñez, S. Recent developments on the catalytic technologies for the transformation of biomass into biofuels: A patent survey. *Renew. Sustain. Energy Rev.* **2015**, *51*, 273–287. [CrossRef]
13. The Concept: From Biomass to Biofuel—CLARA. Available online: https://clara-h2020.eu/the-concept/ (accessed on 17 October 2020).
14. Marx, F.; Dieringer, P.; Ströhle, J.; Epple, B. Design of a 1 MWth pilot plant for chemical looping gasification of biogenic residues. *Energies* **2021**, *14*, 2581. [CrossRef]
15. Di Giuliano, A.; Funcia, I.; Pérez-Vega, R.; Gil, J.; Gallucci, K. Novel application of pretreatment and diagnostic method using dynamic pressure fluctuations to resolve and detect issues related to biogenic residue ash in chemical looping gasification. *Processes* **2020**, *8*, 1137. [CrossRef]

16. Biomass Pre-Treatment—CLARA. Available online: https://clara-h2020.eu/biomass-pre-treatment/ (accessed on 9 November 2020).
17. Dieringer, P.; Funcia, I.; Soleimani, A.; Liese, T. Public Report II. Available online: https://clara-h2020.eu/wp-content/uploads/2020/11/CLARA_PublicReport2.pdf (accessed on 26 May 2021).
18. Tumuluru, J.S.; Sokhansanj, S.; Hess, J.R.; Wright, C.T.; Boardman, R.D. A review on biomass torrefaction process and product properties for energy applications. *Ind. Biotechnol.* **2011**, *7*, 384–401. [CrossRef]
19. Ru, B.; Wang, S.; Dai, G.; Zhang, L. Effect of torrefaction on biomass physicochemical characteristics and the resulting pyrolysis behavior. *Energy Fuels* **2015**, *29*, 5865–5874. [CrossRef]
20. Stelte, W.; Nielsen, N.P.K.; Hansen, H.O.; Dahl, J.; Shang, L.; Sanadi, A.R. Reprint of: Pelletizing properties of torrefied wheat straw. *Biomass Bioenergy* **2013**, *53*, 105–112. [CrossRef]
21. Cen, K.; Zhang, J.; Ma, Z.; Chen, D.; Zhou, J.; Ma, H. Investigation of the relevance between biomass pyrolysis polygeneration and washing pretreatment under different severities: Water, dilute acid solution and aqueous phase bio-oil. *Bioresour. Technol.* **2019**, *278*, 26–33. [CrossRef] [PubMed]
22. Jand, N.; Foscolo, P.U. Decomposition of wood particles in fluidized beds. *Ind. Eng. Chem. Res.* **2005**, *44*, 5079–5089. [CrossRef]
23. Malsegna, B.; Di Giuliano, A.; Gallucci, K. Experimental study of absorbent hygiene product devolatilization in a bubbling fluidized bed. *Energies* **2021**, *14*, 2399. [CrossRef]
24. Shadle, L. F luidized B ed C hemical L ooping. Available online: https://clara-h2020.eu/deliverables/ (accessed on 26 May 2021).
25. Unidad de Pretratamiento—Cener BIO2C. Available online: https://www.bio2c.es/es/unidad-de-pretratamiento/ (accessed on 11 May 2021).
26. Gibilaro, L.G. *Fluidization-Dynamics*; Butterworth-Heinemann: Oxford, UK; Woburn, MA, USA, 2001.
27. Yang, W.-C. *Handbook of Fluidization and Fluid-Particle Systems*; Marcel Dekker: New York, NY, USA, 2003; ISBN 082470259X.
28. Grace, J.R. Fluidized bed hydrodynamics. In *Handbook of Multiphase Systems*; Hemisphere Publishing Corp.: London, UK, 1982; pp. 6–8.
29. Werther, J.; Ogada, T.; Borodulya, V.A.; Dikalenko, V.I. Devolatilisation and combustion characteristics of sewage sludge in a bubbling fluidized bed furnace. In *The Institute of Energy's Second International Conference on Combustion & Emissions Control*; Elsevier: Amsterdam, The Netherlands, 1995; pp. 149–158.
30. Zeng, X.; Wang, Y.; Yu, J.; Wu, S.; Zhong, M.; Xu, S.; Xu, G. Coal pyrolysis in a fluidized bed for adapting to a two-stage gasification process. *Energy Fuels* **2011**, *25*, 1092–1098. [CrossRef]
31. Condori, O.; García-Labiano, F.; de Diego, L.F.; Izquierdo, M.T.; Abad, A.; Adánez, J. Biomass chemical looping gasification for syngas production using ilmenite as oxygen carrier in a 1.5 kWth unit. *Chem. Eng. J.* **2021**, *405*, 126679. [CrossRef]
32. Wang, S.; Song, T.; Yin, S.; Hartge, E.U.; Dymala, T.; Shen, L.; Heinrich, S.; Werther, J. Syngas, tar and char behavior in chemical looping gasification of sawdust pellet in fluidized bed. *Fuel* **2020**, *270*, 117464. [CrossRef]
33. Fan, Y.; Tippayawong, N.; Wei, G.; Huang, Z.; Zhao, K.; Jiang, L.; Zheng, A.; Zhao, Z.; Li, H. Minimizing tar formation whilst enhancing syngas production by integrating biomass torrefaction pretreatment with chemical looping gasification. *Appl. Energy* **2020**, *260*, 114315. [CrossRef]
34. Niu, Y.; Lv, Y.; Lei, Y.; Liu, S.; Liang, Y.; Wang, D.; Hui, S. Biomass torrefaction: Properties, applications, challenges, and economy. *Renew. Sustain. Energy Rev.* **2019**, *115*, 109395. [CrossRef]
35. Medic, D.; Darr, M.; Shah, A.; Potter, B.; Zimmerman, J. Effects of torrefaction process parameters on biomass feedstock upgrading. *Fuel* **2012**, *91*, 147–154. [CrossRef]
36. Zhang, R.; Zhang, J.; Guo, W.; Wu, Z.; Wang, Z.; Yang, B. Effect of torrefaction pretreatment on biomass chemical looping gasification (BCLG) characteristics: Gaseous products distribution and kinetic analysis. *Energy Convers. Manag.* **2021**. [CrossRef]
37. Chen, D.; Mei, J.; Li, H.; Li, Y.; Lu, M.; Ma, T.; Ma, Z. Combined pretreatment with torrefaction and washing using torrefaction liquid products to yield upgraded biomass and pyrolysis products. *Bioresour. Technol.* **2017**, *228*, 62–68. [CrossRef] [PubMed]
38. Chen, Q.; Zhou, J.; Liu, B.; Mei, Q.; Luo, Z. Influence of torrefaction pretreatment on biomass gasification technology. *Chin. Sci. Bull.* **2011**, *56*, 1449–1456. [CrossRef]

applied sciences

MDPI

Review

Design and Implementation of the Solar Field and Thermal Storage System Controllers for a Parabolic Trough Solar Power Plant

Wisam Abed Kattea Al-Maliki [1,2], Nabeel Sameer Mahmoud [2], Hussein M. H. Al-Khafaji [2], Falah Alobaid [1,*] and Bernd Epple [1]

[1] Institut Energiesysteme und Energietechnik, TU Darmstadt, Otto-Berndt-Straße 2, 64287 Darmstadt, Germany; wisam.a.kattea@uotechnology.edu.iq (W.A.K.A.-M.); bernd.epple@est.tu-darmstadt.de (B.E.)

[2] Mechanical Engineering Department, University of Technology, 10066 Baghdad, Iraq; nabeel.s.mahmoud@uotechnology.edu.iq (N.S.M.); Hussein.m.hussein@uotechnology.edu.iq (H.M.H.A.-K.)

* Correspondence: falah.alobaid@est.tu-darmstadt.de; Tel.: +49-6151/1623004; Fax: +49-6151/16-6690

Abstract: Dynamic simulation provides an efficient approach for improving the efficiency of parabolic trough power plants and control circuits. In the dynamic simulation, the possibilities and operating conditions of the plant are evaluated regarding materials, processes, emissions, or economics. Several studies related to the dynamic simulation of the parabolic trough technology are summarised and discussed in this work. This study is the first research that presents a thorough description of the advanced control circuits used in the solar field and thermal storage system of a parabolic trough power plant. This power plant was implemented using advanced process simulation software (APROS). The dynamic model was built based on the real specifications of the power plant.

Keywords: dynamic simulation; parabolic trough power plant; control circuit; solar field; thermal storage system

Citation: Al-Maliki, W.A.K.; Mahmoud, N.S.; Al-Khafaji, H.M.H.; Alobaid, F.; Epple, B. Design and Implementation of the Solar Field and Thermal Storage System Controllers for a Parabolic Trough Solar Power Plant. *Appl. Sci.* **2021**, *11*, 6155. https://doi.org/10.3390/app11136155

Academic Editor: Joachim Müller

Received: 3 June 2021
Accepted: 29 June 2021
Published: 2 July 2021

1. Introduction

Solar energy is one of the best renewable energy sources to meet the energy demand in countries with high solar irradiation. Generally, solar energy is a permanent source of energy, and is locally available. There are two main technologies used in solar power plants—namely, photovoltaic technology, and concentrated solar power (CSP) technology. In general, only direct radiation is used in these systems, while the diffuse part of sunlight cannot be concentrated. Direct normal irradiation (DNI) is reflected by means of mirrors and concentrated on the absorbent surface, leading to a rise in the temperature of the absorbent surface [1,2]. This concentrated solar radiation is then transformed into thermal energy to heat a certain fluid, which can be used directly to generate renewable heat, or can be used for producing electricity. In the case of electricity production, the heated fluid will run a turbine (usually a steam turbine). Thereafter, the mechanical power resulting from the steam turbine will be transformed into electricity by the electrical power generator [3–5]. Today, CSP technology can be divided into four types—namely, linear Fresnel reflector, central tower, parabolic trough, and parabolic dish technology. Among the CSP technologies, parabolic trough technology is the most mature, as has been commercially proven [6–8].

The general design of parabolic trough power plants is principally concentrated on the high performance of the process, while the market requirements increasingly aim to improve the operating flexibility due to the current international trends in renewable energies. A dynamic simulation is a useful tool for enhancing the operation of parabolic trough power plants at different operating periods subject to the vagaries of weather, which in turn leads to load fluctuations and several start-up processes. Certain applications can

be implemented based on the dynamic simulation, such as the optimisation of control circuits, and stress evaluation for critical components.

In the literature review, there are several steady-state models concerning the parabolic trough power plant, while dynamic models are rarely implemented. Among the few dynamic models in the literature, there is no updated work that discusses in detail the description of the advanced controllers used in the solar field (SF) and thermal storage system (TSS) of a parabolic trough power plant.

Feldhoff et al. [9] indicated that the simplified solar field design and a competitive thermal storage system are required in order to make better use of the economic potential of direct steam generation (DSG). Several works have been presented with regards to feasibility of integrating various thermal storage options with parabolic trough (PT) or linear Fresnel reflector (LFR) solar fields using DSG technology. Valenzuela et al. [3] implemented and developed the control strategies for generating steam directly under high pressures and temperatures using parabolic trough solar collectors. The controllability of the power plant was achieved using a PI control scheme during clear days, and even with the transient periods of the solar radiation. Classical controllers were implemented due to the knowledge of power plant operators using PI controllers. Hakkarainen et al. [10] implemented two different DSG solar fields using advanced process simulation software. These models are used to simulate and to optimise thermal energy storage operations. Regarding the solar fields for both technologies (PT and LFR), only the configuration of the solar collector modules was described. Further simulation results for the stable operations and storage requirements in different cases were discussed. Mosleh et al. [11] examined and compared a dynamic simulation with several phase change materials (PCMs) using the TRNSYS program. They have demonstrated that materials whose melting point temperature is close to the superheated steam temperature are suitable for a thermal potential energy storage system. The solar fraction of sodium nitrate is the best choice among other materials. Liu et al. [12] developed model predictive control for a parabolic trough and solar tower combined with the coal-fired power plant using Ebsilon Professional software. Predictive solar radiation data were applied during the period of real electricity generation for 10 consecutive days. The study showed that the average coal consumption decreased by 20% due to the storage system control strategy, which relies on transferring more stored energy to the working cycle. Frejo et al. [13] suggested a new central model for a control algorithm to optimise the thermal energy collected by solar parabolic troughs. The best operation strategy of the power plant was conducted by regulating the valves located at the inlet of each loop, which provided a response superior to those obtained with normal control processes for parabolic trough solar plants. The simulation of the model was performed for two hours for the solar field ACUREX in Spain. This approach significantly increased the produced thermal energy. The proposed model controller, unfortunately, cannot be used realistically for medium and large power plants, due to its computational complexity. The researchers did not take into consideration various possible storage options and their feasibility for these solar fields.

The objectives of this review are explained as follows: First, to review the works that deal with the explanation of the control circuits of the SF and TSS of parabolic trough power plants. To the best of our knowledge, few works in the literature have been studied as important controllers of the SF and TSS in parabolic trough solar power plants. Second, all control circuits of the SF and TSS are described here in detail, based on real data obtained from the Andasol II plant. Third, this is the first study that describes in detail the control circuits of the SF and TSS using APROS software. Finally, the main objective of this research is to provide a useful reference tool for researchers regarding advanced control circuits for parabolic trough power plants.

2. Mathematical Background

There are several simulation programmes that can be used in the implementation and optimisation of control circuits in the dynamic simulation. These programs are improved

by universities or companies, and they are normally not openly available. However, they are applied in scientific research and industrial applications. The cited references of this research are non-exhaustive, and limited to widely known codes that are applied in scientific research and industrial applications. The cited references of this research are in agreement with the related simulation software, such as advanced process simulation software (APROS) [10,14–18], ASPEN Plus DYNAMICS, ASPEN HYSYS [19,20], DYMOLA (based on Modelica language) [21–32], MATHEMATICA [33], SIMULINK [26], RELAP [34], and TRNSYS [35,36].

The Andasol II model is carried out using commercial APROS software developed by VTT Finland [37]. APROS includes many components and solution techniques for a full-scale dynamic simulation of thermal power plants. In addition, it consists of two flow models—namely, a mixture flow model, and a two-fluid flow model. In addition, its ability to accurately follow the changes of load in power plants during their operation was proven in several previous studies. For this reason, this software is used in this study.

The control circuits of SF and TSS for the parabolic trough power plant "Andasol II" are described at a high level of detail. All control circuits used in both parts (SF and TSS) are modelled using APROS software. Figure 1 illustrates the typical setup of a parabolic trough power plant. The APROS model is divided into several nets in order to provide high flexibility and accuracy.

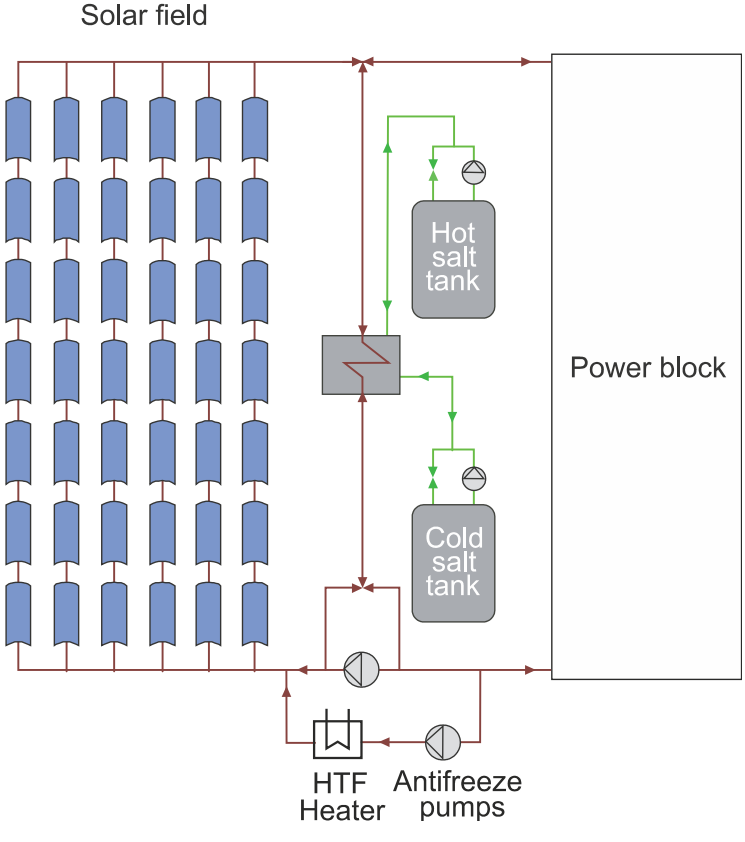

Figure 1. Parabolic trough power plant with thermal storage system.

3. Solar Field Model

The solar field includes four sections. The four sections are evenly distributed across two sectors, which are the south and north sectors. Each sector contains 78 mirror loops. Four main pumps pump the heat transfer fluid (HTF). These are placed between the inlet of the solar field and the outlet of the HP economiser. Then, the heat transfer fluid (HTF) is divided from the main cold line pipes to the south and the north sectors, distributing through 156 loops. The HTF absorbs the solar radiation through the collector loops. The HTF in the north and the south collector loops will meet before the solar field outlet. Two paths of the hot thermal oil are opened at the outlet of the SF. In the first path, the thermal oil is transferred from the SF to the PB. In the second path, the surplus of absorbed heat is transmitted by the thermal oil to the thermal storage system.

The real DNI leaves the control circuit of the DNI and enters the boundary condition transfer modules in the four sections of the solar field. After subtracting the heat losses, the useful thermal power is applied to the HTF (Therminol VP-1), which passes through the heat structure pipes. Firstly, the thermal oil mass flow is raised up to 390 kg/s, and remains unaltered until achieving the designated inlet temperature (295 °C). Hereby, each section in the solar field collects a certain amount of thermal power. After achieving the design inlet temperature, the thermal oil's temperature and mass flow increase gradually in order to achieve the maximum mass flow rate (1170 kg/s) at the design outlet temperature (393 °C). It should be mentioned here that the pressure losses for all of the components of the power plant were previously included in the APROS model. Furthermore, APROS software provides the possibility of defining the type of material depending on some major properties (e.g., the specific heat, the conductivity, and the density). The type of material for each layer was selected to determine the properties of the material and select the thickness of the wall, as well as select the type of fluid inside the pipes. The absorber tubes in the solar field were divided into three layers; each layer represents the type of the material (i.e., stainless steel layer, vacuum layer, and borosilicate glass layer). The insulated pipes were divided into two layers (i.e., steel layer and insulated layer).

3.1. Solar Field Control Structures

In order to control the temperature and thermal oil mass flow in the SF during the dynamic simulation, it is essential to implement control circuits that keep the nominal conditions of thermal power transferred to the power block. Hence, several controllers were modelled in the SF circuit to obtain reasonable responses during the fluctuations in the operating conditions.

3.1.1. DNI Control Circuit

The DNI controller adjusts the amount of solar irradiation collected by the absorber tubes and then transferred to the thermal oil. The useful heat is absorbed using 312 collector rows, as illustrated in Figure 2. After achieving the design mass flow of 1170 kg/s in the SF, the DNI decreases gradually in one collector to maintain the outlet temperature at 393 °C. If the solar irradiance continues to increase, one collector is automatically turned off (i.e., DNI = 0 W/m^2). This process is implemented by the selector, which sends the signal (activated or deactivated) to the actuator. The signal of a selector is limited based on two boundary conditions—the design temperature of the HTF (393 °C) at the SF outlet, and the maximum value of the mass flow (1170 kg/s). After achieving these conditions, the signal passed into the actuator is changed by the selector from an activated to a deactivated signal, as displayed in Figure 2. Hence, the useful heat collected through this collector will not transfer to the HTF in the absorber tubes. Subsequently, the DNI in the second collector begins reducing gradually until the second collector is inactivated. A fully loaded hot storage tank is achieved with a molten salt level of 14 m; this means that the total mass flow of the thermal oil must be reduced by further deactivating the boundary condition modules (BCs), alternately.

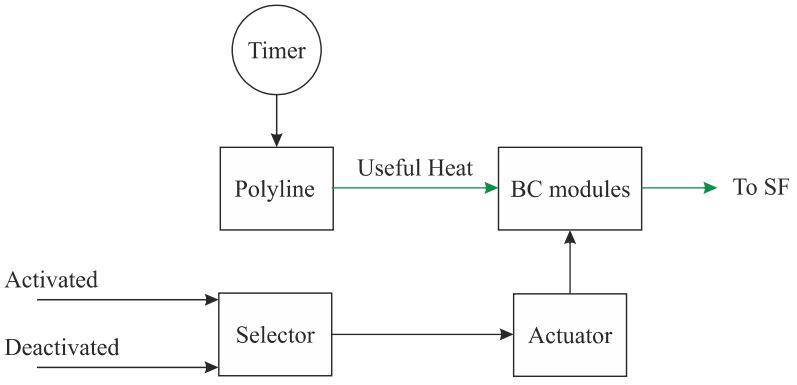

Figure 2. DNI control circuit (Simplified).

3.1.2. HTF Main Control Valve at the Inlet of the SF (HTF MCV)

The HTF temperature at the outlet of the SF is regulated using HTF MCV at the inlet of the SF. This control process is performed by regulating the thermal oil mass flow passing through the SF. Two processes are achieved via this control valve: firstly, after sunrise the thermal oil mass flow in the SF is regulated at a constant value of 2.5 kg/s per loop. The thermal oil flow is kept constant at this value until achieving the design temperature of the HTF (295 °C) at the inlet of the SF. Secondly, the thermal oil temperature at the outlet of the SF continues to rise until it reaches its nominal value of (393 °C). Thereafter, this design outlet temperature of the HTF is kept, using this controller (HTF MCV), by increasing or reducing the thermal oil mass flow passing through the solar field. It is worth mentioning that there is a control valve before the inlet of each loop; these valves are controlled by the same procedure that applies to the HTF MCV. The advantage of using these valves is to maintain the design temperature of thermal oil (393 °C) at the loop outlet, when some clouds prevent the solar radiation from falling on a certain loop. Unfortunately, in this study, the location of loops adversely affected by the existing clouds was not available from the supplier. Therefore, the decrease in the heat collected within the solar field was evenly distributed among all loops. It should be mentioned here that each selector includes two functions. These functions are chosen based on one, two, or more boundary conditions for these selectors. The HTF MCV is modelled with four selectors, as demonstrated in Figures 3 and 4. The boundary condition of selector 1 is when the DNI has reached a value more than 25 W/m^2, when selector 1 will change its function from a certain orifice (which keeps the thermal oil mass flow at 156 kg/s) to the second function (increase HTF mass flow from 156 kg/s to 390 kg/s). The boundary condition of selector 2 is when the thermal oil temperature reaches the design inlet value of 295 °C. After achieving this condition, selector 2 will choose the second function, which regulates the thermal oil mass flow rate to reach the design temperature of the thermal oil at the outlet of the SF (393 °C). Selector 3 consists of two functions; the first function is applied during normal cases (clear periods), and the second function is activated during the cloudy periods. The second function of selector 3 is enabled when two boundary conditions are achieved: the first condition is that the thermal oil mass flow continues decreasing down to a minimum condition value of 312 kg/s, and the second condition is that the HTF temperature decreases to below 393 °C. After achieving both conditions, the thermal oil mass flow is still unaltered at a minimum value of 312 kg/s, despite the decline in the design outlet temperature of the HTF. Two functions are passed through selector 4, the first of which comes from selector 3. When two boundary conditions are achieved (312 kg/s and 377 °C), the second function starts maintaining the thermal oil temperature of 377 °C at the outlet of the SF by closing the HTF MCV gradually until it is totally closed.

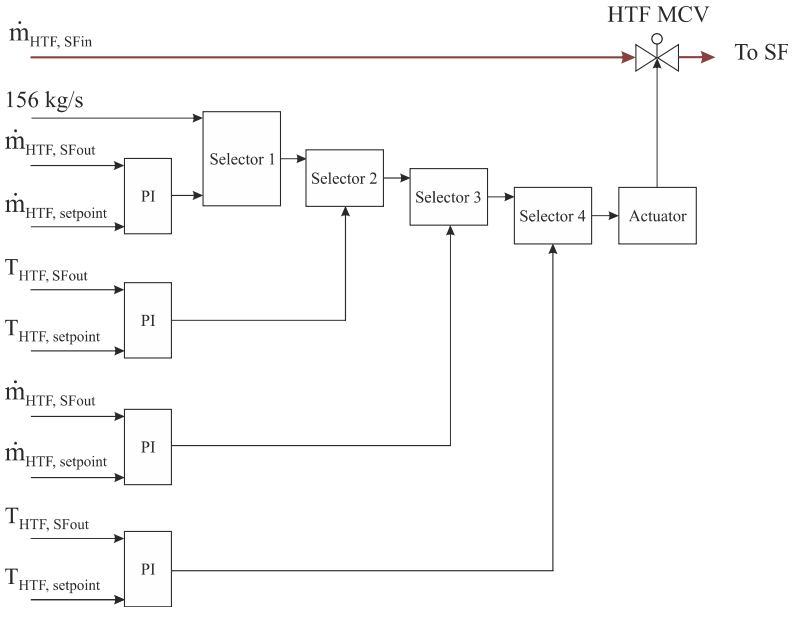

Figure 3. HTF main control valve at the inlet of the SF (simplified).

3.1.3. HTF Control Valve at the Outlet of the SF (to Power Block)

The HTF control valve at the outlet of the SF (or to the power block (PB CV_{in})) adjusts the thermal oil mass flow that is transmitted to the power block (PB). PB CV_{in} is opened when the HTF temperature reaches the design temperature value of 295 °C at the inlet of the SF. Then, it continues opening in order to achieve the nominal value of thermal oil mass flow (600 kg/s), with a temperature of 393 °C. This process is achieved by comparing the thermal oil mass flow rate at the SF outlet with a setpoint of 600 kg/s through PI controller, as shown in Figure 5.

3.1.4. Control Valve of the Thermal Storage System (SF–TS CV)

SF–TS CV is installed between the SF outlet and the TSS inlet; it controls the excess flow of thermal oil into the TSS, as demonstrated in Figure 6. The operational procedures of this control circuit are implemented based on two cases: In the first case, the valve begins to open when the thermal oil mass flow at the SF outlet exceeds the nominal value of 600 kg/s with a temperature of 393 °C. In the second case, the SF–TS CV starts closing when the solar irradiance is low and the thermal oil mass flow is less than the nominal value (600 kg/s).

3.1.5. HTF Redirection Control Valve (RDCV)

In the evening period, the PB is operated based on the TSS. Therefore, the HTF path should be changed to the TSS instead of the solar field. This process is achieved via HTF redirection control valve (RDCV), as illustrated in Figure 7. This control circuit includes one selector, and operates with two functions: The first function is that the RDCV remains closed when solar radiation is available. The second function is that the RDCV is gradually opened in order to redirect the HTF to the TSS, and then transfers the thermal power to the power block. Therefore, the selector will change from the first function to the second function after achieving two boundary conditions: the first condition is that the thermal oil mass flow at the outlet of the SF should be less than the design value of 600 kg/s. The

second condition is that the level of the hot tank must be more than a minimum value of 0.6 m.

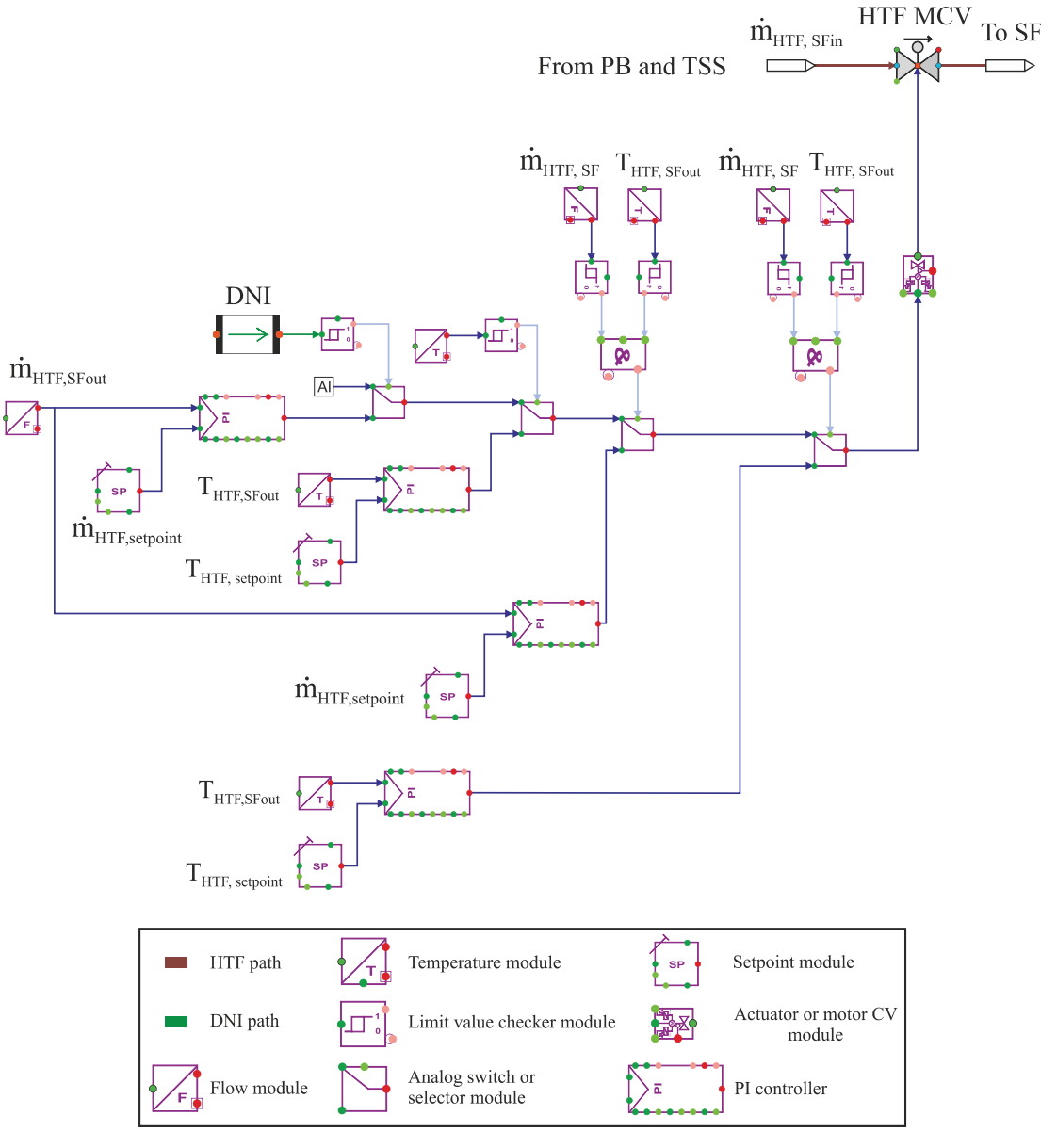

Figure 4. HTF main control valve at the inlet of the SF (APROS model).

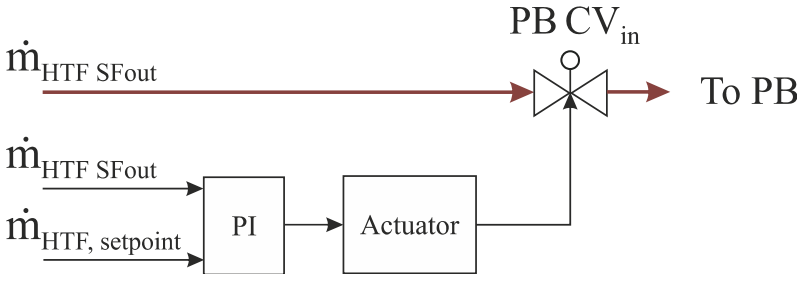

Figure 5. HTF control valve at the outlet of the SF (simplified).

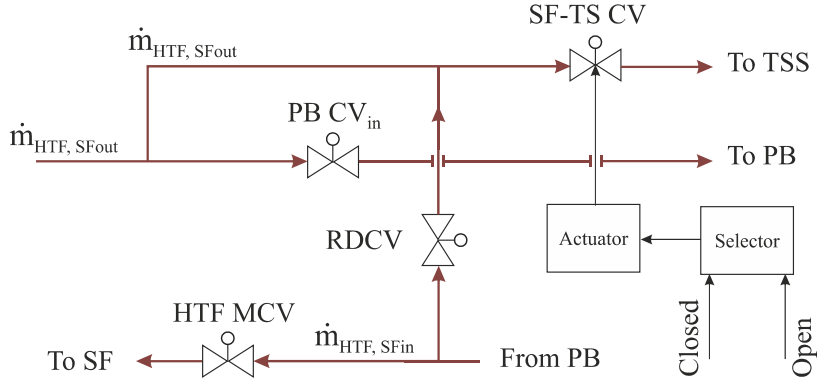

Figure 6. HTF control valve between the SF outlet and the TS inlet (simplified).

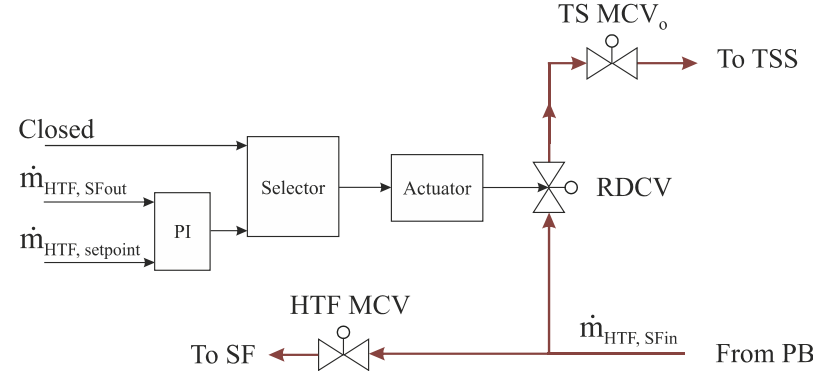

Figure 7. HTF redirection control valve (simplified).

3.1.6. HTF Recirculation Control Valve (RCV)

The HTF recirculation valve (RCV) is installed between the hot header and the cold header in the solar field, as shown in Figure 8. There are two functions in this control circuit: The first is that the RCV remains closed as long as there is stored energy. The second function is activated when the TSS is completely exhausted. Here, the RCV will be opened to regulate the thermal oil mass flow in the SF at a certain value of 156 kg/s, and continues until the sunrise of the second day.

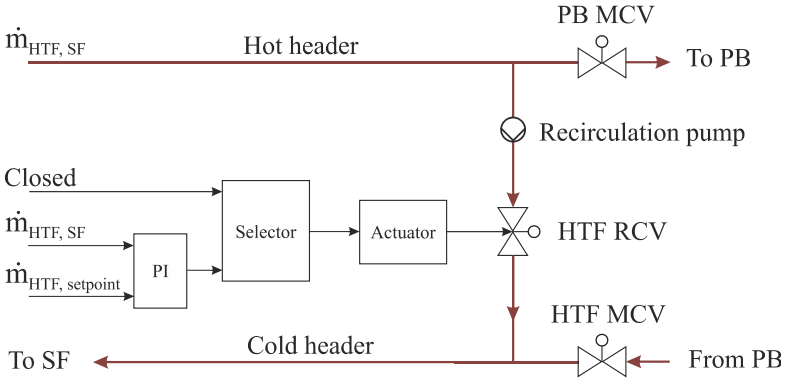

Figure 8. HTF recirculation control valve (simplified).

3.1.7. HTF Protection System

To keep the thermal oil from freezing during the cold periods, a thermal oil protection system is applied in this work. The protection system prevents the thermal oil temperature in the SF from decreasing below a value of 70 °C, and from exceeding the maximum value of 110 °C in the next operation This temperature range is regulated by two protection control valves (PCV_1 and PCV_2), as shown in Figure 9. Accordingly, PCV_2 starts opening in order to pass HTF through the heaters when the thermal oil temperature at the inlet of the SF decreases below 70 °C. On the other hand, PCV_1 starts closing in order to maintain the thermal oil temperature at the SF inlet in the range of 70–110 °C.

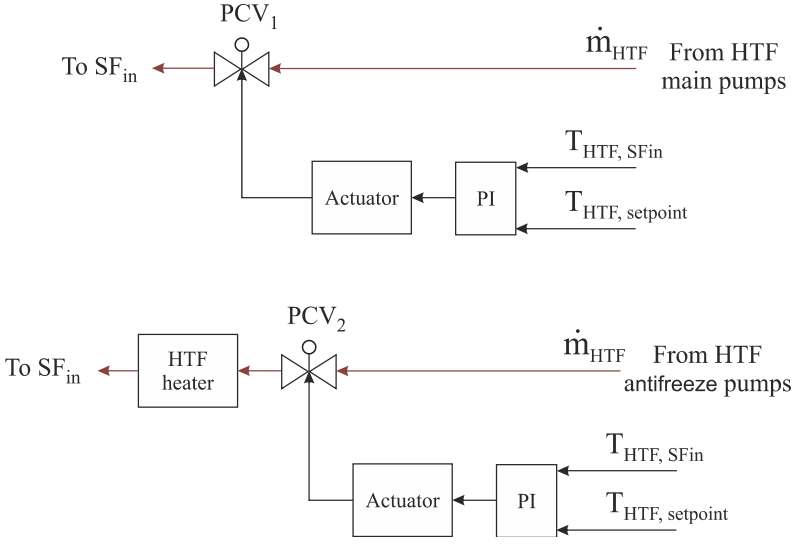

Figure 9. HTF protection control valve (simplified).

4. Thermal Storage Model

As solar irradiation depends on the daylight and the clarity of the sky, CSP plants are usually non-dispatchable. In order to make them highly dispatchable, a TSS can be added to the CSP plants. Although the solar power source is intermittent, continuous electrical power can be produced due to the use of the TSS. A two-operation mode efficiencies

(during charge and discharge modes) of more than 96 % was documented for TSS units consisting of hot and cold storage tanks of the molten salt [38].

The storage system studied in this work will be explained based on two operation modes, including all control circuits.

The excess solar irradiation is transferred to the TSS and provided as a substitute for the energy lost because of the clouds or during the night. This system allows for high operating flexibility, and produces more stable electricity. Hot and cold insulated tanks are connected by heat exchangers in APROS. The molten salt in both tanks is transferred to the heat exchangers by the series of thermal storage pumps that are located after the thermal storage tanks. The molten salt can be defined as a solution of potassium and sodium nitrates with known specifications.

In the charge mode, the thermal oil from the SF heats the molten salt that flows from the cold tank to the hot storage tank, with a temperature of approximately 386 °C. It should be mentioned here that there will be losses in the heat exchangers between the thermal oil and the molten salt. This means that the hot molten salt will reach a temperature below the maximum value of HTF temperature of 393 °C, whereas the hot molten salt will reach a temperature of 386 °C. Note that the capacity of this system can reach a maximum value of about 1025 MW_{th} h.

The thermal energy in the thermal storage system can be used in the discharge mode, where the hot molten salt heats the thermal oil through the heat exchangers. Here, the thermal storage system provides the nominal mass flow of the HTF (600 kg/s) with a temperature of 377 °C in the evening period. This will affect the steam production performance, whereas the nominal amount of generated steam (55 kg/s) in the daylight will not be accomplished during the evening period. However, the hot thermal oil is transmitted to the PB. After that, the thermal oil is returned to a cold tank with a temperature of about 292 °C.

4.1. Thermal Storage Control Structures

In order to regulate the thermal storage process during the dynamic simulation, it is necessary to implement control circuits that maintain the nominal temperature and mass flow rate conditions for the molten salt and the HTF. Hence, three control circuits are modelled in the thermal storage system, in order to obtain reasonable responses during the continuous changes in operating conditions.

4.1.1. Control Valve at the Thermal Storage System Inlet (TS MCVi)

The control valve at the thermal storage system inlet includes two tasks, depending on the operation mode of the thermal storage system, as shown in Figure 10. The first task is applied during charge mode, where this valve allows the surplus of thermal oil with a temperature of 393 °C to pass through it into the heat exchangers in order to transmit the thermal power from the HTF to the molten salt. Thereafter, the HTF leaves the TSS with a temperature of 293 °C through the control valve at the thermal storage system outlet (TS MCV_o). Subsequently, the HTF that exited the thermal storage system will be mixed with the HTF, which comes from the PB and enters the SF again. The second task is activated during the cloudy periods and the evening hours; in the compensation periods, the direction of the HTF flow will be reversed, where the HTF flows directly from the PB to the TSS through the redirection control valve (RDCV), and then through TS MCV_o. Therefore, TS MCV_o and TS MCV_i are considered to be the inlet and outlet of the TSS, respectively. Afterwards, the heated HTF flows to the PB to replenish the rest of the nominal mass flow (600 kg/s).

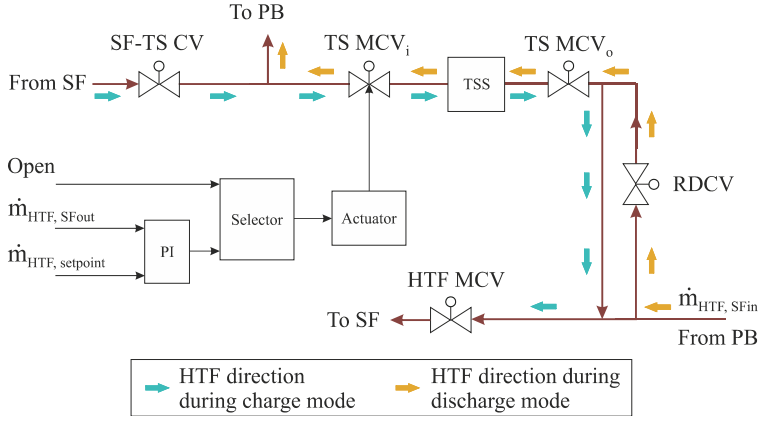

Figure 10. HTF control valve at the thermal storage inlet (simplified).

The HTF flow direction is reversed based on two conditions (T_{HTF} = 393 °C, and $\dot{m}$ = 600 kg/s) that are applied to the selector: Firstly, this control valve remains open when the HTF flow is directed from the SF to the TSS (SF–TS direction) during charge mode, as long as the design temperature of the thermal oil at the outlet of the SF and the nominal HTF mass flow are achieved. Secondly, when the one of the mentioned conditions (393 °C and 600 kg/s) is not accomplished, the discharge mode starts, and the HTF flow direction is changed from the SF–TS to the TS–PB direction.

4.1.2. Control Valve at the Thermal Storage System Outlet (TS MCV$_o$)

The control valve at the outlet of the TSS controls the process of thermal energy compensation. This controller has two functions, as illustrated in Figure 11. The first function is that TS MCV$_o$ remains open, like the TS MCV$_i$, during charge mode, where TS MCV$_i$ and TS MCV$_o$ are considered to be the inlet and outlet of the TSS, respectively. During discharge mode, the second task is enabled, and the thermal oil flow is directed from TS MCV$_o$ to TS MCV$_i$. TS MCV$_o$ regulates the mass flow of the thermal oil in order to maintain the nominal value of 600 kg/s at the PB inlet during the evenings and cloudy periods.

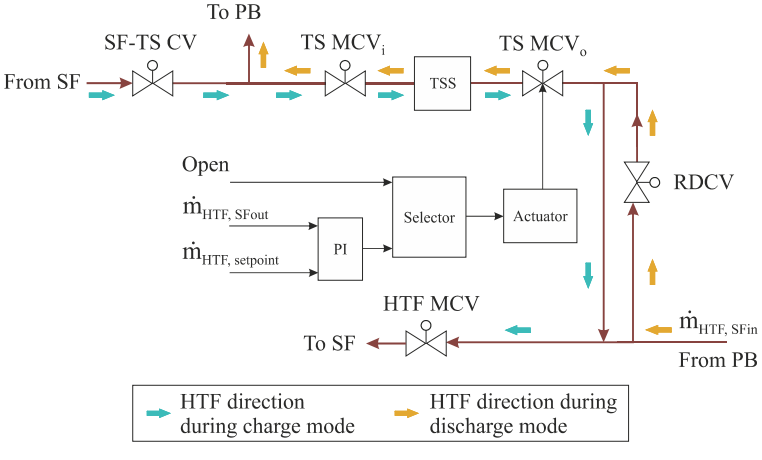

Figure 11. HTF control valve at the thermal storage outlet (simplified).

4.1.3. Hot Tank Control Valve (HTCV)

The hot tank control valve is located after the pumps of the hot tank in the thermal storage system. This control circuit includes two functions, as shown in Figure 12. The first function is that this valve remains closed during charge mode (the molten salt is transferred from the cold drum to the hot drum through the heat exchanger). The second task is enabled when the thermal oil temperature at the outlet of the solar field decreases below the design outlet temperature (393 °C or 377 °C, during the daylight or in the evening period, respectively). It should be mentioned here that the setpoint of the HTF temperature will be changed automatically from 393 °C to 377 °C based on the temperature value, which is regulated by the HTF MCV. However, the hot molten salt is sent to the heat exchangers through the HTCV, which in turn regulates the design HTF temperature at the inlet of the PB during the cloudy and night periods. Thereafter, the energy stored in the hot salt drum is transmitted into the HTF which, in turn, transfers this energy into the power block to produce the steam.

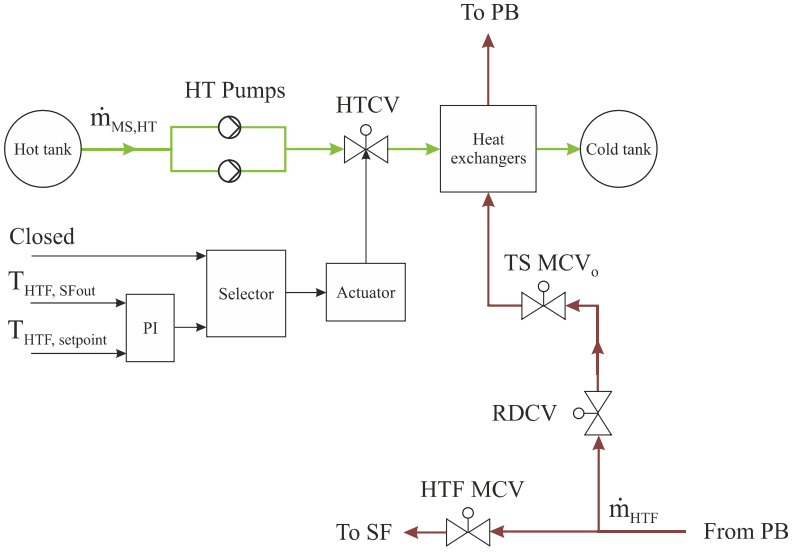

Figure 12. Hot tank control valve (during discharge mode) (simplified).

5. Conclusions

A large number of works can be found regarding parabolic trough power plants; however, few studies focus on the dynamic behaviour of the secondary systems—e.g., the TSS, taking into account stable electrical power and capacitance factor enhancement. A particular focus is placed on the modelling of the SF. Most works refer to the use of a simplified steady-state model instead of a comprehensive dynamic model of these power plants. In order to understand the dynamic behaviour of the secondary systems (SF, TSS, and PB) with high accuracy, more consideration should be devoted to the thorough modelling of the power plants.

In this study, detailed solar field and thermal storage system models for a parabolic trough power plant are implemented based on the specifications from data obtained from Andasol II, located in Spain. In this work, the components of these models have been accurately modelled using APROS software.

A detailed SF model was modelled with 156 collector loops, as well as implementing many control circuits to regulate the operation processes. Therminol VP-1 was used as an HTF in the SF. The reference solar field was designed to operate with maximum HTF mass

flow (1170 kg/s) at the design outlet temperature (393 °C). Hereby, the solar field operates with a total capacity of useful thermal energy of approximately 280 MW_{th}.

A comprehensive TSS was implemented using hot and cold insulated drums and, between them, heat exchangers. Moreover, the control circuits of this system are described. The thermal storage system was operated with two operation modes—namely, charge mode and discharge mode. During charge mode, the HTF from the solar field at a temperature of 393 °C heats the molten salt (sodium and potassium nitrates) that is pumped from the cold tank to the hot tank and stored with temperature of approximately 386 °C. This process continues until achieving a maximum capacity of stored energy of about 1025 MW_{th} h. This thermal storage provides high operational flexibility and stable electricity generation.

On the other mode, the hot salt heats the thermal oil via the heat exchangers. The molten salt exits the heat exchangers and is sent into the cold tank at a temperature of about 292 °C. Accordingly, the thermal storage system will provide the thermal power at the nominal load (125.75 MW_{th}) for a period of approximately 7.5 h in the evening period.

The purpose of this work was to provide reference models for the SF and TSS. This, in turn, will help researchers and designers to understand the advanced control circuits of these stations. In addition, these models can determine the best manner of power plant operation.

Future studies will be focused on a detailed description of the power block controllers.

Funding: This research received no external funding.

Informed Consent Statement: Not applicable.

Data Availability Statement: Not applicable.

Acknowledgments: We acknowledge support from the Deutsche Forschungsgemeinschaft (DFG —German Research Foundation) and the Open Access Publishing Fund of the Technical University of Darmstadt. The first author would like also to thank the University of Technology, Iraq.

Conflicts of Interest: All authors declare no conflict of interest.

Abbreviations

Abbreviations

AD	Adder
BC	Boundary condition
BFP	Boiler feedwater pump
CP	Condenser pump
HP	High pressure
HPRP	High-pressure recirculation pump
HTCV	Hot tank control valve
HTF	Heat transfer fluid
HTF MCV	Heat transfer fluid main control valve
LFR	Linear Fresnel reflector
MS	Molten salt
PB	Power block
PCV1	The first protection control valve
PCV2	The second protection control valve
PD	Parabolic dish
PI	Proportional–integral controller
PT	Parabolic trough
PB CV	Power block control valve
PB MCV	Power block main control valve
RCV	Recirculation control valve
RDCV	Redirection control valve
SF	Solar field

SF–TS CV	Solar field to thermal storage control valve
TSS	Thermal storage system
TS DCV_o	Thermal storage dual control valve at the outlet
TS MCVi	Thermal storage main control valve at the inlet
TS MCV_o	Thermal storage main control valve at the outlet

References

1. Philibert, C. *The Present and Future Use of Solar Thermal Energy as a Primary Source of Energy*; International Energy Agency: Paris, France, 2005.
2. Pérez-Higueras, P.; Rodrigo, P.; Fernández, E.F.; Almonacid, F.; Hontoria, L. A simplified method for estimating direct normal solar irradiation from global horizontal irradiation useful for CPV applications. *Renew. Sustain. Energy Rev.* **2012**, *16*, 5529–5534. [CrossRef]
3. Artola, V.; María, J. Performance of a 50 MW Concentrating Solar Power Plant. Mechanical Engineering Final Thesis, Politecnico Di Bari, Bari, Italy, 2010.
4. Kaygusuz, K. Prospect of concentrating solar power in Turkey: The sustainable future. *Renew. Sustain. Energy Rev.* **2011**, *15*, 808–814. [CrossRef]
5. Desai, N.B.; Bandyopadhyay, S. Optimization of concentrating solar thermal power plant based on parabolic trough collector. *J. Clean. Prod.* **2015**, *89*, 262–271. [CrossRef]
6. Bhutto, A.W.; Bazmi, A.A.; Zahedi, G.; Klemeš, J.J. A review of progress in renewable energy implementation in the Gulf Cooperation Council countries. *J. Clean. Prod.* **2014**, *71*, 168–180. [CrossRef]
7. Fernández-García, A.; Rojas, E.; Pérez, M.; Silva, R.; Hernández-Escobedo, Q.; Manzano-Agugliaro, F. A parabolic-trough collector for cleaner industrial process heat. *J. Clean. Prod.* **2015**, *89*, 272–285. [CrossRef]
8. Sharan, P.; Bandyopadhyay, S. Solar assisted multiple-effect evaporator. *J. Clean. Prod.* **2017**, *142*, 2340–2351. [CrossRef]
9. Feldhoff, J.F.; Schmitz, K.; Eck, M.; Schnatbaum-Laumann, L.; Laing, D.; Ortiz-Vives, F.; Schulte-Fischedick, J. Comparative system analysis of direct steam generation and synthetic oil parabolic trough power plants with integrated thermal storage. *Sol. Energy* **2012**, *86*, 520–530. [CrossRef]
10. Hakkarainen, E.; Kannari, L.; Tähtinen, M. Dynamic modelling of concentrated solar field for thermal energy storage integration. In Proceedings of the 9th International Renewable Energy Storage Conference (IRES 2015), Düsseldorf, Germany, 9–11 March 2015.
11. Mosleh, H.J.; Ahmadi, R. Linear parabolic trough solar power plant assisted with latent thermal energy storage system: A dynamic simulation. *Appl. Therm. Eng.* **2019**, *161*, 114204. [CrossRef]
12. Liu, H.; Zhai, R.; Patchigolla, K.; Turner, P.; Yang, Y. Model predictive control of a combined solar tower and parabolic trough aided coal-fired power plant. *Appl. Therm. Eng. Appl. Therm. Eng.* **2021**, *193*, 116998. [CrossRef]
13. Frejo, J.R.D.; Camacho, E.F. Centralized and distributed Model Predictive Control for the maximization of the thermal power of solar parabolic-trough plants. *Sol. Energy* **2020**, *204*, 190–199. [CrossRef]
14. Terdalkar, R.; Doupis, D.; Clark, M.; Joshi, A.; Wang, C. Transient simulation of high temperature high pressure solar tower receiver. *Energy Procedia* **2015**, *69*, 1451–1460. [CrossRef]
15. Henrion, T.; Ponweiser, K.; Band, D.; Telgen, T. Dynamic simulation of a solar power plant steam generation system. *Simul. Model. Pract. Theory* **2013**, *33*, 2–17. [CrossRef]
16. Hakkarainen, E.; Tähtinen, M.; Mikkonen, H. Dynamic Model Development of Linear Fresnel Solar Field. In Proceedings of the ASME 2015 9th International Conference on Energy Sustainability Collocated with the ASME 2015 Power Conference, the ASME 2015 13th International Conference on Fuel Cell Science, Engineering and Technology, and the ASME 2015 Nuclear Forum, San Diego, CA, USA, 28 June–2 July 2015.
17. Al-Maliki, W.A.K.; Alobaid, F.; Kez, V.; Epple, B. Modelling and dynamic simulation of a parabolic trough power plant. *J. Process Control* **2016**, *39*, 123–138. [CrossRef]
18. Al-Maliki, W.A.K.; Alobaid, F.; Starkloff, R.; Kez, V.; Epple, B. Investigation on the dynamic behaviour of a parabolic trough power plant during strongly cloudy days. *Appl. Therm. Eng.* **2016**, *99*, 114–132. [CrossRef]
19. Greenhut, A.D.; Tester, J.W.; DiPippo, R.; Field, R.; Love, C.; Nichols, K.; Augustine, C.; Batini, F.; Price, B.; Gigliucci, G.; et al. Solar–geothermal hybrid cycle analysis for low enthalpy solar and geothermal resources. In Proceedings of the World Geothermal Congress, Bali, Indonesia, 25–29 April 2010.
20. Zhou, C.; Doroodchi, E.; Moghtaderi, B. An in-depth assessment of hybrid solar–geothermal power generation. *Energy Convers. Manag.* **2013**, *74*, 88–101. [CrossRef]
21. Eck, M.; Hirsch, T. Dynamics and control of parabolic trough collector loops with direct steam generation. *Sol. Energy* **2007**, *81*, 268–279. [CrossRef]
22. Bonilla, J.; Yebra, L.J.; Dormido, S.; Zarza, E. Parabolic-trough solar thermal power plant simulation scheme, multi-objective genetic algorithm calibration and validation. *Sol. Energy* **2012**, *86*, 531–540. [CrossRef]
23. Twomey, B.; Jacobs, P.; Gurgenci, H. Dynamic performance estimation of small-scale solar cogeneration with an organic Rankine cycle using a scroll expander. *Appl. Therm. Eng.* **2013**, *51*, 1307–1316. [CrossRef]

24. Birnbaum, J.; Feldhoff, J.F.; Fichtner, M.; Hirsch, T.; Jöcker, M.; Pitz-Paal, R.; Zimmermann, G. Steam temperature stability in a direct steam generation solar power plant. *Sol. Energy* **2011**, *85*, 660–668. [CrossRef]
25. El Hefni, B.; Soler, R. Dynamic Multi-configuration Model of a 145 MWe Concentrated Solar Power Plant with the ThermoSysPro Library (Tower Receiver, Molten Salt Storage and Steam Generator). *Energy Procedia* **2015**, *69*, 1249–1258. [CrossRef]
26. Liu, S.; Faille, D.; Fouquet, M.; El-Hefni, B.; Wang, Y.; Zhang, J.; Wang, Z.; Chen, G.; Soler, R. Dynamic Simulation of a 1MWe CSP Tower Plant with Two-level Thermal Storage Implemented with Control System. *Energy Procedia* **2015**, *69*, 1335–1343. [CrossRef]
27. Mitterhofer, M.; Orosz, M. Dynamic Simulation and Optimization of an Experimental Micro-CSP Power Plant. In Proceedings of the ASME 2015 9th International Conference on Energy Sustainability collocated with the ASME 2015 Power Conference, the ASME 2015 13th International Conference on Fuel Cell Science, Engineering and Technology, and the ASME 2015 Nuclear Forum, San Diego, CA, USA, 28 June–2 July 2015; American Society of Mechanical Engineers: New York, NY, USA, 2015; p. V001T05A7-VT05A7.
28. El Hefni, B. Dynamic modeling of concentrated solar power plants with the ThermoSysPro library (Parabolic Trough collectors, Fresnel reflector and Solar-Hybrid). *Energy Procedia* **2014**, *49*, 1127–1137. [CrossRef]
29. Österholma, R.; Pålssonb, J. Dynamic modelling of a parabolic trough solar power plant. In Proceedings of the 10th International Modelica Conference, Lund, Sweden, 10–12 March 2014.
30. Rodat, S.; Souza, J.; Thebault, S.; Vuillerme, V.; Dupassieux, N. Dynamic simulations of Fresnel solar power plants. *Energy Procedia* **2014**, *49*, 1501–1510. [CrossRef]
31. Zhang, J.; Valle-Marcos, J.; El-Hefni, B.; Wang, Z.; Chen, G.; Ma, G.; Li, X.; Soler, R. Dynamic Simulation of a 1MWe Concentrated Solar Power Tower Plant System with Dymola®. *Energy Procedia* **2014**, *49*, 1592–1602. [CrossRef]
32. Mertens, N.; Alobaid, F.; Frigge, L.; Epple, B. Dynamic simulation of integrated rock-bed thermocline storage for concentrated solar power. *Sol. Energy* **2014**, *110*, 830–842. [CrossRef]
33. García, I.L.; Álvarez, J.L.; Blanco, D. Performance model for parabolic trough solar thermal power plants with thermal storage: Comparison to operating plant data. *Sol. Energy* **2011**, *85*, 2443–2460. [CrossRef]
34. Russo, V. CSP Plant Thermal-hydraulic Simulation. *Energy Procedia* **2014**, *49*, 1533–1542. [CrossRef]
35. Jones, S.A.; Blair, N.; Pitz-Paal, R.; Schwarzboezl, P.; Cable, R. TRNSYS modeling of the SEGS VI parabolic trough solar electric generating system. In *Proceedings of Solar Forum 2001: Solar Energy: The Power to Choose*; ASME: Washington, DC, USA, 2001.
36. Wahhab, H.A.A.; Al-Maliki, W.A.K. Application of a Solar Chimney Power Plant to Electrical Generation in Covered Agricultural Fields. In *IOP Conference Series: Materials Science and Engineering*; IOP Publishing: Bristol, UK, 2020; p. 012137.
37. VTT. APROS Advanced Process Simulation Software. Available online: https://www.vttresearch.com/en/ourservices/aprosr-dynamic-process-simulation-software (accessed on 30 June 2021).
38. Kuravi, S.; Trahan, J.; Goswami, D.Y.; Rahman, M.M.; Stefanakos, E.K. Thermal energy storage technologies and systems for concentrating solar power plants. *Prog. Energy Combust. Sci.* **2013**, *39*, 285–319. [CrossRef]

applied sciences

MDPI

Review

Biomass-Based Chemical Looping Gasification: Overview and Recent Developments

Nhut Minh Nguyen [1,2,*], Falah Alobaid [1], Paul Dieringer [1] and Bernd Epple [1]

[1] Institute for Energy Systems and Technology, Technische Universität Darmstadt, Otto-Berndt-Straße 2, 64287 Darmstadt, Germany; falah.alobaid@est.tu-darmstadt.de (F.A.); paul.dieringer@est.tu-darmstadt.de (P.D.); bernd.epple@est.tu-darmstadt.de (B.E.)
[2] Department of Chemical Engineering, Can Tho University, 3/2 Street, Can Tho 90000, Vietnam
* Correspondence: nhut.nguyen@est.tu-darmstadt.de

Abstract: Biomass has emerged as one of the most promising renewable energy sources that can replace fossil fuels. Many researchers have carried out intensive research work on biomass gasification to evaluate its performance and feasibility to produce high-quality syngas. However, the process remains the problem of tar formation and low efficiency. Recently, novel approaches were developed for biomass utilization. Chemical looping gasification is considered a suitable pathway to produce valuable products from biomass among biomass conversion processes. This review paper provides a significant body of knowledge on the recent developments of the biomass-based chemical looping gasification process. The effects of process parameters have been discussed to provide important insights into the development of novel technology based on chemical looping. The state-of-the-art experimental and simulation/modeling studies and their fundamental assumptions are described in detail. In conclusion, the review paper highlights current research trends, identifying research gaps and opportunities for future applications of biomass-based chemical looping gasification process. The study aims to assist in understanding biomass-based chemical looping gasification and its development through recent research.

Keywords: biomass; gasification; chemical looping gasification; carbon dioxide capture; oxygen carriers; syngas

Citation: Nguyen, N.M.; Alobaid, F.; Dieringer, P.; Epple, B. Biomass-Based Chemical Looping Gasification: Overview and Recent Developments. *Appl. Sci.* **2021**, *11*, 7069. https://doi.org/10.3390/app11157069

Academic Editor: Borja Velazquez-Marti

Received: 22 June 2021
Accepted: 21 July 2021
Published: 30 July 2021

1. Introduction

The combustion of fossil fuels (coal, petroleum, and natural gas) contributes the largest share of greenhouse gas (GHG) emissions and currently, the mitigation of these emissions is one of the most challenging global issues. The Paris Agreement aims to limit the temperature increase to 1.5 °C above pre-industrial levels [1]. According to international energy outlook 2016 (IEO 2016), the total world energy consumption will predictably increase by 48% from 2012 to 2040 due to growth in non-OECD Asia (including China, India, Southeast Asia), the Middle East, parts of Africa, and America [2]. According to the IEO 2016 reference case, fossil fuels will present the greatest energy source in the world in 2040, accounting for 78% of total world energy consumption [2]. Although coal is the slowest-growing energy source with 0.6% annual growth, it still accounts for a large proportion of world energy consumption. This is due to the fact that coal is abundant and less expensive than natural gas or oil. However, the utilization of coal is related to the challenge of increasing the efficiency of thermal power plants and reducing emissions such as carbon dioxide that is the primary greenhouse gas and its increase in the atmosphere mainly causes global warming. Germany has set a key goal to achieve at least a 40% cut in GHG emissions by 2020 and 80–95% by 2050 compared to its 1990 levels [3]. To reach this target, the increased use of renewable energy will play a key role. By 2050, power generation in Germany must be almost entirely based on renewable energy sources. The

European Union (EU) has planned to achieve a 20% share of renewable energy in total energy consumption across its members by 2020 [4].

Biomass has been considered one of the most important primary and renewable energy resources for a renewable and sustainable energy future due to its carbon-neutral renewable and abundant quantity, which can give more carbon credit for conversion technologies and consequently economic advantages. Additionally, biomass has higher reactivity and higher volatile content, which can promote its conversion reactions. Its low content of sulfur and mercury leads to lower SO_x emissions and pollutants. Other benefits of biomass are low ash content, thereby reducing solid residue, handling, and processing costs overall [5]. Combined with the carbon capture and storage processes, the overall system could achieve carbon negative emissions [6,7].

Biomass conversion pathways can typically be classified as biochemical and thermochemical processes. The biochemical conversion pathway consists of two main processes used, namely fermentation and anaerobic digestion [8]. Fermentation, a metabolic process, converts solid fuels into biofuels or chemicals through the action of enzymes, while anaerobic digestion is a conversion of organic material into biogas in the absence of oxygen. The biochemical processes have main disadvantages such as low energy efficiency, high water requirement, long conversion times, and stringent feedstock requirements [9]. The thermochemical conversion processes mainly include combustion, gasification, and pyrolysis. Biomass thermochemical conversion processes are characterized by low efficiency mainly due to biomass properties such as high moisture content and relatively low energy density. Biomass gasification, a thermochemical conversion approach, is to convert efficiently the solid fuels into a combustible gas mixture, mainly CO and H_2, which can be used as a feedstock in the production of chemicals or power generation. However, the drawback of conventional gasification technology is a demand for a large amount of heat supply for the production of high-quality syngas, making the process less attractive. Therefore, a new technology is required to be more economically feasible to produce enriched hydrogen syngas from biomass.

Ishida et al. [10] firstly proposed the term "chemical looping" for the process, where a metal oxide is used as an oxygen transport medium to perform a redox reaction scheme for an increase of exergy efficiency in power generation. In the chemical looping concept, oxygen carriers (e.g., Me_xO_{y-1}/Me_xO_y) [5–7] are applied for oxygen transport, avoiding direct contact between fuels and air. Chemical looping processes can be used for power generation, production of syngas, chemicals, and liquid fuels through chemical looping combustion (CLC) [9,11,12], chemical looping reforming (CLR) [13,14], and chemical looping gasification (CLG) [9,15]. In the CLC process, metal/metal oxide as oxygen carrier circulates between two reactors to completely combust fuels (gaseous and solid fuels), while the CLR is a process for the partial oxidation of hydrocarbon fuels to produce hydrogen. The CLG shares similar principles with the CLC and CLR, but the CLG can produce useful combustible gas from gaseous and solid carbonaceous materials through the partial oxidation process.

The typical mechanism operation of CLG of the biomass process is illustrated in Figure 1. The configuration mainly consists of an air reactor (AR) and a fuel reactor (FR), where oxidation and reduction reactions take place, respectively.

In the FR, a metal oxide as an oxygen carrier (OC) is reduced to provide oxygen for fuel conversion. Then, the reduced metal oxide is circulated to the AR to be re-oxidized before a new cycle. The general chemical reactions in the FR and AR are shown as follows.

$$\text{Biomass} + Me_xO_y \rightarrow Me_xO_{y-1} + H_2 + CO + CO_2 + CH_4 \quad (1)$$

$$Me_xO_{y-1} + \frac{1}{2} O_2 \rightarrow Me_xO_y \quad (2)$$

where Me_xO_y is the oxidized and Me_xO_{y-1} represents the reduced form of oxygen carrier [16].

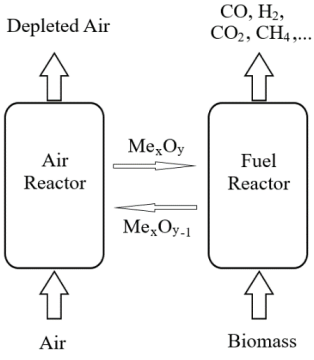

Figure 1. Schematic principles of Biomass chemical looping gasification process.

Biomass-derived chemical looping gasification is a novel technology to convert biomass into renewable hydrogen-enriched syngas. Since most reactions in the FR are endothermic, they require a large energy supply for stable operation. On the other hand, oxidation reactions in the AR are exothermic. Thus, the oxygen carrier, which can circulate between two reactors in the CLG process, can transfer not only oxygen but also heat from the AR to the FR through oxidation-reduction reactions [9,17,18]. Additionally, looping materials (metal oxides) can reduce considerably the amount of tar that causes serious problems in a biomass gasification system. Metal oxides act as an effective catalyst for tar cracking and reduction in tar formation during chemical looping gasification. Mendiara et al. [19] found that the tar content was reduced around 2.4% per degree Celsius with the presence of iron ore. The $NiFe_2O_4$ showed a dual-function of oxidation-catalyst for toluene reduction and significantly promotes toluene converted into carbon and H_2 [20]. Although biomass-based chemical looping gasification currently remains several challenges, the potential achievements may outweigh the challenges. Many studies have been carried out to investigate its nature and to solve operational challenges for the commercialization of this technology. The efforts focus on the development of biomass gasification processes for large-scale applications, improvement in reactivity and stability, as well as the multifunctional nature of looping materials, holistic evaluation for the economic feasibility of biomass-based chemical looping systems, and various types of biomass feedstock for chemical looping processes [9]. Therefore, biomass chemical looping technology has notable potentials to convert biomass-based materials into valuable products and effectively mitigate CO_2 emissions in the atmosphere.

Review papers that systematically analyzed scientific publications on certain topics are very valuable but are only rarely published. Although BCLG has been reviewed in previous works [9,14,15,18], the results and insights of recent studies of BCLG based on oxygen carriers have not been analyzed systematically. This work is to describe the novel gasification technology, which aims to elucidate the latest advances in chemical looping gasification. The objective of this work is to critically approach the research results on the chemical looping gasification technology of biomass and its progress through recent finding experimental and simulation/modeling studies to assist in the knowledge of the behavior and the potentials of using biomass in chemical looping gasification. The review paper is organized into six sections.

Section 2 is dedicated to the process configuration of BCLG, focusing on the key components of a CLG system such as system configurations, reactors. Furthermore, system complexity and its challenges are introduced in this section.

Section 3 presents an overview of looping materials in BCLG. In this section, fundamentals and developments of oxygen carriers used in BCLG are described according to recent studies.

Section 4 analyzes the influence of operating parameters on the performance of BCLG. This section may provide an understanding of the operation of BCLG under various conditions.

Section 5 summarizes the recent results and insights of BCLG through experimental and simulation works across the world. A large number of experimental studies have been developed to evaluate process performance in various operating conditions, system configurations, and types of oxygen carriers. These investigations can be categorized into kinetic studies and pilot-scale investigations. Additionally, simulation/modeling of the BCLG system is mainly developed for prediction, evaluation, and optimization. Their results can offer a good understanding of the feasibility of the commercialization of this process.

The paper closes with Section 6, highlighting the summary of this work and prospects of chemical looping gasification of biomass. Finally, the review paper concludes with concrete recommendations for this field of research.

2. Process of Chemical Looping Gasification of Biomass

Chemical looping gasification is a novel technology to convert biomass into gaseous products; it has been proven that its advantages, e.g., high-quality syngas production, lower CO_2 emissions. Furthermore, heat generated in the air reactor can be supplied to endothermic reactions in the fuel reactor through oxygen carriers, allowing for autothermal operation [17]. Additionally, the inorganic compounds in biomass ash can act as effective catalysts for gasification reactions [9], which is an important benefit for the chemical looping gasification of biomass.

2.1. Process Description

Chemical looping technology is designed to avoid direct contact between air and fuel by circulating metal/metal oxide acting as oxygen carrier between two reactors, i.e., air reactor (AR) and fuel reactor (FR). The metals/metal oxides work as oxygen carriers to transport oxygen from the air to the fuel via reduction-oxidation (redox) reactions. Biomass chemical looping gasification (BCLG) shares the principles with chemical looping technology. A simplistic mechanism of chemical looping gasification is illustrated in Figure 2. Biomass is partially oxidized in the FR by metal oxides (Me_xO_y) to produce a mixture of gases, mainly H_2, CO, and CO_2. Steam or CO_2 may be added to the FR to promote reforming reactions and char gasification reactions. A general description of the overall oxidation reaction in the FR is given in Reaction (4). In the AR, the reduced form of oxygen carriers (Me_xO_{y-1}) in the fuel reactor is oxidized by oxygen from the air as shown in Reaction (3). The key reactions in the fuel reactor are summarized in Table 1.

$$\text{Air reactor: } 2Me_xO_{y-1} + O_2 \rightarrow 2Me_xO_y \quad (3)$$

$$\text{Fuel reactor : Biomass} + Me_xO_y \xrightarrow{H_2O/CO_2} CO + H_2 + CO_2 + CH_4 + \text{tar} + Me_xO_{y-1} \quad (4)$$

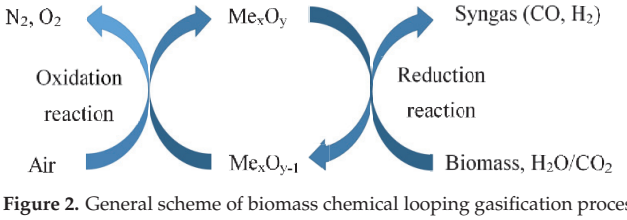

Figure 2. General scheme of biomass chemical looping gasification process.

Table 1. Chemical reactions in fuel reactor [19,21,22].

No.	Name of Reaction	Chemical Reaction
1	Boudouard reaction	$C + CO_2 \boxed{\leftrightarrow} 2CO$
2	Char reforming/water gas	$C + H_2O \boxed{\leftrightarrow} CO + H_2$
3	Methanation	$C + 2H_2 \boxed{\leftrightarrow} CH_4$
4	Water gas shift reaction	$CO + H_2O \boxed{\leftrightarrow} CO_2 + H_2$
5	Steam reforming of methane	$CH_4 + H_2O \boxed{\leftrightarrow} CO + 3H_2$
6	Dry reforming	$CH_4 + CO_2 \boxed{\leftrightarrow} 2CO + 2H_2$
7	Oxygen carrier reduction	$CO + Me_xO_y \rightarrow CO_2 + Me_xO_{y-1}$
8	Oxygen carrier reduction	$H_2 + Me_xO_y \rightarrow H_2O + Me_xO_{y-1}$
9	Oxygen carrier reduction	$CH_4 + Me_xO_y \rightarrow 2H_2 + CO + Me_xO_{y-1}$
10	Oxygen carrier reduction	$C + Me_xO_y \rightarrow CO + Me_xO_{y-1}$
11	Oxygen carrier reduction	$C + 2Me_xO_y \rightarrow CO_2 + 2Me_xO_{y-1}$
12	Tars' reforming	$Tars + H_2O \boxed{\leftrightarrow} CO + H_2 + CO_2 + hydrocabons + \ldots$
13	Hydrocarbon reforming	$Hydrocabons + H_2O \boxed{\leftrightarrow} CO + H_2 + CO2 + \ldots$

2.2. Process Classification

Sharing the basic principles with chemical looping technology, the BCLG process takes place based on many intrinsic components such as the fuel, gasifying agents, reactor configurations, and looping materials. These parameters can be grouped into three main categories as shown in Figure 3. In the following, each of these categories is elucidated in detail.

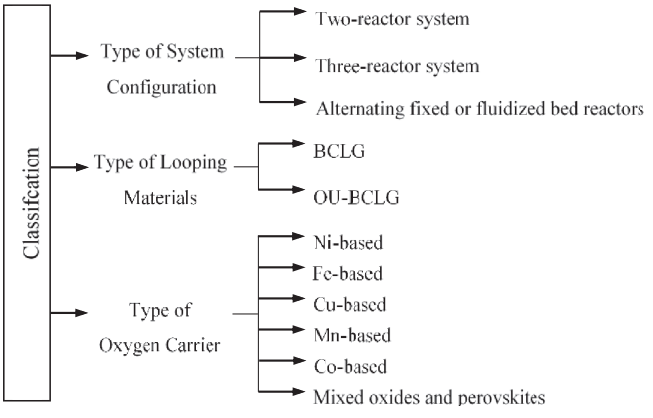

Figure 3. Classification of biomass chemical looping gasification process.

2.2.1. System Configuration

The biomass chemical looping gasification concept is to produce high-quality syngas for further applications. The contact between the fuel and the oxygen carrier plays a key role in the chemical looping system, especially BCLG. Hence, the selection of the reactor configuration is an important criterion for chemical looping processes. The essential requirements for selecting an appropriate BCLG with a continuous operation are as follows [12,17,23]:

(i) There should be sufficient particle circulation between the FR and the AR.
(ii) There should be sufficient contact between the fuel/air and the solid oxygen carriers to achieve maximum conversion.
(iii) High temperature and high-pressure operations must be carried out to achieve higher overall efficiency.
(iv) There should be limited gas leakage between the FR and the AR.

As a part of a chemical looping system, a reactor is a crucial factor that affects process performance. Two common types of reactors have been proposed for chemical looping

applications, namely fixed-bed and fluidized-bed reactors. Fixed-bed reactors are the simplest type of reactor in chemical looping processes ranging from laboratory-scale to pilot plant-scale and commercial-scale. In this type of reactor, the solid materials are stationary and are alternately exposed to reducing and oxidizing conditions through periodic switching of feed streams [24]. The major advantages of the fixed-bed reactor are that separation of gas and solid particles is not required, which allows for better utilization of oxygen carrier. To achieve a high process energy efficiency and continuous operation, two or more fixed bed reactors in parallel can be installed in the system. However, this reactor configuration has not been used widely for BCLG since it shows heat and mass transfer limitations and demands high temperature and a complex flow switching system. In fluidized bed systems, solids behave like a fluid by passing gas or liquid upwards through the bed of particles. The fluidized-bed reactor is extensively used in chemical looping processes. Its advantages over the fixed-bed reactors are uniform temperature distribution, more effective mixing, and higher heat and mass transfer. The behavior of a fluidized bed strongly depends on flow gas velocity and solid properties. Among fluidization regimes, bubbling, turbulent, and fast fluidization are mainly applied in chemical looping processes. However, one of the serious problems in the stable operation of the fluidized-bed reactor is particle segregation leading to poor fluidization. Based on the key requirements and types of reactors in the system mentioned above, it could be proposed to be accomplished in three configurations like a two-reactor system, three-reactor system, and alternating packed or fluidized bed reactor (Figure 4). Many researchers have carried out their studies in different types of reactor systems and different types of oxygen carriers for CLG fitting biomass fuels to evaluate the feasibility of the BCLG process.

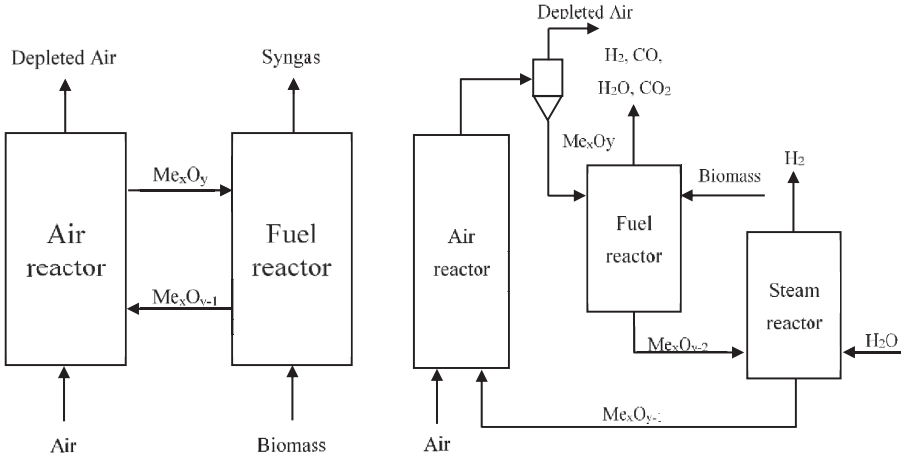

Figure 4. BCLG configurations for hydrogen enrich gas production: (**a**) Two-reactor system and (**b**) Three-reactor system.

Two-Reactor System

The two-reactor system is the most popular configuration for BCLG as shown in Figure 4a [25–28]. The configuration consists of two fluidized bed reactors as the AR and FR, respectively. In the AR, the oxygen carrier materials are oxidized by oxygen from air. The oxidized form of the oxygen carrier is transferred to the FR to react with biomass to produce a gaseous mixture and the reduced form of metal oxides, then they are returned to the AR for regeneration. Additionally, two loop-seal devices are installed between the AR and FR to prevent gas mixing between two reactors. This configuration is based on the reactivity of the oxygen carrier considering that the residence time of the

oxygen carrier required for the reduction reaction is higher than for the oxidation. The AR, a fast fluidized bed reactor, has two objectives: to give the driving force for the solid material circulation and provide sufficient oxygen and heat for fuel conversion in the FR [11]. Interconnected fluid fluidized bed reactors, a type of two-reactor system, comprise mainly two fluidized bed reactors. This configuration normally consists of a high-velocity riser and a low velocity bubbling fluidized-bed as the AR and FR, respectively, being the most popular configuration among all the various types [26,28–33]. Biomass gasification takes place in the FR while the oxygen carrier is oxidized inside the AR. The loop-seals are installed to prevent gas leakage between the AR and the FR. Additionally, cyclones are used to remove solid particles from the gas stream.

Three-Reactor System

The three-reactor system can generate pure hydrogen and syngas separately and simultaneously. It shares similar principles with the chemical looping reforming of methane configuration [14] as shown in Figure 4b. A simplistic mechanism of the three-reactor system for BCLG combined with water splitting is illustrated in Figure 5. Biomass is partially oxidized by the lattice oxygen of the metal oxides in the FR to produce syngas as shown in Reaction (4), but the reduced oxygen carrier is oxidized by steam to regenerate lattice oxygen and produce H_2 in the steam reactor Reaction (5) instead of in the AR. Afterward, the oxygen carrier is fully oxidized in the AR Reaction (3) before continuing the next cycle.

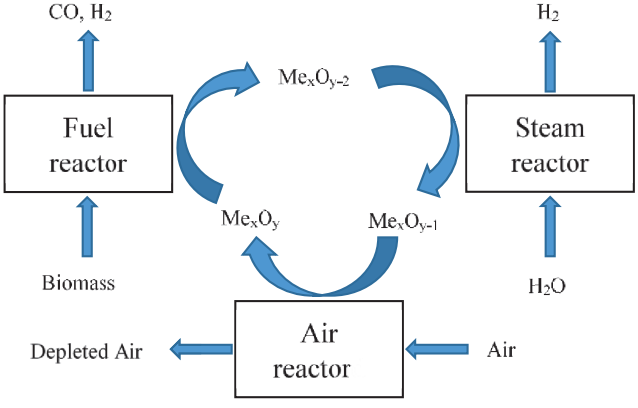

Figure 5. Process scheme of three-reactor system for BCLG.

The reaction in the steam reactor can be illustrated as follows:

$$\text{Steam reactor: } Me_xO_{y-2} + H_2O \rightarrow H_2 + Me_xO_{y-1} \quad (5)$$

where Me_xO_y is an oxygen carrier, Me_xO_{y-1} and Me_xO_{y-2} are the corresponding reduced form of oxygen carriers with different reduction degrees, i.e., the strongly reduced oxygen carriers (Me_xO_{y-2}) leaving the FR are partially oxidized in the steam reactor (Me_xO_{y-1}) before full regeneration in the AR.

Oxygen carrier material used in the process demands a sufficiently high reactivity with biomass, good performance for water splitting to generate hydrogen, and high stability during redox cycles. Additionally, the material should have good resistance to carbon deposition because it may cause contamination of the hydrogen produced. Some metal oxides have been considered as possible oxygen carriers for this configuration such as Fe_3O_4, WO_3, SnO_2, Ni-ferrites, (Zn, Mn)-ferrites, Cu-ferrites, and Ce based oxides [14]. A study was developed in a fixed bed reactor by He et al. [34] to combine BLCG and water/CO_2 splitting using $NiFe_2O_4$ as oxygen carrier. In this study, experimental investigations were

carried out separately in three steps. Firstly, biomass was reduced by $NiFe_2O_4$ to generate syngas in the presence of steam/CO_2. Afterward, the reduced form of oxygen carrier was oxidized partially by steam/CO_2 to produce H_2/CO, then it was fully oxidized by air in the oxidation step. During the investigations, syngas and H_2/CO were obtained separately in different steps. The authors also proposed phase transitions corresponding to different reduction degree of oxygen carrier at different steps as follows:

$$NiFe_2O_4 \rightarrow \text{metallic Fe(Ni)}/FeO_x \rightarrow Ni_{1.43}Fe_{1.7}O_4/Ni \rightarrow NiFe_2O_4$$

The three-reactor configuration has been considered a promising approach since it can produce syngas and pure hydrogen simultaneously. However, there have been very few studies on this configuration. Some research related to the three-reactor system has been focused on gaseous fuels, coal, and $FeO/Fe_3O_4/Fe_2O_3$ materials as looing materials [35–41].

Packed and Fluidized-Bed

The packed bed configuration reactor can be applied for chemical looping gasification of biomass. A simple configuration of this type is shown in Figure 6. The system comprises at least two reactors in parallel working alternately to continuously produce syngas. Each reactor works alternately reduction and oxidation cycles and intermittently alternated with short periods of mild fluidization of the bed after each cycle to level off temperature and concentration profiles [12]. The main advantages of this technology include the separation of gas and particles and the ability to work under high pressure, whereas this technology requires high temperature and a high flow gas switching system [11].

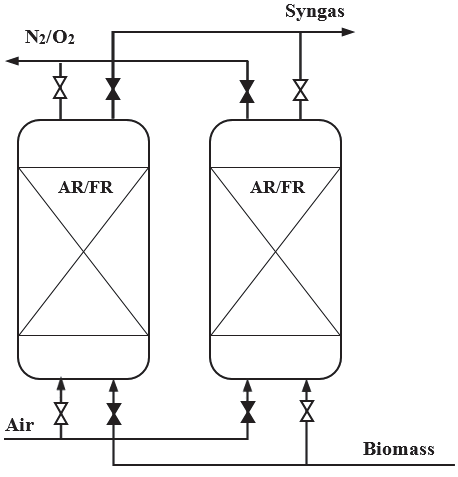

Figure 6. Simple configuration of alternating packed or fluidized bed reactors.

Yan et al. [42] used a fixed bed reactor to study the performance of $Al_2O_3/BaFe_2O_4$ as a synthesized oxygen carrier in BCLG for hydrogen-rich syngas production. Liu et al. [43] conducted a study of chemical looping co-gasification of pinewood and polyethylene in a fixed reactor. The effects of operating conditions during the BCLG process were reported in the investigation. A study of CLG of biomass char using NiO-modified iron ore as an oxygen carrier was carried out by Huang et al. [44]. They reported the reduction of oxygen carrier by biomass char in TGA and a fixed-bed reactor. Liu et al. [45] developed $Ca_2Fe_2O_5$ with Mg/Al/Zn oxides as support materials for BCLG in a fixed bed reaction. This work mainly investigated the effects of Mg/Al/Zn oxides on the reactivity of $Ca_2Fe_2O_5$ and the BCLG performance. Wang et al. [46] presented experimental results in a bubbling fluidized bed reactor for CLG of sawdust pellet with high volatile and low ash content as fuel. It was

found that higher reaction temperatures increased gas production, while the amount of liquid and solid decreased.

2.2.2. System Complexity and Challenges

Although BCLG has many potential advantages over the conventional biomass gasification process, this technology has remained several challenges for widely commercialized applications. Thus, these issues should be considered and solved for its commercialization.

System Complexity

Biomass owns intrinsic characteristics, such as high moisture content, low energy density, various geometrical shapes, ash content, etc. Furthermore, different types of biomass have different properties [47,48]. The bulk density of lignocellulosic biomass materials is relatively low (80–150 kg/m^3 for grass biomass and 160–220 kg/m^3 for woody biomass), which can cause low efficiency in transportation and storage. Therefore, pre-treatment processes are required to homogenize its properties and meet the requirements of chemical looping gasification. These processes possibly include drying, densification, or grinding, etc. These processes require energy and cost resulting in reducing process efficiency.

The BCLG generally operates at high temperatures (over 800 °C) for the production of high calorific value syngas. The process requires a large heat transfer area in a gasifier for a sufficient heat supply for biomass gasification, which increases the operating complexity of the system.

During biomass gasification, biomass ash is produced, which would result in reducing the performance of oxygen carriers. The removal of looping materials from biomass ash (including unreacted carbon) is a considerable challenge to minimize the loss of the looping materials. Additionally, interactions between the ash and looping materials may contribute to a reduction in separation efficiency [9]. Moreover, the syngas produced from the gasification system also contains unwanted substances such as dust, fly ash, tar, alkali metals, nitrogen compounds, sulfur compounds, chlorine, and trace elements. Thus, the CLG system should be integrated with the syngas cleaning system to remove these impurities from syngas before further applications. The required level of syngas cleaning significantly depends on the end-use technology and/or emission standards [49]. There are several methods to remove contaminants which are conveniently categorized according to the process temperature range as hot gas cleanup (HGC) (>300 °C), cold gas cleanup (CGC) (<100 °C), and warm gas cleanup (WGC). The majority of these methods are developed based on using wet scrubbers [49,50].

Typically, biomass gasification system efficiency for power generation would increase corresponding to an increase in unit capacity. However, most of the power plants from biomass are small-scaled and decentralized due to difficulty in the biomass supply chain [51].

The stable load on the chemical plant and long-term operation are among the challenges. Load variations or frequent start-ups and shut-downs could result in damage to the equipment and a reduction in productivity. Moreover, it could cause an increase in cost due to excessive fuel consumption during the start-up and shut-down.

Fouling and Corrosion

Tars are produced during the pyrolysis stage of a gasification process. Certain high molecular weight tar compounds, which start to condense at lower than 450 °C and subsequent polymerization, can cause clogging and blockages in gas lines and filters and reduce process efficiency [52]. Furthermore, the removal of the condensed tars consumes intensive energy and cost. Ash is the remained inorganic residue and exists as particulate after biomass chemical looping processes at temperatures of 800–1200 °C. The particulate of the fuel reactor can deposit in downstream equipment and gas lines resulting in blockages and attrition; however, these particles can be removed by using filters and cyclone separators [5]. Another concern is that biomass fuels have a high content of minerals, including sodium,

potassium, phosphorous, and chloride which can cause potential corrosion for equipment, particularly heat transfer surfaces. Several researchers investigated that chloride has a catalytic effect that promotes the dissociation of the steel material in the heat exchangers, even at low temperatures (100 to 150 °C) [53]. Corrosion mechanisms coexist and occur simultaneously, including several chemical reactions between the metal and metal oxides with gaseous substances of Cl and O, the solid phase of alkali metal salts (K and Na), and ash in the liquid phase and during phase changes [54]. Furthermore, the high content of silica from many types of biomass sources [48] and the formation of molten material in the ash can also cause significant abrasion and erosion on mechanical components and pneumatic ash handling systems [53]. Additionally, biomass-derived tars also have a highly acidic nature (typical pH < 2) and high water content; thus, its presence can cause considerably corrosion-related problems in downstream pipelines and equipment of the system [52].

3. Looping Materials in Chemical Looping Gasification of Biomass

3.1. Looping Materials

In the BCLG process, oxygen carriers are used to transfer lattice oxygen from the air to the fuel via redox reactions to produce syngas, which can avoid the direct contact of air and fuel. Metal oxide materials play a key role in the chemical looping redox processes. These metal oxide materials can be classified as chemical looping gasification (BCLG) and oxygen uncoupling chemical looping gasification (OU-BCLG) based on the properties of looping materials as shown in Figure 3. As can be seen in Figure 7a, biomass fuel is decomposed and cracked down at high temperatures mainly into three products of gas, tar, and char, which can be simplified into volatiles and char. The volatile matter in the biomass, which is reduced to the release of hydrocarbon gases, is constituted by complex organic substances and can be condensed at a sufficiently low temperature to liquid tars. The gaseous fraction is an incondensable mixture of gases at ambient temperature and accounts typically for 70–90 wt.% of the feedstock [55,56]. This mixture of gases consists mainly of hydrogen, carbon monoxide, carbon dioxide, and light hydrocarbon. Afterward, these products react with oxygen carrier particles. Two main types of reactions occur simultaneously in the fuel reactor: homogeneous and heterogeneous. There are two reaction pathways proposed between the oxygen carrier and biomass in the fuel reactor: direct reduction of oxygen carrier by biomass and reduction of oxygen carrier by gaseous biomass gasification products [9]. The first pathway consists of two main reaction types, reactions of volatile matter released from biomass with oxygen carrier (see Reaction (7)), and direct solid-solid reactions. Since solid–solid reactions are very limited due to low contact efficiency, the impact on the final gas composition is negligible in comparison to heterogeneous reactions. Due to a relatively high fraction of volatile matter in biomass, it is a benefit for biomass that a higher proportion of the fuel can directly react with oxygen carrier in a CLG system [9].

The second pathway is an indirect reaction between biomass and oxygen carrier. Firstly, Biomass is gasified with H_2O/CO_2 to produce mainly H_2/CO (see Reactions (8) and (9)), and then gaseous products can readily react with oxygen carrier (see Reactions (6), (10) and (11)).

The general reactions occur in the fuel reactor:

$$\text{Biomass} \rightarrow \text{Volatiles} + \text{Char (mainly C)} + H_2O \quad (6)$$

$$\text{Volatiles} + Me_xO_y \rightarrow CO_2 + H_2O + Me_xO_{y-1} \quad (7)$$

$$\text{Char} + CO_2 \rightarrow 2CO \quad (8)$$

$$\text{Char} + H_2O \rightarrow H_2 + CO \quad (9)$$

$$CO + Me_xO_y \rightarrow CO_2 + Me_xO_{y-1} \quad (10)$$

$$H_2 + Me_xO_y \rightarrow H_2O + Me_xO_{y-1} \quad (11)$$

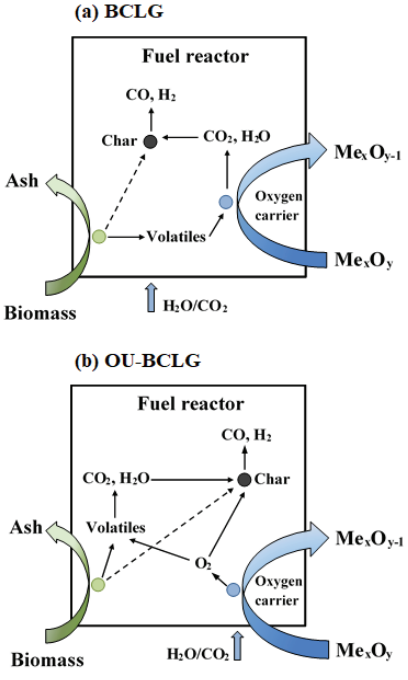

Figure 7. Main reactions in the fuel reactor: (**a**) BCLG and (**b**) OU-BCLG.

The other concept proposed is oxygen uncoupling biomass chemical looping gasification (OU-BCLG). The system is based on the use of an oxygen carrier that can release gaseous oxygen in the fuel reactor to oxidize the fuel as shown in Figure 7b.

$$2Me_xO_y \rightleftharpoons 2Me_xO_{y-1} + O_2 \quad (12)$$

$$Char + O_2 \rightarrow CO + CO_2 \quad (13)$$

$$Volatiles + O_2 \rightarrow CO + CO_2 + H_2O \quad (14)$$

In the OU-BCLG process, the oxygen carrier releases oxygen according to Reaction (12), and the biomass fuel can be decomposed simultaneously into volatiles and char as shown in Reaction (6). Afterward, the devolatilization products are oxidized to CO, CO_2, and H_2O according to Reactions (13) and (14). The remaining char is gasified by CO_2 and H_2O to produce CO and H_2. Moreover, the fuel reactor in both concepts should be fluidized by H_2O, CO_2, or their mixture, which also acts as gasifying agents to accelerate biomass gasification.

There are a limited number of oxygen carrier materials, which have the property of releasing oxygen, that can meet the requirement for multiple cycles of oxygen uncoupling processes. They must be reversible in the reactions of releasing and oxidizing oxygen. In comparison with oxygen carrier for the normal BCLG process, the metal oxides used in OU-BCLG have a suitable equilibrium partial pressure of gas-phase oxygen at a temperature range of 800–1200 °C. Thus, there are three metal oxide system could be used in the OU-BCLG system such as CuO/Cu_2O, Mn_2O_3/Mn_3O_4, and Co_3O_4/CoO. Their reversible reactions are as follows [11]:

$$4CuO \rightleftharpoons 2Cu_2O + O_2 \; \Delta H_{850} = 263.2 \text{ kJ/mol } O_2 \quad (15)$$

$$6Mn_2O_3 \rightleftharpoons 4Mn_3O_4 + O_2 \; \Delta H_{850} = 193.9 \text{ kJ/mol } O_2 \quad (16)$$

$$2Co_3O_4 \rightleftharpoons 6CoO + O_2 \ \Delta H_{850} = 408.2 \text{ kJ/mol } O_2 \quad (17)$$

Unlike the chemical looping combustion process, the BCLG concept is to produce useful combustible gas (CO and H_2, syngas); therefore, the partial oxidation of biomass can be achieved by using oxygen carrier materials suitable for OU-BCLG. Due to the very high reactivity of oxygen uncoupling materials, less metal oxide material used is needed in the system which could reduce the reactor size and associated costs. OU-BCLG is a new concept and a few studies related to OU-CLG have been performed with biomass [57–59].

3.2. Type of Oxygen Carrier

Oxygen carrier plays a key role as the chemical intermediate to indirectly transfer pure oxygen from the air to the fuels via redox reactions in the chemical looping processes. In chemical looping gasification, an oxygen carrier is used to not only provide the oxygen needed for gasification to extremely improve the quality of syngas but also as a thermal carrier that increases heat balance between the two reactors [27]. Furthermore, some metal oxide oxygen carriers may have a catalytic effect on biomass tar cracking [60–62]. Thus, the selection of an appropriate oxygen carrier is one of the most important criteria for the good performance of the chemical looping process. The preferable properties of an oxygen carrier for system performance should be as follows [11,12,63–65]:

(i) Sufficient oxygen transport capacity.
(ii) Favorable thermodynamics and reactivity regarding the solid fuel for the reduction reactions.
(iii) High reactivity in the oxidation reactions.
(iv) Selectivity towards CO and H_2.
(v) Resistance to attrition to minimize losses of elutriated solid.
(vi) Minimal carbon deposition.
(vii) Good fluidization characteristics (no presence of agglomeration) and high melting points.
(viii) Reasonable cyclability/circulation for using over several redox reactions.
(ix) Low cost and long lifetime.
(x) Environmentally friendly properties.
(xi) High mechanical strength and resistance to frictional stresses.
(xii) Capability of converting biomass to gaseous products.
(xiii) Propensity to convert methane

In the chemical looping systems, the lattice oxygen in metal oxides can oxidize partially or fully carbonaceous fuels; therefore, the reduction behavior of the metal oxides significantly affects the performance of chemical looping gasification systems. A modified Ellingham diagram is shown in Figure 8a, which depicts the standard Gibbs free energies of reactions as a function of temperature according to the following reaction:

$$aMe_xO_y + O_2 \rightleftharpoons aMe_xO_{(y+2/a)} \quad (18)$$

The diagram shows the change of the Gibbs free energy with temperature variation, which can be used to evaluate the redox potentials of common oxygen carrier materials. According to the thermodynamic analysis, metal oxides can be mainly categorized in three zones according to their potential to oxidize the fuel or desired applications. In Figure 8b, three zones are bound by three reaction lines as follows:

$$\text{Reaction line 1: } 2CO + O_2 \rightarrow 2CO_2 \quad (19)$$

$$\text{Reaction line 2: } 2H_2 + O_2 \rightarrow 2H_2O \quad (20)$$

$$\text{Reaction line 3: } 2C + O_2 \rightarrow 2CO \quad (21)$$

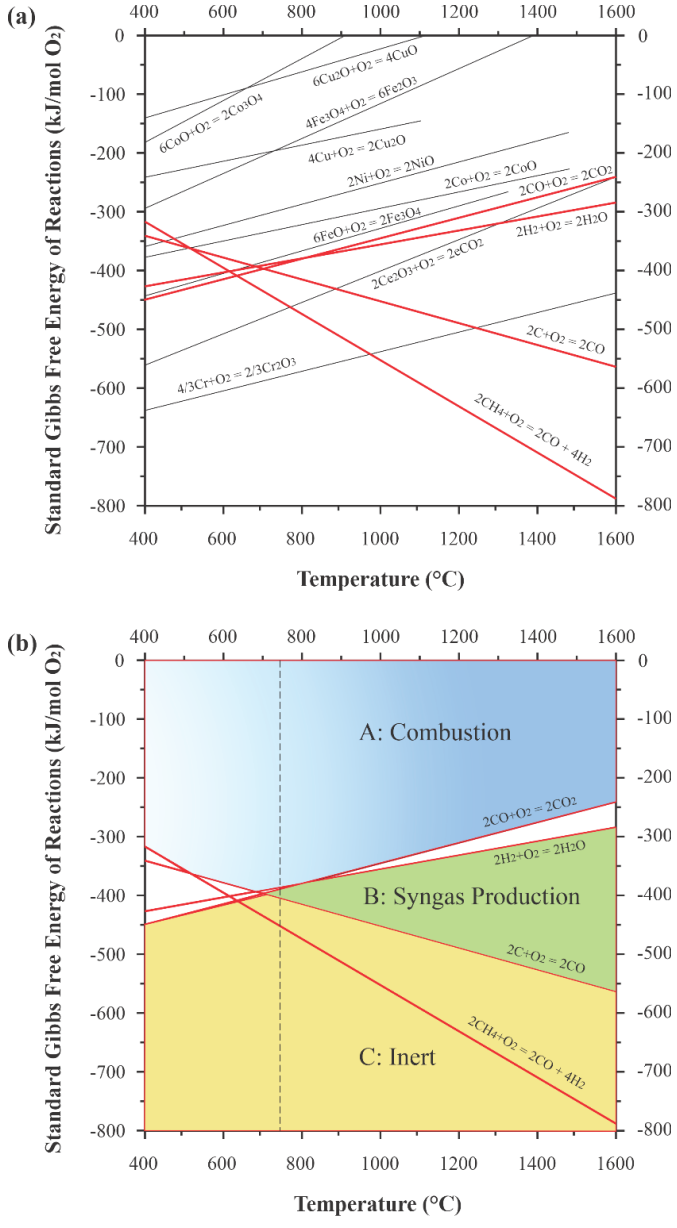

Figure 8. Modified Ellingham diagram for oxygen carrier material: (**a**) standard Gibbs free energy changes of some oxidation reactions and (**b**) reaction zones for syngas production applications [9].

Zone A: metal oxides located in the area above lines 1 and 2 have strong oxidizing properties and can completely or near completely convert the fuel to yield 95% of CO_2 [66]. Metal oxides in this zone consist of CuO, Co_3O_4, Fe_2O_3, Cu_2O, NiO, CoO, and Fe_3O_4.

Zone B: the region is bound in between lines 1 and 3, the materials in this region can partially oxidize the fuel to produce CO or H_2 and an excessive quantity of oxygen

carrier does not yield full oxidation. Thus, metal oxides in zone B are theoretically ideal for chemical-looping gasification applications with 90% of syngas yield [66].

Zone C: the materials in this zone below line 3 cannot be used as oxygen carriers due to their low oxidizing ability; thus, they are considered inert for chemical looping applications.

Ellingham diagrams allow effective evaluation of redox pairs thermodynamically, which can provide theoretical indications for the oxygen carrier's selection. An oxygen carrier performs in a chemical looping system depending on a combination of reaction kinetics, a ratio of oxygen carrier to fuel, contact time, and process design.

To select oxygen carriers for chemical-looping gasification applications, there are two approaches to achieve partial oxidation of fuels [9]. Firstly, metal oxides in zone B are used to mainly produce CO and H_2, which cannot be completely oxidized due to thermodynamic restrictions. The other approach is to use under stoichiometric quantities of materials in zone A.

According to the basis of desired characteristics, various types of oxygen carriers have been investigated for chemical looping gasification of biomass including Fe-based [26,32,43,67–70], Ni-based [25,44], Cu-based [71,72], Mn-based [28], Zn [73], bimetallic oxygen carriers (Fe-Ni [31,74], Fe-Cu [71,75], etc.). They can be classified as follows:

(i) Ni-based oxygen carriers.
(ii) Cu-based oxygen carriers.
(iii) Fe-based oxygen carriers.
(iv) Mn-based oxygen carriers.
(v) Co-based oxygen carriers.
(vi) Perovskite-type complex metal oxides
(vii) Other oxygen carriers.

Several kinds of research have been conducted to compare a large number of oxygen carriers. These results show the general reactivity of the commonly used metal oxides follows orders [9,14,76]:

$$NiO > CuO > Mn_3O_4 > Fe_2O_3 \quad (22)$$

One of important characteristics of an oxygen carrier is oxygen transport capacity, R_O, which is defined as the usable oxygen in the oxygen carrier during one redox cycle, defined by

$$R_O = \frac{m_{ox} - m_{red}}{m_{ox}} \quad (23)$$

where m_{ox} and m_{red} represent the weight of fully oxidized and reduced oxygen carrier in the redox cycle, respectively. The oxygen transport capacity, R_O, determines the fuel conversion and the amount of solid circulation rate.

Table 2 presents the R_O values of different redox couples of oxygen carriers. It can be seen that $CaSO_4$, Co_3O_4, NiO, and CuO have higher R_O values, whereas reduction of Fe_2O_3 to Fe_3O_4 produces only around 3 wt.% of oxygen, the lowest one in the list. The support materials are commonly used to improve the oxygen carrier's performance. The interaction of the metal oxide and the support material can influence the R_O value of oxygen carriers. By using Al_2O_3 supported Fe-based oxygen carriers, more Fe_2O_3 can be reduced to FeO in form of $FeAl_2O_4$ with R_O of 0.045, allowing it to almost completely combust to CO_2 and H_2O in a chemical looping system.

Table 2. Oxygen transport capacity of some Redox couples, R_O [11].

Redox Couples	$CaSO_4/CaS$	Co_3O_4/Co	CuO/Cu	CuO/Cu_2O	NiO/Ni
R_o	0.47	0.27	0.20	0.1	0.21
Redox couples	Mn_2O_3/MnO	Mn_2O_3/Mn_3O_4	Fe_2O_3/FeO	Fe_2O_3/Fe_3O_4	$Fe_2TiO_5/FeTiO_3$
R_o	0.1	0.034	0.1	0.034	0.05
Redox couples	$CuAl_2O_4/Cu.Al_2O_3$	$CuAlO_2/Cu.Al_2O_3$	$CuAl_2O_4/Cu.AlO_2$	$Fe_2O_3/Al_2O_3/FeAl_2O_4$	$FeAl_2O_4/Ni.Al_2O_3$
R_o	0.089	0.066	0.044	0.045	0.091

Among oxygen carriers, the Nikel-based oxygen carriers perform the best reactivity of the reduction and oxidation reactions in chemical looping gasification of biomass [25,31,34]. Due to high oxygen transport capacity, very high chemical reactivity, and almost complete conversion of hydrocarbons, NiO/Ni should be utilized in sub-stoichiometric quantities for chemical looping gasification applications. Additionally, Ni-based oxygen carriers exhibit the potentials for chemical looping process applications at high temperatures in the range of 900–1100 °C, but significant challenges include accumulative chemical and thermal stress, and mechanical degradation with high cycle number [77] along with low reaction rate, high cost, and sulfur deactivation have hindered for their commercial applications.

Copper-based oxygen carriers perform good properties in the chemical-looping process, e.g., high reactivity, oxygen transport capacity, cyclical, and mechanical stability [78]. Reactions of CuO and the gasification products are exothermic thus could promote biomass reforming [71,75]. However, the main challenges of Cu-based oxygen carriers are sintering and de-fluidization due to the low melting temperature of metallic Cu.

The oxygen transport capacity of Fe-based oxygen carriers is relatively low, and it cannot be reduced further than Fe_3O_4 in a fluidized bed reactor because of the thermodynamic limitation [25]. Thus, to improve the reaction rate and characteristics of metal oxides, alkali, and alkaline compounds are added to the oxygen carrier. Yu et al. [79] investigated that the addition of alkali metals to Fe_2O_3 can improve the reaction rate of solid fuel, and Gu et al. [80] reported that K_2CO_3 -added iron ore showed stable catalysis properties for coal chemical looping combustion, whereas calcium oxide exhibited not only catalytic activity but also the ability to capture CO_2 and sulfur compounds [81]. The known benefits of iron oxide are low price, chemical stability, non-toxicity, low sintering temperature needed, and low degree de-fluidization problems, the Fe-based materials are promising oxygen carriers in chemical looping processes. Fe-based oxygen carriers perform differently in their reactivity with various fuels, their reaction rate varies with the following order: H_2 > CO > CH_4 > solid fuels [69,82].

Mn-based oxygen carriers are probably classified into the group of oxygen uncoupling materials with Mn_2O_3/Mn_3O_4 phases, but Mn_2O_3 is not stable at relevant temperatures; therefore, Mn_3O_4/MnO can be the main phase transition in the chemical looping processes which is not possible to release oxygen [28]. Mn-based materials show low-cost and environmentally friendly properties that are similar to Fe-based oxygen carriers. MgO addition improved the oxygen release ability of the oxygen carrier and increased the performance of biomass chemical looping gasification [45]. The theoretical oxygen transport capacity of Mn-based oxygen carriers is higher than that of Fe-based materials, but there are a few reports that have been published regarding these materials in the chemical looping gasification of biomass.

Perovskite-type complex metal oxides have a general formula ABO_3, where A is a lanthanide ion and/or alkaline earth metal and B is a transition metal ion [18]. Many studies pointed out that two different oxygen species being in the perovskite oxides, such surface absorbed oxygen and bulk lattice oxygen which play a different role in chemical looping processes [83]. The surface absorbed oxygen combusts completely methane, whereas the other is responsible for partial oxidation of methane to H_2 and CO. Redox activity of the

perovskite materials is dependent on the mixed-conductivity of the support. Many types of research found that the materials released between 3.44 and 8.23 wt.% of oxygen at 600 °C [18]. Oxygen transport within iron oxide particles can play an important role at the final stage of the reduction, whereas higher Ni^{2+} shows a greater reduction ability. The advantages of the materials are excellent regeneration ability and less agglomeration at temperatures above 100 °C, as well as high thermal stability, good mechanical properties, and high selectivity to synthesis gas.

Along with transition metal oxides, i.e., Ni, Cu, Co, Mn, Fe have been investigated as possible oxygen carriers for the chemical looping gasification process, synthetic oxygen carriers are widely researched, while natural minerals are potentially developed due to their low cost. The low-cost natural minerals are used as oxygen carriers including iron ore, ilmenite, manganese ore, and waste materials from the steel industry and alumina production [63]. Synthetic materials generally comprise single metal oxides, as well as their blend with inert support (Al_2O_3, SiO_2, $MgAl_2O_4$, TiO_2, ZrO_2, CaO, etc.) [11] to improve their reactivity, mechanical properties, and stability, as well as multifunctional properties, including catalytic function, tar decomposition, and CO_2 adsorbent in BCLG. Many studies have been carried out to investigate experimentally the reactivity and stability of different oxygen carriers with various supporting materials, e.g., Al_2O_3 [25,26,33,42,45,78,84], SiO_2 [30], CaO [43,85,86], MgO [45], TiO_2 [69,84]. It was found that the reactivity and stability of oxygen carriers increase significantly during the multiple cycles when supported with Al_2O_3. Additionally, TiO_2 is used as a supporting material with iron oxides for chemical looping processes. The compounds performed high reactivity and stability in various studies [32,69,84]. Ilmenite performed well in the continuous operations of a 1.5 kW_{th} pilot reactor with >90% of biomass conversion and carbon conversion efficiency obtained [32]. It was reported that the presence of MgO and ZrO_2 can increase thermal and chemical stability, as well as specific heat capacity of oxygen carriers [45,87]. The addition of CaO to oxygen carrier has emerged in the chemical looping gasification process for continuous hydrogen production [43,45,85,88–90]. Calcium oxide (CaO) has been known as a catalyst and CO_2 sorbent, which favors hydrogen-rich gas production [43,85,91]. Furthermore, the presence of CaO also works as tar cracking catalyst for hydrogen production in a fluidized bed reactor [92,93]. High hydrogen content (approximately 63%) and hydrogen yield (23.07 mol/kg rice straw) at 800 °C were obtained with the presence of calcium-iron oxide oxygen carriers [86], while Sun et al. [93] reported the maximum hydrogen yield reaches 7.12 mol/kg pine wood at 850 °C.

Many kinds of research have been carried out by mixing different active metal oxides or mixing different oxygen carriers composed of single metal oxides. The major aims of using mixed oxides are desired as follows [11,31,34,78,94,95]:

(i) Increase the reactivity and/or stability of particles.
(ii) Improve the conversion of the fuel gas.
(iii) Improve the mechanical strength and resistance to the attrition of particles.
(iv) Improve tar decomposition.
(v) Improve carbon dioxide adsorption.
(vi) Decrease the carbon deposition.
(vii) Decrease the preparation cost of the oxygen carrier.
(viii) Decrease the use of toxic metals.

Many studies have been carried out to evaluate the performance of many metal oxides as oxygen carrier for hydrogen production. It was found that the Fe-based oxygen carrier shows the most attractive application prospect for the chemical looping applications, particularly for hydrogen production due to its high-temperature stability, low cost, environmentally friendly effects [14,96]. Composite materials of iron oxide and perovskite have been proposed as a potential oxygen carrier material for hydrogen production due to their excellent oxygen transport properties and stability under cycling. Thus, these materials work effectively for catalytic oxidation reactions including hydrogenation, CO oxidation, and catalytic combustion [14]. According to Dueso et al. [97], several oxygen

carrier materials composed of LSF731 and iron oxide showed higher performances in oxygen capacity and stability, as well as hydrogen production compared to iron oxide. The characteristics of common types of oxygen carriers are summarized in Table 3.

Table 3. Overview of common types of oxygen carriers in chemical looping processes [9,11,12,14,18].

Type of OC	Operating Temp. [°C]	Support Materials	Advantage	Disadvantage
Ni-based	900–1100	Al_2O_3, $MgAl_2O_3$, ZrO_2, Bentonite, TiO_2, MgO, SiO_2	Very high reactivity and selectivity, strong catalytic properties for hydrocarbon conversion, high oxygen transport capacity, high stability, low agglomeration	Sulfur deactivation, high cost, health, and safety issues
Fe-based		Al_2O_3, $MgAl_2O_4$, TiO_2, SiO_2, YSZ, CeO_2, ZrO_2	Environmentally friendly and non-toxicity, low cost, high mechanical strength, high chemical stability	Relatively low reactivity, low oxygen transport capacity, agglomeration issue, low solid circulation rate
Cu-based	<800	Al_2O_3, $CuAl_2O_4$, TiO_2, SiO_2, CeO_2, ZrO_2, Bentonite, MgO, $MgAl_2O_4$	High reactivity and oxygen transport capacity, low cost and toxicity, high chemical and mechanical stability, environmentally friendly. No demand for external heat	Agglomeration and de-fluidization due to the low melting point of Cu
Mn-based		Al_2O_3, $MgAl_2O_4$, TiO_2, SiO_2, ZrO_2, bentonite	Low cost and non-toxicity, environmentally friendly	Sulfur deactivation, relatively low oxygen transport capacity, agglomeration, low reactivity with fuels
Co-based		YSZ, Al_2O_3, $CoAl_2O_4$, TiO_2, SiO_2, ZrO_2, bentonite	High oxygen transport capacity, high reactivity with CH_4 and CO	High cost and environmental impact and health issue, low reactivity with fuels

3.3. Performance of Looping Materials

Oxygen carrier is a key factor in chemical looping processes. One of the main challenges of these processes is to stabilize their performance over prolonged redox cycling. However, many reasons may reduce the performance of oxygen carriers during Biomass chemical looping gasification. As discussed above, the agglomeration of oxygen carriers is one of the most serious challenges in chemical looping processes which can lead to bed defluidization and deactivation of oxygen carriers. The Cu metal has a low melting point which can cause agglomeration at high temperatures, and the redox rate of CuO would readily decrease after few reduction-oxidation cycles [98], while several agglomerations of Fe-based oxygen carrier has been reported when the phase change to Fe_3O_4 during oxidized in air. Therefore, different support materials have been used to mitigate this problem. Another concern is the reduction of the mechanical strength of oxygen carriers during chemical looping processes. This problem can lead to attrition and decrease their lifetime. Along with physical attrition, chemical stress during redox cycles is also a reason for the reduction of mechanical strength [9].

In solid–gas reactions, carbon deposition on the solid oxygen carriers is a serious problem, because it can reduce their reactivity and shorten their lifetime. Carbon deposition is a complex phenomenon that is affected by several factors (pressure, temperature, availability of oxygen in the oxygen carrier, contents of water vapor, and CO_2 in the fuel gas) [99]. For Ni- or Cu-based oxygen carriers, carbon deposition was reported when the oxygen

carrier converted more than 75% [9,100]. Additionally, gas sulfur compounds in the syngas possibly react with oxygen carriers and produce various sulfur compounds that may cause the deactivation of looping materials. During thermochemical conversion processes, the inorganic matters in biomass are converted into the solid residual produced that can cause several problems for the performance of oxygen carriers and the system. Biomass ash composition is a complex mixture of inorganic-organic matters with solid, liquid, and gaseous phases from various origins. In the solid phase, ash is composed of inert materials from feedstock and un-reacted matters. In chemical looping processes, the interaction between biomass ash and oxygen carrier could be a significant issue. Gu et al. [101] reported that the performance of iron ore oxygen carrier was significantly influenced by the biomass ash type, resulting in serious particle sintering and subsequent deactivation of oxygen carrier with SiO_2-rich ash, whereas K-rich ash with lower SiO_2 content could efficiently improve the performance of oxygen carrier during cycle experiments. Additionally, biomass ash has considerably low melting temperatures (<800 °C), which is mostly lower than the operating temperatures of the gasification process ranging between 800 and 1000 °C. Consequently, it can cause agglomeration, sintering, and defluidization problems, as well as ash deposition [9,30,102,103].

4. Effect of Process Parameters on Biomass Chemical Looping Gasification

Operating conditions play a key role that significantly influences the process performance, especially the amount of hydrogen in the product gas. The effects of the key process parameters in BCLG are described and analyzed in this section.

4.1. Biomass Characteristics

Biomass is a complex mixture of organic and inorganic substances. Vassile et al. [48] categorized types of biomass based on their biology diversity, source, and origins, such as woody plant, herbaceous and agricultural plants/grasses, aquatic plants, human and animal waste, contaminated and industrial waste biomass, and biomass mixtures. Florin and Harris [104] characterized biomass as follows:

(i) The chemical constituents: cellulose, hemicellulose, and lignin.
(ii) Elemental composition.
(iii) Inherent mineral content.
(iv) Proximate analysis: moisture, volatile, fixed carbon, and ash contents.
(v) Physical properties: particle size, shape, and density.

All these parameters have been investigated their effects on the product gas composition, yield, and process performance. The properties of different types of biomass are shown in Tables 4 and 5. Many studies have been carried out on various types of biomass for gasification and BCLG. Generally, the higher content of cellulose and lignin produces more gaseous products resulting in the increasing potential of hydrogen recovery from biomass. The hydrogen production from biomass gasification is attributed to the intrinsic properties, moisture content, and alkali content [105]. Additionally, biomass with high contents of oxygen and hydrogen results in highly liquid and volatile yields, thereby reducing the overall energy conversion efficiency of the combustion process. Furthermore, higher H/C ratios in fuels generate a greater heat of combustion, whereas higher ratios of O/C produce more CO_2 emission per amount of energy release [47,106]. A simplified summary of biomass pyrolysis is illustrated in Figure 9 [107]. Some studies [108–111] found that biomass with the proportions of cellulose and hemicellulose are directly related to higher CO and CO_2 concentrations, while higher lignin content leads to a higher char yield and CH_4 concentration during the pyrolysis process. Consequently, those intermediate products can vary in the final composition of the product gas. Chang et al. [112] carried out an experimental study on biomass gasification for hydrogen production in a fluidized bed reactor.

Table 4. Biomass constituents (wt.% on a dry basis) [21,29,47].

Biomass Type	Cellulose	Hemicellulose	Lignin
Hardwood	42–50	20–38	16–25
Softwood	35–50	24–35	16–33
Straws	33–40	20–45	15–20
Corn stover	33–35	21–24	17–22
Switchgrass	30–50	10–40	5–20

Table 5. Proximate analysis of some biomass feedstock (wt.%) [32,33,47,49].

Biomass	Moisture [a]	VM	FC	Ash	LHV (MJ/kg)
Wood	20	82	17	1	18.6
Wheat straw	16	59	21	4	17.3
Barley straw	30	46	18	6	16.1
Torrefied woodchips	5.28	70.75	22.82	1.15	19.3
Pine sawdust	-	84.1	15.6	0.4	19.3
Pine wood	5.6	78.5	15.3	0.6	17.4

[a] Intrinsic.

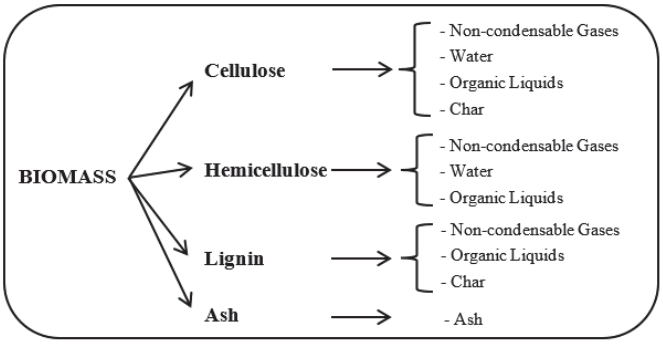

Figure 9. The simplified summary of biomass pyrolysis.

They gasified three different types of biomass (α-cellulose, bagasse, and mushroom waste) at different temperatures (600–1000 °C), steam-to-biomass ratios, and equivalent ratios. The results showed that the highest hydrogen production was obtained in the case of using α-cellulose, which has higher contents of carbon and hydrogen than those of the other species. Raut et al. [113] studied the effect of torrefaction pretreatment on biomass gasification performance at different reaction temperatures (700–850 °C) and the steam-to-biomass ratio (0.6). In the study, biomass feedstock was Poplar wood and its torrefied products. The hydrogen content increased corresponding to the increment of torrefaction degrees.

Biomass particle size influences significantly the performance of biomass gasification and hydrogen production. Biomass with smaller particles provides a larger surface area per unit mass resulting in improving heat and mass transfer which promotes the gasification reactions (Boudouard reaction, water gas reaction) to produce significantly H_2 and CO. Several studies have been conducted to analyze the effect of biomass particle size on gasification reactions. Lv et al. [114] found that CH_4, CO, and C_2H_4 were produced more in the case of the smaller particles while less CO_2 was formed, and larger particles showed greater heat transfer resistance which led to incomplete pyrolysis and a higher amount of unreacted char. Hernández et al. [115] reported that the smaller particle size of the fuel improves mass and heat transfer due to higher external surface area/volume resulting in

more porous owing to a higher amount of volatile release. Therefore, the reactivity of the remaining char increases leading to an increase in the gasification reactions. Di Blasi [116] in his work demonstrated that the smaller particles with a large surface area produce more light gases, as well as less unreacted char and tar. Thus, the particle size of biomass has a significant impact on the product gas yield.

4.2. Gasification Temperature

Temperature is one of the most significant factors in gasification since the gasification process is a thermochemical conversion process that uses heat to convert the fuel into product gas. Generally, most of the biomass gasification reactions are endothermic reactions, an increase in temperature promotes them. Additionally, higher temperatures increase the heating rate among the particles resulting in effective destruction of the particles and proceeds for complete gasification reactions [22]. Consequently, more yield of gaseous products is generated, and the amount of unreacted char reduces.

Many researchers have studied the relationship between gasification temperature and process performance, as well as hydrogen production. As shown in Figure 10, hydrogen content slightly decreases in most cases, whereas studies conducted by Zeng [27] and He [34] show a small increase in hydrogen fraction in the product gas. The possible explanation supporting this trend can be referred to Le Chatelier's principle. Elevated temperatures favor the reactants in exothermic reactions and the products in endothermic reactions. As a result, the endothermic reactions in gasification would be strengthened with an increase in temperature which leads to an increase in the content of H_2 and CO, as well as more solid char is consumed to produce gaseous products. Furthermore, higher temperature also promotes cracking heavier hydrocarbon and tars.

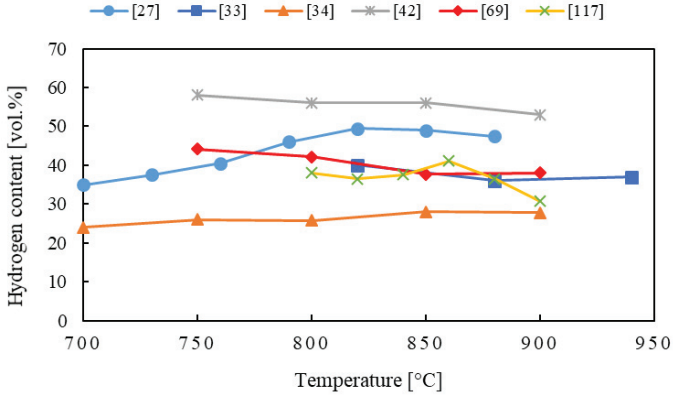

Figure 10. Hydrogen concentration as a function of fuel reactor temperature.

Additionally, elevated temperature improves gas yield and process efficiencies during the BCLG process. Yan et al. [42] reported that the total gas yield increased significantly with the gasification temperature. Additionally, the concentration of CO and CH_4 increased, while there was a slight decrease in the yield of H_2 and CO_2. Zeng et al. [27] investigated that H_2 content increased to the maximum value of 49.47% at 820 °C, then slightly dropped to approximately 47% at 880 °C. They also found that CGE increased with increasing temperature and reached a peak at 820 °C. Ge et al. [117] carried out a study on BCLG in a 25 kW_{th} reactor using natural hematite as oxygen carrier. The temperature range in the study was between 800 and 900 °C. The results showed that hydrogen concentration reached the maximum value at 860 °C, then it decreased considerably to 30.77% at 900 °C. Gas yield showed a similar trend with hydrogen content, while carbon conversion efficiency increased with elevated temperatures. In a study of BCLG using $NiFe_2O_4$ [34], carbon conversion efficiency and syngas yield increased from approximately 26% and

0.32 $m^3/kg_{biomass}$ from 700 to 850 °C. These variations of gas concentrations and total gas yield are related to a series of competing reactions in the gasifier. Under high temperatures, biomass pyrolysis, heavier hydrocarbon, and tars are promoted increasing gas yield and gas concentrations. High temperatures also thermodynamically favor the reactants in exothermic reactions and the products in endothermic reactions. At high temperatures, the reactivity of oxygen carriers with combustible gases is promoted, resulting in a reduction in the content and yield of hydrogen. This is rarely stated in small-scale experimental studies, but larger FR temperatures also mean that a higher heat transport (i.e., solid circulation) is required in the CLG unit.

4.3. Steam-to-Biomass Ratio

Steam-to-biomass ratio (SBR) refers to the amount of steam the mass of biomass fed into the gasifier. SBR is a key parameter strongly affecting hydrogen production and carbon conversion efficiency, as well as total gas yield. High SBRs result in a lower amount of unreacted char and greater both the yield and concentration of hydrogen in the product gas. Many researchers have reported that increasing SBR leads to a rise in hydrogen production and carbon conversion efficiency, as well as a low amount of tar produced. Figure 11 shows that hydrogen content is proportional to the ratio of steam-to-biomass.

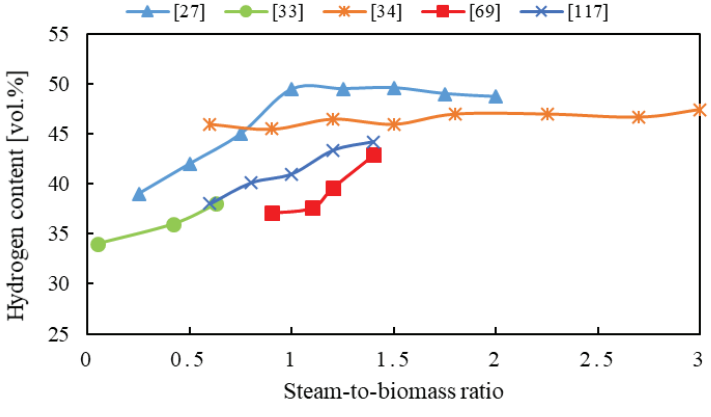

Figure 11. Hydrogen concentration as a function of steam-to-biomass ratio.

In the presence of high steam content in the gasifier, there is an increase in both the yield and content of hydrogen. Along with the increase in hydrogen production, process efficiencies have been improved corresponding to higher SBR. It should be noted that CO content decreases with higher SBRs. These tendencies are probably attributed to water gas shift reaction, char gasification reaction and steam reforming reaction. However, the undesired rise in CO_2 content has been reported which could be problematic in hydrogen-enriched gas production. This fact can be evidenced from study results [27,34,42,114,117,118].

Along with the enhancement of hydrogen production, the higher amount of steam used in the gasifier promotes tar decomposition, which is one of the most serious issues in biomass gasification. It is likely attributed to tar cracking reactions with the presence of steam. Reed [119] found that steam could strengthen participation of tar in steam gasification which leads to the decrease in tar content at higher SBR. Consequently, hydrogen and total gas yields can enhance as products of tar cracking reaction (tar reforming reaction). The addition of steam mainly brings about favorable aspects. Yet, in a large-scale process steam addition is one of the main sources of energy consumption. Hence, one would always try to minimize steam addition to the lowest possible level.

4.4. Oxygen Carrier-to-Biomass Ratio (OBR)

In the CLG process, metal/metal oxide provides lattice oxygen as a gasifying agent for solid fuel gasification. Oxygen carrier-to-biomass ratio (OBR) is defined as the mass ratio of the amount of oxygen carrier per biomass fed into the gasifier being a key factor in a BCLG process. OBR strongly influences the composition of the product gas, gas yields, and the performance of the BCLG process. Many studies have been carried out to evaluate the effect of oxygen carrier (in both type and quantity used) on the performance of BCLG, especially syngas production. It is noted that an increase in the amount of oxygen carrier used leads to further char gasification; therefore, high OBRs are beneficial for carbon conversion efficiency. However, it was found that a rise in OBR cause low content and yield of H_2 and CO in the product gas. It is due to the higher quantity of oxygen carriers that would promote the oxidation reactions of combustible gases including H_2 and CO. On the other hand, a high amount of oxygen carrier could result in a higher gasification temperature, which can enhance the gasification and improve the quality of the product gas to some extent.

Ge et al. [117] reported that a high amount of oxygen carrier could keep gasification temperature stable under the experimental conditions. Additionally, carbon conversion efficiency increased corresponding to the increase in the hematite mass percentage from 40 to 60 wt.%. However, H_2 and CO concentrations declined significantly by around 9% and 5%, respectively, resulting in the reduction in the syngas yield from 0.74 to 0.52 Nm^3/kg. An experimental study on BCLG using $BaFe_2O_4/Al_2O_3$ as an oxygen carrier [42] figured out that CO reduced with the increase of OBR for 30AF, whereas it increased for 30ABF at OBR of 0.6, then dropped down at higher OBRs. Huang et al. [67] used iron ore as an oxygen carrier to oxidize biomass char in a fixed bed reactor. They evaluated the effect of iron ore excess number, Ω, which refers to the ratio of oxygen provided by oxygen carrier to the oxygen required for the complete oxidation of the fuel, on the performance of char gasification. Carbon conversion efficiency increased by approximately 23%, but H_2 and CO contents reduced by 7% and 10%, respectively, when the OBR increased from 0.46 to 1.17. Huijun et al. [25] showed an increase in carbon conversion efficiency while large amounts of H_2 and CO could be consumed with the rise in NiO content resulting in a significant decrease in syngas yield. An interesting result was found in a study on chemical looping co-gasification of biomass and polyethylene [43]. It was noted that there was an opposite variation of the contents of H_2 and CO with the increment of OBR. The concentration of H_2 increased from 34.78 vol.% to 38.15 vol.%, whereas CO and CH_4 contents declined with increasing OBR from 0 to 1.0. Additionally, more syngas yield also was generated with the elevated OBR. It can be considered that syngas production could be promoted by the presence of the oxygen carrier.

4.5. Effect of Operating Conditions on Tar Formation

Tar is a product of the gasification process which is defined as any matter in the product stream that is organic condensable compounds produced in thermochemical reactions [52]. Due to the high content of volatile matters in biomass, a large amount of tar derived from biomass gasification may cause many serious problems for gasifier or downstream processing steps as blockages, clogged filters, and efficiency reduction, but there are few investigations into its formation and effects in biomass chemical looping gasification.

High temperatures can thermally crack tar components efficiently, but they may reduce process efficiency. It was observed that naphthalene reduces by 47% when temperature increases from 820 to 940 °C [33]. Huang et al. [120] reported that the tar content declines from 18.58 to 9.03 g/Nm^3 in the range of operating temperature between 740 and 940 °C. Another study found that about 86% of tar content is eliminated when temperature increases from 500 to 900 °C [121].

Furthermore, the addition of steam in the gasifier can also abate an amount of tar in the product gas through steam reforming reactions of tar. Some publications found that steam

can effectively crack down large tar molecules [15,32,33]. Increasing the SBR would promote cracking reactions. However, this promotion can be less effective at a relatively high value of SBR. Moreover, excess amount of steam causes a temperature reduction in the reactor, resulting in low tar decomposition by temperature effect. Condori et al. [32] investigated the variation of the amount of tar formed as a function of the steam-to-biomass ratio. They found that an increase in the steam-to-biomass ratio results in a decrease in the amount of tar produced with a reduction of approximately 27% at 820 °C when the ratio increases from 0.06 to 0.9. A downward trend of tar yield was observed with a reduction of 73% when steam addition was further increased to the steam-to-biomass of 1.25 in an experimental investigation of biomass chemical looping gasification with Cu_5Fe_5 at 800 °C [121].

Figure 12 presents the tar yields of biomass chemical looping gasification under different gasification conditions and various oxygen carriers. The feedstocks used in these investigations were pine wood and pine wood sawdust. Without an oxygen carrier, the highest amount of tar was produced with about 22 and 17 g/Nm^3. In the presence of an oxygen carrier as catalyst and oxidation agent, tar yield obtained reduces significantly to the lowest yield of around 2 g/Nm^3. A similar trend was observed that tars were obtained between 0.9 and 3.0 g/Nm^3 at different operating conditions with Fe_2O_3/Al_2O_3 as oxygen carrier [33]. It is noteworthy that increasing the oxygen carrier-to-biomass ratio promotes the tar decomposition, but it can decline the reduction degree of the oxygen carrier, resulting in the low catalytic reactivity of the oxygen carrier and reduction in tar removal efficiency. Tian et al. [71] investigated the effect of oxygen carrier-to-biomass ratio on the reforming of tar using Cu_5Fe_5 as oxygen carrier. They found that the total amount of tar obtained reduces strongly by approximately 67% when the oxygen carrier-to-biomass ratio increases from 0 to 0.8. The results also perform that the presence of oxygen carrier can promote the transformation of macromolecular components into smaller molecular species.

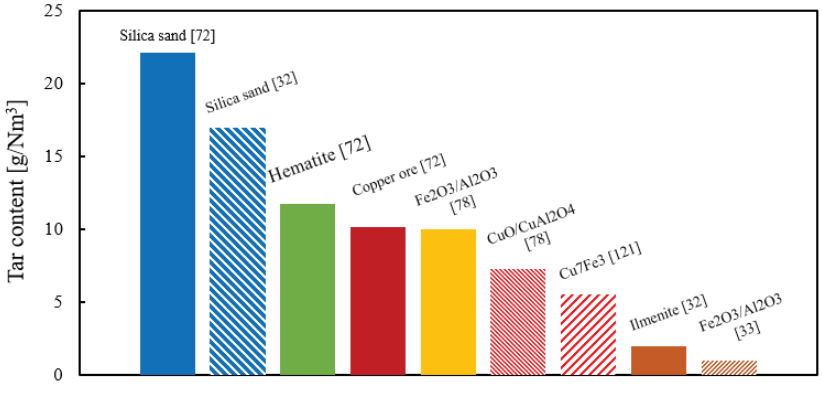

Figure 12. Tar yield (800–880 °C).

Hence, operating conditions have significant influences on tar formation, including its yield and constituents. Increasing operating parameters, i.e., gasification temperature, steam-to-biomass ratio, and oxygen carrier-to-biomass ratio, can be beneficial for tar removal from biomass chemical looping gasification.

5. Progress in Biomass Chemical Looping Gasification

Chemical looping gasification is viewed as a promising gasification technology for high-quality syngas generation. Currently, biomass is emerging as a renewable feedstock for the CLG process. Recent studies have been carried out to analyze kinetics and the process performance in pilot-scale systems, as well as to simulate the process through technical software. However, the research activities on chemical looping gasification of biomass are not

still limited compared to coal by this time, resulting in the lack of good understanding of the process behavior and hindering further large-scale commercial applications.

5.1. Thermodynamic Analysis and Kinetic Studies

Thermodynamic and kinetic studies are to evaluate the energy efficiency of the system and the effects of operation parameters on process performance and the interaction between solid fuel and oxygen carriers, as well as the feasibility of oxygen carrier for chemical looping gasification of biomass. The results obtained will be analyzed to develop pilot-scale and then industrial processes by mostly using thermogravimetric analysis equipment (TGA). Various types of oxygen carriers and their compounds have been investigated to assess their feasibility for the chemical looping gasification process. Many studies have been carried out to analyze the reactivity of an oxygen carrier in various atmospheres and to propose kinetic models to describe the kinetics of the oxygen carrier with different types of fuels [94,96,122–127]. During biomass chemical looping gasification, many gas-solid reactions take place simultaneously in the reactor. Therefore, the knowledge of redox reaction kinetics and their mechanism is necessary for the design of the system [124,125,128].

Yan et al. [122] analyzed system performances of biomass-coal co-gasification with steam. In the study, a coal and biomass-based chemical looping power generation system was developed. Wheat straw and coal were introduced into the reactor to gasify with steam, then the generated syngas would reduce Fe_2O_3 in the reducer. FeO generated from the reducer was oxidized by steam to produce hydrogen, and Fe_3O_4 generated in the oxidizer would be regenerated to form Fe_2O_3 before the next cycle. Hydrogen obtained in the oxidizer then was used as feedstock to generate electric power through the SOFC system. The result of the study was used to analyze the efficiency of energy and exergy of the system, the effect of operation parameters on system performance, and economic feasibility for the removal of NO_x, SO_x, and CO_2. Wang et al. [125] discussed the mechanism of reactions between corn cob and Mn_2O_3 during the chemical looping gasification. Furthermore, the method of Gibbs free energy minimization was used to analyze the thermodynamics of syngas generation from the process. They proposed the optimal ratio of Mn_2O_3/corn cob is 0.18 to obtain the maximum yields of H_2 and CO, and the total dry concentration of CO and H_2 could gain 98.8% at 1000 °C and atmospheric pressure. Additionally, the carbon conversion also increases in the presence of steam used as a gasifying agent.

Non-isothermal experiments were carried out by Huang et al. [128] to develop the kinetic analysis of oxygen carrier reduction by char. A mixture of biomass char and $NiFe_2O_4$ as oxygen carrier was introduced into the TG-MS system and then heated to 1250 °C with different heating rates under the inert environment. The study investigated that the increase of activation energy of redox reaction corresponds to conversion ratio, and the random nucleation and subsequent growth model can be used to describe the kinetic mechanism. A new concept for syngas production was proposed to use a liquid metal oxide as an oxygen carrier for chemical looping gasification. The proposed configuration comprises two interconnected bubble reactors as the fuel and air reactors, and a liquid form of oxygen carrier is circulated between two reactors to provide the required heat and oxygen for the gasification reaction. The proposed concept could prevent the challenges from the solid oxygen carrier system such as agglomeration and sintering. Wu et al. [94] carried out a thermodynamic analysis to investigate the performance of four bimetallic oxygen carriers ($BaFe_2O_4$, $BaMn_2O_4$, $CaFe_2O_4$, $CaFe_2O_4$) for CLG of biomass-based lignin. The kinetic behavior and reaction performance of lignin pyrolysis and gasification was evaluated through a TGA-MS system. According to the results, $BaFe_2O_4$ and $CaFe_2O_4$ showed good syngas selectivity, while $BaFe_2O_4$ exhibited excellent reactivity and regeneration in the air after reduction.

5.2. Pilot-Scale Investigations

Along with thermodynamic analysis and kinetic study, BCLG in experimental test rigs has been intensively investigated in the temperature range of 600–1300 °C using vari-

ous types of biomass, typically woody biomass to evaluate the feasibility of the process. Different pilot-scale configurations have been used in the BCLG studies, commonly fixed bed [42,43,45,90] and fluidized bed reactors [25,26,32,33]. One of the key performances in those studies is the reactivity of oxygen carriers in the BCLG process. Various oxygen carriers have been investigated including Fe-based [26,32,43,67–70], Ni-based [25,44], Cu-based [71,72], Mn-based [28], Zn [73], bimetallic oxygen carriers (Fe-Ni [31,74], Fe-Cu [71,75], etc.). Additionally, the oxygen carriers were supported by supporting materials, such as SiO_2 [30], Al_2O_3 [26,33,42], CaO [43,85,86], MgO [45], TiO_2 [69,84], etc., to improve their reactivity and multifunctional properties, including catalytic function, tar decomposition and CO_2 adsorbent.

A 25 kW_{th} system was developed by Ge et al. [30] to investigate the performance of rice husk gasification chemical looping using hematite as an oxygen carrier. The system mainly consists of a high-velocity fluidized bed as the AR and a bubble fluidized bed as the FR. The main components of hematite are Fe_2O_3, SiO_2, and Al_2O_3 with 83.21 wt.%, 7.06 wt.%, and 5.37 wt.%, respectively. The higher performance of BCLG with hematite, such as higher carbon could obtain at 860 °C, while carbon conversion efficiency reached a peak at oxygen carrier/biomass ratio of 1.0. Wei et al. [31] experimentally investigated the performance of Fe-Ni bimetallic oxides as oxygen carriers that were applied for biomass chemical looping gasification. The experiments were performed in a 10 $\underline{kW_{th}}$ interconnected circulating fluidized bed which mainly consists of a fast fluidized bed as the AR and a bubbling bed as the FR. Sawdust of pine was used as feedstock. The experimental results indicated that the content of CO, H_2, and CH_4, as well as process performance, increased with the rising gasification temperature. The Fe-Ni bimetallic oxygen carriers displayed a higher gasification efficiency of biomass and showed a stable reactivity and good sintering resistance. Chuayboon et al. [73] proposed a novel process for chemical looping gasification. The high-temperature solar-driven chemical looping gasification of lignocellulosic with ZnO/Zn redox pair was developed to evaluate the advantages and reliability of the combined process. Experiments were carried out in a lab-scale solar reactor at a range temperature from 1050 to 1300 °C with a biomass/solid ratio from 0.5 to 1. Biomass feedstock was beech wood for the experiments. The experimental set-up mainly consists of the solar reactor, solar concentration system, gas injection, and particle feeding system, filtering unit, and gas analysis unit. A fixed ratio mixture of ZnO and biomass particles was placed in the hopper, and then the reactor was heated up to the required temperature by concentrated sunlight. During the study, the influence of temperature and reactant molar ratio on syngas production was analyzed. The result successfully demonstrated the feasibility of the process for the first time, and optimal operating conditions for the study were found at 1250 °C and a biomass/ZnO molar ratio of 0.75. Additionally, the temperature of Zn production was lower than that for ZnO thermal dissociation.

A study was carried out to evaluate the multi-functional oxygen carrier for hydrogen-rich syngas production [129]. An iron-based oxygen carrier was developed from the Bauxite residual of the alumina industry (red mud). It was evaluated the capacity of transport oxygen and heat from the air reactor to the fuel reactor to promote gasification, and catalytic function for fuel gasification and syngas reforming. Four series of experiments took place in a Bench-scale fluidized bed at 950 °C and atmospheric pressure to examine the performance of the process and oxygen carrier. Those experiments demonstrated that the oxygen carrier was able to promote endothermic gasification due to its stable transport capacity of oxygen and heat during multiple redox cycles. Furthermore, its reduced forms could strongly catalyze internal syngas reforming. Red mud oxygen carrier has a high melting point and proper heat capacity; thus, it can be operated at a high temperature in the FR.

Shen et al. [75] combined Fe_2O_3 and CuO to produce a novel oxygen carrier for biomass gasification. It was found that the bimetallic oxides showed advantages over two mono-metallic oxygen carriers in the investigation. A ratio of 50 wt.% of Fe_2O_3 and 10 wt.% CuO was selected as an optimal ratio in the study. Furthermore, the best per-

formance was observed at the O/C ratio of 0.75 and 900 °C. However, the combined oxygen carrier performed the worst reactivity after three cycles. It was mainly attributed to sintering caused by Cu atomic that resulted in the reactivity decline. During steam gasification of biomass, undesirable CO_2 and tar would be produced, which will reduce the quality of the hydrogen stream and process efficiency. The adding of calcium oxide (CaO) could be used to overcome such challenges. Calcium oxide could work as a tar reforming catalyst and CO_2 sorbent, and thereby increase hydrogen-rich gas production. However, the deactivation of calcium oxide after the carbonation reaction is a challenge for continuous hydrogen production and economic issues [91]. A study was conducted to evaluate the effects of Fe/Ca ratio on hydrogen production from chemical looping gasification of rice straw [86]. Synthesized bimetallic Fe-Ca oxides were used as an oxygen carrier in the study. Its results found that there are two types of calcium ferrites ($Ca_2Fe_2O_5$ and $CaFe_2O_4$) formed with different ratios of Fe/Ca; and at the Fe:Ca ratio of 1:1, the highest hydrogen yield was obtained with 23.07 mmol/g biomass at 800 °C. Furthermore, the process temperature needed for the completed redox of $Ca_2Fe_2O_5$ was higher than 800 °C during chemical looping gasification with steam.

Wu et al. [85] investigated CLG of biomass using steam and CaO additive. It found that CaO showed a positive effect on gasification performance, and worked mainly as a CO_2 absorbent at low temperature but as a catalyst above 700 °C. It was also found to retard the sintering and porosity reduction of Fe_2O_3. A novel process was proposed to combine BCLG and CO_2 splitting using $Ca_2Fe_2O_5$ aerogel as an oxygen carrier [90]. In the process, pine wood was decomposed with the presence of an oxygen carrier in the FR to produce syngas, phenolic-rich bio-oil, and biochar. The reduced oxygen carrier was re-oxidized in the AR by CO_2 instead of air to generate CO. The results showed that $Ca_2Fe_2O_5$ aerogel is a promising oxygen carrier due to its redox activity, phase reversibility and cyclic stability. The study also investigated the mechanism of the synergistic enhancement of chemical looping-based CO_2 splitting using biomass cascade. It was found that the products from biomass fast pyrolysis and oxygen carrier reduction can further benefit oxygen carrier reduction and biomass conversion, respectively, as well as enhance CO_2 reduction in the AR.

Continuous operations in a 1.5 kW_{th} pilot were conducted for syngas production using pine wood as fuel and ilmenite [32], Fe_2O_3/Al_2O_3 [33] as oxygen carriers. A new method was proposed [32] for controlling the lattice oxygen used in the fuel reactor for syngas production by controlling the oxygen fed into the air reactor. The operating parameters in the BCLG in those studies were found that a high content of syngas components was produced during the process with 27–30% of H_2, 17–21% of CO for ilmenite and 37% of H_2, 21% of CO for Fe_2O_3/Al_2O_3 at autothermal conditions. It is noteworthy that tar generated in the studies was in the range of 0.9–3.0 g/Nm^3, being lower than that reported by other gasification technologies. Tian et al. [71] indicated that operating parameters strongly influence tar reforming in a BCLG process. The research results showed that tar decomposition is promoted at higher gasification temperatures, steam-to-biomass ratios and oxygen carrier-to-biomass ratios, resulting in the conversion of large molecular compounds into small ones. They also found that the presence of Cu in the oxygen carrier could enhance the decomposition of small molecular compounds in tar, while the Fe composition is favorable for a reduction in the yield of large molecular compounds in tar.

A novel oxygen carrier was synthesized for BCLG with additional functionalities of its reduced form acting as a catalyst for tar decomposition and a CO_2 adsorbent in syngas [130]. Fe_2O_3 is supported on silicalite-1 (Fe/S-1) was synthesized and characterized with different loadings as multi-functional materials to improve the quality of syngas and the efficiency of BCLG. The results found that the iron supported on silicalite-1 performed high thermal/chemical stability in a multi-cycle process and better catalytic activity in tar decomposition compared to the iron on a conventional silica support. An experimental investigation of CLG of torrefied woodchips using iron-based oxygen carriers was conducted in a bubbling fluidized bed reactor to evaluate the effects of operating parameters and the reactivity of oxygen carriers during the process [69]. The authors found that the operating

conditions strongly influence the process performance in terms of process efficiencies, gas yields. It was noted that the reactivity of iron-based oxygen carriers with different gaseous fuels follows the order $H_2 > CO > CH_4$. Additionally, the calcination temperature of oxygen carriers plays a key factor in the reactivity of oxygen carriers in the BCLG process. The other recent experimental studies of BCLG in the pilot-scale reactors are summarized and tabulated in Table 6.

Table 6. Summary of the key information of recent experimental studies in BCLG.

References	Biomass	Type of OC	Fuel Reactor	Air Reactor	Remarks
Huijun et al. [25] Interconnected FB (25 kW_{th})	Rice straw	NiO/A_3	Bubbling fluidized bed Operating temperature: 650–850 °C	High-velocity fluidized bed	• Max. syngas yield (0.33 Nm3/kg) at 750 °C. • Carbon conversion efficiency: max. value (60.28%) at SBR of 1.2 • The addition of CaO improved Biomass gasification performance.
Huseyin et al. [26] Interconnected FB (10 kW_{th})	Sawdust of Pine	Fe_2O_3/Al_2O_3	Bubbling fluidized bed Operating temperature: 750–900 °C	Fast fluidized bed	• H_2 production was the highest value at 870 °C. • Carbon conversion rate and gasification efficiency increased at higher temperatures. • Oxygen carrier used has good stability and resistance to sintering
He et al. [34]	Biomass	$NiFe_2O_4$	Fixed bed Operating temperature 700–900 °C	Fixed bed	• BCLG coupled with steam/CO_2 splitting. • Producing syngas and pure H_2 or CO separately.
Yan et al. [42]	Sawdust	$BaFe_2O_4/Al_2O_3$	Fixed bed reactor Operating temperature: 750–900 °C	-	• 30ABF showed high activity with char, but low reactivity with syngas. • Max. syngas yield was at 850 °C, O/B of 0.6 and steam fraction of 33.6%.
Liu et al. [43]	Pine wood + polyethylene	CaO/Fe_2O_3	Fixed bed reactor Operating temperature: 750–850 °C	Fixed bed reactor	• The optimal product was obtained at 850 °C and Fe_2O_3/feedstock of 0.25. • The addition of 75% polyethylene increased H_2 yield to 1.59 Nm^3/kg. • Cold gas efficiency and H_2/CO ratio were improved to 89.30% and 1.88.

Table 6. *Cont.*

References	Biomass	Type of OC	Fuel Reactor	Air Reactor	Remarks
Liu et al. [45]	Pine sawdust	$CaFe_2O_5$/MgO, ZnO, Al_2O_3	Fixed bed reactor Operating temperature: 850 °C	Fixed bed reactor	• The study evaluated the effects of Mg/Al/Zn oxides as support materials on $CaFe_2O_5$ reactivity in BCLG. • Al oxide promoted the oxygen release rate by breaking the OC structure, but the syngas selectivity was reduced. • ZnO showed higher reactivity in BCLG, but it was reduced into metal Zn before the reduction of the OC. • MgO addition improved the oxygen release ability of the OC, as well as increased the performance of BCLG.
Zeng et al. [68]	Pine sawdust	Natural hematite (Fe_2O_3)	Fixed bed reactor Operating temperature: 800 °C	-	• The moisture content of biomass increased the gas yield to 1.1646 Nm^3/kg while steam increased the ratio of H_2/CO by about 16%. • The diffusion of moisture content and steam showed opposite directions resulting in differing gasification reactivity.
Huang et al. [67]	Biomass char	Hematite (Fe_2O_3)	Fixed bed reactor Operating temperature: 850 °C	Fixed bed reactor	• Iron ore remained a good reactivity after 20 cycles. • Fe_2O_3 was reduced into Fe_3O_4 and FeO under steam and inert atmosphere, respectively, during CLG of biomass char.
Hedayati et al. [28]	Woody based biomass	Mn ores	300 W fluidized bed reactor 850–900 °C	Fluidized bed	• C_3 components were completely converted in all operating conditions. • Syngas yield obtained was promoted by high fuel flow rate and high temperature.

Table 6. *Cont.*

References	Biomass	Type of OC	Fuel Reactor	Air Reactor	Remarks
Hildor et al. [131]	Wood pellet	Steel converter slag (LD slag)	Batch fluidized bed 820–970 °C		• LD slag performed a high gasification rate/char conversion rate. • LD slag acted as a catalytic for water gas shift reaction. • Temperatures above 920 °C may increase the CO/C ratio and reduce the H_2/CO ratio. • No CO_2 adsorption at temperatures above 800 °C due to carbonation.

5.3. Simulation/Modeling Studies

Simulation and modeling of the CLG system are applied for prediction, evaluation, optimization. The most common configuration of chemical looping gasification mainly comprises two interconnected fluidized bed reactors and separators. Unlike the CLC process, minimal research has been conducted regarding the simulation and modeling of CLG by this time, particularly BCLG. The modeling of the system mainly includes its reaction kinetics, heat and mass transfer, and process performance. The most challenging issue is to describe the behavior of the gas-solid interactions inside the reactors. The model normally requires the configuration of the reactors, operational parameters, and the properties of gas and solids as input parameters to derive the combination of output parameters such as pressure and temperature distribution, composition and content of the stream, and energy and process efficiencies. The simulation of the gasification process can be developed based on [132]:

- Thermodynamic equilibrium
- Restricted thermodynamic equilibrium
- Kinetic mechanism
- Experimental data

Mathematical models of the CLG process available in the literature are mostly based on the computational fluid dynamic (CFD) technique. Currently, three main methods have been developed for the CFD modeling of fluidized-bed gasifiers such as the Eulerian-Eulerian approach, the Eulerian-Lagrangian approach, and the hybrid Eulerian-Lagrangian approach [133]. An alternative simulation approach for the gasification process is neural network modeling, but this method requires extensive experimental data, thus it is not often readily available [132]. An overall summary of simulation studies is tabulated in Table 7.

Table 7. Summary of the key information of recent simulation studies in BCLG.

References	Biomass	Type of OC	Type of Model	Remarks
Gopaul et al. [134]	Poultry litter	CaO and Fe_3O_4	ASPEN Plus (process modeling)	• The study compared the simulations of two CLG types for H_2 production. • The iron-based OC model showed higher syngas yield obtained with 2.54 kmol/kmol biomass while the first model with CaO sorbent produced H_2-enriched syngas with 92.45 mol.%.
Detchusananard et al. [135]	Wood residue	NiO/CaO	ASPEN Plus (process modeling)	• CaO added played two roles of tar cracking catalyst and CO_2 sorbent. • The simulation was developed based on the second-order respond surface model to analyze the process's energy efficiency performance. • The maximum energy efficiency performance was obtained at S/C ratio of 2.6, 636 °C, CaO/C ratio of 1 and OC/C ratio of 1.06.
Cormos et al. [136]	Sawdust Coal/sawdust	Ilmenite	Computational methods	• The models were developed for the techno-economic evaluation of H_2 and power co-generation based on BCLG. • The model used an ilmenite-based system to produce 400–500 MW net power with flexible H_2 output. • The energy efficiencies obtained up to 42% with 99% of the carbon capture rate.
Aghabararnejad et al. [137]	Biomass	Co_3O_4/Al_2O_3	ASPEN Plus (process modeling)	• A $7MW_{th}$ CLG model was developed in ASPEN Plus for techno-economic comparison with conventional systems. • The CLG system had a higher total capital investment, but the annual operating cost was lower compared to other systems.
Li et al. [138]	Dried poplar	Iron-based (Fe_2O_3)	ASPEN Plus (process modeling)	• A BDCL process was developed with the three-reactor configuration based on a multistage model to simulate the performance of the process. • The BDCL system showed a better performance compared to other conventional processes, and the feasibility of CO_2 capture.
Ge et al. [139]	Rice straw	Hematite (Fe_2O_3)	ASPEN Plus (process modeling)	• A CLG-BIGCC system was simulated using ASPEN Plus software. • The model results showed a better performance with up to 4% higher compared to existing BIGCC plants in China. • Five optimization schemes about CLG-BIGCC with nitrogen reinjection were proposed and investigated.

Table 7. *Cont.*

References	Biomass	Type of OC	Type of Model	Remarks
Kuo et al. [140]	Raw wood and torrefied wood	Iron-based	Matlab and ASPEN Plus	• A BSG-CLHP-CHP system was developed. • The results showed the effects of operating conditions on the process performance. • Hydrogen thermal efficiency and hydrogen yield of TW-derived syngas increased by 8.3% and 22%, respectively.
Li et al. [141]	Pine sawdust	Iron-based (Fe_2O_3)	Numerical method (CFD)	• The numerical method was developed to integrate the Eulerian multi-fluid model and the chemical reaction models to predict the concentrations of five gas components over time. • The model is validated well by the experimental data from the literature. • The results showed the continuous pine sawdust and mixing and segregation behaviors between fuel and OC particles strongly impact the concentrations of gas species and the evolution of the solid particle in the CLG system.
Li et al. [142]	Microalgae	Fe_2O_3	Numerical method	• A one-dimensional transient model for BCLG was developed based on hydrodynamics and chemical reactions. • The numerical model is to predict the time-varying outlet concentrations of gaseous components and process efficiencies. • Energy and exergy analyses were carried out based on the validated model.
Dieringer et al. [17]	Wood pellet	Ilmenite	Matlab and ASPEN Plus (equilibrium process modeling)	• Two approaches for autothermal CLG behavior were analyzed. • Evaluation of dilution of oxygen carrier with inert bed material. • Optimizing process efficiency.

Gopaul et al. [134] simulated two chemical looping gasification types using the ASPEN Plus simulation software for H_2 production. The research aimed to compare the performance of two systems. The first CLG model used in situ CO_2 capture utilizing a CaO sorbent for the production of CO_2-rich stream for sequestration, and the second model used iron-based oxygen carriers in redox cycles to 99.8% of Fe_3O_4 recovery and higher syngas yields. The main findings of the model were syngas yields, gas content. The model showed that the second model produced more syngas yields, while the concentration of H_2 in the first model was higher than that of the second one. Furthermore, sensitivity analyses of temperature and pressure were carried out on the main factors to determine optimal operating conditions. A model was implemented by Detchusananard et al. [135] to investigate the sorption enhanced biomass chemical looping gasification without heating and cooling system for enriched hydrogen production. During the steam gasification, calcium oxide and solid oxygen carrier (NiO) were added as bed material. The model of gasification was developed using the ASPEN Plus process simulator to analyze the energy efficiency performance of the process. It is noticed that the energy efficiency depended on the steam to carbon molar ratio and gasifying temperature.

A large-scale biomass chemical looping for hydrogen and power co-production was assessed by Cormos [136]. This study aimed to evaluate the techno-economic feasibility of hydrogen and power co-generation based on the biomass direct chemical looping (BDCL) concept. The net power output of a plant model of about 400–500 MW_{th} with a flexible hydrogen output in a range of 0 to 200 MW_{th} (LHV) was developed for the assessment of the BDCL and the benchmark power plant concept. Computational methods (using ChemCAD software) based on mass and energy balances were used for in-depth techno-economic analysis. The influence of various technical and economic parameters on economics was considered through the sensitivity study. A 7-MW_{th} CLG system was simulated to compare with conventional gasification processes using ASPEN Plus [137]. The CLG consists of a bubbling fluidized-bed gasifier and a fast fluidized-bed oxidized. Along with the comparison in the process performance, the economic aspects were also evaluated in the study. The results showed that the CLG system had a higher total capital investment compared to that of the conventional gasification process with pure oxygen but the annual operating cost of the CLG is $0.58M less resulting in the CLG as a feasible solution for biomass gasification.

Li et al. [138] developed a biomass direct chemical looping process (BDCL) for hydrogen and electricity co-production based on a multistage model using ASPEN Plus. The BDCL process configuration consists mainly of biomass preparation, the chemical looping system, heat recovery and steam generation (HRSG), gas cleanup units, and power generation systems. The BDCL process can produce hydrogen and/or electricity at any ratio, and it is 10–25% more efficient compared to conventional biomass combustion and gasification processes. The BDCL process also generated a high CO_2 concentration stream which could lead to a carbon-negative process from the life cycle standpoint. A system of biomass-based integrated gasification combined cycle coupling with CLG (CLG-BIGCC) for power generation was simulated by Ge et al. [139]. The system, mainly consisting of BCLG, gas cleaning, heat recovery steam generator (HRSG), and gas/steam turbine cycles, was developed with ASPEN Plus software. The simulation results were compared with the experimental data from a 25 kW_{th} interconnected fluidized bed reactor under the same operating conditions. The power efficiency of the CLG-BIGCC system was 33.51%, the gas turbine efficiency obtained 33.24% and the efficiency of the steam turbine was 34.01%. Those efficiencies are higher than the existing BIGCC plants in China with a range of 30–32%. Moreover, a sensitivity analysis on the CLG-BIGCC was carried out to obtain the optimal gasification conditions, and five optimization schemes about CLG-BIGCC with nitrogen reinjection were proposed and investigated. Kuo et al. [140] developed a new system for the co-production of electricity and hydrogen with CO_2 capture using biomass as fuel. The model integrated a biomass steam gasification (BSG) with an iron-based chemical looping hydrogen production (CLHP) system and a combined heat and power (CHP) system. The fuel used in the study was raw wood (RW) and torrefied wood (TW). The results were used to evaluate the effects of operating conditions on the process performance and syngas derived from RW and TW. Using TW can improve the BSG-CLHP-CHP system's performance. Hydrogen thermal efficiency and hydrogen yield of TW-derived syngas increased by 8.3% and 22%, respectively.

Li et al. [141] developed a numerical model to investigate biomass gasification with iron-based oxygen carrier in a bubbling bed reactor. The model integrated the Eulerian multi-fluid model and the chemical reaction models including the decomposition of biomass, gasification of char, water-gas-shift reaction and the heterogeneous reactions between gases and metal oxides. It is validated well by the experimental data from the literature. The results were used to analyze the impacts of the mixing and segregation behaviors between two solid phases on the gas composition distribution at various operating conditions. A one-dimensional transient model, including the hydrodynamics and chemical reactions, was developed for biomass gasification using chemical looping technology to investigate the outlet concentrations of gaseous species and efficiencies at various operating conditions [142]. In the study, the numerical model was validated

against the experimental results utilizing Fe_2O_3 as oxygen carrier and microalgae as fuel. Additionally, the validated model also analyzed energy and exergy values to evaluate the energy sources. The analysis showed that the presence of oxygen carrier can improve the quantity and quality of syngas. [1,2]

6. Conclusions and Future Prospects

Biomass has been considered as a potential renewable source to replace fossil fuels for energy generation and chemical production. Due to the carbon cycle of biomass, the use of biomass as a feedstock can achieve significant environmental benefits of mitigation of net greenhouse gas emissions. However, biomass is currently less attractive in conventional thermochemical processes since it owns low energy density, high moisture content, complex ash composition, and highly distributed resource.

The comprehensive summary of biomass chemical looping gasification basis and its developments through recent studies will be of great benefit for the readers. This study is structured to investigate key components in a BCLG process. Therefore, through the existing knowledge and recent research, the potentials and challenges of BCLG are summarized in this study, as follows:

- Description of principles and developments of biomass-based chemical looping gasification technology.
- Recent research strategies and achievements in biomass-based chemical looping gasification.
- Prospects and challenges of biomass-based chemical looping gasification towards commercialization.

As discussed in the study, chemical looping technology can produce high-quality syngas using for energy generation or chemical production. Thus, using biomass as a feedstock for chemical looping gasification has many potential advantages over the conventional methods in biomass conversion and coal-fueled chemical looping processes. However, the chemical looping technologies are mostly in the R&D phase since they remain several challenges. Oxygen carrier is a key factor in the chemical looping concept, the selection of suitable oxygen carrier materials is one of the most important issues in terms of redox behavior, stability, availability, process performance, costs, environmental, and safety aspects. Additionally, tar formation from biomass chemical looping gasification has been considered increasingly. Tars formed during the process cause serious problems for the BCLG system, resulting in a decrease in the process efficiency. However, research on tar formation and elimination in BCLG is still limited. A better understanding of tars and finding efficient approaches to minimize their effects on the system are necessary for the commercialization of BCLG. Numerous studies on the chemical looping process of biomass have been carried out over the years, and many various carriers were investigated in a pilot-scale system of chemical looping gasification plants for their feasibility. The recent developments of biomass CLG have been carried out on a pilot-scale system ranging from a few kW to MW. This is the basis for the massive scale-up of the process that is necessary for commercial power plant and syngas production along with CO_2 capture. Furthermore, syngas cleanup technologies have been improving to mitigate problems regarding failure and blockage, as well as the loss of efficiency. Additionally, economic evaluation for each specific biomass feedstock, operational flexibility in the variation of feedstock composition is to respond to the changes in supply and demand of the feedstock market [9]. Those challenges should be solved to meet the coming future regarding the commercialization of this technology. Hence, chemical looping gasification using biomass as feedstock shows promising applications in the future in the continued fight against climate change [2].

Author Contributions: N.M.N. is responsible for administration, conceptualization, the original draft, and the applied methodology. F.A. supported the writing process with his review and edits. P.D. supported the writing process with his review and edits. B.E. supervised the research progress the presented work. All authors have read and agreed to the published version of the manuscript.

Funding: This work received no external funding. The corresponding author would like to thank the Techical University of Darmstadt, enabling the open-access publication of this paper.

Institutional Review Board Statement: Not applicable.

Informed Consent Statement: Not applicable.

Data Availability Statement: The data presented in this study are available in the article.

Acknowledgments: The authors would like to thank Technische Universität Darmstadt and the Institute for Energy Systems and Technology for support.

Conflicts of Interest: The authors declare no conflict of interest.

Abbreviations

Abbreviations

AR	Air reactor
BCLG	Biomass chemical looping gasification
CFD	Computational fluid dynamics
CLC	Chemical looping combustion
CLG	Chemical looping gasification
CLR	Chemical looping reforming
CGC	Cold gas cleanup
CV	Calorific value
FR	Fuel reactor
GHG	Greenhouse gas
HHV	Higher heating value
LHV	Lower heating value
IEO	International energy outlook
LM	Looping material
HGC	Hot gas cleanup
OC	Oxygen carrier
WGC	Warm gas cleanup
TGA	Thermogravimetric analysis

References

1. United Nations. Paris Climate Agreement. 2015. Available online: https://unfccc.int/process-and-meetings/the-paris-agreement/the-paris-agreement (accessed on 10 May 2021).
2. Administration USEI. *International Energy Outlook 2016 with Projections to 2040*; U.S. Energy Information Administration: Washington, DC, USA, 2016; p. 290.
3. Federal Ministry for the Environment NC, Building and Nuclear Safety. *Climate Action Plan 2050. Principles and Goals of the German Government's Climate Policy*; Federal Ministry for the Environment, Nature Conservation, Building and Nuclear Safety: Berlin, Germany, 2016; p. 92.
4. Lamers, P.; Hoefnagels, R.; Junginger, M.; Hamelinck, C.; Faaij, A. Global solid biomass trade for energy by 2020: An assessment of potential import streams and supply costs to North-West Europe under different sustainability constraints. *GCB Bioenergy* **2015**, *7*. [CrossRef]
5. Kumar, A.; Jones, D.D.; Hanna, M.A. Thermochemical Biomass Gasification: A Review of the Current Status of the Technology. *Energies* **2009**, *2*, 556–581. [CrossRef]
6. Mendiara, T.; García-Labiano, F.; Abad, A.; Gayán, P.; de Diego, L.F.; Izquierdo, M.; Adánez, J. Negative CO2 emissions through the use of biofuels in chemical looping technology: A review. *Appl. Energy* **2018**, *232*, 657–684. [CrossRef]
7. Mattison, T.; Hildor, F.; Li, Y.; Linderholm, C. Negative emissions of carbon dioxide through chemical-looping combustion (CLC) and gasification (CLG) using oxygen carriers based on manganese and iron. *Mitig. Adapt. Strat. Glob. Chang.* **2020**, *25*, 497–517. [CrossRef]
8. McKendry, P. Energy production from biomass (part 2): Conversion technologies. *Bioresour. Technol.* **2002**, *83*, 47–54. [CrossRef]
9. Zhao, X.; Zhou, H.; Sikarwar, V.S.; Zhao, M.; Park, A.-H.A.; Fennell, P.S.; Shen, L.; Fan, L.-S. Biomass-based chemical looping technologies: The good, the bad and the future. *Energy Environ. Sci.* **2017**, *10*, 1885–1910. [CrossRef]
10. Ishida, M.; Zheng, D.; Akehata, T. Evaluation of a chemical-looping-combustion power-generation system by graphic exergy analysis. *Energy* **1987**, *12*, 147–154. [CrossRef]

11. Adanez, J.; Abad, A.; García-Labiano, F.; Gayan, P.; de Diego, L.F. Progress in Chemical-Looping Combustion and Reforming technologies. *Prog. Energy Combust. Sci.* **2012**, *38*, 215–282. [CrossRef]
12. Nandya, A.; Lohaa, C.; Gub, S.; Sarkarc, P.; Karmakara, M.K.; Chatterjeea, P.K. Present status and overview of Chemical Looping Combustion technology. *Renew. Sustain. Energy Rev.* **2016**, *59*, 597–619. [CrossRef]
13. Pujara, M.; Sheth, M.; Rachchh, N.; Bhoraniya, R.; Harichandan, A.B. Chemical looping reforming (CLR) system for H2 production—A review. In *Blockchain Technology and Innovations in Business Processes*; Springer: Berlin, Germany, 2020; pp. 267–276.
14. Luo, M.; Yi, Y.; Wang, S.; Wang, Z.; Du, M.; Pan, J.; Wang, Q. Review of hydrogen production using chemical-looping technology. *Renew. Sustain. Energy Rev.* **2018**, *81*, 3186–3214. [CrossRef]
15. Lin, Y.; Wang, H.; Wang, Y.; Huo, R.; Huang, Z.; Liu, M.; Wei, G.; Zhao, Z.; Li, H.; Fang, Y. Review of Biomass Chemical Looping Gasification in China. *Energy Fuels* **2020**, *34*, 7847–7862. [CrossRef]
16. Cuadrat, A.; Abad, A.; García-Labiano, F.; Gayán, P.; de Diego, L.; Adánez, J. Relevance of the coal rank on the performance of the in situ gasification chemical-looping combustion. *Chem. Eng. J.* **2012**, *195*, 91–102. [CrossRef]
17. Dieringer, P.; Marx, F.; Alobaid, F.; Ströhle, J.; Epple, B. Process Control Strategies in Chemical Looping Gasification—A Novel Process for the Production of Biofuels Allowing for Net Negative CO2 Emissions. *Appl. Sci.* **2020**, *10*, 4271. [CrossRef]
18. Protasova, L.; Snijkers, F. Recent developments in oxygen carrier materials for hydrogen production via chemical looping processes. *Fuel* **2016**, *181*, 75–93. [CrossRef]
19. Mendiara, T.; Abad, A.; de Diego, L.F.; García-Labiano, F.; Gayan, P.; Adanez, J. Biomass combustion in a CLC system using an iron ore as an oxygen carrier. *Int. J. Greenh. Gas Control.* **2013**, *19*, 322–330. [CrossRef]
20. Huang, Z.; Zheng, A.; Deng, Z.; Wei, G.; Zhao, K.; Chen, D.; He, F.; Zhao, Z.; Li, H.; Li, F. In-situ removal of toluene as a biomass tar model compound using NiFe2O4 for application in chemical looping gasification oxygen carrier. *Energy* **2020**, *190*, 116360. [CrossRef]
21. Molino, A.; Chianese, S.; Musmarra, D. Biomass gasification technology: The state of the art overview. *J. Energy Chem.* **2016**, *25*, 10–25. [CrossRef]
22. Parthasarathy, P.; Narayanan, K.S. Hydrogen production from steam gasification of biomass: Influence of process parameters on hydrogen yield—A review. *Renew. Energy* **2014**, *66*, 570–579. [CrossRef]
23. Wolf, J. CO2 Mitigation in Advanced Power Cycles. Ph.D. Thesis, KTH-Royal Institute of Technology, Kemiteknik, Stockholm, Sweden, 2004.
24. Noorman, S.; Annaland, M.V.S.; Kuipers, H. Packed Bed Reactor Technology for Chemical-Looping Combustion. *Ind. Eng. Chem. Res.* **2007**, *46*, 4212–4220. [CrossRef]
25. Huijun, G.; Laihong, S.; Fei, F.; Shouxi, J. Experiments on biomass gasification using chemical looping with nickel-based oxygen carrier in a 25 kWth reactor. *Appl. Therm. Eng.* **2015**, *85*, 52–60. [CrossRef]
26. Huseyin, S.; Wei, G.-Q.; Li, H.-B.; He, F.; Huang, Z. Chemical-looping gasification of biomass in a 10 kWth interconnected fluidized bed reactor using Fe2O3/Al2O3 oxygen carrier. *J. Fuel Chem. Technol.* **2014**, *42*, 922–931. [CrossRef]
27. Zeng, J.; Xiao, R.; Zhang, H.; Wang, Y.; Zeng, D.; Ma, Z. Chemical looping pyrolysis-gasification of biomass for high H2/CO syngas production. *Fuel Process. Technol.* **2017**, *168*, 116–122. [CrossRef]
28. Hedayati, A.; Soleimanisalim, A.H.; Linderholm, C.J.; Mattisson, T.; Lyngfelt, A. Experimental evaluation of manganese ores for chemical looping conversion of synthetic biomass volatiles in a 300 W reactor system. *J. Environ. Chem. Eng.* **2021**, *9*, 105112. [CrossRef]
29. Marx, F.; Dieringer, P.; Ströhle, J.; Epple, B. Design of a 1 MWth pilot plant for Chemical looping gasification of Biogenic Residues. *Energies* **2021**, *14*, 2581. [CrossRef]
30. Acharya, B.; Dutta, A.; Basu, P. Chemical-Looping Gasification of Biomass for Hydrogen-Enriched Gas Production with In-Process Carbon Dioxide Capture. *Energy Fuels* **2009**, *23*, 5077–5083. [CrossRef]
31. Wei, G.; He, F.; Zhao, Z.; Huang, Z.; Zheng, A.; Zhao, K.; Li, H. Performance of Fe–Ni bimetallic oxygen carriers for chemical looping gasification of biomass in a 10 kWth interconnected circulating fluidized bed reactor. *Int. J. Hydrogen Energy* **2015**, *40*, 16021–16032. [CrossRef]
32. Condori, O.; García-Labiano, F.; de Diego, L.F.; Izquierdo, M.T.; Abad, A.; Adánez, J. Biomass chemical looping gasification for syngas production using ilmenite as oxygen carrier in a 1.5 kWth unit. *Chem. Eng. J.* **2021**, *405*, 126679. [CrossRef]
33. Samprón, I.; de Diego, L.F.; García-Labiano, F.; Izquierdo, M.T.; Abad, A.; Adánez, J. Biomass Chemical Looping Gasification of pine wood using a synthetic Fe2O3/Al2O3 oxygen carrier in a continuous unit. *Bioresour. Technol.* **2020**, *316*, 123908. [CrossRef] [PubMed]
34. He, F.; Huang, Z.; Wei, G.; Zhao, K.; Wang, G.; Kong, X.; Feng, Y.; Tan, H.; Hou, S.; Lv, Y.; et al. Biomass chemical-looping gasification coupled with water/CO2-splitting using NiFe2O4 as an oxygen carrier. *Energy Convers. Manag.* **2019**, *201*, 112157. [CrossRef]
35. Wolf, J.; Yan, J. Parametric study of chemical looping combustion for tri-generation of hydrogen, heat, and electrical power with CO2 capture. *Int. J. Energy Res.* **2005**, *29*, 739–753. [CrossRef]
36. Cormos, C.-C. Hydrogen production from fossil fuels with carbon capture and storage based on chemical looping systems. *Int. J. Hydrogen Energy* **2011**, *36*, 5960–5971. [CrossRef]
37. Chiesa, P.; Lozza, G.; Malandrino, A.; Romano, M.C.; Piccolo, V. Three-reactors chemical looping process for hydrogen production. *Int. J. Hydrogen Energy* **2008**, *33*, 2233–2245. [CrossRef]

38. Xiang, W.; Chen, S.; Xue, Z.; Sun, X. Investigation of coal gasification hydrogen and electricity co-production plant with three-reactors chemical looping process. *Int. J. Hydrogen Energy* **2010**, *35*, 8580–8591. [CrossRef]
39. Fan, L.-S.; Li, F. Chemical Looping Technology and Its Fossil Energy Conversion Applications. *Ind. Eng. Chem. Res.* **2010**, *49*, 10200–10211. [CrossRef]
40. Gupta, P.; Velazquez-Vargas, L.G.; Fan, L.-S. Syngas Redox (SGR) Process to Produce Hydrogen from Coal Derived Syngas. *Energy Fuels* **2007**, *21*, 2900–2908. [CrossRef]
41. Li, F.; Kim, H.R.; Sridhar, D.; Wang, F.; Zeng, L.; Chen, J.; Fan, L.-S. Syngas Chemical Looping Gasification Process: Oxygen Carrier Particle Selection and Performance. *Energy Fuels* **2009**, *23*, 4182–4189. [CrossRef]
42. Yan, J.; Sun, R.; Shen, L.; Bai, H.; Jiang, S.; Xiao, Y.; Song, T. Hydrogen-rich syngas production with tar elimination via biomass chemical looping gasification (BCLG) using BaFe2O4/Al2O3 as oxygen carrier. *Chem. Eng. J.* **2020**, *387*, 124107. [CrossRef]
43. Liu, Q.; Hu, C.; Peng, B.; Liu, C.; Li, Z.; Wu, K.; Zhang, H.; Xiao, R. High H2/CO ratio syngas production from chemical looping co-gasification of biomass and polyethylene with CaO/Fe2O3 oxygen carrier. *Energy Convers. Manag.* **2019**, *199*, 111951. [CrossRef]
44. Huang, Z.; He, F.; Feng, Y.; Zhao, K.; Zheng, A.; Chang, S.; Wei, G.; Zhao, Z.; Li, H. Biomass Char Direct Chemical Looping Gasification Using NiO-Modified Iron Ore as an Oxygen Carrier. *Energy Fuels* **2014**, *28*, 183–191. [CrossRef]
45. Liu, G.; Liao, Y.; Wu, Y.; Ma, X. Enhancement of Ca2Fe2O5 oxygen carrier through Mg/Al/Zn oxide support for biomass chemical looping gasification. *Energy Convers. Manag.* **2019**, *195*, 262–273. [CrossRef]
46. Wang, S.; Song, T.; Yin, S.; Hartge, E.-U.; Dymala, T.; Shen, L.; Heinrich, S.; Werther, J. Syngas, tar and char behavior in chemical looping gasification of sawdust pellet in fluidized bed. *Fuel* **2020**, *270*, 117464. [CrossRef]
47. McKendry, P. Energy production from biomass (part 1): Overview of biomass. *Bioresour. Technol.* **2002**, *83*, 37–46. [CrossRef]
48. Vassilev, S.V.; Baxter, D.; Andersen, L.K.; Vassileva, C.G. An overview of the chemical composition of biomass. *Fuel* **2010**, *89*, 913–933. [CrossRef]
49. Woolcock, P.J.; Brown, R.C. A review of cleaning technologies for biomass-derived syngas. *Biomass Bioenergy* **2013**, *52*, 54–84. [CrossRef]
50. Sharma, S.; Dolan, M.; Park, D.; Morpeth, L.; Ilyushechkin, A.; McLennan, K.; Harris, D.; Thambimuthu, K. A critical review of syngas cleaning technologies—Fundamental limitations and practical problems. *Powder Technol.* **2008**, *180*, 115–121. [CrossRef]
51. Asadullah, M. Barriers of commercial power generation using biomass gasification gas: A review. *Renew. Sustain. Energy Rev.* **2014**, *29*, 201–215. [CrossRef]
52. Milne, T.A.; Evans, R.J.; Abatzaglou, N. *Biomass Gasifier "Tars": Their Nature, Formation, and Conversion*; National Renewable Energy Laboratory: Golden, CO, USA, 1998.
53. Nunes, L.; Matias, J.; Catalão, J.P.S. Biomass combustion systems: A review on the physical and chemical properties of the ashes. *Renew. Sustain. Energy Rev.* **2016**, *53*, 235–242. [CrossRef]
54. Heakal, F.E.-T.; Fouda, A.; Radwan, M. Inhibitive effect of some thiadiazole derivatives on C-steel corrosion in neutral sodium chloride solution. *Mater. Chem. Phys.* **2011**, *125*, 26–36. [CrossRef]
55. Roos, C.J. *Clean Heat and Power Using Biomass Gasification for Industrial and Agricultural Project*; U.S. Department of Energy, Northwest CHP Application Center: Washington, DC, USA, 2010; p. 64.
56. Schmid, J.C.; Wolfesberger, U.; Koppatz, S.; Pfeifer, C.; Hofbauer, H. Variation of feedstock in a dual fluidized bed steam gasifier-influence on product gas, tar content, and composition. *Environ. Prog. Sustain. Energy* **2012**, *31*, 205–215. [CrossRef]
57. Ran, J.; Fu, F.; Qin, C.; Zhang, P.; Yang, L.; Wang, W. Evaluation of CuO/MgAl2O4 in Biomass Chemical Looping Gasification with Oxygen Uncoupling. *Bioresources* **2016**, *11*, 2109–2123. [CrossRef]
58. Zhang, B.; Wu, Z.; Zhang, J.; Guo, W.; Yang, B. Chemical Looping with Oxygen Uncoupling of the Lignocellulosic Biomass Main Model Compound: Product Distribution and Kinetic Analysis on Lignin. *Energy Fuels* **2020**, *34*, 10968–10979. [CrossRef]
59. Wang, M.; Li, T.; Xiao, Y.; Wang, W. Study of chemical looping co-gasification of lignite and rice husk with Cu-Ni oxygen carrier. *Int. J. Low-Carbon Technol.* **2021**. [CrossRef]
60. Mendiara, T.; Johansen, J.M.; Utrilla, R.; Jensen, A.D.; Glarborg, P. Evaluation of different oxygen carriers for biomass tar reforming (II): Carbon deposition in experiments with methane and other gases. *Fuel* **2011**, *90*, 1370–1382. [CrossRef]
61. Park, H.J.; Park, S.H.; Sohn, J.M.; Park, J.; Jeon, J.-K.; Kim, S.-S.; Park, Y.-K. Steam reforming of biomass gasification tar using benzene as a model compound over various Ni supported metal oxide catalysts. *Bioresour. Technol.* **2010**, *101*, S101–S103. [CrossRef] [PubMed]
62. Sonoyama, N.; Nobuta, K.; Kimura, T.; Hosokai, S.; Hayashi, J.-I.; Tago, T.; Masuda, T. Production of chemicals by cracking pyrolytic tar from Loy Yang coal over iron oxide catalysts in a steam atmosphere. *Fuel Process. Technol.* **2011**, *92*, 771–775. [CrossRef]
63. Wang, P.; Means, N.; Shekhawat, D.; Berry, D.; Massoudi, M. Chemical-Looping Combustion and Gasification of Coals and Oxygen Carrier Development: A Brief Review. *Energies* **2015**, *8*, 10605–10635. [CrossRef]
64. Guo, Q.; Cheng, Y.; Liu, Y.; Jia, W.; Ryu, H.-J. Coal Chemical Looping Gasification for Syngas Generation Using an Iron-Based Oxygen Carrier. *Ind. Eng. Chem. Res.* **2013**, *53*, 78–86. [CrossRef]
65. Voitic, G.; Hacker, V. Recent advancements in chemical looping water splitting for the production of hydrogen. *RSC Adv.* **2016**, *6*, 98267–98296. [CrossRef]

66. Zhu, X.; Li, K.; Neal, L.M.; Li, F. Perovskites as Geo-inspired Oxygen Storage Materials for Chemical Looping and Three-Way Catalysis: A Perspective. *ACS Catal.* **2018**, *8*, 8213–8236. [CrossRef]
67. Huang, Z.; Zhang, Y.; Fu, J.; Yu, L.; Chen, M.; Liu, S.; He, F.; Chen, D.; Wei, G.; Zhao, K.; et al. Chemical looping gasification of biomass char using iron ore as an oxygen carrier. *Int. J. Hydrogen Energy* **2016**, *41*, 17871–17883. [CrossRef]
68. Zeng, J.; Xiao, R.; Zhang, H.; Chen, X.; Zeng, D.; Ma, Z. Syngas production via biomass self-moisture chemical looping gasification. *Biomass-Bioenergy* **2017**, *104*, 1–7. [CrossRef]
69. Nguyen, N.M.; Alobaid, F.; Epple, B. Chemical looping gasification of torrefied woodchips in a bubbling fluidized bed test rig using iron-based oxygen carriers. *Renew. Energy* **2021**, *172*, 34–45. [CrossRef]
70. Huang, Z.; Xu, G.; Deng, Z.; Zhao, K.; He, F.; Chen, D.; Wei, G.; Zheng, A.; Zhao, Z.; Li, H. Investigation on gasification performance of sewage sludge using chemical looping gasification with iron ore oxygen carrier. *Int. J. Hydrogen Energy* **2017**, *42*, 25474–25491. [CrossRef]
71. Tian, X.; Niu, P.; Ma, Y.; Zhao, H. Chemical-looping gasification of biomass: Part II. Tar yields and distributions. *Biomass-Bioenergy* **2018**, *108*, 178–189. [CrossRef]
72. Guo, L.; Zhao, H.; Zheng, C. Synthesis Gas Generation by Chemical-Looping Reforming of Biomass with Natural Copper Ore as Oxygen Carrier. *Waste Biomass-Valorization* **2015**, *6*, 81–89. [CrossRef]
73. Chuayboon, S.; Abanades, S.; Rodat, S. Solar chemical looping gasification of biomass with the ZnO/Zn redox system for syngas and zinc production in a continuously-fed solar reactor. *Fuel* **2018**, *215*, 66–79. [CrossRef]
74. Huang, Z.; Deng, Z.; He, F.; Chen, D.; Wei, G.; Zhao, K.; Zheng, A.; Zhao, Z.; Li, H. Reactivity investigation on chemical looping gasification of biomass char using nickel ferrite oxygen carrier. *Int. J. Hydrogen Energy* **2017**, *42*, 14458–14470. [CrossRef]
75. Shen, T.; Ge, H.; Shen, L. Characterization of combined Fe-Cu oxides as oxygen carrier in chemical looping gasification of biomass. *Int. J. Greenh. Gas Control.* **2018**, *75*, 63–73. [CrossRef]
76. Adanez, J.; de Diego, L.F.; García-Labiano, F.; Gayan, P.; Abad, A.; Palacios, J.M. Selection of Oxygen Carriers for Chemical-Looping Combustion. *Energy Fuels* **2004**, *18*, 371–377. [CrossRef]
77. Shen, L.; Wu, J.; Gao, Z.; Xiao, J. Reactivity deterioration of NiO/Al2O3 oxygen carrier for chemical looping combustion of coal in a 10kWth reactor. *Combust. Flame* **2009**, *156*, 1377–1385. [CrossRef]
78. Zhao, H.; Guo, L.; Zou, X. Chemical-looping auto-thermal reforming of biomass using Cu-based oxygen carrier. *Appl. Energy* **2015**, *157*, 408–415. [CrossRef]
79. Yu, Z.; Li, C.; Fang, Y.; Huang, J.; Wang, Z. Reduction Rate Enhancements for Coal Direct Chemical Looping Combustion with an Iron Oxide Oxygen Carrier. *Energy Fuels* **2012**, *26*, 2505–2511. [CrossRef]
80. Gu, H.; Shen, L.; Xiao, J.; Zhang, S.; Song, T.; Chen, D. Iron ore as oxygen carrier improved with potassium for chemical looping combustion of anthracite coal. *Combust. Flame* **2012**, *159*, 2480–2490. [CrossRef]
81. Andrus, H.E.; Chiu, J.H.; Thibeault, P.R.; Brautsch, A. Alstom's Calcium Oxide Chemical Looping Combustion Coal Power Technology Development. In Proceedings of the 34th International Technical Conference on Clean Coal and Fuel Systems, Clearwater Beach, FL, USA, 31 May–4 June 2009; pp. 1179–1900.
82. Yu, Z.; Yang, Y.; Yang, S.; Zhang, Q.; Zhao, J.; Fang, Y.; Hao, X.; Guan, G. Iron-based oxygen carriers in chemical looping conversions: A review. *Carbon Resour. Convers.* **2019**, *2*, 23–34. [CrossRef]
83. Chen, Y.; Galinsky, N.; Wang, Z.; Li, F. Investigation of perovskite supported composite oxides for chemical looping conversion of syngas. *Fuel* **2014**, *134*, 521–530. [CrossRef]
84. Chen, S.; Shi, Q.; Xue, Z.; Sun, X.; Xiang, W. Experimental investigation of chemical-looping hydrogen generation using Al2O3 or TiO2 -supported iron oxides in a batch fluidized bed. *Int. J. Hydrogen Energy* **2011**, *36*, 8915–8926. [CrossRef]
85. Wu, Y.; Liao, Y.; Liu, G.; Ma, X. Syngas production by chemical looping gasification of biomass with steam and CaO additive. *Int. J. Hydrogen Energy* **2018**, *43*, 19375–19383. [CrossRef]
86. Hu, Q.; Shen, Y.; Chew, J.W.; Ge, T.; Wang, C.-H. Chemical looping gasification of biomass with Fe2O3/CaO as the oxygen carrier for hydrogen-enriched syngas production. *Chem. Eng. J.* **2020**, *379*, 122346. [CrossRef]
87. Kang, K.-S.; Kim, C.-H.; Bae, K.-K.; Cho, W.-C.; Kim, S.-H.; Park, C.-S. Oxygen-carrier selection and thermal analysis of the chemical-looping process for hydrogen production. *Int. J. Hydrogen Energy* **2010**, *35*, 12246–12254. [CrossRef]
88. Zheng, Z.; Luo, L.; Feng, A.; Iqbal, T.; Li, Z.; Qin, W.; Dong, C.; Zhang, S.; Xiao, X. CaO-Assisted Alkaline Liquid Waste Drives Corn Stalk Chemical Looping Gasification for Hydrogen Production. *ACS Omega* **2020**, *5*, 24403–24411. [CrossRef]
89. Acharya, B.; Dutta, A.; Basu, P. An investigation into steam gasification of biomass for hydrogen enriched gas production in presence of CaO. *Int. J. Hydrogen Energy* **2010**, *35*, 1582–1589. [CrossRef]
90. Sun, Z.; Wu, X.; Russell, C.K.; Dyar, M.D.; Sklute, E.C.; Toan, S.; Fan, M.; Duan, L.; Xiang, W. Synergistic enhancement of chemical looping-based CO2 splitting with biomass cascade utilization using cyclic stabilized Ca2Fe2O5 aerogel. *J. Mater. Chem. A* **2019**, *7*, 1216–1226. [CrossRef]
91. Udomsirichakorn, J.; Salam, P.A. Review of hydrogen-enriched gas production from steam gasification of biomass: The prospect of CaO-based chemical looping gasification. *Renew. Sustain. Energy Rev.* **2014**, *30*, 565–579. [CrossRef]
92. Han, L.; Wang, Q.; Yang, Y.; Yu, C.; Fang, M.; Luo, Z. Hydrogen production via CaO sorption enhanced anaerobic gasification of sawdust in a bubbling fluidized bed. *Int. J. Hydrogen Energy* **2011**, *36*, 4820–4829. [CrossRef]

93. Sun, Z.; Chen, S.; Russell, C.K.; Hu, J.; Rony, A.H.; Tan, G.; Chen, A.; Duan, L.; Boman, J.; Tang, J.; et al. Improvement of H2-rich gas production with tar abatement from pine wood conversion over bi-functional Ca2Fe2O5 catalyst: Investigation of inner-looping redox reaction and promoting mechanisms. *Appl. Energy* **2018**, *212*, 931–943. [CrossRef]
94. Wu, J.; Bai, L.; Tian, H.; Riley, J.; Siriwardane, R.; Wang, Z.; He, T.; Li, J.; Zhang, J.; Wu, J. Chemical looping gasification of lignin with bimetallic oxygen carriers. *Int. J. Greenh. Gas Control* **2020**, *93*, 102897. [CrossRef]
95. He, F.; Galinsky, N.; Li, F. Chemical looping gasification of solid fuels using bimetallic oxygen carrier particles—Feasibility assessment and process simulations. *Int. J. Hydrogen Energy* **2013**, *38*, 7839–7854. [CrossRef]
96. Huang, Z.; He, F.; Zhu, H.; Chen, D.; Zhao, K.; Wei, G.; Feng, Y.; Zheng, A.; Zhao, Z.; Li, H. Thermodynamic analysis and thermogravimetric investigation on chemical looping gasification of biomass char under different atmospheres with Fe2O3 oxygen carrier. *Appl. Energy* **2015**, *157*, 546–553. [CrossRef]
97. Dueso, C.; Thompson, C.; Metcalfe, I. High-stability, high-capacity oxygen carriers: Iron oxide-perovskite composite materials for hydrogen production by chemical looping. *Appl. Energy* **2015**, *157*, 382–390. [CrossRef]
98. de Diego, L.F.; García-Labiano, F.; Adánez, J.; Gayán, P.; Abad, A.; Corbella, B.M.; Palacios, J.M. Development of Cu-based oxygen carriers for chemical-looping combustion. *Fuel* **2004**, *83*, 1749–1757. [CrossRef]
99. Wang, B.; Yan, R.; Lee, D.H.; Liang, D.T.; Zheng, Y.; Zhao, H.; Zheng, C. Thermodynamic Investigation of Carbon Deposition and Sulfur Evolution in Chemical Looping Combustion with Syngas. *Energy Fuels* **2008**, *22*, 1012–1020. [CrossRef]
100. de Diego, L.F.; Gayán, P.; García-Labiano, F.; Celaya, J.; Abad, A.; Adánez, J. Impregnated CuO/Al2O3 Oxygen Carriers for Chemical-Looping Combustion: Avoiding Fluidized Bed Agglomeration. *Energy Fuels* **2005**, *19*, 1850–1856. [CrossRef]
101. Gu, H.; Shen, L.; Zhong, Z.; Zhou, Y.; Liu, W.; Niu, X.; Ge, H.; Jiang, S.; Wang, L. Interaction between biomass ash and iron ore oxygen carrier during chemical looping combustion. *Chem. Eng. J.* **2015**, *277*, 70–78. [CrossRef]
102. Niu, X.; Shen, L.; Gu, H.; Jiang, S.; Xiao, J. Characteristics of hematite and fly ash during chemical looping combustion of sewage sludge. *Chem. Eng. J.* **2015**, *268*, 236–244. [CrossRef]
103. Niu, X.; Shen, L.; Gu, H.; Song, T.; Xiao, J. Sewage sludge combustion in a CLC process using nickel-based oxygen carrier. *Chem. Eng. J.* **2015**, *260*, 631–641. [CrossRef]
104. Florin, N.; Harris, A.T. Enhanced hydrogen production from biomass with in situ carbon dioxide capture using calcium oxide sorbents. *Chem. Eng. Sci.* **2008**, *63*, 287–316. [CrossRef]
105. de Lasa, H.; Salaices, E.; Mazumder, J.; Lucky, R. Catalytic Steam Gasification of Biomass: Catalysts, Thermodynamics and Kinetics. *Chem. Rev.* **2011**, *111*, 5404–5433. [CrossRef] [PubMed]
106. Rinaldi, R.; Schüth, F. Design of solid catalysts for the conversion of biomass. *Energy Environ. Sci.* **2009**, *2*, 610–626. [CrossRef]
107. Brown, R. Biochar production technology. In *Biochar for Environmental Management*; Routledge: London, UK, 2009; p. 448.
108. Burhenne, L.; Messmer, J.; Aicher, T.; Laborie, M.-P. The effect of the biomass components lignin, cellulose and hemicellulose on TGA and fixed bed pyrolysis. *J. Anal. Appl. Pyrolysis* **2013**, *101*, 177–184. [CrossRef]
109. Mok, W.S.-L.; Antal, M.J. Effects of pressure on biomass pyrolysis. II. Heats of reaction of cellulose pyrolysis. *Thermochim. Acta* **1983**, *68*, 165–186. [CrossRef]
110. Volpe, R.; Zabaniotou, A.A.; Skoulou, V.K. Synergistic Effects between Lignin and Cellulose during Pyrolysis of Agricultural Waste. *Energy Fuels* **2018**, *32*, 8420–8430. [CrossRef]
111. Pasangulapati, V.; Ramachandriya, K.D.; Kumar, A.; Wilkins, M.; Jones, C.L.; Huhnke, R.L. Effects of cellulose, hemicellulose and lignin on thermochemical conversion characteristics of the selected biomass. *Bioresour. Technol.* **2012**, *114*, 663–669. [CrossRef] [PubMed]
112. Chang, A.C.-C.; Chang, H.-F.; Lin, F.-J.; Lin, K.-H.; Chen, C.-H. Biomass gasification for hydrogen production. *Int. J. Hydrogen Energy* **2011**, *36*, 14252–14260. [CrossRef]
113. Raut, M.K.; Basu, P.; Acharya, B. The Effect of Torrefaction Pre-Treatment on the Gasification of Biomass. *Int. J. Renew. Energy Biofuels* **2016**, *2016*, 1–14. [CrossRef]
114. Lv, P.; Xiong, Z.; Chang, J.; Wu, C.; Chen, Y.; Zhu, J. An experimental study on biomass air–steam gasification in a fluidized bed. *Bioresour. Technol.* **2004**, *95*, 95–101. [CrossRef]
115. Hernández, J.J.; Aranda-Almansa, G.; Bula, A. Gasification of biomass wastes in an entrained flow gasifier: Effect of the particle size and the residence time. *Fuel Process. Technol.* **2010**, *91*, 681–692. [CrossRef]
116. Di Blasi, C. Kinetic and Heat Transfer Control in the Slow and Flash Pyrolysis of Solids. *Ind. Eng. Chem. Res.* **1996**, *35*, 37–46. [CrossRef]
117. Ge, H.; Guo, W.; Shen, L.; Song, T.; Xiao, J. Biomass gasification using chemical looping in a 25kWth reactor with natural hematite as oxygen carrier. *Chem. Eng. J.* **2016**, *286*, 174–183. [CrossRef]
118. Nguyen, N.M.; Alobaid, F.; May, J.; Peters, J.; Epple, B. Experimental study on steam gasification of torrefied woodchips in a bubbling fluidized bed reactor. *Energy* **2020**, *202*, 117744. [CrossRef]
119. Reed, T.B. Biomass Gasification: Principle and Technology. *Energy Technol. Rev.* **1981**, *67*, 123.
120. Huang, Z.; He, F.; Zhao, K.; Feng, Y.; Zheng, A.; Chang, S.; Zhao, Z.; Li, H. Natural iron ore as an oxygen carrier for biomass chemical looping gasification in a fluidized bed reactor. *J. Therm. Anal. Calorim.* **2014**, *116*, 1315–1324. [CrossRef]
121. Niu, P.; Ma, Y.; Tian, X.; Ma, J.; Zhao, H. Chemical looping gasification of biomass: Part I. screening Cu-Fe metal oxides as oxygen carrier and optimizing experimental conditions. *Biomass-Bioenergy* **2018**, *108*, 146–156. [CrossRef]

122. Yan, L.; Yue, G.; He, B. Thermodynamic analyses of a biomass–coal co-gasification power generation system. *Bioresour. Technol.* **2016**, *205*, 133–141. [CrossRef]
123. Sarafraz, M.; Jafarian, M.; Arjomandi, M.; Nathan, G. Potential use of liquid metal oxides for chemical looping gasification: A thermodynamic assessment. *Appl. Energy* **2017**, *195*, 702–712. [CrossRef]
124. Riley, J.; Siriwardane, R.; Tian, H.; Benincosa, W.; Poston, J. Kinetic analysis of the interactions between calcium ferrite and coal char for chemical looping gasification applications: Identifying reduction routes and modes of oxygen transfer. *Appl. Energy* **2017**, *201*, 94–110. [CrossRef]
125. Wang, K.; Yu, Q.; Qin, Q.; Hou, L.; Duan, W. Thermodynamic analysis of syngas generation from biomass using chemical looping gasification method. *Int. J. Hydrogen Energy* **2016**, *41*, 10346–10353. [CrossRef]
126. Chein, R.-Y.; Hsu, W.-H. Thermodynamic equilibrium analysis of H2-rich syngas production via sorption-enhanced chemical looping biomass gasification. *Renew. Energy* **2020**, *153*, 117–129. [CrossRef]
127. Yang, J.; Ma, L.; Yang, J.; Liu, H.; Liu, S.; Yang, Y.; Mu, L.; Wei, Y.; Ao, R.; Guo, Z.; et al. Thermodynamic and kinetic analysis of CuO-CaSO4 oxygen carrier in chemical looping gasification. *Energy* **2019**, *188*, 116109. [CrossRef]
128. Huang, Z.; Deng, Z.; Chen, D.; He, F.; Liu, S.; Zhao, K.; Wei, G.; Zheng, A.; Zhao, Z.; Li, H. Thermodynamic analysis and kinetic investigations on biomass char chemical looping gasification using Fe-Ni bimetallic oxygen carrier. *Energy* **2017**, *141*, 1836–1844. [CrossRef]
129. Chen, L.; Yang, L.; Liu, F.; Nikolic, H.S.; Fan, Z.; Liu, K. Evaluation of multi-functional iron-based carrier from bauxite residual for H2-rich syngas production via chemical-looping gasification. *Fuel Process. Technol.* **2017**, *156*, 185–194. [CrossRef]
130. Li, X.; Wang, L.; Zhang, B.; Khajeh, A.; Shahbazi, A. Iron oxide supported on silicalite-1 as a multifunctional material for biomass chemical looping gasification and syngas upgrading. *Chem. Eng. J.* **2020**, *401*, 125943. [CrossRef]
131. Hildor, F.; Leion, H.; Linderholm, C.J.; Mattisson, T. Steel converter slag as an oxygen carrier for chemical-looping gasification. *Fuel Process. Technol.* **2020**, *210*, 106576. [CrossRef]
132. Myöhänen, K.; Palonen, J.; Hyppänen, T. Modelling of indirect steam gasification in circulating fluidized bed reactors. *Fuel Process. Technol.* **2018**, *171*, 10–19. [CrossRef]
133. Liu, H.; Cattolica, R.J.; Seiser, R. CFD studies on biomass gasification in a pilot-scale dual fluidized-bed system. *Int. J. Hydrogen Energy* **2016**, *41*, 11974–11989. [CrossRef]
134. Gopaul, S.G.; Dutta, A.; Clemmer, R. Chemical looping gasification for hydrogen production: A comparison of two unique processes simulated using ASPEN Plus. *Int. J. Hydrogen Energy* **2014**, *39*, 5804–5817. [CrossRef]
135. Detchusananard, T.; Ponpesh, P.; Saebea, D.; Authayanun, S.; Arpornwichanop, A. Modeling and Analysis of Sorption Enhanced Chemical Looping Biomass Gasification. *Chem. Eng. Trans.* **2017**, *57*, 6.
136. Cormos, C.-C. Biomass direct chemical looping for hydrogen and power co-production: Process configuration, simulation, thermal integration and techno-economic assessment. *Fuel Process. Technol.* **2015**, *137*, 16–23. [CrossRef]
137. Aghabararnejad, M.; Patience, G.S.; Chaouki, J. Techno-Economic Comparison of a 7-MWthBiomass Chemical Looping Gasification Unit with Conventional Systems. *Chem. Eng. Technol.* **2015**, *38*, 867–878. [CrossRef]
138. Li, F.; Zeng, L.; Fan, L.-S. Biomass direct chemical looping process: Process simulation. *Fuel* **2010**, *89*, 3773–3784. [CrossRef]
139. Ge, H.; Zhang, H.; Guo, W.; Song, T.; Shen, L. System simulation and experimental verification: Biomass-based integrated gasification combined cycle (BIGCC) coupling with chemical looping gasification (CLG) for power generation. *Fuel* **2019**, *241*, 118–128. [CrossRef]
140. Kuo, P.-C.; Chen, J.-R.; Wu, W.; Chang, J.-S. Hydrogen production from biomass using iron-based chemical looping technology: Validation, optimization, and efficiency. *Chem. Eng. J.* **2018**, *337*, 405–415. [CrossRef]
141. Li, Z.; Xu, H.; Yang, W.; Zhou, A.; Xu, M. CFD simulation of a fluidized bed reactor for biomass chemical looping gasification with continuous feedstock. *Energy Convers. Manag.* **2019**, *201*, 112143. [CrossRef]
142. Li, Z.; Xu, H.; Yang, W.; Xu, M.; Zhao, F. Numerical investigation and thermodynamic analysis of syngas production through chemical looping gasification using biomass as fuel. *Fuel* **2019**, *246*, 466–475. [CrossRef]

applied sciences

MDPI

Article

A Comparison Study on the Improved Operation Strategy for a Parabolic trough Solar Power Plant in Spain

Wisam Abed Kattea Al-Maliki [1,2], Adnan G. Tuaamah Al-Hasnawi [3], Hasanain A. Abdul Wahhab [2], Falah Alobaid [1,*] and Bernd Epple [1]

[1] Institute Energiesysteme und Energietechnik, Technische University Darmstadt, Otto-Berndt-Straße 2, 64287 Darmstadt, Germany; wisam.a.kattea@uotechnology.edu.iq (W.A.K.A.-M.); bernd.epple@est.tu-darmstadt.de (B.E.)
[2] Mechanical Engineering Department, University of Technology—Iraq, Baghdad 10066, Iraq; 20085@uotechnology.edu.iq
[3] Electromechanical Engineering Department, University of Technology—Iraq, Baghdad 10066, Iraq; 10597@uotechnology.edu.iq
* Correspondence: falah.alobaid@est.tu-darmstadt.de; Tel.: +49-6151-16-6691; Fax: +49-6151-16-5685

Abstract: The present work focuses on the development of a detailed dynamic model of an existing parabolic trough solar power plant (PTSPP) in Spain. This work is the first attempt to analyse the dynamic interaction of all parts, including solar field (SF), thermal storage system (TSS) and power block (PB), and describes the heat transfer fluid (HTF) and steam/water paths in detail. Advanced control circuits, including drum level, economiser water bypass, attemperator and steam bypass controllers, are also included. The parabolic trough power plant is modelled using Advanced Process Simulation Software (APROS). An accurate description of control structures and operation strategy is necessary in order to achieve a reasonable dynamic response. This model would help to identify the best operation strategy due to DNI (direct normal irradiation) variations during the daytime. The operation strategy used in this model has also been shown to be effective compared to decisions made by operators on cloudy periods by improving power plant performance and increasing operating hours.

Keywords: parabolic trough power plant; dynamic simulation; APROS; operation strategy; comparative study

Citation: Al-Maliki, W.A.K.; Al-Hasnawi, A.G.T.; Abdul Wahhab, A.A.; Alobaid, F.; Epple, B. A Comparison Study on the Improved Operation Strategy for a Parabolic trough Solar Power Plant in Spain. *Appl. Sci.* **2021**, *11*, 9576. https://doi.org/10.3390/app11209576

Academic Editor: Yosoon Choi

Received: 3 September 2021
Accepted: 12 October 2021
Published: 14 October 2021

1. Introduction

Solar power plants are a very important factor in the countries that depend on renewable energy sources for their energy system because they can also produce electrical power in the night. Current estimates of the amount of power supplied by solar thermal power plants in the world are at approximately 6.2 GW by 2020. For example, in Spain there are 2.3 GW produced by 47 parabolic trough power plants, 51 MW by three solar power plants and 31 MW by two linear Fresnel power plants.

There are 2.194 GW under construction around the world [1,2]. The estimated power is expected to reach more than 11 GW by 2030 depending on an average development of the CSP technology. Approximately 15% of these power plants will be installed in Europe, 30% in northern Africa and 55% in the Middle East [3–6].

In the following study, an overview of the dynamic simulation models for parabolic trough power plants will be presented that have been implemented in the past to improve and evaluate methods for increasing the operational flexibility of these plants. Due to DNI and demand variations, the use of dynamic models is of great importance. These variations in the performance need to use the transient solution of three conservation laws (energy, mass and momentum), dynamic conditions, controllers and accompanied parts.

There are several commercial programs for power plant modelling used in solar thermal applications, namely TRNSYS, EcoSimPro, EBSILON Professional, IPSEpro, GATECYCLE, MATHEMATICA, DYMOLA and APROS [5,7,8].

In general, there are few researchers who have studied the dynamic simulation of parabolic trough power plants. In particular, most researchers have not addressed optimising the performance of these plants. For this reason, we will review the most important works that have dealt with parabolic trough power plants.

Masero et al. [9] developed a control predictive model to optimise thermal power on a large scale for solar parabolic trough plants. The power plant is divided into several subsystems. They are controlled by their loop control valves to improve the performance and reduce the computation time of control inputs. The operation strategy is evaluated by decentralised and centralised control predictive models in two simulated solar fields. Frejo and Camacho [10] optimised the solar field of a parabolic trough power plant using a centralised predictive model. The best operating strategy of the power plant is implemented by regulating a group of control valves installed at the beginning of each collector loop. This leads to improving the response obtained from classic control processes for this type of power plant. The implemented control model is applied for a small parabolic trough power plant. The simulated control models are evaluated based on the data of the collector of solar fields for ACUREX (Almería, Spain) over two hours. The results of the suggested algorithm showed a good agreement with the centralised algorithm. Sánchez et al. [11] performed a control predictive model for analysis of deconcentrating control for different collector loops. The HTF temperature is controlled by deconcentrating two and four collector loops in different cases. The results showed better performance when four complexes were not concentrated in addition to maintaining the deconcentrating procedures in the areas with high control power. Montañés et al. [12] developed dynamic models of a 50 MW parabolic trough power plant using Modelica language to assess the behaviour of stored energy and its mechanism of action with the solar field (SF) and the power block (PB). The steady-state results were compared with the original plant data. Regarding dynamic behaviour, the response of the PB showed good behaviour because the chosen days were clear. Larrain et al. [13] implemented a thermal model to evaluate the reserve part required for 100 MW_{el} hybrid-fossil-solar PTSPP. The performance was predicted and its usefulness was explored in aiding suitable site selection among four sites. García et al. [14] provided a dynamic model of a PTSPP without power block simulation using Wolfram's Mathematica 7 programme. The model deals only with the thermal oil behaviour within the SF and TSS. The results were compared with experimental data for a 50 MW_{el} of PTSPP in Spain during summer. Diendorfer et al. [15] dynamically simulated the optical performance of the collector platform. The floating stability of the existing platform design was experimentally verified, and the performance influence to go offshore was small. Schenk et al. [16] dynamically implemented a model PTSPP by DYMOLA. A transient behaviour was evaluated for the start-up case based on thermal oil behaviour. This model was checked with the Ebsilon model since there were no experimental data to investigate the model. Luo et al. [17] built a dynamic parabolic trough collector model and validated it depending on the photothermal conversion process for a parabolic trough technology. Together with the verified model with pumps, the thermal oil/water heat exchangers and other existing components, a solar field was simulated.

The review research reveals that most modelling studies found in the literature are focused on the work of specific parts of the PTSPP, such as the solar field or the thermal storage system or the power block during certain periods (clear periods). In addition, they do not address the operation of the control units and the operational strategy used in these power plants.

In this work, a detailed dynamic model of the PTSPP (Andasol II) with all control circuits is developed employing (APROS) software. The dynamic behaviour of the investigated power plant is assessed during a strongly cloudy day. The solar data is computed depending on satellite measurements and databases from ground weather stations.

Specifically, the novelty of this study can be summarised as follows:

1. A detailed dynamic model of a PTSPP, including the SF, the TSS, and the PB, has been extended based on our previous studies presented. In addition, the dynamic behaviour of the thermal oil path of the power plant during heavily cloudy days in summer is discussed. The steam behaviour in the high pressure (HP)/low pressure (LP) turbine stages is also investigated. Such dynamic simulation modelling cannot be found in the literature.
2. This model can also determine the best operating strategy of the power plant, taking into account the DNI variations during the day, compared to the decisions made by operators in the absence of a dynamic modelling approach.
3. For model validation, the simulation results for the most important properties of the solar field, storage system, and power block are compared with measurements. The comparative work is of great interest to designers of PTSPP and scientific researchers.

2. Power Plant Operation Strategy in Dynamic Simulation

The operation strategy performed in the dynamic simulation of the parabolic trough power plant for a single day can be defined based on six operation periods, as explained below and depicted in Figure 1:

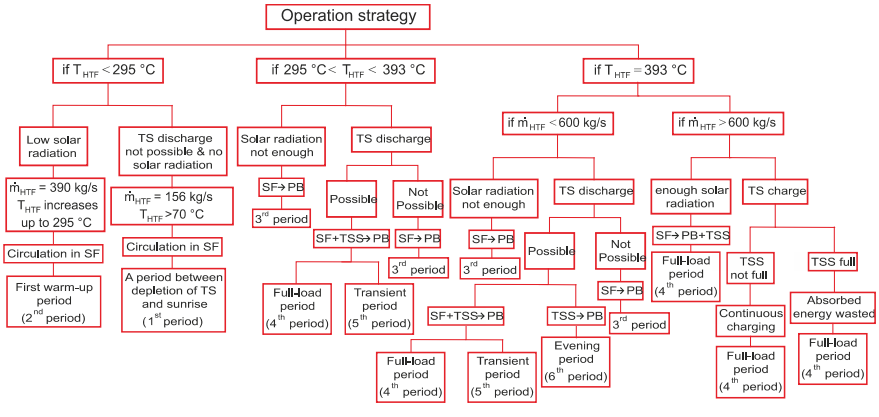

Figure 1. Schematic diagram of the operation strategy during a single day for a PTSPP model.

- The first period is the period between the time of thermal storage depletion and sunrise.
- The second period represents the first warm-up period of HTF, when the HTF temperature in the SF reaches the designated temperature at the inlet (295 °C).
- The third period corresponds to the second warm-up period of HTF, where the temperature of HTF in the SF achieves the designated temperature at the outlet (393 °C).
- The fourth period represents a full-load operation period during the daytime.
- The fifth period represents the transient period that precedes the sunset.
- The sixth period is the evening period, where the thermal storage is discharged until it is completely depleted.

This operation strategy carried out in the dynamic simulation model represents the best approach comparing with the operator decisions implemented in the Andasol II.

During the first and the sixth periods (night periods), the dynamic model checks firstly whether the thermal storage discharge is available, taking into consideration the boundary conditions of the power plant. If the discharge mode is available, the power plant produces electrical power (48 MWth). On the other hand, the HTF is not circulated in the solar field. Thermal storage continues discharging during night hours until stored energy is depleted.

Conversely, when the thermal storage discharge is not available, electrical power is not produced by the steam turbine. The HTF is still circulated by the recirculation pumps within the SF at 1 kg/s for one loop as long as the design inlet temperature (295 °C) is not achieved. When the thermal oil temperature at the outlet of each loop decreases lower than 70 °C (minimum input value when there is no solar radiation or stored energy), the HTF protection system is activated to prevent the thermal oil temperature in the SF from dropping below a specified minimum temperature.

The second period (first HTF warm-up period) starts when the sun rises and continues until the designated temperature at the inlet (295 °C) is reached. After sunrise, the thermal oil in the SF is circulated with mass flow of 390 kg/s until the designate inlet temperature (295 °C) is reached. During this period the thermal oil is not transferred to the PB as the useful thermal power in the SF is still equal to zero.

Subsequently, the third period (second HTF warm-up period) begins when the design inlet temperature (295 °C) is achieved. Thereafter, the temperature and mass flow of HTF will increase together, where the design outlet temperature (393 °C) is first achieved and then the nominal value of mass flow (600 kg/s). This amount of thermal oil mass flow sent to the PB must not exceed its limit value (600 kg/s) in order to avoid the production of more steam than required. It is worth mentioning that the useful thermal energy is sent to the PB on the HTF in this period. Coinciding with the third period, the start-up period of steam turbine starts until the steam production reaches its nominal value (55 kg/s).

The assumptions implemented in the dynamic model of PTSPP are made to simulate the measured data curves for a 50 MW_{el} PTSPP, located in Spain. The simulation indicates an excellent agreement compared to the experimental data collected from Andasol II.

The fourth period (full-load operation period) begins after the second warm-up period of HTF, where the design conditions of HTF (600 kg/s and 393 °C) are reached at the power block inlet. This period continues during daytime until sunset. Under high DNI conditions the specified conditions of HTF are achieved, and the surplus of HTF is transferred to the TSS to start the charge phase. When the TSS is completely charged, i.e., maximum TSS capacity of 1025 MW_{th} h is reached, some SCAs are faced to the ground (stow mode) in order to avoid a further increase in the collected thermal energy.

Optionally, the nominal HTF mass flow can be reduced below 600 kg/s when clouds prevent the DNI from falling on a number of loops. In this case, the thermal storage is discharged, if possible, in order to maintain the target heat flow to the PB. The storage discharge period can be classified during the daylight into cases: first, if the thermal oil mass flow in the SF continues decreasing from 600 kg/s down to a minimum value of 312 kg/s, a part of the HTF coming from the PB is redirected to the thermal storage system and the rest of the thermal oil is sent to the solar field. If the DNI is still low, the operation strategy proceeds to maintain the thermal oil mass flow at a designated minimum value of 312 kg/s. Here, the power plant is operated by transferring all the useful thermal power absorbed within the SF to the PB and compensating the rest of HTF from the thermal storage system if a discharge mode is available.

Once the HTF mass flow in the SF falls below a minimum value of 312 kg/s due to the decrease in solar radiation, the designated temperature of thermal oil at the PB inlet is changed to 377 °C instead of 393 °C, and the nominal mass flow of thermal oil remains unaltered at 600 kg/s. As a result, if the mass flow of thermal oil in the SF continues falling to zero, the TSS supplies the nominal thermal power (125.75 MW_{th}) similar to the night period, as long as the storage discharge is possible. In this mode, 600 kg/s of HTF are directed to the TSS heat exchangers, hence no HTF is circulated in the solar field.

Whenever thermal storage discharge is not possible and there is a lack of DNI, the PB is stopped, and the thermal oil is circulated in the SF at 1 kg/s as in the first period. Hence, if the turbine is stopped several times during daytime hours because of cloudy periods, the HTF will be warmed up again which in turn leads to a second start-up process. Therefore, several start-ups can occur during the day depending on meteorological data. After the

clouds pass over, the HTF can be routed to the solar field again and the process repeats starting from the third phase, as explained above.

The fifth phase (transient period) starts when the HTF mass flow falls to a value of 312 kg/s during the sunset period. The designated HTF temperature at the SF outlet is altered from 393 °C to 377 °C and the PB is operated based on the stored energy until the complete depletion of the TSS.

Fossil fuel is used in the real power plant when there is no energy stored in the storage system. However, the fossil fuel backup system has not been included in the APROS model for the results obtained in this study since the data of the real fossil fuel backup system were not available.

Finally, this operation strategy is applied in the validated power plant model for the cloudy summer day selected in this study.

3. Simulation Programme

Dynamic simulation can be a useful tool for determining the design of a new power plant, as well as to aid selection of the best operating strategy. The investigation of the dynamic behaviour of thermal power plants needs a detailed description of the thermal processes. The large fluctuations that occur during the operation of solar power plants require the use of a large number of controllers. Therefore, the process of controlling a specific property is complex, and for the purpose of achieving long-term dynamic simulation of a power plant it requires sophisticated modelling programs that include numerical solutions as well as solving differential conservation correlations.

Andasol II plant is modelled by APROS software. This programme consists of many components and different solutions which can be used for dynamic simulation. APROS implements the dynamic simulation based on homogenous and heterogeneous flow models.

Different approaches for the modelling of two-phase flow in a thermal power plant can be found in the literature, such as mixture-flow and six-equation flow models. In the mixture-flow model, the three characteristic fluid variables are calculated, including local pressure, total mass flow, and temperature or enthalpy, which are represented by three conservation equations (mass, momentum and energy) of the mixture:

Mass balance:

$$\frac{\partial \rho}{\partial t} + \frac{\partial (\rho u)}{\partial z} = 0 \tag{1}$$

Momentum balance:

$$\frac{\partial (\rho u)}{\partial t} + \frac{\partial \left(\rho u^2\right)}{\partial z} + \frac{\partial p}{\partial z} = F_{grav} + F_w \tag{2}$$

Energy balance:

$$\frac{\partial (\rho h)}{\partial t} + \frac{\partial (\rho u h)}{\partial z} = \frac{\partial p}{\partial t} + Q_w \tag{3}$$

Here, ρ denotes the density of the flow mixture, u represents the longitudinal velocity of fluid, p and h refer to the static pressure and overall enthalpy, respectively. The parameters Q_w, F_{grav} and F_w represent the heat transfer across the walls, the gravitational force and the friction force, respectively.

The six-equation model is more suitable for certain applications because it allows the inclusion of thermodynamic non-equilibrium states in the formulation. Here, two sets of conservation equations are formulated to determine the mass, momentum and energy balance for each phase:

Mass balance:

$$\frac{\partial (\chi_k \rho_k)}{\partial t} + \frac{\partial (\chi_k \rho_k u_k)}{\partial z} = \Gamma_k \tag{4}$$

Momentum balance:

$$\frac{\partial (\chi_k \rho_k u_k)}{\partial t} + \frac{\partial \left(\chi_k \rho_k u_k^2\right)}{\partial z} + \chi_k \frac{\partial p}{\partial z} = \Gamma_k u_{ik} + \chi_k F_{grav,k} + F_{wk} + F_{ik} + F_{va} + F_{fl} + \Delta P_{pu} \tag{5}$$

Energy balance:

$$\frac{\partial(\chi_k \rho_k h_k)}{\partial t} + \frac{\partial(\chi_k \rho_k u_k h_k)}{\partial z} = \chi_k \frac{\partial p}{\partial t} + \Gamma_k h_{ik} + Q_{wk} + Q_{ik} + F_{ik} u_{ik} \quad (6)$$

The symbol k is either l = liquid or g = gas, the indices i and w refer to the interface of two phases and the wall, respectively. The variable Γ denotes the mass transfer rate between the phases. The parameters F_{va}, F_{fl} and ΔP_{pu} are valve friction, friction loss and head difference of pump, respectively. The coefficient h in Equation (6) is the overall enthalpy which includes the kinetic energy and Q_{ik} is the heat transfer at the interface.

Several equations are required to model the process components of the power plant. The equations for modelling these process components can be found in a comprehensive review of dynamic simulation of thermal power plants published by Alobaid et al. [18].

The solution method applied in APROS is the finite volume method. This is in turn used to find a solution for the one-dimensional partial differential correlations, which are discretised regarding time and space. In addition, the non-linear expression is linearised. The density, pressure and enthalpy are computed in the centre of the mesh cells while the velocity at the boundary of two mesh cells is computed. Furthermore, the first-order upwind scheme is used to find the enthalpy solution. In the mesh cell, average quantities are calculated across the entire grid. The implicit solution is used for temporal assessment. Some properties, such as linear equation set of the void fraction, enthalpy and pressure, are computed one by one. Furthermore, the density is updated as a function of a given enthalpy and pressure.

4. Solar Field Calculations

The direct normal irradiation data were not available from the existing measurements. Furthermore, APROS can only provide an average value of DNI. Therefore, the Meteonorm software provides detailed calculations of DNI at any time in Granada (location of Andasol II) depending on satellite measurements and databases from ground weather stations. Thence, the obtained DNI values were used in the absorbed heat correlation, then the obtained values from this equation were entered into the SF as input values, as explained below.

In our work, the typical meteorological year (TMY) data for the selected day from [19] were calculated from several weather stations at the Andasol II site with a time step of 10 min between TMY data points.

Absorbed Solar Radiation Calculations

The absorbed heat $\left(S_{absorb,loop}\right)$ by thermal oil passing through the absorbers for one loop is calculated as follows:

$$S_{absorb,loop} = DNI\ A_c IAM\ cos\theta\ \eta_{opt,0}\ \eta_{track} f_{end,loss} f_{row,shadow}\ f_{dust} f_{add}\ f_{clean} \quad (7)$$

where:

DNI:Direct normal irradiance [W/m^2], the DNI data is measured at the Andasol 2 power plant site in Spain. Then, these measured data are entered into the APROS model.

A_c: Mirror aperture area for one loop [m^2]; the value of A_c used in Equation (7) is 3270 m^2.

IAM: Incidence angle modifier, used to modify additional optical and geometric losses due to an incident angle more than 0°. It is calculated from this equation:

$$IAM = \frac{K}{cos\theta_i}$$

where $K = cos\theta_i - 0.000525\ \theta_i - 0.00002859(\ \theta_i)^2$

θ_i: Angle of incidence [deg], the angle between the incident solar radiation on a surface and the plane perpendicular to the aperture of the parabolic trough.

$\eta_{opt,0}$: A peak optical efficiency determined at an incidence angle of zero. The value used in Equation (7) is 0.81, based on García IL correlation.
η_{track}: The tracking coefficient is a measure of how accurate a solar tracking system is to get the best amount of solar radiation. It ranges between 0 and 1, where a value of 1 indicates that the tracking system follows the sun with high accuracy. The unity value is used in this study.
$f_{end,loss}$: End loss factor refers to the ratio between the effective length and the actual length of the mirror in a solar collector assembly. It is calculated depending on STUETZLE TA formula.
$f_{row,shadow}$: Shadow factor represents the ratio between the effective width of trough aperture and its real total width. It is computed based on STUETZLE TA equation.
f_{dust}: This coefficient is used to describe the absorption due to dust on the absorber glass cover. Its value ranges between zero and unity. Zero values mean that the absorber is dusty and there is no absorption. The value 1 means the absorber is clear and there is complete absorption. The value of 0.98 was chosen in this study.
f_{add}: This factor is used to calculate the additional reduction in the absorbed solar radiation. It ranges between 0 and 1, where the value of 1 is the ideal case and used in this work.
f_{clean}: This factor refers to mirror cleanliness. The values range of this factor is between zero and 1, where the zero value represents no solar radiation of the mirrors to the absorber tube and the unity value denotes that the whole solar radiation falling on the mirrors is reflected. The value of 0.97 was selected in this work.

The total heat losses of the pipes and absorbers are calculated based on experimental equations in [20,21]. The results obtained in this work are calculated depending on subtraction the total thermal losses in the SF from the absorbed heat in 156 loops in order to send the net thermal power to the PB.

5. PTSPP Model Description

A schematic diagram of (PTSPP) "Andasol II" in Andalusia is demonstrated in Figure 2, including all parts (SF, TSS and PB).

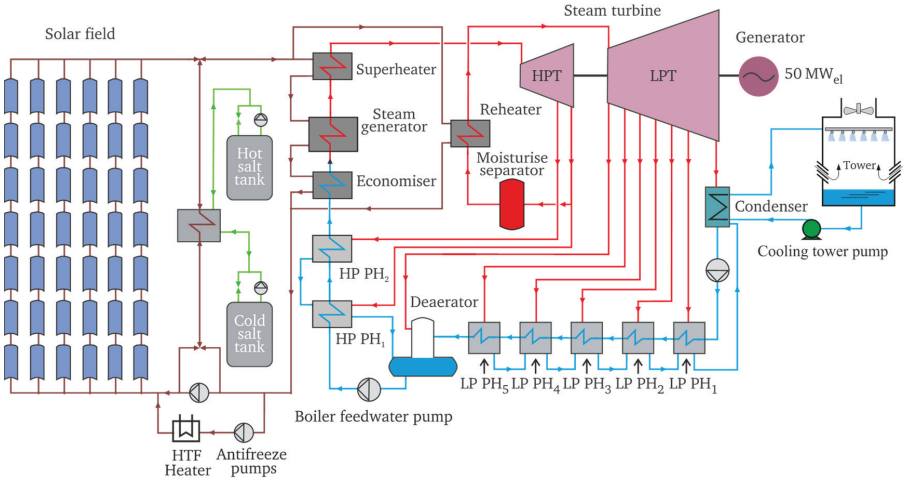

Figure 2. Parabolic trough solar power plant (PTSPP).

5.1. Solar Field (SF)

The solar field includes north and south sectors. Each sector includes two sections which contain 78 collector loops for both. The thermal oil coming from the economiser with 295 °C is pumped to the inlet of the solar field, as illustrated in Figure 3. Thereafter, the thermal oil is streamed to the north and the south sections through 312 collector rows.

The HTF circulated through the collector loops is heated by solar radiation. The HTF in the north and the south loops will meet before the SF outlet. At the SF outlet, the hot HTF will be flow to either the power block, a storage system or to both.

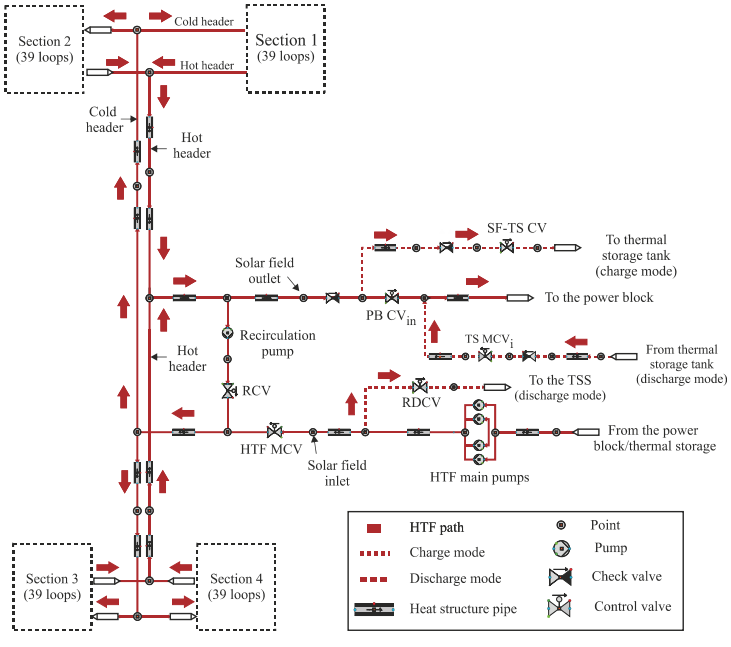

Figure 3. Solar field circuit.

The measured DNI represents the input into this model. Initially, the HTF mass flow rate is increased to 390 kg/s and is maintained until the designed inlet temperature (295 °C) is reached. In this process, each section of the SF accumulates a specific amount of thermal energy. After reaching the designated temperature at the entrance, the mass flow rate of the thermal oil and its temperature gradually increase until the maximum mass flow rate (1170 kg/s) is reached at the designated exit temperature (393 °C). Furthermore, the pressure losses for the power plant components are already included in this model.

In dynamic simulation it is very important to use the controllers to complete the simulation with high accuracy. Only the most important control circuits will be described briefly:

(1) The SF-TS valve regulates the surplus thermal oil to the hot storage tank. This valve is opened when the HTF mass flow threshold value is 600 kg/s and the temperature is 393 °C.
(2) The PB CVin adjusts the nominal value of HTF mass flow of 600 kg/s to the PB.
(3) The DNI controller sets the real data of solar radiation measured in Spain to the HTF in four sections.
(4) The HTF MCV valve at the SF inlet controls HTF temperature at the SF outlet. This valve performs two functions: First, it adjusts a mass flow of 390 kg/s after sunrise in the SF and remains at this value until the HTF temperature at the outlet of SF has been raised up to 295 °C due to the increase in DNI. Second, after achieving 295 °C of thermal oil temperature at the outlet of SF, the second function is enabled. This valve controls the temperature of HTF at the outlet of SF to obtain the design temperature at the SF exit (393 °C).

5.2. Thermal Storage System (TSS)

This system provides the stability in the production of electric power and high flexibility in operation. Two insulated tanks connected to each other by six heat exchangers are used to model the storage system in APROS. A series of heat pumps are installed beyond the storage tanks to pump the molten salt into the heat exchangers. The density and specific heat properties of the molten sodium and potassium nitrate salt mixture are known as a function of temperature.

In the charging phase (high solar radiation), the molten salt from the cold tank is heated by HTF up to approximately 386 °C and it is then sent to the hot salt tank. At this point it should be mentioned that there are losses between the HTF and the molten salt in the series of heat exchangers. That means that the temperature of the hot molten salt drops under the maximum HTF temperature of 393 °C, while the hot molten salt achieves a temperature of 386 °C. Consider that the maximum capacity of the TSS is approximately 1025 MW_{th} h.

In the discharging phase (evening or cloudy periods), the HTF is heated using hot molten salt. In this case, the TSS supplies the HTF's nominal mass flow (600 kg/s) with a temperature of 377 °C in the night hours. This affects the steam generation capacity, while the nominal amount of steam generated during the day (55 kg/s) is not reached in the evening hours. When the heat exchange between molten salt and thermal oil has been completed, the cold molten salt with a temperature of 292 °C enters the cold tank.

5.3. Power Block (PB)

The boiler in this power plant consists of a series of heat exchangers. Each line includes a superheater, evaporator, economiser and reheater. The steam–water path is designed based on two pressure sections, namely the main system pressure and reheat sections, as described in Figure 4.

The water coming from the condenser enters a low-pressure feedwater circuit. Thereafter, it passes through five low-pressure preheaters to raise the temperature from 35 °C to 165 °C at the outlet of LP PH_5 (low pressure preheater) using the steam extracted from the LP turbine. The water is then collected in the deaerator, which is considered a type of open water heater. It is then pumped to the HP preheaters before entering the steam generator. In the deaerator, the water is purged of oxygen by HP steam flowing from the HP turbine to avoid corrosion.

Both HP and LP preheaters work by the steam extracted from the turbine. These heat exchanger preheaters contain tube and shell sides where the extracted steam is condensed in the shell side while the water is heated in the tube side. Although the steam extracted from the turbine reduces the turbine power production, it also raises the feedwater temperature in the tubes, resulting in an improvement in the plant cycle efficiency.

The steam exits the economiser and streams into the HP feedwater tank. The level of the HP tank is regulated by the HP feedwater main control valve (FW MCV_{HP}). The circulation process between the evaporators and HP tank is carried out by the HP recirculation pump (HPRP) which generates saturated steam. Here, the HP tank works as a separator. While the water remains in the drum and mixes with water coming from the economisers, the saturated steam leaves the drum and enters to the HP superheaters, and here saturated steam absorbs additional heat from the thermal oil. Then, the HP superheated steam enters the HP turbine part. The steam temperature is kept from increasing above 384 °C at the turbine inlet by the HP attemperator, which is placed at the superheater outlet. The HP attemperator is supplied the feedwater by the HP feedwater pump.

The pressure and temperature of steam entering the steam turbine are 106 bar and 384 °C, respectively. On the one hand, part of the steam is extracted to the high-pressure preheater (HP PH), while on the other hand, part of the steam is streamed to the reheaters in order to reheat the steam up to 383 °C. Thereafter, the reheated steam enters the LP turbine with a pressure of 19.4 bar. At the outlet of the LP turbine, the steam flows into the

condenser. After condensing the steam, the water is pumped using condenser pumps to the LP preheaters and then the cycle will continue in the power plant again.

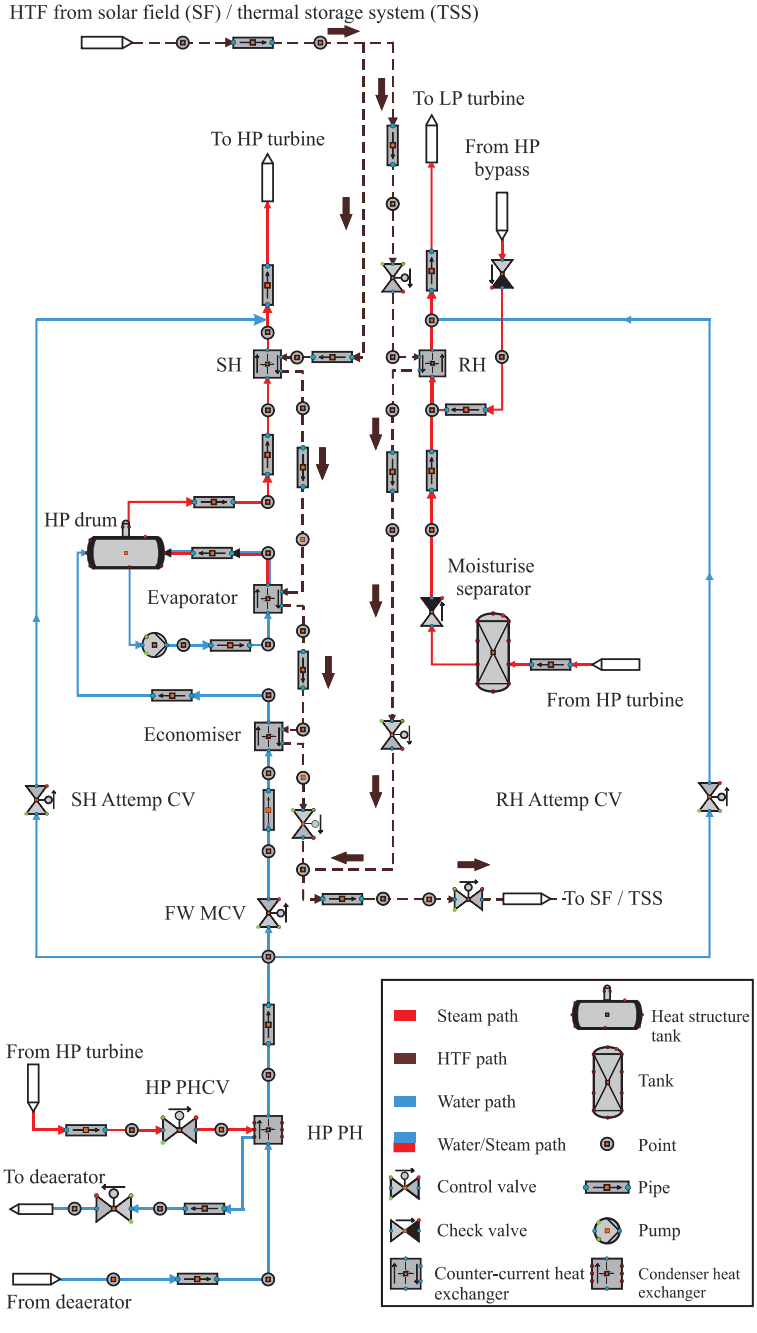

Figure 4. Steam generator circuit.

Table 1 shows the properties of steam and HTF obtained from the Andasol II plant at the nominal load.

Table 1. Technical data of the real power plant.

Andasol II	Units	SF	TSS	HP Turbine	RH/LP Turbine
Working Fluid		HTF (Thermal Oil)	HTF (Thermal Oil)	Steam	
Conditions at the inlet	(bar)	P = 31.3	P = 17.5	P = 104	P = 19.4
	(°C)	T = 295	T = 393	T = 384	T = 383
	(kg/s)	$\dot{m}$ = 1100	$\dot{m}$= 500	$\dot{m}$= 54	$\dot{m}$= 44.3
Conditions at the outlet	(bar)	P = 18.2	P = 12	P = 20.5	P = 0.05
	(°C)	T =393	T = 293	T = 215	T = 30
	(kg/s)	$\dot{m}$ = 1100	$\dot{m}$= 500	$\dot{m}$= 47.7	$\dot{m}$= 33.7

To regulate the operating process of the power plant, it is essential to have control circuits. Here, the controllers for the LP/HP preheater level, the SH and RH attemperator, the drum level, the economiser water bypass and the steam bypass control circuits are implemented in this model.

- Undesired steam is bypassed by HP and LP bypass controllers to the reheater and condenser before entering the HP and LP turbine, respectively. These controllers are used in the shutdown and start-up processes as well as for the steam turbine trip of any load.
- The attemperators (SH Attemp CV and RH Attemp CV) adjust the steam temperature to (384 °C) at the turbine inlet. This cooling process is implemented by injecting some of the water from the boiler water pump to the attemperators.
- In order to achieve the stability of flow in the evaporator, a small amount of water transferred from the economiser inlet is bypassed into the inlet of the drum. Here, the water temperature at the outlet of the last economiser is kept under the boiling temperature with a sub-cooling temperature of 5 °C by the economiser water bypass controller.
- The drum-level control valve adjusts the mass flow flowing into the drum in order to avoid instability caused by fluctuations in the water level in the tank.
- Seven control valves of LP/HP preheater level keep the water level of preheaters at certain values due to changes caused by condensation of extracted steam on the shell side.

6. Results

The suggested model was verified against the experimental data obtained from Andasol II in [22]. The simulated results in this section were compared with the experimental data on 2 July 2010 to generalize the model validity and test the effectiveness of the adopted operating strategy. The power plant operation strategy is dynamically controlled by many control circuits during the day regardless of DNI oscillations. The strategy of the developed model was compared versus the strategy of the real power plant through the measured data on this day. This day in July was cloudy. The simulated predictions for the dynamic HTF behaviour in the SF, the TSS and the PB are displayed. In addition, the model results of the dynamic behaviour of steam in the power block are discussed.

6.1. Heat Transfer Fluid Behaviour

The simulation results and experimental data are compared on 2 July 2010, including (DNI), the HTF temperature at the exit of SF, the thermal energy transmitted to the PB and the thermal stored energy accumulated in the TSS.

In Figure 5, DNI data were measured in several weather stations on a selected day at the location of Andasol II. The average values of this data were used as inputs to the power plant model for the chosen day.

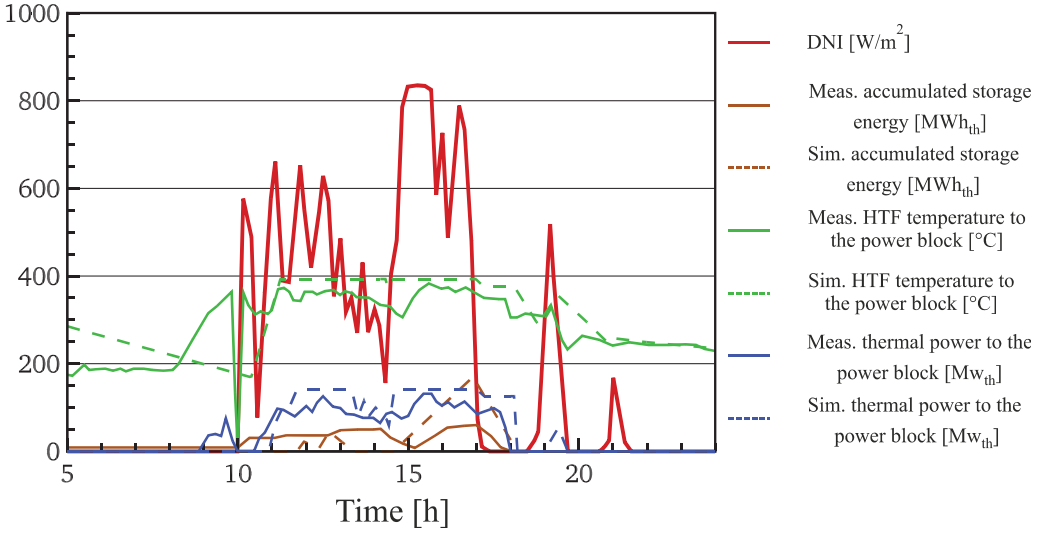

Figure 5. Comparison of simulations and measurements on 2 July 2010.

After the outlet of SF, the simulated thermal oil temperature on 2 July 2010 displayed a good match with the measurements, as illustrated in Figure 5. At t = 9:59, a technical fault occurred, causing a drop in the measured temperature of HTF to 0 °C. The warm-up periods in the SF include two phases. The first phase begins at sunrise. As a consequence, the temperature of HTF raises from 170 °C to the designated temperature at the inlet of the SF (295 °C).

In the second of the warm-up phase, the simulated temperature of thermal oil continues to rise until the designated temperature of the SF outlet (393 °C) is at t = 11:13. Additional heating of the HTF temperature is avoided by controlling the HTF flow through the SF to maintain the temperature of HTF at the designated outlet temperature (393 °C). Between t = 11:13 and t = 14:18, the temperature is kept stable at 393 °C despite severely fluctuating DNI values. After t = 14:18, the HTF temperature drops and reaches 375 °C because of the absence of stored energy and low DNI. At t = 14:30, the temperature of thermal oil increases to the designated outlet temperature. Thereafter, the temperature of thermal oil remains constant until t = 16:59, and here the HTF temperature decreases to 377 °C at t = 17:10 because the power plant operates in thermal storage mode. At t = 18:04, the simulated HTF temperature decreases from 377 °C to 287 °C at t = 18:49 because of the absence of stored energy, and DNI is completely absent due to dense clouds. After t = 18:49, the power plant continues operating only with the thermal storage until the end of the day. After the clouds clear, the thermal oil temperature rises again to 355 °C at t = 19:22. Afterwards it decreases to 250 °C because of heavily cloudy skies. At t = 21:00, the temperature increases again to 293 °C because of the removal of clouds. Thereafter, the temperature drops because of the sunset.

Thermal power transferred to the PB is calculated based on the HTF mass flow at the inlet of PB and the variation between the thermal oil temperature at the inlet and the outlet of SF. In the actual power plant between t = 8:49 and t = 9:59, thermal power is generated even though there is no DNI, and storage power is exhausted. This indicates that the power plant was running on the fuel system during this period. Hence, this difference affects the production of electricity, which is dependent on the thermal energy behaviour. At t = 10:53 thermal power is produced based on DNI and reaches and reaches 101 MW_{th} at t = 11:17, as shown in Figure 5. After that, the transferred thermal power drops to 99 MW_{th} and shows

a decline of solar radiation suddenly. At t = 11:42, the maximum value of the transferred thermal power (140.72 MW_{th}) is achieved.

Then, this continues constantly until t = 13:18. This is due to the presence of solar radiation and adequate thermal storage. After t = 13:20, the thermal power drops to 80 MW_{th} at t = 13:30 because the PB only works with the SF mode. From t = 13:30 to t = 14:24, the experimental and simulated thermal power oscillates because of changes in the total HTF mass flow to keep the designated outlet temperature.

Thereafter, the thermal energy transferred to the PB rises again to the set value and maintains this value after t = 14:33 because of the increase in DNI. The transmitted thermal power reduces to 125.75 MW_{th} as a result of decreasing the design outlet temperature to around 377 °C. After t = 18:04, the thermal power reduces to zero and remains constant because of the depletion of stored energy. After the demise of the clouds, the thermal power reaches 54 MW_{th} at t = 19:24 and then reduces to the zero value as a result of the DNI reduction. Although the DNI was high again after heavily cloudy periods, the thermal power transferred to the PB remained at a zero value until sunset. This is because the designated temperature at the inlet (295 °C) was not achieved as the solar radiation was not enough.

In Figure 5, the experimental stored energy accumulated in the TSS shows a good match with simulated energy. At t = 11:42, a set value of the transferred thermal power to the PB is achieved. As a result, the excess heat is either transferred to the hot salt tank or dissipated when the hot salt tank is completely filled, i.e., reached 1025 MW_{th} h. The thermal oil (HTF) enters and exits the TSS at temperatures of 393 °C and 293 °C, respectively. In the storage discharge period, the temperature of thermal oil is set to be 293 °C and 377 °C at the inlet and outlet of TSS, respectively. From t = 11:43 to t = 13:22, the thermal power transferred to the PB is collected from the SF and the TSS. At t = 13:22, the TSS is exhausted and remains empty until t = 14:32. At t = 16:52, the thermal storage capacity reaches 170 MW_{th} h. After that, the discharge period lasts about 1.35 h until the TSS is fully exhausted. From t = 18:12 to sunset, all the heat absorbed in the SF is transmitted to the PB to achieve the specified values of thermal oil mass flow and temperature of 600 kg/s and 393 °C, respectively. Therefore, no excess heat is found in TSS because of heavily cloudy periods. On the other hand, the measured stored energy is sent to the thermal storage system at t = 9:59 instead of the power block, then this process continues until t = 10:27. From t = 10:27 to t = 14:09, the collected heat is sent together to the PB and to the TSS despite nominal thermal power still not being achieved. Thereafter, the measured stored energy is decreased to replenish the lost heat due to the cloud cover. The measured storage energy rises again at t = 15:09 and continues increasing until t = 16:59, accompanied by oscillations in the measured transmitted thermal power. The accumulated thermal storage then drops to (0 MW_{th} h) at t = 17:59 due to the real power plant operating in storage mode.

Figure 6 shows the simulated HTF mass flow to the TSS and to the PB on 2 July 2010. The operating principle that was adopted to obtain these results shown in Figure 6 ensures the nominal HTF mass flow (600 kg/s). The surplus of thermal energy is transferred to the TSS, and this energy is also used to compensate for the shortfall in thermal power.

Finally, the comparison of simulation predictions and experimental data displays a good agreement until t = 17:59 on 2 July. This does not prevent some differences between the simulation and experimental after t = 17:59, as previously demonstrated. The discrepancies between the simulation and experimental are explained as follows: The operational steps were taken in the Andasol II plant to transfer the thermal power to TSS instead of transferring the power to the PB.

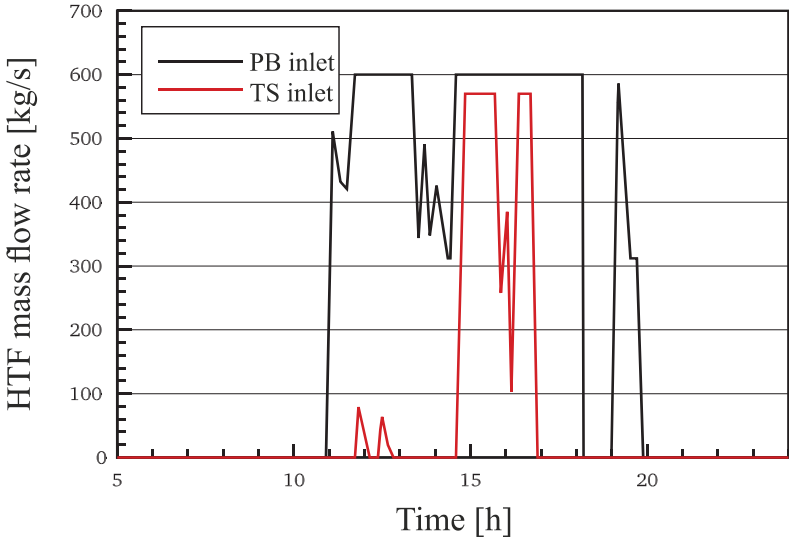

Figure 6. Simulated results of HTF mass flow rate to the PB and to the TSS.

6.2. Steam Behaviour

In this section, the steam parameters (steam mass flow and steam pressure) in different points in the Andasoll II are measured for the specified day at the nominal load. The dynamic behaviour of these parameters in the PB will be explained below.

The HP cycle is implemented between the exit of the HP feedwater pumps (HP FP) and the outlet of the last superheater. The dynamic behaviour of the water/steam path is presented by the following figures.

The model results of the mass flow of steam at the inlet and outlet of the HP turbine are demonstrated in Figure 7 for the selected day.

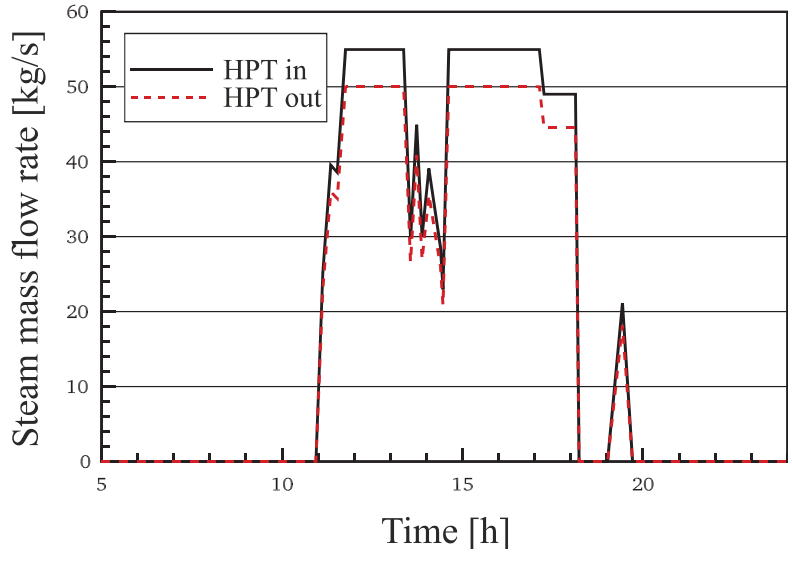

Figure 7. Simulated steam mass flow at the inlet and outlet of the HP turbine.

At t = 10:50, the mass flow of steam begins to increase until its specified value reaches about 55 kg/s at t = 11:40. The HP steam mass flow remains at this value until t = 13:20. Then, the mass flow of steam drops to 25 kg/s at t = 13:32 because of the lack of stored energy and the oscillations of HTF mass flow due to clouds. Here, the PB is only operated in SF mode. Between t = 14:33 and t = 17:06, the steam mass flow remains constant (55 kg/s). Between t = 17:14 and t = 18:06, the steam mass flow reduces down to 44.5 kg/s since the power plant operates only in storage mode. Then it drops to zero at t = 18:12 when the storage energy is exhausted. The steam mass flow increases at t = 19:54 again to 21 kg/s due to higher solar radiation. Thereafter, it drops to zero and continues at this value until sunrise the next day.

The steam mass flow at the outlet of the HP turbine displays similar behaviour to that of the steam mass flow at the inlet of the HP turbine for the chosen day, as illustrated in Figure 7. The difference in the steam mass flow between the HPT inlet and outlet is due to the steam extractions that are connected with the HP preheaters.

Figure 8 displays the dynamic behaviour of the steam pressure at the inlet of the HP turbine. The pressure of steam rises to a set value of 106 bars due to the generation of steam in the PB. After that, it continues at this value in the period between t = 11:44 and t = 13:20. From t = 13:20; the steam pressure decreases to 57 bars. Then, it fluctuates until t = 14:26. The steam pressure rises again to its set value at t = 14:35 and then it continues constant until t = 17:06. The steam pressure decreases to 94.42 bars and is kept constant for one hour, then decreased to (0 bars) at t = 18:12. At t = 18:59, the steam pressure rises again to 40.64 bars due to higher DNI. Subsequently, the vapour pressure drops to zero at t = 19:41 and remains to sunset because there is no storage energy and there is no solar radiation due to the clouds. The steam pressure of the LP turbine behaves the same as the steam pressure of the HP turbine.

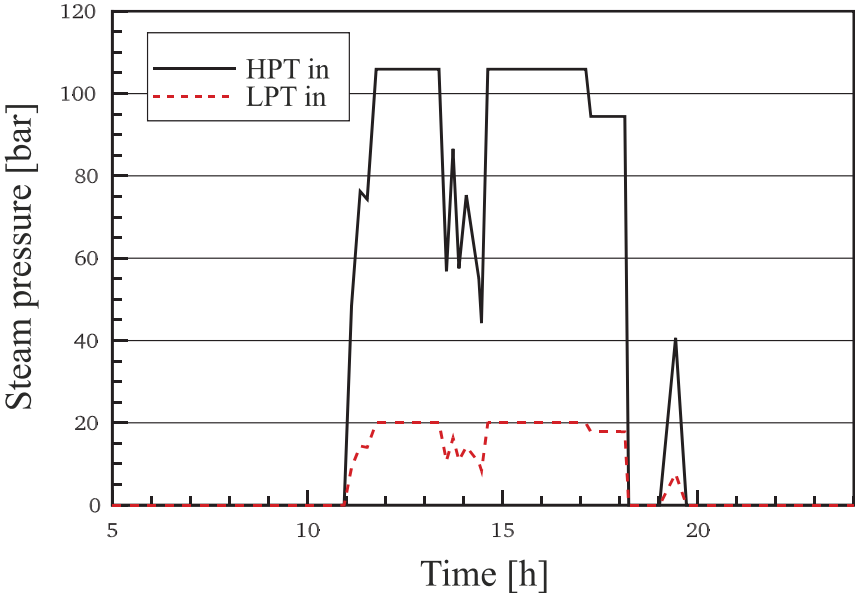

Figure 8. Simulated results of steam pressure at the inlet of the high- and low-pressure turbine.

7. Conclusions

A detailed dynamic model of a parabolic trough solar power plant (Andasol II) was carried out by (APROS) Software with required control circuits. The model was

implemented using the realistic details obtained from a real plant. A comparison between the simulations results and experimental data from "Andasol II" was applied.

It is obvious that the model results agree well with the experimental data in some periods ranging between t = 10:28–17:59 for the selected day. Conversely, several discrepancies can be observed between the simulated results and the experimental data for the rest of the day. This is due to the fact that, on the one hand, the operator's decision during overcast periods was different from that performed in the model, and on the other hand the power plant was operated based on the fossil fuel system during some periods, as well as a technical fault in the measured data that occurred around t = 9:53. Note that the operator's decisions can also be included by the APROS model, but that will be at the expense of the dynamic behaviour of simulation, i.e., the simulation will be conducted as a steady-state model. However, the operation strategy applied in the dynamic model during cloudy day improves the electrical power production compared to the operator's decisions that were implemented in the real power plant. About 28% (about 2.7–3.1 h) of electric power generation was increased during the discharge and charge phases of the chosen days.

This model is important for understanding the operation strategy of the power plant and possibly for other plants in other operating conditions to benefit from it.

Author Contributions: Methodology, W.A.K.A.-M. and H.A.A.W.; software, W.A.K.A.-M. and A.G.T.A.-H.; investigation, W.A.K.A.-M., A.G.T.A.-H. and H.A.A.W.; writing—original draft preparation, W.A.K.A.-M.; writing—review and editing, W.A.K.A.-M. and F.A.; supervision, B.E. All authors have read and agreed to the published version of the manuscript.

Funding: This research received no external funding.

Informed Consent Statement: Not applicable.

Data Availability Statement: Not applicable.

Acknowledgments: We acknowledge support by the Deutsche Forschungsgemeinschaft (DFG—German Research Foundation) and the Open Access Publishing Fund of Technical University of Darmstadt. The authors would like also to thank the University of Technology—Iraq.

Conflicts of Interest: All authors declare no conflict of interest.

References

1. Kaygusuz, K. Prospect of concentrating solar power in Turkey: The sustainable future. *Renew. Sustain. Energy Rev.* **2011**, *15*, 808–814. [CrossRef]
2. Teske, S.L.J.; Crespo, L.; Bial, M.; Dufour, E.; Richter, C. Solar thermal electricity. *Glob. Outlook.* 2016. Available online: https://www.estelasolar.org/wp-content/uploads/2016/02/GP-ESTELA-SolarPACES_Solar-Thermal-Electricity-Global-Outlook-2016_Full-report.pdf (accessed on 3 September 2021).
3. Philibert, C. *Technology Roadmap: Solar Thermal Electricity*; OECD/IEA: Paris, France, 2014.
4. Izquierdo, S.; Montanes, C.; Dopazo, C.; Fueyo, N. Analysis of CSP plants for the definition of energy policies: The influence on electricity cost of solar multiples, capacity factors and energy storage. *Energy Policy* **2010**, *38*, 6215–6221. [CrossRef]
5. Wahhab, H.A.A.; Al-Maliki, W.A.K. Application of a Solar Chimney Power Plant to Electrical Generation in Covered Agricultural Fields. In *IOP Conference Series: Materials Science and Engineering*; IOP Publishing: Bristol, UK, 2020; p. 012137.
6. Ismaeel, A.A.; Wahhab, H.A.A.; Naji, Z.H. *Performance Evaluation of Updraft Air Tower Power Plant Integrated with Double Skin Solar Air Heater*; Transdisciplinary Research and Education Center for Green Technologies, Kyushu University: Fukuoka, Japan, 2021.
7. Lovegrove, K.; Stein, W. *Concentrating Solar Power Technology: Principles, Developments and Applications*; Elsevier: Amsterdam, The Netherlands, 2012.
8. Al-Maliki, W.A.K.; Mahmoud, N.S.; Al-Khafaji, H.M.; Alobaid, F.; Epple, B. Design and Implementation of the Solar Field and Thermal Storage System Controllers for a Parabolic Trough Solar Power Plant. *Appl. Sci.* **2021**, *11*, 6155. [CrossRef]
9. Masero, E.; Frejo, J.R.D.; Maestre, J.M.; Camacho, E.F. A light clustering model predictive control approach to maximize thermal power in solar parabolic-trough plants. *Sol. Energy* **2021**, *214*, 531–541. [CrossRef]
10. Frejo, J.R.D.; Camacho, E.F. Centralized and distributed Model Predictive Control for the maximization of the thermal power of solar parabolic-trough plants. *Sol. Energy* **2020**, *204*, 190–199. [CrossRef]
11. Sánchez, A.; Gallego, A.; Escaño, J.; Camacho, E. Parabolic Trough Collector Defocusing Analysis: Two control stages vs four control stages. *Sol. Energy* **2020**, *209*, 30–41. [CrossRef]
12. Montañés, R.M.; Windahl, J.; Pålsson, J.; Thern, M. Dynamic modeling of a parabolic trough solar thermal power plant with thermal storage using modelica. *Heat Transf. Eng.* **2018**, *39*, 277–292. [CrossRef]

13. Larraín, T.; Escobar, R.; Vergara, J. Performance model to assist solar thermal power plant siting in northern Chile based on backup fuel consumption. *Renew. Energy* **2010**, *35*, 1632–1643. [CrossRef]
14. García, I.L.; Álvarez, J.L.; Blanco, D. Performance model for parabolic trough solar thermal power plants with thermal storage: Comparison to operating plant data. *Sol. Energy* **2011**, *85*, 2443–2460. [CrossRef]
15. Diendorfer, C.; Haider, M.; Lauermann, M. Performance analysis of offshore solar power plants. *Energy Procedia* **2014**, *49*, 2462–2471. [CrossRef]
16. Schenk, H.; Hirsch, J.D.T.; Polklas, T. Transient Simulation of the Power Block in a Parabolic Trough Power Plant. In Proceedings of the 11th International Modelica Conference, Versailles, France, 21–23 September 2015.
17. Luo, N.; Yu, G.; Hou, H.; Yang, Y. Dynamic Modeling and Simulation of Parabolic Trough Solar System. *Energy Procedia* **2015**, *69*, 1344–1348. [CrossRef]
18. Alobaid, F.; Mertens, N.; Starkloff, R.; Lanz, T.; Heinze, C.; Epple, B. Progress in dynamic simulation of thermal power plants. *Prog. Energy Combust. Sci.* **2017**, *59*, 79–162. [CrossRef]
19. Wilcox, S.; Marion, W. *Users Manual for TMY3 Data Sets*; National Renewable Energy Laboratory Golden: Golden, CO, USA, 2008.
20. Patnode, A.M. *Simulation and Performance Evaluation of Parabolic Trough Solar Power Plants*; University of Wisconsin-madison: Madison, WI, USA, 2006.
21. Burkholder, F.; Kutscher, C. *Heat-Loss Testing of Solel's UVAC3 Parabolic Trough Receiver*; National Renewable Energy Laboratory (NREL): Golden, CO, USA, 2008.
22. Al-Maliki, W.A.K.; Alobaid, F.; Kez, V.; Epple, B. Modelling and dynamic simulation of a parabolic trough power plant. *J. Process Control* **2016**, *39*, 123–138. [CrossRef]

applied sciences

MDPI

Article

Experimental Study of the Influence of Gas Flow Rate on Hydrodynamic Characteristics of Sieve Trays and Their Effect on CO_2 Absorption

Adel Almoslh *, Falah Alobaid, Christian Heinze and Bernd Epple

Institut Energiesysteme und Energietechnik, Technische Universität Darmstadt, Otto-Berndt-Straße 2, 64287 Darmstadt, Germany; falah.alobaid@tu-darmstadt.de (F.A.); christian.heinze@tu-darmstadt.de (C.H.); bernd.epple@tu-darmstadt.de (B.E.)

* Correspondence: adel.almoslh@wihi.tu-darmstadt.de; Tel.: +49-(61)-511623004; Fax: +49-(06)-1511622690

Abstract: An experimental study was conducted in the sieve tray column to investigate the influence of gas flow rate on the hydrodynamic characteristics of the sieve tray, such as total tray pressure drop, wet tray pressure drop, dry tray pressure drop, clear liquid height, liquid holdup, and froth height. The hydrodynamic characteristics of the sieve tray were investigated for the gas/water system at different gas flow rates from 12 to 24 Nm^3/h and at different pressures of 0.22, 0.24, and 0.26 MPa. In this study, a simulated waste gas was used that consisted of 30% CO_2 and 70% air. The inlet volumetric flow rate of the water was 0.148 m^3/h. The temperature of the inlet water was 19.5 °C. The results showed that the gas flow rate has a significant effect on the hydrodynamic characteristics of the tray. The authors investigated the effect of changing these hydrodynamic characteristics on the performance of a tray column used for CO_2 capture.

Keywords: CO_2 capture; CO_2 absorption; liquid holdup; pressure drop; clear liquid height; froth height; experimental study

Citation: Almoslh, A.; Alobaid, F.; Heinze, C.; Epple, B. Experimental Study of the Influence of Gas Flow Rate on Hydrodynamic Characteristics of Sieve Trays and Their Effect on CO_2 Absorption. *Appl. Sci.* **2021**, *11*, 10708. https://doi.org/10.3390/app112210708

Academic Editor: Teemu Turunen-Saaresti

Received: 4 October 2021
Accepted: 9 November 2021
Published: 12 November 2021

1. Introduction

Absorption is a separation process used to capture many gases—such as CO_2—which, when released into the atmosphere, contributes to the increase of global warming. The absorption technology for CO_2 capture mainly consists of the absorber column and the regeneration unit. The absorber column can be a plate column or packed column. The absorbent enters the absorber from the top, and the waste gas containing CO_2 enters the absorber from the bottom. The gas and liquid phases come into contact with each other on the trays or packing. The trays or packing material increase the gas–liquid interface, which increases mass and heat transfer between the contact phases. The CO_2 component passes from the gas phase to a liquid phase and is then absorbed. Knowledge of the hydrodynamic properties of trays is necessary for the design and operation of absorption columns because they control the liquid height on the trays and affect the pressure drop, tray efficiency, and flow conditions on the trays (Wijn, et al., 1999) [1].

In the literature, various studies can be found on the influence of the inlet gas flow on the hydrodynamic characteristics and mass transfer in gas–liquid systems. Some studies discuss the influence of gas velocity on froth height and the height of clear liquid on the trays.

Dhulesia, H. (1984) [2] tested the effect of gas velocity on the height of clear liquid for three sieve trays. They plotted the height of the clear liquid versus the flow ratio $\Psi^{0.25}$, they found that the height of the clear liquid was proportional to the flow ratio for froth regime. However, for the spray regime, they stated that the dependence of clear liquid height on the flow ratio group could not be detected. Dhulesia, H. (1984) [2] also investigated the influence of liquid and gas rates on the clear liquid height by using a valve tray with a

weir height of 25 mm. They established that the clear liquid height increases with liquid volume, where the clear liquid height decreases with increasing superficial air velocity.

Badssi, Bugarel et al. (1988) [3] explored the effect of the superficial velocity of gas on the interfacial area in two different gas–liquid systems CO_2-DEA and CO_2-NaOH. The experiment was carried out in a laboratory column equipped with cross-flow sieve trays. They found that the total interfacial area increased when the superficial velocity was increased.

Wijn (1999) [1] stated that the liquid height depends on the gas and liquid loads, gas and liquid properties, and some geometrical parameters such as the height and length of the weir, free hole area, hole diameter, etc.

Van Baten, Ellenberger et al. (2001) [4] investigated the hydrodynamics of a sieve tray column for reactive distillation. The author observed that the clear liquid decreased significantly when the superficial velocity of the gas increased between 0.4–1 m/s.

Furzer et al. (2001) [5] determined the height of froth and the height of clear liquid on dual-flow trays with 20% free area; the authors stated that there is a strong relationship between the height of froth and the height of clear liquid, as the height of froth increases when the height of clear liquid increases. The authors noted that the height of the clear liquid increases with the vapour velocity.

Rahimi, Zarei et al. (2010) [6] studied hydraulic parameters such as dry pressure drop in a column with a diameter of 1.22 m. The column has two sieve trays and two chimney trays; the author observed that the pressure drop increases when the Fs factor is increased. Their experiments were conducted in a round tower with a diameter of 1.22 m for the air/water system; The author observed that the height of the clear liquid decreases as the velocity of the gas increases.

R Brahem et al. (2015) [7] reviewed experimental measurements of hydrodynamic and interface parameters performed on two pilot-scale rectangular valve tray columns. They present their results for the height of the clear liquid as a function of the flow ratio Ψ and show that the height of the clear liquid increases as the flow ratio Ψ increases. In the same study, they also plot that the tray pressure drop increases by increasing the gas kinetic factor, Fa.

Kurella, Bhukya et al. (2017) [8] studied the effect of the gas velocity on the average height of the clear liquid that is on the tray; their experimental study was conducted in a dual-flow sieve plate scrubber. The authors found that at constant liquid flow rates, the average clear liquid height increased as the gas loading factor (Fs) was increased.

Kurella, Bhukya et al. (2017) [8] examined the effects of gas and liquid flow rates on the percent removal of H_2S at H_2S input concentrations of 50–300 ppm. Their experiments were performed in a lab-scale three-stage dual-flow sieve plate column scrubber. The authors concluded that the percentage of H_2S removal increases as the gas flow rate is increased.

Feng, Fan et al. (2018) [9] analysed the effects of the Fs factor on dry pressure drop, wet pressure drop, clear liquid height, and froth height. Their experiments were conducted using a folding sieve tray (FST), which consists of double-perforated oblique planes folding at a specific angle. The author found that the dry pressure drop, wet tray pressure drop, clear liquid height, and froth height increased when the Fs factor of the gas was increased, while the clear liquid height decreased when the Fs factor was increased.

There are numerous studies in the literature investigating the effect of parameters such as temperature, flow rate of the solvent flow rate of the inlet gas on CO_2 absorption, but the study of the correlation between the hydrodynamic characteristics of the sieve tray and CO_2 absorption is still limited.

The objectives of this study are summarized as follows:

(1) To experimentally investigate the effect of inlet gas flow rate on the hydrodynamic properties of the sieve tray column, such as total tray pressure drop, wet tray pressure drop, dry tray pressure drop, clear liquid height, liquid holdup, and froth height, an absorber test rig was constructed and operated.
(2) Investigating the influence of inlet gas flow rate on the hydrodynamic characteristics of the sieve tray and its effect on the performance of a sieve tray absorber for CO_2 capture using water as the absorbent.

2. Experimental

2.1. Test Rig Setup

Figures 1 and 2 show an absorber test rig that was constructed at the Technical University of Darmstadt. The absorber test rig consists of four main parts: an absorber column, a regeneration unit, a gas mixing unit, and a gas analysis unit. The absorber consists of a glass column with an inner diameter of 152 mm and a height of 1500 mm. The upper and lower parts of the column were closed by suitable metal flanges. The lower flange contains the outlet of the liquid and the upper flange contains the outlet of the gas. The column has 12 glass nozzles to which metal flanges can be connected, 10 nozzles of which are used to measure the temperatures and pressures in the absorber, and 2 nozzles for the entrance of the liquid and gas into the absorber. Figure 3 shows a cross section of the sieve tray used in the absorber, five sieve trays are fixed with threaded rods and inserted into the absorber. The diameter of the sieve tray is 150 mm, the space between the sieve tray and the glass wall is sealed with rubber seals. The percentage of the sieve holes area in the active area is 0.071, the diameter of the hole in the sieve tray is 2 mm, the vertical and horizontal pitch between the holes is 6 mm, and the height of the weir is 15 mm. The tray spacing is 240 mm. The mixing unit consists of two lines connected to a manifold in front of the absorber. One of the lines is connected to cylinders filled with CO_2 gas, while the other is connected to an air compressor. The MFC is used to control the flow rate of the gases introduced into the absorber. A gas analyser is connected to the gas outlet line to measure the volume fraction of CO_2 at the outlet of the absorber.

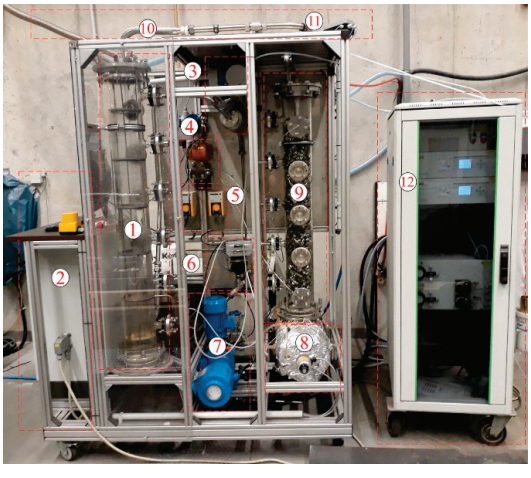

Figure 1. Side view of the absorber test rig: 1, absorber column; 2, control panel; 3, Coriolis device; 4, pressure difference transmitter; 5, make-up pump; 6, liquid level control valve; 7, recycling pump; 8, re-boiler; 9, packed column; 10, gas outlet; 11, pressure control valve; 12, gas analysis unit.

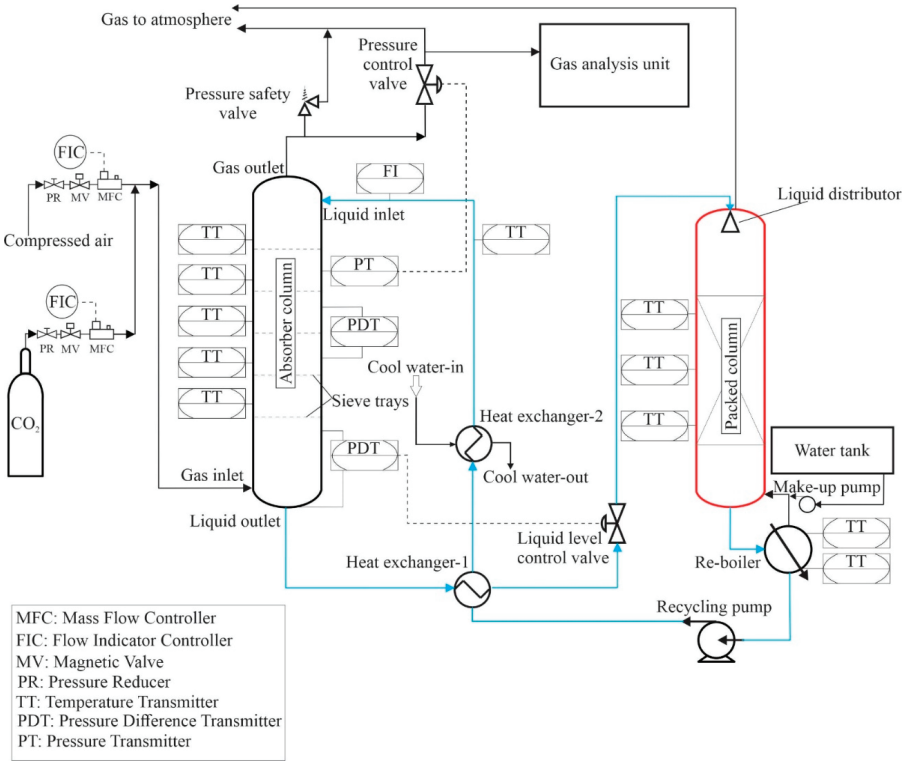

Figure 2. Schematic diagram of the absorber test rig.

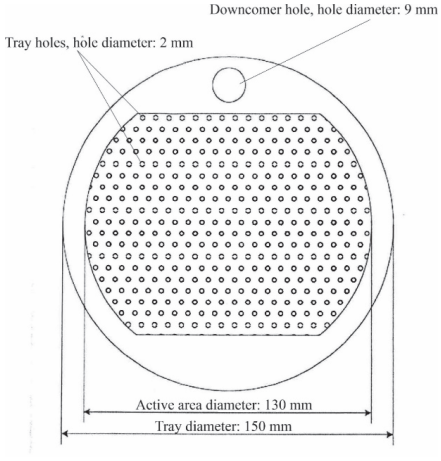

Figure 3. A cross-section of the sieve tray used in the absorber.

The regeneration unit is used to regenerate the absorbent and recycle it to the absorber as a lean absorbent. It consists of a packed column, a reboiler, two heat exchangers, a recycle pump and a make-up pump. The packed column was made of a glass column with a height of 1300 mm and a diameter of 152 mm. The packed column is filled with a metallic packing of the Pall-Ring 15 mm type with a specific surface area of 360 m^2/m^3 and a free

volume of 95%. The height of the packed column is 1 m. The rich absorbent enters the packed column through a liquid distributor to uniformly distribute the absorbent over the top of the packed column. The shaped liquid distributor is of spray type, which contains 13 holes uniformly arranged on the liquid distributor. The packed column is installed on the reboiler, a heating coil with a heating capacity of 4.5 kW was inserted into the reboiler to heat and regenerate the absorbent. A circulation pump is connected to the reboiler, which draws the water from the reboiler and pumps it into the absorber. The lean hot absorbent is cooled by two heat exchangers. In the first heat exchanger, the lean hot absorbent is precooled by heat exchange with the absorbent leaving the absorber, while in a second heat exchanger the precooled absorbent is cooled by heat exchange with cold water.

2.2. Instrumentation and Control Equipment of the Test Rig

The test stand is equipped with various devices and control circuits installed to measure the required parameters of the absorption process and for safe operation. A pressure reducer is installed on each line of the gas mixer to set the maximum pressure of the gas entering the absorber. After the pressure reducer, a magnetic valve is installed, which allows opening or closing the gas supply and can be closed in case of emergency. An MFC is attached to each line of the gas mixer to control the volume flow. A temperature sensor is placed near each absorber tray to measure the temperature of the liquid on that tray. A Coriolis device is placed at the inlet of the fluid to measure the temperature and flow rate of the water entering the absorber. A pressure difference meter was attached to the absorber column to estimate the total pressure drop in the tray.

The test rig is equipped with five control loops for control. The first control loop is used to regulate the pressure to the set point and to prevent the pressure from rising above 0.6 MPa (permissible internal pressure of the glass absorber). The pressure control circuit consists of a control valve and a pressure sensor. The control valve is attached to the gas outlet of the absorber, while the pressure sensor is attached to the column. The pressure control loop starts controlling the pressure after the gas enters the absorber, resulting in a pressure increase. The pressure sensor sends a signal with the actual value of the pressure to a PID controller. The PID controller compares the set point of the pressure with the actual value of the pressure and gives a signal to the control valve, which opens or closes with the percentage value to keep the pressure at the desired set point. At the outlet of the absorber, there is a safety pressure valve that releases the pressure in the absorber when it reaches the value of 0.45 MPa. This design protects the glass absorber from unexpected pressure development above 0.45 MPa.

The second control circuit is used to control the liquid level at the bottom of the absorber. The liquid level control is necessary because it prevents the gas from flowing from the liquid outlet and prevents the accumulation of the liquid in the absorber to a high level. The level control circuit consists of a pressure differential device and a control valve. The pressure differential device is installed in the sump of the column, while the control valve is attached to the liquid outlet of the absorber. The third control circuit regulates the level of absorbent in the reboiler, since a certain loss of absorbent occurs due to the evaporation of water. The control circuit consists of a make-up pump and a level sensor. The level sensor sends a signal to the make-up pump when the absorbent level falls below the set point to pump fresh absorbent into the reboiler. The fourth control loop is used to control the temperature of the absorbent in the reboiler. The purpose of this control circuit is to regenerate the absorbent by heating it using the heating coil installed in the reboiler. Since the third control circuit may not work for unexpected reasons, a control circuit (the fifth control circuit) is installed in the reboiler to protect the heating coil, which switches off the heating element when the liquid level in the reboiler drops below the set value of the absorbent level.

2.3. Test Procedure

The CO_2 gas was mixed with air in the gas mixing unit; the air served as the carrier gas. The CO_2 volume fraction was 0.3 in all experiments, and the inlet gas flow rate was varied in the ranges 12–24 Nm^3/h. The pressure of the absorber was varied at 0.22, 0.24, and 0.26 MPa. Distilled water was used as the absorbent. The volume flow rate of the feed water was almost constant at 0.148 m^3/h, and the temperature was controlled at 19.5 °C. The regeneration unit was operated with a thermal power of 4.5 kW over time.

3. Results and Discussion

3.1. Effect of the Inlet Gas Flow Rate on Outlet CO_2 Volume Fraction

The absorber test rig is run for 10 min under specified conditions for every measurement, resulting in time-dependent values for each measured parameter (i.e., pressure, temperature, and gas concentrations). The standard deviation, which indicates the range of variation of each measured parameter, is then calculated to estimate the random error. The systematic error of the measuring instruments is constant for all tests and is therefore not presented additionally in this chapter. In general, the measurement uncertainty of directly measured values (e.g., temperature, pressure, and flue gas concentrations) depends only on the relative uncertainty of the measuring instruments and is given by the relative error. For indirectly measured parameters or calculated values (e.g., volumetric flow rate, where the pressure difference and temperature are used in the calculation), the Gaussian error propagation method is applied, assuming normally distributed uncertainties. In this study, the volumetric concentrations are determined with the gas analysis unit, and the maximum relative error for CO_2 in the different process streams is about 3%.

Figure 4 demonstrates the effect of inlet gas flow rate on the outlet volume fraction of CO_2 at pressures of 0.22, 0.24, and 0.26 MPa. From Figure 4, it can be shown that increasing the inlet gas flow rate has a significant effect on the volume fraction of CO_2. The volume fraction of CO_2 goes up with the increase of the inlet gas flow rate from 12 to 16 Nm^3/h and from 20 to 24 Nm^3/h, while an increase of the inlet gas flow rate between 16 and 20 Nm^3/h has a slight effect on the volume fraction of CO_2. The trend of this effect is similar for all pressure values investigated.

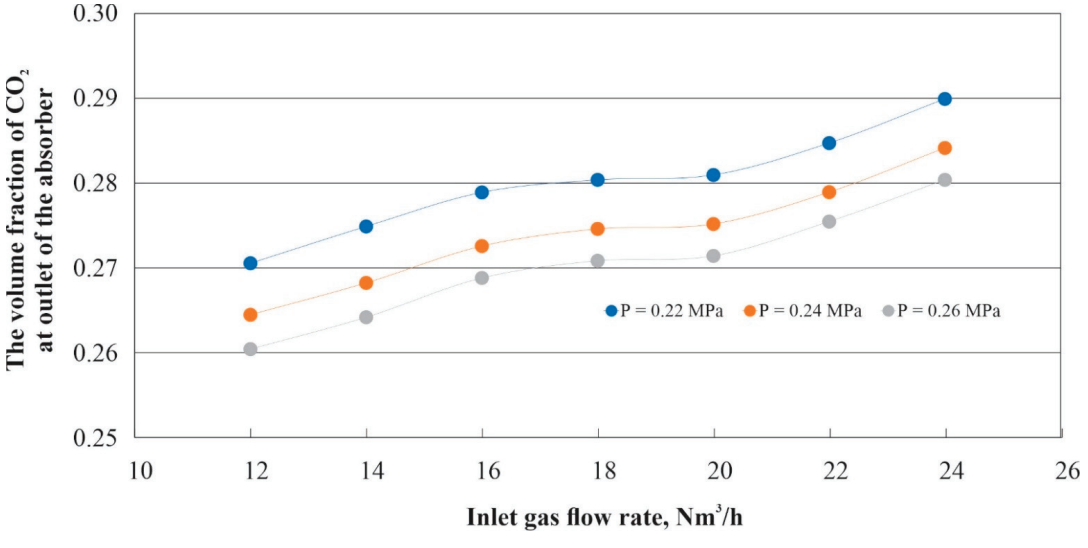

Figure 4. Effect of the inlet gas flow rate on the volume fraction of CO_2 at the outlet of the absorber.

The principal explanation for this effect may be that a change in the gas flow rate will influence the hydrodynamic characteristics of the tray—such as clear liquid height, the liquid holdup of the tray, and the froth height on the tray—which will be studied later.

The standard errors of the measurements of CO_2 volume fraction are shown in Table 1.

Table 1. Standard errors of the measurements of CO_2 volume fraction.

Inlet Gas Flow Rate, Nm^3/h	The Standard Errors of the Measurements		
	P = 0.22 MPa	P = 0.24 MPa	P = 0.26 MPa
12	0.00043	0.00003	0.00011
14	0.00025	0.00027	0.00007
16	0.00023	0.00014	0.00024
18	0.00017	0.00017	0.00022
20	0.00011	0.00015	0.00029
22	0.00014	0.00015	0.00017
24	0.00016	0.00015	0.00025

3.2. Effect of the Inlet Gas Flow Rate Hydrodynamic Characteristics of Sieve Tray

3.2.1. Effect of the Inlet Gas Flow Rate on Tray Pressure Drop

To study the effect of the inlet gas flow rate on tray pressure drop, the absorber test rig is equipped with a pressure difference device that measures the pressure difference before and after the third tray as shown in Figure 2. The pressure difference device measures the total pressure drop of the tray, which is the sum of the dry and wet pressure drops, is calculated as

$$\Delta P_{total,\ tray} = \Delta P_{dry,\ tray} + \Delta P_{wet.\ tray} \quad (1)$$

where $\Delta P_{total,\ tray}$ is the total tray pressure drop, $\Delta P_{dry,\ tray}$ is the dry tray pressure drop, and $\Delta P_{wet.\ tray}$ is the wet tray pressure drop. $\Delta P_{total,\ tray}$ is measured during performing the experiments when the liquid and the gas are coming into the column, in contrast $\Delta P_{dry,\ tray}$ is measured when only the gas is coming into the column at operating conditions of gas flow rates between 12 to 24 Nm^3/h and different pressure with 0.22, 0.24, and 0.26 MPa.

By measuring both $\Delta P_{total,\ tray}$, $\Delta P_{dry,\ tray}$ one can get the ΔP_{wet} as

$$\Delta P_{wet.\ tray} = \Delta P_{total,\ tray} - \Delta P_{dry,\ tray} \quad (2)$$

Figure 5 shows the impact of the gas flow rate on the total tray pressure drop, dry tray pressure drop, and wet tray pressure drop. It can be observed that both the total tray pressure drop and the wet tray pressure drop increase smoothly between 12 and 20 Nm^3/h, and these pressure drops are almost constant when the inlet flow rate increases between 20 and 24 Nm^3/h, while the dry pressure drop increases due to an increase in the gas flow rate between 12 and 24. It is clear that the trend of this effect is similar for all pressure values studied.

The standard errors of the measurements of total tray pressure drop are shown in Table 2.

3.2.2. Effect of the Inlet Gas Flow Rate on Clear Liquid Height

Since wet pressure drop is equivalent to the clear liquid high on the tray, one can calculate clear liquid height as

$$h_{cl} = \Delta P_{wet,tray} \times 1.01972 \times 10^{-2} \quad (3)$$

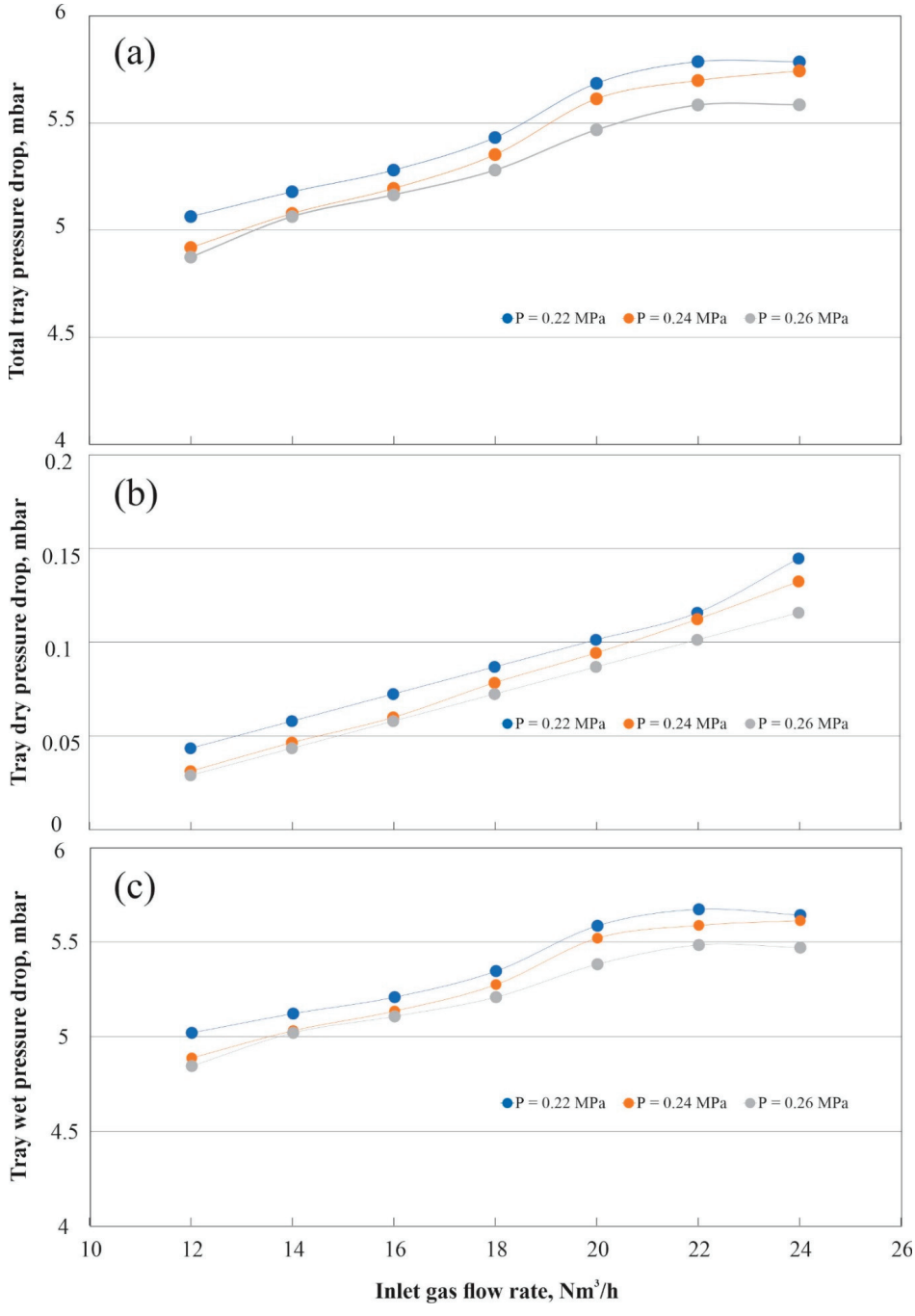

Figure 5. Effect of the inlet gas flow rate on (**a**) total tray pressure drop, (**b**) dry tray pressure drop, (**c**) wet tray pressure drop.

Table 2. Standard errors of the measurements of total tray pressure drop.

Inlet Gas Flow Rate, Nm^3/h	The Standard Errors of the Measurements		
	P = 0.22 MPa	P = 0.24 MPa	P = 0.26 MPa
12	0.00555	0.00535	0.00525
14	0.01886	0.01299	0.03397
16	0.01482	0.00982	0.01135
18	0.02145	0.01216	0.01368
20	0.02208	0.01817	0.01705
22	0.03704	0.03629	0.01956
24	0.04720	0.04783	0.03811

There are several correlations in the literature for estimating the clear liquid head. Francis (1883) [10] proposed an equation to calculate the liquid flow rate across the exit weir with rectangular cross section. The Francis equation is

$$Q = 3.33{h_1}^{3/2}(L - 0.2h_1) \tag{4}$$

where Q = discharge in f^3/s neglecting velocity of approach, L = the length of weir in ft, h_1 = head on the weir in ft.

From this equation, we can conclude that the height of the clear liquid and the liquid accumulation are only affected by the change in liquid flow. The gas flow has no influence.

Bennett et al. (1983) [11] developed a correlation for clear liquid height as

$$h_{cl} = \alpha_e \left[h_W + C\left(\frac{Q_L/W}{\alpha_e} \right)^{0.67} \right] \tag{5}$$

$$\alpha_e = exp\left[-12.55\left(u_b \left(\frac{\rho_G}{\rho_L - \rho_G} \right)^{0.5} \right)^{0.91} \right] \tag{6}$$

$$C = 0.5 + 0.438exp(-137.8h_W) \tag{7}$$

where h_{cl} is the clear liquid height, h_W is the outlet weir height, C empirical constant, Q_L is the liquid flow rate, W is the weir length, u_b is the bubbling velocity, ρ_G is the density of gas m^3/kg, ρ_L is the density of liquid m^3/kg, and α_e is the effective liquid volume fraction. It can be noted that the liquid clear high is a function of the bubbling velocity and the liquid/gas density.

Hofhuis et al. (1979) [12] have developed an Empirical correlation as

$$h_{cl} = 0.6\Psi^{0.25}{h_W}^{0.5}A^{0.25} \tag{8}$$

$$\Psi = \frac{Q_L/W}{u_s}\sqrt{\frac{\rho_L}{\rho_G}} \tag{9}$$

where A is the hole pitch, m; and u_s is superficial velocity.

It can be see that Hofhuis equation is a function of flow ratio group Ψ, weir height, and hole pitch. Hofhuis model can be applied to both froths and spray regimes (Wang, Chao, et al., 2018) [13].

Taking into account these studies, the Hofhuis correction can be modified to accommodate the height of the clear liquid on the sieve tray studied as

$$h_{cl} = 1.75\Psi^{-0.1}{h_W}^{0.5}P^{0.25} \tag{10}$$

Figure 6 shows the comparison between the experimental data and the results from Equation (10). It appears that there is agreement within the relative error ±5.5%.

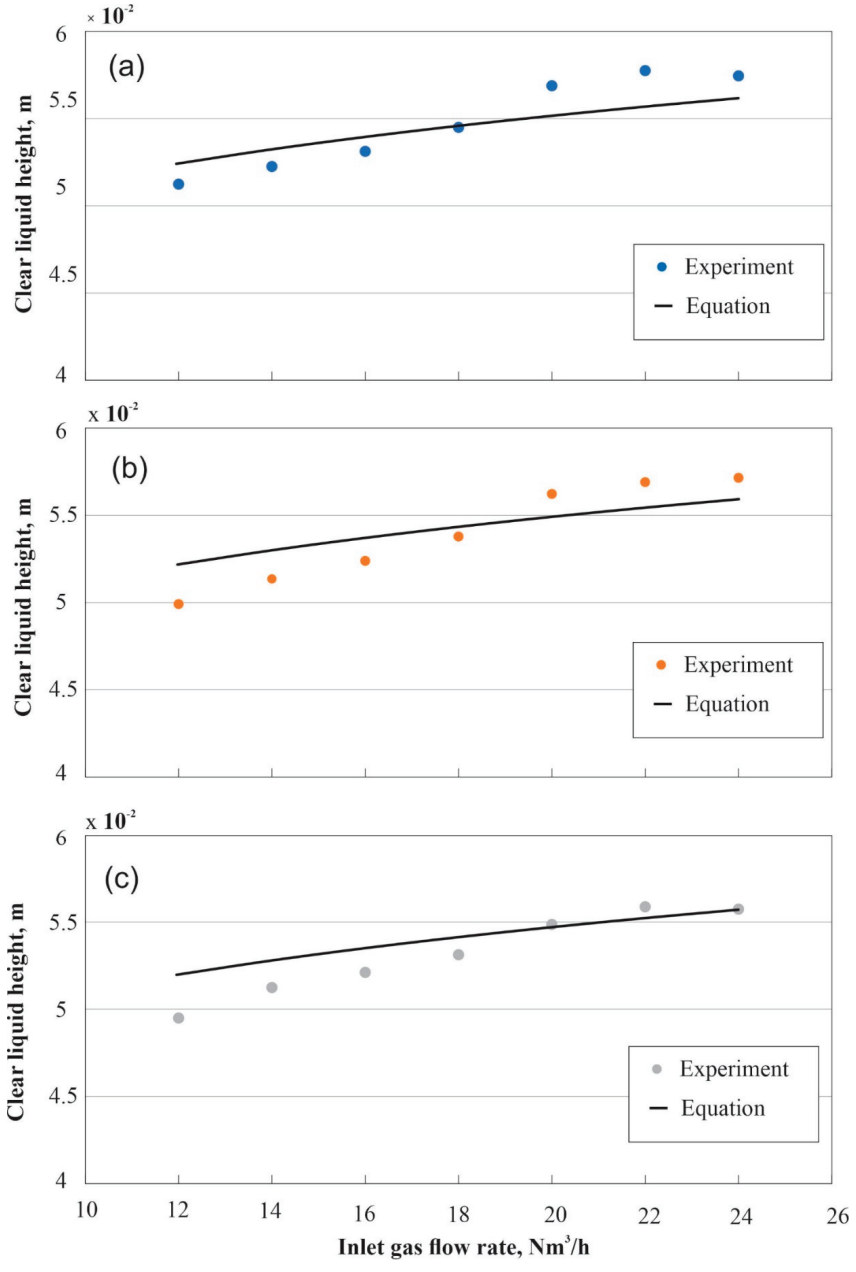

Figure 6. Effect of inlet gas flow rates on clear liquid height compared with Equation (10), at pressure 0.22 MPa (**a**), 0.24 MPa (**b**), and 0.26 MPa (**c**).

3.2.3. Effect of the Inlet Gas Flow Rate on Tray Liquid Holdup

One can calculate liquid holdup as

$$h_L = A_{tray} \times h_{cl} \tag{11}$$

Figure 7 shows the liquid holdup on the tray when the inlet gas flow rate is increased. Figure 7 shows that increasing the gas volume flow rate has a significant effect on liquid holdup on the tray. The liquid holdup on the tray is drastically increased when the gas volume flow rate is increased between 12 and 20 Nm^3/h. It is noted that the increase in flow rate between 16 and 20 Nm^3/h is more significant than the increase in flow rate between 12 and 16 Nm^3/h, while the increase in flow rate between 20 and 24 Nm^3/h has a small effect on liquid holdup. The trend of this effect is similar for all pressure values studied. The possible reason for this behavior is the increase in the superficial velocity of the gas in the absorber due to the increase in inlet gas flow rate, the increase in gas velocity causes the liquid to be trapped on a tray, resulting in the accumulation of the liquid on the tray, and as a result, the liquid holdup will increase. It appears also that when the gas inlet flow rate is increased after 20 Nm^3/h, the liquid holdup is almost constant. This trend may be due to the high gas velocity accelerates the liquid to flow into the downcomer, resulting in a steady liquid holdup.

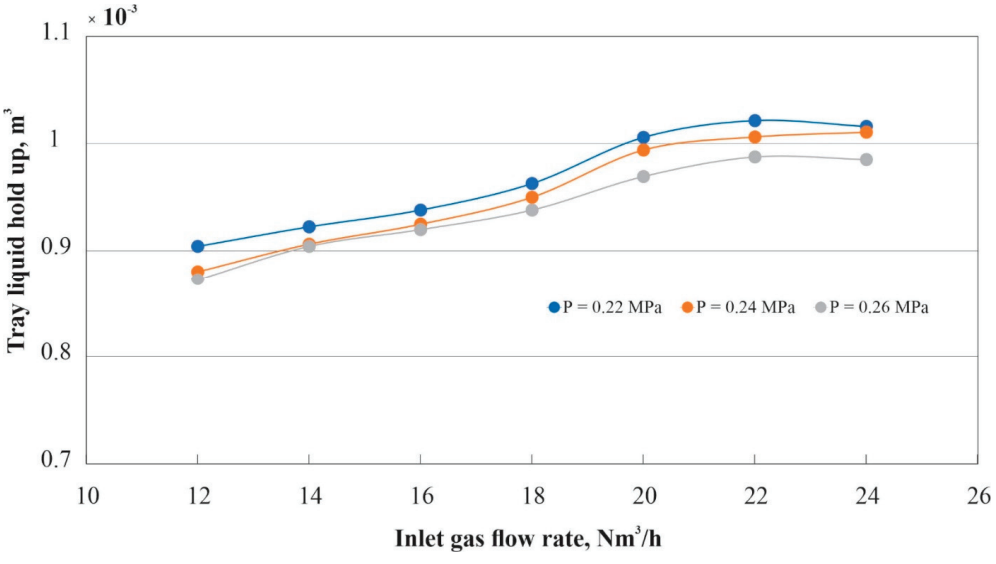

Figure 7. Effect of the inlet gas flow rate on the tray liquid holdup.

3.2.4. Effect of the Inlet Gas Flow Rate on Froth Height

To investigate the effect of gas flow rate on froth height, the absorber was fitted with a ruler to observe froth formation above the tray. It can be seen from Figures 8 and 9 that the froth height above the tray goes up as the flow rate progresses. The trend of this effect is similar for all pressure values studied. This trend can be explained by the increasing of the superficial velocity of the gas into the absorber through the increase of the flow rate, leading to an increase of the liquid holdup, as can be seen in Figure 7. The increase of the tray liquid holdup will increase the height of the froth on the tray.

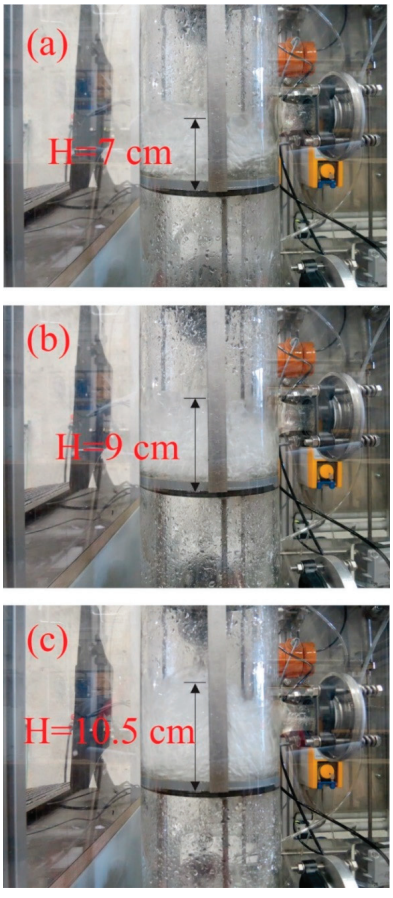

Figure 8. Froth height above the tray at inlet gas flow rate (**a**) 12 Nm^3/h, (**b**) 16 Nm^3/h, and (**c**) 18 Nm^3/h.

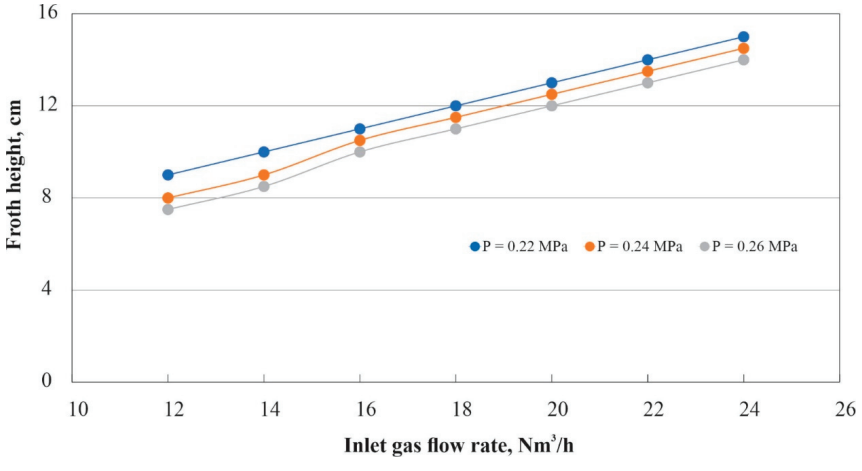

Figure 9. Effect of the inlet gas flow rate on froth height.

3.3. Studying the Effect of the Inlet Gas Flow Rate on the Performance of the Absorber

The performance of the absorber for CO_2 capture was measured by estimating the absorbed rate of CO_2. The absorbed rate N_{CO_2} of CO_2 was calculated using the equation

$$N_{CO_2} = \left[\left(y_{CO_2,\text{in}} - y_{CO_2,\text{out}}\right) F_{gas,in}\right] \quad (12)$$

where $y_{CO_2,\text{in}}$ is the inlet volumetric fraction of CO_2, $y_{CO_2,\text{out}}$ is the outlet volumetric fraction of CO_2, and $F_{gas,in}$ is the inlet gas flow rate. $y_{CO_2,\text{out}}$ was measured by the gas analysis unit, where $y_{CO_2,\text{in}}$ was calculated as

$$y_{CO_2,\text{in}} = \frac{F_{CO_2,\text{ in}}}{F_{gas,in}} = \frac{F_{CO_2,\text{ in}}}{F_{CO_2,\text{ in}} + F_{air,in}} \quad (13)$$

$F_{CO_2,\text{ in}}$ is the inlet CO_2 flow rate, and $F_{air,in}$ is the inlet air flow rate.

Figure 10 illustrates the effect of inlet gas flow rate on CO_2 absorption rate when the inlet gas flow rate is changed in the range of 12–24 Nm^3/h. There is a significant effect on the CO_2 absorption rate. The trend of this effect is similar for all pressure values studied. It can be seen that the CO_2 absorption rate is almost constant when the flow rate is changed between 12 and 16 Nm^3/h, whereas the CO_2 absorption rate increases clearly when the gas flow rate is increased between 16 and 20 Nm^3/h, while the CO_2 absorption rate decreases significantly when the flow rate is increased between 20 and 24 Nm^3/h.

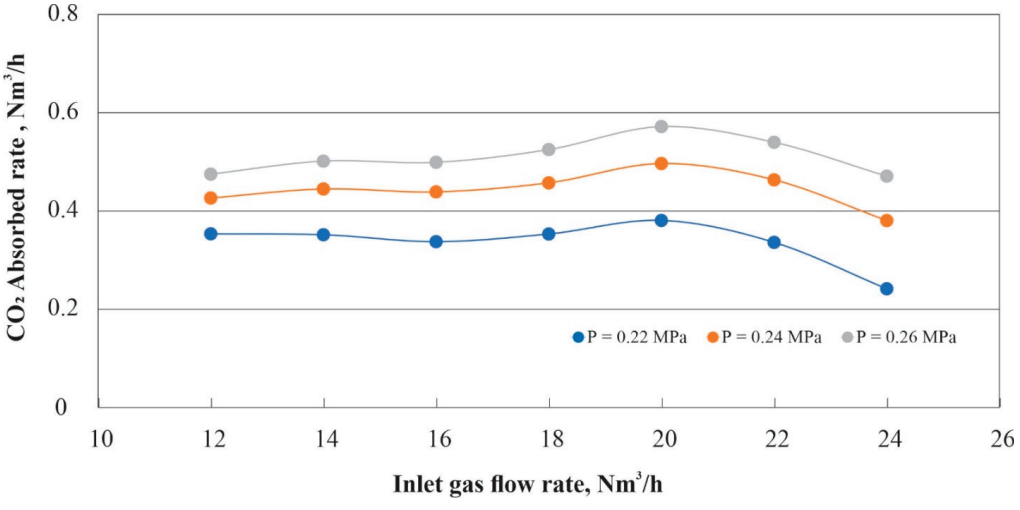

Figure 10. Effect inlet gas flow rates on the absorbed rate of CO_2 at pressure 0.22, 0.24, and 0.26 MPa.

Such trends in absorber performance can be interpreted by the increasing superficial velocity of the gas in the absorber as the flow rate increases. Increasing the gas velocity has different effects on the absorber performance. Increasing the superficial velocity of the gas affects the hydrodynamic characteristics of the tray, as shown in Figures 5–9. Specifically, in the case of liquid holdup, increasing the liquid holdup on the tray improves the mass transfer between the liquid and gas phases, resulting in an increase in the amount of CO_2 absorbed, and vice versa. In addition, as the superficial velocity of the gas increases, the interfacial area between the gas and liquid phases increases, as seen in the increase in froth height when the gas flow rate at the inlet is increased (as seen in Figure 9), leading to an increase in mass transfer and the amount of CO_2 absorbed.

On the other hand, increasing the superficial velocity above a certain value does not enhance the liquid holdup, as can be seen in Figure 7. In addition, increasing the superficial velocity will decrease the residence time of the gas in the absorber, thus decreasing the contact time between the gas and liquid phases, leading to a decrease in mass transfer between the gas and liquid phases, which could explain the decrease in CO_2 absorption rate when the flow rate is increased between 20 and 24 Nm^3/h.

4. Conclusions

Our study contributes to the body of literature on CO_2 absorption. An absorber test rig was built and operated. The effect of gas flow rate on the hydrodynamic properties of a sieve tray was experimentally investigated, and an analytical study of the effect of the hydrodynamic properties of a sieve tray on the CO_2 absorption process was presented, highlighting the following points.

(1) The inlet gas flow rate is found to have a significant effect on the hydrodynamic properties of the sieve tray. Increasing the inlet gas flow rate up to a certain value increases the liquid holdup, but increasing the inlet gas flow rate above this value does not improve the liquid holdup.
(2) There is a correlation between the absorber performance and tray liquid holdup. An increase in liquid holdup due to an increase in inlet flow rate increases the performance of the CO_2 absorber.
(3) This study gives us an idea of how the interface between the gas and liquid phases changes due to a change in gas flow rate. The increase of froth height is considered as a parameter which gives an idea of how big the interfacial area is between the gas and liquid phases.
(4) The study of the hydrodynamic properties of the tray is essential for the selection of the optimal operating conditions of the absorber. Through this study, it is possible to determine the optimal range of inlet flow rate of gas and also to determine the range of inlet flow rate of gas that causes a drop in absorber performance.

This work is a contribution to the knowledge available for studies o CO_2 absorption using water as an absorbent in the sieve tray column. Our results confirm other quotes in the literature, which are still limited to this issue.

Author Contributions: Conceptualization, A.A., F.A. and C.H.; methodology, A.A.; formal analysis, A.A. and F.A.; resources, B.E.; data curation, A.A.; writing—original draft preparation, A.A.; writing—review and editing, A.A. and F.A.; visualization, C.H. and A.A.; supervision, B.E.; project administration, B.E. All authors have read and agreed to the published version of the manuscript.

Funding: The authors received no specific funding for this work. The corresponding author would like to thank the Technical University of Darmstadt, enabling the open-access publication of this paper.

Institutional Review Board Statement: Not applicable.

Informed Consent Statement: Not applicable.

Data Availability Statement: Not applicable.

Acknowledgments: We acknowledge support by the Deutsche Forschungsgemeinschaft (DFG—German Research Foundation) and the Open Access Publishing Fund of Technical University of Darmstadt.

Conflicts of Interest: The authors declare no conflict of interest.

Abbreviations

Nomenclatures	
F_s	$F\ factor = V_s\sqrt{\rho_G}$, $\left[\mathrm{m/s(kg/m^3)^{0.5}}\right]$
F_a	kinetic gas factor based on velocity toward active area $Pa^{0.5}$
V_s	gas phase superficial velocity based on the bubbling area, [m/s]
ρ_G	gas density, $\left[\mathrm{kg/m^3}\right]$
$F_{gas,in}$	inlet gas flow rate, $\left[\mathrm{Nm^3/h}\right]$
$F_{\mathrm{CO_2,in}}$	inlet CO_2 flow rate $\left[\mathrm{Nm^3/h}\right]$
$F_{air,in}$	inlet air flow rate, $\left[\mathrm{Nm^3/h}\right]$
$N_{\mathrm{CO_2}}$	the absorbed rate of CO_2, $\left[\mathrm{Nm^3/h}\right]$
$y_{\mathrm{CO_2,in}}$	inlet volumetric fraction of CO_2, $[-]$
$y_{\mathrm{CO_2,in}}$	outlet volumetric fraction of CO_2, $[-]$
$\Delta P_{total,tray}$	total tray pressure drop, [mbar]
$\Delta P_{wet,\ tray}$	wet tray pressure drop, [mbar]
$\Delta P_{dry,\ tray}$	dry tray pressure drop, [mbar]
h_L	liquid holdup, $\left[\mathrm{m^3}\right]$
A_{tray}	Tray surface area, $\left[\mathrm{m^2}\right]$
h_{cl}	clear liquid height, [m]
h_W	weir height, [m]
C	empirical constant, $[-]$
Q_L	liquid flow rate, $\left[\mathrm{m^3/s}\right]$
W	weir length, [m]
u_b	bubbling velocity, [m/s]
ρ_G	density of gas, $\left[\mathrm{kg/m^3}\right]$
ρ_L	density of liquid, $\left[\mathrm{kg/m^3}\right]$
α_e	effective liquid volume fraction, $[-]$
Q	discharge in f^3/s neglecting velocity of approach, $\left[f^3/s\right]$
L	length of weir, $[f]$
h_1	head on the weir, $[f]$
A	the hole pitch, [m]
Ψ	flow ratio group
Abbreviations	
$\mathrm{Nm^3/h}$	a cubic meter of gas per hour at the normal temperature and pressure
PID controller	proportional–integral–derivative controller
MFC	mass flow controller
kW	kilowatt
DEA	2,2′-iminodiethanol
FST	folding sieve tray

References

1. Wijn, E.F. Weir flow and liquid height on sieve and valve trays. *Chem. Eng. J.* **1999**, *73*, 191–204. [CrossRef]
2. Dhulesia, H. Clear liquid height on sieve and valve trays. *Chem. Eng. Res. Des.* **1984**, *62*, 321–326.
3. Badssi, A.; Bugarel, R.; Blanc, C.; Peytavy, J.-L.; Laurent, A. Influence of pressure on the gas-liquid interfacial area and the gas-side mass transfer coefficient of a laboratory column equipped with cross-flow sieve trays. *Chem. Eng. Process. Process. Intensif.* **1988**, *23*, 89–97. [CrossRef]
4. Van Baten, J.; Ellenberger, J.; Krishna, R. Hydrodynamics of reactive distillation tray column with catalyst containing envelopes: Experiments vs. CFD simulations. *Catal. Today* **2001**, *66*, 233–240. [CrossRef]
5. Furzer, I.A. Froth heights on dual-flow trays with a heterogeneous binary azeotropic system and a heterogeneous ternary system with a homogeneous azeotrope. *Ind. Eng. Chem. Res.* **2001**, *40*, 4951–4966. [CrossRef]
6. Zarei, A.; Rahimi, R.; Zarei, T.; Naziri, N. A study on sieve tray lower operating limit. Distillation Absorption. In Proceedings of the 50th Distillation & Absorption Conference, Eindhoven, The Netherlands, 12–15 September 2010; pp. 479–484.
7. Brahem, R.; Royon-Lebeaud, A.; Legendre, D. Effect of path length on valve tray columns: Experimental study. *Chem. Eng. Sci.* **2015**, *126*, 517–528. [CrossRef]

8. Kurella, S.; Bhukya, P.K.; Meikap, B. Removal of H_2S pollutant from gasifier syngas by a multistage dual-flow sieve plate column wet scrubber. *J. Environ. Sci. Health Part A* **2017**, *52*, 515–523. [CrossRef] [PubMed]
9. Feng, W.; Fan, L.; Zhang, L.; Xiao, X. Hydrodynamics analysis of a folding sieve tray by computational fluid dynamics simulation. *J. Eng. Thermophys.* **2018**, *27*, 357–368. [CrossRef]
10. Francis, J.B. *Lowell Hydraulic Experiments*; Van Nostrand: New York, NY, USA, 1883.
11. Bennett, D.L.; Agrawal, R.; Cook, P.J. New pressure drop correlation for sieve tray distillation columns. *AIChE J.* **1983**, *29*, 434–442. [CrossRef]
12. Hofhuis, P.A.M. Sieve Plates: Dispersion Density and Flow Regimes. *Distillation* **1979**, *2*, 2/1–2/26.
13. Wang, C.; McCarley, K.; Cai, T.; Vennavelli, A. Study of clear liquid height and dry pressure drop models for valve trays. *Chem. Eng.* **2018**, *69*, 409–414. [CrossRef]

applied sciences

MDPI

Article

Dynamic Process Simulation of a Molten-Salt Energy Storage System

Wisam Abed Kattea Al-Maliki [1,2], Falah Alobaid [1,*], Alexander Keil [1] and Bernd Epple [1]

[1] Institut Energiesysteme und Energietechnik, Maschinenbau, Technische Universität Darmstadt, Otto-Berndt-Straße 2, 64287 Darmstadt, Germany; wisam.a.kattea@uotechnology.edu.iq (W.A.K.A.-M.); AD.Keil@web.de (A.K.); bernd.epple@est.tu-darmstadt.de (B.E.)
[2] Mechanical Engineering Department, University of Technology-Iraq, Bagdad P.O. Box 10066, Iraq
* Correspondence: falah.alobaid@est.tu-darmstadt.de; Tel.: +49-6151-16-23004

Abstract: The main objective of this work was the construction of a numerical model using Advanced Process Simulation Software to represent the dynamic behaviour of a thermal storage system (TSS). The storage model was validated by comparing the results with the measured data of the storage process of the Andasol 2 solar power plant. Subsequently, a system analysis and system optimisation were carried out, and the stand-alone concept of the thermal storage system is presented. Stand-alone refers to an isolated use of the storage system without a solar power plant. During power peaks, this storage medium is heated with excess electrical power and later returned to the electrical grid through a steam cycle. Then, the system was optimised by modelling four models based on the type of storage medium and the temperature difference of the storage system. The four models, Andasol 2, SSalt max, Hitec, and Carbonate, were evaluated and compared in terms of the improvement in capacity and efficiency that can be achieved. The comparison shows that the preferred storage medium is carbonate salt due to the increases in both efficiency and capacity. The greatest increase in efficiency in terms of power generation can also be achieved with the Carbonate model (18.2%), whereas the amount of increase was 9.5% and 7.4% for each of SSalt max and Hitec, respectively. The goal of this analysis and system optimisation of a thermal salt storage system is to stabilise and relieve the local power grid.

Keywords: dynamic simulation; stand-alone system; molten salt; thermal storage system; combined cycle plants

Citation: Al-Maliki, W.A.K.; Alobaid, F.; Keil, A.; Epple, B. Dynamic Process Simulation of a Molten-Salt Energy Storage System. *Appl. Sci.* **2021**, *11*, 11308. https://doi.org/10.3390/app112311308

Academic Editors: Miguel R. Oliveira Panão and Agus Pulung Sasmito

Received: 5 October 2021
Accepted: 25 November 2021
Published: 29 November 2021

1. Introduction

The depletion of fossil fuels and the increasing number of problems caused by global warming have increased interest in renewable energy sources in recent years [1]. At present, 46% of the electricity generated in Germany is obtained from renewable energy sources. As a result of the increasing share of sustainable power generation, the load on the power grid has increased because such power generation has significant dependencies on meteorological influences. In order to enable a further expansion of renewable energy sources, it is necessary to relieve and stabilise the power supply through the use of energy storage devices.

Energy storage is divided into electrical, chemical, mechanical and thermal energy storage according to its operating principle [2]. Electrical storage uses electrical and magnetic fields to store energy (for a short time). Chemical storage is the storage of energy with the help of material energy carriers [3]. In electrochemical storage systems, the stored energy is in chemical form in the electrodes. These also act as energy stores and converters. They have a fast response time, but have a short lifespan (<10 years) and show a constant loss of capacity. Mechanical storage uses the forced change in position (potential), speed (kinematics) or the thermodynamic state (pressure) of a material to store energy [4].

Thermal energy storage is discussed as the last operating principle, and can be divided into three types of thermal storage: latent, thermochemical, and sensitive. It is expected that thermal storage will gain increasing importance in the future because the heating sector is the largest energy sector in Europe, accounting for approx. 50% of energy consumption [1].

The most important type of energy storage for this work is that of sensible heat storage. In this type, heat is stored based on temperature difference. More precisely, a medium is heated during charging in order to absorb (excess) heat, and cooled during discharging, or the thermal energy is removed again. In sensible heat storage, the heat capacity of the storage medium, the mass, and the temperature difference are important. Furthermore, effective thermal insulation is essential, especially for long-term storage. Because of its low price and high level of development, it is currently the most common form of heat storage.

Thermal salt storage systems are currently used in a large number of solar power plants to ensure a constant power supply even though the solar radiation fluctuates in daylight and disappears during the night. The research and development of these storage systems are currently largely limited to steady-state process simulation models [5]. These do not require any control structures and are mathematically based on mass, momentum, and energy balances, which simplifies the initial system description. However, the transient and continuous changes in operating conditions can influence the efficiency of the investigated power plant. A recent literature review shows that there are few studies regarding the optimisation of the parabolic trough power plant employing dynamic and steady-state models.

A high temperature storage model of a solar tower power plant can be explained with open volumetric receiver technology using air as the heat transfer fluid (HTF) [6]. The model of the storage system was designed in the MATLAB/Simulink. The type of storage system investigated in this study is a bed-packed thermal energy storage system that has regeneration properties. It was used to develop various models of thermal storage systems using the lumped parameter method. First, the implemented models were stimulated to achieve high accuracy for the obtained results. Second, the dynamic properties of the thermal storage systems were extensively evaluated by applying turbulence of 15% to the mass flow. The results indicate that the charge and discharge properties of the three developed storage models have the same behaviour [7]. A dynamic solar field (SF) and thermal storage system (TSS) model of a 1 MW solar tower power plant was implemented in Beijing using Modelica software. The transient behaviour of charge storage and release processes for inlet and outlet steam quality was tested [8]. A proposed model was designed to provide a complete simulation of a thermocline tank operated at the lowest computing cost and to address the shortcomings of models developed in the previous studies. The suggested model was then integrated into a system-level model of a 100 MW_{el} solar tower power plant to study the storage capability in long-term service. The heliostat array and solar absorber tubes were modelled using DELSOL software, whereas the transient absorber tubes response was simulated using SOLERGY software. The study showed that the efficiency of the thermocline tank in accumulating and releasing thermal energy is approximately 99% year-round. Despite the excellent level of thermal efficiency, the structural stability of the thermocline tank remains a problem due to the high thermal expansion of the internal quartzite stone at high temperatures of the molten salt [9]. A 50 MW_{el} parabolic trough power plant has been modelled with (TRNSYS© software, 2007). Two heat transfer fluids (thermal oil and molten salt) were applied in this model. Seven operation strategies for charging and discharging modes were analysed to determine the most appropriate mode of operation that will minimise the difference in annual return between the two systems [10]. A parabolic trough power model was developed using APROS. A precise specification of the control response structures and operating approach was implemented to ensure appropriate dynamic performance. The operating strategies used in this model were also proven to be effective in enhancing power plant output and improving power plant operating hours using TSS compared to the operator's choices under cloudy sky conditions [11]. The periodic processes of molten salt storage system

thermoclines for parabolic trough solar plants were systematically evaluated using two temperature models. These models were designed by Fluent 6.1 and investigated with measured data. It was found that cycle efficiency is improved for smaller Reynolds numbers of molten salt, larger aspect ratios (distance of flow of molten salt in half a cycle relative to the diameter of the filler particles), and larger tank height. It was shown that the diameter of the filler particles and the capacity of the tank significantly affect the efficiency of the cycle [12]. A ceramic honeycomb TSS was modelled for a 10 kW solar air Brayton cycle system in this study using steady-state cycle analysis. The TSS showed very good operational efficiencies under the charge and discharge experimental tests, which were 79.6% and 76.5%, respectively. This study provides a contribution to the designing and modelling of TSS for solar-air Brayton cycle systems and to the analysis of the power plant operation strategy [13]. The binary nitrate (KNO_3 + Ca $(NO_3)_2$) with a melting point of 116.9 °C was chosen as the heat storage media in this research. The objective of this study was to achieve a stable and constant heat discharge performance of the TSS with a single tank of molten salt. A comparative study was undertaken of three different inlet velocity conditions, such as a steady value, automatic adjustment, and manual adjustment. According to the results, the heat discharge power decreases with increasing heat discharge period at a constant inlet velocity. The heat discharge period reduces as the inlet velocity increases, but the heat discharge power increases as the inlet velocity increases. The heat discharge power under automatic and manual adjustment of inlet speed varies by ±3% and ±10% from the set value, respectively [14]. A numerical model was built using enthalpy porosity model and two-temperature energy equations to evaluate thermal energy storage, extract the latent thermal energy from a storage system, and understand detailed heat transfer properties during a phase change material. The results showed that coating molten salt with nickel foam to effectively improve the thermal conductivity of the phase change material can enhance the performance of these types of systems [15]. A mathematical model for simulating the thermal performance of the high-temperature latent heat storage system in concentrating solar power plants was proposed, and satisfactory agreements were obtained between the simulated results and the empirical measurements. It can be seen that the average charging and discharging rates are enhanced by 6.8% and 9.1%, respectively, and the total thermal storage efficiency of the latent heat storage system increases from 34.4% to 44.1% due to the installation of circular fins [16]. The optimal design and technical and economic analysis of the stand-alone hybrid energy system was addressed for a rural city in China. A composite integer linear optimisation model was proposed with the objective of minimum overall annual cost depending on the assessment of current domestic renewable energy capacity potential and the study of heat and electricity consumption behaviour [17].

In order to ensure a realistic view of the efficiency and a precise design of the process components, a dynamic representation of the system is required. The originality of this work can be summarised as follows: In this study, the dynamic model of a thermal salt storage facility was modelled in APROS. The purpose is thus to represent the reference process as precisely as possible and to analyse the possible system improvements by changing the storage medium, which therefore produces differences in temperature for each medium used. The most important problem addressed by this study is how to utilise the surplus electricity generated from renewable energy sources during molten salt heating to be used later for electricity generation. Subsequently, a system analysis and system optimisation was performed and the stand-alone concept of the thermal salt storage system is presented.

Here, the structure and further development of the model is discussed in detail using APROS and any assumptions and simplifications made are presented. The model was then validated by comparing it with the storage process of the Andasol 2 thermal power plant. After the model was validated, further storage fluids were inserted into the model in order to analyse them with regard to system optimisation. In the following sections, a description of the system, modelling and simulation, results, and conclusions are presented.

2. Description of the System

The combined cycle power plant system with a storage system consists of the water/steam paths, gas turbine section, and thermal storage system (TSS). The schematic representation of the combined cycle power plant with the thermal storage system (TSS) can be seen in Figure 1. In this work, the TSS is only implemented with hot and cold tanks connected via heat exchangers. Two working media (molten salt and heat transfer fluid (HTF)) are used in the TSS. Each of the two salt tanks has a diameter of 38.5 m and a height of 14 m. The total amount of molten salt used is about 28,500 t. The TSS and the process of charging and discharging are explained in more detail in the following sections.

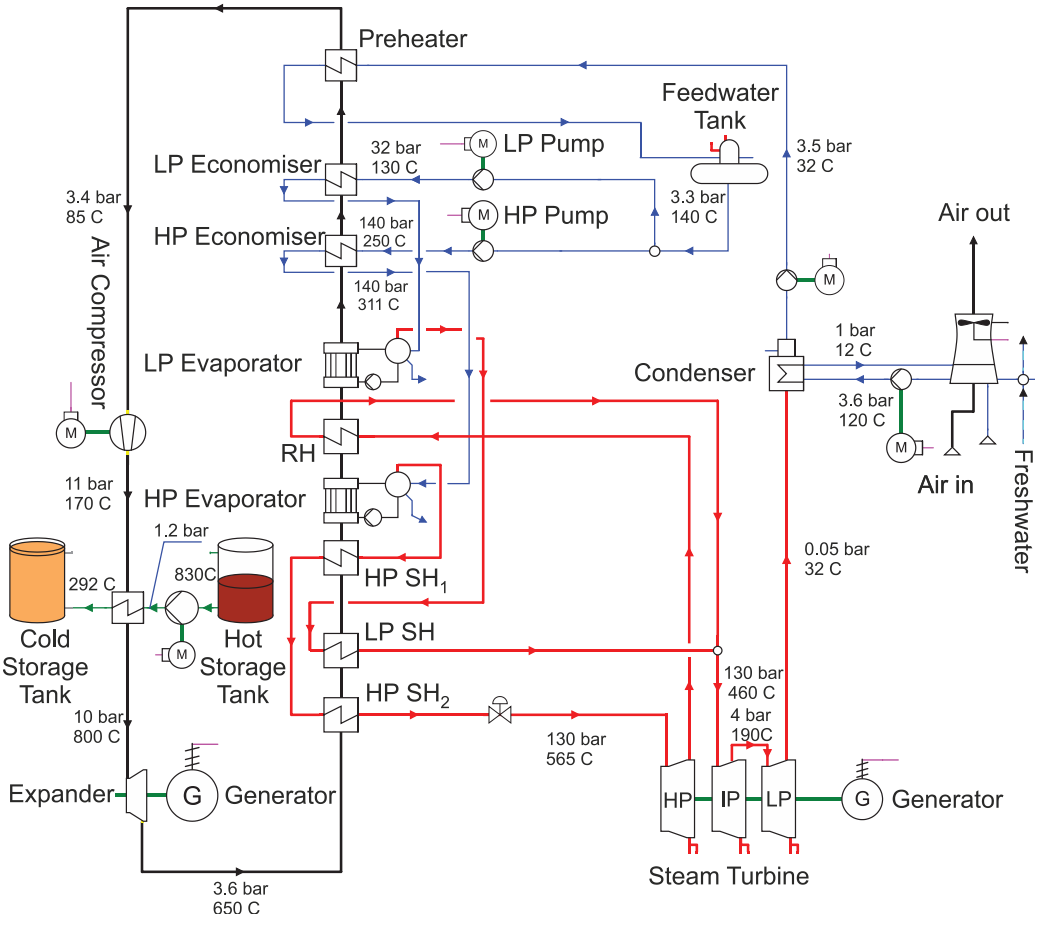

Figure 1. Schematic structure of a combined cycle power plant with a storage system (discharge path).

2.1. Working Cycle

The working cycle of TSS can be divided into two operating periods of charge and discharge. In the charge period, the molten salt coming from the CST is heated by surplus electricity generated using any renewable energy sources, as shown in Figure 2. Then, the hot molten salt is stored in the HST. The charging process continues until the HST is completely filled or the surplus electricity from renewable sources is reduced.

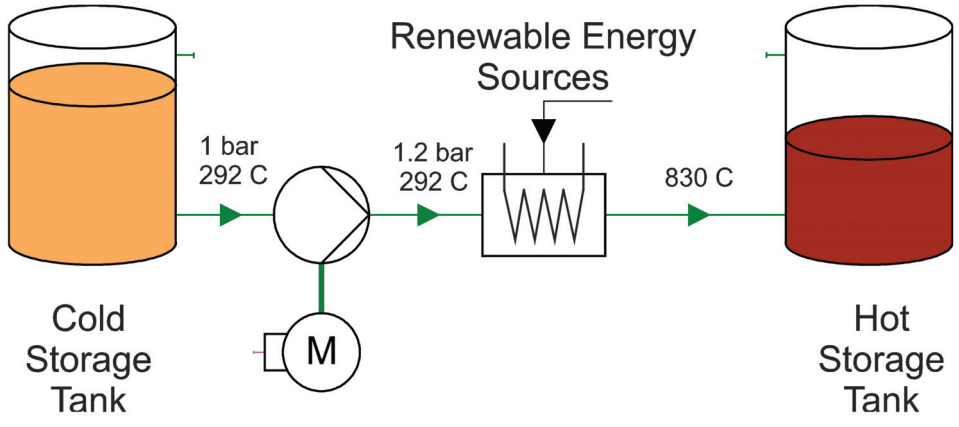

Figure 2. Schematic structure of a thermal storage system during charge mode.

During the charge period, on the one side, the air coming from the air compressor enters the heat exchanger of TSS, while on the other side the hot molten salt is pumped to the same heat exchangers in order to heat the airflow, as demonstrated in Figure 3. Then, the hot air enters the expander to generate electricity. After that, the expanded hot air flows into HRSG to complete the steam cycle with three pressure circuits. Thereafter, this process continues until the HST is completely depleted. It should be mentioned here that three types of molten salt will be used in this study.

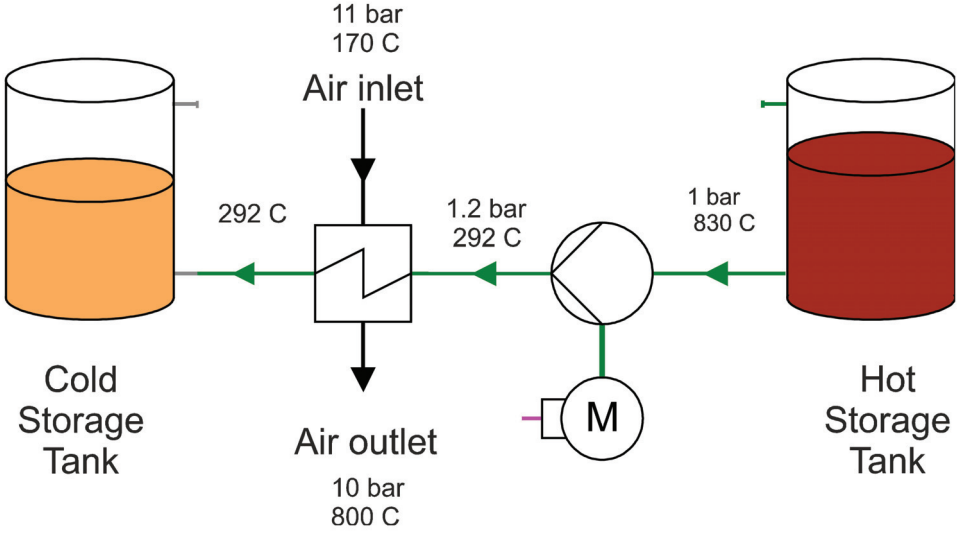

Figure 3. Schematic structure of a thermal storage system during discharge mode.

2.2. Working Media

Due to the high costs compared to molten salt and the limited temperature range, salt storage is more commonly used. Therefore, this paper discusses the two main types of molten salt.

2.2.1. Liquid Salt

Liquid salt is the name given to salt compounds that are used above their melting point. The most widely used liquid salts for thermal storage in the industry are the nitrate salts Hitec and Solar Salt. Hitec is a ternary liquid salt (53% KNO_3, 40% $NaNO_2$, 7% $NaNO_3$) with a melting point of approx. 142 °C [18]. It can be operated up to 535 °C. At temperatures above 535 °C, it decomposes and becomes unusable for further use. Solar Salt is a binary nitrate salt (60% $NaNO_3$, 40% KNO_3). It can be operated from approx. 220 to 585 °C.

Due to the large temperature range in which liquid salts are used, they are particularly suitable for storing thermal energy. Compared with thermal oil, they are also cheaper, more readily available, and less harmful to the environment, Moreover, although thermal oil and molten salt have almost the same specific heat capacity, the density of molten salt is about twice as high. Therefore, with the same storage capacity, thermal oil storage tanks accordingly have a volume that is twice as large. The main difficulty with using molten salt is the risk of solidification. If the temperature falls below the melting point, the salt solidifies and the volume contracts, causing irreversible destruction of the system [19].

It must therefore be ensured at all times that the salt is constantly kept above its melting point at all points in the system.

2.2.2. Carbonate Salt

In order to work in temperature ranges of over 500 °C, carbonate salts instead of nitrate salts may be used in the future. These is not currently used as a storage medium and in this respect the level of development is very low. In a study by Wu, Ren, Wang and Ma [20], it was shown that carbonate salts are suitable as a high-temperature storage medium. More precisely, 36 carbonate salts were tested in the study, which differed only in the concentration of their three inorganic salts—K_2CO_3, Li_2CO_3, Na_2CO_3. The advantage of carbonate salts compared to nitrate salts is, as mentioned above, the working temperature. The melting temperature for the carbonate salt specified as optimal in [20] is 400 °C. The decomposition temperature is correspondingly higher (830 °C), which not only promises a greater temperature range than nitrate salt, but also a higher efficiency can be achieved when generating electricity later due to the high temperature [20]. It should be noted here that a carbonate salt storage facility can only be implemented as a direct storage facility, as there is currently no HTF that can be used in a temperature range of 400–850 °C. This means that the carbonate salt must be a storage medium and HFF at the same time. The specific heat capacity is discussed in more detail below when presenting the implementation of carbonate salt in APROS.

3. Modelling and Simulation

Following the above description of the working cycle, the modelling process and assumptions made are presented. First, the basic model is described, on which the further modelling is based. Then the weaknesses of the system are identified and the system is further developed. A distinction must be made between the process and the so-called automation. Both the process and the associated automation are APROS work areas. In the process, the physical components of the system are modelled (for example pumps, pipes, tanks, and valves). Signals and electrical components are displayed in automation. This includes the control and regulation of the system, but also signals and external influences, such as the power at which the system is charged by renewable energy sources. After the further development of the model, the validation follows. This checks how closely the simulation results align with subsequent practical results.

In this work, a one-dimensional, homogeneous two-phase pressure-flow model (referred to as a homogeneous model in APROS) was used. This is based on the dynamic conservation equations for mass, momentum and energy. APROS calculates the thermodynamic state from the known enthalpy, composition of the fluid, and pressure for each individual calculation node in each time step. From this, the respective node temperature,

the gas volume fraction, the phase composition and the individual fluid properties, such as density, dynamic viscosity, and heat capacity, are calculated [21–24].

3.1. Basic Model

An APROS 6 model of a thermal storage tank was developed in this work and used as the basis for the modelling. The schematic structure of the basic thermal storage model can be seen in Figure 4. The model consists of two tanks (CST and HST), two valves (V_1 and V_2), two pumps (P_1 and P_2), and two heat exchangers (Q_1 and Q_2). The individual components are connected by pipes.

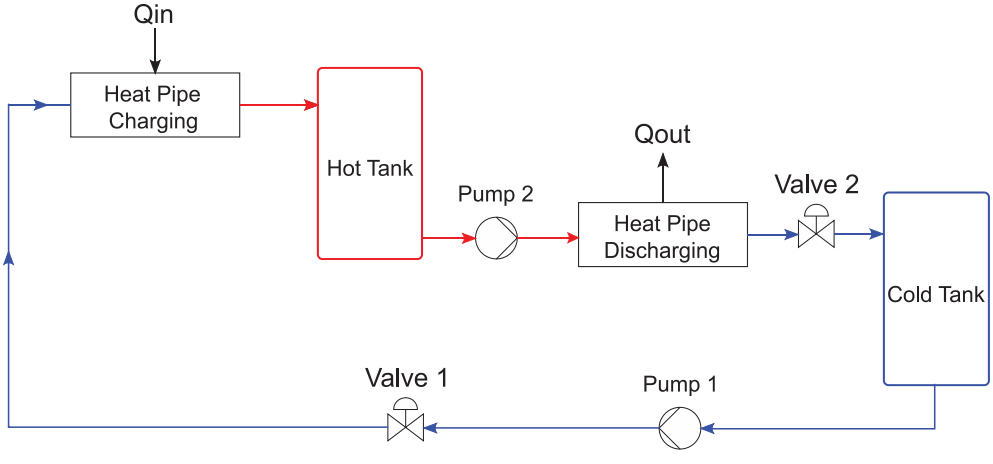

Figure 4. Schematic structure of the APROS basic model.

In contrast to Figure 1, the charging and discharging of the salt storage in the APROS model is realised with two different pipe systems. The reason for this is that APROS can only calculate flows in a certain direction. Thus, if the fluid in the same component is allowed to flow in the opposite direction, the simulation is aborted. However, the use of two different pipe systems instead of one should not affect subsequent results.

The salt storage tanks are modelled with the Heat_Tank component from the APROS library. The dimensions are taken as described above [25]. At an initial temperature of 282 °C, a temperature difference of 28 °C was determined over a period of six weeks with an outside temperature between 2 and 6 °C. This corresponds to a daily loss of 0.66 °C, which is negligible. The pumps are modelled with the BASIC_PUMP component. This defines the pump by the following five parameters: nominal flow rate, nominal delivery head, maximum delivery head, length, and flow cross-section.

The pump is controlled via the rotational speed, as a percentage, depending on the maximum speed. The power calculated from this assumes that the pump works isentropically [26].

The valves are modelled with the component CONTROL_VALVE. To fully define a valve, the program requires the following five parameters: valve length, flow cross-section, nominal mass flow, loss of nominal pressure, and nominal density.

The valves are controlled by their percentage of opening, where 100% represents a fully open valve.

The heat exchangers are modelled with the components HEAT_PIPE and BOUNDARY_CONDITION. With the component HEAT_PIPE, only a pipe with thermal insulation is initially implemented. The BOUNDARY_CONDITION is used to supply the fluid in the pipe with a heat flow in W_{th} in one or more nodes. In this case, the heat is transferred through three nodes. This promises a more accurate result than feeding through a single node. Alternatively, it would also be possible to model a countercurrent heat exchanger

with an HTF mass flow on one side and the molten salt mass flow on the other. However, it would not be possible to precisely record the supplied thermal energy, which is essential for subsequent validation of the model. Unknown characteristic values are left at the standard value (from APROS) or modified according to the cycle process so that APROS-does not display any error messages. After the basic model was implemented in APROS 6, the model was further developed in the next step. The following concrete objectives were set for this: implementation of molten salt as a storage medium; implementation of the constant pressure of 1 bar in the storage tanks during a complete charging cycle; implementation of heat supply and removal that is as realistic as possible; limitation of the working temperature in each working step to the working range of the liquid salt that is possible in reality; and expansion of the control range of the valves (in the basic model, these constantly operated in an opening range of less than 1%). In addition, it should be determined whether the pumps must run continuously at maximum output (as in the basic model) or whether power reduction is possible during certain periods of the work cycle.

3.1.1. Further Development of the Model

As a first step, the storage fluid was changed from water to molten salt. For this purpose, a predefined fluid introduced with APROS 6 is used, which is referred to as SOLAR_SALT1. This can be found in the database and describes the binary nitrate salt Solar Salt used in the industry, which is also used in the comparison process of Andasol 2. In APROS, a fluid is defined by the correlation of five material properties as a function of temperature. The required material properties are density, dynamic viscosity, specific heat capacity, thermal conductivity, and adiabatic compressibility.

The next objective was to equalise the pressure in the individual storage tanks to a constant pressure level of 1 bar. This pressure equalisation is required because APROS assumes that empty space in the tank is filled by a non-condensable gas and is not filled with selected fluid. If the pressure is now set to 1 bar in the initial state and the level is set to, e.g., 4 m, there is an increase in pressure when fluid is pumped into the tanks as the volume of the unfilled area decreases. As a first solution, the two tanks are connected to each other, whereby the connection point of both tanks is set at a height of 13.9 m. This results in a large fluctuation around the ambient pressure during a working cycle. The reason for this is that the pressure is the same in both storage tanks, but in the discharge state there is significantly more gas in the hot tank than in the cold one, which results in an increase in the total pressure due to thermal expansion. The second and final approach is to use pressure equaliser tanks. These are also implemented with the Heat_TANK component and connected to the storage tanks at a height of 13.9 m. The level of pressure equaliser is set to 5 m. In addition, the two components are removed from the dynamic simulation using the Exclude From Simulation function. This means that they do not change their state during the simulation; thus, the equaliser tanks always remain at a pressure of 1 bar and a fill level of 5 m. As expected, the pressure now remains at 1 bar during a working cycle. This completes the modelling of the process work area, as shown in Figure 5.

Next, the charge and discharge processes were implemented in the APROS model. The thermal energy available in the model is determined by the radiant power of the sun and the temperature is controlled via the mass flow. In order to enable a later validation of the system, exactly 1025 $MW_{th}h$ are fed into the system, which exactly corresponds to the amount of energy required to fully charge the storage unit.

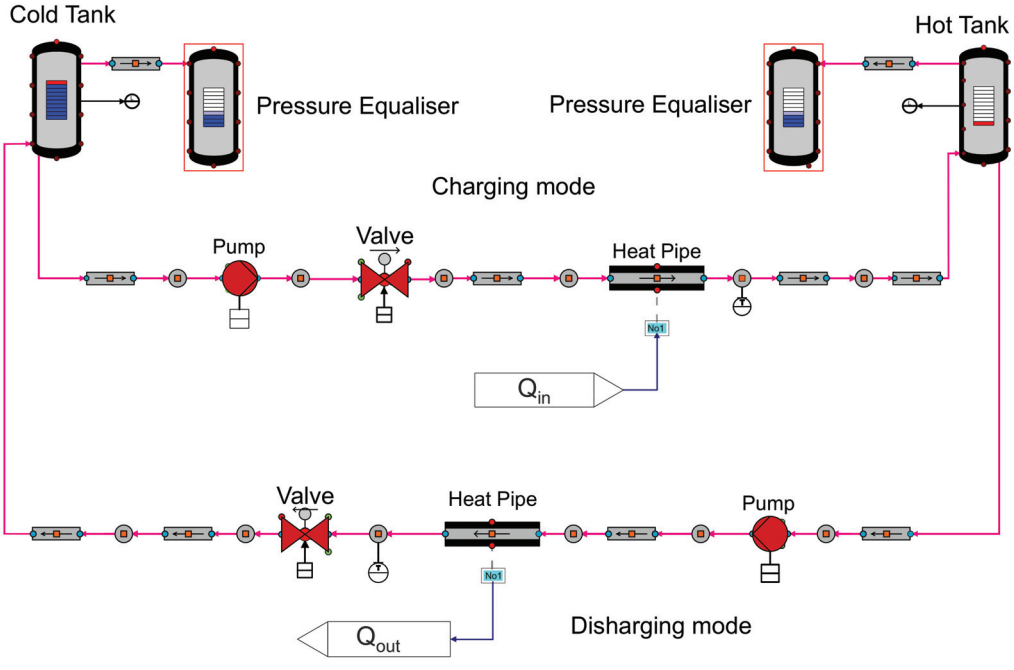

Figure 5. Schematic structure of the APROS basic model.

It can be seen from [25] that in the tests carried out on Andasol 2, a charging time of approximately 10 h is expected. Accordingly, the charging period is set to 10 h in the modelling. In order to keep the regulation as close as possible to reality, sunrise and sunset are also taken into account. In order to supply 1025 $MW_{th}h$ to the system in 10 h, the system must be charged with a constant charge power of 102.5 MW_{th}. The integral of the charging power over time corresponds to the thermal energy supplied to the system. During the night, in order to obtain the same thermal energy for the same period of daytime operation, the charge power must be increased. From Figure 6, in the left figure, it can be seen that the difference between a constant power and the consideration of the sunrise and sunset is exactly the thermal energy that would be supplied to the system in 40 min by a constant charging power of 102.5 MW_{th}. The power must be selected accordingly so that the 1025 $MW_{th}h$ would be reached in 9 h and 20 min, which leads to the following calculation:

$$\frac{1025\ MW_{th}h}{9.33\ \text{h}} = 109.82\ MW_{th} \tag{1}$$

The required charging power is thus 109.82 MW_{th}. This is implemented using the GRADIENT component. This is a dynamic component that limits the rate at which the value of an input signal can change. In this case, the rate for both the increase and the decrease in the input value is limited to 2.75 MW_{th} min, which can be seen from the following calculation:

$$\frac{109.82\ MW_{th}h}{40\ \text{min}} = 2.75\frac{MW_{th}}{\text{min}} \tag{2}$$

The model for heat supply created in APROS can be also seen in Figure 7. This is clearly discussed below:

The setpoint SP01 describes a digital input signal that is sent to a system. In this, the input signal represents the charging power. SP01 and SP05 (the discharging power) are the only variables in the model that must be changed externally during a simulation cycle.

All other variables are derived from these or are regulated based on them. SP01 and SP05 are changed by the so-called queue. Queues are around process logs that can be used to influence a system according to a specific schedule. As described above, this input signal first runs through the gradient component and then to the binary switch ASW03. The signal is measured twice between them and sent to other systems as a digital signal. The switch is used in the event that the CST is empty and can no longer be pumped. In this case, the charging power must be set to 0 MW_{th} immediately, otherwise, the temperature in the model will approach infinity if the mass flow rate decreases. After the binary switch, the signal passes through two gain components. In the first component, the signal is multiplied by a factor of 10^6 because the following boundary condition is calculated in watts. In the second gain block, the signal is divided by a factor of 3. The charging power is then output via three nodes. The Boundary_Conditions, which convert the digital signal into a heat flow, follow the gain components. Finally, the three heat flows are measured and fed to the heat_pipe in the storage system.

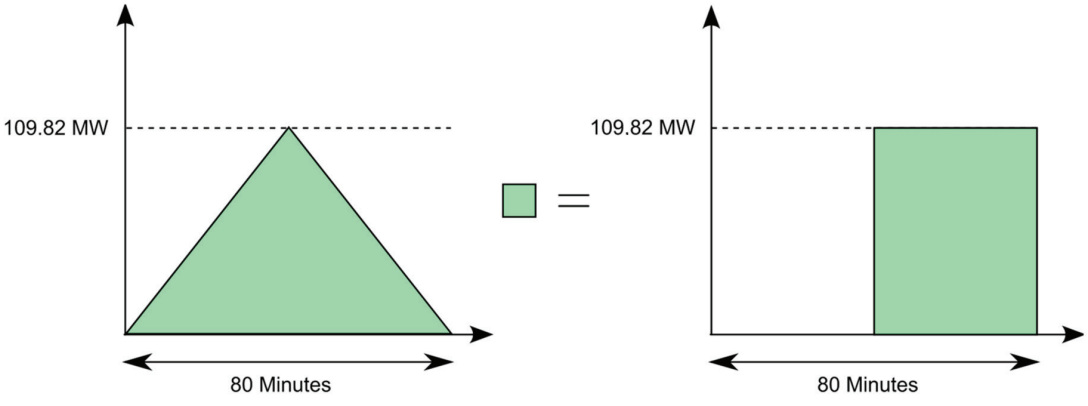

Figure 6. Visualisation of the equivalence between the energy supplied by sunrise and sunset and a constant output of 109.82 MW_{th} over 40 min; filled area represents the service supplied.

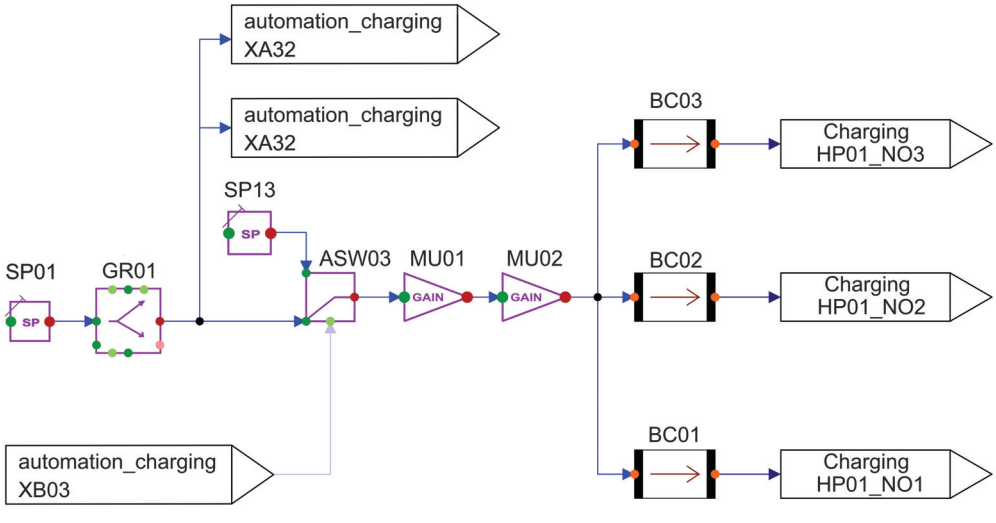

Figure 7. Control circuit for heat flow during charging by APROS.

According to [25], the discharge takes 7.5 h. This results in a discharge power of $-136.67\ MW_{th}$, as shown in the equation (3).

$$\frac{-1025\ MW_{th}h}{7.5\ \text{h}} = -136.66\ MW_{th} \tag{3}$$

The associated modelling can be seen in Figure 8. This only differs in the input signal and the subsequent component. While a gradient is used for charging to describe sunrise and sunset, only a filter is used for discharging to prevent overheating due to sudden changes in charging power. This means that the heat flow cannot suddenly change to a value of $-136.67\ MW_{th}$ when the input signal changes.

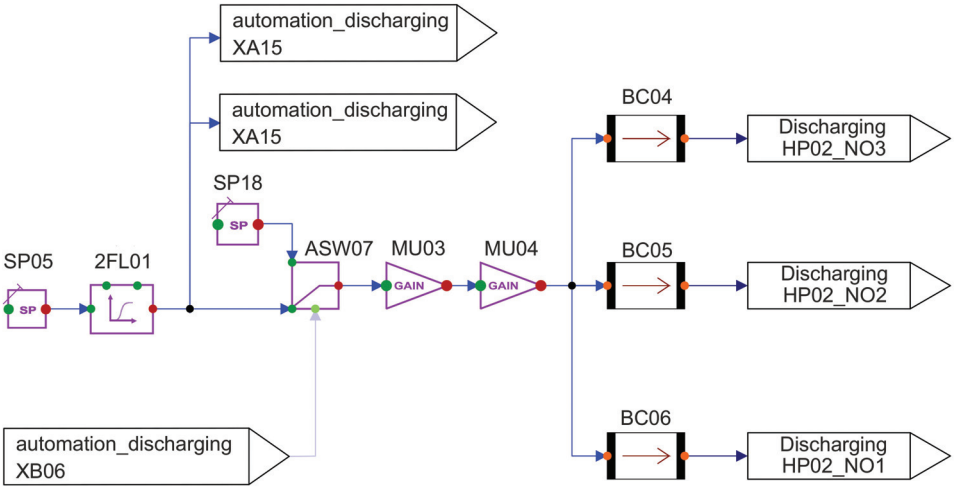

Figure 8. Control circuit for heat flow during discharging by APROS.

The remaining goals are handled by modifying the regulation and control of the process.

3.1.2. Regulation and Control

Then, the working temperature limits are dealt with at each work step of the real working range of the molten salt. As in the comparison process, this is achieved by regulating the mass flow. The associated APROS automation can be seen in Figure 9 and is explained and described in more detail below:

The temperature at the heat exchanger outlet is measured from the APROS process (Figure 9 top left) and converted into a digital signal with the measurement component TI01. This is compared in the PI controller with the setpoint SP09, which sets a target temperature of 386 °C. A PI controller is used because, according to [19], this is the type of controller commonly used in the industry.

The controller then forwards a signal between 0.1 and 1, which is converted into a valve position between 10% and 100% with the aid of the ACT05 actuator component. A valve position of over 10% is used here to ensure a constant mass flow of >0 kg/s. If the controller has to regulate the mass flow to 0 kg/s in the meantime, nothing will change in the temperature after the heat exchanger, because the heated fluid will not reach the measuring point. The binary_switch ASW01 between the actuator and the PI controller has the function of completely closing the valve if necessary because the PI controller cannot do this due to its working range of 0.1–1 described above. This is needed in two cases. The first case describes the end of the charging process, that is, when no more heat flows into the system. If the measured heat flow (middle left) falls below the value of 0.5, the

output signal of the limit-value checker LVC03 changes from true to false. The following OR component then also changes its output signal to false (because one of its input values is false), which leads to the binary_switch jumping to the setpoint SP02 = 0, which results in a valve position of 0%. The second case in which the valve needs to be fully closed occurs when the system is fully charged; this means when the CST falls below 0.65 m level. As shown in Figure 9, this is also modelled using a measured signal and a limit-value checker.

The control of the discharge line is equivalent to that of the charging line, except that the control parameters are adapted to the discharge process (e.g., target temperature = 292 °C).

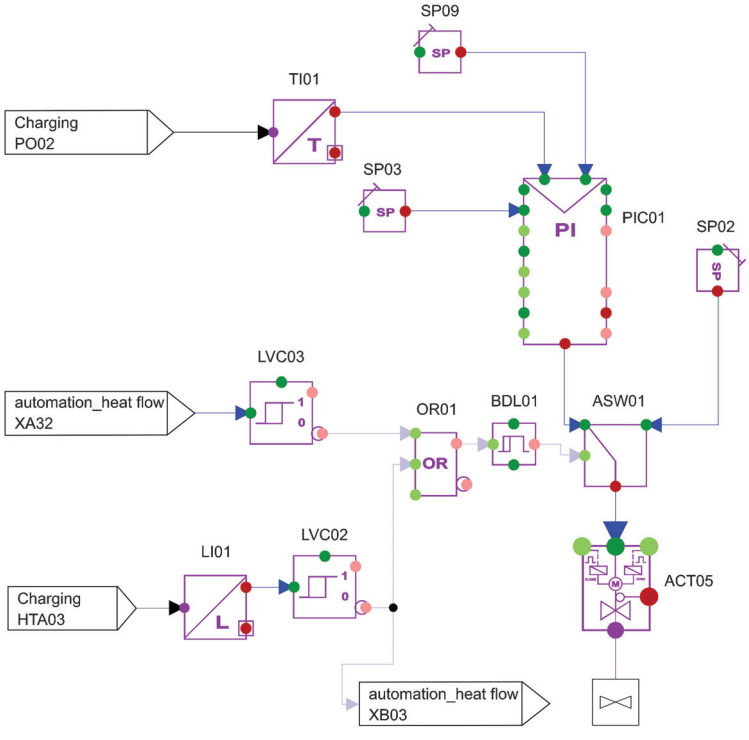

Figure 9. Mass flow controller during charge mode.

The next step is to try to optimise the pump performance. In the basic model, these pumps ran at 100% performance regardless of the fill level of the tanks and the required mass flow. The reason for this is the associated simplification of the regulation, because the valve regulates continuously at the same pump output and can therefore easily keep the mass flow constant compared to when the pump output changes. However, full power is not always required. For example, when the HST is low, the power required is less than when the level is high. However, it must be ensured here that the pump performance is not directly dependent on the mass flow because this can lead to an interference with the control of mass flow by the valve. As a solution, the pump is controlled based on the charging capacity and the geodetic height difference. The associated APROS automation can be seen in Figure 10 and is described below:

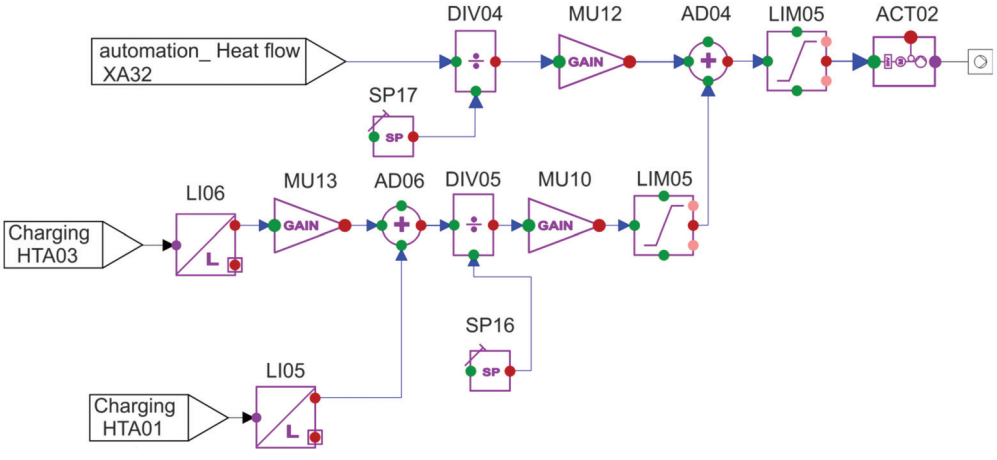

Figure 10. Mass flow controller during discharge mode.

Automation begins with the design principle of the pump to overcome a height difference of 13 m with a capacity of 100% while providing the required mass flow at full discharge capacity. On this basis, the automation shown in Figure 10 calculates the required power and passes it on to the pump via the ACT02 actuator. As described above, two variables are used to determine the power: the geodetic height difference and the charging power. The discharge power is flowed in the upper line, divided by the maximum discharge power (109.83 MW_{th}) and then multiplied again by a factor of 100. This gives a value showing the percentage of the maximum discharge power currently affecting the system. Between 0 and 50% is deducted from this maximum discharge power by the summation block (AD04) because at full discharge capacity and a geodetic height difference of 13 m (the maximum difference in level between HST and CST), this is slightly more than 50% of the maximum pump capacity. After the summation block (AD04), the signal runs through a limiter, which limits the signal to a range from 10% to 100% in order to always ensure a mass flow >0 kg/s.

The control of the pump in the discharging line is equivalent to the control of the charge line, where 136.67 MW_{th} of the discharge line is selected as the maximum power.

3.2. Model Validation

After the modelling was completed, the model was validated. As described above in Section 3.1, 1025 $MW_{th}h$ is fed into the system in 10 h and then discharged again in 7.5 h. In the ideal modelling, the CST should be completely filled out after the charging cycle, as in the comparison process of the Andasol 2. Figure 11 shows the level of the comparison process with the APROS model.

The filling level of storage tanks in the APROS model is approximately 12.7 m and in the comparison process is 13.6 m. Accordingly, the deviation of the model is 6.62%, which justifies a confirmation of the system. The error can result from the assumption of an adiabatic change in volume, failure to consider friction, any differences in the physical properties of the modelled liquid salt, or the assumption of an isentropic pump. It should be noted that the error does not come from modelling the sunrise and sunset, as the graph indicates, because the amount of heat supplied is the same.

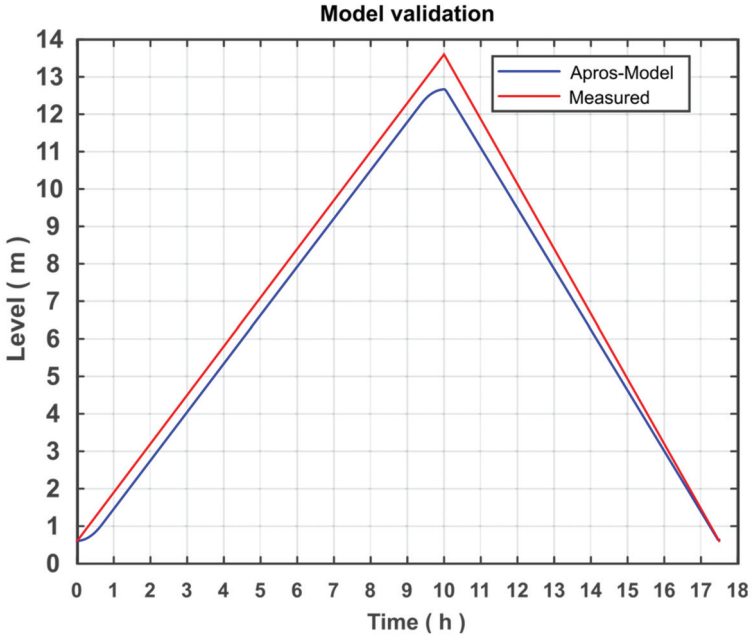

Figure 11. A validation model for a thermal storage system during a working cycle.

3.3. Design of the Process for Other Storage Fluids

After modelling and model validation are completed, three new models with different storage media or other temperature ranges were created based on the developed model in order to analyse differences and optimisation options. First, the TSS system is operated by the fluid Solar Salt, but the temperature range is extended to the maximum possible range. Because the melting temperature of Solar Salt is 220 °C and the decomposition temperature is 580 °C, the temperature range was set to 240 to 560 °C. The following components must be adapted to the new process requirements: regulation of the mass flows, pump parameters, and valve parameters. The rest of the modelling could be performed.

Second, the Hitec fluid from the APROS database is used. This has a melting temperature of 142 °C and a decomposition temperature of 535 °C. Accordingly, the temperature range is set to 162 to 515 °C. Here, the same components must be adapted as when the working area of the Solar Salt was expanded.

Third, the carbonate salts are used, which have a working temperature higher than nitrate salts. The melting temperature for the carbonate salt specified as optimal in [20] is 400 °C. The decomposition temperature is correspondingly higher (830 °C), which not only promises a greater temperature range than nitrate salt, but also a higher degree of efficiency can be achieved. The specific heat capacity is discussed in the next section in more detail later when implementing carbonate salt in APROS.

Implementation of Carbonate Salt in APROS 6

As the last storage medium, carbonate salt is included in the process so that it can also be compared with the other storage media. Carbonate salt is not one of the predefined fluids that APROS provides, which is why a new fluid must be created in APROS. As described above, the following values are required to define the carbonate salt in APROS: the density, the dynamic viscosity, the specific heat capacity, the thermal conductivity, and the adiabatic compressibility—all depending on the temperature. The selection of the carbonate salt follows the study [20], with the 36 carbonate salts in terms of their usability

as a storage medium in sensible heat storage as part of a solar power plant. This identified two suitable carbonate salt compositions: 3% K_2CO_3, 10% Li_2CO_3, 60% Na_2CO_3 and 20% K_2CO_3, 10% Li_2CO_3, 70% Na_2CO_3. The first composition was used in this work because it has a higher decomposition temperature (850 °C). The working temperature range is set to 446 to 830 °C because a distance of 20 degrees from the melting and decomposition point must be maintained. Melting and decomposition points were also taken from [20].

Based on [27], the density of the salt is modelled as a linear function. However, the literature values, which are given in Kelvin, must be converted to degrees Celsius, as APROS only accepts temperatures in Celsius:

$$\rho \left[\mathrm{kg{\cdot}m^{-3}}\right] = 2323 - 0.4613 \times (T) \tag{4}$$

In the following, the correlation of the dynamic viscosity is required. This can be found in [28]:

$$\eta[\mathrm{mPa{\cdot}s}] = 0.1012 \times e^{33400/R \cdot T} \tag{5}$$

With

$$R \left[\mathrm{J{\cdot}K^{-3}{\cdot}mol^{-3}}\right] = 8.3143 \tag{6}$$

However, only correlations in the form of polynomials can be inserted into APROS, which is why the formula given in Equation (5) is approximated with a second-degree polynomial for the range from 446 to 830 °C.

A polynomial of the 2nd degree can be formed with these values. The temperature is converted back to Celsius when setting up the polynomial. Thus, the final correlation of the dynamic viscosity and the temperature in degrees Celsius is:

$$\eta[\mathrm{Pa{\cdot}s}] = 1.9436 \times 10^{-7} \times T^2 - 3.0871 \times 10^{-4} \times T + 0.126 \tag{7}$$

No studies or other results can be found on the thermal conductivity of carbonate salt. The only evidence about the thermal conductivity λ of such salt can be found in [29]. In that study, the thermal conductivity of $LiNO_3$, $NaNO_3$, KNO_3, which is also a carbonate salt and has a similar melting temperature and density, was measured. The thermal conductivity of this salt was determined to be λ = 1.17 $\mathrm{W{\cdot}m^{-1}{\cdot}{^\circ}C^{-1}}$, which is why a thermal conductivity of λ_{carb} = 1 $\mathrm{W{\cdot}m^{-1}{\cdot}{^\circ}C^{-1}}$ was assumed for the further simulation.

Because the adiabatic compressibility of liquids is negligible, but a value for the compressibility must be assumed in APROS, the value was taken from Solar Salt. Accordingly, the compressibility was set as $K_{carb} = 1.8 \times 10^{-8}$ $\mathrm{Pa^{-1}}$. The fluid is now fully defined and could be implemented in APROS.

4. Results

In this section, the results of the various simulations are presented and discussed. First, simulations were carried out with the validated Andasol 2 model and it was checked whether the goals set in the modelling are achieved. The results of the system were also be collected and documented for any weaknesses that may still be present in the model to facilitate further work. The change in the system was then analysed by changing the storage fluid and the temperature range. The associated simulations were compared to each other. Furthermore, the comparison was evaluated based on their storage utilisation and change in efficiency in the thermodynamic cycle. The work cycle of one day (24 h) was used in all simulations.

4.1. System Analysis of the Andasol 2 Model

First, the process values of the Andasol 2 system were analysed and it was determined whether the objectives set in the modelling were achieved. For this purpose, as described above, 24 h were simulated. This was implemented with the help of the full day of the work queue, with which process values and input variables were changed at certain time intervals. The simulation begins at a virtual time of 8:00 a.m. with the loading of the initial

conditions (initial condition = 8:00 a.m.) of the process and is thus reset to the initial state, as shown in Figure 11. In this, the mass flow of the two molten salt lines is equal to 0 kg/s, there is no heat flow on the system, the CST is completely filled with a fill level of 13.6 m, and the HST is completely emptied with a fill level of 0.6 m. At 9:30 a.m. the heat flow of the charging line is set to 109.82 MW_{th}—charging begins. After 10 h the maximum charging capacity of HST is reached. At 19.30 p.m. the charging process is completed and the heat flow is set to 0 MW_{th} due to the discontinuation of electrical energy from renewable energy sources. Then, the discharging process begins for 7 h and 30 min. For this, the value of the heat flow in the discharge line is set to 136.67 MW_{th}, which is slowed by the filter after approximately 100 s. At 3:00 a.m. the end of the discharge time is reached and the heat flow of the discharge line is set to 0 MW_{th} again. From 3:00 a.m. to 8:00 a.m., the system maintains its state without charge or discharge processes, so that at 8:00 a.m., with ideal modelling, the initial conditions should be given again.

In the first step, it is simulated whether the temperature of the molten salt remains within the real working range during the entire process. For this purpose, Figure 12 shows the temperature of the molten salt after the heat exchangers (referred to as heat exchanger in the illustration) in the two charging lines over a 24 h period. As can be seen, the working range of 220 to 580 °C is not exceeded. Furthermore, the set temperature is missed by a maximum of 14 °C (start of discharge) due to the transient behaviour of the control, which corresponds to a maximum control deviation of 4.79%. This means that the goal of delimiting the work area can be classified as achieved. It should be noted that the modelling of sunrise and sunset lengthens the transient process, which can be clearly seen when comparing the two temperature curves. This is an important finding for further simulations and a confirmation of the relevance of modelling the sunrise and sunset. Another relevant finding from the simulation is that the valve after the heat exchanger must be designed for the entire temperature range. As can be seen in the simulation, the valve in the discharge line is only set with a temperature of 292 °C during the discharge period, but it is exposed to the full 386 °C in the rest phase. One explanation for this is that the mass flow of the discharging line is only set to 0 kg/s after the discharge process has ended, so that small amounts of hot fluids can still reach the valve. If an attempt is made to end the discharge process and the mass flow at the same time, a temperature peak occurs shortly before the discharge power and the mass flow are stopped.

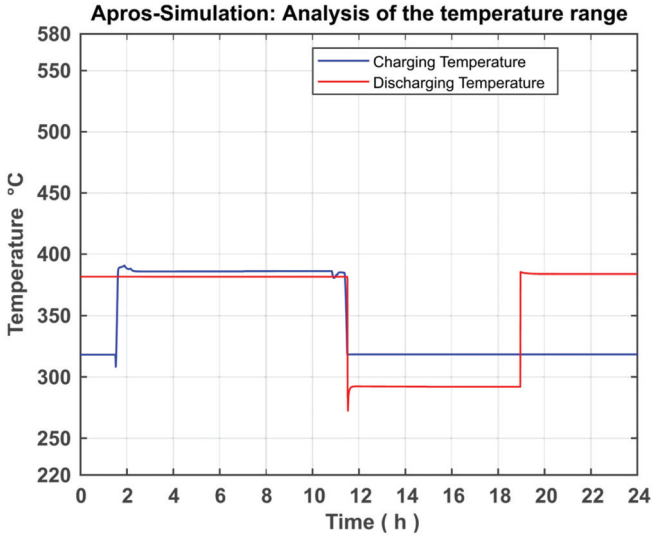

Figure 12. Simulated temperature after the heat exchangers during charging.

In the second step, it is simulated in which area the valves work in the further developed form of the model. The current valve position is plotted as a percentage of the maximum degree of opening. As can be seen in Figure 13, the valves operate in a range of 0–75%, which means that the goal of expanding the control range of the valves has been achieved. This is important for the subsequent construction of the system because with a low degree of opening there are constant flow losses, which further confirms the success of the simulation. It should be noted that an expansion to 0–100% operating range should be a goal. This may be part of further work.

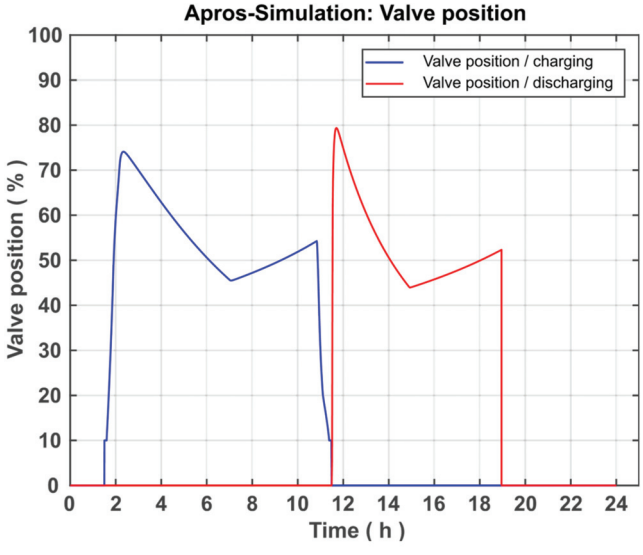

Figure 13. Simulated valve position of the two control valves in the charging line during a working cycle.

The third simulation shows how the current pump output behaves as a percentage compared to the maximum output during the 24 h. Significant reductions in energy consumption can be achieved here in some sections of the working cycle, as can be seen in Figure 14. It should be noted here, however, that it can be further reduced because the pump in the discharge line is not necessary during the charging period and vice versa. In the simulation shown, however, the performance of the pumps is always >0%, which is why further energy savings are possible. In this way, all of the goals set in the modelling have been achieved, with the possibility of further implementation of these goals as part of the ongoing work.

4.2. System Optimisation

In the following part, the consequences of a change in the temperature range and the storage fluid on the storage tank capacity and the subsequent thermodynamic cycle efficiency should be determined. For this purpose, the three models SSalt max, Hitec, and Carbonate were tested and analysed under the same initial conditions and with the same heat flows as the Andasol 2 model. In detail, all models had the same queue applied to them. The simulation results were then compared with each other and evaluated with regard to a possible increase in storage capacity. In the second part, the individual storage media and working temperatures were evaluated with regard to the resulting change in the efficiency of electricity generation.

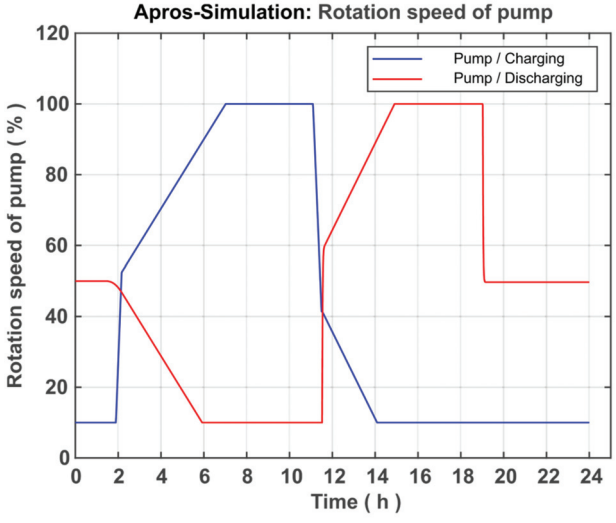

Figure 14. Simulated pump utilisation of the two pressure pumps in the charging lines.

4.2.1. Increase in Capacity

Figure 15 shows the respective fill levels of the HST of the four models during a working cycle. As expected, charging the same amount of heat with the SSalt max, Hitec, and Carbonate models leads to a significantly lower fill level than with the Andasol 2 model, because this work used a significantly greater temperature difference, which is presumably with the help of a specific comparable heat capacity, and should be explained using the following formula:

$$Q = m \cdot cp \cdot (T_2 - T_1) \tag{8}$$

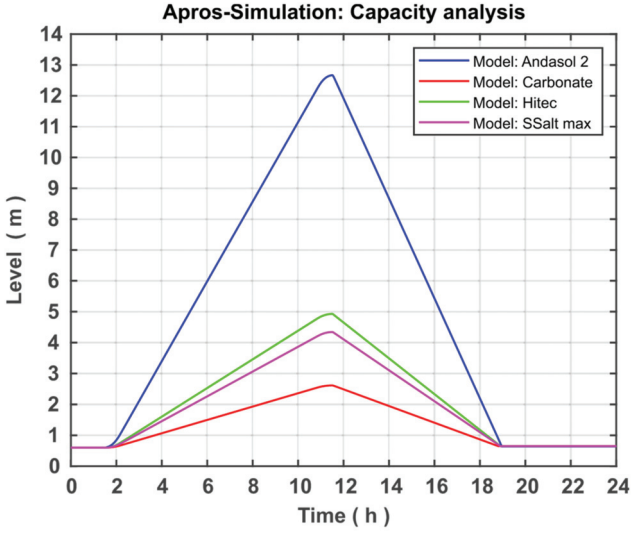

Figure 15. Simulated fill levels of the four models during a working cycle.

The fill levels of the charging state and the associated increase in storage capacity compared to the Andasol 2 model can be seen in Table 1.

Table 1. Shows the maximum fill level and increased capacity.

	SSalt Max	Hitec	Carbonate
Fill level max. in m	4.3	4.9	2.61
Increased Capacity in %	295	259	487

It must be taken into account that these values are theoretical values that can only be approximated in practice, because, for example, it is only possible with a great deal of effort to design a storage system that approaches the melting and decomposition temperature of the storage medium up to 20 °C as in the simulations. Particularly when carbonate salt is used, the assumption of an adiabatic storage system is associated with a significant error due to the high temperature level, which must be taken into account in practice. Furthermore, the collector principle must be changed regarding system optimisation for the Andasol 2 test facility, because the PT collectors do not allow temperatures above 400 °C due to the mandatory use of thermal oil as HTF.

4.2.2. Increase in Efficiency

When optimising a heat storage system, however, it is not only the capacity increase but also the increase in the efficiency of the thermal power process used to generate electricity in the power plant that must be taken into account, which is associated with an increase in the temperature difference. For this, the theoretically possible thermal efficiency η_c is calculated by the following formula:

$$\eta_c = 1 - \frac{T_s}{T_q} \tag{9}$$

where T_s is the temperature of the heat sink and T_q is the temperature of the heat source.

The temperatures are taken from Figures 16 and 17 to calculate the thermal efficiency. The inflection across the simulation results is deliberately performed in order to check the models for correctness in the same step. This can be confirmed here directly, because all models work with their specified temperature difference. It should be noted that the Hitec model shows a pronounced transient process, which can cause problems in practice. In addition, however, an incorrect design of the controller is also possible.

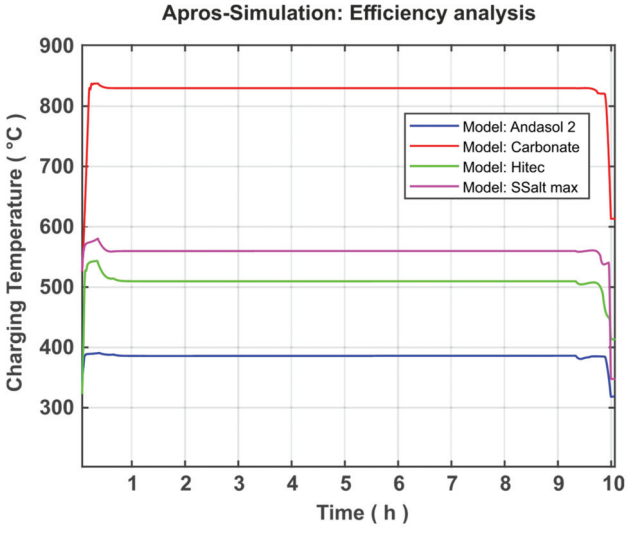

Figure 16. Simulated temperature after the heat exchanger of the four models in the charging line.

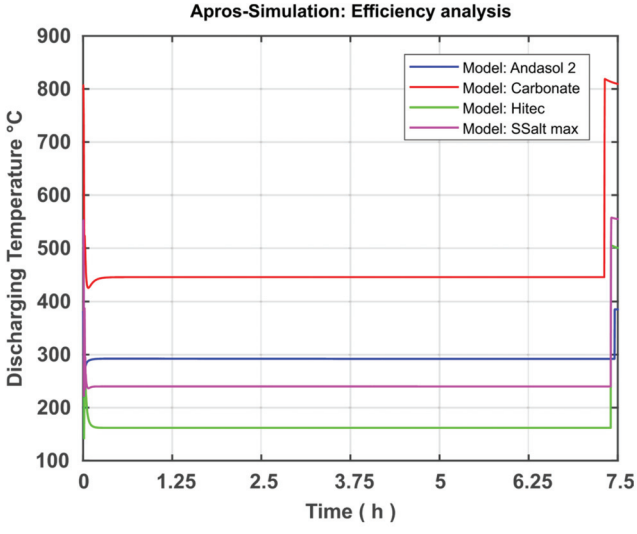

Figure 17. Simulated temperature after the heat exchanger of the four models in the discharging line.

The comparison shows that the storage medium to be chosen should be carbonate salt, both for increasing efficiency and increasing capacity. With a theoretical increase in efficiency in the thermal power process of up to 18.2%, it exceeds all other storage media and their associated temperature levels.

In addition, the carbonate model has the opportunity to switch two thermodynamic cycle processes one after the other in order to approach the Carnot efficiency [20]. First, a Joule process can be applied to use the temperature range above 600 °C to generate electricity, followed by a steam power cycle, which can use the remainder of the temperature difference. A potential difficulty in the Joule cycle can be found because of the heat exchangers, which must have a high volume due to gas operation. It should be noted here that the consideration of the efficiency is limited to the maximum achievable thermal efficiency, which allows sufficient quantification for a comparison of the processes, but does not provide any information about the real efficiency.

$$\eta_c^{\text{Andasol 2}} = 1 - \frac{(25 + 273.15)K}{(386 + 273.15)K} = 0.547 \tag{10}$$

$$\eta_c^{\text{Hitec}} = 1 - \frac{(25 + 273.15)K}{(515 + 273.15)K} = 0.621 \tag{11}$$

$$\eta_c^{\text{SSalt max}} = 1 - \frac{(25 + 273.15)K}{(560 + 273.15)K} = 0.642 \tag{12}$$

$$\eta_c^{\text{Carbonate}} = 1 - \frac{(25 + 273.15)K}{(830 + 273.15)K} = 0.73 \tag{13}$$

During the charging step, an efficiency of 95% was assumed due to heat losses and HTF pump consumption and other requirements (i.e., each 1 MW_{el} h was converted to 0.95 $MW_{th}h$ in the molten slat). During the discharging step and according to the previous calculation, the optimal efficiency is 0.73, so that the optimal round-trip efficiency is 0.73 × 0.95 = 0.69. In real cases, the achievable thermal efficiency is lower for a combined cycle power plant. The nominal process efficiency of the combined-cycle power plant (CCPP) can reach 60%. Large-scale combined-cycle power plants with a net electrical power of 780 MW_{el} and an efficiency level up to 62.2% are now running in Irsching,

Germany [30,31], Bouchain, France [32,33], and Tambak Lorok, Indonesia [34,35]. The real round-trip efficiency is expected to $0.62 \times 0.95 = 0.589$.

5. Conclusions

The present study focused on the creation and further development of a numerical model in APROS for the dynamic system analysis of thermal salt storage facilities. The aim here was the system analysis and optimisation of the thermal salt storage with regard to a stand-alone solution. For this purpose, the theoretical fundamentals were first researched and the properties of power plants and thermal storage systems were explained. In addition, the possibilities of using a TSS in a solar power plant or a stand-alone system were demonstrated. The discussion was extended to the fact that the range of the temperature difference and the storage medium selection is very relevant to TSS optimisation. In the section on modelling and simulation, the development of the model was discussed. The basic model was presented and goals were set for expanding the model. The model was further developed on the basis of these goals. This included the modification of the Andasol 2 comparison system located in Granada, Spain. In the course of this approximation, the created model can be validated by comparing the level of both systems after supplying an identical amount of heat in the same period of time. The discrepancy between both systems was approximately 6.62%, indicating a satisfactory accuracy and allowing the validation of the system. Three additional models were created based on the validated model to analyse the temperature difference and the storage medium. The simulations of the individual models were presented and discussed in the Results section. First, the simulations of the Andasol 2 model were presented. The focus here was on the goals set in the modelling. Both the successful limitation of the working temperature to a technically possible range and the expansion of the valve working range can be recorded. In addition, the pump capacity could be significantly reduced by controlling the pump based on the amount of heat added and the geodetic height difference of the individual storage reservoirs. Then, the four models Andasol 2, SSalt max, Hitec, and Carbonate Salt were evaluated and compared in terms of possible capacity increase and efficiency increase. For the capacity analysis, all models were charged with the same heat quantity as previously and the levels were compared at full fill. The largest increase in capacity of 487% was achieved with the Carbonate Salt model. The greatest increase in efficiency in terms of power generation can also be achieved with the carbonate model (18.2%), whereas the amount of increase was 9.5% and 7.4% for each of SSalt max and Hitec, respectively. With regard to the goal of a stand-alone version, Carbonate Salt can be determined as the optimal storage fluid, as this promises the highest increase in capacity as well as efficiency.

For the stand-alone system, it was found that the charge efficiency is 95%, whereas the discharge efficiency (similar to the existing combined cycle) is 60%. The expected round-trip efficiency of the system is 0.589%, which should be analysed in detail in a future work.

Author Contributions: Methodology, W.A.K.A.-M. and A.K.; software, W.A.K.A.-M. and A.K.; investigation, W.A.K.A.-M. and A.K.; writing—original draft preparation, W.A.K.A.-M. and A.K.; writing—review and editing, W.A.K.A.-M. and F.A.; supervision, B.E. All authors have read and agreed to the published version of the manuscript.

Funding: This research received no external funding.

Institutional Review Board Statement: Not applicable.

Informed Consent Statement: Not applicable.

Data Availability Statement: Not applicable.

Acknowledgments: We acknowledge Support from the Deutsche Forschungsgemeinschaft (DFG—German Research Foundation) and the Open Access Publishing Fund of the Technical University of Darmstadt. The first author would like also to thank the University of Technology-Iraq.

Conflicts of Interest: All authors declare no conflict of interest.

Abbreviations

Abbreviations

ACT	actuator
AD	adder
APROS	advanced process simulation software
ASW	binary switch
BC	boundary condition
CST	cold storage tank
DIV	divider
GR	gradient
HST	hot storage tank
HP	high pressure
HTF	heat transfer fluid
LVC	limit-value checker
LI	level measurement component
LP	low pressure
MU	gain
OR	or component
PI	proportional–integral controller
SP	set point
TI	temperature measurement component

References

1. Sterner, M.; Stadler, I. *Definition und Klassifizierung von Energiespeichern*; Springer: Singapore, 2014; pp. 25–46.
2. Wahhab, H.A.A.; Al-Maliki, W.A.K. Application of a Solar Chimney Power Plant to Electrical Generation in Covered Agricultural Fields. In *IOP Conference Series: Materials Science and Engineering*; IOP Publishing: Kerbala, Iraq, 2020; p. 012137.
3. Sterner, M.; Stadler, I. *Energiespeicher-Bedarf, Technologien, Integration*; Springer: Berlin/Heidelberg, Germany, 2014.
4. Stephan, P.; Schaber, K.; Stephan, K.; Mayinger, F. *Thermodynamik: Grundlagen und Technische Anwendungen-Band 2: Mehrstoffsysteme und Chemische Reaktionen*; Springer: Berlin/Heidelberg, Germany, 2018.
5. Medrano, M.; Gil, A.; Martorell, I.; Potau, X.; Cabeza, L.F. State of the art on high-temperature thermal energy storage for power generation. Part 2—Case studies. *Renew. Sustain. Energy Rev.* **2010**, *14*, 56–72. [CrossRef]
6. Kronhardt, V.; Alexopoulos, S.; Reißel, M.; Sattler, J.; Hoffschmidt, B.; Hänel, M.; Doerbeck, T. High-temperature Thermal Storage System for Solar Tower Power Plants with Open-volumetric Air Receiver Simulation and Energy Balancing of a Discretized Model. *Energy Procedia* **2014**, *49*, 870–877. [CrossRef]
7. Yu, Q.; Li, X.; Wang, Z.; Zhang, Q. Modeling and dynamic simulation of thermal energy storage system for concentrating solar power plant. *Energy* **2020**, *198*, 117183. [CrossRef]
8. Liu, S.; Faille, D.; Fouquet, M.; El-Hefni, B.; Wang, Y.; Zhang, J.; Wang, Z.; Chen, G.; Soler, R. Dynamic Simulation of a 1MWe CSP Tower Plant with Two-level Thermal Storage Implemented with Control System. *Energy Procedia* **2015**, *69*, 1335–1343. [CrossRef]
9. Flueckiger, S.M.; Iverson, B.; Garimella, S.V.; Pacheco, J.E. System-level simulation of a solar power tower plant with thermocline thermal energy storage. *Appl. Energy* **2014**, *113*, 86–96. [CrossRef]
10. Biencinto, M.; Bayon, R.; Rojas, E.; González, L. Simulation and assessment of operation strategies for solar thermal power plants with a thermocline storage tank. *Sol. Energy* **2014**, *103*, 456–472. [CrossRef]
11. Al-Maliki, W.A.K.; Al-Hasnawi, A.G.T.; Wahhab, H.A.A.; Alobaid, F.; Epple, B. A Comparison Study on the Improved Operation Strategy for a Parabolic trough Solar Power Plant in Spain. *Appl. Sci.* **2021**, *11*, 9576. [CrossRef]
12. Yang, Z.; Garimella, S.V. Cyclic operation of molten-salt thermal energy storage in thermoclines for solar power plants. *Appl. Energy* **2013**, *103*, 256–265. [CrossRef]
13. Zhou, X.; Xu, H.; Xiang, D.; Chen, J.; Xiao, G. Design and modeling of a honeycomb ceramic thermal energy storage for a solar thermal air-Brayton cycle system. *Energy* **2021**, *239*, 122405. [CrossRef]
14. Zhang, C.; Lu, Y.; Shi, S.; Wu, Y. Comparative research of heat discharging characteristic of single tank molten salt thermal energy storage system. *Int. J. Therm. Sci.* **2021**, *161*, 106704. [CrossRef]
15. Zhang, P.; Ma, F.; Xiao, X. Thermal energy storage and retrieval characteristics of a molten-salt latent heat thermal energy storage system. *Appl. Energy* **2016**, *173*, 255–271. [CrossRef]
16. Ma, Z.; Yang, W.-W.; Yuan, F.; Jin, B.; He, Y.-L. Investigation on the thermal performance of a high-temperature latent heat storage system. *Appl. Therm. Eng.* **2017**, *122*, 579–592. [CrossRef]

17. Ji, L.; Liang, X.; Xie, Y.; Huang, G.; Wang, B. Optimal design and sensitivity analysis of the stand-alone hybrid energy system with PV and biomass-CHP for remote villages. *Energy* **2021**, *225*, 120323. [CrossRef]
18. Boerema, N.; Morrison, G.; Taylor, R.; Rosengarten, G. Liquid sodium versus Hitec as a heat transfer fluid in solar thermal central receiver systems. *Sol. Energy* **2012**, *86*, 2293–2305. [CrossRef]
19. Hakkarainen, E.; Tähtinen, M. Dynamic modelling and simulation of linear Fresnel solar field model based on molten salt heat transfer fluid. In *AIP Conference Proceedings*; AIP Publishing LLC: Melville, NY, USA, 2016; p. 070014.
20. Wu, Y.-t.; Ren, N.; Wang, T.; Ma, C.-f. Experimental study on optimized composition of mixed carbonate salt for sensible heat storage in solar thermal power plant. *Sol. Energy* **2011**, *85*, 1957–1966. [CrossRef]
21. Silvennoinen, E.; Juslin, K.; Hänninen, M.; Tiihonen, O.; Kurki, J.; Porkholm, K. *The APROS Software for Process Simulation and Model Development*; VTT Technical Research Centre of Finland: Espoo, Finland, 1989.
22. Al-Maliki, W.; Mahmoud, N.; Al-Khafaji, H.; Alobaid, F.; Epple, B. Design and Implementation of the Solar Field and Thermal Storage System Controllers for a Parabolic Trough Solar Power Plant. *Appl. Sci.* **2021**, *11*, 6155. [CrossRef]
23. Lappalainen, J.; Hakkarainen, E.; Sihvonen, T.; Rodríguez-García, M.M.; Alopaeus, V. Modelling a molten salt thermal energy system—A validation study. *Appl. Energy* **2019**, *233*, 126–145. [CrossRef]
24. Al-Maliki, W.A.K.; Alobaid, F.; Starkloff, R.; Kez, V.; Epple, B. Investigation on the dynamic behaviour of a parabolic trough power plant during strongly cloudy days. *Appl. Therm. Eng.* **2016**, *99*, 114–132. [CrossRef]
25. Al-Maliki, W.A.K.; Alobaid, F.; Kez, V.; Epple, B. Modelling and dynamic simulation of a parabolic trough power plant. *J. Process Control* **2016**, *39*, 123–138. [CrossRef]
26. Herrmann, U.; Kelly, B.; Price, H. Two-tank molten salt storage for parabolic trough solar power plants. *Energy* **2004**, *29*, 883–893. [CrossRef]
27. Kojima, T.; Miyazaki, Y.; Nomura, K.; Tanimoto, K. Density, surface tension, and electrical conductivity of ternary molten carbonate system Li_2CO_3–Na_2CO_3–K_2CO_3 and methods for their estimation. *J. Electrochem. Soc.* **2008**, *155*, F150. [CrossRef]
28. Ejima, T.; Sato, Y.; Yamamura, T.; Tamai, K.; Hasebe, M.; Bohn, M.S.; Janz, G.J. Viscosity of the eutectic dilithium carbonate-disodium carbonate-dipotassium carbonate melt. *J. Chem. Eng. Data* **1987**, *32*, 180–182. [CrossRef]
29. Wang, T.; Mantha, D.; Reddy, R.G. Novel high thermal stability LiF–Na_2CO_3–K_2CO_3 eutectic ternary system for thermal energy storage applications. *Sol. Energy Mater. Sol. Cells* **2015**, *140*, 366–375. [CrossRef]
30. Ratcliff, P.; Garbett, P.; Fischer, W. The new Siemens gas turbine SGT5-8000H for more customer benefit. *VGB Powertech* **2007**, *87*, 128–132.
31. Scholz, C.; Zimmermann, H. First Long-Term Experience with the Operational Flexibility of the SGT5-8000H. In Proceedings of the 8. VDI Symposium "Stationary Gas Turbines of All Performance Classes in a Flexible Power Supply Operation", Mainz, Germany, 20–21 November 2012.
32. Vandervort, C.; Leach, D.; Scholz, M. Advancements in H Class Gas Turbines for Combined Cycle Power Plants for High Efficiency, Enhanced Operational Capability and Broad Fuel Flexibility. The Future of Gas Turbine Technology. In Proceedings of the 8th International Gas Turbine Congress, Brussels, Belgium, 12–13 October 2016.
33. Vandervort, C.; Wetzel, T.; Leach, D. Engineering and Validating a World Record Gas Turbine. *Mech. Eng.* **2017**, *139*, 48–50. [CrossRef]
34. Vandervort, C.; Leach, D.; Walker, D.; Sasser, J. *Commercialization and Fleet Experience of the 7/9HA Gas Turbine Combined Cycle. Turbo Expo: Power for Land, Sea, and Air*; American Society of Mechanical Engineers: New York, NY, USA, 2019; p. V003T08A6.
35. Müller-Steinhagen, H.; Fa, T.F. *Concentrating Solar Power. A Review of the Technology*; Institute of Technical Thermodynamics, German Aerospace Centre: Stuttgart, Germany, 2004; p. 9.

applied sciences

MDPI

Article

A High Thermal Conductivity of MgO-H_2O Nanofluid Prepared by Two-Step Technique

Hadia Kadhim Judran [1], Adnan G. Tuaamah Al-Hasnawi [1], Faten N. Al Zubaidi [1], Wisam Abed Kattea Al-Maliki [2,3], Falah Alobaid [3,*] and Bernd Epple [3]

[1] Electromechanical Engineering Department, University of Technology-Iraq, Baghdad 19006, Iraq; 50100@uotechnology.edu.iq (H.K.J.); 10597@uotechnology.edu.iq (A.G.T.A.-H.); 50241@uotechnology.edu.iq (F.N.A.Z.)
[2] Mechanical Engineering Department, University of Technology-Iraq, Baghdad 19006, Iraq; wisam.a.kattea@uotechnology.edu.iq
[3] Institut Energiesysteme und Energietechnik, TU Darmstadt, Otto-Berndt-Straße 2, 64287 Darmstadt, Germany; bernd.epple@est.tu-darmstadt.de
* Correspondence: falah.alobaid@est.tu-darmstadt.de

Abstract: In this paper, the main goal is to study the impact of nanopowder volume concentration and ultrasonication treatment time on the stability and thermophysical properties of MgO-DW nanofluid at room temperature. The co-precipitation method was utilized to prepare pure MgO nanoparticles with an average particle size of 33 nm. The prepared MgO nanopowder was characterized by using XRD, SEM, and EDX analyses. Then, MgO-DW nanofluid was obtained with different volume concentrations (i.e., 0.05, 0.1, 0.15, 0.2, and 0.25 vol.%) and different ultrasonication time periods (i.e., 45, 90, 135, and 180 min) by using a novel two-step technique. With volume concentration and ultrasonication time of 0.15 vol.% and 180 min, respectively, good stability was achieved, according to the zeta potential analysis. With increasing volume concentration and ultrasonication time period of the nanofluid samples, the thermal conductivity measurements showed significant increases. As a result, the maximum enhancement was found to be 25.08% at a concentration ratio of 0.25 vol.% and agitation time of 180 min. Dynamic viscosity measurements revealed two contrasting trends with volume concentration and ultrasonication time. The lowest value of relative viscosity was gained by 0.05 vol.% MgO-DW nanofluid. The chemical and physical interactions between MgO nanoparticles and DW molecules play an important function in determining the thermal conductivity and dynamic viscosity of MgO-DW nanofluid. These findings exhibit that MgO-DW nanofluid has the potential to be used as an advanced heat transfer fluid in cooling systems and heat exchangers.

Keywords: MgO-DW nanofluid; two-step technique; co-precipitation; XRD and SEM; thermal conductivity; dynamic viscosity

Citation: Judran, H.K.; Al-Hasnawi, A.G.T.; Al Zubaidi, F.N.; Al-Maliki, W.A.K.; Alobaid, F.; Epple, B. A High Thermal Conductivity of MgO-H_2O Nanofluid Prepared by Two-Step Technique. *Appl. Sci.* **2022**, *12*, 2655. https://doi.org/10.3390/app12052655

Academic Editor: Jianzhong Lin

Received: 10 January 2022
Accepted: 2 March 2022
Published: 4 March 2022

1. Introduction

High thermal conductivity fluids are referred to as nanofluids and are employed rather than regular fluids to increase heat transfer properties or to prevent overheating. Numerous studies have demonstrated that standard fluids used in heat exchangers, such as water, oil, ethylene glycol, and glycerol, have low thermal conductivity as compared with metallic and ceramic materials [1–3]. Therefore, praiseworthy attempts have been made to improve the thermal conductivity of traditional fluids, by distributing ultrafine solid particles. The growing requirement for high efficiency in heat exchangers, storage materials in electronic devices, chemical reactions, boiling processes, and solar energy has prompted researchers to focus on dispersed particles, particularly within a size range of 1–100 nm, within the base fluid [4–9].

Maxwell [10,11] was the first to conduct practical research to increase heat conductivity, and he was supported by a large number of researchers. Among the most prominent, Choi,

suggested the concept of blending nanoparticles into traditional working fluids to enhance the thermophysical properties and heat transfer characteristics of the working fluids.

Choi formulated the idiom "nanofluid" at the Argonne National Laboratory in the United States of America in 1995 [12]. Nanofluids have unique and effective features such as larger specific surface area (SSA) nanoparticles, high suspension stability (longer suspension time), reduced erosion of ducts, significant energy saving, minimal viscosity increase, and higher heat transfer rate as compared with the milli- and micro-sized suspension fluids proposed by Maxwell [13,14]. Therefore, different aspects of nanofluids have been studied such as synthesis techniques [15–17], thermophysical properties such as thermal conductivity and dynamic viscosity [18–23], and nanofluid applications [16,24]. Because of its clear influence on heat transfer, thermal conductivity is worth investigating. Accordingly, researchers have worked hard to investigate aspects that have an impact on thermal conductivity, such as the shape (morphology) and size of the dispersed phase (nanopowder), type of the base fluid, temperature, synthesis technique, using or not using and type of surfactant (additives), pH, nanopowder concentration, and ultrasonication time [25–30]. Metal oxide nanopowders are widely used in nanofluid preparation due to their chemical stability as compared with metals, as well as their good thermal conductivity, abundance, and cheapness [31,32]. Metal oxide nanoparticles such as MgO, CuO, Al_2O_3, ZnO, TiO_2, Fe_2O_3, and SiO_2 are suitable candidates for the development of effective heat transfer fluids due to their significant properties. Among these particles, MgO has played a critical role in improving the thermal properties of traditional fluids. In addition, MgO nanofluid has been employed in various applications including catalysis, catalyst supports, nuclear reactors, storage materials, and boiling processes [33–37].

Subsequently, investigators have extensively examined MgO nano oxides. Various physical and chemical methods have been used for preparation of MgO nanopowder, involving vapor deposition [38], co-precipitation [39,40], sol-gel [41,42], molecular beam epitaxial [43], spray pyrolysis [44], ultrasonic irradiation [45], microwave irradiation [46], hydrothermal [39], plasma irradiation [47], surfactant methods [48], combustion method [49], solvothermal [50], and thermal evaporation [51], in addition to biological sterilization methods [52], such as fungal strain *Aspergillus terreus* [53], and so-called green synthesis [54,55]. Although MgO nanopowder can be prepared via the different previously mentioned approaches, the co-precipitation method has several advantages due to its simplicity, effectiveness, high surface area of the nano product, and economic route [56]. There are two major techniques that can be used to synthesize nanofluid, i.e., single-step and two-step techniques. Nevertheless, in terms of a two-step procedure, any of the aforementioned methods can synthesize MgO nanofluid. In both techniques, applying the ultrasonication treatment is the pivotal operator for breaking down the agglomerated nanoparticles to attain a high stable nanofluid [4]. Thermal conductivity and viscosity of the MgO/propylene glycol nanofluid were extensively improved by S. Manikandan and K. S. Rajan [57] at various MgO nanopowder concentrations (0–2 vol.%), temperatures (20–60 °C), and ultrasonication times (0–30 h). Firstly, MgO nanopowder with an average particle size of 35 nm was prepared by a simple chemical reaction route. Then, a two-step technique was devoted to synthesizing the nanofluid using probe ultrasonication for 25 h. The average thermal conductivity enhancement was 20% for 2 vol.% MgO/propylene glycol nanofluid and was detected to be independent of temperature. The relative viscosity of the nanofluid was decreased with nanoparticle concentration at a temperature of 30 °C. At a higher ultrasonication time, both thermal conductivity and viscosity were clearly improved with ultrasonication time up to 0.243 (W/M·°K) and 25 (mPa·sec), respectively. M. H. Esfa et al. [58] prepared MgO nanofluid by suspending nanoparticles (40 nm) in a binary base fluid of water and ethylene glycol (60:40) using a two-step technique. In this technique, an ultrasonication treatment time of up to 4 h was applied. The impact of different solid concentrations and different temperatures were investigated. The results showed that the thermal conductivity of MgO/H_2O-EG nanofluid increased with an increase in nano MgO volume concentration and temperature. Using a two-step technique, a hybrid

nanofluid of Ag-MgO/water was also conducted by the M. H. Esfa research group [5]. The nanofluid was produced by mixing 25 nm nano Ag (50%), 40 nm nano MgO (50%), and water. Ultrasonic vibration for 3 h and CTAB surfactant were employed to ensure better stability.

Thermal conductivity and dynamic viscosity were measured as a function of nanoparticle volume fraction range between 0% and 2%. The obtained results revealed that both thermal conductivity and dynamic viscosity were increased with increases in the volume fraction of (Ag + MgO) nanoparticles. The effects of particle size, solid concentration, and temperature on the dynamic viscosity of ethylene glycol-based nanofluid containing MgO nanoparticles have been studied by K. Yapici et al. [59]. They conducted experiments at concentrations ranging from 5 to 20 wt.% of MgO nanopowder with particle sizes of 20 and 40 nm. MgO/EG nanofluid was agitated in an ultrasonic bath for 6 h by using a two-step technique. Nonlinear results revealed that the 20 nm and 40 nm MgO nanoparticles exhibited non-Newtonian behavior at weight concentrations higher than 5%. J. Lu et al. [60] used molten salt $LiNO_3$-$NaNO_3$-KNO_3 with MgO nanoparticles to prepare nanofluid via a two-step technique. The synthesis technique was concluded by heating the mixture of molten salt and MgO nanoparticles to 350 °C and ultrasonication time for 1 h. The effect of nanoparticles on thermal properties was studied with different sizes ranges of 20–100 nm, weight concentrations from 0.5 to 2.0 wt.%, and temperature. The results showed that the enhancement of thermal conductivity of salt with 1 wt.% nano-MgO could be 5.3–11.7%. In an experimental environment, S. R. Nfawa et al. [61] improved the thermal conductivity of a CuO-MgO/H_2O hybrid nanofluid in an experimental setting. The hybrid nanofluid was synthesized and investigated at various volume fractions (i.e., 0.125–1.25%) of 80% CuO and 20% MgO nanoparticles which were dispersed in water at temperatures ranging from 25 to 50 °C. The zeta potential measurement indicated that the 0.25% (CuO-MgO)/H_2O hybrid nanofluid had a good stability of −45.1 mV. The study results showed that by increasing the concentration ratio, the CuO-MgO/H_2O hybrid nanofluid's thermal conductivity was clearly enhanced; however, this enhancement began to decline when the concentration was higher than 1 vol.% as a result of nanoparticle precipitation.

The two-step approach is often supported by the aid of relatively high temperatures, and/or the use of surfactants, and/or a long ultrasonication treatment time, and/or organic base fluids. Therefore, in the present study, we aimed at preparing MgO-DW nanofluid with efficient thermal properties such as better stability, high thermal conductivity, and low viscosity, without using surfactants or stabilizers, and with environmentally friendly nanofluid at room temperature.

Furthermore, the plurality of the concerned investigations has been considered in order to exploit MgO nanopowder as an additive or to synthesize hybrid nanofluid with other nanomaterials, as cited in [62–66]. However, in this work, pure MgO-DW nanofluid was produced with functional properties. This was achieved by using MgO nanopowder with a unique morphology of feathery or fluffy-like nanostructure, while usually, the nano shape used in nanofluid preparation is spherical particles. The abovementioned aspects are all assumed to be novel, making MgO-DW nanofluid an excellent alternative for heat transfer applications.

2. Experimental Details

2.1. Materials and Method

The co-precipitation method was used to create MgO nanopowder. Analytical grade chemicals such as magnesium sulfate ($MgSO_4 \cdot 7H_2O$), sodium bicarbonate ($NaHCO_3$), ammonium hydroxide (NaOH), and sodium dodecyl sulfate (SDS) were utilized without additional purification. NaOH and SDS were both used as a surfactant at room temperature. The chemicals used were all from BDH Chemicals Ltd., Poole, Dorset, UK. First, a 0.8 M solution of $NaHCO_3$ and NaOH was prepared by dissolving a suitable quantity in deionized water. Similarly, Mg precursor solution was prepared by dissolving $MgSO_4 \cdot 7H_2O$ in deionized water. Next, 50 mL of 0.5 M $MgSO_4$ and SDS solution were blended fully by

stirring vigorously by utilizing a magnetic stirrer for 20 min at room temperature. Then, using a burette, 50 mL of 0.8 M $NaHCO_3$ solution was gently poured into it, while it was constantly stirred. Then, 50 mL of 1 M NaOH solution was added in batches into the above resulting solution under stirring. The final combination was left to swirl for 4 h after adding the surfactant and precipitating agent, with no parameters being modeled.

The extremely finely powdered white precipitate MgO was collected at the bottom of the preparation flask once the time was up. The fine powder was carefully separated using a centrifuge. The whole precipitation was washed several times with distilled water. The main purpose of the washing process was to ensure that the precipitate was free from foreign trace elements, especially SDS residue. The resulting MgO powder was dried in an air oven at 60 °C for 2 h. Then, the prepared MgO nanopowder was produced via a calcination process using a furnace at 350 °C for 1 h. All details of the preparation method are explained in Figure 1 (first step).

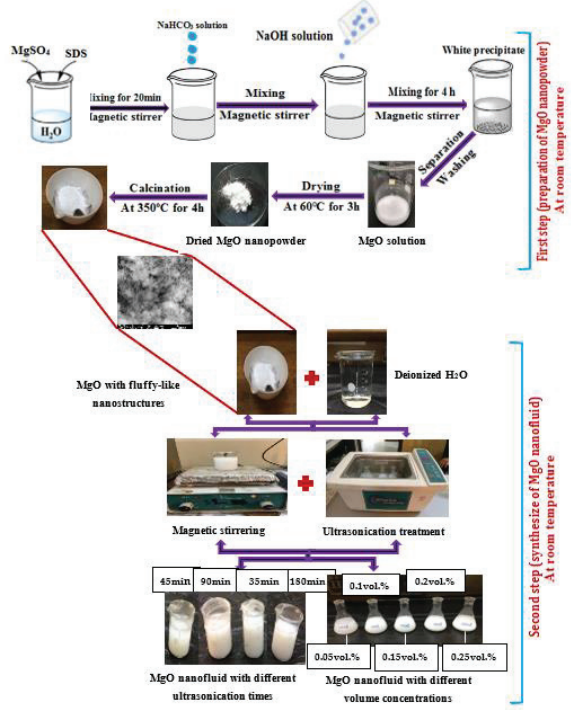

Figure 1. Synthesize of MgO-DW nanofluid via a two-step technique.

2.2. Preparation of MgO Nanofluid

A two-step technique was used to make the MgO nanofluid. The first step, i.e., nanopowder preparation, was completed (as described above). The second step involved synthesis of the nanofluid using mechanical procedures. The mechanical procedures were carried out using primary mechanical stirring for 30 min, and then ultrasonic agitation as shown in Figure 1 (second step). Different ultrasonication periods and volume concentrations were used to prepare the nanofluid samples. They were synthesized via dispersing MgO nanoparticles in 100 mL of deionized water as a base fluid without the use of any dispersants or heat. The ultrasonication times were 45, 90, 135, and 180 min. The following

relationship [67] was used to compute the volume concentration ratios of 0.05, 0.1, 0.15, 0.2, and 0.25 vol.%:

$$\phi = \frac{V_P}{V_T} \quad (1)$$

where ϕ is the volume concentration of MgO nanofluid, V_P is the volume of MgO nanopowder, and V_T is the total volume of nanofluid sample.

Depending on nanopowder density (ρ_P) and base fluid density (ρ_{bf}), the volume was measured as follows:

$$\begin{aligned} \text{Since, } V_p = \frac{m_p}{\rho_p},\ V_T = V_p + V_{bf} = \frac{m_p}{\rho_p} + \frac{m_{bf}}{\rho_{bf}} \\ \text{So, } \phi = \frac{(m_p/\rho_p)}{(m_p/\rho_p) + (m_{bf}/\rho_{bf})} \end{aligned} \quad (2)$$

where m_p and m_{bf} are the masses of MgO nanopowder and base fluid (deionized water), respectively; ρ_p and ρ_{bf} are the densities of nanopowder and base fluid, respectively. According to the final relation, the weights of MgO nanopowder required to prepare nanofluid samples with different volume ratios are listed in Table 1.

Table 1. Weights of MgO nanoparticles corresponding to the volume concentrations.

Volume Concentrations Ratio	Weights of MgO Nanopowder (g)
0.05 vol.%	0.1433
0.1 vol.%	0.2867
0.15 vol.%	0.4326
0.2 vol.%	0.5772
0.25 vol.%	0.7178

2.3. The Characterization Techniques

The structural characteristics of MgO nanopowder were achieved using an XRD-6000 Shimadzu X-ray diffractometer with Cu Kα radiation (λ = 1.5406 Å) in the 2θ range of (10−80°) in a step of 0.05° and a scan speed of 5 degree/min. A scanning electron microscope (SEM) analysis was also performed to test the surface morphology of the prepared nanopowder. The SEM device was a Mira 3-scan (Metrohm France, Villebon-sur-Yvette, France) type that ran at a 15 kV accelerating voltage. An EDX approach equipped with a SEM instrument was used to assess the composition and purity of the nanopowder.

2.4. The Stability and Particle Size Analysis

Zeta potential was employed as an index of the surface charge of the MgO nanoparticles in the base fluid. The surface charge was considered to be an indicator of the dispersion stability of the MgO nanosuspension. The suspension with high zeta potential was stabilized, while the sample with low value tended to accumulate and suffer from sedimentation, according to ASTM standard (D4187-82) of zeta potential ranges in Table 2 [68,69]. MgO-DW nanofluid samples at different concentration ratios (0.05 vol.%, 0.1 vol.%, 0.15 vol.%, 0.2 vol.%, and 0.25 vol.%) were mixed with the KCl solution, then, mechanically stirred for 30 min with ultrasonic agitation for 90 min, and then tested by the device. The same procedure was followed in the case of 0.15 vol.% MgO-DW nanofluid samples at different ultrasonication times (45, 90, 135, and 180 min).

Table 2. The ASTM standard of zeta potential ranges.

Zeta Potential Range (mV)	Stability Behavior
<±5	Rapid coagulation or flocculation
±10 to ±30	Incipient instability
±30 to ±40	Moderate stability
±40 to ±60	Good stability
>±61	Excellent stability

The measurements were carried out using a zeta potential analyzer (Zeta Plus (21521), power 100–240 V 50/60 Hz, USA). To ensure data reliability, each experiment was repeated three times before the mean results were estimated. After four days of preparation, the zeta potential measurements were obtained. A particle size analyzer (Zetasizer, Brookhaven Instruments, New York, NY, USA) can also detect particle size by using a dynamic light scattering (DLS) process. The container is illuminated by a laser, and the particles scatter the light which is measured using a detector. A fundamental property of Brownian motion is that small particles move much faster than large particles. There is an association between the size of a particle and its velocity due to Brownian motion. Based on this physical feature, a particle size analyzer measures the Brownian motion of the particles in a specimen and connects this to a size based on established theories [70]. Therefore, a particle size analyzer was used to determine the average particle size of the prepared MgO nanopowder at room temperature. The scattering angle and polydispersity index were 15° and 0.061, respectively.

2.5. Measurements of Thermophysical Properties

With varying volume concentrations of 0.05, 0.1, 0.15, 0.2, and 0.25 vol. percent, the thermal conductivity and dynamic viscosity of MgO-DW nanofluid were measured. They were also measured with various ultrasonication treatment times of 45, 90, 135, and 180 min. The thermal conductivity was tested using a Sweden company device (Hot Disk TPS 500 S, KIJTALEY, Johanneberg Science Park, Göteborg, Sweden), which is a type of thermal constants analyzer that uses the standard isotropic method. The dynamic viscosity measurements were carried out using a viscometer, Model HTD13145 Six-Speed Rotational Viscometer (Qingdao Haitongda Special Instrument Co., Ltd., Qingdao, China). The thermal conductivity and dynamic viscosity measurements were both achieved at room temperature. The enhancement ratio of thermal conductivity values of MgO-DW nanofluid can be estimated using the following relationship [71]:

$$\mathrm{TCE\%} = \frac{K_{nf} - K_{bf}}{K_{bf}} * 100 \quad (3)$$

where K_{nf} and K_{bf} are the thermal conductivity of the nanofluid and the base fluid, respectively.

3. Results and Discussion

3.1. The Structural Studies

Figure 2 shows the XRD spectrum used to analyze the crystalline structure of the obtained MgO nanopowder. The pattern shows an ordered polycrystalline structure with five intense peaks. The low intensity of the diffraction background was clearly indicative of the pure phase of the intended material. Therefore, no distinguishing peaks of any impurities were discovered. The surfactant SDS [$CH_3(CH_2)_{11}OSO_3Na$] acts as a catalyst, preventing any fast reactions in the solution. In addition, it acts as a dispersion factor of the formed particles [72].

Hence, the synthesized material is of high purity, free of any secondary products, and nanoscale. The diffraction peaks at 2θ values of 36.9271°, 42.8937°, 62.2626°, 74.6169°, and 78.5795° correspond to the crystalline planes of (111), (200), (220), (311), and (222), respectively. A strong preferential orientation was observed at a diffraction angle of 42.8937° with Miller indices (200). Similar results have been reported in the literature [73,74]. The specified X-ray peaks matched well with the crystallographic structure according to the JCPDS standard file no. 45-0946 of polycrystalline MgO. The crystallite size (D) was calculated based on the full width at half maximum (FWHM) of the intensive diffraction peak (i.e., the plane 200) by using the Debye–Scherrer's formula [75,76]:

$$D = \frac{A\lambda}{(FWHM)\cos\theta} \quad (4)$$

where A is an empirical shape factor equal to 0.94, λ is the wavelength of the X-ray source, and θ is the angular position of the diffraction peak.

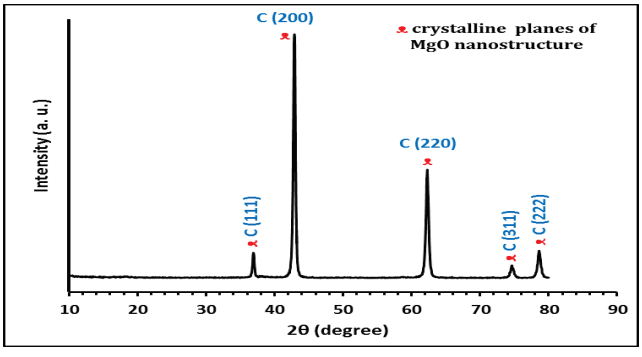

Figure 2. XRD pattern of MgO nanopowder prepared by the co-precipitation method.

The crystallite size was calculated to be 22.78 nm. The sharp diffraction peaks indicated a high degree of crystallization. The nanostructure of the prepared MgO particles was also revealed by the average particle size of less than 100 nm. All the diffraction peaks of MgO nanopowder revealed an obvious shift towards lower 2θ positions, as seen in Table 3. This result may be attributed to the nano scale of the prepared particles, whereas the high density of crystalline boundaries in the nano structure may cause microstrain.

Table 3. Positions of X-ray diffraction peaks (2θ) of MgO nanopowder prepared by the co-precipitation.

Crystalline Planes (hkl)	C (111)	C (200)	C (220)	C (311)	C (222)
Measured (XRD) 2θ (deg.)	36.9271	42.8937	62.2626	74.6169	78.5795
Standard 2θ (deg.) (JCPD S card no. 45-0946)	36.9360	42.9160	62.3020	74.6890	78.6280

The lattice constant and the unit cell volume were estimated by using the Formulas (5) and (6) [75], respectively:

$$\frac{1}{d^2_{(hkl)}} = \frac{h^2 + k^2 + l^2}{a^2} \quad (5)$$

$$V = a^3 \quad (6)$$

where d_{hkl} is the interplanetary crystalline distance; h, k, and l are the Miller indices; and "a" is the lattice constant.

From the results in Table 4, it can be noticed there is relative stretching in the d_{hkl} spacing and lattice constant values as compared with the standard values, since the variation in both is approximately 0.0011 Å of the interplanetary distance and 0.0023 Å of lattice constant. Consequently, the volume of the unit cell showed relative enlargement, which might be due to the nanoscale of MgO particles.

Table 4. XRD results of MgO nanopowder prepared by the co-precipitation method at room temperature.

The Value	Crystal Structure and (hkl)	d_{hkl}-Spacing (Å)	Lattice Constant (Å)	Unit Cell Volume (Å^3)
Measured (XRD)	Cubic (200)	2.1067	4.2135	74.8047
Standard (JCPDS card no. 45-0946)	Cubic (200)	2.1056	4.2112	74.6823

The elemental structure, purity, and surface morphology of the synthesized MgO nanostructure were tested using SEM and EDX techniques. The energy dispersive X-ray spectrum was achieved at the range of 0–10 keV, as shown in Figure 3a. One can clearly observe three evident bands at nearly 0.25 keV, 0.55 keV, and 1.3 keV which correspond to the elements of C, O, and Mg, respectively. The spectrum demonstrated a distinct absorption band of magnesium element with weight and atomic ratios of 50.08% and 47.55%, respectively. As stated in the inset table inside the Figure, the oxygen element ratios are 46.95% and 50.76%. Therefore, the EDX spectroscopy results confirmed the formation of MgO, as was previously demonstrated by XRD analysis. In addition, according to XRD results the prepared material has a pure phase, but the EDX results show a small band of carbon element.

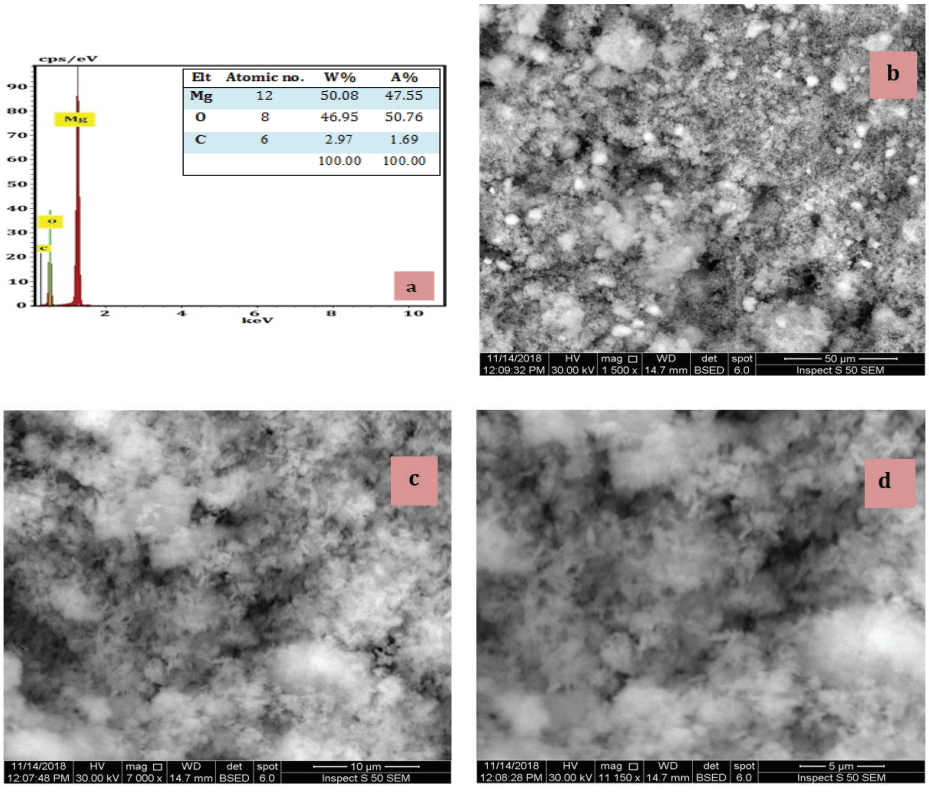

Figure 3. MgO nanopowder prepared by using the co-precipitation method: (**a**) EDX analysis. Typical SEM images at different scale bars of: (**b**) 50 um; (**c**) 10 um; (**d**) 5 um.

The presence of carbon peak in the prepared sample was attributed to the carbon holder utilized in the imaging and/or the sodium carbonate used in the preparation process. A similar result was reported in the literature [77]. The morphology of MgO nanostructure was anatomized at various magnifications, as displayed in Figure 3b–d. Figure 3b exhibits agglomerated structures with high density. It shows what looks like snowballs or bright white cotton balls that are diffused on the surface of the agglomerated structures. Interestingly, the SEM images (Figure 3c,d) exhibit feathery or fluffy-like nanostructures that assemble together to form dense clouds.

The fluffy-like nanostructures have varied orientations, resulting in the intermingled morphology within the clouds. The average particle size of MgO nanostructures was measured to be 33 nm.

3.2. Stability Measurement of MgO-DW Nanofluid

The stability of the nano suspension contents in the base medium must be carefully monitored since it has a significant influence on the thermal characteristics. Nanoparticle aggregation may cause precipitation and blockage, hence, decreasing the thermal conductivity of the nanofluid. The zeta potential refers to the quantity of electrostatic repulsion potential presented between the charged nanoparticles and the base fluid. The zeta potential was investigated at various volume concentrations and ultrasonication times of MgO-DW nanofluid, as listed in the Table 5A,B. It can be seen that all the values of zeta potential have a negative sign, due to the adsorption of the OH^- ions (negative ions) on the surface of MgO nanoparticles. The states of zeta potential values were determined according to the ASTM standard in Table 2 (experimental part). The specimens in part A were conducted with an ultrasonication time of 90 min. Mostly, the zeta potential values exhibited that as the volume ratios increased from 0.05 to 0.25 vol.%, the ZP values of the synthesized MgO-DW nanofluid decreased from −41.0 to −30.3 mV. This behavior cannot be extended as a general rule, as shown in the 0.15 vol.% MgO nanofluid sample, which recorded a zeta potential value of −47.0 mV. Hence, in the case of this sample, an increase in solid volume concentration did not cause a decrease in the zeta potential value, as shown in other samples.

Table 5. Zeta potential analysis of MgO nanofluids prepared using the two-step technique.

A			B		
Volume Ratios ϕ (vol.%)	**Zeta Potential (mV)**	**The State**	**Ultrasonication Time (min)**	**Zeta Potential (mV)**	**The State**
0.05	−41.0	Good stability	45	−38.9	Moderate stability
0.1	−38.2	Moderate stability	90	−45.0	Good stability
0.15	−45.0	Good stability	135	−54.7	Good stability
0.2	−35.7	Moderate stability	180	−62.1	Good stability
0.25	−30.3	Moderate stability			

Good stability was obtained when the electrostatic repulsion forces overcame the attraction forces such as Van der Waals forces between the MgO nanoparticles. For this reason, this phenomenon could prevent accumulation, therefore, no sedimentation of dispersion nanoparticles occurred within the base fluid. A low zeta potential value was found at 0.25 vol.% MgO-DW nanofluid, which indicated the presence of some clusters or aggregates. However, this sample was moderately stable. All the samples in part B were prepared with a concentration ratio of 0.15 vol.% nanoparticles. It can be seen that ultrasonication time is directly proportional to zeta potential values. Therefore, as ultrasonication time increased from 45 to 180 min, the ZP values of the synthesized MgO nanofluids also increased from −38.9 to −62.1 mV. The portion of nanoparticles that survive in a well dispersed state in nanofluid increases as the ultrasonication treatment period increases, raising the zeta potential values. The last result confirmed the possibility

of improving the dispersion stability of the nanofluids via an increasing ultrasonication agitation time. The current findings agree with those reported in [61].

3.3. Thermophysical Properties Measurements

3.3.1. Thermal Conductivity

The thermal conductivity of MgO-DW nanofluid is one of the most important operators that has a direct effect on heat transfer rate. Variations in thermal conductivity and relative thermal conductivity with respect to the nanoparticle concentration ratio ranging from 0.05 to 0.25 vol.% was studied at room temperature 27 °C ± 2, as shown in Figure 4a,b. It is apparent from Figure 4 that the thermal conductivity and relative thermal conductivity increased with the solid content of dispersed MgO nanostructures.

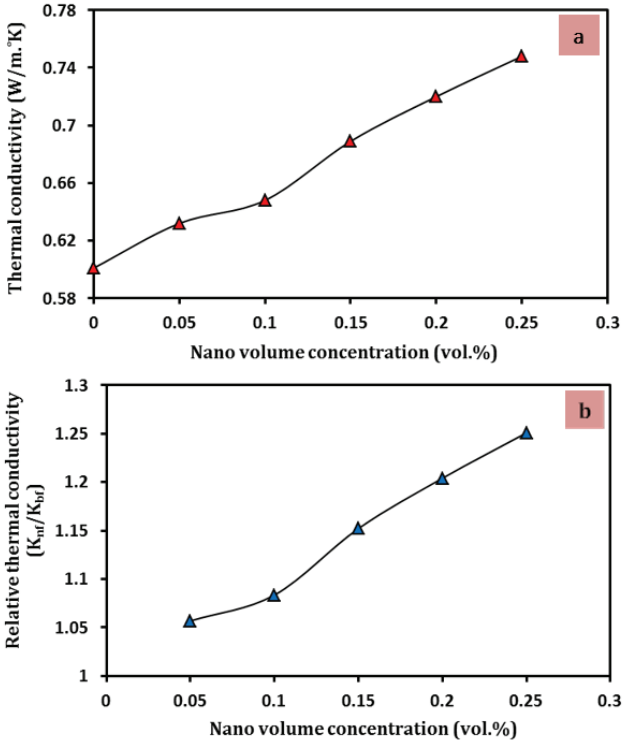

Figure 4. (**a**) The thermal conductivity and (**b**) relative thermal conductivity (K_{nf}/K_{bf}), as a function of solid volume concentration of MgO-DW nanofluid at room temperature.

The thermal conductivity of MgO is approximately 48.4 (W/m·°K) [57] which is significantly greater than water's value of 0.598 (W/M·°K) [78]. As a result, raising the concentration ratio of MgO nanopowder would undoubtedly improve and increase the thermal conductivity of the prepared nanofluid. Notably, the utilized MgO nanoparticles have a high specific surface area that comes from a nanoscale of 33 nm. Hence, there is a significant rate of heat transfer between dispersed nanoparticles and deionized water molecules, which increases as their volume concentrations increase.

In other words, an improvement in relative thermal conductivity means increased interactions between nanoparticles. The interactions are ascribed to the evolution of intense networks of dispersed nanoparticles inside the base fluid and the stir action caused by the Brownian motion of these nanoparticles. Furthermore, the Brownian motion becomes faster in the case of a nanostructure.

The greatest thermal conductivity enhancement (by using Relation (3)) was found to be 25.08% at the highest concentration of 0.25 vol.%. In addition, the lowest improvement was 5.68% at a volume concentration of 0.05 vol.%, as observed in Table 6. Generally, increasing the volume concentrations of MgO nanoparticles in the fluid minimizes the distance between moving particles, resulting in more molecular collisions. An increase in the accelerated nanoparticles in the base fluid enhances the thermal conductivity of the nanofluid.

Table 6. The improvement ratios of the thermal conductivity with solid volume concentrations of MgO/DW nanofluid at room temperature.

Concentration Ratios ϕ (vol.%)	Thermal Conductivity Enhancement (TCE%)
0.05	5.685
0.1	8.361
0.15	15.217
0.2	20.401
0.25	25.084

Furthermore, the development of clusters and aggregates can take the shape of chain-like structures which provide a transformation path of the thermal energy among the nanoparticles. This may explain the high improvement ratio of thermal conductivity in the case of 0.25 vol.% MgO-DW nanofluid, despite the low zeta potential value of this sample. The results agree very well with the researchers' observations in [79–81].

The major aim of ultrasonication treatment is to ensure proper dispersion and break up of any residual agglomerations in the dispersed phase (MgO nanopowder) within the base fluid. Figure 5 reveals the changes in thermal conductivity with respect to the ultrasonication treatment time of MgO-DW nanofluid. The evident trend in Figure 5 is that the values of thermal conductivity increase with ultrasonication time.

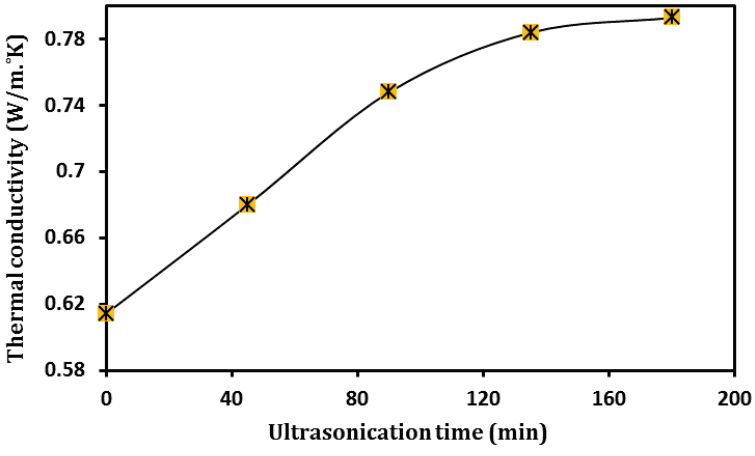

Figure 5. The thermal conductivity as a function of ultrasonication time of 0.25 vol.% MgO-DW nanofluid at room temperature.

The increase in thermal conductivity with an increase in ultrasonication time may be attributed to enhancing dispersion stability, which was confirmed via zeta potential analysis (see Table 5). Therefore, the majority of the nanoparticles in the MgO nanosuspension will participate in the heat transfer process, increasing with ultrasonication agitation time, thereby, increasing its thermal conductivity. The differences in thermal conductivity

were constrictive between 135 and 180 min of ultrasonication, and hence, ultrasonication influence was marginalized after 135 min. Therefore, the enhancement rate in thermal conductivity was insignificant over these periods, as shown in Table 7. The authors in [82–86] found a similar behavior when they investigated the thermal conductivity of MWCNT, Fe_3O_4/CNT, TiO_2, CNT, and Al_2O_3 nanofluids, respectively, at various ultrasonication times. Therefore, at the ultrasonication time of 180 min, the 0.25 vol.% MgO-DW nanofluid showed better thermal transport characteristics due to the higher volume concentration of MgO nanoparticles in the suspended state.

Table 7. The improvement ratios of the thermal conductivity with ultrasonication time of MgO-DW nanofluid at room temperature.

Concentration Ratios ϕ (vol.%)	Improvement of Thermal Conductivity (K_{nf}%)
45	13.71
90	25.08
135	31.10
180	32.61

3.3.2. Dynamic Viscosity

The concentration ratio of nanoparticles and ultrasonication time are major factors that influence the viscosity of nanofluids. Figure 6a,b shows the changes in viscosity and relative viscosity with volume concentration ratios of MgO-DW nanofluid, at room temperature.

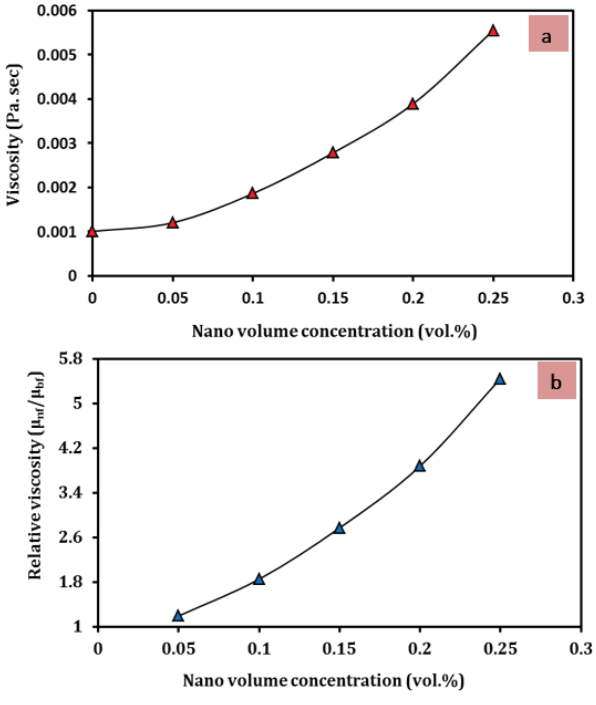

Figure 6. (**a**) The viscosity; (**b**) the relative viscosity (μ_{nf}/μ_{bf}), as a function of solid volume concentration of MgO-DW nanofluid at room temperature.

Figure 6a shows that the viscosity of MgO-DW nanofluid is directly proportional to the MgO nanoparticles loading. The viscosity of nanofluid samples was gradually increased

with increasing concentrations of MgO nanopowder. The intersection on the viscosity axis corresponded to the viscosity value of base fluid as 0.001 (Pa·sec). The increase in nanofluid viscosity is narrow over the range of nanoparticle concentration of ≤0.05 vol.%, while the increasing is fast over a range of more than 0.05 to 0.25 vol.% of the MgO nanoparticle concentration. Furthermore, the resistance to flow increased to 0.0052 (Pa·Sec) at a higher solid content of 0.25 vol.% MgO-DW nanofluid. The dynamic viscosity behavior of MgO-DW nanofluid is harmonious with the predictions in [87,88]. The viscosity of nanofluids is compared to that of base fluid producing relative viscosity, as seen in Figure 6b. It shows how much the nanofluid viscosity differs from the viscosity of the base fluid. From Figure 6, it can be observed that the relative viscosity increases with increasing volume concentrations of MgO-DW nanofluid.

The lowest value of relative viscosity, i.e., 1.2, was obtained by 0.05 vol.% MgO-DW nanofluid, with respect to a base fluid viscosity, while the higher value was obtained by nano solid content of 0.25 vol.%. When the MgO nanoparticle content increases within the base fluid, the Brownian motion is restricted as a result of intense collisions between nanoparticles. Subsequently, the relative viscosity of MgO-DW nanofluid increases with nanopowder volume concentration.

The effects of ultrasonication time on the viscosity of the MgO-DW nanofluid were investigated, as shown in Figure 7. The results show that the viscosity experiences a sharp decrease by increasing the ultrasonication treatment time.

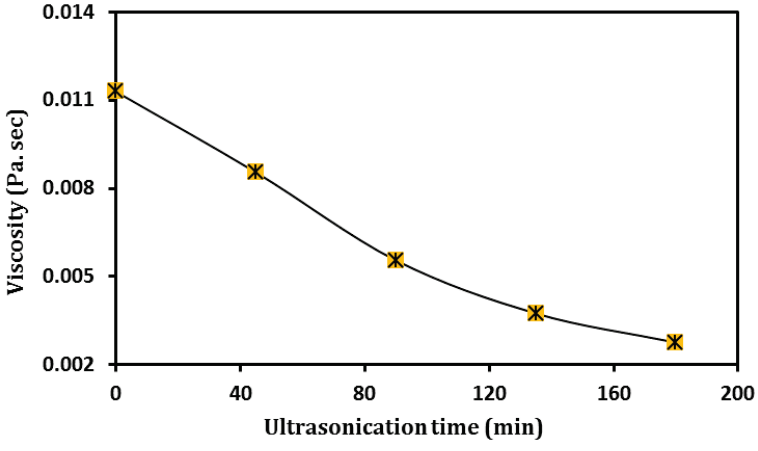

Figure 7. The viscosity as a function of ultrasonication time of 0.25 vol.% MgO-DW nanofluid at room temperature.

On the one hand, the minimal value of dynamic viscosity was measured at 180 min of ultrasonication treatment, indicating a decreasing tendency. On the other hand, the maximum value of viscosity was obtained by the nanofluid sample which was synthesized by stirring only without ultrasonication treatment of 0.0122 Pa·sec. This trend is identical to the results reported by A. Asadi et al. [89] and I. M. Mahbubul et al. [90]. Because the nanoparticles are uniformly dispersed in the base fluid, there are few or no clusters. As a result, the majority of nanoparticles, if not all, are involved in the flow, lowering the resistance to the viscometer's spindle. Additionally, the motion of the various layers of the nanofluid is made easier, hence, the dynamic viscosity decreases.

It is worth noting that increasing the ultrasonication time improves the dispersion stability and the thermal conductivity, while decreasing the dynamic viscosity of the prepared nanofluid. Ultrasonication time and dynamic viscosity are highly important in engineering applications where both of them have direct influences on the heat transfer performance, pumping power, and pressure drop.

4. Conclusions

A novel two-step technique was employed for preparing efficient MgO-DW nanofluid, at room temperature, without using surfactants and/or organic base fluids. Based on the experimental valuation, the following conclusions can be drawn:

- The co-precipitation method was followed to make crystalline and pure MgO nanopowder with an average particle size of 33 nm.
- SEM images revealed unique feathery or fluffy-like nanostructures of the prepared MgO nanopowder.
- MgO-DW nanofluid was synthesized with volume concentrations ranging from 0.05 to 0.25 vol.%, and ultrasonication treatment times ranging from 45 to 180 min, at room temperature.
- Zeta potential results showed that good stability was obtained with nano MgO content of 0.15 vol.% and a higher ultrasonication time of 180 min.
- The addition of MgO nanoparticles to traditional fluid as DW improved its thermal conductivity, where the highest value of thermal conductivity enhancement of 25.08% was found at 0.25 vol.% concentration and 180 min ultrasonication time.
- The effect of ultrasonication time on thermal conductivity improvement was similar to the impact of the nanoparticles volume concentration. However, this enhancement in the conductivity became limited after an ultrasonication time of 135 min.
- The dynamic viscosity measurements were revealed as directly proportional to the volume concentration of MgO-DW nanofluids, until recording the highest value of 0.0052 (Pa·Sec) at a higher solid content of 0.25 vol.% MgO-DW nanofluid. On the contrary, an increase in ultrasonication time resulted in a sharp decrease in the viscosity of the nanofluid samples.
- An MgO-DW nanofluid with good dispersion stability, high thermal conductivity, and low viscosity was created by controlling ultrasonication time and/or volume concentration.
- The produced MgO-DW nanofluid has the potential for exploitation in various implementations such as working fluid in cooling systems and heat exchangers. Therefore, it can be used as a working fluid in a hybrid solar collector, to study the effect of different flow rates on electrical and thermal efficiency.

Author Contributions: Methodology, H.K.J., A.G.T.A.-H. and F.N.A.Z.; investigation, H.K.J., A.G.T.A.-H., F.N.A.Z. and W.A.K.A.-M.; writing—original draft preparation, H.K.J., A.G.T.A.-H. and F.N.A.Z.; writing—review and editing, H.K.J., W.A.K.A.-M. and F.A.; supervision, B.E. All authors have read and agreed to the published version of the manuscript.

Funding: This research received no external funding.

Acknowledgments: We acknowledge support by the Deutsche Forschungsgemeinschaft (DFG) German Research Foundation and the Open Access Publishing Fund of the Technical University of Darmstadt. The authors would like to also thank the University of Technology-Iraq.

Conflicts of Interest: The authors declare no conflict of interest.

Nomenclature

MgO	Magnesium oxide
DW	Deionized water
SSA	Specific surface area
CuO	Copper oxide
Al_2O_3	Aluminum oxide
ZnO	Zinc oxide
TiO_2	Titanium oxide
Fe_2O_3	Iron oxide
EG	Ethylene glycol

$LiNO_3$	Lithium nitrate
$NaNO_3$	Sodium nitrate
KNO_3	Potassium nitrate
CTAB	Cetyl trimethylammonium bromide
ϕ	Volume concentration ratio
V_P	Volume of nanopowder
V_T	Total volume of nanofluid
ρ_P	Nanopowder density
ρ_{bf}	Base fluid density
m_p	Mass of nanopowder
m_{bf}	Mass of base fluid
TCE	Thermal conductivity enhancement
K_{nf}	Thermal conductivity of nanofluid
K_{bf}	Thermal conductivity of base fluid
JCPDS	Joint committee of powder diffraction standards
D	Crystallite size
V	Volume of unit cell
θ	Diffraction Angle of X-ray
d_{hkl}	Interplaner crystalline distance
hkl	Miller indices
a	Lattice constant
FWHM	Full width at half maximum of the X-ray diffraction peak.
ZP	Zeta potential
MWCT	Multi-walled carbon nanotubes
vol.%	Volume percentage
μ_{nf}	Viscosity of nanofluid
μ_{bf}	Viscosity of base fluid

References

1. Hashim, A.A. (Ed.) *Smart Nanoparticles Technology*; IntechOpen: Rijeka, Croatia, 2012.
2. Das, S.K.; Choi, S.U.; Yu, W.; Pradeep, T. *Nanofluids, Science and Technology*; John Wiley & Sons Inc.: Hoboken, NJ, USA, 2008.
3. Waqas, H.; Farooq, U.; Muhammad, T.; Manzoor, U. Importance of shape factor in Sisko nanofluid flow considering gold nanoparticles. *Alex. Eng. J.* **2022**, *61*, 3665–3672. [CrossRef]
4. Bharat, B.; Baral, D. *Nanofluids for Heat and Mass Transfer (Fundamentals, Sustainable Manufacturing and Applications)*, 1st ed.; Elsevier: Amsterdam, The Netherlands, 2021.
5. Esfe, M.H.; Arani, A.A.A.; Rezaie, M.; Yan, W.-M.; Karimipour, A. Experimental determination of thermal conductivity and dynamic viscosity of Ag–MgO/water hybrid nanofluid. *Int. Commun. Heat Mass Transf.* **2015**, *66*, 189–195. [CrossRef]
6. Gonçalves, I.; Souza, R.; Coutinho, G.; Miranda, J.; Moita, A.; Pereira, J.E.; Moreira, A.; Lima, R. Thermal Conductivity of Nanofluids: A Review on Prediction Models, Controversies and Challenges. *Appl. Sci.* **2021**, *11*, 2525. [CrossRef]
7. Ali, N.; Teixeira, J.A.; Addali, A. A Review on Nanofluids: Fabrication, Stability, and Thermophysical Properties. *J. Nanomater.* **2018**, *2018*, 6978130. [CrossRef]
8. Ali, N.; Bahman, A.M.; Aljuwayhel, N.F.; Ebrahim, S.A.; Mukherjee, S.; Alsayegh, A. Carbon-Based Nanofluids and Their Advances towards Heat Transfer Applications—A Review. *Nanomaterials* **2021**, *11*, 1628. [CrossRef] [PubMed]
9. Chamsa-ard, W.; Brundavanam, S.; Fung, C.C.; Fawcett, D.; Poinern, G. Nanofluid Types, Their Synthesis, Properties and Incorporation in Direct Solar Thermal Collectors: A Review. *Nanomaterials* **2017**, *7*, 131. [CrossRef]
10. Maxwell, J.C. *Electricity and Magnetism*; Clarendon Press: Oxford, UK, 1873.
11. Maxwell, J.C. *A Treatise on Electricity and Magnetism*; Clarendon Press: Oxford, UK, 2010; Volume 1.
12. Choi, S.U.S. *Enhancing Thermal Conductivity of Fluids with Nanoparticles*; ASME: New York, NY, USA, 1995; Volume 66, pp. 99–105.
13. Judran, H.K. Preparation and Investigation Study on (CuO/H_2O) Nanofluid for Improving the Performance of (PV/T) Hybrid System. Ph.D. Thesis, University of Technology, Baghdad, Iraq, 2016.
14. Keblinski, P.; Eastman, J.A.; Cahill, D.G. Nanofluids for thermal transport (review). *Annu. Rev. Mater. Res.* **2005**, *8*, 36–44.
15. Terekhov, V.I.; Kalinina, S.V.; Lemanov, V.V. The mechanism of heat transfer in nanofluids: State of the art (review). Part1. Synthesis and properties of nanofluids. *Thermophys. Aeromechanics* **2010**, *17*, 1–14. [CrossRef]
16. Tarafdar, A.; Negi, T.; Badgujar, P.C.; Shahi, N.C.; Kumar, S.; Sim, S.; Pandey, A. Nanofluid research advances: Preparation, characteristics and applications in food processing. *Food Res. Int.* **2021**, *150*, 110751. [CrossRef]
17. Babar, H.; Ali, H.M. Towards hybrid nanofluids: Preparation, thermophysical properties, applications and challenges. *J. Mol. Liq.* **2019**, *281*, 598–633. [CrossRef]
18. Esfe, M.H.; Saedodin, S.; Asadi, A.; Karimipour, A.; Ali, H.M. Thermal conductivity and viscosity of $Mg(OH)_2$-ethylene glycol nanofluids. Finding a critical temperature. *J. Therm. Anal. Calorim.* **2015**, *120*, 1145–1149. [CrossRef]

19. Safaei, M.R.; Hajizadeh, A.; Afrand, M.; Qi, C.; Yarmand, H.; Zulkifli, N.W.B. Evaluating the effect of temperature and concentration on the thermal conductivity of ZnO-TiO_2/EG hybrid nanofluid using artificial neural network and curve fitting on experimental data. *Phys. A Stat. Mech. Appl.* **2019**, *519*, 209–216. [CrossRef]
20. Asadi, A.; Pourfattah, F. Heat transfer performance of two oil-based nanofluids containing ZnO and MgO nanoparticles; a comparative experimental investigation. *Powder Technol.* **2019**, *343*, 296–308. [CrossRef]
21. Shahsavar, A.; Khanmohammadi, S.; Karimipour, A.; Goodarzi, M. A novel comprehensive experimental study concerned synthesizes and prepare liquid paraffin-Fe_3O_4 mixture to develop models for both thermal conductivity & viscosity: A new approach of GMDH type of neural network. *Int. J. Heat Mass Transf.* **2019**, *131*, 432–441.
22. Goodarzi, M.; Toghraie, D.; Reiszadeh, M.; Afrand, M. Experimental evaluation of dynamic viscosity of ZnO–MWCNTs/engine oil hybrid nanolubricant based on changes in temperature and concentration. *J. Therm. Anal. Calorim.* **2019**, *136*, 513–525. [CrossRef]
23. Bioucas, F.E.B.; Rausch, M.H.; Schmidt, J.; Bück, A.; Kolle, T.M.; Fröba, A.P. Effective Thermal Conductivity of Nanofluids: Measurement and Prediction. *Int. J. Thermophys.* **2020**, *41*, 55. [CrossRef]
24. Mahbubul, I.M. *Preparation, Characterization, Properties, and Application of Nanofluid*, 1st ed.; William Andrew: Norwich, NY, USA, 2018.
25. Pourpasha, H.; Farshad, P.; Heris, S.Z. Modeling and optimization the effective parameters of nanofluid heat transfer performance using artificial neural network and genetic algorithm method. *Energy Rep.* **2021**, *7*, 8447–8464. [CrossRef]
26. Puneeth, V.; Baby, A.K.; Manjunatha, S. The analogy of nanoparticle shapes on the theory of convective heat transfer of Au-Fe_3O_4 Casson hybrid nanofluid. *Heat Transf.* **2021**, *3*, 1–18.
27. Junankar, A.A.; Parate, S.R.; Dethe, P.K.; Dhote, N.R.; Gadkar, D.G.; Gadkar, D.D.; Gajbhiye, S.A. A Review: Enhancement of turning process performance by effective utilization of hybrid nanofluid and MQL. *Mater. Today Proc.* **2021**, *38*, 44–47. [CrossRef]
28. Jawad, M.; Saeed, A.; Gul, T.; Shah, Z.; Kumam, P. Unsteady thermal Maxwell power law nanofluid flow subject to forced thermal Marangoni Convection. *Sci. Rep.* **2021**, *11*, 7521.
29. Waqas, H.; Manzoor, U.; Shah, Z.; Arif, M.; Shutaywi, M. Magneto-Burgers Nanofluid Stratified Flow with Swimming Motile Microorganisms and Dual Variables Conductivity Configured by a Stretching Cylinder/Plate. *Math. Probl. Eng.* **2021**, *2021*, 8817435. [CrossRef]
30. Acharya, N.; Mabood, F.; Shahzad, S.A.; Badruddin, I.A. Hydrothermal variations of radiative nanofluid flow by the influence of nanoparticles diameter and nanolayer. *Int. Commun. Heat Mass Transf.* **2022**, *130*, 105781. [CrossRef]
31. Suganthi, K.S.; Rajan, K.S. Metal oxide nanofluids: Review of formulation, thermo-physical properties, mechanisms, and heat transfer performance. *Renew. Sustain. Energy Rev.* **2017**, *76*, 226–255. [CrossRef]
32. Porgar, S.; Rahmanian, N. *Investigation of Effect of Aluminium Oxide Nanoparticles on the Thermal Properties of Water-Based Fluids in a Double Tube Heat Exchanger*; University of Bradford: Bradford, UK, 2022; Volume 12, pp. 2618–2628.
33. Dahkaee, K.P.; Sadeghi, M.T.; Khroueian, Z.F.; Esmaeilzadeh, P. Effect of NiO/SiO_2 nanofluids on the ultra-interfacial tension reduction between heavy oil and aqueous solution and their use for wettability alteration of carbonate rocks. *J. Pet. Sci. Eng.* **2019**, *176*, 11–26. [CrossRef]
34. Yang, L.; Hu, Y. Toward TiO_2 Nanofluids Part1: Preparation and Properties. *Nanoscale Res. Lett.* **2017**, *12*, 417.
35. Maseer, M.M.; Alnaimi, F.B.I.; Hannun, R.M.; Al-Gburi, K.A.H.; Mezan, S.O. A review of the characters of nanofluids used in the cooling of a photovoltaic -thermal collector. *Mater. Today Proc.* **2021**, 1–9. [CrossRef]
36. Sone, B.T.; Diallo, A.; Fuku, X.G.; Gurib-Fakim, A.; Maaza, M. Biosynthesized CuO nano-platelets: Physical properties and enhanced thermal conductivity nanofluidics. *Arab. J. Chem.* **2018**, *13*, 160–170. [CrossRef]
37. Abbas, F.; Ali, H.M.; Shaban, M.; Janjua, M.M.; Doranehgard, M.H.; Ahmadlouydarab, M.; Farukh, F. Towards convective heat transfer optimization in aluminum tube automotive radiators: Potential assessment of novel Fe_2O_3-TiO_2/water hybrid nanofluid. *J. Taiwan Inst. Chem. Eng.* **2021**, *14*, 424–436. [CrossRef]
38. Lai, Y.F.; Chaudouët, P.; Charlot, F.; Matko, I.; Dubourdieu, C. Magnesium oxide nanowires synthesized by pulsed liquid-injection metal organic chemical vapor deposition. *Appl. Phys. Lett.* **2009**, *94*, 022904. [CrossRef]
39. Hornak, J. Synthesis, Properties, and Selected Technical Applications of Magnesium Oxide Nanoparticles: A Review. *Int. J. Mol. Sci.* **2021**, *22*, 12752. [CrossRef]
40. Rane; Kanny, A.V.; Abitha, K.; Thomas, V.K. Chapter 5-Methods for Synthesis of Nanoparticles and Fabrication of Nanocomposites. In *Synthesis of Inorganic Nanomaterials*; Micro and Nano Technologies; Wood Head Publishing: Cambridge, UK, 2018; pp. 121–139.
41. Mehta, M.; Mukhopadhyay, M.; Christian, R.; Mistry, N. Synthesis and characterization of MgO nanocrystals using strong and weak bases. *Powder Technol.* **2012**, *226*, 213–221. [CrossRef]
42. Thamilvanan, D.; Jeevanandam, J.; Hii, Y.S.; Chan, Y.S. Sol-gel coupled ultrasound synthesis of photo-activated magnesium oxide nanoparticles: Optimization and antibacterial studies. *Can. J. Chem. Eng.* **2021**, *99*, 502–518. [CrossRef]
43. Niu, F.; Meier, A.L.; Wessels, B.W. Epitaxial growth and strain relaxation of MgO thin films on Si grown by molecular beam epitaxy. *J. Vac. Sci. Technol. B* **2006**, *24*, 2586–2591. [CrossRef]
44. Pradita, T.; Shih, S.J.; Aji, B.B.; Sudiby. Synthesis of MgO powder from magnesium nitrate using spray pyrolysis. In *International Conference on Chemistry*; Chemical Process and Engineering (IC3PE), AIP Conf. Proc. 1823, (020016-1)-(020016-5); AIP Publishing: New York, NY, USA, 2017.

45. Alavi, M.A.; Morsali, A. Syntheses and characterization of $Mg(OH)_2$ and MgO nanostructures by ultrasonic method. *Ultrason. Sonochem.* **2010**, *17*, 441–446. [CrossRef] [PubMed]
46. Gajengi, A.L.; Sasaki, T.; Bhanage, B.M. Mechanistic aspects of formation of MgO nanoparticles under microwave irradiation and its catalytic application. *Adv. Powder Technol.* **2017**, *28*, 1185–1192. [CrossRef]
47. Sirota, V.; Selemenev, V.; Kovaleva, M.; Pavlenko, I.; Mamunin, K.; Dokalov, V.; Prozorova, M. Synthesis of Magnesium Oxide Nanopowder by Thermal Plasma Using Magnesium Nitrate Hexahydr. *Phys. Res. Int.* **2016**, *2016*, 6853405. [CrossRef]
48. Ouraipryvan, P.; Sreethawong, T.; Chavadej, S. Synthesis of crystalline MgO nanoparticle with mesoporous-assembled structure via a surfactant-modified sol-gel process. *Mater. Lett.* **2009**, *63*, 1862–1865. [CrossRef]
49. Stojanovic, B.D.; Dzunuzovic, A.S.; Ilic, N.I. 17-Review of methods for the preparation of magnetic metal oxides. In *Magnetic, Ferroelectric, and Multiferroic Metal Oxides (Metal Oxides)*; Elsevier: Amsterdam, The Netherlands, 2018; pp. 333–359.
50. Feng, S.-H.; Li, G.-H. Hydrothermal and Solvothermal Syntheses. In *Modern Inorganic Synthetic Chemistry*, 2nd ed.; Xu, R., Xu, Y., Eds.; Elsevier: Amsterdam, The Netherlands, 2017; pp. 73–104.
51. Yang, Q.; Sha, J.; Wang, L.; Wang, J.; Yang, D. MgO nanostructures synthesized by thermal evaporation. *Mater. Sci. Eng. C* **2006**, *26*, 1097–1101. [CrossRef]
52. Ngo, C.; Voorde, C.; van de Voorde, M.H. *Nanotechnology in a Nutshell: From Simple to Complex Systems*; Atlantis Press: Paris, France, 2014.
53. Saied, E.; Eid, A.M.; Hassan, S.E.D.; Salem, S.S.; Radwan, A.A.; Halawa, M.; Saleh, F.M.; Saied, E.M.; Fouda, A. The Catalytic Activity of Biosynthesized Magnesium Oxide Nanoparticles (MgO-NPs) for Inhibiting the Growth of Pathogenic Microbes, Tanning Effluent Treatment and Chromium Ion Removal. *Catalysts* **2021**, *11*, 821. [CrossRef]
54. Faisal, F.S.; AslamKhan, M.; Rizwan, M.; Hussain, Z.; Zaman, N.; Afsheen, Z.; Uddin, M.N.; Bibi, N. Exploring the therapeutic potential of Hibiscus rosa sinensis synthesized cobalt oxide (Co_3O_4-NPs) and magnesium oxide nanoparticles (MgO-NPs). *Saudi J. Biol. Sci.* **2021**, *28*, 5157–5167.
55. Pal, G.; Rai, P.; Pandey, A. Chapter 1-Green synthesis of nanoparticles: A greener approach for a cleaner future. In *Green Synthesis, Characterization and Applications of Nanoparticles (Micro and Nano Technologies)*; Elsevier: Amsterdam, The Netherlands, 2019; pp. 1–26.
56. Singh, J.P.; Singh, V.; Sharma, A.; Pandey, G.; Chae, K.H.; Lee, S. Approaches to synthesize MgO nanostructures for diverse applications. *Heliyon* **2020**, *6*, e04882. [CrossRef] [PubMed]
57. Manikandan, S.; Rajan, K.S. Rapid synthesis of MgO nanoparticles & their utilization for formulation of a propylene glycol based nanofluid with superior transport properties. *RSC Adv.* **2014**, *4*, 1830–51837.
58. Esfe, M.H.; Afrand, M.; Karimipour, A.; Yan, W.-M.; Sina, N. An experimental study on thermal conductivity of MgO nanoparticles suspended in a binary mixture of water and ethylene glycol. *Int. Commun. Heat Mass Transf.* **2015**, *67*, 173–175. [CrossRef]
59. Yapici, K.; Osturk, O.; Uludag, Y. Dependency of nanofluid rheology on particle size and concentration of various metal oxide nanoparticles. *Braz. J. Chem. Eng.* **2018**, *35*, 575–586. [CrossRef]
60. Lu, J.; Zhang, Z.; Wang, W.; Ding, J. Effects of MgO Nanoparticles on Thermo-Physical Properties of $LiNO_3$-$NaNO_3$-KNO_3 for Thermal Energy Storage. *Energies* **2021**, *14*, 677. [CrossRef]
61. Nfawa, S.R.; Talib, A.R.A.; Basri, A.A.; Masuri, S.U. Novel use of MgO nanoparticle additive for enhancing the thermal conductivity of CuO/water nanofluid. *Case Stud. Therm. Eng.* **2021**, *27*, 101279. [CrossRef]
62. Saufi, M.A.B.; Mamat, H.B. A Review on Thermophysical Properties for Heat Transfer Enhancement of Carbon-Based Nanolubricant. *Adv. Eng. Mater.* **2021**, *23*, 2100403. [CrossRef]
63. Vafaei, M.; Afrand, M.; Sina, N.; Teimouri, H. Evaluation of thermal conductivity of MgO-MWCNTs/EG hybrid nanofluids based on experimental data by selecting optimal artificial neural networks. *Phys. E Low-Dimens. Syst. Nanostruct.* **2017**, *85*, 90–96. [CrossRef]
64. Mousavi, S.M.; Esmaeilzadeh, F.; Wang, X.P. Effects of temperature and particles volume concentration on the thermophysical properties and the rheological behavior of $CuO/MgO/TiO_2$, aqueous ternary hybrid nanofluid: Experimental investigation. *J. Anal. Calorim.* **2019**, *137*, 879–901. [CrossRef]
65. Mousavi, S.M.; Esmaeilzadeh, F.; Wang, X.P. A detailed investigation on the thermo-physical and rheological behavior of MgO/TiO_2 aqueous dual hybrid nanofluid. *J. Mol. Liq.* **2019**, *282*, 323–339. [CrossRef]
66. Bhattad, A.; Sarkar, J.; Ghosh, P. Hydrothermal performance of different alumina hybrid nanofluid types in plate heat exchanger: Experimental study. *J. Therm. Anal. Calorim.* **2020**, *139*, 3777–3787. [CrossRef]
67. Hussein, M.A.; Sharma, K.V.; Bakar, R.A.; Kadirgama, K. The Effect of Nanofluid Volume Concentration on Heat Transfer and Friction Factor inside a Horizontal Tube. *J. Nanomater.* **2013**, *2013*, 1–12. [CrossRef]
68. Hunter, R.J. *Zeta Potential in Colloid Science, Principles and Applications*, 1st ed.; Academic Press: Cambridge, MA, USA, 1988.
69. Zainon, S.N.M.; Azmi, W.H. Recent Progress on Stability and Thermo-Physical Properties of Mono and Hybrid towards Green Nanofluids. *Micromachines* **2021**, *12*, 176. [CrossRef]
70. Washington, C. *Particle Size Analysis in Pharmaceutics and other Industries: Theory and Practice*; Ellis Horwood Limited: Chichester, UK, 1992.
71. Bianco, V.; Manca, O.; Nardini, S.; Vafai, K. *Heat Transfer Enhancement with Nanofluids. Routledge (Taylor & Francis Group)*, 1st ed.; CRC Press: Boca Raton, FL, USA, 2017.

72. Sabeeh, S.H.; Hussein, H.A.; Judran, H.K. Synthesis of a complex nanostructure of CuO via a coupled chemical route. *Mater. Res. Express* **2016**, *3*, 125025. [CrossRef]
73. Wahhab, H.A.A.; Al-Maliki, W.A.K. Application of a Solar Chimney Power Plant to Electrical Generation in Covered Agricultural Fields. In *IOP Conference Series: Materials Science and Engineering*; IOP Publishing: Kerbala, Iraq, 2020; p. 012137.
74. Ammulu, M.A.; Viswanath, K.V.; Giduturi, A.K.; Vemuri, P.K.; Mangamuri, U.; Poda, S. Phytoassisted synthesis of magnesium oxide nanoparticles from *Pterocarpus marsupium* rox.b heartwood extract and its biomedical applications. *J. Genet. Eng. Biotechnol.* **2021**, *19*, 21. [CrossRef] [PubMed]
75. Cullity, B.D. *Elements of X-ray Diffraction*, 3rd ed.; Wesley Publishing Company: Boston, MA, USA, 1967.
76. Sabeeh, S.H.; Hussein, H.A.; Judran, H.K. Effect of Cu Salt Molarity on the Nanostructure of CuO Prolate Spheroid. *Int. J. Nanosci.* **2016**, *15*, 1650034. [CrossRef]
77. Wong, C.W.; Chan, Y.S.; Jeevanandam, J.; Pal, K.; Bechelany, M.; Elkodous, M.A.; El-Sayyad, G.S. Response Surface Methodology Optimization of Mono-dispersed MgO Nanoparticles Fabricated by Ultrasonic-Assisted Sol–Gel Method for Outstanding Antimicrobial and Antibiofilm Activities. *J. Clust. Sci.* **2019**, *31*, 367–389. [CrossRef]
78. Chang, M.-H.; Liu, H.-S.; Tai, C.Y. Preparation of copper oxide nanoparticles and its application in nanofluid. *Powder Technol. J.* **2011**, *207*, 378–386. [CrossRef]
79. Al-Maliki, W.; Mahmoud, N.; Al-Khafaji, H.; Alobaid, F.; Epple, B. Design and Implementation of the Solar Field and Thermal Storage System Controllers for a Parabolic Trough Solar Power Plant. *Appl. Sci.* **2021**, *11*, 6155. [CrossRef]
80. Wang, S.; Li, Y.; Zhang, H.; Lin, Y.X.; Li, Z.; Wang, W.; Wu, Q.; Qian, Y.; Hong, H.; Zhi, C. Enhancement of thermal conductivity in water-based nanofluids employing TiO_2/reduced graphene oxide composites. *J. Mater. Sci.* **2016**, *51*, 10104–10115. [CrossRef]
81. Moradikazerouni, A.; Hajizadeh, A.; Safaei, M.R.; Afrand, M.; Yarmand, H.; Zulkifli, N.W.B.M. Assessment of thermal conductivity enhancement of nano-antifreeze containing single-walled carbon nanotubes: Optimal artificial neural network and curve-fitting. *Phys. A Stat. Mech. Appl.* **2019**, *521*, 138–145. [CrossRef]
82. Asadi, A.; Alarifi, I.M.; Ali, V.; Nguyen, H.M. An experimental investigation on the effects of ultrasonication time on stability and thermal conductivity of MWCNT-water nanofluid: Finding the optimum ultrasonication time. *Ultrason. Sonochem.* **2019**, *58*, 104639. [CrossRef] [PubMed]
83. Shahsavar, A.; Salimpour, M.R.; Saghafian, M.; Shafii, M.B. An experimental study on the effect of ultrasonication on thermal conductivity of ferrofluid loaded with carbon nanotubes. *Thermochim. Acta* **2015**, *617*, 102–110. [CrossRef]
84. Mahbubul, I.M.; Elcioglu, E.B.; Saidur, R.; Amalina, M.A. Optimization of ultrasonication period for better dispersion and stability of TiO_2-water nanofluid. *Ultrason. Sonochem.* **2017**, *37*, 360–367. [CrossRef]
85. Sadri, R.; Ahmadi, G.; Togun, H.; Dahari, M.; Kazi, S.N.; Sadeghinezhad, E.; Zubir, N. An experimental study on thermal conductivity and viscosity of nanofluids containing carbon nanotubes. *Nanoscale Res. Lett.* **2014**, *9*, 151. [CrossRef]
86. Michael, M.; Zagabathuni, A.; Sikdar, S.; Pabi, S.K.; Ghosh, S. Effect of dispersion behavior on the heat transfer characteristics of alumina nanofluid: An experimental investigation and development of a new correlation function. *Int. Nano Lett.* **2020**, *10*, 207–217. [CrossRef]
87. Peñas, J.R.V.; Zárate, J.M.; Khayet, M. Measurement of the thermal conductivity of nanofluids by the multi current hot-wire method. *J. Appl. Phys.* **2008**, *104*, 044314. [CrossRef]
88. Amin, A.-T.M.; Hamzah, W.A.W.; Oumer, A.N. Thermal conductivity and dynamic viscosity of mono and hybrid organic- and synthetic-based nanofluids: A critical review. *Nanotechnol. Rev.* **2021**, *10*, 1624–1661. [CrossRef]
89. Asadi, A.; Pourfattah, F.; Szilágyi, I.M.; Afrandf, M.; Żyła, G.; Ahn, H.S.; Wongwisesi, S.; Nguyen, H.M.; Arabkoohsa, A.; Mahian, O. Effect of sonication characteristics on stability, thermophysical properties, and heat transfer of nanofluids: A comprehensive review. *Ultrason. Sonochem.* **2019**, *58*, 104701. [CrossRef]
90. Mahbubul, I.M.; Chong, T.H.; Khaleduzzaman, S.S.; Shahrul, I.M.; Saidur, R.; Long, B.D.; Amalina, M.A. Effect of Ultrasonication Duration on Colloidal Structure and Viscosity of Alumina-Water Nanofluid. American Chemical Society. *Ind. Eng. Chem. Res.* **2014**, *53*, 6677–6684. [CrossRef]

applied sciences

MDPI

Review

Application of Nanofluids in CO_2 Absorption: A Review

Babak Aghel [1,2,*], Sara Janati [2], Falah Alobaid [1], Adel Almoslh [1] and Bernd Epple [1]

[1] Institut Energiesysteme und Energietechnik, Technische Universität Darmstadt, Otto-Berndt-Straße 2, 64287 Darmstadt, Germany; falah.alobaid@tu-darmstadt.de (F.A.); adel.almoslh@wihi.tu-darmstadt.de (A.A.); bernd.epple@tu-darmstadt.de (B.E.)

[2] Department of Chemical Engineering, Faculty of Energy, Kermanshah University of Technology, Kermanshah 6715685420, Iran; s.janati@kut.ac.ir

* Correspondence: babak.aghel@est.tu-darmstadt.de; Tel.: +49-(0)-6151-16-22673; Fax: +49-(0)-6151-16-22690

Abstract: The continuous release of CO_2 into the atmosphere as a major cause of increasing global warming has become a growing concern for the environment. Accordingly, CO_2 absorption through an approach with maximum absorption efficiency and minimum energy consumption is of paramount importance. Thanks to the emergence of nanotechnology and its unique advantages in various fields, a new approach was introduced using suspended particles in a base liquid (suspension) to increase CO_2 absorption. This review article addresses the performance of nanofluids, preparation methods, and their stability, which is one of the essential factors preventing sedimentation of nanofluids. This article aims to comprehensibly study the factors contributing to CO_2 absorption through nanofluids, which mainly addresses the role of the base liquids and the reason behind their selection.

Keywords: CO_2 capture; nanofluid; absorption; improvement; solvent

Citation: Aghel, B.; Janati, S.; Alobaid, F.; Almoslh, A.; Epple, B. Application of Nanofluids in CO_2 Absorption: A Review. *Appl. Sci.* **2022**, *12*, 3200. https://doi.org/10.3390/app12063200

Academic Editor: Luca Fiori

Received: 3 February 2022
Accepted: 8 March 2022
Published: 21 March 2022

1. Introduction

The European Union (EU) has long term strategies to reduce carbon-based energy systems till 2030 and 2050. This energy strategy is set to reduce Greenhouse Gas (GHG) emissions, increase the efficiency of energy systems, and gradually substitute fossil fuels with renewable energy sources (RES). One of the targets is to reduce carbon emissions by about 40% by 2030 [1]. CO_2 is the main greenhouse gas and constitutes about 77% of the emissions all around the world. The emission of an excessive amount of CO_2 intensifies global warming. Fossil fuel burning and the production of cement are the two main CO_2 emitting sources [2]. One way of decreasing the emission rate of CO_2 to the atmosphere is its separation and collection, utilization, or storage for further application. There are several separation methods to capture CO_2 from various gas streams. Adsorption, absorption, cryogenic, and membrane separation are the main technologies used in CO_2 capture [3,4]. Much progress has been made in CO_2 absorption by gas-liquid, some of them are proposed to reduce the energy demand. The gas-liquid absorption technique can also be applied to other renewable energies for the absorption of carbon dioxide. Typically, the novel absorption methods that use solvents benefit from physical and/or chemical phenomena to improve the absorption process. This technique has higher efficiency in low concentrations of CO_2, therefore it has a better performance in separating CO_2 from the flue gas mixtures of post-combustion processes that contain low concentrations of CO_2 [5]. The probable chemical absorption mechanism of CO_2 is that one NH_2 group attacks CO_2 with the free electron pairs of its N atom and as a result, a hydrogen bond is formed with another NH_2 group. The chemical absorption of CO_2 in flue gas by a solvent is a selective and reversible chemical reaction. One of the major challenges is to minimize the energy demand of this process [6].

Many different solvents have been used for CO_2 chemical absorption so far. The selection criteria of a suitable solvent are: fast kinetics of the reaction; high capacity of

absorbent; low regeneration energy demand; and low rate of solvent degradation [7]. Today, amine solvents are the most widely utilized chemical solvents for CO_2 capture. The reasons are their high capacity, high thermal stability, and the high reaction rate of amine solvents with carbon dioxide molecules [8]. The sterically hindered amines and simple alkanolamines are the two major types of amine absorbents. Monoethanolamine (MEA), diethanolamine (DEA), and methyldiethanolamine (MDEA) are primary, secondary, and tertiary amines that are classified as simple alkanolamines. All amine absorbents are different in some respects, such as stability, absorption capacity for CO_2, the kinetics of reaction with CO_2, and corrosion products. MEA is considered the standard amine solvent for carbon dioxide absorption; the reason being the high efficiency (90%) of CO_2 capture, fast kinetics, high mass transfer rate, and capability of CO_2 absorption even at atmospheric and low pressures of flue gases [9]. Nevertheless, since absorption of CO_2 with chemical solvents containing amines is a mature and economically feasible method, that can be used on large scale to treat flue gas streams with high volumes, it has been at the center of attention in recent years [10,11]. This method also has some drawbacks including high energy demand for solvent recovery, expensive materials, weak performance in selective absorption from acidic gases, corrosivity, the occurrence of side reactions, and resultant water-saturated gas, and being detrimental to the environment [12,13]. CO_2 absorption processes with the physical solvents Selexol and Rectisol need high-pressure conditions and are governed by Henry's law. Despite chemical absorption, there is no need for heat in physical absorption, and the solvent is recovered by pressure reduction in these processes [14–16]. However, physical solvents have some drawbacks; they are sensitive to the partial pressure of acid gas (acid gas partial pressure should be high), they hardly meet H_2S specifications, the concentration of inert gases must be low [14]. Some of the commonly used physical solvents are NMP (N-Methyl-2-Pyrrolidone), DEPG (Dimethyl Ether of Polyethylene Glycol), and PC (Propylene Carbonate) [17].

The cryogenic processes is another CO_2 absorption process that takes advantage of the intrinsic properties of components of a gas mixture; CO_2 capture is done using the distinct desublimation and condensation properties of CO_2 and its carrier gas. The high purity of CO_2 (99.99%) is achieved in a highly efficient (99.99%) process, compared to other CO_2 capture techniques [18]. In this process, a CO_2 phase change occurs in flue gases, after several stages of compression and cooling. Other constituents of the mixture will invariably experience phase change, too. CO_2 might be separated as a liquid or a solid along with other components and can be further purified by distillation. However, the absorbent pores are at risk of blockage by the water from other components, and in this case, the cost of CO_2 capture will increase [19]. One of the commercial gas separation and purification processes is membrane separation. This highly efficient, environmentally friendly technique is utilized in some gas purifying systems like natural gas sweetening and air separation and can compete with the other absorption systems for CO_2 removal from flue gas [20]. The concept of membrane separation is very simple. Nevertheless, in the case of post-combustion capture, some membrane properties like permeability and selectivity, limit its utilization. As an example, 95% purification of CO_2 with a 90% CO_2 capture rate is not feasible with a single-stage membrane. When talking about using membrane separation in gas-transport pipeline systems for CO_2 capture, we face two conflicting effects, high energy consumption in low membrane areas and high investment cost for large membrane areas [21].

Adsorption is a promising alternative to chemical adsorption processes; the process in which one or more components are removed by attachment to a solid surface is called adsorption. The basis of adsorption is the intermolecular interactions between solid materials surface (like activated carbon or molecular sieve) and the adsorbed gas (like CO_2). Single or multilayer adsorption depends on the variables of the partial pressure of the absorbed gas, temperature, adsorbent pore sizes, and surface forces [22]. Activated carbon, metal–organic frameworks, zeolites, and microporous organic polymers are solid absorbents that have some superiorities in CO_2 adsorption capture. The lower energy consumption of CO_2 capture by adsorption is attracting increasing attention. Gas streams

with different CO_2 content can be treated with temperature vacuum swing (TVS), vacuum swing adsorption (VSA), temperature swing adsorption (TSA), electrical swing adsorption (ESA), and pressure swing adsorption (PSA) [23].

In addition, there are other processes for CO_2 absorption, such as Ionic Liquids (Ils), electrochemical conversion, photochemical, thermochemical, and biochemical, using organic/metallic (organometallic) catalysts on chemical and hybrid rings. Even though all of these methods are promising in CO_2 absorption, they are still being evaluated with respect to the obstacles pertinent to cost, energy, and also their application at large scales [24,25].

Over the recent years, CO_2 absorption through nanofluid has captured interest due to its unique advantages in adjusting physical and chemical properties and its special applications and high specific area. Due to their porosity, nanomaterials, such as nano-sized zeolites, metal, and metal oxide nanoparticles, metal-organic frameworks (MOFs), covalent organic frameworks (COPs) promisingly increase the efficiency of CO_2 absorption [26].

This article is a comprehensive review of the summary of the last advances in nanofluids in increasing CO_2 absorption. In addition to describing nanofluids, properties, and applications, this study also elaborately introduces the factors contributing to increasing CO_2 absorption. In the following, the nanofluid preparation methods consisting of one-step and two-step methods will be explained. Afterward, nanofluid stability, mechanisms of increasing mass transfer in nanofluids (shuttle effect, bubble breakage effect, and micro convection), and the factors affecting CO_2 absorption through the nanofluid will be discussed and summarized. Ultimately, based on the base liquid, nanofluids will be categorized into three categories (water, amine, and methanol), and a conclusion and viewpoint in reaching favorable CO_2 absorption in nanotechnology will be provided. By describing the application of nanofluid in the CO_2 absorption field, this article evaluates and helps understand this novel technology and compares it with conventional methods.

2. Nanofluid

Nanofluids are prepared by dispersing nanosized materials (nanotubes, nanoparticles, nanorods, nanofibers, nanodroplets, and nanosheets) in a base fluid [27]. Nano-sized materials are determined according to their strict definition that specifies materials with at least one dimension (length, diameter, or thickness) in the range of 1–100 nm. This definition is widely accepted by nanotechnology researchers. The origin of this definition comes back to the fact that when the particle size is decreased, the ratio of surface area to volume increases rapidly, therefore 100 nm was set as a criterion for nanomaterials. Nanofluids are typically prepared by dispersion of ceramics (PNP, aluminum nitride, cellulose, etc.), carbonaceous materials (fullerene, graphene, carbon nanotubes, etc.), metals (gold, copper, aluminum, etc.), and inorganic oxides (silicon dioxide, zinc oxide, iron oxide, etc.) in a base fluid [28]. A refrigerant, mineral oils, liquids with high viscosity like ethylene glycol, and low viscosity liquids like water, or a blend of various liquids (propylene/water, water/EG, etc.) may be used as base fluid.

The researchers found that the addition of nanoparticles to the base fluid led to changes in the thermophysical properties of the nanofluid. In other words, Nanofluids caused changes in the base fluid due to their unique thermophysical properties such as density, thermal conductivity, viscosity, and other thermodynamic properties. Table 1 summarizes some of the thermophysical properties of common nanoparticles.

Table 1. Properties of nanoparticles.

Nanoparticle	Average Particle Size [nm]	Morphology	Surface Area [m^2/g]	Density [kg/m^3]	Thermal Conductivity (W/m·K)	
Al_2O_3	<40	Spherical	-	4700	36–40	[24]
MWCNT	10–20	Tubular	200	2100	-	[29]
ZnO	10–30	Nearly spherical	20–60	5606	29	[30]
TiO_2	<50	Spherical	50 ± 15	5500–6000	-	[29,30]
SiO_2	10–15	Spherical	180–270	2200	-	[31]

Table 1. *Cont.*

Nanoparticle	Average Particle Size [nm]	Morphology	Surface Area [m^2/g]	Density [kg/m^3]	Thermal Conductivity (W/m·K)	
Fe_3O_4	4	Spherical	40–60	5200	17.65	[32]
CNT	10–20	-	332	1800	-	[33]
NiO_2	50	-	-	6670	-	[34]
MgO	-	Cubic	-	2900	48.4	[35]

Choi was the first one who proposed this definition for nanofluids in 1995 that two-phase, uniform and stable suspensions resulted from the dispersion of nanoparticles in an inorganic or organic liquid phase with a pre-specified proportion [36]. Nanofluids are theoretically classified as colloidal dispersion systems with properties that are related to the characteristics of the nanoparticles like shape, properties, scale, content, or their chemical or physical properties of nanoparticles [37]. Tests that have been carried out on nanofluids also indicated many beneficial points; when compared to particles with millimeter or micrometer sizes, nanofluids are more stable and have higher thermal conductivity, pressure drop and erosion are lower, especially in microchannels, when using nanofluids. Many industries benefit from nanofluids like the chemical industry, electronics and machinery, aerospace, biomedicine, energy, and power. Nevertheless, the application of nanofluids as mass and heat transfer media has attracted special attention due to their high mass and heat transfer coefficients [38,39]. These advantages of using nanofluids have made researchers eager to discover other fields of application of nanofluids.

Since mass transfer and heat transfer have similar basic principles, nanoparticles can also influence mass transfer by a fluid. Researchers concluded that using small quantities of soluble particles will considerably increase the gas absorption rate. The enhancement in mass transfer rate was later proved by Ruthiya et al., who assessed four probable mechanisms to improve mass transfer in gas–liquid systems [40]. Krishnamurthy et al., were one of the first groups that studied mass transfer improvement in nanofluids. They compared the diffusivity of fluorescein dye droplets in deionized water and a mixture of nanofluids in water [41]. Now, the focus of the studies is on using nanoparticles to increase the rate of absorption, mass transfer, and carbon loading in nanofluids [42]; this way, the resistance against mass transfer between liquid and gas phases will be decreased. The application of nanofluid as CO_2 absorbent could reduce the cost of energy in CO_2 capture systems by the enhancement of absorption rate. As an example, one way of reducing the energy consumption and cost of a CO_2 capture plant is to utilize nanographene oxide (NGO) nanofluids in CO_2 capture and sequestration (CCS) recovery that benefits from the gas hydrate formation process [43]. The dispersion of nanoparticles in an absorption solvent can improve the absorption performance due to the high surface area of these particles that creates Brownian motion, micro convection, and shuffle effects. The small size of nanoparticles also increase the rate and capacity of CO_2 absorption compared to the same particles with larger sizes [44]. However, if the concentration of nanoparticles exceeds the optimal point, nanoparticles will be agglomerated and prevent gas absorption into the liquid phase. Several gas absorption investigations were carried on using nanofluids while an external magnetic field was also applied to the gas absorption in a column [45]. In this respect, the convective mass transfer under the influence of nanoparticle dispersion in the fluid was also investigated in several liquid–gas absorption systems such as a tray and packed absorption column, wetted-wall column (WWC), gas–liquid hollow fiber membrane contactor, liquid–liquid extraction (LLE), gas-sparged stirred absorption vessel, bubble-type column absorber, and three-phase airlift reactor [46].

2.1. The Method of Nanofluid Preparation

Nanofluid preparation is the principal stage in experiments. However, the superb performance of a nanofluid highly depends on its method of preparation [47]. Nanofluids are not a simple dispersion of solids in liquids. Nanofluids should necessarily be stable, durable, and even suspensions with minor agglomerations that do not experience any

chemical change of the fluid, etc. The agglomeration of nanoparticles is one of the main challenges of nanofluid preparation. Therefore, the formulation of a highly efficient CO_2 absorber nanofluid is a fundamental stage in the preparation of CO_2 absorption nanofluids. According to Figure 1, nanofluids are prepared using the (a) one-step method (Vapor deposition), and (b) two-step method (mixing) [48].

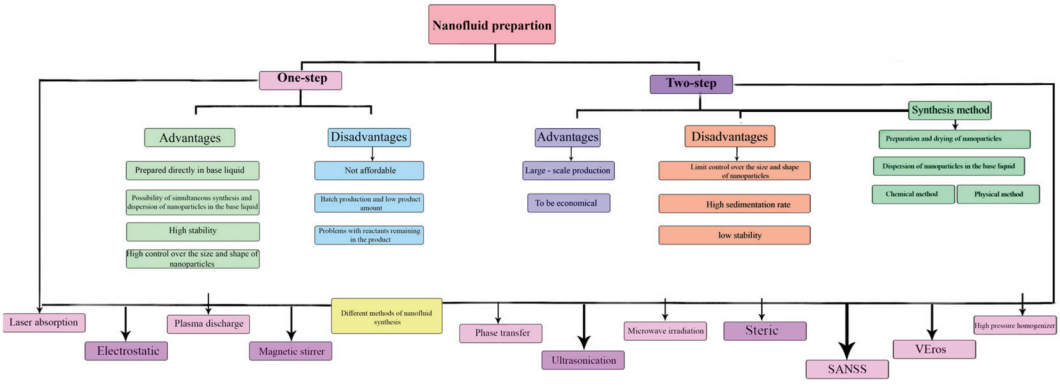

Figure 1. Different methods of preparing nanofluids.

2.1.1. One-Step Synthesis Method

In the one-step method, nanofluid is directly prepared in the base fluid and there is no need for intermediate phases like storage or drying of nanoparticles and their dispersion in the base fluid [49]. This means, the synthesis and dispersion of nanoparticles take place at the same time and inside the base fluid, this hinders oxidation of nanoparticles. Some technologies like plasma, microwaves, or lasers can help this process. Nanoparticles like Au, Ag and Cu have been successfully synthesized via a single-step method [50]. This process was also used by some researchers for the preparation of nanofluids. To prevent the agglomeration of nanoparticles, dispersion, drying, transportation, and storage are eluded in this method, this will increase the stability of nanofluid and lower the production costs. Generally, since single-step nanofluid preparation is a rather costly method, it is not practical in large-scale production. Thus, special focus has been placed on the single-step chemical process, which is a relatively cost-effective method of nanofluid preparation [49].

2.1.2. Two-Step Method

In this method, different nanopowder materials like nanoparticles, etc., are utilized by physical, chemical, and mechanical methods [51]. The direct method of application includes first the dispersion of nanoparticles in the base fluid and then using a stabilization method. Although the resultant nanofluids have small size nanoparticles with high surface activity, they easily agglomerate. Ultrasonic waves are utilized to increase the stability of the obtained nanofluid and yield a dispersible suspension of nanoparticles. Some of the advantages of the two-step method are the low cost, simple process, large-scale nanofluid preparation, and industrial realization [52]. However, the stability of the nanofluids prepared in this way is weak, and using surfactants is not applicable at high temperatures. Therefore, some dispersing methods such as using ultrasound vibration, the addition of surfactant, pH variation of the base fluid, and ultrasonication are combined in some cases, to reach a suspension with better dispersion performance [53]. Nevertheless, it is recommended that nanofluids containing oxide nanoparticles may better be prepared by a two-step process, while this method is not suitable for metallic nanoparticles [54].

2.2. Nanofluid Stability

Stability is a main problem of nanofluids. Van der Waals forces are the reason for the instability of nanofluids and are intensified by the increased number of nanoparticle collisions

with each other due to Brownian movements, and the large surface area of nanoparticles themselves [55]. Nanofluids are susceptible to destabilization and leave deposits under the influence of gravitational force, electrostatic repulsive force, Van der Waals attraction, and buoyancy forces. The function of gravitational force and Van der Waals force is toward the destabilization of any colloidal suspension [56]. This means that these forces help the dispersed particles in adhering to each other and aggregates with bigger sizes will form as a result. These large particles will precipitate from the suspension under the influence of gravitational force and form deposits at the bottom of the container [57]. The settlement of the particles is due to their heavier weight that prevents Brownian motions maintaining the particles in a stable suspension. Based on theory, the main features that remarkably increase the conductivity of nanofluids and their stability are aggregation and clustering. However, this theory merely applies to specific groups of nanoparticles like single-wall nanotubes that have a high aspect ratio [58]. Therefore, destabilization of the nanofluid occurs as a result of the susceptibility of nanoparticles to form aggregates and clusters in the suspension. Accordingly, the two major stability aspects of nanofluids are nanoparticle aggregation and sedimentation.

In the past few years, some of the many attempts for the preparation of stable nanofluids were partially successful. Different methods have been utilized for the stabilization of suspended nanoparticles (colloids) in nanofluids [59]. Thus, it is necessary to investigate the stability of nanofluids for suitable utilization in proper applications. The determination of effective factors on the stability of nanofluids is also of great importance [60]. Generally, several techniques are used for the evaluation of nanofluid stability; some of them are spectral absorbance and measurement of transmittance, settlement and centrifugation, 3ω method, measurement of zeta potential, TEM (transmission electron microscopy), and DLS (dynamic light scattering [38]. In general, two methods can improve the stability of nanofluids, which can be divided into two major categories: Physical methods and chemical methods as shown in Figure 2.

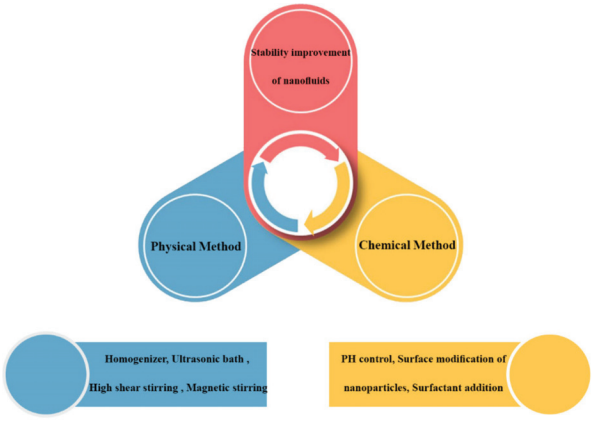

Figure 2. Methods for improving the stability of nanofluids.

2.2.1. Sedimentation and Centrifugation

The most commonly utilized method for stability assessment is sedimentation. The basis of this method is the settlement of nanoparticles out of the nanofluid under the influence of gravity [61]. The volume or weight of sediment is a good indication of nanofluid stability. If the concentration of supernatant particles remains unchanged over time then the nanofluid is considered stable [62]. The method deals with the observation of nanoparticle settlement from a nanofluid in a container over time. Generally, most papers have considered the stability time frame as the time during which obvious sedimentation does not occur, or at least negligibly occurs, in the nanofluid. Some researchers accepted the

sedimentation method as a criterion for the assessment of the stability of a nanofluid [63]. But the sedimentation technique is not a time-efficient method [64]. To overcome this problem, researchers use the centrifugation method which is a more time-efficient method for the assessment of nanofluid stability. In this method, sedimentation is accelerated under the influence of centrifugal force which is much stronger than the gravitational force [65].

2.2.2. Zeta Potential

Another method of stability determination of a nanofluid is using the zeta-potential test in which mutual repulsion happens between nanoparticles with the same charge. Thus, there is little agglomeration tendency between the particles with high surface charge, in their collisions [66]. This method can help describe the differences in some experimental data, where the structure of the suspension and the nanoparticles' surface charges are altered by using surfactants [67]. The zeta potential technique is a basic test for determining nanofluid stability, which considers the electrophoretic behavior of the fluid [68]. According to the theory of electrophoresis, the zeta potential measures the repulsion force between two particles [69]. Based on the stabilization theory, a high value of zeta potential is an indication of a high solubility of particles in the suspension, which is due to increased electrostatic repulsion between particles [70]. It is suggested that suspensions with 5 mV zeta potential or less are not stable and experience agglomeration, those with 20 mV have limited stability, but the suspensions with >30 mV have physical stability and if their zeta potential is greater than 60 mV they will have excellent stability [71].

2.3. The Mechanisms of Enhancement in Nanofluids

Many research works have focused on the role of fine particles in the enhancement of mass transfer in gas–liquid systems. These findings indicated that partial pressure enhancement will give rise to the gas absorption capacity, meanwhile, temperature enhancement decreases the gas solubility in the liquid phase, which is in accordance with the ideal gas law [72]. The theory that suggests enhancement in mass transfer by using nanoparticles has not been established. Several mechanisms are accepted: micro convection; mixed boundary layer; bubble coalescence prevention; and the shuttle mechanism. The bubble breaking effect, shuttle mechanism, and micro convection are discussed in this paper as shown in Figure 3 [73].

2.3.1. Shuttle (Grazing) Effect

The shuttle effect was proposed by Kars et al., who discussed the rate enhancement of gas absorption in liquid in a gas–liquid-solid three-phase system when solid particles are present, using a theoretical model [74]. The grazing effect states that the gas absorption from liquid can be enhanced by using particles that can penetrate the gas–liquid mass transfer membranes to absorb a specific amount of gas [75].

Also, the shuttle effect considers that particles could enter the gas–liquid mass transfer membrane and absorb a certain amount of gas. And due to the concentration difference, particles carrying absorbed gas return to the bulk liquid and then desorb [76]. Owing to the strong adsorption of the diffusing gas phase component in the dispersed phase particles, the concentration of this gas-phase reactant in the liquid phase near the interface will be decreased, resulting in an increment in the absorption rate [77].

2.3.2. Bubble Breaking Effect

Krishnamurthy et al., have concluded that the velocity disturbance field is the reason for the enhancement of mass transfer, which is formed due to the movements of nanoparticles [41]. In the bubble absorption process, the collision of nanoparticles and nanoparticles with bubbles occurs. When the bubbles move toward the interface and form a dynamic movement, the nanoparticles strike the interface of gas–liquid and this results in breaking the bubbles [78]. This phenomenon increases the diffusion area. Considering that this enhancement in the specific interfacial area occurred due to the particles, it can be concluded that they can increase the overall mass transfer coefficient [79].

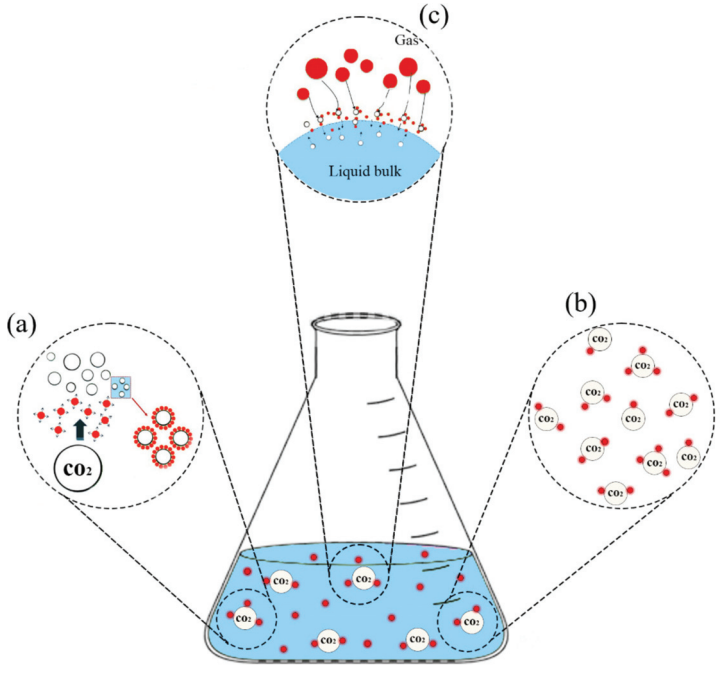

Figure 3. The schematic of (**a**) Bubble breaking, (**b**) Brownian motion, and (**c**) Grazing effect mechanisms in the improvement of CO_2 absorption.

2.3.3. Micro-Convection

The convective mass transfer process is strongly influenced by the Brownian motions and the resultant micro-advection near the particles that scatter a considerable fraction of the measured species molecules [80]. The solute diffusion can also be enhanced by micro-convection that is promoted by Brownian movements, this enhancement will also improve the diffusion coefficient. There is also a synergistic effect between the mass and heat transfer. When heat transfer is enhanced, changes in the gas–liquid phase temperature result in an enhancement in the potential for absorption [81]. The governing mechanism is that the micro-convection is enhanced by the fluid disturbance, the liquid disturbance is caused by random particle movement called Brownian motion [82]. The determination of the optimal nanoparticle concentration in a liquid depends on the Brownian motion that creates micro-convection. The mentioned three mechanisms play key roles in the enhancement of CO_2 mass transfer [83].

3. Effective Factors in the CO_2 Absorption by Nanofluid

Nanofluids' properties have opened a new research field in new technologies. Researchers started investigations on various nanofluids to be used as absorbents in CO_2 absorption processes. In this respect, different metal oxide, metallic, and nonmetallic nanoparticles were examined for CO_2 absorption enhancement; some of them are TiO_2, MgO, SiO_2, Cu, CuO, Al_2O_3, and carbon nanotubes [84]. The dominant parameters were determined according to the results of CO_2 absorption using nanoparticles. These factors are nanoparticle type, morphology, size, and concentration in the base fluid, flow rate of gas, concentration of CO_2 in the feed stream, and base fluid type, flow rate, pressure, temperature, and hydrodynamics as presented in Figure 4 [53].

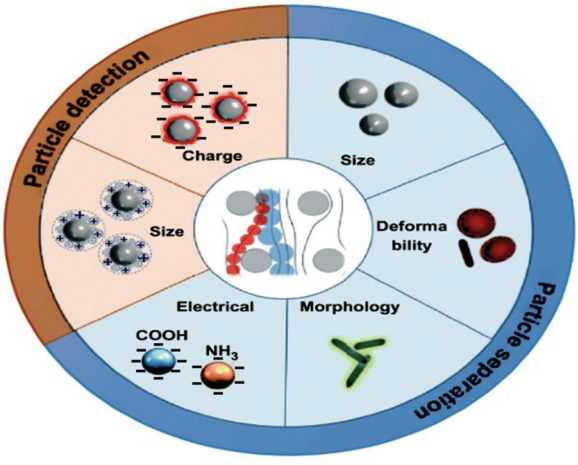

Figure 4. The main parameters of nanoparticles in CO_2 absorption.

3.1. Effect of Nanoparticle Type

Ganapathy et al., observed gas–liquid absorption enhancement when using nanoparticles in the form of nanofluids in bubbling absorption systems for CO_2 capture, which was different for each nanoparticle type. When equilibrium is reached in a gas–liquid absorption system, the gas concentration slightly increases in the liquid phase [85]. In a research study, Fang et al., used a bubbling ammonia system for the investigation of nanoparticles' effects on CO_2 absorption. The relationship between the type of nanoparticle and the efficiency of CO_2 capture was determined. The sequence of CO_2 capture efficiency was TiO_2 > CuO > SiO_2 [86]. The CO_2 removal efficiency of a stirred reactor containing CNT and Al_2O_3 nanoparticles was studied by Sumin et al. The results of their experiments indicated a considerably enhanced CO_2 capture when using carbon nanotubes in the absorption solvent [33]. In a study, Pineda et al. investigated the effect of TiO_2, SiO_2, and Al_2O_3 nanoparticle addition to the absorption solvent in a new annular contactor (AC) that utilized a tray absorber. This study suggested up to 5%, 6% and 10% enhancement in the absorption rate when using TiO_2, SiO_2, and Al_2O_3 nanoparticles, respectively [87]. Zhang et al., used a stirred reactor to examine the influence of TiO_2 nanoparticle addition into propylene carbonate, on the capture rate of the system; the effects of particle size and the optimum concentration of nanoparticles were also analyzed in their experiments [73]. Golkhar et al., used a gas–liquid hollow fiber membrane contactor to remove CO_2 with a nanofluid containing silica nanoparticles and carbon nanotubes. Their findings showed that CNT nanofluid has better performance in CO_2 removal with up to 40% efficiency [31].

3.2. Effect of Nanoparticle Concentration

In one investigation, an isothermal quasi-static high pressure stirred reactor was utilized to study the effect of temperature and concentration of ZnO and SiO_2 nanoparticles in water-based nanofluid on CO_2 absorption. Results indicated temperature enhancement slightly reduces the CO_2 absorption, whereas the addition of 0.1 wt.% ZnO and SiO_2 increases the CO_2 absorption by 14% and 7%, respectively [88]. The influence of MWCNTs addition to the CO_2 absorbent fluid was investigated by Nabipour et al., and the outcomes indicated that 0.02 wt.% concentration of MWCNTs with carboxyl functional groups in Sulfinol-M absorber results in a 23.2% enhancement in CO_2 equilibrium solubility compared to the base fluid [89]. CO_2 absorption in a bubble absorber system was studied by Kim et al., to evaluate the performance of a nanofluid containing SiO_2 nanoparticles on CO_2 absorption. The 0.21 wt.% nanofluid showed a 24% enhancement in CO_2 absorption performance compared to pure water as its base fluid [90]. Peng et al., investigated the

effect of Ag nanoparticle addition into water/NH_3 mixture on the mass transfer performance of an absorption column, they found that the rate of CO_2 absorption was increased by 55% when 0.02 wt.% Ag nanoparticles were added to the solution [91]. Lee and Kang used a bubble column system to investigate the influence of Al_2O_3 nanoparticles addition to a NaCl solution on the CO_2 absorption performance of the system and observed that only 0.01 vol% of Al_2O_3 nanoparticles can improve the CO_2 solubility. All these investigations indicate that the addition of small amounts of nanoparticles to an absorption fluid can enhance its absorption capacity [92]. The CO_2 absorption capacity of a nanofluid containing Fe_2O_3 nanoparticles was recently investigated by Darvanjooghi et al. [93] and it was shown that the maximum mean CO_2 flux of 2.8×10^{-5} mol/(m^2.s) was achieved at a Fe_2O_3 concentration of 1 wt.%, which decreased after a while. The effect of HKUST-1 with polyethyleneimine functional groups was studied on the CO_2 absorption capacity of an aqueous solution of 40 wt.%. This study which was carried out by Irani et al., showed a 16% enhancement in CO_2 absorption capacity when only 0.2 wt.% nanoparticles were used [94]. Periasamy Manikandan et al., studied the influence of Al_2O_3 nanoparticles on mass transfer of a water-based nanofluid and reported the maximum CO_2 absorption enhancement at 0.6 vol% concentration of Al_2O_3 nanoparticle [95]. Huang et al. [96] and Park et al. [97,98] added SiO_2 nanoparticles to a solution mixture of MEA, DEA, and Diisopropanolamine to evaluate its performance in CO_2 absorption in a stirred cell. They witnessed a reduction in the CO_2 absorption rate by increasing the nanoparticle concentration, which is believed to be related to the elasticity of the solution [99]. According to these investigations, the addition of small amounts of nanoparticles to a fluid significantly enhances the CO_2 absorption of the nanofluid.

3.3. Effect of Nanoparticle Size

Many different types of nanoparticles were used in investigations of CO_2 mass transfer efficiency enhancement by the addition of nanoparticles to aqueous solutions as Al_2O_3, SiO_2, and TiO_2 nanoparticles [100,101]. Nagy et al., achieved more than 200% mass transfer enhancement by the addition of 10 vol% of n-hexadecane nanoparticles with 65 nm size into a fluid. According to the results, the rate of mass transfer increases rapidly at low concentrations of nanoparticles, whereas its enhancement is slow at higher concentrations of particles (more than 6 vol%) [102]. Lee and Kang, concluded that the addition of smaller Al_2O_3 nanoparticles to a NaCl solution shows higher enhancement in the CO_2 absorption capacity of the fluid [92]. Zhu et al., used an agitated microreactor to show the superiority of a nanofluid containing mesoporous silica materials (MCM41) with a mean particle size of 250 nm compared to micro-sized silica particles (1.4 and 7 mm), in CO absorption by water [103]. A study of the literature shows that Kim et al., were the only research group that studied the influence of nanoparticles on the mass transfer performance of nanofluids. They dispersed silica nanoparticles with average particle sizes of 30, 70, and 120 nm in water to reach a nanofluid with 0.021 wt.% nanoparticle concentration. Results showed up to 76% enhancement in CO_2 absorption of a nanofluid containing 0.021 wt.% nanoparticles, 24% of this enhancement occurred in the first minute of a total 8 min duration of the absorption process. These increases were 11% and 12%, respectively, for nanofluids containing K_2CO_3 nanoparticles. The conclusion of their investigation was the contribution of small bubbles that exist in nanofluids in the enhancement of mass transfer [90]. Huang et al. suggested that the improvement of volumetric mass transfer coefficient continues until the particle size reaches 60 nm, and a further increase in particle size does not affect the efficiency of nanofluid CO_2 absorption [96]. Generally, increasing the volume fraction of nanoparticles will increase the enhancement factor, while enhancement of nanoparticle size decreases this enhancement factor [47].

3.4. Effect of Temperature

Temperature also plays a key role in CO_2 absorption enhancement by nanofluids. Lee and Kang introduced a novel CO_2 absorbent consisting of a NaCl aqueous solution

containing Al_2O_3 nanoparticles. They assessed the solubility of CO_2 in this nanofluid at different temperatures and concentrations of Al_2O_3. They reached 11%, 12.5%, and 8.7% enhancement in CO_2 capture at 30 °C, 20 °C, and 10 °C, respectively, when Al_2O_3 nanoparticle concentration was 0.01 vol% in the solution [92]. Another study carried out by Lee et al., that was carried out in a bubble reactor indicated that the rate of CO_2 absorption increased by 4.5% at 20 °C and Al_2O_3 concentration of 0.01 vol%; this enhancement was 5.6% when Al_2O_3 was substituted by SiO_2 nanoparticles at the same temperature [104]. Jung et al., achieved an eight percent enhancement in CO_2 absorption rate in a bubble reactor at Al_2O_3 nanoparticle concentration of 0.01% and 10 °C. These results imply that better mass transfer efficiency was obtained at lower concentrations of nanoparticles [105].

4. Classification of Nanofluids Based on Base Liquid

Determination of the most suitable solvent for CO_2 absorption is another challenge. A suitable solvent must be cheap with high availability, non-toxic, non-corrosive, non-flammable, and should have a low vapor pressure. Brine, water, ionic liquids, amines, alcohols, amines, and piperazine (PZ) are the most commonly used solvents for this purpose [106]. Three types of nanofluids named water mixtures, amines, and methanol are introduced in the following.

4.1. Amine-Based Nanofluid

Amine absorption of CO_2 is classified as a chemical process in which a gas–liquid phase mass transfer occurs. Absorption and desorption columns are used for this purpose. The gas–liquid equilibrium determines the absorption performance of the selected amine [107]. Amines have fast kinetics in CO_2 absorption. The water solubility is increased and the vapor pressure is reduced by the hydroxyl functional group in the amine, while the alkalinity is facilitated by the amino groups in an aqueous solution [108]. Accordingly, aqueous alkanolamine solutions are the most common solvent used in industrial gas sweetening processes in scrubbers.

Generally, the number of hydrogen atoms of an ammonia molecule substituted with other functional groups is the basis of the classifications for amines into three groups that are primary amines like MEA, secondary amines including DEA, and tertiary amines like MDEA; secondary amines have fast reactions with acidic gases like CO_2 with a higher rate of regeneration energy consumption in comparison to the tertiary amines [109]. The most commonly used amine solvent in large plants is the primary amine of MEA, which is highly reactive and is economically feasible. Nevertheless, this solvent is corrosive and requires a high amount of energy for regeneration.

Several MEA mixtures are proposed in the literature to reduce the energy consumption of this solvent; A mixture of tertiary amines with primary amines is often desirable [110]. The favorable acid gas loading of MEDA has made it a cost-efficient solvent for gas sweetening processes. This solvent has low corrosivity and needs lesser amounts of heat for regeneration. The problem is the weak selectivity of MDEA for CO_2 in the presence of H_2S. One way of increasing CO_2 selectivity is to activate it before being used in CO_2 separation processes; this activation can be achieved through some additives like PZ or MEA [84]. PZ is another attractive candidate for CO_2 absorption due to a higher reactivity than MEA. But, PZ has also some drawbacks such as higher volatility compared to MEA, higher cost-intensive implementation in CO_2 than MEA which is still in the development phase. Lots of papers are available in the literature that consider the efficiency, advantage, and disadvantages of amine solvents. For instance, AMP (2-Amino-2-Methyl-1-Propanol) is a primary amine with steric hindrance with higher CO_2 absorption capacity (due to bi-carbonate formation), furthermore, it is less corrosive compared with MEA.

According to the literature, CO_2 is soluble in aqueous solutions containing alkanolamines. This absorption can be further improved by the addition of PZ as an activator, similarly the additives can also enhance and accelerate the absorption of CO_2. On the other hand, since different species exist in different amines, the chemical stability and corrosivity

of the products of CO_2 absorption will be different from one another. Corrosion causes some problems for the process including the reduction of equipment lifetime. Besides, the strong chemical bonds of amine solvents with CO_2 require high amounts of energy for the desorption process. This high energy demand of the solvent recovery process and corrosion of scrubbers used for CO_2 capture (water-based alkanolamine solutions) led to the idea of developing solid sorbents [10].

Many research studies suggested that the addition of promoters or the dispersion of a third phase such as solid particles, can considerably increase the gas absorption performance [33]. In other words, one way of increasing the rate of CO_2 absorption in CO_2 capture processes is to increase the CO_2 mass transfer. This mass transfer improvement can be achieved by the addition of fine particles to the solvent, which increases the rate of gas removal in gas–liquid mass transfer processes in the absorption columns, therefore, the equipment size will be reduced. It means that in the processes where CO_2 diffusion is involved, the acceleration of the absorption rate is achieved by the enhancement of mass transfer. Therefore, fine particles were added to the liquid phase to increase the mass transfer; it also increases the efficiency of gas–liquid absorption columns or decreases the required size of the equipment due to the enhancement in removal rate of the mass transfer process from gas to the liquid phase.

Thus, the substitution of amine solvents with amine-based nanoparticle absorbents that are dispersed in the liquid phase can save a significant amount of energy since these absorbents do not require high amounts of energy for heating and cooling cycles to recover the liquid solvent [111]. An overview of the recent works in the CO_2 absorption with amine-based nanoparticles is presented in Table 2.

Wang et al., used dispersions of Al_2O_3, SiO_2, and TiO_2 nanoparticles in MEA base fluid to be used in CO_2 capture processes. TiO_2 showed the highest improvement in CO_2 absorption [112]. Similar reports are available in the literature. Jiang et al. carried out some experiments to determine the effect of four nanoparticles of SiO_2, MgO, TiO_2, and Al_2O_3, on the improvement of CO_2 capture. They found that TiO_2-MDEA nanofluids have the best CO_2 absorption performance among the four solutions. Since TiO_2 has the highest CO_2 adsorption capacity, its solution shows the maximum absorption performance due to the higher gradient of CO_2 concentration that it provides in the solution. Furthermore, the CO_2 absorption performance of TiO_2-MEA nanofluid was better than TiO_2-MDEA nanofluid; the reason was the higher rate of the chemical reaction between MEA and CO_2 [105]. Hwang et al. [96] and Park et al. [97–99] studied the impact of SiO_2 nanoparticles addition to MEA, DEA, and DIPA aqueous solutions, on CO_2 absorption rate in a stirred cell. Results indicated that the enhancement of nanoparticle concentration reduces the absorption rate due to the solution's elasticity. The absorption enhancement performance of Al_2O_3 and SiO_2 nanoparticles were assessed when they were dispersed in three different base fluids of MDEA, PZ, and MEA. The coefficient of mass transfer measured at the liquid side indicated a significant enhancement in absorption kinetic of PZ absorbent after the addition of nanoparticles [113]. Komati et al., enhanced the absorption rate of CO_2 capture by amine solutions when nanoferrofluids were used as the enhancement agent. They indicated that the addition of 0.39 vol% of nanoparticles to the base fluid results in a 92.8% enhancement in the absorption capacity compared to the base fluid [99].

The utilization of a nanofluid mixture of graphene-Oxide/MDEA in the gas sweetening process was assessed by Irani et al. [114]. The addition of only 0.1 wt.% graphene oxide to the solvent could promote its absorption capacity by 9.1% which is attributed to the increased mass transfer coefficient due to the hydroxyl functional groups on the graphene oxide surface. In another study, Park et al., studied the impact of colloidal nanosilica addition to 2-amino-2-methyl-1-propanol solvent on CO_2 absorption performance in a stirred vessel. They found that as the concentration of nanoparticles increases the absorption rate and the volumetric mass transfer coefficient in the liquid side decreases [115]. Rahmatmand et al. [84] have also witnessed that the addition of CNT nanoparticles does not significantly affect the DEA absorption performance because DEA is a powerful chem-

ical absorbent of CO_2. Nevertheless, CNTs could significantly enhance the absorptionn capacity of MDEA-based nanofluid for CO_2 capture.

In general, it can be concluded that absorption capacity increases by increasing nanoparticle concentration in the base fluid [89].

Table 2. Summary of various types of amine-based nanofluids.

Researchers	Base Fluid	Nanoparticle	Size of Nanoparticle (nm)	Contactor Type	Enhancement %	Absorbent Loading
Rahimi et al. [116]	MDEA	nMWCNT	11.6	Stirred reactor	141.6	0.05 wt.%
	MEA		11.6		20.79	0.1 wt.%
Jiang et al. [42]	MEA	TiO_2	20	Bubbling reactor	9	0.6 kg/m^3
	MDEA	TiO_2	20		30	0.4 kg/m^3
	MEA	Al_2O_3	20		4	0.6 kg/m^3
	MDEA	Al_2O_3	20		15	0.8 kg/m^3
Irani et al. [114]	MDEA	GO	29.3–35.16	Stirred cell reactor	10.4	0.2 wt.%
Taheri et al. [117]	DEA	Al_2O_3	10–20	WWC	33	0.05 wt.%
		SiO_2	10–15		40	0.05 wt.%
Irani et al. [94]	MDEA	PEI-HKUST-1	-	PSE	16	0.2 wt.%
Aghehrochaboki et al. [72]	MDEA	GO	-	Stirred cell reactor	10.4	0.2 wt.%
		PEI-GO	-		15	0.1 wt.%
Rahmatmand et al. [84]	MDEA	CNT	*	Batch vessel	23	0.02 wt.%
Pashaei et al. [118]	PZ	TiO_2	20	Stirrer Bubble column	14.7	0.05 wt.%
		ZnO	10–30		16.6	0.1 wt.%
		ZrO_2	20		3.7	0.05 wt.%
Li et al. [119]	MDEA	TiO_2	15	Stirred cell reactor	11.54	0.8 wt.%
Komati et al. [99]	MDEA	Fe_3O_4	15	WWC	90	0.39 vol%
Wang et al. [112]	MEA	Al_2O_3	15	Bubble Column	10	0.06 wt.%
		SiO_2	15		10	0.06 wt.%
		TiO_2	15		13	0.06 wt.%
Wang et al. [113]	MEA	Al_2O_3	20	WWC	7	0.02 wt.%
		SiO_2	15		10	0.06 wt.%
Elhambakhsh et al. [120]	MDEA	Fe_3O_4@SiO_2-NH_2	31–39	Stirred cell reactor	16.36	0.1 wt.%
		Fe_3O_4-proline	10–16		6.78	0.02 wt.%
		Fe_3O_4-lysine	13–18		12.13	0.1 wt.%
Jiang et al. [121]	TETA	SiO_2	45	Bubble reaction system	29	0.10 wt.%

*: Outside diameter = 8 nm, Inside diameter = 2.5 nm and Length= 10 μm.

4.2. Water-Based Nanofluid

Water as a non-toxic natural absorber can physically bond with CO_2 and H_2S. Some advantages of distilled water (DW) when being used as an absorber are its high surface tension and proper capacity for CO_2 absorption. Nevertheless, it has a weak performance in CO_2 recovery and has a low absorption rate [122]. Thus, many researchers suggested that dispersing nanoparticles in raw water can considerably increase gas absorption into the resultant nanofluid as depicted in Table 3.

For instance, the CNT-water was used by Ma et al., as a binary nanofluid for the absorption of ammonia. The experiment results indicated that a solution mixture of 0.23 wt.% CNTs in water yields a 16.2% improvement in the absorption of the fluid [123]. Periasamy et al., have dispersed copper and graphene nanoparticles in a solution mixture of water and ethylene glycol and reported a considerable improvement on the base fluid thermophysical properties [124]. A numerical investigation was carried out by Darabi et al. on the carbon dioxide adsorption by hollow fiber membranes using two different solutions of SiO_2/water and CNT/water. The CNT/water fluid had better performance compared to SiO_2 nanoparticles and its rate of CO_2 capture was 16% higher than the other solution. The reason is the lower adsorption capacity of SiO_2 nanoparticles compared to CNT nanoparticles [125]. The suspension of SiO_2 in water was also assessed from mass and heat transfer aspects and a significant enhancement was observed in mass and heat transfer rates that were 18% and 47%, respectively [126].

Komati et al., used magnetic nanoparticles to enhance the CO_2 absorption rate of the base fluid [99]. Salimi et al., used Fe_3O_4 and NiO suspension in water for the absorption of CO_2 in a packed bed. The results indicated an improvement in mass transfer performance

of the nanofluid after the addition of magnetic nanoparticles in the CO_2 capture process [34]. Samadi et al., could achieve 22.35% and 59% enhancement in CO_2 mass flux and mass transfer coefficient just by using a wetted wall column for CO_2 absorption, which was equipped with an external magnetic field. The nanofluid that was used in their experiments was Fe_3O_4/water [127]. The Fe_3O_4 nanofluid was also examined by Darvanjooghi et al., for the CO_2 absorption in constant and alternating magnetic fields. The results indicated that high strength magnetic fields increase both mass transfer rate and solubility of CO_2. The results showed a maximum value of CO_2 solubility and the average molar flux of absorption into the nanofluid when an AC field was applied. They indicated that as the strength of the magnetic field increases, the renewal surface factor and CO_2 mass diffusivity in the nanofluid increase as well, while the thickness of the diffusion layer decreases [93]. Haghtalab et al., utilized a batch stirred vessel to study CO_2 solubility in SiO_2/water and ZnO/water nanofluids. The ZnO/water nanofluid showed better CO_2 absorption than the SiO_2/water nanofluid in their experiments. Furthermore, CO_2 absorption was examined by some researchers in membrane contactors with water as the absorption media. They found that the addition of some materials as promoters to deionized water can enhance the absorption rate and capacity of CO_2 [88].

Table 3. Overview of water-based nanofluids for improvement of CO_2 absorption.

Researchers	Base Fluid	Nanoparticle	Size of Nanoparticle (nm)	Contactor Type	Enhancement %	Absorbent Loading
Arshadi et al. [111]	Water	Fe_3O_4@SiO_2-SNH_2	50	Bubble column	70.3	0.4 wt.%
Kim et al. [90]	Water	SiO_2	30	Bubble column	24	0.021 wt.%
Jorge et al. [128]	Water	FCNT [a]	10	Bubble column	36	4 vol%
Rahmatmand et al. [84]	Water	SiO_2	15	Batch vessel	21	0.1 wt.%
	Water	Al_2O_3	20	Batch vessel	18	0.1 wt.%
		Fe_3O_4	4		24	0.02 wt.%
		CNT	*		34	0.02 wt.%
Peyravi et al. [32]	Water	Fe_3O_4	4	HFMC	43.8	0.15 wt.%
		CNT	*		38	0.1 wt.%
		SiO_2	15		25.9	0.05 wt.%
		Al_2O_3	20		3	0.05 wt.%
Haghtalab et al. [88]	Water	SiO_2	30–40	Bubble column	7	0.1 wt.%
	Water	ZnO	11.5		14	0.1 wt.%
Salimi et al. [129]	Water	Al_2O_3	15–20	Packed column	14	0.05 vol%
		Al_2O_3-SiO_2	10–15		10	0.05 vol%
Salimi et al. [34]	Water	Fe_3O_4	8	Packed column	12	0.005 vol%
		NiO	50		9.5	0.01 vol%
Samadi et al. [127]	Water	Al_2O_3	25	WWC	40–55	1 vol%
Darvanjooghi et al. [93]	Water	SiO_2	62	Bubble column	40	0.01 wt.%
Ghasem [130]	Water	CNT	*	HFMC	45 [1]	0.25 wt.%
Rezakazemi et al. [131]	Water	SiO_2	15	HFMC	16	0.05 wt.%
		CNT	*		34	0.05 wt.%
Zare et al. [29]	DI Water	ZnO	10–30	PP HFMC	130	0.15 wt.%
		TiO_2	21		60	0.15 wt.%
		MWCNT	10–20		60	0.15 wt.%
Rahimi et al. [116]	Water	nMWCNT	11.6	Stirred reactor	25.1	0.02 wt.%
Devakki et al. [24]	DI Water	TiO_2	<50	Stirred cell reactor	39.81	0.1 wt.%
		Al_2O_3	<40		22.3	0.14 wt.%
Hafizi et al. [132]	Water	DETA@ECH@ Fe_3O_4	40	Batch equilibrium vessel	77.3	0.5 wt.%
Esmaeili-Faraj et al. [133]	Water	EGO	20	Bubble column	diminished to zero	<0.02 wt.%
Elhambakhsh et al. [134]	DI Water	Fe_3O_4@SiO_2-lysine	17–20	Bubble Column	88	0.125 wt.%
Karamian et al. [135]	Water	Al_2O_3	20–60	Single-Bubble Column	117	0.1 wt.%
		Fe_2O_3	30–80		103	1 wt.%
		SiO_2	20–60		88	0.01 wt.%
Lee et al. [136]	DI Water	Al_2O_3	45	Bubble Column	23.5	0.01 vol%
		SiO_2	15		23.5	0.01 vol%
Ansaripour et al. [137]	DI Water	α- Al_2O_3	80	HFMC	12.2	0.02 vol%
		γ- Al_2O_3	20		21.6	0.02 vol%
Golkhar et al. [31]	DI Water	CNT	*	HFMC	40	0.5 wt.%
		SiO_2	10–15		20	0.5 wt.%
Choi et al. [138]	DI Water	SiO_2	15	Stirred cell reactor	13.1	0.01 vol%

Table 3. *Cont.*

Researchers	Base Fluid	Nanoparticle	Size of Nanoparticle (nm)	Contactor Type	Enhancement %	Absorbent Loading
Elhambakhsh et al. [120]	DI Water	Fe_3O_4-proline	10–16	Stirred cell reactor	25.07	0.02 wt.%
		Fe_3O_4-lysine	13–18		31.04	0.1 wt.%
		Fe_3O_4@SiO_2-NH_2	31–39		34.23	0.1 wt.%
Manikandan et al. [95]	Water	Al_2O_3	-	WWC	19	0.6 vol%
Manikandan et al. [139]	Water	TiO_2	-	Packed column	65	1.0 vol%
		MWCNT	10	Bubble Column	36	40 Mg/L

[1]: CO_2 removal% *: Outside diameter = 8 nm, Inside diameter = 2.5 nm and Length= 10 μm. [a]: Hollow fiber membrane contactors.

Nanofluids containing different nanoparticles like SiO_2, Fe_3O_4, carbon nanotubes, or Al_2O_3 in a base fluid including amine-based solutions or deionized water were also used for gas absorption in a membrane contactor. The CO_2 absorption performance of different nanofluids from gas streams was also experimentally studied to determine the influence of different nanoparticles (Al_2O_3, SiO_2, Fe_3O_4, and CNT), in low concentrations, on the improvement of CO_2 absorption. It was revealed that unlike Al_2O_3 and SiO_2 which have better CO_2 absorption performance at high concentrations, CNT and Fe_3O_4 nanoparticles better enhance CO_2 absorption at low concentrations [84,102]. In general, when water is used as the base fluid in absorption processes, hydrophobic nanoparticles have better dispersion and a higher rate of collisions with CO_2 bubbles; consequently, the rate of CO_2 bubble cracking and as a result, the mass transfer between the two phases increases [111].

4.3. Methanol-Based Nanofluid

The methanol-based nanofluids are another kind of absorbent that improves CO_2 absorption in synthetic natural gas (SNG) systems. The high selectivity and low cost of this absorbent and the possibility of being used for high-pressure natural gas streams have made it a good candidate for these processes. Another advantage of this absorbent is the requirement of low temperatures for the regeneration process compared to the aqueous solutions since it has smaller latent heat and a lower boiling point. Therefore, the non-aqueous alkanolamines are good candidates to enhance the CO_2 absorption performance. But, according to Henry's law of solubility, it is required to keep the temperature of the absorbent at about −20 °C to be able to increase the rate of absorption [104,140]. Therefore, it needs a lot of energy to keep methanol at such a low temperature. The addition of nanoparticles to the base fluids is a perfect way of CO_2 absorption enhancement. The present research efforts are summarized in Table 4.

Table 4. Common use of methanol-based nanofluids in CO_2 absorption.

Researchers	Base Fluid	Nanoparticle	Particle Size (nm)	Contactor Type	Enhancement %	Absorbent Loading
Pineda et al. [87]	Methanol	Al_2O_3	40–50	AC, T-CA	1.2, 10	0.05 vol%
		TiO_2	<25		4.6, 5	0.05 vol%
		SiO_2	10–20		1.1, 6	0.05 vol%
Jung et al. [105]	Methanol	Al_2O_3	40–50	Bubble column	8.3	0.01 vol%
Pineda et al. [141]	Methanol	Al_2O_3	40–50	Tray column	9.4	0.05 vol%
		SiO_2	10–20		9.7	0.05 vol%
Lee et al. [104]	Methanol	Al_2O_3	40–50	Bubble column	4.5	0.01 vol%
		SiO_2	10–20		5.6	0.01 vol%
Kim et al. [78]	Methanol	Al_2O_3	40–50	Bubble column	26	0.01 vol%

Accordingly, extensive investigations were done by Jung et al., with nanofluids containing Al_2O_3 dispersed nanoparticles with 0.005–0.1 vol% concentrations. They achieved the highest CO_2 elimination of 8.3% at nanoparticle a concentration of 0.01 vol% compared to pure methanol as the absorbent. The suggested that the reason for this enhancement is

the Brownian motion that induces particle-laden flows and consequently creates the mixing effects by Al_2O_3 nanoparticles [105].

Pineda et al., used a tray column to study the impact of Al_2O_3 and SiO_2 on CO_2 absorption rate when they are dispersed in a methanol-based solution. Results of their experiments showed a 9.4% and 9.7% enhancement, respectively, in the absorption capacity of nanofluids containing Al_2O_3 and SiO_2, when the optimum concentration of 0.05% of the nanoparticles was used [141]. Lee et al., also investigated the absorption performance of different methanol-based nanofluids containing different concentrations of silica and alumina particles. It was observed that the highest CO_2 absorption compared to pure methanol is achieved when 0.01 vol% Al_2O_3 or 0.01 vol% SiO_2 are dispersed in the pure methanol, in this case, 4.5% and 5.6% improvement will occur in the absorption process, respectively [104]. In another investigation, Peng et al., utilized the transient hot-wire method to determine the thermal conductivity nanofluids in which SiO_2 and Al_2O_3 are dispersed in methanol. The maximum increase in thermal conductivity was 14.29% when the nanoparticle concentration was in the range of 0.005–0.5 vol% [142]. Jung et al., utilized a bubble column to evaluate the performance of nanofluids containing Al_2O_3 dispersed in methanol-based fluids in the absorption rate of CO_2. They found that the absorption rate of the nanofluid is 8.3% higher compared to the pure base fluid [105].

In the end, different base fluids for nanofluids for the improvement of CO_2 absorption in the literature are compared in Table 5. The results indicate that the nanofluids in these fluids showed proper activity as compared with those reported in earlier studies.

Table 5. Different based nanofluids for the improvement of CO_2 absorption.

Researchers	Base Fluid	Nanoparticle	Size of Nanoparticle (nm)	Contactor Type	Enhancement %	Absorbent Loading
Devakki et al. [24]	Salt solutions	Al_2O_3	<40	Stirred cell reactor	−5.68 [1]	1 to 3.1 wt.%
		TiO_2	<50		−11.93 [1]	1 to 3.1 wt.%
Lee et al. [92]	NaCl solution	Al_2O_3	40–50	Bubble column	12.5	0.01 vol%
Nabipour et al. [89]	Sulfinol-M	Fe_3O_4	**	Quasi-static high pressure	14.7	0.02 wt.%
		MWCNT	20–30		23.2	0.02 wt.%
Zhang et al. [83]	Ammonia solutions	Fe_3O_4	20	Bubbling reactor	14.5	0.3 g/L

[1]: decreases the absorption **: Inside diameter: 5–10 nm, outside diameter: 20–30 nm and length: 10–30 µm.

5. Future Perspective

Currently, due to their positive approaches in CO_2 absorption, hybrid systems can replace common processes. Due to their novelty, on the other hand, hybrid systems require further studies to understand the effect of parameters, the performance of nanomaterials, and analysis of the process to reach an optimum rate of absorption. Some of the challenges in using hybrid systems include blockage, phase stability, lack of sufficient data in examining solvent properties, pump power, and costs of solid materials, increasing heat and energy transfer, and imposing additional investment costs. In this regard, by proper selection of nanoparticles and base liquid, two problems of energy and economy can be controlled in these systems in addition to accelerating mass transfer and increasing gas-phase absorption by solid particles. Generally, a promising perspective can be imagined in the future and at large scales by studying the relationship between mechanisms and conducting comprehensive studies on nanofluids' role in CO_2 absorption. Furthermore, CO_2 removal and absorption processes using nanoparticles and new methods will be paid more scientific attention in the future.

6. Conclusions

In this study, we have investigated hybrid systems, unique properties of nanomaterials, and their wide application in CO_2 absorption. In the last few decades, the properties of nanoparticles on a small scale with different structures have been significantly efficient in the energy field. Accordingly, we believe that such technology provides one of the effective

solutions for CO_2 absorption. In this review study, in addition to the nanofluid explanation, its application, and properties using the nanofluid preparation, we have tried to address the reasons behind the base liquid selection, stability, mass transfer enhancement mechanisms in the nanofluids (shuttle effect, Bubble Breakup effect, and micro convection), and the CO_2 absorption increasing factors following the nanofluids. One of the most important points of the hybrid systems is the role of the base solvent, in which by properly selecting the nanoparticles–base solvent pair, the mass transfer rate and mechanism for CO_2 absorption have been substantially increased, accelerating the CO_2 reaction kinetics. On the contrary, lower energy consumption is required for solvent regeneration in the desorption process by decreasing the heat transfer in such systems. For this reason, in this study, the effect of 3 types of base liquid, e.g., water, amine and methanol, with different nanoparticles have been evaluated on the CO_2 absorption level. In the following, we will briefly explain the main results of this short review.

1. CO_2 absorption using nanofluids depends on several factors, i.e., particle size, nanoparticle type, temperature, and base liquid.

2. The nanoparticles preparation method and their stability are some of the important properties of nanofluids that should be taken into consideration. This is because the hybrid systems create sediments and settle over time. Accordingly, in order to control this issue, we can reform the nanoparticles' surface or the low-cost dispersions so that the stability of the nanofluids is increased.

3. The suspension preparation process is of paramount importance in terms of the type and the extent of solid particles since the nanoparticles' cost as an additive solid material to the base solvent is one of the important economic issues. Similarly, in hybrid systems, the nanoparticles synthesis is usually done using the 2-step method that is cost-effective.

4. The main mechanisms for the CO_2 absorption, the shuttle effect, bubble break-up, and the Brownian motion leading to the nanoparticles' micro convection have been thoroughly explained. It is expected that other mechanisms will be explained in this field in the future.

5. The CO_2 absorption in the nanofluid depends on the different surfaces of the nanoparticles; as a nanoparticle has a larger surface, it is dispersed better in the base liquid, increasing the absorption level.

6. There are different nanoparticles with particular applications and properties, but among them, making use of the metal oxide nanoparticles, e.g., Fe_3O_4, ZnO, Al_2O_3, TiO_2, etc., have captured significant interest in industrial applications due to being cheaper.

7. The CO_2 absorption has been investigated using three base liquids (water, amine, and methanol). Water has captured more interest among researchers as a base liquid than the two other base liquids due to availability and being cheaper.

In general, according to the research conducted in the realm of mass transfer and CO_2 absorption so far, we can conclude that using nanofluids is an effective method for increasing the CO_2 absorption in terms of the base liquid that can decrease the energy consumption and equipment costs.

Author Contributions: Conceptualization, Methodology, Investigation, Resources, Writing—Original Draft, Writing—Review, and Editing, Visualization, B.A.; Methodology, Investigation, Validation, S.J.; Methodology, Investigation, Resources, Visualization, Writing—Review and Editing, F.A.; Methodology, Investigation, Visualization, A.A.; Resources, Supervision, B.E. All authors have read and agreed to the published version of the manuscript.

Funding: This research received no external funding.

Acknowledgments: We acknowledge support by the Deutsche Forschungsgemeinschaft (DFG—German Research Foundation) and the Open Access Publishing Fund of Technical University of Darmstadt. The first author acknowledges the support provided by Alexander von Humboldt Foundation through the project IRN 1218321 GF-E for the experienced researcher.

Conflicts of Interest: The authors declare no conflict of interest.

Abbreviations

AC	Annular contactor
AMP	2-Amino-2-Methyl-1-Propanol
CCS	CO_2 capture and sequestration
COPs	Covalent organic frameworks
DEA	Diethanolamine
DEPG	Dimethyl ether of polyethylene glycol
DLS	Dynamic light scattering
DW	Distilled water
EU	European Union
ESA	Electrical swing adsorption
GHG	Greenhouse gas
HFCM	Hollow fiber ceramic membrane
IIS	lonic liquids
LLE	Liquid–liquid extraction
MDEA	Methyldiethanolamine
MEA	Monoethanolamine
MOFs	Metal-organic frameworks
MWCNT	Multi-walled carbon nanotube
NGO	Nanographene oxide
NMP	N-Methyl-2-Pyrrolidone
NP	Nanoparticle
PC	Propylene carbonate
PNP	Pnitrophenol
PSA	Pressure swing adsorption
PZ	Piperazine
RES	Renewable energy sources
SNG	Synthetic natural gas
TEM	Transmission electron microscopy
TSA	Temperature swing adsorption
TVS	Temperature vacuum adsorption
VSA	Vacuum swing adsorption
WWC	Watted-wall column
Fe_3O_4@SiO_2-NH_2	Synthesiz of Fe_3O_4
Fe_3O_4-lysine	Synthesiz of Fe_3O_4
Fe_3O_4-proline	Synthesiz of Fe_3O_4

References

1. Koytsoumpa, E.I.; Bergins, C.; Kakaras, E. The CO_2 economy: Review of CO_2 capture and reuse technologies. *J. Supercrit. Fluids* **2018**, *132*, 3–16. [CrossRef]
2. Wojtacha-Rychter, K.; Kucharski, P.; Smolinski, A. Conventional and alternative sources of thermal energy in the production of cement—An impact on CO_2 emission. *Energies* **2021**, *14*, 1539. [CrossRef]
3. Aghel, B.; Sahraie, S.; Heidaryan, E. Comparison of aqueous and non-aqueous alkanolamines solutions for carbon dioxide desorption in a microreactor. *Energy* **2020**, *201*, 117618. [CrossRef]
4. Zheng, W.; Liu, Z.; Ding, R.; Dai, Y.; Li, X.; Ruan, X.; He, G. Constructing continuous and fast transport pathway by highly permeable polymer electrospun fibers in composite membrane to improve CO_2 capture. *Sep. Purif. Technol.* **2021**, *285*, 120332. [CrossRef]
5. Liu, L.; Fang, M.; Xu, S.; Wang, J.; Guo, D. Development and testing of a new post-combustion CO_2 capture solvent in pilot and demonstration plant. *Int. J. Greenh. Gas Control* **2022**, *113*, 103513. [CrossRef]
6. Garg, B.; Pearson, P.; Cousins, A.; Verheyen, V.; Puxty, G.; Feron, P. Experimental evaluation of methods for reclaiming sulfur loaded amine absorbents. In Proceedings of the 14th Greenhouse Gas Control Technologies Conference, Melbourne, VIC, Australia, 21–25 October 2018; pp. 21–26.
7. Krótki, A.; Solny, L.W.; Stec, M.; Spietz, T.; Wilk, A.; Chwoła, T.; Jastrząb, K. Experimental results of advanced technological modifications for a CO_2 capture process using amine scrubbing. *Int. J. Greenh. Gas Control* **2020**, *96*, 103014. [CrossRef]
8. Aghel, B.; Sahraie, S.; Heidaryan, E.; Varmira, K. Experimental study of carbon dioxide absorption by mixed aqueous solutions of methyl diethanolamine (MDEA) and piperazine (PZ) in a microreactor. *Process Saf. Environ. Prot.* **2019**, *131*, 152–159. [CrossRef]

9. Janati, S.; Aghel, B.; Shadloo, M.S. The effect of alkanolamine mixtures on CO_2 absorption efficiency in t-shaped microchannel. *Environ. Technol. Innov.* **2021**, *24*, 102006. [CrossRef]
10. Mukhtar, A.; Saqib, S.; Mellon, N.B.; Babar, M.; Rafiq, S.; Ullah, S.; Bustam, M.A.; Al-Sehemi, A.G.; Muhammad, N.; Chawla, M. CO_2 capturing, thermo-kinetic principles, synthesis and amine functionalization of covalent organic polymers for CO_2 separation from natural gas: A review. *J. Nat. Gas Sci. Eng.* **2020**, *77*, 103203. [CrossRef]
11. Babar, M.; Bustam, M.A.; Maulud, A.S.; Ali, A.; Mukhtar, A.; Ullah, S. Enhanced cryogenic packed bed with optimal CO_2 removal from natural gas; a joint computational and experimental approach. *Cryogenics* **2020**, *105*, 103010. [CrossRef]
12. Chawla, M.; Saulat, H.; Masood Khan, M.; Mahmood Khan, M.; Rafiq, S.; Cheng, L.; Iqbal, T.; Rasheed, M.I.; Farooq, M.Z.; Saeed, M.; et al. Membranes for CO_2/CH_4 and CO_2/N_2 gas separation. *Chem. Eng. Technol.* **2020**, *43*, 184–199. [CrossRef]
13. Hu, X.E.; Liu, L.; Luo, X.; Xiao, G.; Shiko, E.; Zhang, R.; Fan, X.; Zhou, Y.; Liu, Y.; Zeng, Z.; et al. A review of N-functionalized solid adsorbents for post-combustion CO_2 capture. *Appl. Energy* **2020**, *260*, 114244. [CrossRef]
14. Li, C.; Shi, X.; Shen, S. Performance evaluation of newly developed absorbents for solvent-based carbon dioxide capture. *Energy Fuels* **2019**, *33*, 9032–9039. [CrossRef]
15. Aghel, B.; Sahraie, S.; Heidaryan, E. Carbon dioxide desorption from aqueous solutions of monoethanolamine and diethanolamine in a microchannel reactor. *Sep. Purif. Technol.* **2020**, *237*, 116390. [CrossRef]
16. Aghel, B.; Maleki, M.; Sahraie, S.; Heidaryan, E. Desorption of carbon dioxide from a mixture of monoethanolamine with alcoholic solvents in a microreactor. *Fuel* **2021**, *306*, 121636. [CrossRef]
17. Carranza-Abaid, A.; Wanderley, R.R.; Knuutila, H.K.; Jakobsen, J.P. Analysis and selection of optimal solvent-based technologies for biogas upgrading. *Fuel* **2021**, *303*, 121327. [CrossRef]
18. Babar, M.; Bustam, M.A.; Ali, A.; Maulud, A.S.; Shafiq, U.; Mukhtar, A.; Shah, S.N.; Maqsood, K.; Mellon, N.; Shariff, A.M. Thermodynamic data for cryogenic carbon dioxide capture from natural gas: A review. *Cryogenics* **2019**, *102*, 85–104. [CrossRef]
19. Song, C.; Liu, Q.; Ji, N.; Deng, S.; Zhao, J.; Li, Y.; Kitamura, Y. Reducing the energy consumption of membrane-cryogenic hybrid CO_2 capture by process optimization. *Energy* **2017**, *124*, 29–39. [CrossRef]
20. Saqib, S.; Rafiq, S.; Muhammad, N.; Khan, A.L.; Mukhtar, A.; Mellon, N.B.; Man, Z.; Nawaz, M.H.; Jamil, F.; Ahmad, N.M. Perylene based novel mixed matrix membranes with enhanced selective pure and mixed gases (CO_2, CH4, and N2) separation. *J. Nat. Gas Sci. Eng.* **2020**, *73*, 103072. [CrossRef]
21. Jeong, Y.; Kim, S.; Lee, M.; Hong, S.; Jang, M.-G.; Choi, N.; Hwang, K.S.; Baik, H.; Kim, J.-K.; Yip, A.C.K.; et al. A hybrid zeolite membrane-based breakthrough for simultaneous CO_2 capture and CH_4 upgrading from biogas. *ACS Appl. Mater. Interfaces* **2022**, *14*, 2893–2907. [CrossRef]
22. Zhang, S.; Shen, Y.; Wang, L.; Chen, J.; Lu, Y. Phase change solvents for post-combustion CO_2 capture: Principle, advances, and challenges. *Appl. Energy* **2019**, *239*, 876–897. [CrossRef]
23. Raganati, F.; Miccio, F.; Ammendola, P. Adsorption of carbon dioxide for post-combustion capture: A review. *Energy Fuels* **2021**, *35*, 12845–12868. [CrossRef]
24. Devakki, B.; Thomas, S. Experimental investigation on absorption performance of nanofluids for CO_2 capture. *Int. J. Air-Cond. Refrig.* **2020**, *28*, 2050017. [CrossRef]
25. Kumar, R.; Mangalapuri, R.; Ahmadi, M.H.; Vo, D.-V.N.; Solanki, R.; Kumar, P. The role of nanotechnology on post-combustion CO_2 absorption in process industries. *Int. J. Low Carbon Technol.* **2020**, *15*, 361–367. [CrossRef]
26. Yu, W.; Wang, T.; Park, A.-H.A.; Fang, M. Review of liquid nano-absorbents for enhanced CO_2 capture. *Nanoscale* **2019**, *11*, 17137–17156. [CrossRef] [PubMed]
27. Mehdipour, M.; Keshavarz, P.; Rahimpour, M.R. Rotating liquid sheet contactor: A new gas-liquid contactor system in CO_2 absorption by nanofluids. *Chem. Eng. Process. Process Intensif.* **2021**, *165*, 108447. [CrossRef]
28. Ma, B.; Banerjee, D. A review of nanofluid synthesis. In *Advances in Nanomaterials*; Springer: Cham, Switzerland, 2018; pp. 135–176; ISBN 978-3-319-64715-9.
29. Zare, P.; Keshavarz, P.; Mowla, D. Membrane absorption coupling process for CO_2 capture: Application of water-based ZnO, TiO_2, and multi-walled carbon nanotube nanofluids. *Energy Fuels* **2019**, *33*, 1392–1403. [CrossRef]
30. Pordanjani, A.H.; Aghakhani, S.; Afrand, M.; Mahmoudi, B.; Mahian, O.; Wongwises, S. An updated review on application of nanofluids in heat exchangers for saving energy. *Energy Convers. Manag.* **2019**, *198*, 111886. [CrossRef]
31. Golkhar, A.; Keshavarz, P.; Mowla, D. Investigation of CO_2 removal by silica and CNT nanofluids in microporous hollow fiber membrane contactors. *J. Membr. Sci.* **2013**, *433*, 17–24. [CrossRef]
32. Peyravi, A.; Keshavarz, P.; Mowla, D. Experimental investigation on the absorption enhancement of CO_2 by Various nanofluids in hollow fiber membrane contactors. *Energy Fuels* **2015**, *29*, 8135–8142. [CrossRef]
33. Sumin, L.U.; Min, X.; Yan, S.U.N.; Xiangjun, D. Experimental and theoretical studies of CO_2 absorption enhancement by nano-Al_2O_3 and carbon nanotube particles. *Chin. J. Chem. Eng.* **2013**, *21*, 983–990.
34. Salimi, J.; Haghshenasfard, M.; Etemad, S.G. CO_2 absorption in nanofluids in a randomly packed column equipped with magnetic field. *Heat Mass Transf.* **2015**, *51*, 621–629. [CrossRef]
35. Yu, W.; Xie, H. A review on nanofluids: Preparation, stability mechanisms, and applications. *J. Nanomater.* **2011**, *2012*, 1–17. [CrossRef]
36. Choi, S.U.S.; Eastman, J.A. *Enhancing Thermal Conductivity of Fluids with Nanoparticles*; Argonne National Lab.: Lemont, IL, USA, 1995.

37. Elsaid, K.; Olabi, A.; Wilberforce, T.; Abdelkareem, M.A.; Sayed, E.T. Environmental impacts of nanofluids: A review. *Sci. Total Environ.* **2021**, *763*, 144202. [CrossRef]
38. Chakraborty, S.; Panigrahi, P.K. Stability of nanofluid: A review. *Appl. Therm. Eng.* **2020**, *174*, 115259. [CrossRef]
39. Yahya, S.I.; Rezaei, A.; Aghel, B. Forecasting of water thermal conductivity enhancement by adding nano-sized alumina particles. *J. Therm. Anal. Calorim.* **2021**, *145*, 1791–1800. [CrossRef]
40. Ruthiya, K.C.; van der Schaaf, J.; Kuster, B.F.M.; Schouten, J.C. Mechanisms of physical and reaction enhancement of mass transfer in a gas inducing stirred slurry reactor. *Chem. Eng. J.* **2003**, *96*, 55–69. [CrossRef]
41. Krishnamurthy, S.; Bhattacharya, A.P.; Phelan, P.E.; Prasher, R.S. Enhanced mass transport in nanofluids. *Nano Lett.* **2006**, *6*, 419–423. [CrossRef]
42. Jiang, J.; Zhao, B.; Zhuo, Y.; Wang, S. Experimental study of CO_2 absorption in aqueous MEA and MDEA solutions enhanced by nanoparticles. *Int. J. Greenh. Gas Control* **2014**, *29*, 135–141. [CrossRef]
43. ZareNezhad, B.; Montazeri, V. Nanofluid-assisted gas to hydrate (GTH) energy conversion for promoting CO_2 recovery and sequestration processes in the petroleum industry. *Pet. Sci. Technol.* **2016**, *34*, 37–43. [CrossRef]
44. Rashidi, H.; Mamivand, S. Experimental and numerical mass transfer study of carbon dioxide absorption using Al_2O_3/water nanofluid in wetted wall column. *Energy* **2022**, *238*, 121670. [CrossRef]
45. Selvi, P.P.; Baskar, R. CO_2 absorption in nanofluid with magnetic field. *Chem. Ind. Chem. Eng. Q.* **2020**, *26*, 321–328. [CrossRef]
46. Jiang, J.-Z.; Zhang, S.; Fu, X.-L.; Liu, L.; Sun, B.-M. Review of gas–liquid mass transfer enhancement by nanoparticles from macro to microscopic. *Heat Mass Transf.* **2019**, *55*, 2061–2072. [CrossRef]
47. Zhang, N.; Zhang, X.; Pan, Z.; Zhang, Z. A brief review of enhanced CO_2 absorption by nanoparticles. *Int. J. Energy Clean Environ.* **2018**, *19*, 3–4. [CrossRef]
48. Babar, H.; Ali, H.M. Towards hybrid nanofluids: Preparation, thermophysical properties, applications, and challenges. *J. Mol. Liq.* **2019**, *281*, 598–633. [CrossRef]
49. Ma, B.; Shin, D.; Banerjee, D. One-step synthesis of molten salt nanofluid for thermal energy storage application—A comprehensive analysis on thermophysical property, corrosion behavior, and economic benefit. *J. Energy Storage* **2021**, *35*, 102278. [CrossRef]
50. Torres-Mendieta, R.; Mondragón, R.; Juliá, E.; Mendoza-Yero, O.; Lancis, J.; Mínguez-Vega, G. Fabrication of high stable gold nanofluid by pulsed laser ablation in liquids. *Adv. Mater. Lett.* **2015**, *6*, 1037–1042. [CrossRef]
51. El-Salamony, R.A.; Morsi, R.E.; Alsabagh, A.M. Preparation, stability and photocatalytic activity of titania nanofluid using gamma irradiated titania nanoparticles by two-step method. *J. Nanofluids* **2015**, *4*, 442–448.
52. Sarkar, J.; Ghosh, P.; Adil, A. A review on hybrid nanofluids: Recent research, development and applications. *Renew. Sustain. Energy Rev.* **2015**, *43*, 164–177. [CrossRef]
53. Zhang, Z.; Cai, J.; Chen, F.; Li, H.; Zhang, W.; Qi, W. Progress in enhancement of CO_2 absorption by nanofluids: A mini review of mechanisms and current status. *Renew. Energy* **2018**, *118*, 527–535. [CrossRef]
54. Solangi, K.; Kazi, S.; Luhur, M.; Badarudin, A.; Amiri, A.; Sadri, R.; Zubir, M.; Gharehkhani, S.; Teng, K. A comprehensive review of thermo-physical properties and convective heat transfer to nanofluids. *Energy* **2015**, *89*, 1065–1086. [CrossRef]
55. Ilyas, S.U.; Pendyala, R.; Narahari, M.; Susin, L. Stability, rheology and thermal analysis of functionalized alumina-thermal oil-based nanofluids for advanced cooling systems. *Energy Convers. Manag.* **2017**, *142*, 215–229. [CrossRef]
56. Said, Z.; Hachicha, A.A.; Aberoumand, S.; Yousef, B.A.; Sayed, E.T.; Bellos, E. Recent advances on nanofluids for low to medium temperature solar collectors: Energy, exergy, economic analysis and environmental impact. *Prog. Energy Combust. Sci.* **2021**, *84*, 100898. [CrossRef]
57. Syarif, D.G.; Prajitno, D.H. Synthesis and characterization of Fe3O4 nanoparticles for nanofluids from local material through carbothermal reduction and precipitation. *J. Aust. Ceram. Soc.* **2016**, *52*, 76–81.
58. Sandhya, M.; Ramasamy, D.; Sudhakar, K.; Kadirgama, K.; Harun, W.S.W. Ultrasonication an intensifying tool for preparation of stable nanofluids and study the time influence on distinct properties of graphene nanofluids—A systematic overview. *Ultrason. Sonochemistry* **2021**, *73*, 105479. [CrossRef]
59. Sadeghinezhad, E.; Togun, H.; Mehrali, M.; Nejad, P.S.; Latibari, S.T.; Abdulrazzaq, T.; Kazi, S.N.; Metselaar, H.S.C. An experimental and numerical investigation of heat transfer enhancement for graphene nano-platelets nanofluids in turbulent flow conditions. *Int. J. Heat Mass Transf.* **2015**, *81*, 41–51. [CrossRef]
60. Farahmandjou, M.; Sebt, S.A.; Parhizgar, S.S.; Aberomand, P.; Akhavan, M. Stability investigation of colloidal Fe, Pt nanoparticle systems by spectrophotometer analysis. *Chin. Phys. Lett.* **2009**, *26*, 27501. [CrossRef]
61. Sofiah, A.; Samykano, M.; Shahabuddin, S.; Kadirgama, K.; Pandey, A. A comparative experimental study on the physical behavior of mono and hybrid RBD palm olein based nanofluids using Cu, O nanoparticles and PANI nanofibers. *Int. Commun. Heat Mass Transf.* **2021**, *120*, 105006. [CrossRef]
62. Kong, L.; Sun, J.; Bao, Y. Preparation, characterization and tribological mechanism of nanofluids. *RSC Adv.* **2017**, *7*, 12599–12609. [CrossRef]
63. Ettefaghi, E.; Ghobadian, B.; Rashidi, A.; Najafi, G.; Khoshtaghaza, M.H.; Pourhashem, S. Preparation and investigation of the heat transfer properties of a novel nanofluid based on graphene quantum dots. *Energy Convers. Manag.* **2017**, *153*, 215–223. [CrossRef]
64. Yang, X.-F.; Liu, Z.-H. Pool boiling heat transfer of functionalized nanofluid under sub-atmospheric pressures. *Int. J. Therm. Sci.* **2011**, *50*, 2402–2412. [CrossRef]

65. Thakur, P.; Sonawane, S.S.; Sonawane, S.H.; Bhanvase, B.A. Nanofluids-based delivery system, encapsulation of nanoparticles for stability to make stable nanofluids. In *Encapsulation of Active Molecules and Their Delivery System*; Elsevier: Amsterdam, The Netherlands, 2020; p. 141.
66. Bhattacharjee, S. DLS and zeta potential—What they are and what they are not? *J. Control. Release* **2016**, *235*, 337–351. [CrossRef] [PubMed]
67. Jung, J.-Y.; Yoo, J.Y. Thermal conductivity enhancement of nanofluids in conjunction with electrical double layer (EDL). *Int. J. Heat Mass Transf.* **2009**, *52*, 525–528. [CrossRef]
68. Kamalgharibi, M.; Hormozi, F.; Zamzamian, S.A.H.; Sarafraz, M.M. Experimental studies on the stability of CuO nanoparticles dispersed in different base fluids: Influence of stirring, sonication and surface active agents. *Heat Mass Transf.* **2016**, *52*, 55–62. [CrossRef]
69. Zhu, H.; Zhang, C.; Tang, Y.; Wang, J.; Ren, B. Preparation and thermal conductivity of suspensions of graphite nanoparticles. *Carbon* **2007**, *45*, 226–228. [CrossRef]
70. Choudhary, R.; Khurana, D.; Kumar, A.; Subudhi, S. Stability analysis of Al_2O_3/water nanofluids. *J. Exp. Nanosci.* **2017**, *12*, 140–151. [CrossRef]
71. Mehrali, M.; Sadeghinezhad, E.; Latibari, S.T.; Kazi, S.N.; Mehrali, M.; Zubir, M.N.B.M.; Metselaar, H.S.C. Investigation of thermal conductivity and rheological properties of nanofluids containing graphene nanoplatelets. *Nanoscale Res. Lett.* **2014**, *9*, 15. [CrossRef]
72. Aghehrochaboki, R.; Chaboki, Y.A.; Maleknia, S.A.; Irani, V. Polyethyleneimine functionalized graphene oxide/methyldiethanolamine nanofluid: Preparation, characterization, and investigation of CO_2 absorption. *J. Environ. Chem. Eng.* **2019**, *7*, 103285. [CrossRef]
73. Zhang, Y.; Zhao, B.; Jiang, J.; Zhuo, Y.; Wang, S. The use of TiO_2 nanoparticles to enhance CO_2 absorption. *Int. J. Greenh. Gas Control* **2016**, *50*, 49–56. [CrossRef]
74. Kars, R.L.; Best, R.J.; Drinkenburg, A.A.H. The sorption of propane in slurries of active carbon in water. *Chem. Eng. J.* **1979**, *17*, 201–210. [CrossRef]
75. Vinke, H.; Hamersma, P.; Fortuin, J. Enhancement of the gas-absorption rate in agitated slurry reactors by gas-adsorbing particles adhering to gas bubbles. *Chem. Eng. Sci.* **1993**, *48*, 2197–2210. [CrossRef]
76. Kluytmans, J.; van Wachem, B.; Kuster, B.; Schouten, J. Mass transfer in sparged and stirred reactors: Influence of carbon particles and electrolyte. *Chem. Eng. Sci.* **2003**, *58*, 4719–4728. [CrossRef]
77. Holstvoogd, R.; van Swaaij, W. The influence of adsorption capacity on enhanced gas absorption in activated carbon slurries. *Chem. Eng. Sci.* **1990**, *45*, 151–162. [CrossRef]
78. Kim, J.H.; Jung, C.W.; Kang, Y.T. Mass transfer enhancement during CO_2 absorption process in methanol/Al_2O_3 nanofluids. *Int. J. Heat Mass Transf.* **2014**, *76*, 484–491. [CrossRef]
79. Craig, V.S. Bubble coalescence and specificion effects. *Curr. Opin. Colloid Interface Sci.* **2004**, *9*, 178–184. [CrossRef]
80. Koo, J.; Kleinstreuer, C. Impact analysis of nanoparticle motion mechanisms on the thermal conductivity of nanofluids. *Int. Commun. Heat Mass Transf.* **2005**, *32*, 1111–1118. [CrossRef]
81. Lu, S.; Song, J.; Li, Y.; Xing, M.; He, Q. Improvement of CO_2 absorption using Al_2O_3 nanofluids in a stirred thermostatic reactor. *Can. J. Chem. Eng.* **2015**, *93*, 935–941. [CrossRef]
82. Saien, J.; Bamdadi, H. Mass transfer from nanofluid single drops in liquid–liquid extraction process. *Ind. Eng. Chem. Res.* **2012**, *51*, 5157–5166. [CrossRef]
83. Zhang, Q.; Cheng, C.; Wu, T.; Xu, G.; Liu, W. The effect of Fe_3O_4 nanoparticles on the mass transfer of CO_2 absorption into aqueous ammonia solutions. *Chem. Eng. Process. Process Intensif.* **2020**, *154*, 108002. [CrossRef]
84. Rahmatmand, B.; Keshavarz, P.; Ayatollahi, S. Study of absorption enhancement of CO_2 by Si, O_2, Al_2O_3, CNT, and Fe_3O_4 nanoparticles in water and amine solutions. *J. Chem. Eng. Data* **2016**, *61*, 1378–1387. [CrossRef]
85. Ganapathy, H.; Shooshtari, A.; Dessiatoun, S.; Alshehhi, M.; Ohadi, M.M. Experimental investigation of enhanced absorption of carbon dioxide in diethanolamine in a microreactor. In *International Conference on Nanochannels, Microchannels, and Minichannels*; American Society of Mechanical Engineers: New York, NY, USA, 2013.
86. Fang, L.; Liu, H.; Zhu, Y.; Zhang, H.; Cao, T. Influence of nanoparticles on bubble absorption of gaseous CO_2 in ammonia water. *Chem. Eng. China* **2016**, *5*, 6.
87. Pineda, I.T.; Choi, C.K.; Kang, Y.T. CO_2 gas absorption by CH_3OH based nanofluids in an annular contactor at low rotational speeds. *Int. J. Greenh. Gas Control* **2014**, *23*, 105–112. [CrossRef]
88. Haghtalab, A.; Mohammadi, M.; Fakhroueian, Z. Absorption and solubility measurement of CO_2 in water-based ZnO and SiO_2 nanofluids. In *Fluid Phase Equilibria*; Elsevier: Amsterdam, The Netherlands, 2015; Volume 392, pp. 33–42.
89. Nabipour, M.; Keshavarz, P.; Raeissi, S. Experimental investigation on CO_2 absorption in sulfinol-M based Fe_3O_4 and MWCNT nanofluids. *Int. J. Refrig.* **2017**, *73*, 1–10. [CrossRef]
90. Kim, W.-G.; Kang, H.U.; Jung, K.-M.; Kim, S.H. Synthesis of silica nanofluid and application to CO_2 absorption. *Sep. Sci. Technol.* **2008**, *43*, 3036–3055. [CrossRef]
91. Pang, C.; Wu, W.; Sheng, W.; Zhang, H.; Kang, Y.T. Mass transfer enhancement by binary nanofluids (NH3/H2O+ Ag nanoparticles) for bubble absorption process. *Int. J. Refrig.* **2012**, *35*, 2240–2247. [CrossRef]
92. Lee, J.W.; Kang, Y.T. CO_2 absorption enhancement by Al_2O_3 nanoparticles in NaCl aqueous solution. *Energy* **2013**, *53*, 206–211. [CrossRef]

93. Darvanjooghi, M.H.K.; Esfahany, M.N.; Esmaeili-Faraj, S.H. Investigation of the effects of nanoparticle size on CO_2 absorption by silica-water nanofluid. *Sep. Purif. Technol.* **2018**, *195*, 208–215. [CrossRef]
94. Irani, V.; Tavasoli, A.; Maleki, A.; Vahidi, M. Polyethyleneimine-functionalized HKUST-1/MDEA nanofluid to enhance the absorption of CO_2 in gas sweetening process. *Int. J. Hydrogen Energy* **2018**, *43*, 5610–5619. [CrossRef]
95. Manikandan, S.P.; Akila, S.; Deepapriya, N. Mass transfer performance of Al_2O_3 nanofluids for CO_2 absorption in a wetted wall column. *Int. Res. J. Eng. Technol.* **2019**, *6*, 1329–1331.
96. Hwang, B.-J.; Park, S.-W.; Park, D.-W.; Oh, K.-J.; Kim, S.-S. Absorption of carbon dioxide into aqueous colloidal silica solution with different sizes of silica particles containing monoethanolamine. *Korean J. Chem. Eng.* **2009**, *26*, 775–782. [CrossRef]
97. Park, S.-W.; Choi, B.-S.; Kim, S.-S.; Lee, J.-W. Chemical absorption of carbon dioxide into aqueous colloidal silica solution containing monoethanolamine. *J. Ind. Eng. Chem.* **2007**, *13*, 133–142.
98. Park, S.-W.; Choi, B.-S.; Kim, S.-S.; Lee, B.-D.; Lee, J.-W. Absorption of carbon dioxide into aqueous colloidal silica solution with diisopropanolamine. *J. Ind. Eng. Chem.* **2008**, *14*, 166–174. [CrossRef]
99. Komati, S.; Suresh, A.K. CO_2 absorption into amine solutions: A novel strategy for intensification based on the addition of ferrofluids. *J. Chem. Technol. Biotechnol.* **2008**, *83*, 1094–1100. [CrossRef]
100. Lee, J.W.; Pineda, I.T.; Lee, J.H.; Kang, Y.T. Combined CO_2 absorption/regeneration performance enhancement by using nanoabsorbents. *Appl. Energy* **2016**, *178*, 164–176. [CrossRef]
101. Said, S.; Govindaraj, V.; Herri, J.-M.; Ouabbas, Y.; Khodja, M.; Belloum, M.; Sangwai, J.; Nagarajan, R. A study on the influence of nanofluids on gas hydrate formation kinetics and their potential: Application to the CO_2 capture process. *J. Nat. Gas Sci. Eng.* **2016**, *32*, 95–108. [CrossRef]
102. Nagy, E.; Feczkó, T.; Koroknai, B. Enhancement of oxygen mass transfer rate in the presence of nanosized particles. *Chem. Eng. Sci.* **2007**, *62*, 7391–7398. [CrossRef]
103. Zhu, H.; Shanks, B.H.; Heindel, T.J. Enhancing CO−water mass transfer by functionalized MCM41 nanoparticles. *Ind. Eng. Chem. Res.* **2008**, *47*, 7881–7887. [CrossRef]
104. Lee, J.W.; Jung, J.-Y.; Lee, S.-G.; Kang, Y.T. CO_2 bubble absorption enhancement in methanol-based nanofluids. *Int. J. Refrig.* **2011**, *34*, 1727–1733. [CrossRef]
105. Jung, J.-Y.; Lee, J.W.; Kang, Y.T. CO_2 absorption characteristics of nanoparticle suspensions in methanol. *J. Mech. Sci. Technol.* **2012**, *26*, 2285–2290. [CrossRef]
106. Lin, P.-H.; Wong, D.S.H. Carbon dioxide capture and regeneration with amine/alcohol/water blends. *Int. J. Greenh. Gas Control* **2014**, *26*, 69–75. [CrossRef]
107. Mandal, B.; Guha, M.; Biswas, A.; Bandyopadhyay, S. Removal of carbon dioxide by absorption in mixed amines: Modelling of absorption in aqueous MDEA/MEA and AMP/MEA solutions. *Chem. Eng. Sci.* **2001**, *56*, 6217–6224. [CrossRef]
108. Mazari, S.A.; Ghalib, L.; Sattar, A.; Bozdar, M.M.; Qayoom, A.; Ahmed, I.; Muhammad, A.; Abro, R.; Abdulkareem, A.; Nizamuddin, S.; et al. Review of modelling and simulation strategies for evaluating corrosive behavior of aqueous amine systems for CO_2 capture. *Int. J. Greenh. Gas Control* **2020**, *96*, 103010. [CrossRef]
109. Hafizi, A.; Mokari, M.; Khalifeh, R.; Farsi, M.; Rahimpour, M. Improving the CO_2 solubility in aqueous mixture of MDEA and different polyamine promoters: The effects of primary and secondary functional groups. *J. Mol. Liq.* **2020**, *297*, 111803. [CrossRef]
110. Garcia, M.; Knuutila, H.K.; Aronu, U.E.; Gu, S. Influence of substitution of water by organic solvents in amine solutions on absorption of CO_2. *Int. J. Greenh. Gas Control* **2018**, *78*, 286–305. [CrossRef]
111. Arshadi, M.; Taghvaei, H.; Abdolmaleki, M.; Lee, M.; Eskandarloo, H.; Abbaspourrad, A. Carbon dioxide absorption in water/nanofluid by a symmetric amine-based nanodendritic adsorbent. *Appl. Energy* **2019**, *242*, 1562–1572. [CrossRef]
112. Wang, T.; Yu, W.; Liu, F.; Fang, M.; Farooq, M.; Luo, Z. Enhanced CO_2 absorption and desorption by monoethanolamine (MEA)-based nanoparticle suspensions. *Ind. Eng. Chem. Res.* **2016**, *55*, 7830–7838. [CrossRef]
113. Wang, T.; Yu, W.; Fang, M.; He, H.; Xiang, Q.; Ma, Q.; Xia, M.; Luo, Z.; Cen, K. Wetted-wall column study on CO_2 absorption kinetics enhancement by additive of nanoparticles. *Greenh. Gases Sci. Technol.* **2015**, *5*, 682–694. [CrossRef]
114. Irani, V.; Maleki, A.; Tavasoli, A. CO_2 absorption enhancement in graphene-oxide/MDEA nanofluid. *J. Environ. Chem. Eng.* **2019**, *7*, 102782. [CrossRef]
115. Park, S.-W.; Choi, B.-S.; Lee, J.-W. Effect of elasticity of aqueous colloidal silica solution on chemical absorption of carbon dioxide with 2-amino-2-methyl-1-propanol. *Korea Aust. Rheol. J.* **2006**, *18*, 133–141.
116. Rahimi, K.; Riahi, S.; Abbasi, M. Effect of host fluid and hydrophilicity of multi-walled carbon nanotubes on stability and CO_2 absorption of amine-based and water-based nanofluids. *J. Environ. Chem. Eng.* **2020**, *8*, 103580. [CrossRef]
117. Taheri, M.; Mohebbi, H.A.; Hashemipour, H.; Rashidi, A. Simultaneous absorption of carbon dioxide (CO_2) and hydrogen sulfide (H2S) from CO_2–H_2S–CH_4 gas mixture using amine-based nanofluids in a wetted wall column. *J. Nat. Gas Sci. Eng.* **2016**, *28*, 410–417. [CrossRef]
118. Pashaei, H.; Ghaemi, A.; Nasiri, M.; Heydarifard, M.; Heydarifaed, M. Experimental investigation of the effect of nano heavy metal oxide particles in piperazine solution on CO_2 absorption using a stirrer bubble column. *Energy Fuels* **2018**, *32*, 2037–2052. [CrossRef]
119. Li, S.H.; Ding, Y.; Zhang, X.S. Enhancement on CO_2 bubble absorption in MDEA solution by TiO_2 nanoparticles. *Adv. Mater. Res.* **2013**, *631*, 127–134.

120. Elhambakhsh, A.; Keshavarz, P. Investigation of carbon dioxide absorption using different functionalized Fe3O4 magnetic nanoparticles. *Energy Fuels* **2020**, *34*, 7198–7208. [CrossRef]
121. Jiang, Y.; Zhang, Z.; Fan, J.; Yu, J.; Bi, D.; Li, B.; Zhao, Z.; Jia, M.; Mu, A. Experimental study on comprehensive carbon capture performance of TETA-based nanofluids with surfactants. *Int. J. Greenh. Gas Control* **2019**, *88*, 311–320. [CrossRef]
122. Elhajj, J.; Al-Hindi, M.; Azizi, F. A review of the absorption and desorption processes of carbon dioxide in water systems. *Ind. Eng. Chem. Res.* **2014**, *53*, 2–22. [CrossRef]
123. Ma, X.; Su, F.; Chen, J.; Bai, T.; Han, Z. Enhancement of bubble absorption process using a CNTs-ammonia binary nanofluid. *Int. Commun. Heat Mass Transf.* **2009**, *36*, 657–660. [CrossRef]
124. Periasamy, S.M.; Baskar, R. Assessment of the influence of graphene nanoparticles on thermal conductivity of graphene/water nanofluids using factorial design of experiments. *Period. Polytech. Chem. Eng.* **2018**, *62*, 317–322. [CrossRef]
125. Darabi, M.; Rahimi, M.; Dehkordi, A.M. Gas absorption enhancement in hollow fiber membrane contactors using nanofluids: Modeling and simulation. *Chem. Eng. Process. Process Intensif.* **2017**, *119*, 7–15. [CrossRef]
126. Kim, J.-K.; Park, C.W.; Kang, Y.T. The effect of micro-scale surface treatment on heat and mass transfer performance for a falling film H2O/LiBr absorber. *Int. J. Refrig.* **2003**, *26*, 575–585. [CrossRef]
127. Samadi, Z.; Haghshenasfard, M.; Moheb, A. CO_2 absorption using nanofluids in a wetted-wall column with external magnetic field. *Chem. Eng. Technol.* **2014**, *37*, 462–470. [CrossRef]
128. Jorge, L.; Coulombe, S.; Girard-Lauriault, P.-L. Nanofluids containing MWCNTs coated with nitrogen-rich plasma polymer films for CO_2 absorption in aqueous medium. *Plasma Process. Polym.* **2015**, *12*, 1311–1321. [CrossRef]
129. Salimi, J.; Salimi, F. CO_2 capture by water-based Al_2O_3 and Al_2O_3-Si, O_2 mixture nanofluids in an absorption packed column. *Rev. Mex. Ing. Química* **2016**, *15*, 185–192.
130. Ghasem, N. Modeling and simulation of CO_2 absorption enhancement in hollow-fiber membrane contactors using CNT–water-based nanofluids. *J. Membr. Sci. Res.* **2019**, *5*, 295–302.
131. Rezakazemi, M.; Darabi, M.; Soroush, E.; Mesbah, M. CO_2 absorption enhancement by water-based nanofluids of CNT and SiO_2 using hollow-fiber membrane contactor. *Sep. Purif. Technol.* **2019**, *210*, 920–926. [CrossRef]
132. Hafizi, A.; Rajabzadeh, M.; Khalifeh, R. Enhanced CO_2 absorption and desorption efficiency using DETA functionalized nanomagnetite/water nano-fluid. *J. Environ. Chem. Eng.* **2020**, *8*, 103845. [CrossRef]
133. Esmaeili-Faraj, S.H.; Esfahany, M.N. Absorption of hydrogen sulfide and carbon dioxide in water based nanofluids. *Ind. Eng. Chem. Res.* **2016**, *55*, 4682–4690. [CrossRef]
134. Elhambakhsh, A.; Zaeri, M.R.; Mehdipour, M.; Keshavarz, P. Synthesis of different modified magnetic nanoparticles for selective physical/chemical absorption of CO_2 in a bubble column reactor. *J. Environ. Chem. Eng.* **2020**, *8*, 104195. [CrossRef]
135. Karamian, S.; Mowla, D.; Esmaeilzadeh, F. The effect of various nanofluids on absorption intensification of CO_2/SO_2 in a single-bubble column. *Processes* **2019**, *7*, 393. [CrossRef]
136. Lee, J.S.; Lee, J.W.; Kang, Y.T. CO_2 absorption/regeneration enhancement in DI water with suspended nanoparticles for energy conversion application. *Appl. Energy* **2015**, *143*, 119–129. [CrossRef]
137. Ansaripour, M.; Haghshenasfard, M.; Moheb, A. Experimental and numerical investigation of CO_2 absorption using nanofluids in a hollow-fiber membrane contactor. *Chem. Eng. Technol.* **2017**, *41*, 367–378. [CrossRef]
138. Choi, I.D.; Lee, J.W.; Kang, Y.T. CO_2 capture/separation control by SiO_2 nanoparticles and surfactants. *Sep. Sci. Technol.* **2014**, *50*, 772–780. [CrossRef]
139. Manikandan, S.P.; Sundar, G.D.; Perumal, C.C.; Aminudin, U. CO_2 absorption using TiO_2 nanoparticle suspended water solvent in a packed bed absorption column. *Int. J. Appl. Innov. Eng. Manag.* **2019**, *8*, 51–55.
140. Budzianowski, W.M. *Energy Efficient Solvents for CO_2 Capture by Gas-Liquid Absorption: Compounds, Blends and Advanced Solvent Systems*; Springer: Berlin/Heidelberg, Germany, 2016.
141. Pineda, I.T.; Lee, J.W.; Jung, I.; Kang, Y.T. CO_2 absorption enhancement by methanol-based Al_2O_3 and SiO_2 nanofluids in a tray column absorber. *Int. J. Refrig.* **2012**, *35*, 1402–1409. [CrossRef]
142. Pang, C.; Jung, J.-Y.; Lee, J.W.; Kang, Y.T. Thermal conductivity measurement of methanol-based nanofluids with Al_2O_3 and SiO_2 nanoparticles. *Int. J. Heat Mass Transf.* **2012**, *55*, 5597–5602. [CrossRef]

applied sciences

MDPI

Article

Thermal Performance Evaluation of a Tubular Heat Exchanger Fitted with Combined Basket–Twisted Tape Inserts

Hayder Q. A. Khafaji [1], Hasanain A. Abdul Wahhab [2], Sajda S. Alsaedi [2], Wisam Abed Kattea Al-Maliki [2,3], Falah Alobaid [3,*] and Bernd Epple [3]

[1] Department of Electromechanical Engineering, University of Technology-Iraq, Baghdad 19006, Iraq; 50092@uotechnology.edu.iq
[2] Mechanical Engineering Department, University of Technology-Iraq, Baghdad 19006, Iraq; 20085@uotechnology.edu.iq (H.A.A.W.); sajda.s.alsaedi@uotechnology.edu.iq (S.S.A.); wisam.a.kattea@uotechnology.edu.iq (W.A.K.A.-M.)
[3] TU Darmstadt, Institut Energiesysteme und Energietechnik, Otto-Berndt-Straße 2, 64287 Darmstadt, Germany; bernd.epple@est.tu-darmstadt.de
* Correspondence: falah.alobaid@est.tu-darmstadt.de; Tel.: +49-6151-16-6691; Fax: +49-6151-16-5685

Abstract: Features of the tubular type of heat exchanger were examined experimentally in the current study. A rig is fitted with a novel insert as a negative heat transfer increase technique. The core fluid used is air under steady heat flux and a turbulent discharge state ($6000 \leq Re \leq 19{,}500$) conditions. Two heat transfer augmentation inserts are employed; one is the basket turbulators utilized as a turbulator and placed inside the heat exchanger with a constant pitch ratio (PR = 150 mm), and the other is the basket turbulators together with twisted tape that are installed at the core of the basket turbulators. The measurements illustrated that the Nusselt number (*Nu*) was found to be higher by about 131.8%, 169.5%, 187.7%, and 206.5% in comparison with the plain heat exchanger for basket turbulators and the combined basket–twisted tape inserts with y/w = 6, 3, and 2, respectively. The highest thermal efficiency factor of the increased tubular heat exchanger is 1.63 times more elevated than that of the simple heat exchanger on average, due to a binary basket-quirky strip for a twisting percentage y/w equal to 2 under steady pumping energy. Further, practical correlations for the Nusselt number, as well as friction characteristics, were established and presented.

Keywords: heat transfer enhancement; binary basket–twisted strip inserts; friction characteristics; thermal performance characteristics; turbulent flow

Citation: Khafaji, H.Q.A.; Abdul Wahhab, H.A.; Alsaedi, S.S.; Al-Maliki, W.A.K.; Alobaid, F.; Epple, B. Thermal Performance Evaluation of a Tubular Heat Exchanger Fitted with Combined Basket–Twisted Tape Inserts. *Appl. Sci.* **2022**, *12*, 4807. https://doi.org/10.3390/app12104807

Academic Editor: Luisa F. Cabeza

Received: 29 March 2022
Accepted: 5 May 2022
Published: 10 May 2022

1. Introduction

Owing to the growing energy costs and manufacturing materials, researchers have given significant attention to building up efficient, compact, and economical thermal systems for different engineering applications such as nuclear reactors, chemical processing industries, solar heaters, etc. A highly efficient thermal system comes with augmented heat transfer using passive, active, or a combination of multiple passive or active techniques. The primary goals of these strategies are to increase the thermal efficiency of the existing systems whilst also actually reducing their size, weight, and operating costs. Consequently, the suitable design of these approaches constitutes a difficult problem in order to achieve heat transfer optimisation at reasonable increase in frictional forces. Using a passive strategy based on introducing turbulators in the flow route as augmentations, such as helical inserts [1,2], it was found that with increasing pitch, vortex shedding frequencies also rise, and that the highest amplitude of the vortex generated by conical-ring turbulators occurred at low pitches. It is discovered that the Nu number grows with rising Re number, and the optimum heat transfer is reached for the arrangement with the smallest pitch, for corrugated and grooved geometries [3–5]. As the pitch length is increased, the frequency of vortex shedding is also observed to rise, and the peak amplitude of vortex generated by

conical-ring turbulators occurs at small pitches. Findings were made to show increasing Nu with rising Re, and maximum heat transfer is achieved at the minimum pitch configuration for ribbed and grooved geometries [3–5]. The dimensions of the grooves, the rotational speed, and the axial velocity of the fluid show a significant impact on their heat transfer. The results of vortex generators [6,7] show that increases in distance between two vortex generators increase the mean Nusselt number, and other types of turbulators [8–10] are commonly used to improve heat transfer inside thermal systems due to the simple manufacturing process, easily employed compared to the active technique. Employing conical-ring turbulators at three-pitch ratios (PR) 2, 3, and 4, Ibrahim et al. [11] demonstrated augmentations of 330, 419, and 765 percent, respectively. They also discovered that using the diverging conical-ring with a smaller setup can increase the enhancement effectiveness by 1.291 (PR). Xu et al. [12] examined the effect of winglet vortex generators on a horizontal circular tube in a forced convection setting with a Re number range of 6000–34,000. They concluded that winglet tensor flow with a pitch ratio of 1.6, a barrier ratio of 0.3, and an attack angle of 45° boosted the heat transfer rate by up to 4.88 times under constant heat flux conditions. The perforated inserts are usually used to generate strong turbulence/vortex flows, which helps further improvement of turbulence intensity with reasonable increment in pressure loss. Chamoli et al. [13] performed an investigation of the perforated vortex generators' influences on forced convection in a circular tube. They observed that the perforated insert improves the thermal performance by 1.65 times under constant pumping power conditions. In comparison with the conventional conical-ring, Nakhchi et al. [14] claimed that the recirculation flow by holes of perforated conical-rings with varying geometrical characteristics can improve the heat transfer rate by about 35.48% and decrease the pressure loss by about 88.06%. Attempts to enhance thermal efficiency took place by utilising the advantages of twisted-tape swirl generator inserts as cross hollow twisted-tape [15]. A plain tube's experimental data are compared to the standard validation. With the increase in the hollow width from 6 mm to 10 mm, the Nu number and friction factor (f) subsequently increase. Compared to the flat tube, Nu and f increase by 93 percent–120 percent and 883 percent–1042 percent, respectively, for the 6 mm hollow width rise. Perforated double and triple counter twisted-tape [16,17] evaluated the impacts of perforated double and triple-counter twisted-tapes on heat transmission and fluid friction properties in a heat exchanger tube. Except for 1.2 percent porosity, the measurements showed that the Nu, f, and thermal enhancement efficiency improved with porosity reduction. The findings also demonstrated better heat transfer of the tape-fitted tube, accompanied by a consequent rise in the f. The thermohydraulic features inside the heat exchanger tube inserted with multiple-twisted-tapes [18]. The measurements revealed a signed rise in heat transfer and f in comparison with single-twisted tape, compound-twisted tape, and twisted tube [19]. An effort to examine the thermo-fluidic transportation capability of a laminar flow passing through tubular-heat exchangers utilizing a composite design consisting of the combination of twisted-tapes and twisted-tubes. The results show that raising the twist-pitch and Re improves the total efficiency with twisted-tape with rectangular-cut [20]. Nu numbers in a tube with a rectangular-cut twisted-tape insert increased 2.3–2.9 times while f increased 1.4–1.8 times to a smooth tube with perforated helical twisted-tapes [21]. The testing findings show that using perforated helical twisted-tapes reduces friction loss when compared to helically twisted-tape and helical screw-tape [22]. Heat transfer properties and f were tested on helical screw elements with variable twisted ratios and helical screw inserts with various pitch lengths. The research reveals that the total Nu and f reduce as the spacer length or twisted ratio increases for flat tube, spiral ribs, and twisted-tapes [23]. The findings of V-Shape twisted jaw [24] reveal in excess of unity thermal power factor readings with an increasing trend as the number of turbulators increases, demonstrating the practicality of employing these turbulators realistically. For the tube with punched delta-winglet vortex generators [25], a better temperature distribution is obtained, resulting in a better temperature gradient than that obtained with the smooth tube. It was also discovered that, as the attack angle increases, the temperature distribution also follows a trend towards a rel-

atively homogenous temperature profile, and tape inserts combined with cables nails [26]. Prior research indicated that the twisted-tape swirl generator has excellent heat transfer performance by producing strong swirling flow and that the perforated twisted-tape was helpful in lowering pressure loss. However, according Promvonge et al. [27], a composite heat transfer enhancement achieved by combining various heat transfer augmentation approaches may be used to provide an augmentation that improves the thermal performance of either of the procedures functioning independently. They discovered that using a conical-ring and twisted-tape with a twisted ratio TR = 3.75 increases the enhancement efficiency by 1.96 times. Eiamsa et al. [28] offered another experimental research to clarify the impact of the combination insert of regularly/constant wire coil pitch ratio and the twisted-tape on thermal performance behaviours. According to the findings, combining inserts with decreasing coil pitch ratios can boost enhancement efficiency by up to 1.25 times.

Kurnia et al. [29,30] summarized the contribution of entropy production due to both heat transfer and viscous dissipation, in addition to the Bejan number over different twisted band designs, and found that helical tubes having twisted-tape inserts exhibit poorer heat entropy production compared to tubes without. This suggests that for heat transfer equipment, a helical tube with a twisted-tape insert appears to be more effective. The augmentation of heat transmission by various types of inserts, as described in the preceding literature, is largely reliant on the designs and geometries of the inserts. In light of this, it is created a novel design of inserts (basket turbulators) to improve a tubular heat exchanger. When compared to a heat exchanger without inserts, basket turbulators with a spacing ratio of 4.2 can increase heat transfer rate by 115.9 percent, according to their research. The analysis of the work [31] indicates promising findings on the problem of heat transfer augmentation and inspires the current effort to extend the research using basket turbulators in conjunction with twisted-tapes swirl generators placed inside a circular tube under the same operating circumstances. The compound augmentation is supposed to provide a high heat transfer rate by introducing swirl flow and significant fluctuation. As a result, the thermal performance, heat transfer, and friction losses of a tubular heat exchanger coupled with compound augmentation, i.e., basket turbulators with twisted-tapes swirl generator with three twist ratios (y/w = 2, 3, and 6) are investigated experimentally in the current work. There is no evidence of such coupled augmentations in the literature. The experiments were divided into three parts: a study of the thermal performance, heat transfer rate, and friction losses of the basket turbulators in a turbulent flow regime ($6000 \leq Re \leq 19{,}500$) under constant heat flux, the introduction of a novel compound augmentation, and the development of empirical correlations to predict the rate of heat transfer and friction losses. Therefore, the novelty of the current paper is carrying out an experimental study on novel inserts using basket turbulators with twisted-tapes swirl generators.

2. Experimental Apparatus Description

To perform the experiments, an open-loop experimental apparatus located in a normal environment (1 atm) is used. The experimental apparatus is shown by the photographic view and schematic diagram in Figures 1 and 2. The experimental setup mainly consists of a tubular heat exchanger, augmentation inserts, a data collection method, and measurement devices. The heat exchanger is built of an aluminium conduit with an outside diameter of 5 cm, an inner diameter of 4.5 cm, a thick of 0.25 cm, and a length of 13.50 cm. Figure 3 shows the geometric configurations of the tubular heat exchanger, basket turbulators, and twisted-tapes inserts. The twisted-tapes are made of galvanized iron and have twist ratios of TR = 2, 3, and 6 (w = 1.5 cm, y = 3–9 cm). Five pieces of basket turbulators, which are made from the iron bar, are used in this experiment with a constant distance between them (PR = 150 mm). The basket turbulators are inserted into the heat exchanger in a wall-attached position, and the twisted tapes are tightly fitted into the centre of the basket turbulators. The heat exchanger is Ohmically heated using continuously whining flexible nickel–chrome wire to obtain a boundary condition with a homogeneous heat flux. A voltage regulator is applied

to regulate the input power and automatically maintain the heat flux within acceptable limits along with the heat exchanger. Twenty-two calibrated thermocouples (type k) with a temperature range from −58 to 1298 °C are used in positions which are eighteen thermocouples installed along the heat exchanger's wall to determine the distribution of the wall temperature. To acquire the bulk air temperature, four thermocouples are fitted in the input and exit sections. Table 1 shows the placement of the thermocouple along the heat exchanger. All thermocouples are linked to a selection switch, which is subsequently linked to a multi-channel digital data logger system. The exterior surface of the heat exchanger was thermally insulated by an asbestos layer and a fibreglass sheet to reduce heat loss.

Figure 1. Photographic view of the using experimental apparatus.

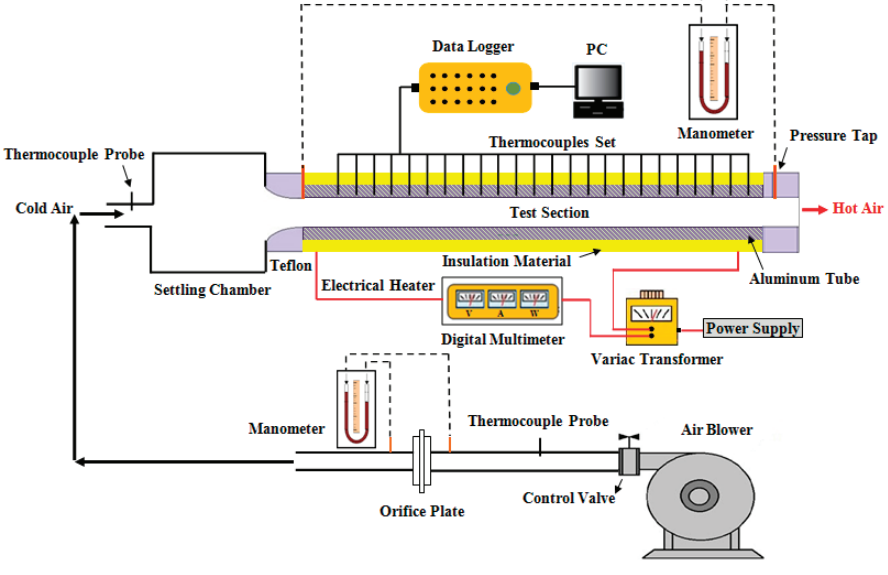

Figure 2. Schematic of the using experimental apparatus.

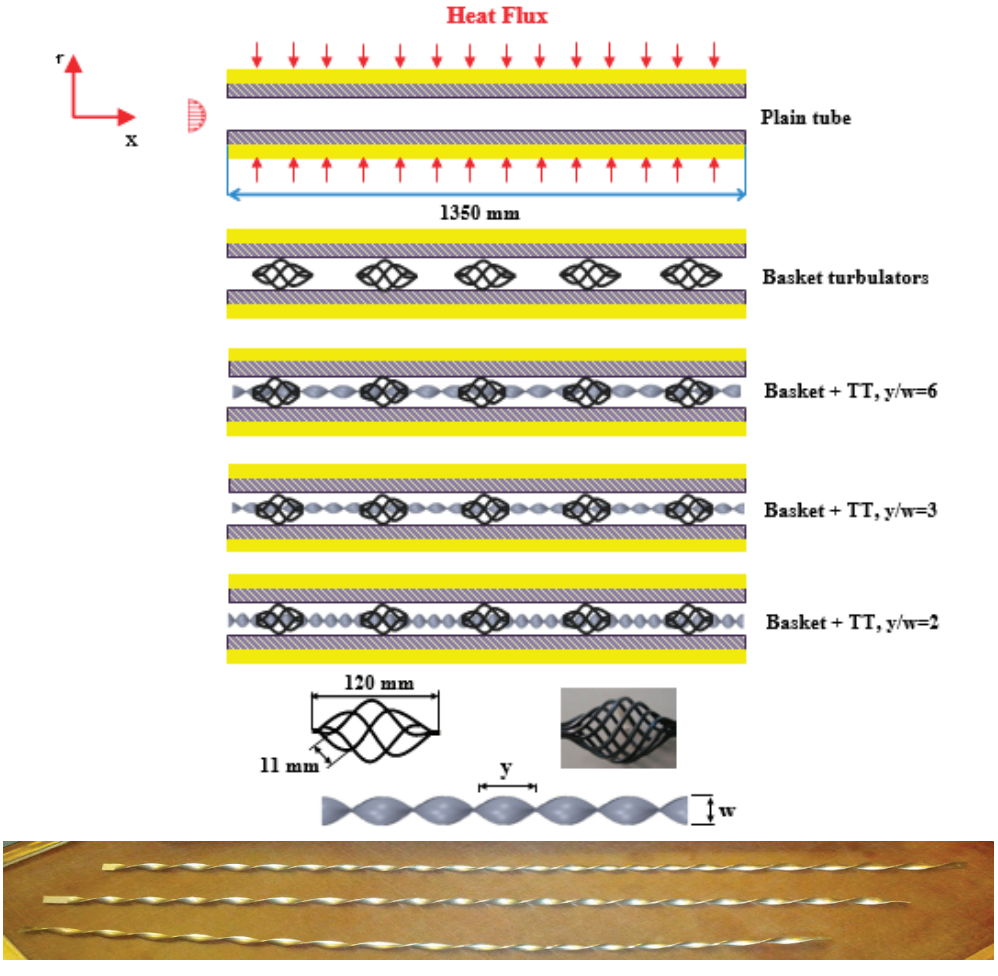

Figure 3. Geometric configurations of twisted tapes.

Table 1. Thermocouple's location.

No.	1	2	3	4	5	6	7	8	9	10	11	12	13	14	15	16	17	18
Position-x-(mm)	10	20	30	50	70	90	130	170	230	290	380	470	570	670	770	900	1040	1180

3. Governing Equations

In this experiment, air supplied by an electrical blower serves as the working fluid and is circulated through the heat exchanger. In a steady-state instance, the net heat energy transmitted from the electrical heater to the air through the heat exchanger wall was calculated as Equation (1), whereas real heat was specified as follows [31,32]:

$$Q_{net} = V_{input} \cdot I_{input} - Q_{ls.}; \quad (1)$$

$$Q_{actual} = \frac{Q_{net} + Q_{con.}}{2}; \quad (2)$$

where:

$$Q_{con.} = \dot{m}_a \cdot C_{p,a} \cdot (T_{b,o} - T_{b,i}); \quad (3)$$

Based on Equation (2), the mean rate of heat transfer is denoted as:

$$\overline{h} = \frac{Q_{actual}}{A_{tt} \cdot (T_{av,w} - T_b)}; \quad (4)$$

where $T_{av,w}$, T_b are the air bulk temperature and average wall temperature, respectively, which are obtained as follows [32]:

$$T_b = \frac{(T_{b,o} + T_{b,i})}{2}; \quad (5)$$

$$T_{av,w} = \frac{\sum_{i=1}^{18} T_{wi}}{18}; \quad (6)$$

The (Nu) mean is defined as below [29]:

$$Nu_d = \frac{h \cdot D_h}{k_a}; \quad (7)$$

The (Re) can be expected as below:

$$Re = \frac{U \cdot D_h}{\nu_a}; \quad (8)$$

Friction factor (f) is estimated as follows:

$$f = \frac{\Delta P}{\left(\frac{L}{D}\right)\left(\frac{\rho U^2}{2}\right)}; \quad (9)$$

Enhancement efficiency (ξ) was calculated as follows for a constant pumping power [33]:

$$\xi = \frac{h}{h_0} = \frac{Nu}{Nu_0} = \left(\frac{Nu}{Nu_0}\right)\left(\frac{f}{f_0}\right)^{-1/3} \quad (10)$$

4. Error Analysis and Uncertainties of Experimental Data

The experimental data are always subjected to a certain level of uncertainty due to the errors in the measuring devices. Based on the ANSI/ASME standard [34], the approach proposed by McClintock and Kline [35], the uncertainty of experimental measurements is determined by the following equations.

$$\left(\frac{\Delta Nu}{Nu}\right) = \sqrt{\frac{1}{Nu}\left[\left(\frac{\partial}{\partial \overline{h}}(Nu)\Delta\overline{h}\right)^2 + \left(\frac{\partial}{\partial D_h}(Nu)\Delta D_h\right)^2 + \left(\frac{\partial}{\partial k}(Nu)\Delta k\right)^2\right]} \quad (11)$$

$$\left(\frac{\Delta \overline{h}}{\overline{h}}\right) = \sqrt{\frac{1}{\overline{h}}\left[\left(\frac{\partial}{\partial q}\left(\overline{h}\right)\Delta q\right)^2 + \left(\frac{\partial}{\partial T_w}\left(\overline{h}\right)\Delta T_w\right)^2 + \left(\frac{\partial}{\partial T_b}\left(\overline{h}\right)\Delta T_b\right)^2\right]} \quad (12)$$

Reynolds number:

$$\left(\frac{\Delta Re}{Re}\right) = \sqrt{\frac{1}{Re}\left[\left(\frac{\partial}{\partial u}(Re)\Delta(u)\right)^2 + \left(\frac{\partial}{\partial \rho}(Re)\Delta\rho\right)^2 + \left(\frac{\partial}{\partial D_h}(Re)\Delta D_h\right)^2 + \left(\frac{\partial}{\partial \mu}(Re)\Delta\mu\right)^2\right]} \quad (13)$$

Friction factor:

$$\left(\frac{\Delta f}{f}\right) = \sqrt{\frac{1}{f}\left[\left(\frac{\partial}{\partial \Delta P}(f)\Delta(\Delta P)\right)^2 + \left(\frac{\partial}{\partial L}(f)\Delta L\right)^2 + \left(\frac{\partial}{\partial D_h}(f)\Delta D_h\right)^2 + \left(\frac{\partial}{\partial Re}(f)\Delta Re\right)^2\right]} \quad (14)$$

The greatest uncertainties for the *Nu*, *Re*, and *f* were determined as 4.12 percent, 1.85 percent, and 3.6 percent, respectively. Table 2 lists the accuracy values of measuring instruments.

Table 2. Accuracy of Measurement Instruments.

Measured Parameters	Value
Temperature	± 0.5 °C
Air velocity	±0.75 m/s
Current of the heater	±0.0003 Amp
Voltage of the heater	0.04 Vol

5. Results

5.1. Confirmation of the Plain Heat Exchanger Findings

The findings of the linked experiment's heat transfer were referred to as the (*Nu*), while the results of the friction losses were referred to as the (*f*). Prior to conducting the tests, the *Nu* and *f* values of the heat exchanger without inserts were recorded and verified to assess the reliability of the measurement and test equipment over the entire test range. The *Nu* and *f* findings were compared to previous empirical correlations of Promvonge [27] for *Nu* number and Blasius [36] and Petkhov [37] for f under comparable conditions, as shown in Figures 4 and 5, respectively. These findings show that the *Nu* and *f* values match well to values derived from prior empirical correlations available within 5.4 percent and 4.47 percent, respectively.

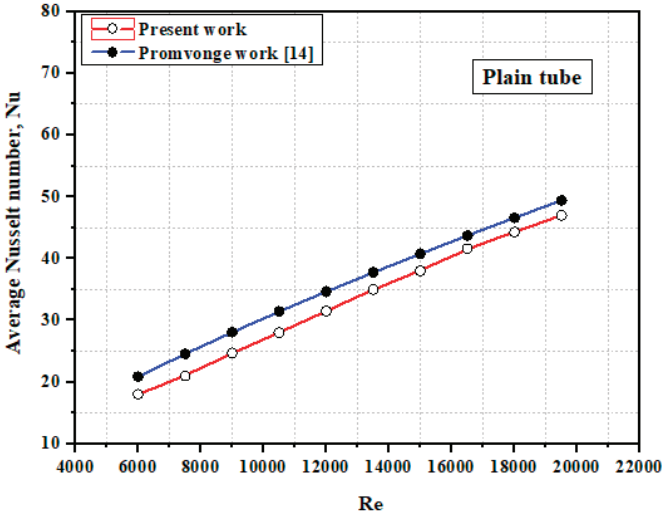

Figure 4. Confirmation of Nusselt number for plain heat exchanger.

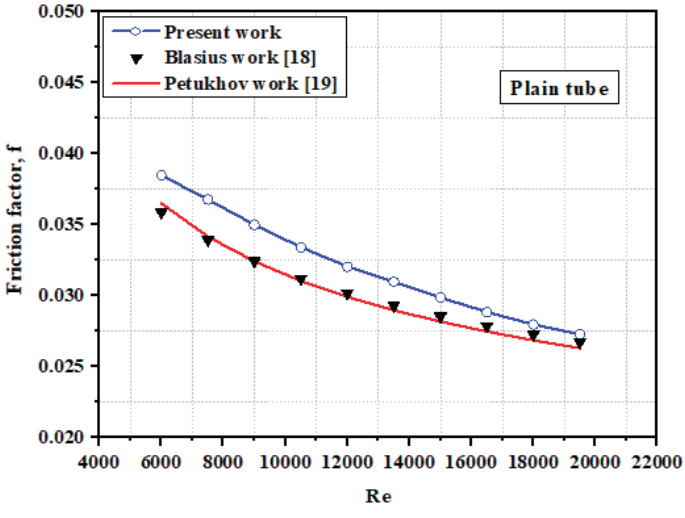

Figure 5. Confirmation of friction factor for plain heat exchanger.

5.2. Impact of Combined Basket–Twisted Tape Inserts

Figure 6 depicts the impact of the basket and combination basket–twisted tape inserts on heat transfer rate. The average *Nu* and *Re* numbers were noted to be directly related to each other. This might be related as the turbulence intensity goes up with rising *Re*, which resulted in an increase in convective heat transfer. The use of basket turbulators alone resulted in a considerable increase in heat transmission rate with variation in Re. The average *Nu* of the basket turbulators was found to be around 131.8 percent greater than that of the ordinary heat exchanger for constant pitch ratio (PR = 150 mm). The reason for this might be related to the heat exchanger creating a spiral or secondary flow with relatively high turbulent intensity, which leads to the disruption and reintegration of the thermal boundary layer, which further improves the convection heat transfer and momentum process. Using twisted-tape in combination with basket turbulators results in stronger swirl flow around the core region and more mixing occurring within the heat exchanger core and the wall region, which is why the average *Nu* is higher than that of basket turbulators alone. Figure 6 shows that when the combined basket–twisted tape is introduced with a rising *Re* number and decreasing twist ratio, the average Nusselt number increases. Due to the increased turbulence intensity and longer flow length with a low twist ratio (y/w = 2), the greatest heat transfer rate was attained. The average *Nu* of the combined basket–twisted tape inserts was increased by 169.5 percent, 187.7 percent, and 206.5 percent for y/w = 6, 3, and 2, respectively, when compared to the simple heat exchanger. Figure 7 depicts the fluctuation of the *f* with the Re number. The employment of basket and coupled basket–twisted tape inserts results in an extra pressure loss when compared to the basic heat exchanger, as predicted. The dissipation of dynamic pressure owing to increased forces generated by swirling flow, as well as the increase in air contact surface area induced by the presence of basket–twisted tape inserts, account for a major portion of the pressure loss. The *f* of basket turbulators can be up to three and a half times that of a conventional heat exchanger, while the variation in friction factors induced by differing twist ratios might be up to 5–6.5 times greater.

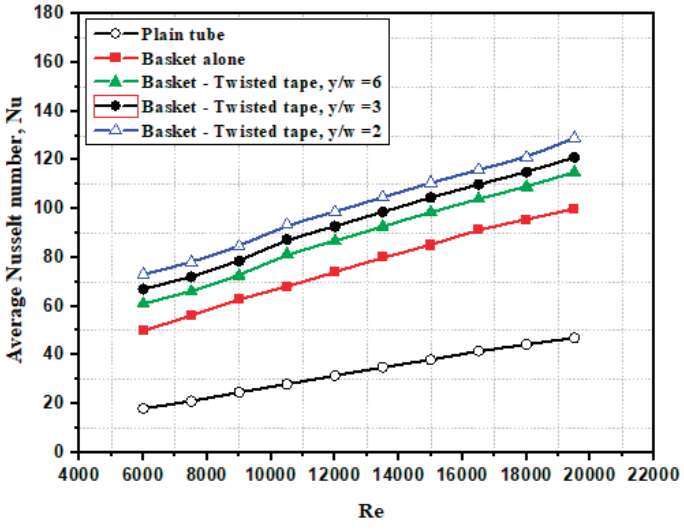

Figure 6. Difference of Nusselt number and Re number for heat exchanger trim by basket alone and combined basket–twisted tape inserts.

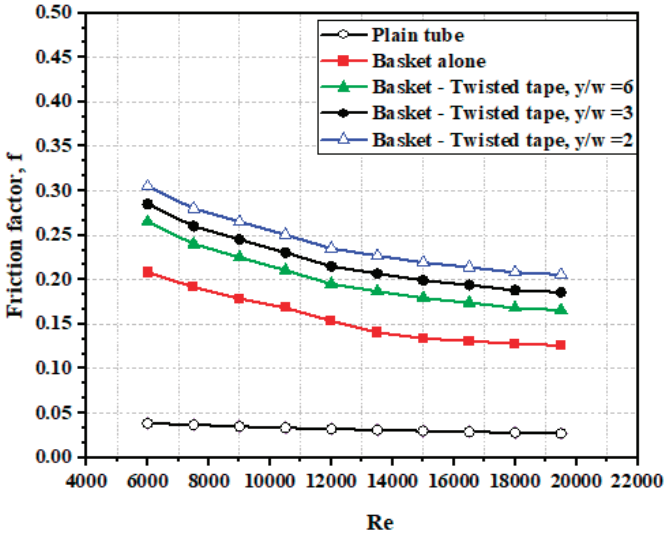

Figure 7. Difference of friction factor with and Reynolds number for heat exchanger trim by basket alone and combined basket–twisted tape inserts.

5.3. Thermal Performing Assessment

Figure 8 illustrates the fluctuation of thermal performance factor (ξ), computed by Equation (10), with Re number. It is evident that the thermal efficiency reduces with the rising Re number and increases with the use of basket and combination basket–twisted tape inserts, notably in the 6000–12,000 *Re* number range. It is worth mentioning that the case of combined basket–twisted tape with a modest twist ratio outperforms those with a greater twist ratio and the case of basket alone in terms of thermal performance. Figure 9 compares all of the evaluated instances and their influence on the thermal performance factor. When

basket and combination basket–twisted tape inserts with N = 5 and y/w = 6, 3, and 2 are used, the average thermal performance factor is 1.40, 1.49, 1.56, and 1.63 times, respectively.

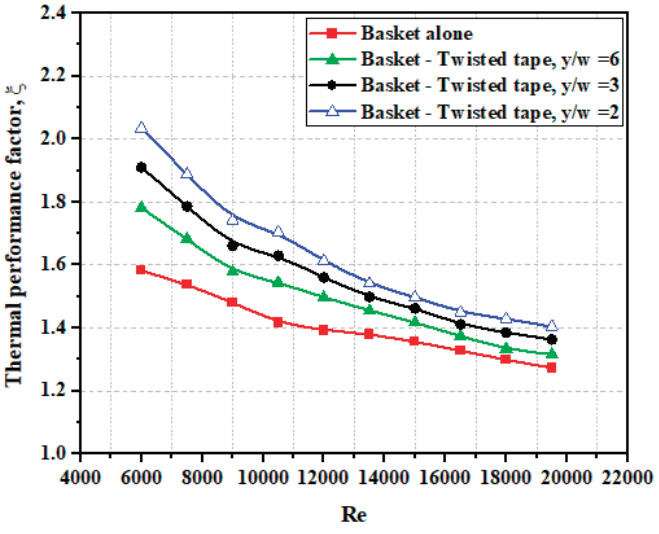

Figure 8. Variation of thermal performance factor with Reynolds number for heat exchanger fitted with basket alone and combined basket–twisted tape inserts.

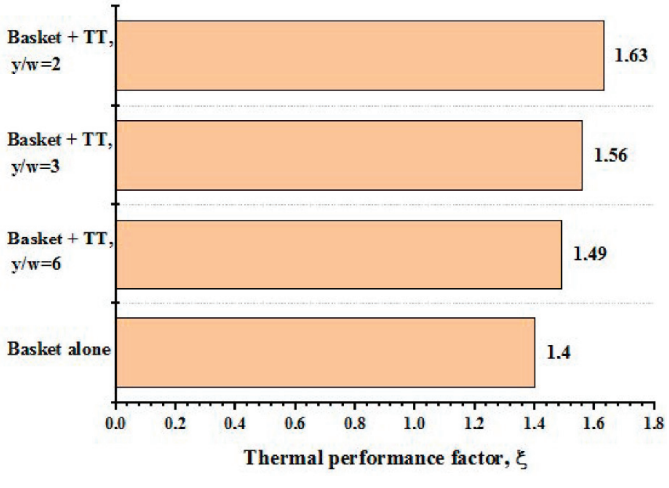

Figure 9. Percentage of thermal performance factor enhancement.

5.4. Empirical Correlations

Using coupled basket–twisted tape inserts with y/w = 6, 3, and 2, empirical correlations were generated for turbulent flow regimes with Re numbers ranging between 6000–19,500. The *Nu* and *f* of the plain heat exchanger were correlated based on the experimental results and are provided below in Equations (15) and (16), respectively [37,38].

$$Nu = 0.0158Re^{0.825}Pr^{0.4} \quad (15)$$

$$f = 0.5229Re^{-0.298} \quad (16)$$

Correlations depending on (*Re*), (*Re*), Prandtl number (*Pr*), number of basket inserts (N), and twist ratio (y/w) were suggested for the case of combined basket–twisted tape inserts as follows [37,38]:

$$Nu = 0.11618 Re^{0.625} Pr^{0.4} \mathrm{N}^{0.541} (\mathrm{y/w})^{-0.011} \quad (17)$$

$$f = 0.6284 Re^{-0.285} \mathrm{N}^{0.99} (\mathrm{y/w})^{-0.0001} \quad (18)$$

The predicted values of the *Nu* were found to be within 7.2 percent of the experimental data for the average *Nu*, as shown in Figure 10.

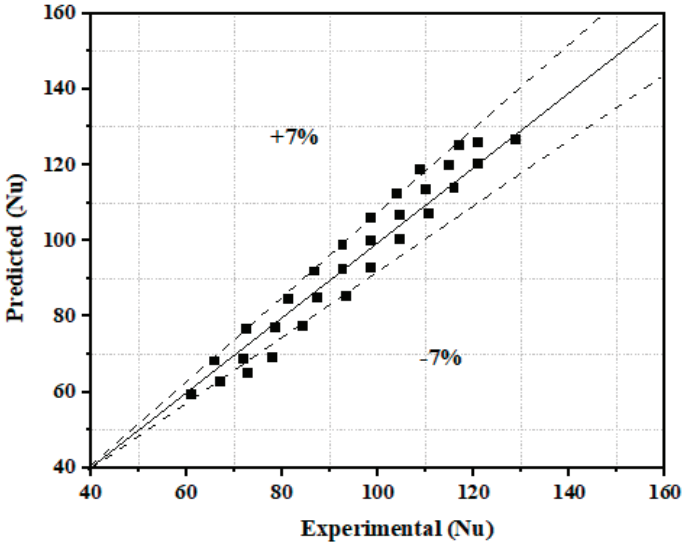

Figure 10. Expected data of Nu vs. trial data.

6. Conclusions

The heat transfer and pressure drops of a circular heat exchanger with a basket and combined basket–twisted inserts are investigated using three types of twist ratios (TR = 2, 3, and 6) in a turbulent flow condition with Re values varying between 6000–19,500. The experimental findings show that using combination basket–twisted tape inserts generates greater heat transfer rates than using a basket alone in a heat exchanger.

For y/w = 6, 3, and 2, the greatest rate of heat transfer attained by utilizing the combination basket–twisted tape improved by 169.5, 187.7, and 206.5 percent, respectively, as compared to the simple heat exchanger. For y/w = 6, 3, and 2, the thermal performance factor attained by employing the combination basket–twisted tape inserts improved by 1.49, 1.56, and 1.63 times, respectively, in comparison with the simple heat exchanger.

Author Contributions: Data curation, H.Q.A.K., S.S.A. and F.A.; Formal analysis, S.S.A. and W.A.K.A.-M.; Investigation, H.Q.A.K., H.A.A.W. and S.S.A.; Methodology, H.A.A.W. and W.A.K.A.-M.; Supervision, B.E.; Visualization, H.A.A.W. and F.A.; Writing—original draft, H.Q.A.K. and W.A.K.A.-M. All authors have read and agreed to the published version of the manuscript.

Funding: This research received no external funding.

Acknowledgments: We acknowledge support by the Deutsche Forschungsgemeinschaft (DFG) German Research Foundation and the Open Access Publishing Fund of the Technical University of Darmstadt. The authors would like to also thank the University of Technology- Iraq.

Conflicts of Interest: The authors declare no conflict of interest.

Nomenclature

A_{tt}	Inner Surface Area of tube Test Section, m^2
$C_{p\cdot a}$	Specific Heat of Air, J/kg.K
D	Hydraulic Diameter, m
f	Friction Factor
$\dot{\mathbf{h}}$	Coefficient of Heat Transfer, W/m2.K
I	Current, A
V	Voltage, volt
K_a	Thermal Conductivity, W/m.K
L	Length of Tube Test Section, m
$\dot{\mathbf{m}}_a$	Air Mass Flow Rate, kg/s
N	Number of Turbulators pieces
Nu_d	Average Nusselt Number of Plain tube Case
Pr	Prandtl Number
$\mathbf{Q_{los}}$	Heat losses, W
$\mathbf{Q_{con.}}$	Convective Heat Transfer from the Test Section, W
Re	Reynolds Number
$T_{b,I}$	Temperature of Air at the Test Section Entrance, °K
$T_{b,o}$	Temperature of Air at the Test Section Exit, °K

References

1. Yakut, K.; Sahin, B. Flow-induced vibration analysis of conical rings used for heat transfer enhancement in heat exchangers. *Appl. Energy* **2004**, *78*, 273–288. [CrossRef]
2. Mashayekhi, R.; Khodabandeh, E.; Bahiraei, M.; Bahrami, L.; Toghraie, D.; Akbari, O.A. Application of a novel conical strip insert to improve the efficacy of water–Ag nanofluid for utilization in thermal systems: A two-phase simulation. *Energy Convers. Manag.* **2017**, *151*, 573–586. [CrossRef]
3. Gravndyan, Q.; Akbari, O.A.; Toghraie, D.; Marzban, A.; Mashayekhi, R.; Karimi, R.; Pourfattah, F. The effect of aspect ratios of rib on the heat transfer and laminar water/TiO_2 nanofluid flow in a two-dimensional rectangular microchannel. *J. Mol. Liq.* **2017**, *236*, 254–265. [CrossRef]
4. Wahhab, H.A.A.; Al-Maliki, W.A.K. Application of a Solar Chimney Power Plant to Electrical Generation in Covered Agri-cultural Fields. In *IOP Conference Series: Materials Science and Engineering*; IOP Publishing: Kerbala, Iraq, 2020; p. 012137.
5. Nouri-Borujerdi, A.; Nakhchi, M. Heat transfer enhancement in annular flow with outer grooved cylinder and rotating inner cylinder: Review and experiments. *Appl. Therm. Eng.* **2017**, *120*, 257–268. [CrossRef]
6. Khoshvaght-Aliabadi, M.; Zangouei, S.; Hormozi, F. Performance of a plate-fin heat exchanger with vortex-generator channels: 3D-CFD simulation and experimental validation. *Int. J. Therm. Sci.* **2015**, *88*, 180–192. [CrossRef]
7. Mamourian, M.; Shirvan, K.M.; Mirzakhanlari, S.; Rahimi, A. Vortex generators position effect on heat transfer and nanofluid homogeneity: A numerical investigation and sensitivity analysis. *Appl. Therm. Eng.* **2016**, *107*, 1233–1247. [CrossRef]
8. Sawhney, J.; Maithani, R.; Chamoli, S. Experimental investigation of heat transfer and friction factor characteristics of solar air heater using wavy delta winglets. *Appl. Therm. Eng.* **2017**, *117*, 740–751. [CrossRef]
9. Al-Maliki, W.A.K.; Al-Khafaji, H.M.H.; Alobaid, F.; Epple, B. Design and Implementation of the Solar Field and Thermal Storage System Controllers for a Parabolic Trough Solar Power Plant. *Appl. Sci.* **2021**, *11*, 6155. [CrossRef]
10. Chamoli, S.; Lu, R.; Xie, J.; Yu, P. Numerical study on flow structure and heat transfer in a circular tube integrated with novel anchor shaped inserts. *Appl. Therm. Eng.* **2018**, *135*, 304–324. [CrossRef]
11. Ibrahim, M.; Essa, M.; Mostafa, N. A computational study of heat transfer analysis for a circular tube with conical ring turbulators. *Int. J. Therm. Sci.* **2019**, *137*, 138–160. [CrossRef]
12. Xu, Y.; Islam, M.; Kharoua, N. Experimental study of thermal performance and flow behaviour with winglet vortex generators in a circular tube. *Appl. Therm. Eng.* **2018**, *135*, 257–268. [CrossRef]
13. Chamoli, S.; Lu, R.; Yu, P. Thermal characteristic of a turbulent flow through a circular tube fitted with perforated vortex generator inserts. *Appl. Therm. Eng.* **2017**, *121*, 1117–1134. [CrossRef]
14. Nakhchi, M.; Esfahani, J. Numerical investigation of different geometrical parameters of perforated conical rings on flow structure and heat transfer in heat exchangers. *Appl. Therm. Eng.* **2019**, *156*, 494–505. [CrossRef]
15. He, Y.; Liu, L.; Li, P.; Ma, L. Experimental study on heat transfer enhancement characteristics of tube with cross hollow twisted. *Appl. Therm. Eng.* **2018**, *131*, 743–749. [CrossRef]
16. Bhuiya, M.; Roshid, M.; Talukder, M.; Rasul, M.; Das, P. Influence of perforated triple twisted tape on thermal performance characteristics of a tube heat exchanger. *Appl. Therm. Eng.* **2020**, *167*, 114769. [CrossRef]
17. Bhuiya, M.; Azad, A.; Chowdhury, M.; Saha, M. Heat transfer augmentation in a circular tube with perforated double counter twisted tape inserts. *Int. Commun. Heat Mass Transf.* **2016**, *74*, 18–26. [CrossRef]

18. Piriyarungrod, N.; Kumar, M.; Thianpong, C.; Pimsarn, M.; Chuwattanakul, V.; Eiamsa-ard, S. Intensification of thermo-hydraulic performance in heat exchanger tube inserted with multiple twisted-tapes. *Appl. Therm. Eng.* **2018**, *136*, 516–530. [CrossRef]
19. Khoshvaght-Aliabadi, M.; Feizabadi, A. Performance intensification of tubular heat exchangers using compound twisted-tape and twisted-tube. *Chem. Eng. Process. Process. Intensif.* **2020**, *148*, 107799. [CrossRef]
20. Salam, B.; Biswas, S.; Saha, S.; Bhuiya, M.M.K. Heat Transfer Enhancement in a Tube using Rectangular-cut Twisted Tape Insert. *Procedia Eng.* **2013**, *56*, 96–103. [CrossRef]
21. Nanan, K.; Thianpong, C.; Promvonge, P.; Eiamsa-ard, S. Investigation of heat transfer enhancement by perforated helical twisted-tapes. *Int. Commun. Heat Mass Transf.* **2014**, *52*, 106–112. [CrossRef]
22. Ibrahim, E.Z. Augmentation of laminar flow and heat transfer in flat tubes by means of helical screw-tape inserts. *Energy Convers. Manag.* **2011**, *52*, 250–257. [CrossRef]
23. Pal, S.; Saha, S.K. Laminar fluid flow and heat transfer through a circular tube having spiral ribs and twisted tapes. *Exp. Therm. Fluid Sci.* **2015**, *60*, 173–181. [CrossRef]
24. Abed, A.H.; Hussein, N.F.; Abdulmunem, A.R. Effect of V-Shape Twisted Jaw Turbulators on Thermal Performance of Tube heat exchanger: An Experimental Study. *Eng. Technol. J.* **2018**, *36*, 1158–1164.
25. Wijayanta, A.T.; Aziz, M.; Kariya, K.; Miyara, A. Numerical study of heat transfer enhancement of internal flow using double-sided delta-winglet tape insert. *Energies* **2018**, *11*, 3170. [CrossRef]
26. Murugesan, P.; Mayilsamy, K.; Suresh, S. Heat Transfer and Friction Factor Studies in a Circular Tube Fitted with Twisted Tape Consisting of Wire-nails. *Chin. J. Chem. Eng.* **2010**, *18*, 1038–1042. [CrossRef]
27. Promvonge, P.; Eiamsaard, S. Heat transfer behaviors in a tube with combined conical-ring and twisted-tape insert. *Int. Commun. Heat Mass Transf.* **2007**, *34*, 849–859. [CrossRef]
28. Eiamsa-ard, S.; Nivesrangsan, P.; Chokphoemphun, S.; Promvonge, P. Influence of combined non-uniform wire coil and twisted tape inserts on thermal performance characteristics. *Int. Commun Heat Mass Transf.* **2010**, *37*, 850–856. [CrossRef]
29. Kurnia, J.C.; Chaedir, B.A.; Sasmito, A.P. Laminar convective heat transfer in helical tube with twisted tape insert. *Int. J. Heat Mass Transfer.* **2020**, *150*, 119309. [CrossRef]
30. Kurnia, J.C.; Chaedir, B.; Wijayanta, A.T.; Sasmito, A.P. Convective Heat Transfer Enhancement of Laminar Herschel–Bulkley Non-Newtonian Fluid in Straight and Helical Heat Exchangers with Twisted Tape Inserts. *Ind. Eng. Chem. Res.* **2021**, *61*, 814–844. [CrossRef]
31. Al-Maliki, W.A.K.; Al-Hasnawi, A.G.T.; Wahhab, H.A.A.; Alobaid, F.; Epple, B. A Comparison Study on the Improved Operation Strategy for a Parabolic Trough Solar Power Plant in Spain. *Appl. Sci.* **2021**, *11*, 9576. [CrossRef]
32. Tamna, S.; Yingyong, K.; Sompol, S.; Pongjet, P. Heat transfer enhancement in tubular heat exchanger with double V-ribbed twisted-tapes. *Case Stud. Therm. Eng.* **2016**, *7*, 14–24. [CrossRef]
33. Bucak, H.; Yılmaz, F. The current state on the thermal performance of twisted tapes: A geometrical categorisation approach. *Chem. Eng. Process. Process. Intensif.* **2020**, *153*, 107929.
34. Abernethy, B.; Benedict, R.P.; Dowdell, R.B. ANSI/ASME. In *Measurement Uncertainty*; University of Rhode Island: Kingston, RI, USA, 1985; Volume 107, pp. 161–164.
35. Kline, S.J.; McClintock, F.A. Describing uncertainties in single sample experiments. *Mech. Eng.* **1953**, *75*, 385–387.
36. Man, C.; Lv, X.; Hu, J.; Sun, P.; Tang, Y. Experimental study on effect of heat transfer enhancement for single-phase forced convective flow with twisted tape inserts. *Int. J. Heat Mass Transf.* **2017**, *106*, 877–883. [CrossRef]
37. Incropera, F.; Dewitt, P.D. *Introduction to Heat Transfer*, 3rd ed.; John Wiley & Sons Inc: New York, NY, USA, 1996.
38. Al-Maliki, W.A.K.; Alobaid, F.; Keil, A.; Epple, B. Dynamic Process Simulation of a Molten-Salt Energy Storage System. *Appl. Sci.* **2021**, *11*, 11308. [CrossRef]

applied sciences

MDPI

Article

Microstructural Analysis and Mechanical Properties of a Hybrid Al/Fe_2O_3/Ag Nano-Composite

Khansaa Dawood Salman [1], Wisam Abed Kattea Al-Maliki [2,3], Falah Alobaid [2,*] and Bernd Epple [2]

[1] Department of Electromechanical Engineering, University of Technology-Iraq, Baghdad 19006, Iraq; 50123@uotechnology.edu.iq
[2] TU Darmstadt, Institut Energiesysteme und Energietechnik, Otto-Berndt-Straße 2, 64287 Darmstadt, Germany; wisam.a.kattea@uotechnology.edu.iq (W.A.K.A.-M.); bernd.epple@est.tu-darmstadt.de (B.E.)
[3] Mechanical Engineering Department, University of Technology-Iraq, Baghdad 19006, Iraq
* Correspondence: falah.alobaid@est.tu-darmstadt.de; Tel.: +49-6151-16-6691; Fax: +49-6151-16-5685

Abstract: This work aims to define the microstructure and to study the mechanical properties of an Al matrix incorporated with various amounts of Fe_2O_3 (3, 6, 9, 12 and 15 wt.%) with a constant amount of Ag at 1 wt.%. Al/Fe_2O_3 + Ag hybrid nano-composite samples are manufactured using powder metallurgy. An aluminum matrix is considered an important alloy, owing to its properties such as being lightweight, strong and corrosion and wear resistant, which enable it to be used in many applications, such as electronics, aerospace and automotive purposes. Various examinations have been performed for the samples of this work, such as Field Emission Scanning Electron Microscopy (FESEM) and X-ray Diffraction (XRD) analysis to estimate the microstructure and phases of manufactured nano-composites. Mechanical testing is also carried out, such as micro-hardness testing, compressive testing and wear testing, to estimate the mechanical properties of the hybrid nano-composites. The results of FESEM and XRD demonstrate that Fe_2O_3 and Ag nanoparticles are uniformly distributed and dispersed into the Al matrix, whereas the mechanical tests show that enhancement t micro-hardness, compressive strength of 12 wt.% Fe_2O_3 + 1Ag and wear rate decrease to a minimum value of 12 wt.% of Fe_2O_3 + 1Ag.

Keywords: hybrid nano-composites; powder metallurgy; Fe_2O_3; Ag; microstructure; mechanical properties; wear

Citation: Salman, K.D.; Al-Maliki, W.A.K.; Alobaid, F.; Epple, B. Microstructural Analysis and Mechanical Properties of a Hybrid Al/Fe_2O_3/Ag Nano-Composite. *Appl. Sci.* **2022**, *12*, 4730. https://doi.org/10.3390/app12094730

Academic Editor: Laurens Katgerman

Received: 2 April 2022
Accepted: 5 May 2022
Published: 8 May 2022

1. Introduction

Aluminum matrix nano-composites (AMNCs) are materials reinforced with metal or ceramic materials used to obtain nano-composite materials for different industrial applications. Al alloys are characterized as having a high strength/light weight, having resistance to the environment and having strong mechanical characteristics. These characteristics make them convenient for use in metal matrix composites (MMCs) [1]. Various reinforcement materials are utilized to enhance their mechanical and physical features. Improvements of these properties have been made in their manufacturing (AMNCs), which are utilized for high-technique engineering components, such as for aerospace, automotive purposes, and engineering shipbuilding. They are quite attractive for this purpose, as reinforced aluminum matrix composites with nano iron oxide (Fe_2O_3) are used in many aeronautical, automotive, etc., purposes due to their excellent efficiency and ratios of strength/weight and stiffness/weight [2].

AMNCs exhibit strong physical properties (electrical and magnetic properties) which enable them to be as lightweight as a multi-functional alloy. However, they do not have high wear resistance [3]. Mechanical properties of aluminum matrix composites, such as hardness, strength, modulus of elasticity and wear resistance, may be improved when the dispersed particles are nano-sized. Improvements in mechanical properties by using nanoparticles incorporated in aluminum matrices have been interesting in recent years [4].

However, the mechanical properties of AMNCs are affected by the manufacturing method used to synthesize nano-composites. Many different processing techniques have been used to manufacture composite and nano-composite materials involving melting casting and powder metallurgy [5]. However, the powder metallurgy technique appears to be the preferred method, owing to its ability to produce a homogeneous dispersion of additive materials into an aluminum matrix. In addition, the powder metallurgy technique gives better mechanical and physical properties. There are many advantages of powder metallurgy techniques, such as good bindings between the additive materials and the matrix, simple technique, easy control of the matrix's microstructure, near-net dimensions and shapes of the product and low cost. It is worth noting that products of powder metallurgy are affected by the particle size of additive materials (nano or micro) and their weight percentages.

Various reinforcing materials may be used to produce aluminum composites or nano-composites for many applications, such as in aircrafts and electrical motors. Many investigations have been conducted in the same fields to obtain composites and nano-composites with unique properties, which are related to the size of the reinforcing materials, their dispersion into the matrix and the grain size of the matrix particles [6–8]. AA7068 alloy is used in different industrial engineering applications, including medical equipment, automobile parts and aerospace. The powder metallurgy technique is utilized to produce AA7068/MgO composites. Additive particles are mixed carefully to obtain a homogeneous dispersion into the matrix. The additive of MgO particles increases the mechanical properties of the product of composite materials, and, as a reinforcing material into the AA7068 alloy, it extensively increases wear resistance [9,10]. In present times, there are many additive materials that are used to improve mechanical properties, such as Al_2O_3, ZrO_2 and TiC, or electrical and magnetic properties, such as Fe_2O_3, Fe_3O_4, Ag and Co. In addition, other additive materials, such as Fe_2O_3, ZnO, TiO_2, WO_3 and $BiVO_4$, which are known as semiconductor photo anode materials [11], are used to improve the efficiency of solar cells. Fe_2O_3 and Fe_3O_4 have received great attention, owing to their unique properties, such as being easy to fabricate, having a low cost, being non-toxic and being thermodynamically stable. Fe_2O_3 exhibits various crystal phases (α, β, γ and ε) which enable it to be used in many applications, such as in photocatalysts, adsorbents and biological and medical applications [12], solar cells. There have been many investigations dealing with hybrid nano-composites with aluminum matrices. Marcu D.F. et al. (2018) studied the mechanical and physical properties of a hybrid nano-composite ($Al/Al_2O_3/Gr$) prepared by powder metallurgy. Al_2O_3 was added by 10, 15 and 20 wt.%, whereas Gr was added by 1, 2 and 3 wt.%. The microstructure analysis was defined using FESEM, XRD and EDS. The results of FESEM, XRD and EDS show that the additive nanomaterials (Al_2O_3 and Gr) dispersed homogeneously into the Al matrix, and they created a fine grain structure at 295 nm–1.63 μm. Moreover, improvements in physical properties reveal that the densities of the sintered samples were higher than those of the compacted samples. Finally, the results of a hardness test show that hardness increases with increasing weight percentages of the additive nano-materials [13].

L.F.P. Ferreiraa et al. (2017) [14] studied the mechanical properties of hybrid nano-composites $Al/Fe_3O_4/TiO_2$ manufactured by powder metallurgy. TiO_2 was added by 2.5 wt.%, 5 wt.%, 75 wt.% and 10 wt.%, whereas Fe_3O_4 was added by 10 wt.% into the aluminum matrix. The microstructures of the samples were analyzed by scanning electron microscope (SEM), and the mechanical properties were defined by micro-hardness and wear tests. The results of this work show that a homogeneous dispersion of TiO_2 and Fe_3O_4 into the Al matrix also improve mechanical properties, such as the micro-hardness, strength and wear resistance of the samples, with increasing weight percentages of TiO_2. In addition, the experimental density of green compacts increases with increasing weight percentages of TiO_2 depending on the applied load, and then they improve the sintered densities of the samples.

Negin Ashrafi et al. (2020) [15] synthesized a hybrid nano-composite of $Al/Fe_3O_4/SiC$ using the powder metallurgy technique for Fe_3O_4 with varied weight percentages of 10,

20, 30 and 40 wt.% and with a constant weight percentage of SiC (20 wt.%). The objective of this research is to investigate the impacts of nanomaterials (Fe_3O_4 and SiC) on the microstructures and on the mechanical properties, such as corrosion resistance and wear behavior, of the products. The results of this study show a homogeneous dispersion of the additive nanoparticles (Fe_3O_4 and SiC) into the Al matrix, which also improves micro-hardness and wear resistance. The preferred sintered density and micro-hardness were obtained for Al/30 Fe_3O_4/20 SiC as 2.69 g/cm^3 and 91 HV, respectively, and the friction coefficient for the applied load 10 N decreased from 0.601 to 0.412 for the sample of Al/30 Fe_3O_4/20 SiC. The results of the corrosion test show that the corrosion resistance for Al/30Fe_3O_4/20 SiC is about 99.83%, and the corrosion resistance for Al/30 Fe_3O_4 is about 88.07%.

Recently, the challenge of developing a hybrid nano-composite with great performance is addressing its limitations. There are many problems and difficulties in manufacturing a hybrid nano-composite, including the type of the matrix alloy as well as the additive materials and manufacturing conditions.

Generally, good interfacial bindings between the matrix and additive materials are difficult. Moreover, the aggregation of additive nanomaterials leads to creating many imperfections, which in turn minimize the physical and mechanical properties. Many processes have been used to improve the dispersion problem of additive materials into the matrix. Therefore, powder metallurgy can be used to overcome this problem and then to improve the mechanical properties.

The aim of the proposed study is to examine the influence of Fe_2O_3 and Ag nanoparticles on the microstructures and mechanical properties of Al matrices during manufacturing by the powder metallurgy technique.

2. Experimental Section

2.1. Raw Substrates

In this work, aluminum powder was used with a grain size of 40 μm and a purity of 99.9%, reinforced with nano iron oxide powder (Fe_2O_3) at a grain size of 31 nm and a purity of 99.8% and with silver (Ag) nanoparticles at a grain size of 25 nm and a purity of 99.9%. The varied weight percentages of Fe_2O_3 powders were 3, 6, 9, 12 and 15 wt.%, and Ag was added as a constant with 1 wt.%.

2.2. Preparing Hybrid Nano-Composites

All samples of hybrid nano-composites were prepared by the PM technique, and the powders were mixed using planetary ball milling (QM-ISPO4). The powder mixture consisted of Al powder as a matrix, iron oxide (Fe_2O_3) powder with different weight percentages (3, 6, 9,12 and 15 wt.%) and constant Ag (1 wt.%) powder as a reinforcing material. The mixing process was performed at a speed of 450 rpm for 0.5 h at room temperature without lubricant materials due to high ductility for the Al matrix to obtain a homogeneous distribution and a dispersion of additive materials into Al matrix. After the mixing process, the powder mixture was compacted by uniaxial pressure at 4 tons to obtain green compacts in the cylindrical samples of 12.65 mm in diameter. The green compacts were sintered at 500 °C for 1.5 h in an electrical furnace under an argon atmosphere to prevent oxidation.

2.3. Microstructural Examination

Microstructural examination was conducted by field emission scanning electron microscopy (FESEM) (model cam scan MV-2300) for the received samples and for after incorporating the iron oxide (Fe_2O_3) at different weight percentages and the silver at a constant wt.% into the aluminum matrix. Before the examination, the samples were ground by using emery paper with a grit size of 1000 μm, and then the samples were polished using polishing cloth. This examination was carried out to define the dispersion of the additive

materials, the pressure influences and sintering temperature on the microstructures of the prepared samples.

2.4. Examination by X-ray Diffraction (XRD)

An examination by X-ray diffraction was implemented using XRD-6000 equipment (SHIMADZU model) for all the samples to determine the phases of the prepared nano-composites. This examination studied the effects of Fe_2O_3 at different wt.% and at constant wt.% of Ag on the resultant phases of the prepared samples of AMNCs.

2.5. Mechanical Properties Definitions

Here, the mechanical properties of the samples involved micro-hardness, wear testing and compressive testing.

2.5.1. Micro-Hardness Testing

Vickers micro-hardness testing according to the ASTM (E384-99) standard was carried out to determine the micro-hardness of the prepared samples for pure Al and Al/Fe_2O_3 + Ag of hybrid nano-composites. The values of the Vickers micro-hardness for the samples (Al/Fe_2O_3 + Ag) were measured before the sintering samples were ground by grinding papers at a grit size of 500 μm, and then they were polished by polishing cloth. Afterwards, the samples were tested by Vickers micro-hardness apparatus (HVS 1000) digital micro-hardness testing for 15 s. A minimum of four measurements for each sample was obtained, and then the average value of micro-hardness was calculated.

2.5.2. Wear Testing

Wear testing was conducted by the pin-on-disc technique according to the ASTM (G99-95) standard to calculate the wear rate of pure Al and Al/Fe_2O_3 + Ag hybrid nano-composite. The samples used for wear testing were fabricated at 1.2 cm in diameter and 2 cm in length. The samples for wear testing were fixed against the hardened disc, which was rotating at 400 rpm for 5 min. Wear testing was carried out by changing the applied loads at values of 2, 4, 6, 8 and 10 N. The wear rate for the samples was determined by the following equations [16]:

$$\text{Wear rate} = \Delta w / 2\pi\, r \cdot n \cdot t \ (g/cm) \quad (1)$$

$$\Delta w = w_1 - w_2 \quad (2)$$

where:

Δw: the difference in weight of the samples (g);
w_1, w_2: weight of the sample before and after wear testing (g);
r: rotating disc radius(cm);
n: revolutions per min (rpm);
t: sliding time (min).

2.5.3. Compressive Testing

Compressive testing was conducted by a universal testing machine for the samples, which were the neat Al and Al/Fe_2O_3 + Ag hybrid nano-composites according to ASTM (G1-90).

2.6. FTIR Examination

Fourier-Transform Infrared Spectroscopy (FTIR) examination was carried out using an FTIR apparatus to give information on the molecules which constituted the prepared nano-composites and on the vibrational reaction of (IR) radiation of the molecules. This was performed at wave numbers of about 4000–400 cm^{-1}, and they registered with an electromagnetic sample absorption. The radiations of the band were absorbed in the spectrum at a specific frequency, which exited a certain binding or many bindings in the molecules

that made the atoms vibrate with each other. The peaks of infrared spectra were obtained from the changes in the frequencies of binding mode and binding stretching depending on the strength of binding and on the atom mass attached to the binding. To understand the interactions between reinforcing nanoparticles and the Al matrix, the surface chemistry and chemical properties for each sample of Al/Fe_2O_3 + Ag nano-composite were analyzed through an FTIR apparatus (SHIMADZU IRA affinity-1) at a range of about 4000–400 cm^{-1} (made in Japan).

3. Results

3.1. Results of FESEM Examination

Figure 1 depicts the photomicrographs of FESEM examination of the Al/Fe_2O_3 + Ag hybrid nano-composites with different weight percentages of Fe_2O_3 and with a constant weight percentage of Ag. The reinforcement materials can be seen to be homogeneously distributed, have low porosity and no cracks. The reinforcing materials Fe_2O_3 and Ag are diffused at the interfaces between Fe_2O_3 and Ag with the Al matrix. The role of Ag metal is to create new phases with the Al matrix and then to be diffused at the grain boundaries between Al grains and Ag. Moreover, the dispersion of Ag is to minimize porosity and then to improve the mechanical properties.

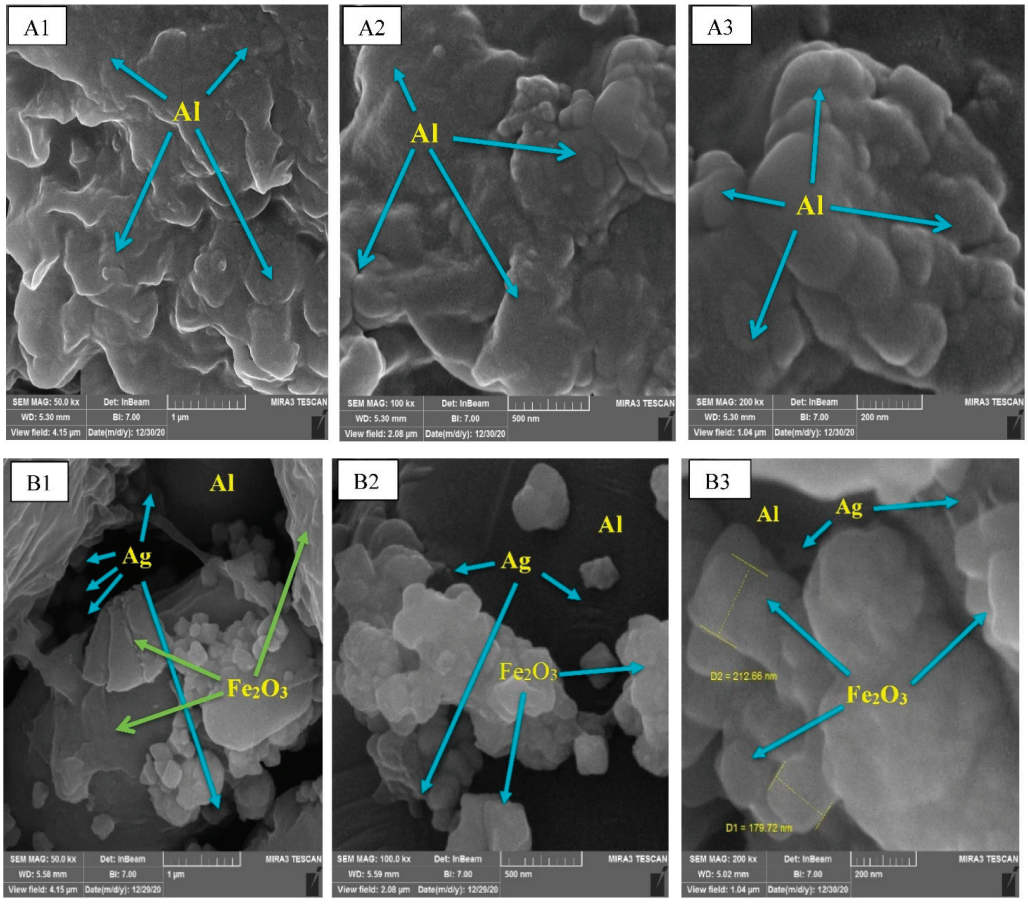

Figure 1. *Cont.*

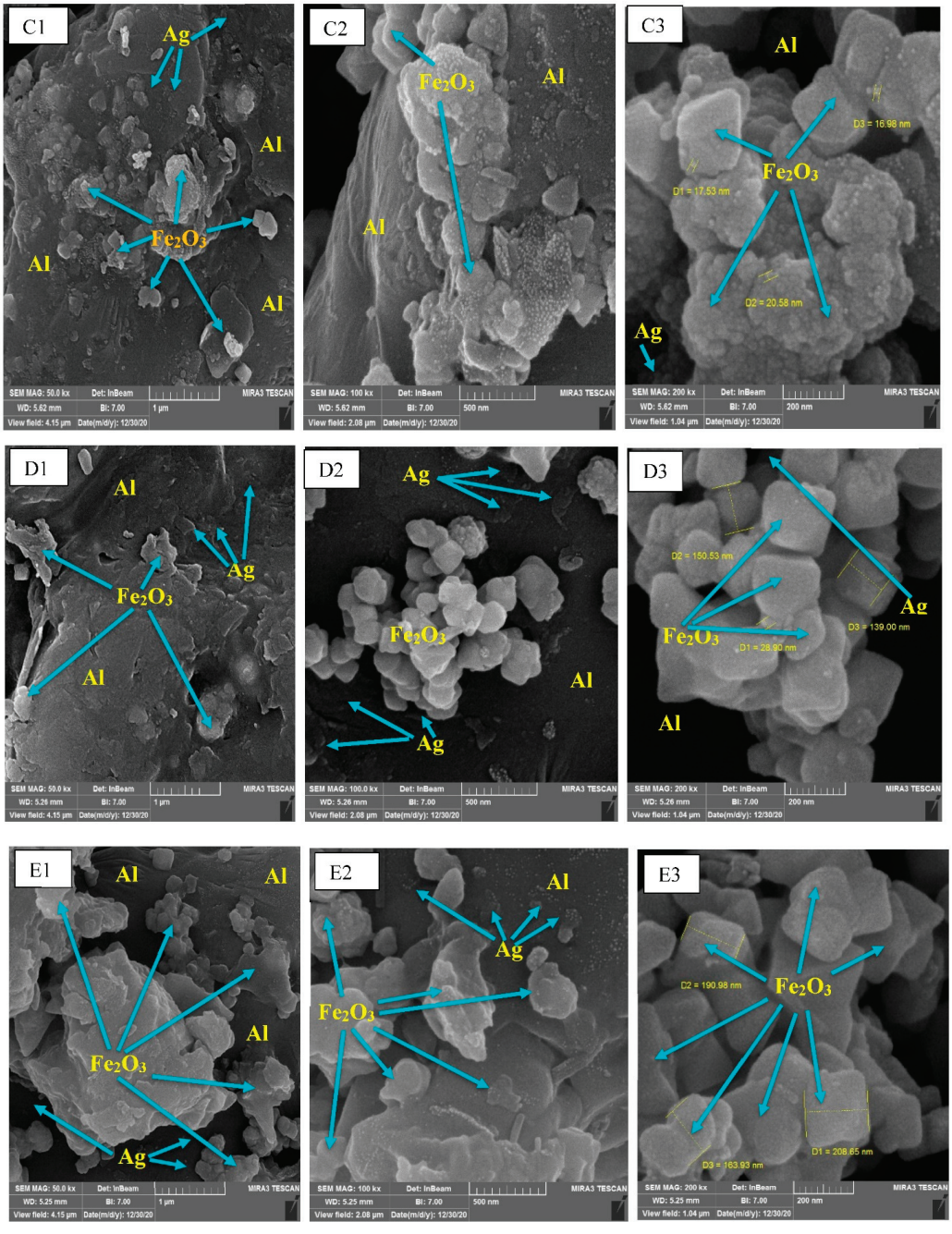

Figure 1. *Cont.*

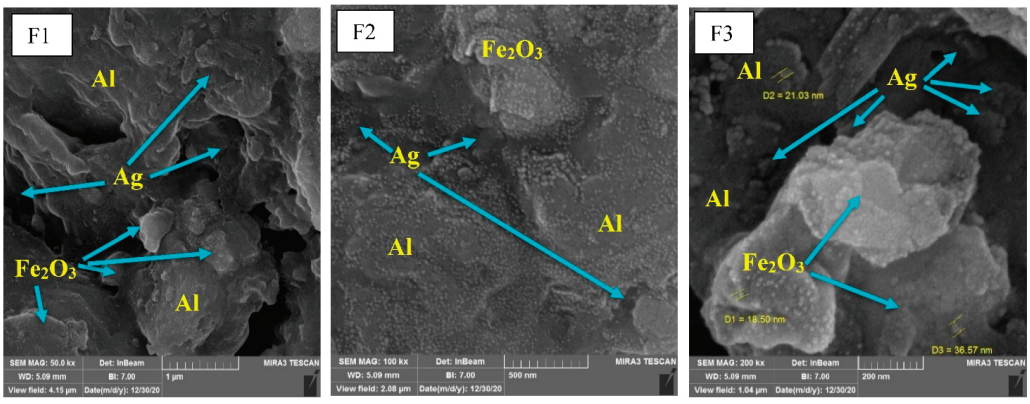

Figure 1. FESEM images of the samples with different percentages of Fe_2O_3 and 1% Ag: (**A1**–**A3**) pure Al; (**B1**–**B3**) Al/3 wt.% Fe_2O_3 +1 wt.% Ag; (**C1**–**C3**) Al/6 wt.% Fe_2O_3 + 1 wt.% Ag; (**D1**–**D3**) Al/9 wt.% Fe_2O_3 + 1 wt.% Ag; (**E1**–**E3**) Al/12 wt.% Fe_2O_3 + 1 wt.% Ag; and (**F1**–**F3**) Al/15 wt.% Fe_2O_3 + 1 wt.% Ag.

3.2. Results of X-ray Diffraction

Figure 2 shows X-ray diffraction (XRD) peaks for the samples before and after adding Fe_2O_3 + Ag. The results of XRD analysis for the samples of Al reinforced by Fe_2O_3 depict that increasing the wt.% of Fe_2O_3 with a constant wt.% of Ag leads to an increase in the peaks of Fe_2O_3 phase and Ag phase. In fact, the results of the XRD examination reveal that the increase in the wt.% of the reinforcement materials leads to an increase in the intensity of diffraction peaks. Moreover, there are no other possible intermetallic inclusions, most likely created between Al and Fe_2O_3 + Ag in a thermo-dynamically steady state [17].

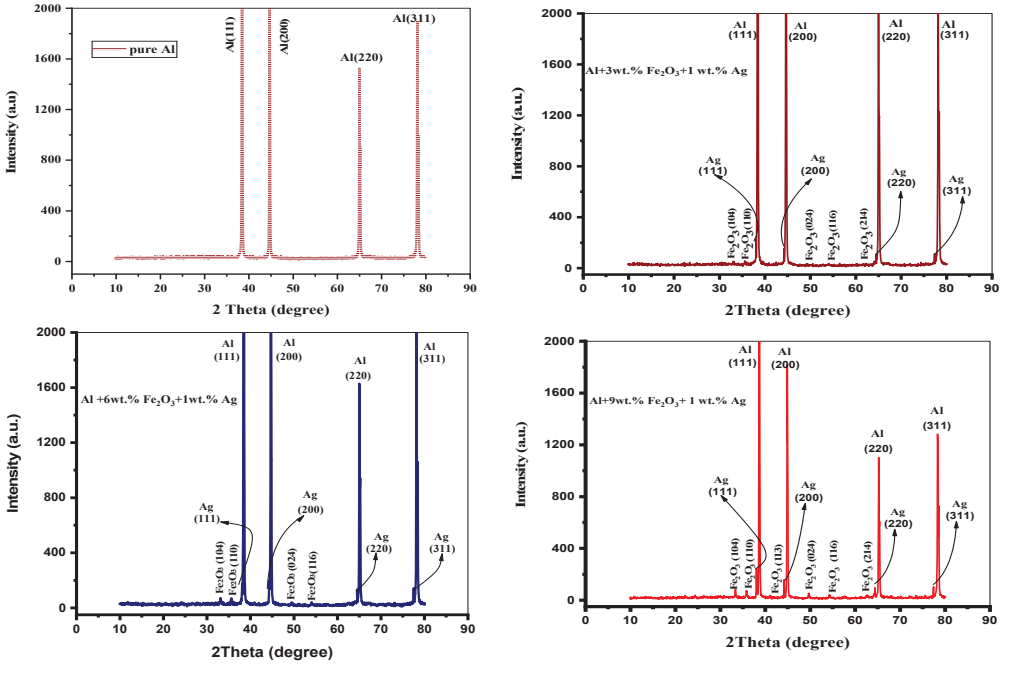

Figure 2. *Cont.*

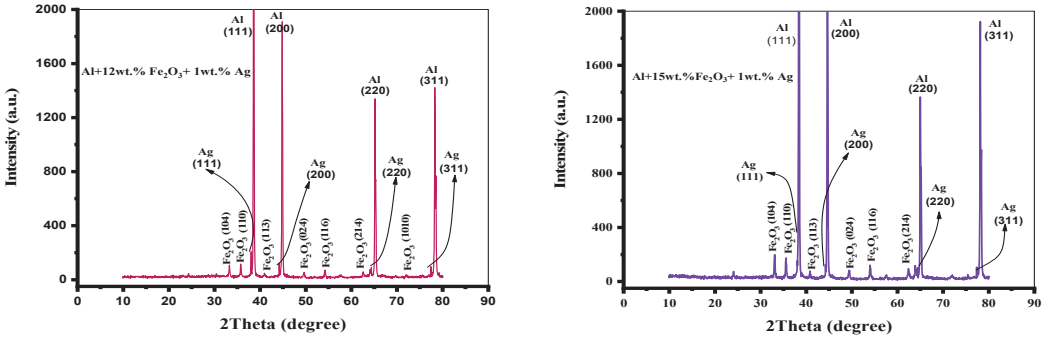

Figure 2. X-ray diffraction spectra of pure Al and Al/Fe_2O_3 + Ag hybrid nano-composites.

As shown in Figure 2, for the XRD data for the pure Al sample, the Al phase formed at 2θ (38.485°, 44.735°, 65.135° and 78.285°) for the planes at hkl (111, 200, 220 and 311), respectively. For the XRD data for the Al/3Fe_2O_3 + 1Ag sample, in addition to the Al phase, the Ag phase formed at 2θ (38.035°, 44.185, 64.385° and 77.435°) for the planes at hkl (111, 200, 200 and 311), and the Fe_2O_3 phase was created at 2θ (33.185°, 35.585°, 49.485°, 54.085° and 62.485°) for the planes at hkl (104, 110, 024, 116 and 214), respectively. For the XRD data for the Al/6Fe_2O_3 + 1Ag sample, in addition to the Al and Ag phases, the Fe_2O_3 phase formed at 2θ (33.185°, 35.585°, 49.485° and 54.085°) for the planes at hkl (104, 110, 024 and 116), respectively. For the Al/9Fe_2O_3 + 1Ag sample, in addition to the Al and Ag phases, the Fe_2O_3 phase formed at 2θ (33.185°, 35.585°, 40.885°, 49.485°, 54.085° and 62.485°) for the planes at hkl (104, 110, 113, 024, 116 and 214), respectively. In addition, the XRD data for the Al/12Fe_3O_3 + 1Ag sample show that, in addition to Al and Ag phases, the Fe_2O_3 phase was created at 2θ (33.185°, 35.585°, 40.885°, 49.485°, 54.085°, 62.485° and 71.935°) for the planes at hkl (104, 110, 113, 024, 116, 214 and hkl 1010), respectively. Finally, for the XRD data for the Al/15Fe_2O_3 + 1Ag sample, in addition to the Al and Ag phases, the Fe_2O_3 phase was created at 2θ (33.185°, 35.585°, 40.885°, 49.485°, 54.085° and 62.485°) for the planes at hkl (104, 110, 113, 024, 116 and 214), respectively.

3.3. Results of Mechanical Testing

3.3.1. Results of Micro-Hardness Testing

Micro-hardness values of the prepared Al/Fe_2O_3 + Ag hybrid nano-composites are extremely dependent on the compacting pressure, sintering temperature and weight percentages of the reinforcing nano-materials. Table 1 shows the Vickers micro-hardness results for the specimens of Al/Fe_2O_3 + 1 wt.%Ag. The results of micro-hardness increase with increasing wt.% of Fe_2O_3 + Ag until reaching 12 wt.% Fe_2O_3 + 1Ag, and then it drops down. This is because the hardness of Fe_2O_3 is higher than that of the Al matrix. The increase in the weight fraction wt.% of Fe_2O_3 and the steady wt.% of Ag leads to decreases in the porosity of nano-composites by filling the pores and then virtually affecting micro-hardness, as illustrated in Figure 3.

Table 1. Micro-hardness values of the samples of Al/Fe_2O_3 + 1 wt.%Ag.

Sample No.	Fe_2O_3 + 1Ag (wt.%)	Micro-Hardness (HV)	STD Error Bars
1	0	17.13	3.14
2	3	23.01	3.61
3	6	26.23	3.95
4	9	31.04	4.17
5	12	34.19	4.47
6	15	30.22	4.10

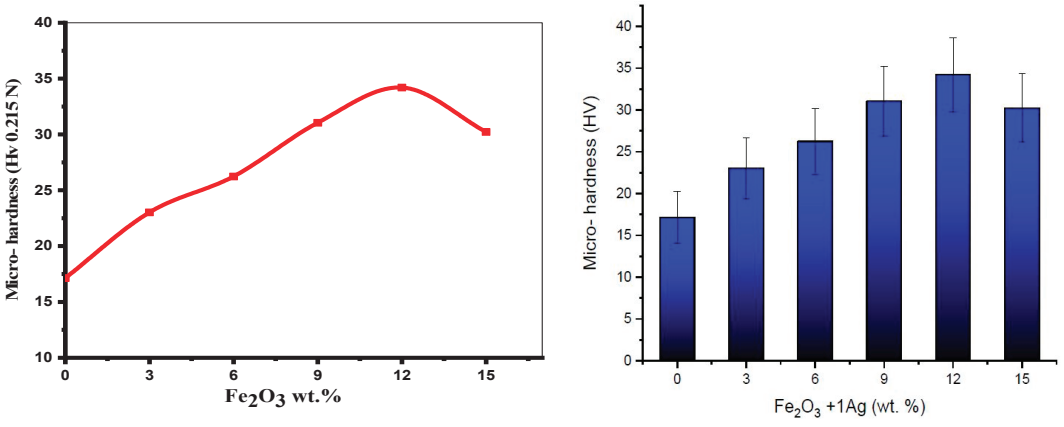

Figure 3. The variation of micro-hardness with different wt.% of Fe_2O_3.

Finally, micro-hardness testing is considered an important tool to define the microstructures and mechanical properties of nano-composites [18].

As shown in Figure 3, the maximum micro-hardness of Al/12Fe_2O_3 + 1Ag is most likely a result of the phase created especially for the Fe_2O_3 phase created at 2θ (71.935°) for the hexagonal plane at hkl (1010), which in turn increases the micro-hardness for this sample.

3.3.2. Results of Wear Testing

Figure 4 shows the results of wear rate with varied weight percentages of Fe_2O_3 and with a constant weight percentage of Ag for Al/Fe_2O_3+ Ag hybrid nano-composites by changing loads by 2, 4, 6, 8 and 10N with a constant sliding velocity of 750 rpm. Wear rate minimizes with increases in the weight percentage of Fe_2O_3 nanoparticles, and the improving of the wear resistance of Al/Fe_2O_3 + Ag nano-composites is a result of good chemical bonding at the interfaces between Fe_2O_3 ceramic nanoparticles and Ag with the Al matrix. Moreover, strain fields are formed around Fe_2O_3 because of the difference in the thermal expansion coefficient of Fe_2O_3 and Al. These strain fields make networks of dislocations at the interfaces between the Fe_2O_3 and Al matrix, which in turn constrains the propagation of cracks. The uniform dispersion of Fe_2O_3 and Ag nanoparticles into the Al matrix improves the Orwan strengthening of the product [19]. Therefore, the wear resistance of Al/Fe_2O_3 + Ag nano-composites is improved and, in turn, enhances the tribological characteristics between the pin (Al/Fe_2O_3 + Ag nano-composites) and the hardened steel disc, which reduces shear stresses between them. The preferred low wear rate for Al/12Fe_2O_3 + 1Ag is a result of the same reasons mentioned for the micro-hardness and compressive tests. This is agreed with in [20].

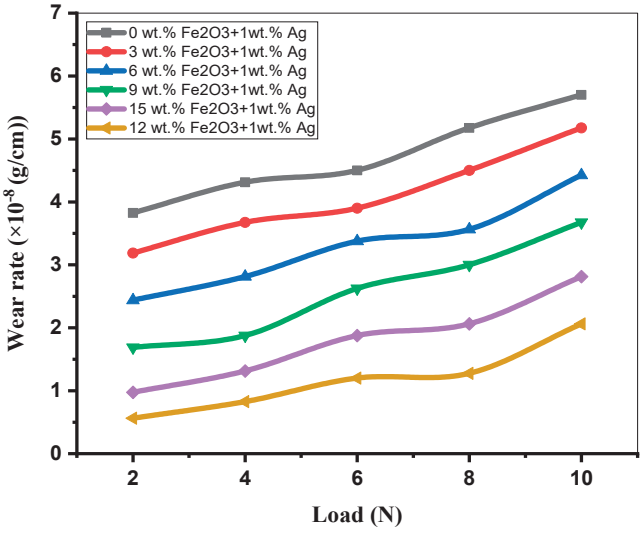

Figure 4. The variation of wear rate as a function of normal loads for pure Al and Al/Fe_2O_3 + Ag hybrid nano-composites.

3.3.3. Results of Compressive Testing

Figure 5 demonstrates the stress–strain curves of compression testing for Al and Al/Fe_2O_3 + Ag hybrid nano-composites with different percentages of Fe_2O_3 and with a constant weight percentage of Ag. The figure shows that the introduction of Fe_2O_3 and Ag nanoparticles increases compressive strength until reaching 12 wt.% Fe_2O_3 + 1 wt.% Ag at about 84 MPa. This is a result of decreases in ductility with increasing amounts of Fe_2O_3 nanoparticles. The highest value of compressive strength is attributed to the strong interfacial bindings between Fe_2O_3, Ag nanoparticles and the Al matrix [21].

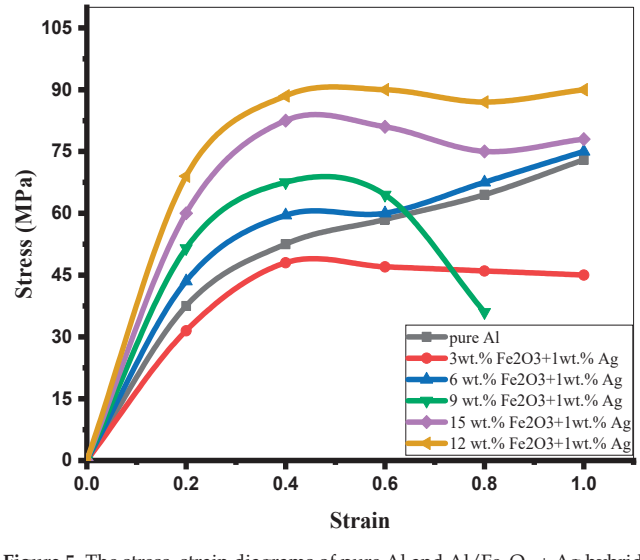

Figure 5. The stress–strain diagrams of pure Al and Al/Fe_2O_3 + Ag hybrid nano-composites.

The increases in the compressive resistances of nano-composites are associated with the introduction of the hard ceramic materials of Fe_2O_3. However, the increase in Fe_2O_3 of more than 12 wt.% can increase brittleness and decrease compressive strength, and it can then inhibit elastic deformation and prevent failure at the rimmed area on the surface.

3.3.4. Results of FTIR Examination

The FTIR spectra of pure Al and Al/Fe_2O_3 + Ag hybrid nano-composites is shown in Figure 6. There are similar features in FTIR spectra between pure Al and Al/Fe_2O_3 + Ag hybrid nano-composites. The peak at 3700 cm^{-1} is compatible with the oscillations of hydroxyl (OH) groups, indicating that OH structures exist on the face of the nanoparticles. The OH groups can be seen on the nanoparticles, as OH groups attach to absorbed water molecules. The strong and broad absorption bands in the range of 2955 cm^{-1}–2840 cm^{-1} correspond to C-H stretching vibration modes. The peaks that appear in the range of 1750 cm^{-1}–1535 cm^{-1} in nano-composites correspond to carbonyl group stretching vibrations C=O. The absorption bands in the range of about 1500 cm^{-1}–1250 cm^{-1} are related to C-O stretching vibrations. When the spectra are at 1020 cm^{-1}, new bindings form for the Al-O stretching mode. The absorption bands for the hybrid nano-composites that are seen in the range of about 900 cm^{-1}–450 cm^{-1} are attributed to the formation of new bindings for the Fe-O stretching mode. Finally, absorption bands at 1000 cm^{-1}–500cm^{-1} correspond to C-N vibration modes [22].

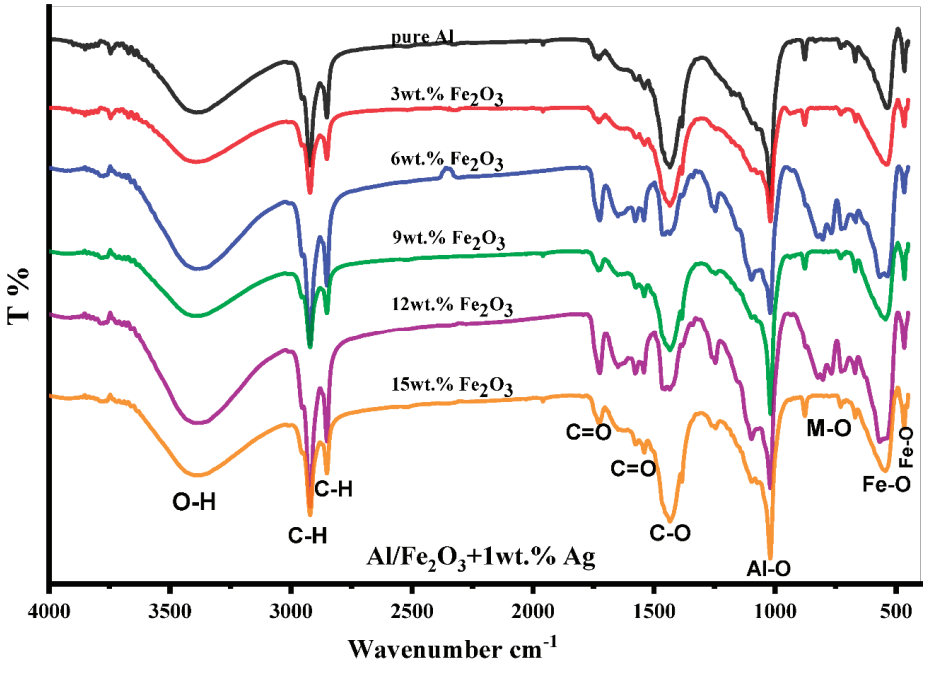

Figure 6. FTIR spectra of pure Al and Al/Fe_2O_3 + Ag hybrid nano-composites.

4. Conclusions

In this investigation, a hybrid nano-composite (Al/Fe_2O_3 + Ag) was composed of an Al matrix reinforced by different wt.% of (Fe_2O_3) and a constant wt.% of (Ag). Al/Fe_2O_3 + Ag hybrid nano-composites were successfully synthesized by powder metallurgy, and the microstructure was depicted by (FESEM) and (XRD) examinations. The mechanical properties were calculated by micro-hardness testing, compressive testing and wear testing. The results of FESEM and XRD examinations reveal good dispersion and distribution of rein-

forcing additives, Fe_2O_3 and Ag nanoparticles, into the aluminum matrix. The results of this work show enhancements in mechanical properties. The values of mechanical testing increased with increases in weight percentages of the reinforcing nanoparticles until reaching 12 wt.% Fe_2O_3. For Al/12 wt.% Fe_2O_3 + 1 wt.% Ag hybrid nano-composites, the microhardness was about 34.19 HV, the compressive strength was 89.9 MPa and the decreasing wear rate was the same weight percentage as that of Al/12 wt.% Fe_2O_3 + 1 wt.% Ag of about 1.8×10^{-8} g/cm compared with pure Al. This is a result of Aluminum matrix. The results of this work show enhancements in mechanical properties. The values of mechanical testing increased with the increases in weight percentages of the reinforcing nanoparticles until reaching 12 wt.% Fe_2O_3. For Al/12Fe_2O_3 + 1Ag hybrid nano-composites, the microhardness increased with increases in wt.% of Fe_2O_3 compared with pure Al, and the wear rate decreased with increases in the weight percentages of Fe_2O_3. The introduction of Fe_2O_3 and Ag nanoparticles increased the compressive strength to 12 wt.% Fe_2O_3 + 1 wt.% Ag compared with the pure Al. This was a result of decreases in ductility with increases in the weight percentages of nanoparticles. Generally, the highest compressive strength is attributed to strong interfacial bindings between Fe_2O_3, Ag nanoparticles and the Al matrix.

Author Contributions: Data curation, K.D.S.; Formal analysis, K.D.S.; Investigation, K.D.S. and F.A.; Methodology, K.D.S. and W.A.K.A.-M.; Supervision, B.E.; Validation, W.A.K.A.-M.; Visualization, F.A.; Writing—original draft, K.D.S.; Writing—review & editing, W.A.K.A.-M. All authors have read and agreed to the published version of the manuscript.

Funding: This research received no external funding.

Acknowledgments: We acknowledge support by the Deutsche Forschungsgemeinschaft (DFG) German Research Foundation and the Open Access Publishing Fund of the Technical University of Darmstadt. The authors would like to also thank the University of Technology-Iraq.

Conflicts of Interest: The authors declare no conflict of interest.

References

1. Megahed, M.; Attia, M.A.; Abdelhameed, M.; El-Shafei, A.G. Tribological Characterization of Hybrid Metal Matrix Composites Processed by Powder Metallurgy. *Acta Met. Sin.* **2017**, *30*, 781–790. [CrossRef]
2. Bayraktar, E.; Ayari, F.; Tan, M.J.; Tosun-Bayraktar, A.; Katundi, D. Manufacturing of aluminum matrix composites reinforced with iron oxide (Fe_3O_4) nanoparticles: Microstructural and mechanical properties. *Metall. Mater. Trans. B* **2014**, *45*, 352–362. [CrossRef]
3. Ferreira, L.F.P.; Bayraktar, E.; Miskioglu, I.; Robert, M.H. Recycle of aluminium (A356) for processing of new composites reinforced with magnetic nano iron oxide and molybdenum. In *Mechanics of Composite and Multi-functional Materials*; Springer: Cham, Switzerland, 2017; Volume 7, pp. 153–161.
4. Mazahery, A.; Abdizadeh, H.; Baharvandi, H.R. Development of high-performance A356/nano-Al_2O_3 composites. *Mater. Sci. Eng. A* **2009**, *518*, 61–64. [CrossRef]
5. Mummoorthi, D.; Rajkumar, M.; Kumar, S.G. Advancement and characterization of Al-Mg-Si alloy using reinforcing materials of Fe_2O_3 and B_4C composite produced by stir casting method. *J. Mech. Sci. Technol.* **2019**, *7*, 3213–3222. [CrossRef]
6. Ferreira, L.-M.; Bayraktar, E.; Miskioglu, I.; Robert, M.-H. New magnetic aluminum matrix composites (Al-Zn-Si) reinforced with nano magnetic Fe_3O_4 for aeronautical applications. *Adv. Mater. Process. Technol.* **2018**, *4*, 358–369. [CrossRef]
7. Alemdağ, Y.; Beder, M. Microstructural, mechanical and tribological properties of Al–7Si–(0–5) Zn alloys. *Mater. Des.* **2014**, *63*, 159–167. [CrossRef]
8. Kurşun, A.; Bayraktar, E.; Robert, M.H. Low cost manufacturing of aluminium-alumina composites. *Adv. Mater. Process. Technol.* **2015**, *1*, 515–528. [CrossRef]
9. Joshua, K.J.; Vijay, S.; Ramkumar, P.; Selvaraj, D.P.; Kim, H.G. Investigation of microstructure and mechanical properties of AA7068 reinforced with MgO prepared using powder metallurgy. In Proceedings of the 2017 First International Conference on Recent Advances in Aerospace Engineering (ICRAAE), Coimbatore, India, 3–4 March 2017; pp. 1–6.
10. Azhar, A.Z.A.; Mohamad, H.; Ratnam, M.M.; Ahmad, Z.A. The effects of MgO addition on microstructure, mechanical properties and wear performance of zirconia-toughened alumina cutting inserts. *J. Alloys Compd.* **2010**, *497*, 316–320. [CrossRef]
11. Liu, Y.; Zhao, G.J.; Zhang, J.X.; Bai, F.Q.; Zhang, H.X. First-principles investigation on the interfacial interaction and electronic structure of $BiVO_4/WO_3$ heterostructure semiconductor material. *Appl. Surf. Sci.* **2021**, *549*, 149309. [CrossRef]
12. Jian, W.; Wang, S.P.; Zhang, H.X.; Bai, F.Q. Disentangling the role of oxygen vacancies on the surface of Fe_3O_4 and γ-Fe_2O_3. *Inorg. Chem. Front.* **2019**, *6*, 2660–2666. [CrossRef]

13. Marcu, D.F.; Buzatu, M.; Ghica, V.G.; Petrescu, I.M.; Popescu, G. Expermintal characterztation of aluminum based hybrid composites obtained through powder. In *Proceedings of the IOP Conference Series Materials Science and Engineering*; IOP Publishing: Tokyo, Japan, 2018; Volume 374.
14. Erreria, L.F.P.; Bayraktar, I.M.E.; Robert, M.H. Aluminium matrix composite reinforced by nano Fe_3O_4 doped with TiO_2 by thermomechanical process. *Mech. Compos. Multi-Funct. Mater.* **2017**, *7*, 251–259.
15. Ashrafi, N.; Azmah Hanim, M.A.; Sarrf, M.; Sulaiman, S.; Hong, T.S. Microstructural, Tribology and Corrosion Properties of Optimized Fe_3O_4-SiC Reinforced Aluminum Matrix Hybrid Nano Filler Composite Fabricated through Powder Metallurgy Method. *Materials* **2020**, *13*, 4090. [CrossRef] [PubMed]
16. Tabrizi, A.T.; Aghajani, H.; Saghafian, H.; Laleh, F.F. Correction of Archard equation for wear behavior of modified pure titanium. *Tribol. Int.* **2021**, *155*, 106772. [CrossRef]
17. Nassar, A.E.; Nassar, E.E. Properties of aluminum matrix Nano composites prepared by powder metallurgy processing. *J. King Saud Univ.-Eng. Sci.* **2017**, *29*, 295–299. [CrossRef]
18. Chen, T.; Cao, Z.; Guo, X.; Nie, J.; Xu, J.; Fan, Z.; Du, B. Preparation and characterization of thermosensitive organic–inorganic hybrid microgels with functional Fe_3O_4 nanoparticles as crosslinker. *Polymer* **2011**, *52*, 172–179. [CrossRef]
19. Zhang, Z.; Chen, D.L. Consideration of Orowan strengthening effect in particulate- reinforced metal matrix nanocomposites: A model for predicting their yield strength. *Scr. Mater.* **2006**, *54*, 1321–1326. [CrossRef]
20. Rajeshkumar, L.R.K. Dry sliding wear behavior of AA2219 reinforced with magnesium oxide and graphite hybrid metal matrix composites. *Int. J. Eng. Res. Technol.* **2018**, *6*, 3–8.
21. Yan, S.; Dai, S.; Zhang, X.; Yang, C.; Hong, Q.; Chen, J.; Lin, Z. Investigating aluminum alloy reinforced by graphene nanoflakes. *Mater. Sci. Eng. A* **2014**, *612*, 440–444. [CrossRef]
22. Madani, H.R. (Cu/Ni)—Al layered double hydroxides@ Fe_3O_4 as efficient magnetic nanocomposite photocatalyst for visible-light degradation of methylene blue. *Res. Chem. Intermed.* **2017**, *43*, 5795–5810. [CrossRef]

applied sciences

MDPI

Article

Microstructural Analysis and Mechanical Characterization of Shape Memory Alloy Ni-Ti-Ag Synthesized by Casting Route

Khansaa Dawood Salman [1], Wisam Abed Kattea Al-Maliki [2,3], Falah Alobaid [2,*] and Bernd Epple [2]

[1] Department of Electromechanical Engineering, University of Technology, Baghdad 19006, Iraq; 50123@uotechnology.edu.iq
[2] TU Darmstadt, Institut Energiesysteme und Energietechnik, Otto-Berndt-Straße 2, 64287 Darmstadt, Germany; wisam.a.kattea@uotechnology.edu.iq (W.A.K.A.-M.); bernd.epple@est.tu-darmstadt.de (B.E.)
[3] Mechanical Engineering Department, University of Technology, Baghdad 19006, Iraq
* Correspondence: falah.alobaid@est.tu-darmstadt.de; Tel.: +49-61-5116-6691; Fax: +49-61-5116-5685

Abstract: The purpose of the current research is to study the microstructure and mechanical properties of Ni-Ti-Ag shape memory alloys prepared by the casting route. Ag (grain size at 1 mm) was incorporated into Ni-Ti alloys at varying percentages of weight (0, 1.5, 3 and 4.5 wt.% Ag) to produce shape memory alloys using a Vacuum Arc Re-melting (VAR) furnace. Microstructural analysis was defined by FESEM microscopy and XRD examinations, while the transformation temperatures of the Ni-Ti-Ag shape memory alloy were determined by DSC examination. On the other hand, determination of mechanical properties was carried out using micro-hardness and compressive tests. The results of this work show that Ag was dispersed homogeneously into the Ni-Ti alloy. Moreover, two primary phases (austenite phase and martensite phase) emerged with few impurities. The results of the XRD examination show that the number of Ag peaks increased with the increase in weight percentage of Ag. The transformation temperature of the austenitic phase was defined as −1.6 °C by DSC. The mechanical characterizations increased with the increase in weight percentages of Ag (1.5, 3 and 4.5 wt.%), and significantly affected the mechanical properties of the Ni-Ti alloy. An improvement in compressive strength (42.478%) was found for the alloy with 3 wt.% Ag, while the micro-hardness results show a slight decrease in micro-hardness (8.858%) for the alloy with 4.5 wt.% Ag.

Keywords: shape memory alloys; Ni-Ti-Ag; casting; VAR furnace; microstructure; XRD; mechanical properties

Citation: Salman, K.D.; Al-Maliki, W.A.K.; Alobaid, F.; Epple, B. Microstructural Analysis and Mechanical Characterization of Shape Memory Alloy Ni-Ti-Ag Synthesized by Casting Route. *Appl. Sci.* **2022**, *12*, 4639. https://doi.org/10.3390/app12094639

Academic Editor: Laurens Katgerman

Received: 5 April 2022
Accepted: 4 May 2022
Published: 5 May 2022

Publisher's Note: MDPI stays neutral with regard to jurisdictional claims in published maps and institutional affiliations.

1. Introduction

Shape memory alloys (SMAs) are the main classification of smart alloys owing to their unique properties. Smart materials are metallic alloys that respond to mechanical stresses and temperature, creating internal deformation of about 2–10%. Smart alloys are considered thermo-mechanical materials used in many mechanical applications due to their ability to return (remember) to their shape after the removal of external loads [1]. The shape memory effect is created when the SMAs undergo applied stresses at a constant temperature, while super elasticity is created at a temperature higher than the austenite finish temperature (Af) and constant stress; hence, the SMAs return to their original shape after removing the load. Ni-Ti alloys (Nitinol) are important shape memory alloys that consist of two main phases; the first phase is austenite (B2) and the second phase is martensite (B19). The austenite phase is created at a high temperature and transforms into the martensite phase at a low temperature. Phase transformation from the austenite phase to the martensite phase is affected by many factors such as the heating–cooling cycle, Ni concentration, and the processing conditions when using the casting route [2]. Shape memory alloys are commonly used in mechanical and biological applications that require smart alloys due to their unique properties, such as recovery to their original shape, with a large amount of

deformations. Each one of these properties consists of two-phase transformations: the first is the martensite phase, which occurs at high pressure and low temperature (Mf), and the second is the austenite phase, which occurs at low pressure and high temperature (Af). For a specific temperature that is lower than the transformation temperature, the martensite phase was created (twin) as a soft phase and was deformed by (de-twinning). Many metal alloys tend to draw back to their original shape when heated above the transformation temperature; however, increasing the applied stress can create plastic deformation. Many metallic alloys have a recovery of about 0.1%, while the SMAs have a recovery of about 7–8% [1,3].

Generally, there are two techniques used to fabricate SMAs: powder metallurgy or the casting method, which are classified as vacuum induction melting (VIM), electron beam melting (EBM) and vacuum arc re-melting (VAR). The preferred technique is vacuum arc re-melting (VAR) as it offers a high purity shape memory alloy, especially Ni-Ti-Ag. On the other hand, Ni-Ti based SMAs are not suitable for many purposes; therefore, to improve the properties of Ni-Ti SMAs, various elements have been added such as Fe, Co and V, which are used to decrease the transformation temperature. Au, Zr, Pt and Hf are used to raise the transformation temperature, and Cu is used to decrease the hysteresis loop, especially when adding Fe and Nb [2]. Ag is an important element due to its superior and anti-bacterial material and its stability. Hence, Ag is considered the best element incorporated into Ni-Ti-based alloys to produce Ni-Ti-Ag composite material with higher strength compared with Ni-Ti-based alloys and higher anti-bacterial activity [4–11]. The main manufacturing processes used to produce SMAs are the casting method and powder metallurgy method, followed by heat treatment to minimize the internal stresses and improve the properties of the manufactured SMAs [12]. The aim of this work is to synthesize Ni-Ti-Ag SMAs by the casting method using a VAR furnace and to study the effect of the addition of Ag on the microstructure and mechanical properties of SMAs.

2. Experimental Procedures

In the present work, commercially pure Ni, Ti and Ag were used with the composition of Ni (50) wt.% with Ti (50, 48.5, 47, 45.5) wt.% and Ag (0, 1.5, 3, 4.5) wt.%. Ni-Ti-Ag shape memory alloys were synthesized by the casting route using a vacuum arc re-melting (VAR) furnace. The arc-melting process was carried out in an inert Ar atmosphere (99.99 vol.% purity) at approximately 500 mbar pressure. Prior to arc melting, a vacuum was applied to a bell jar at a double pressure of about 5×10^{-4} mbar, followed by refilling with argon gas. To improve the mixing process, it was necessary to turn the button over after each arc melting stage and repeat it until the arc-melting process was complete. After repeating the arc-melting process four times, samples with dimensions of about (10 cm × 2.5 cm × 1 cm) inside the furnace tube were homogenized in accordance with the heating cycle under an Ar gas atmosphere. Fast heating was carried out at 600 °C using about 15 °C/min heating rate, which was subsequently followed by heat treatment at a slow warming level of 600–1000 °C, using about 15 °C/min heating rate maintained at 1000 °C for 8 h, followed by rinsing with water.

3. Characterization

X-ray diffraction (XRD) patterns were used to identify each phase, using the X-ray diffractometer model (Panalytical X'pert) with CuKα radiation at λ = 1.5405 A° at an ambient temperature. The microstructure of Ni-Ti-Ag samples was analysed on a Field Emission Scanning Electron Microscopy (FESEM) model (ZEISS SIGMA VP), which was used to describe the surface morphology characteristics. The phase transformation behaviour of the experimental samples was investigated by differential scanning calorimetry (DSC), using a (NETZSCH DSC 214 Polyma) calorimeter with a heating rate of about 10°/min. The mechanical properties and stress–strain curves of the Ti-Ni-Ag alloys were studied in compression testing. Compression testing was carried out by (STM-50), a universal testing machine with a 5 mm/min testing speed. Micro-hardness testing of the samples

was carried out by Vickers apparatus (Diamond pyramid) according to ASTM E92 standard, and Force applied (Kgf): 10 HV with Duration of force: 10–15 s.

4. Results

4.1. Microstructure Analysis

The microstructure of the shape memory alloys, which contain different wt.% of Ag particles, was achieved using FESEM testing, as shown in Figure 1A–D. The photomicrographs reveal the homogeneous dispersion of Ag particles in the Ni-Ti alloys with observed voids. Particles of Ag were melted and filled the interstitial voids between the Ni-Ti alloy elements, owing to the low melting point for Ag. Parallel lines can be seen in the FESEM photomicrographs of the homogenized alloys in Figure 1C,D. These lines are considered the martensite phase (B19′), formed as a result of the thermal transformation of austenitic (B2) Ni-Ti shape memory alloys. This first-order phase transformation provides SMAs with the ability to recover their unique shape [13].

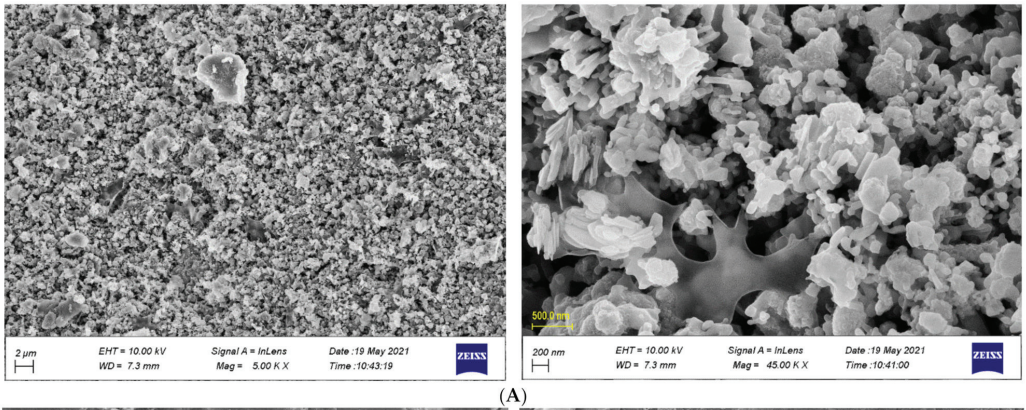

(**A**)

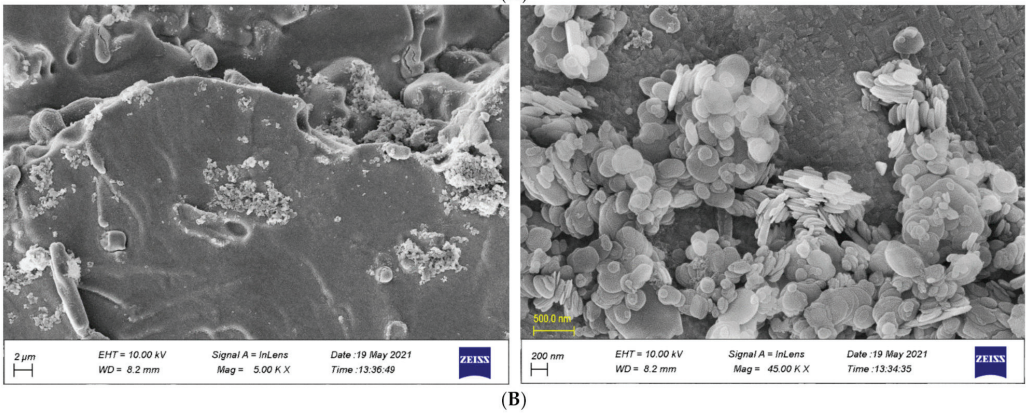

(**B**)

Figure 1. *Cont.*

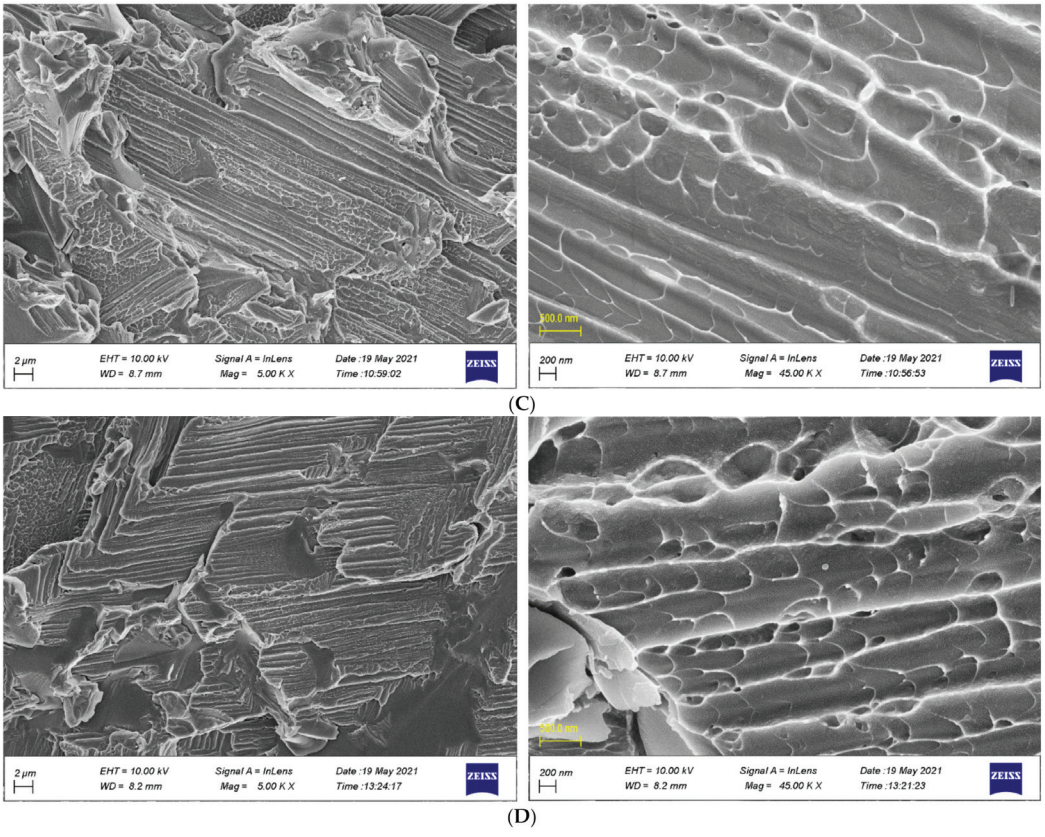

Figure 1. (**A**): 0 wt.% Ag; (**B**) 1.5 wt.% Ag; (**C**) 3 wt.% Ag; (**D**) 4.5 wt.% Ag.

4.2. XRD Results

Figure 2a reveals XRD peaks of the Ni-Ti shape memory alloy (0 wt.% Ag) calculated at room temperature with a diffraction angle (2θ) varying about 25–80°. The strongest peaks for the Ti phase formed at (2θ): 36.12°, 39.24°, 54.35°, 56.7°, 62.77°, 64.12°, 68.9° and 76.4°, respectively, for hkl (100), (101), (102), (200), (110), (211), (103) and (112). While the Ni phase was created at (2θ): 27.47°, 41.38°, 44.47°, 46.54° and 51.74° for hkl (101), (002), (111), (011) and (200), respectively. This is owed to the formation of Ti2Ni (Austenite phase) and M or Ti002 (martensite phase). Figure 2b reveals XRD peaks for the Ni-Ti shape memory alloy for (1.5 wt.% Ag); this created three principal phases: Ni, Ti and Ag phases, which appear at (2θ), varying between 30 and 80°. The Ti phase was created at (2θ): 42.51°, 61.5° and 71.0° for hkl (101), (110) and (103), respectively. In addition, the Ni phase was generated at (2θ) at around 41.8° and 77.5° for the planes (111) and (220), respectively. The addition of element (Ag) was generated at (2θ): 38.26°, 44.45°, and 64.58° for hkl (111), (220) and (311), respectively, while Figure 2c reveals the XRD peaks for the Ni-Ti shape memory alloy for (3 wt.% Ag), producing three major phases: Ni, Ti and Ag phases at (2θ), varying between 30 and 80°. The Ti phase was created at (2θ): 29.57°, 41.57°, 42.32°, 61.43° and 70.84° for hkl (100), (002), (101), (102) and (103), respectively, while the Ni phase formed at (2θ): 44.17° and 64.53° for hkl (011) and (220). The Ag phase formed at (2θ): 38.24°, 44.35° and 77.4° for hkl (111), (200) and (311), respectively. Finally, Figure 2d reveals the XRD peaks for the Ni-Ti shape memory alloy with (4.5 wt.% Ag). Three principal phases were formed: Ni, Ti and Ag phases. Together, these phases formed at (2θ) in the range of 30–80°. The Ti

phase was created at (2θ): 25.29°, 41.43°, 42.35°, 54.3°, 56.53°, 61.53°, 64.38° and 70.85° for hkl (100), (002), (101), (102), (200), (110), (211) and (103), respectively, while the Ni phase formed at (2θ): 46.4°, 46.53° and 51.55° for hkl (111), (011) and (200), respectively. The Ag phase formed at (2θ): 27.38°, 44.23° and 77.53° for hkl (111), (220) and (311), respectively.

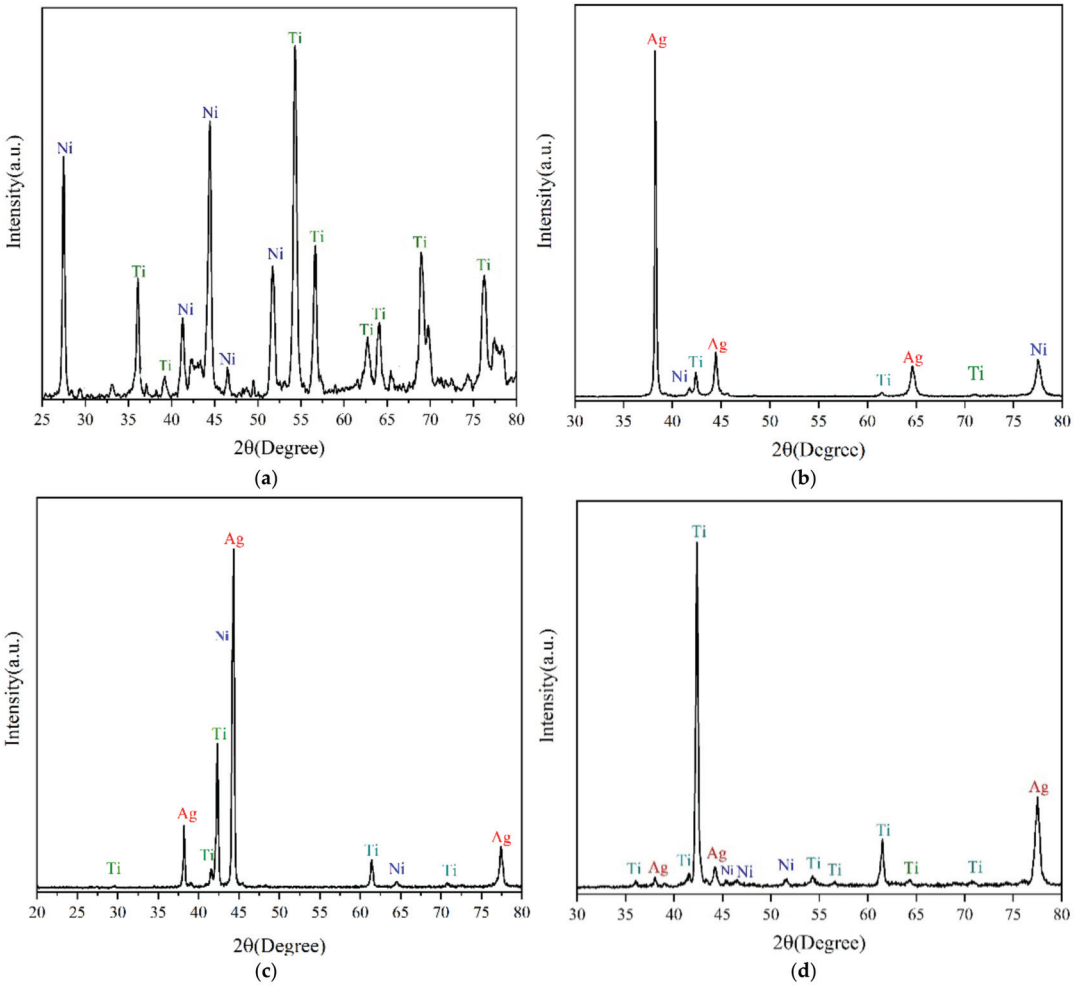

Figure 2. X-ray diffraction patterns for, (**a**): Ni-Ti, (**b**): Ni-Ti-Ag 1.5 wt.%, (**c**): Ni-Ti-Ag 3 wt.% and (**d**): Ni-Ti-Ag 4.5 wt.%.

4.3. DSC Results

Figure 3a–d shows the transformation temperatures for the alloys for all the specimens of shape memory alloys, with and without adding Ag. The transformation temperature was measured as the intersection of the two tangential lines of the curves. Ni-Ti was indicated at the austenitic transformation initial temperature of around −1.6 °C, and for the Ni-Ti-Ag alloys at about 19.7 °C, 12.7 °C and 12.3 °C, for Ag contents of 1.5, 3 and 4.5 wt.%. It should be mentioned here that the specific heat of Ni-Ti-Ag alloy (Cp*) is variable. The Ni-Ti-Ag alloys showed higher transformation temperatures compared with Ni-Ti-based alloys. In spite of the transformation temperatures of the Ni-Ti-Ag alloys, a slight decrease was observed with the rising weight percentages of Ag.

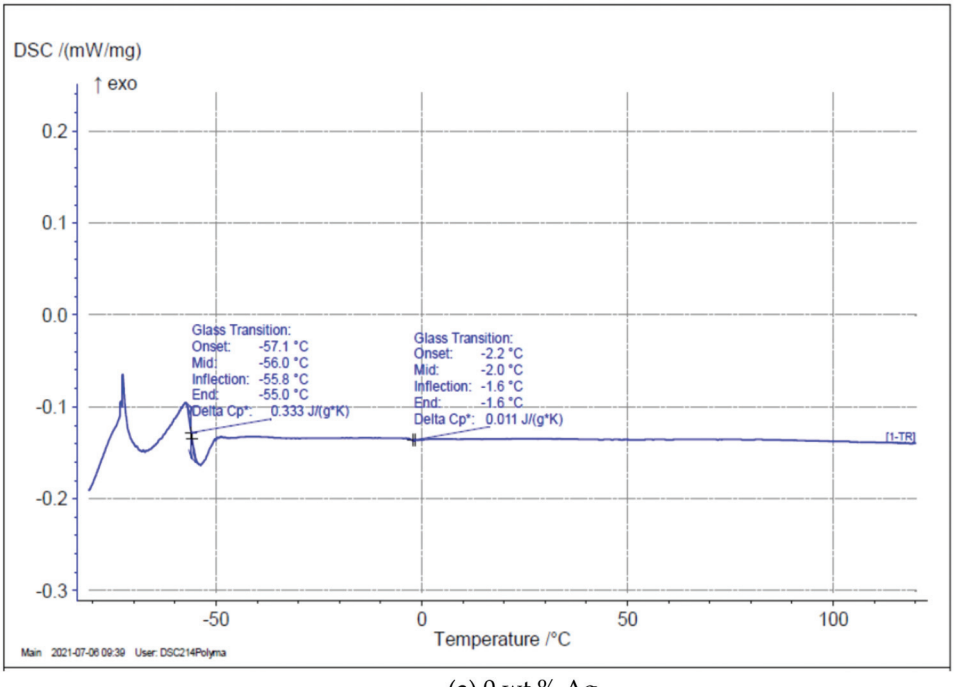

(**a**) 0 wt.% Ag

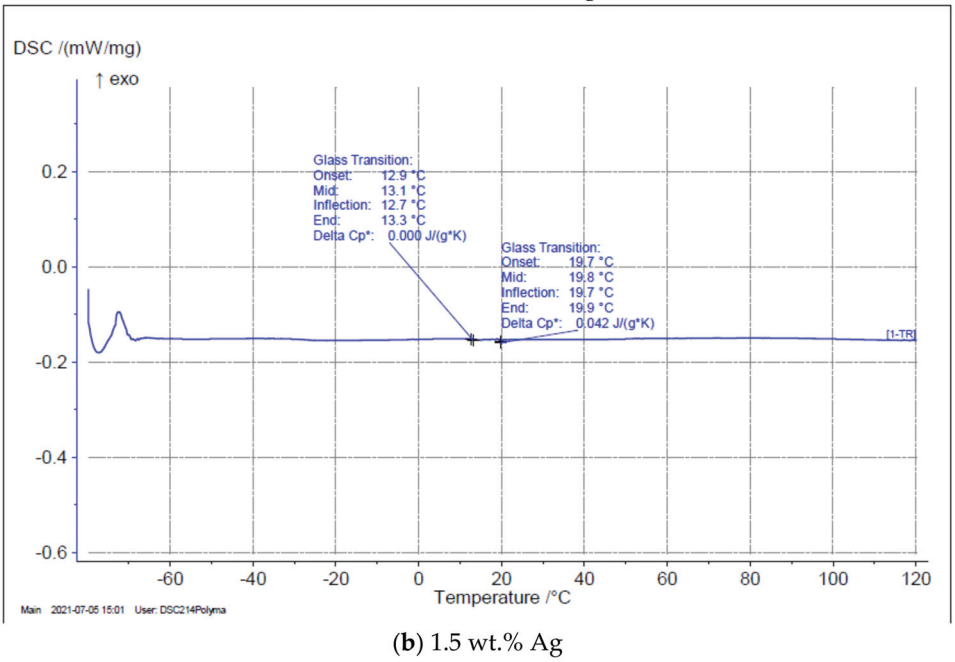

(**b**) 1.5 wt.% Ag

Figure 3. *Cont.*

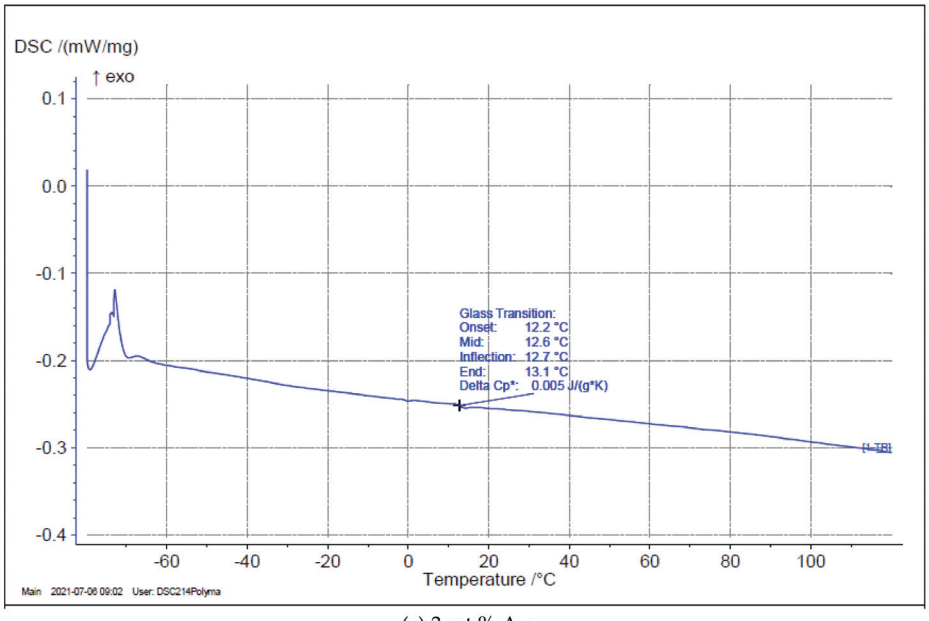

(**c**) 3 wt.% Ag

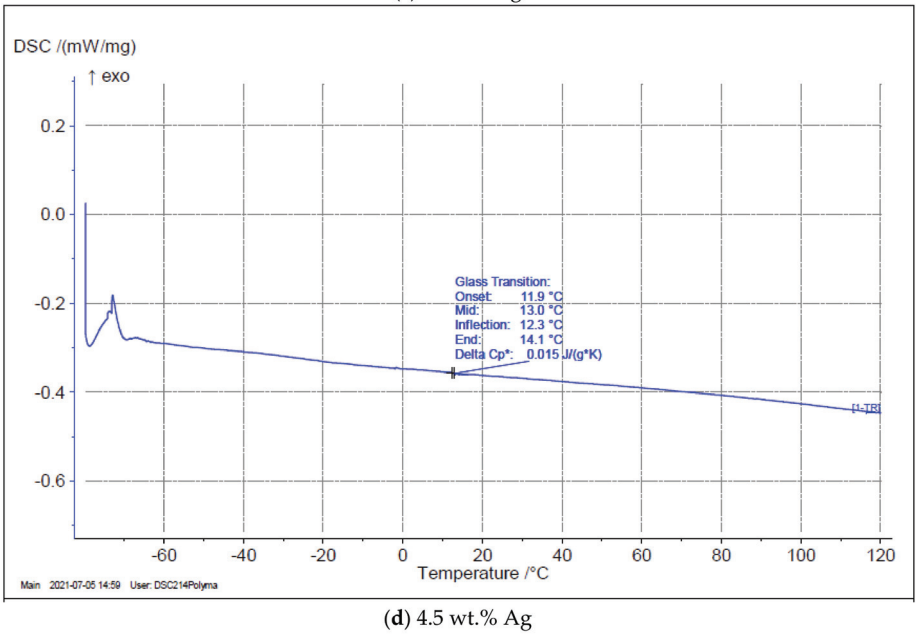

(**d**) 4.5 wt.% Ag

Figure 3. The DSC curves of Ni-Ti-Ag alloys.

4.4. Compression Results

Figure 4 shows the mechanical characteristics of the Ti-Ni matrix alloys for various wt.% of Ag during compression testing at room temperature. Compression testing showed that B2→R→B19′ martensite transformation was carried out by the deformation that occurs in all alloys before fracture. According to the stress–strain behaviour, the deformation

process of Ti-Ni-Ag alloys can be divided into three stages. The first phase, B2, is characterized by the initial linear fraction and strain accumulation due to elastic deformation of the martensite phase. The martensitic second phase R appears in the presence of the stress plateau, which indicates that the martensite transformation process occurred. In the third stage of deformation, the martensite phase, B19, can be seen, owing to the permanent deformation of this phase [14,15]. Moreover, the crystal structure of Ag was FCC, therefore, with increasing the wt.% of Ag incorporated into the Ni-Ti matrix, the volume fraction increased. Afterwards, Ag particles caused internal stresses in the Ni-Ti matrix through the deformation process and made the alloy brittle. The homogeneity dispersion of nanoparticles with a significant volume fraction of reinforcing material into Ti-Ni resulted in the high strength of the Ti-Ni alloy incorporated with 3 wt.% Ag. Additionally, the increment in densities of grain boundaries created the homogeneity of plastic strain in the matrix and then increased the volume; the level of internal stresses then decreased [15].

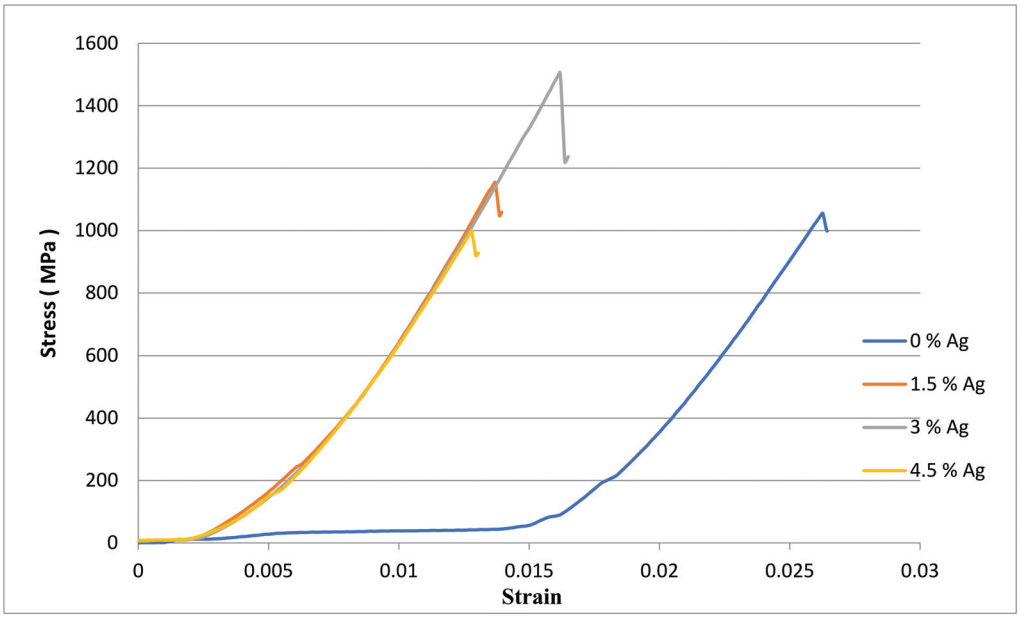

Figure 4. Compressive stress–strain curves of the Ni-Ti-Ag samples.

4.5. Micro-Hardness Results

Figure 5 and Table 1 show the values of the micro-hardness (Vickers Hardness) for the Ni-Ti-Ag SMAs with different weight percentages of Ag. For each sample, four readings were taken and then their average value was calculated. The results of this test showed a slight decrease in micro-hardness with the increase in weight percentages of Ag. The decrease in micro-hardness of the Ni-Ti-Ag SMAs was due to the ductility of silver and its lower scratching resistance than the Ni-Ti matrix.

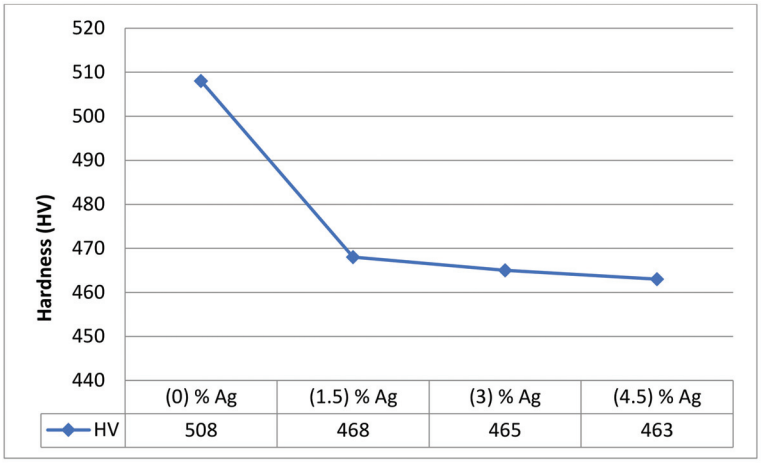

Figure 5. Micro-hardness (Hv) of Ti-Ni-Ag alloys.

Table 1. Compressive stress and microhardness results.

Test \ Sample	0% Ag	1.5% Ag	3% Ag	4.5% Ag
Compression stress (MPa)	1055	1155	1507	1000
Hardness (HV)	508	468	465	463

5. Conclusions

Ni-Ti-Ag shape memory alloys have been successfully synthesized by the casting technique using a VAR furnace. Ag, as an additive material, was incorporated into Ni-Ti based alloys at different weight percentages (1.5, 3 and 4.5 wt.%). The result of the FESEM analysis showed that Ag homogeneously dispersed into the Ni-Ti-based alloy, creating two main phases (austenite and martensite). While XRD analysis demonstrated the emergence of the main phases: Ni, Ti and Ag, as evidenced in the XRD peaks. In addition, the increase in weight percentage of Ag led to an increase in Ag peaks. DSC examination demonstrated that the austenite transformation starting temperature at (−1.6 °C) and transformation temperatures with increasing Ag wt.% are 19.7 °C, 12.7 °C and 12.3 °C, respectively. The addition of Ag significantly affected the mechanical properties of the Ni-Ti-based alloy in regard to its micro-hardness and compressive strength. The maximum value of compressive strength was obtained in the alloy with 3 wt.% Ag, while the results of micro-hardness testing showed a slight decrease with the increase in weight percentage of Ag.

Author Contributions: Data curation, K.D.S. and W.A.K.A.-M.; Formal analysis, F.A.; Investigation, K.D.S. and W.A.K.A.-M.; Methodology, K.D.S. and W.A.K.A.-M.; Resources, W.A.K.A.-M.; Supervision, B.E.; Validation, W.A.K.A.-M.; Visualization, F.A.; Writing—original draft, K.D.S.; Writing—review & editing, W.A.K.A.-M. All authors have read and agreed to the published version of the manuscript.

Funding: This research received no external funding.

Acknowledgments: We acknowledge support by the Deutsche Forschungsgemeinschaft (DFG) German Research Foundation and the Open Access Publishing Fund of the Technical University of Darmstadt. The authors would like to also thank the University of Technology- Iraq.

Conflicts of Interest: The authors declare no conflict of interest.

References

1. Riad, A.; Ben Zohra, M.; Mansouri, M.; Alhamany, A. The shape memory alloy controlled by the sun's radiation effect. *J. Comput. Methods Sci. Eng.* **2018**, *18*, 117–127. [CrossRef]
2. Wang, J.; Moumni, Z.; Zhang, W.; Zaki, W. A thermomechanically coupled finite deformation constitutive model for shape memory alloys based on Hencky strain. *Int. J. Eng. Sci.* **2017**, *117*, 51–77. [CrossRef]
3. Vyavahare, P.V.; Karthikeyan, C.P. Shape memory effect and performance of a nitinol engine. *Aust. J. Eng. Technol. Res.* **2017**, *2*, 109–119.
4. Wahhab, H.A.A.; Al-Maliki, W.A.K. Application of a Solar Chimney Power Plant to Electrical Generation in Covered Agri-cultural Fields. In *IOP Conference Series: Materials Science and Engineering*; IOP Publishing: Kerbala, Iraq, 2020; p. 012137.
5. Al-Maliki, W.; Mahmoud, N.; Al-Khafaji, H.; Alobaid, F.; Epple, B. Design and Implementation of the Solar Field and Thermal Storage System Controllers for a Parabolic Trough Solar Power Plant. *Appl. Sci.* **2021**, *11*, 6155. [CrossRef]
6. Sanaani, Y.T.; Alshorman, A.; Alshurman, K. A Novel Design of Flexure Based, Shape Memory Alloy Actuated Microgripper. In Proceedings of the ASME International Mechanical Engineering Congress and Exposition, Tampa, FL, USA, 3–9 November 2017; American Society of Mechanical Engineers: Tampa, FL, USA, 2017; Volume 58370, p. V04AT05A023.
7. Copaci, D.; Moreno, L.; Blanco, D. Two-Stage Shape Memory Alloy Identification Based on the Hammerstein–Wiener Model. *Front. Robot. AI* **2019**, *6*, 83. [CrossRef] [PubMed]
8. Shelyakov, A.; Sitnikov, N.; Borodako, K.; Koledov, V.; Khabibullina, I.; von Gratowski, S. Design of microgrippers based on amorphous-crystalline TiNiCu alloy with two-way shape memory. *J. Micro-Bio Robot.* **2020**, *16*, 43–51. [CrossRef]
9. Hussain, S.; Pandey, A.; Dasgupta, R. Designed polycrystalline ultra-high ductile boron doped Cu–Al–Ni based shape memory alloy. *Mater. Lett.* **2019**, *240*, 157–160. [CrossRef]
10. Al-Maliki, W.A.K.; Al-Hasnawi, A.G.T.; Wahhab, H.A.A.; Alobaid, F.; Epple, B. A Comparison Study on the Improved Operation Strategy for a Parabolic trough Solar Power Plant in Spain. *Appl. Sci.* **2021**, *11*, 9576. [CrossRef]
11. Álvares da Silva, G.H.; Otubo, J. Designing NiTiAg Shape Memory Alloys by Vacuum Arc Remelting: First Practical Insights on Melting and Casting. *Shape Mem. Superelast.* **2018**, *4*, 402–410. [CrossRef]
12. Zeng, Z.; Oliveira, J.P.; Ao, S.; Zhang, W.; Cui, J.; Yan, S.; Peng, B. Fabrication and characterization of a novel bionic manipulator using a laser processed NiTi shape memory alloy. *Opt. Laser Technol.* **2020**, *122*, 105876. [CrossRef]
13. Khalil-Allafi, J.; Dlouhy, A.; Eggeler, G. Ni_4Ti_3-precipitation during aging of NiTi shape memory alloys and its influence on martensitic phase transformations. *Acta. Mater.* **2002**, *50*, 793. [CrossRef]
14. Zheng, Y.; Zhang, B.; Wang, B.; Wang, Y.; Li, L.; Yang, Q.; Cui, L. Introduction of antibacterial function into biomedical TiNi shape memory alloy by the addition of element Ag. *Acta. Biomater.* **2011**, *7*, 2758–2767. [CrossRef]
15. Baigonakova, G.; Marchenko, E.; Chekalkin, T.; Kang, J.-H.; Weiss, S.; Obrosov, A. Influence of Silver Addition on Structure, Martensite Transformations and Mechanical Properties of TiNi–Ag Alloy Wires for Biomedical Application. *Materials* **2020**, *13*, 4721. [CrossRef] [PubMed]

MDPI
St. Alban-Anlage 66
4052 Basel
Switzerland
Tel. +41 61 683 77 34
Fax +41 61 302 89 18
www.mdpi.com

Applied Sciences Editorial Office
E-mail: applsci@mdpi.com
www.mdpi.com/journal/applsci

MDPI
St. Alban-Anlage 66
4052 Basel
Switzerland

Tel: +41 61 683 77 34

www.mdpi.com

ISBN 978-3-0365-5146-3